Lehrstuhl für Elektrische Energiespeichertechnik
Fakultät für Elektrotechnik und Informationstechnik
Technische Universität München

State-Estimation of Lithium-Ion Batteries using Physicochemical Models and Experimental Characterization Techniques

Johannes Jörg Sturm, M.Sc.

Vollständiger Abdruck der von der Fakultät für Elektrotechnik und Informationstechnik der Technischen Universität München zur Erlangung des akademischen Grades eines

Doktor-Ingenieurs (Dr.-Ing.)

genehmigten Dissertation.

Vorsitzende:		Prof. Dr.-Ing. Sandra Hirche
Prüfer der Dissertation:	1.	Prof. Dr.-Ing. Andreas Jossen
	2.	Prof. Dr. Hubert A. Gasteiger

Die Dissertation wurde am 25.09.2020 bei der Technischen Universität München eingereicht und durch die Fakultät für Elektrotechnik und Informationstechnik am 24.01.2021 angenommen.

Abstract

Continuously rising energy densities and falling manufacturing costs for lithium-ion battery systems are expected to facilitate market penetration of electric vehicles (EVs), provided that fundamental requirements such as power capability, safety and lifetime are invariably guaranteed. The advancements on electrode, cell, module, and battery pack level and the demand for optimized operation such as fast charging of EVs challenge the battery management system to monitor and control the required safe, efficient and durable operation of the battery. Advanced control methods ideally give insights into the battery's internal states to design safe fast charging procedures, which can hardly be satisfactorily achieved by state-of-the-art state-estimation techniques, relying on empirical or semi-empirical approaches. In this thesis, the development of physicochemical model based state-estimation algorithms is presented, which offer the desired estimation not only on a global scale via cell voltage, current and temperature, but also on a local scale describing lithium-ion concentrations and potentials along the electrode stack. The underlying structure of the physicochemical pseudo two-dimensional model (p2D), its parametrization, solving process and validity towards experimental data are presented with focus on a cylindrical high energy lithium-ion battery. The validity of the p2D towards describing spatial imbalances of the battery's internal states is referenced towards a more complex 3D multidimensional-multiphysics model. The resulting error of the p2D can be considered for the state-estimation algorithm to account for the spatial inhomogeneity in the battery. Further, the impact of cylindrical cell format and current collector design on the spatial inhomogeneity in lithium-ion batteries are investigated using the 3D model and suitable fast charging protocols are developed, which avoid safety issues such as overheating and early aging. Albeit the simplification of the physicochemical model structure from 3D to p2D, real-time operation as required in battery management systems is challenging for the p2D, which is why further numerical or physical model reduction is required. A variety of reduced p2Ds are compared and transferred into an embedded software for micro-controller implementation, where performance features of computation speed, memory footprint and model accuracy are evaluated. For the state-estimation process, the reduced p2Ds are extended to recursive state observer models together with a non-linear Kalman filter on the cell's voltage to estimate the lithium-ion battery's global and internal states, which offers the desired insights into the battery's behavior. Safety and lifetime limitations are of crucial importance when defining a suitable operating window of a lithium-ion battery and are therefore separately examined in this thesis by means of experiment and simulation based studies of external and local short-circuit scenarios as well as a cyclic aging study correlating mechanical swelling, capacity decay and impedance rise. By combining experiment and physicochemical simulation, a deeper understanding of a lithium-ion battery's behavior and, consequently, a more efficient operation compared to state-of-the-art control approaches can be guaranteed.

Kurzfassung

Aller Voraussicht nach werden künftig höhere Energiedichten für Lithium-Ionen Batteriespeicher zu geringeren Kosten verfügbar sein, was die Verbreitung von Elektrofahrzeugen am Markt stärken wird, sofern essentielle Anforderungen wie Leistungsfähigkeit, Sicherheit und Lebensdauer weiterhin gewährleistet werden können. Der allgemeine Fortschritt der Batterietechnologie auf Elektroden-, Zell-, Modul- und Batteriespeicher-Ebene und optimierte Betriebsstrategien wie das Schnelladen von Elektrofahrzeugen stellen das Batteriemanagementsystem vor neue und zunehmend komplexere Anforderungen, um einen sicheren, effizienten und langlebigen Betrieb der Batterie zu gewährleisten. Zukunftsfähige Regelungssysteme ermöglichen idealerweise Einblicke in die internen Zustände einer Lithium-Ionen-Batterie, um beispielsweise sicheres Schnelladen zu realisieren, die mit heutzutage verfügbaren empirischen oder semi-empirischen Zustandsschätzern nicht zufriedenstellend ermöglicht werden können. In dieser Arbeit wird die Entwicklung von physikochemischen, modellbasierten Zustandsschätzern vorgestellt, die neben globalen Zustandsgrößen wie Zellspannung, Strom und Temperatur auch die gewünschten internen Größen wie Lithium-Ionen Konzentrationen und Potentiale entlang des Elektrodenstapels simulieren können. Die zugrundeliegende Modellbildung des pseudo zweidimensionalen Modells (p2D), die Parametrierung, die Lösungsberechnung und die Bestimmung der Modellgenauigkeit anhand experimenteller Daten werden für eine zylindrische Hoch-Energie Lithium-Ionen Zelle bestimmt. Die Validität zur Abbildung der örtlichen Verteilung der internen Zustände wird für das p2D in Referenz zu einem rechenintensiveren dreidimensionalen (3D) multiphysikalischen Modell ermittelt. Mithilfe des ermittelten Modellfehlers kann der Zustandsschätzer im Hinblick auf die nicht vom p2D abgebildete örtliche Inhomogenität in der Batterie korrigiert werden. Des Weiteren werden die Auswirkungen von zylindrischen Zellformaten und des Stromableiterdesign auf die örtliche Inhomogenität in der Batterie mittels des 3D Modells diskutiert und geeignete Stromprofile für das Schellladen entworfen, die eine sicherheitskritische Überhitzung und vorzeitige Alterung in der Batterie vermeiden. Trotz der Vereinfachung der Modellstruktur des p2D im Vergleich zum komplexen 3D Modell kann die Echtzeitfähigkeit – wie sie im Batteriemanagementsystem gefordert ist – nur unter Anwendung von weiteren numerischen oder physikalischen Modellreduktionsverfahren gewährleistet werden. Verschiedene, reduzierte Varianten des p2D werden miteinander verglichen und in eine Hardware-nahe Software zur Implementierung in einen Mikrocontroller überführt. Die Leistungsfähigkeit der reduzierten Modellvarianten für eine echtzeitfähige Simulation auf Mikrocontrollern wird anhand von Rechengeschwindigkeit, Speicherplatzbelegung und Modellgenauigkeit bewertet. Die reduzierten Modelle des p2D werden schließlich zur Entwicklung von rekursiven Zustandsschätzmodellen unter Zuhilfenahme eines nichtlinearen Kalman Filters für die Zellspannung verwendet, die neben der Schätzung von globalen auch die gewünschten internen Größen einer Lithium-Ionen-Batterie zur Verfügung stellen. Einschränkungen des Betriebsbereichs zur Erhöhung der Sicherheit und Lebensdauer von Lithium-Ionen-Batterien werden in dieser Arbeit zusätzlich durch experimentelle Studien von externen und internen Kurzschlüssen sowie zyklischen Alterungsreihen zur Bestimmung der Korrelation von Kapazitätsabnahme, mechanischer Dickenzunahme und Widerstandsanstieg untersucht. Die Kombination aus Experiment und physikochemischer Simulation ermöglicht ein tieferes Verständnis in das Verhalten einer Lithium-Ionen-Batterie und folglich kann ein effizienterer Betrieb im Vergleich zu bestehenden Regelungssystemen umgesetzt werden.

Contents

Contents

Abbreviations

AFV   . . . . alternative fuel vehicle

Al_2O_3 . . . . . . aluminum oxide

ARC   . . . . accelerating rate calorimetry

BC   . . . . boost current

BEV   . . . . battery electric vehicle

BMS   . . . . battery management system

C   . . . . graphite

CAN   . . . . controller area network

CC   . . . . constant current

CEI   . . . . cathode electrolyte interphase

CO_2 . . . . carbon dioxide

DEC   . . . . diethyl carbonate

DMC   . . . . dimethyl carbonate

DVA   . . . . differential voltage analysis

E85   . . . . vehicle powered by fuel containing at least $85\,\%$ of ethanol

EC   . . . . ethylene carbonate

ECM   . . . . equivalent circuit model

EKF   . . . . extended Kalman filter

EMC   . . . . ethylmethyl carbonate

EoL   . . . . end of life

EU   . . . . European Union

EV   . . . . electric vehicle

FCEV   . . . . . . fuel cell electric vehicle

FDM   . . . . finite difference method

FEM   . . . . finite element method

HEV . . . . hybrid electric vehicle

HMI . . . . human machine interface

ICE . . . . internal combustion engine

ICP-OES . . . . . inductively coupled plasma-optical emission spectroscopy

KF . . . . Kalman filter

LCO . . . . lithium cobalt oxide

LFP . . . . lithium iron phosphate

LIB . . . . lithium-ion battery

LiO . . . . lithium-air battery

$LiPF_6$ . . . . . lithium hexafluorophosphate

LiS . . . . lithium-sulfur battery

LMO . . . . lithium manganese oxide

LPG . . . . liquefied petroleum gas

LTO . . . . lithium titanate

MC . . . . micro-controller

MCMB . . . . . mesocarbon microbeads

MJ1 . . . . LG Chem INR18650-MJ1 lithium-ion battery

MuDiMod . . . . multidimensional model

NCA . . . . lithium nickel cobalt aluminum oxide

NGV . . . . natural gas vehicle

NMC . . . . lithium nickel manganese cobalt oxide

NMC-111 . . . . lithium nickel manganese cobalt oxide $Li(Ni_{0.33}Mn_{0.33}Co_{0.33})O_2$

NMC-811 . . . . nickel-rich lithium nickel manganese cobalt oxide $Li(Ni_{0.8}Mn_{0.1}Co_{0.1})O_2$

NT . . . . Newman-Tiedemann model

OCP . . . . open-circuit potential of the half-cell vs. Li/Li^+

OCV . . . . open-circuit voltage of the full-cell

p2D . . . . pseudo two-dimensional model

p3D . . . . pseudo three-dimensional model

PC . . . . pulsed current

PE . . . . polyethylene

PHEV . . . . plug-in hybrid electric vehicle

PP . . . . polypropylene

RAM . . . . random access memory

RC . . . . resistor and capacity parallel circuit

REEV . . . . . . range extended electric vehicle

ROM . . . . reduced order model

RuL . . . . remaining useful life

SEI . . . . solid electrolyte interphase

SiC . . . . silicon-graphite

SiO . . . . silicon oxide

SoC . . . . state of charge

SoF . . . . state of function

SoH . . . . state of health

SoS . . . . state of safety

SPM . . . . single particle model

TiO_2 . . . . titanium dioxide

TRL . . . . technology readiness level

UK . . . . United Kingdom

Symbols

The following symbols with their respective meaning are defined as used in the main part of this thesis and may vary in the presented articles due to journal requirements or special usage in the presented content. All symbols are defined in each integrated article individually.

a_s . . . . specific electrode area in m^{-1}

$A_\oslash$ . . . . cross-section area in m^2

A_act . . . . active electrode area in m^2

A_surf . . . . surface area in m^2

c_l . . . . lithium-ion concentration in the electrolyte in $\mathrm{mol\,m}^{-3}$

c_p . . . . isobaric gravimetric heat capacity in $\mathrm{J\,kg}^{-1}\,\mathrm{K}^{-1}$

c_s . . . . lithium-ion concentration in active material in $\mathrm{mol\,m}^{-3}$

$c_\mathrm{s,max}$ . . . . . . maximum lithium-ion concentration in the active material in $\mathrm{mol\,m}^{-3}$

c_ss . . . . lithium-ion concentration at the surface of the active material particle in $\mathrm{mol\,m}^{-3}$

D_l . . . . diffusion coefficient in the electrolyte in $\mathrm{m}^2\,\mathrm{s}^{-1}$

D_s . . . . diffusion coefficient in the active material in $\mathrm{m}^2\,\mathrm{s}^{-1}$

E . . . . cell/terminal voltage in V

E_eq . . . . equilibrium potential vs. $\mathrm{Li/Li}^+$ in V

$\frac{\partial E_\mathrm{eq}}{\partial T}$ . . . . entropic coefficient in $\mathrm{V\,K}^{-1}$

$f_\pm$ . . . . mean molar activity coefficient

F . . . . Faraday's constant, $96\,485\,\mathrm{A\,s\,mol}^{-1}$

i_0 . . . . exchange current density in $\mathrm{A\,m}^{-2}$

i_app . . . . applied current density in $\mathrm{A\,m}^{-2}$

i_l . . . . ionic current density in the liquid phase in $\mathrm{A\,m}^{-2}$

i_n . . . . reaction current density in $\mathrm{A\,m}^{-2}$

i_p2D . . . . through-plane current density in the MuDiMod in $\mathrm{A\,m}^{-2}$

i_s . . . . electronic current density in the solid phase in $\mathrm{A\,m}^{-2}$

I . . . . applied current in A

j_n . . . . pore wall flux density in $\mathrm{mol\,m^{-2}\,s^{-1}}$

k_a . . . . anodic reaction rate constant in $\mathrm{m\,s^{-1}}$

k_c . . . . cathodic reaction rate constant in $\mathrm{m\,s^{-1}}$

l . . . . length in m

n . . . . number of electrons

N_M . . . . MacMullin number

q_cond . . . . heat flux density from heat conduction in $\mathrm{W\,m^{-2}}$

q_conv . . . . convective heat flux density in $\mathrm{W\,m^{-2}}$

q_l . . . . heat flux density from the liquid phase in $\mathrm{W\,m^{-2}}$

q_p2D . . . . total heat flux density in the p2D in $\mathrm{W\,m^{-2}}$

q_r . . . . reaction heat flux density in $\mathrm{W\,m^{-2}}$

q_rad . . . . radiative heat flux density in $\mathrm{W\,m^{-2}}$

q_rev . . . . entropic heat flux density in $\mathrm{W\,m^{-2}}$

q_s . . . . heat flux density from the solid phase in $\mathrm{W\,m^{-2}}$

r . . . . radial coordinate in the particle domain of the p2D in m

r'' . . . . radial coordinate in the 3D model in m

R . . . . universal gas constant, $8.314\,\mathrm{J\,mol^{-1}\,K^{-1}}$

R_ext . . . . resistance in Ω

R_f . . . . film resistance in $\Omega\,\mathrm{m^2}$

R_p . . . . radius of the active material particles in m

s . . . . stoichiometric coefficient

t . . . . time in s

t_+^0 . . . . transference number of lithium-ions

t_a . . . . thickness of the anode coating in m

t_c . . . . thickness of the cathode coating in m

t_cc . . . . thickness of the current collector foil in m

t_sep . . . . thickness of the separator in m

T . . . . cell temperature in K

T_∞ . . . . ambient temperature in K

T_{ref} . . . . reference temperature in K

V . . . . volume in m^3

x . . . . main coordinate of the p2D in m

x' . . . . spatial coordinate along the length of the 2D model in m

x'' . . . . first cartesian coordinate in the 3D model in m

y' . . . . spatial coordinate along the height of the 2D model in m

y'' . . . . second cartesian coordinate in the 3D model in m

z'' . . . . third cartesian coordinate in the 3D model in m

$\alpha_{\mathrm{a/c}}$ . . . . anodic/cathodic charge transfer coefficient

α_{conv} . . . . . . convective heat transfer coefficient in $\mathrm{W\,m^{-2}\,K^{-1}}$

ε_{l} . . . . porosity

$\varepsilon_{\mathrm{rad}}$ . . . . . . emissivity

ε_{s} . . . . volume fraction of the electrode's active material

$\varepsilon_{\mathrm{s,na}}$ . . . . . . volume fraction of the electrode's non-active material

η . . . . reaction overpotential in V

κ_{l} . . . . ionic conductivity of the electrolyte in $\mathrm{S\,m^{-1}}$

λ . . . . heat conduction coefficient in $\mathrm{W\,m^{-1}\,K^{-1}}$

ρ_{stack} . . . . . . volumetric mass density in $\mathrm{kg\,m^{-3}}$

σ_{b} . . . . Stefan-Boltzmann's constant, $5.67 \times 10^{-8}\,\mathrm{W\,m^{-2}\,K^{-4}}$

σ_{cc} . . . . electrical conductivity of the current collector in $\mathrm{S\,m^{-1}}$

σ_{s} . . . . electrical conductivity of the solid phase in $\mathrm{S\,m^{-1}}$

τ . . . . tortuosity

φ_{cc} . . . . electrical potential in the current collector foils in V

Φ_{l} . . . . electrical potential in the electrolyte in V

Φ_{s} . . . . electrical potential in the active material in V

χ . . . . volumetric share for calculating the heat generation in the 3D model

ψ . . . . azimuthal angle in polar coordinates of the 3D model in rad

1 Introduction to State-Estimation of Lithium-Ion Batteries

Worldwide emission regulations for internal combustion engine (ICE) vehicles such as diesel or petrol powered cars appeared in the last decade and further restrictions are expected for the next decade looking into governmental campaigns for reducing greenhouse-gas emissions [1]. First consequences emerge in the passenger transport sector, where a significant push in the market share of alternatively powered vehicles can be observed. Especially the EV experiences a significant increase in market share. The development of the passenger car sector can be analyzed on a global perspective as shown in Fig. 1.1a, which depicts the most important sales markets on a territorial world map. Considering the worldwide registrations of battery electric vehicles (BEVs), plug-in hybrid electric vehicles (PHEVs),
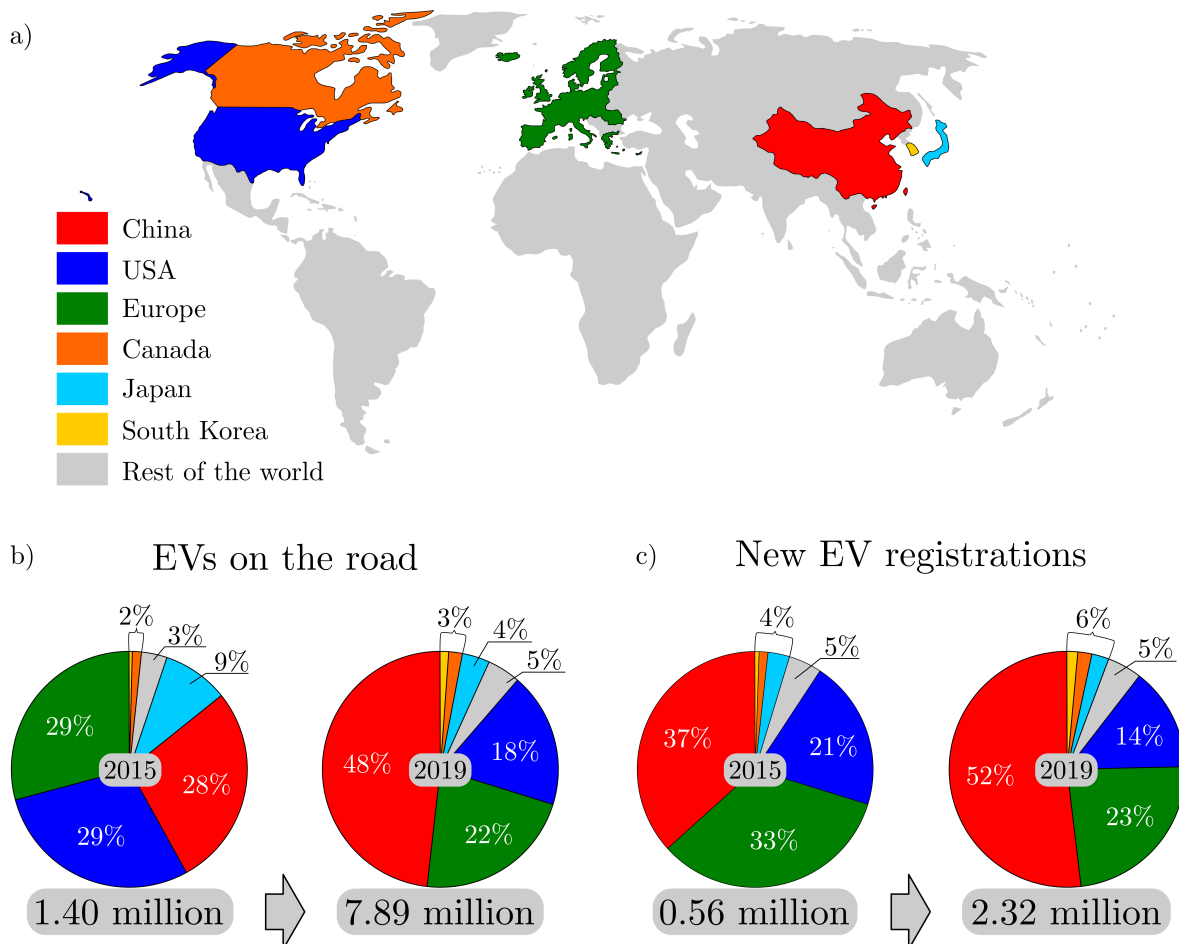

Figure 1.1: Overview of EVs on the road and new registrations of EVs on the world sales market of the passenger car sector. Subplot a) shows the dominant submarkets and illustrates the share of registrations in total (b) and new (c) EV registrations between the years 2015 and 2019 (data as from February 2020, figure derived from Ref. [2]).

and extended range electric vehicle (REEVs), the total number of these EVs on the road increased between the years 2015 and 2019 from 1.4 to 7.89 million cars as shown in Fig. 1.1b. The most important markets appear in China followed by Europe and the USA [2]. Similarly, more than four times more new EVs were registered in 2019 compared to 2015 as shown in Fig. 1.1c, where at most 2.32 million EVs were registered all over the world [2]. Albeit the remarkable market development in China, roughly one out of four EVs worldwide is still registered in Europe.

The new EV registrations are analyzed in terms of the national market share at the entire passenger car sector and the total number of cars for seven European countries, which revealed the highest number of total registrations in the first quarter of 2020. The results are summarized in Fig. 1.2. As a reference, the EV sales figures of the first quarter in 2019 are used to determine the growth in market share and total number of cars. New EV registrations experienced a significant push within a single year in countries with a low market share of EVs as seen in Germany with an increase of the total number of EVs by +125 %, in France by +144 %, in the United Kingdom (UK) by +119 % or in Italy by +268 %. A stagnating market growth appears for Norway, which already has a high market share of EVs at levels beyond 60 % for the last two years. Compared to the remaining European countries, the number of new EV registrations in Norway is still the fourth biggest. Overall, the EV market share increased in all European countries from 2 % up to 15 % within a single year.
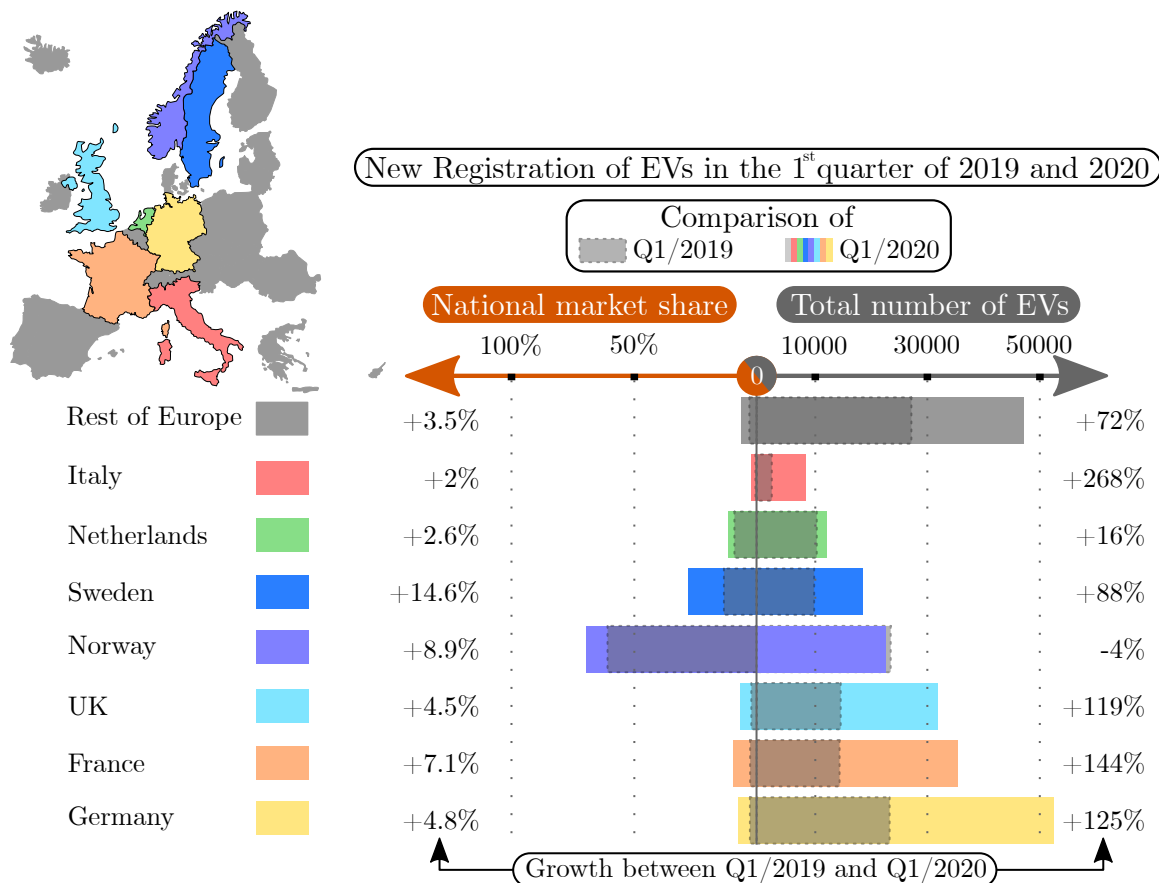

Figure 1.2: The territorial map (upper left) highlights the seven European countries with the highest number of new EV registrations between the first quarter (Q1) in 2019 and 2020. The national market share of the passenger car sector (left-hand side) and the total numbers of new registrations (right-hand side) are shown for the EV per country in the bar charts (data as from May 2020, figure derived from Ref. [2, 3]) .

The market share of newly registered EVs accounted for 6.8 % in Europe in the first quarter of 2020, which still accumulates to a minor share of 17.8 % considering also hybrid electric vehicle (HEV) and alternative fuel vehicle (AFV) (i.e. vehicle powered by fuel containing at least 85 % of ethanol (E85), liquefied petroleum gas (LPG) and natural gas vehicle (NGV)) compared to the dominant ICE cars with a combined share of 82.2 % as shown in Fig. 1.3. Against the overall decline in new registrations of
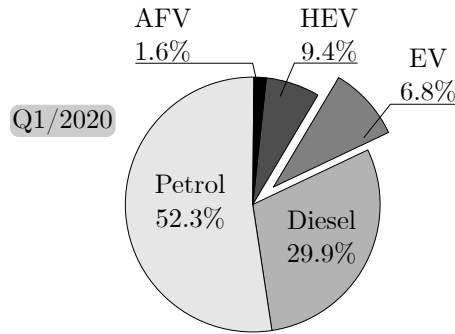

Figure 1.3: Market share in the European passenger car sector showing the number of new registration consisting of EVs, HEVs, alternative fuel (AFV), petrol and diesel powered cars (data as from May 2020, figure derived from Ref. [3]).

passenger cars due to the COVID-19 outbreak [3], the currently imposed regulations for ICE vehicles [4, 5] boosted the market share in Europe between the first quarter of 2019 and 2020 by +4.3 % for EVs, which comprise BEVs, fuel cell electric vehicles (FCEVs), PHEVs, and REEVs [3]. Tumbling shares appear at the same time at a decrease of −5.4 % for petrol and −3.3 % for diesel powered passenger cars. Regarding all vehicles on the road, the current numbers of registered passenger cars in Germany sum up to 65.9 % of petrol and to 31.7 % of diesel powered cars, whereas only 0.5 % (i.e. 239.299 cars) represent the share of EVs [6]. In Europe (see territorial map in Figure 1.2) the total number of EVs on the road accounts to 1.72 million [2] cars, which represents a similar market share of approximately 0.3 %. Again, this is a marginal share compared to petrol and diesel powered cars [7].

Even if the actual numbers of EVs on the road are still marginal in Germany and the rest of Europe compared to the fleet of ICE powered cars, the increasing market share for new registrations of EVs together with the decreasing sales figures of ICE powered cars on national, European and worldwide markets most likely indicate the onset of a possible turnaround to electrified mobility in the passenger car sector.

The success of consistent market penetration of EVs is correlated to governmental regulations and incentive programs [1, 8], the technology readiness level (TRL) of the battery system, the charging infrastructure and the demand of the customers [5]. Especially regulations [1] have a dominant impact such as the efforts of the European Union (EU) on reducing greenhouse gases by 80 % up to 95 % in the years from 1990 to 2050 [9]. It noticeably affects the passenger car fleet offered by the car manufacturers since 2007 with a regulatory framework for average carbon dioxide (CO_2) emissions to decelerate the climate change, which required $130\,g$ of CO_2 per $1\,km$ in 2015, a decrease to $95\,g\,km^{-1}$ in 2020 and a further reduction to $85\,g\,km^{-1}$ until 2024 [9, 10]. Together with an increase of supplied batteries at lower costs by the cell manufacturers and an extended electrified product line-up by the car manufacturers [5], the turnaround from ICE cars to EVs in the passenger transportation sector will be facilitated. National incentive programs such as financial support to purchase EVs or guaranteed tax exemptions for electrified cars [5, 8, 11] are typically used to promote the electrified mobility and enhance sales figures. Improved battery technology can offer an extended driving range of more than

560 km [12], lower battery prices and overall lower costs of ownership of EVs compared to ICE cars, which further promotes the suitability of EVs for the mass market [5]. First national collaborations [5, 13] focus on establishing sufficient charging infrastructures to fulfil the increasing demand of electrical power to recharge the growing EV fleet. Nevertheless, a consistently operating grid for recharging a large EV fleet at the same time is challenging and may become a bottleneck for the electrified mobility in the future [14]. Nowadays government and industry seem to willingly push electrified mobility, but the customer's demand is still the most challenging and the most unpredictable factor, which determines the success of a sustainable EV market penetration [5].

The expected increasing demand for EVs comes with intensified efforts in industry and research to further develop and optimize the battery technology, that is a key component of the required electrical energy storage system. The lithium-ion battery (LIB) is the state-of-the-art technology used for electrical energy storage in EVs and is most promising for application in next-generation EVs [15, 16]. LIBs are also the common technology for energy storage in mobile applications such as tablets or smart phones and stationary storage systems, which can use former EV battery packs and enable a useful second life application [17]. However, the current LIB technology reveals still potential for improvement in terms of energy density, safety characteristics, lower costs and longer lifetime [16]. Improving the battery's energy density can increase acceptance of the customers, as the extension of the EV driving range will ease the "range anxiety", whereby a positive effect on sales figures is expected [18]. Similarly, doubts about a sufficient charging speed of an EV can be addressed by improvements of the battery charging performance and the charging strategy of the battery management system (BMS). Improvements of the LIB system can be applied on single cell, module and battery pack level [18]. The LIB technology can be improved regarding hardware features such as the cell format, the incorporated materials like electrode, separator and electrolyte or the geometrical design of the electrode stack. Software based improvements address the algorithms incorporated in the BMS, which monitor and control the single cell, the module and the entire battery pack. Significant improvement of the battery's efficiency without changing the actual physical settings of a LIB is expected via using advanced software algorithms in the BMS [18].

Exemplary, the Electric Vehicle Enhanced Range, Lifetime And Safety Through INGenious battery management (EVERLASTING) project from the European commission's Horizon 2020 research and innovation program [19] aims to keep the battery in a safe and optimal operational state with more than $+10\%$ increased battery efficiency using sophisticated software algorithms, which estimate the state of a LIB more precisely than state-of-the-art state-estimation techniques. The more accurate estimation of the battery's states can exemplary yield to an extended operating range due to decreased safety buffer zones such as upper and lower limits for the battery's state of charge (SoC), terminal voltage, surface temperature or the applied current. Increasing the capacity of LIBs generally comes with a larger geometrical battery size, which could partly be reduced when an advanced BMS operates the LIB more efficiently and consequently enables for a reduction of the overall size. Considering a hypothetical $+10\%$ efficiency increase along with a corresponding -10% decrease of the battery's size, a total of 39.5 GWh in electrical energy could be saved assuming an average 50 kWh [20] LIB pack for the worldwide total amount of today's 7.89 million EVs. Assuming a footprint of 100 kg of CO_2 for producing a battery capacity of 1 kWh [20, 21], a promising amount of 3.9 million tons of CO_2 could possibly be saved in the battery manufacturing process due to the smaller geometrical size at the same level of usable energy content.

Furthermore, an advanced BMS not only offers potentials to improve the efficiency and sustainability of LIB technology, but can also lower customer reservations such as range anxiety or reduce customer

complaints about slow charging processes. The estimate of remaining energy or safety and lifetime critical charging limitations can be identified more accurately with the aid of advanced BMS.
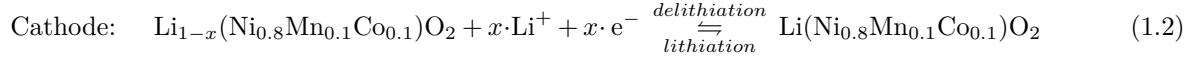
To conclude, the rise of electrified mobility could benefit from advanced techniques describing the complex behavior of LIBs. In this context, the development and application of experimental and model based simulation methods is required, which is the motivation of this thesis. A variety of model based simulation and estimation methods are discussed for describing the electrochemical-thermal behavior of LIBs ranging from a 3D, computationally expensive multidimensional model (MuDiMod) to BMS-suitable, p2D based state-estimation algorithms, which can operate under real-time requirements in embedded systems. In this matter, impacts of cell format and electrode design on the local imbalanced utilization of cylindrical LIBs are discussed within this thesis. With the aid of the MuDiMod, spatial inhomogeneity of utilization within a single cell can be emulated, which cannot be described by the p2Ds applied for the state-estimation algorithms. The computational complexity of the model structure and the time intense solving process practically exclude the application of the MuDiMod for the BMS, which is why reduced p2Ds are required for the state-estimation algorithms. However, the model-to-model comparison between the MuDiMod and the simplified, reduced p2D results in the model error caused by neglecting spatially imbalanced utilization of the LIB, which can be considered for the state-estimation algorithms. To enable real-time computation of the p2D, different model reduction schemes are compared to find the most suitable model implementation for embedded systems. The extension to observer models is outlined as the last step of developing the p2D based state-estimation algorithms. Additionally, selected experimental studies focusing on short-circuit events and cyclic aging are presented to better understand and predict energy and power capability, safety and lifetime, which is relevant to design optimized operational strategies for current and next-generation LIBs.

1.1 Functionality of Lithium-Ion Batteries

Understanding the working principles of a LIB is essential to develop any suitable modeling approach. The functionality of state-of-the-art LIBs is presented together with a review of its key components in the following section. Within this thesis, the commercial LG Chem INR18650-MJ1 lithium-ion battery (MJ1) is used as a representative of state-of-the-art high energy LIBs, as it shows one of the highest energy density of current commercially available LIBs.

The operating principle of a LIB follows the "rocking-chair" concept [22], where lithium-cations are reversibly transferred between electrodes. Lithium-ions intercalate into the electrodes. The electrodes comprise a composite consisting of the active material, binder and additives such as electrically conductive carbon [23], which is coated on a current collector foil like copper for the anode, or aluminum for the cathode. Lithium-ion transfer and de-/intercalation reactions are coupled to electron transfer into non-occupied electronic states in the electrodes [22]. To enable a transfer of lithium-ions between the electrodes, typically a liquid electrolyte consisting of solute and solvents is used, where an electrical insulation between the electrodes is applied via a porous separator membrane. Together with an external circuit for the electron flow, the operation of a LIB can be controlled. During discharge, the electron flow and lithium-ion flux are oriented towards the reduced electrode, where the lithium-ion intercalates. While both electrodes can be reduced or oxidized depending on the direction of the reaction/operational mode of the battery, the discharge case is set as standard to define the nomenclature to anode and cathode. Therefore, the reduced electrode during discharge is defined as the cathode and the oxidized electrode (i.e. the de-intercalated electrode) as the anode. Considering

the applied active materials silicon-graphite (SiC) and nickel-rich lithium nickel manganese cobalt oxide $\text{Li}(\text{Ni}_{0.8}\text{Mn}_{0.1}\text{Co}_{0.1})\text{O}_2$ (NMC-811) in the MJ1 battery, the simplified "half-cell" reactions can be described as follows

$$\text{Anode:} \qquad \text{Li}_x\text{SiC} \underset{delithiation}{\overset{lithiation}{\rightleftharpoons}} x\cdot\text{Li}^+ + x\cdot\text{e}^- + \text{SiC} \qquad (1.1)$$

$$\text{Cathode:} \quad \text{Li}_{1-x}(\text{Ni}_{0.8}\text{Mn}_{0.1}\text{Co}_{0.1})\text{O}_2 + x\cdot\text{Li}^+ + x\cdot\text{e}^- \underset{lithiation}{\overset{delithiation}{\rightleftharpoons}} \text{Li}(\text{Ni}_{0.8}\text{Mn}_{0.1}\text{Co}_{0.1})\text{O}_2 \qquad (1.2)$$

The simplified "full-cell" charge and discharge reaction in a LIB superimposes the simplified anode's and cathode's half-cell reactions of Eq. 1.1 and Eq. 1.2 as

$$\text{Anode + Cathode: } \text{Li}_{1-x}(\text{Ni}_{0.8}\text{Mn}_{0.1}\text{Co}_{0.1})\text{O}_2 + \text{Li}_x\text{SiC} \underset{discharging}{\overset{charging}{\rightleftharpoons}} \text{Li}(\text{Ni}_{0.8}\text{Mn}_{0.1}\text{Co}_{0.1})\text{O}_2 + \text{SiC} \quad (1.3)$$

Fig. 1.4 shows a schematic structure of the SiC/NMC-811 LIB. For simplicity, binder and additives are neglected, which represent the non-reactive part of the composite. The reactive surface between the electrodes and the electrolyte is the solid-liquid interface in the porous structure of the electrodes, wherein the pores are filled with electrolyte. In the following, a brief review of state-of-the-art and
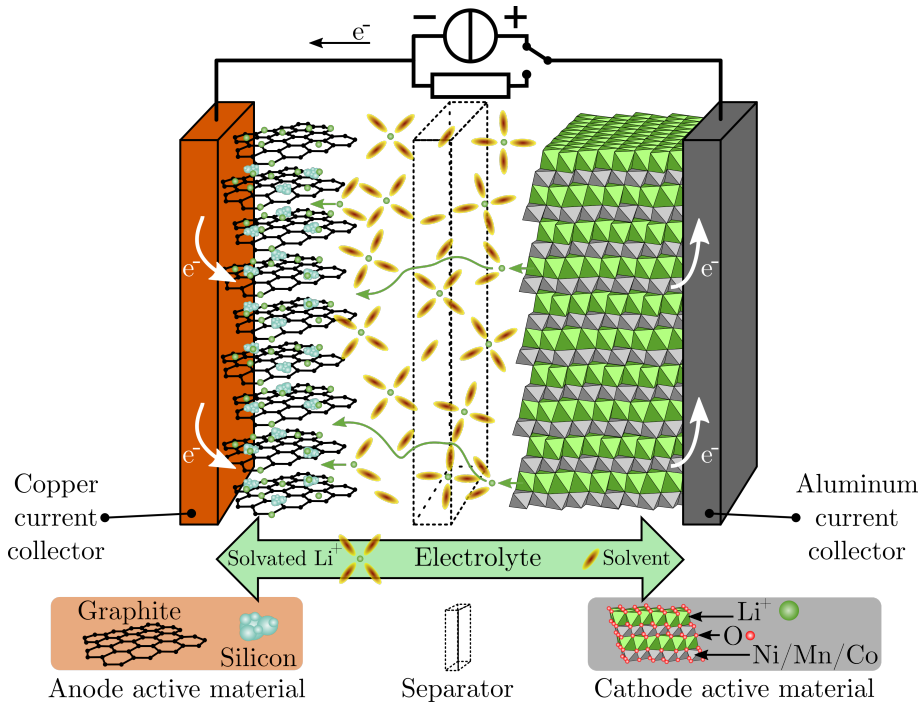

Figure 1.4: Schematic structure of a SiC/NMC-811 LIB such as the MJ1. The copper (anode-side) and aluminum (cathode-side) current collector carry the composites incorporating the SiC or NMC-811 active materials, which are isolated by the separator. For simplicity, binder and additives are not shown and the cathode host lattice is simplified by neglecting oxygen in the upper illustration. The pores throughout the porous anode, separator and cathode domain are filled with electrolyte, which incorporates the solvated lithium-ions species. The LIB's terminal voltage E is measured between the negative and positive current collector under the illustrated charging mode, which determines the direction of electron flow and lithium-ion flux (derived from Ref. [22, 24–30]).

prospective components used for LIBs is presented and discussed in the context of the MJ1 LIB, which is investigated in the main part of this thesis.

Anode active materials   For more than two decades, graphite (LiC_6, $372 \, \text{mAh} \, \text{g}^{-1}$ [27, 31, 32]) has been the state-of-the-art anode active material in commercial LIBs because of its sufficient capability of hosting intercalated lithium between its flexible graphene layers and its beneficial surface passivation towards electrolyte decomposition [33]. Graphite is typically available in natural or synthetic form, where the synthetic types come with a higher market price [33, 34]. Despite the increased costs, synthetic graphite offers increased purity, improved thermal stability and a lower thermal expansion alongside with improved reaction kinetics and lower capacitive formation losses due to the adjustable crystalline orientation during the manufacturing process [33]. Anodes of lithium titanate (LTO) are less common as lower cell voltage in full-cell operation are caused by the higher open-circuit potential of the half-cell vs. Li/Li^+ (OCP) as seen in Fig. 1.5a, beside the lower gravimetric capacity. The current trend towards increasing the energy density in LIBs exceeds the capacitive resources of
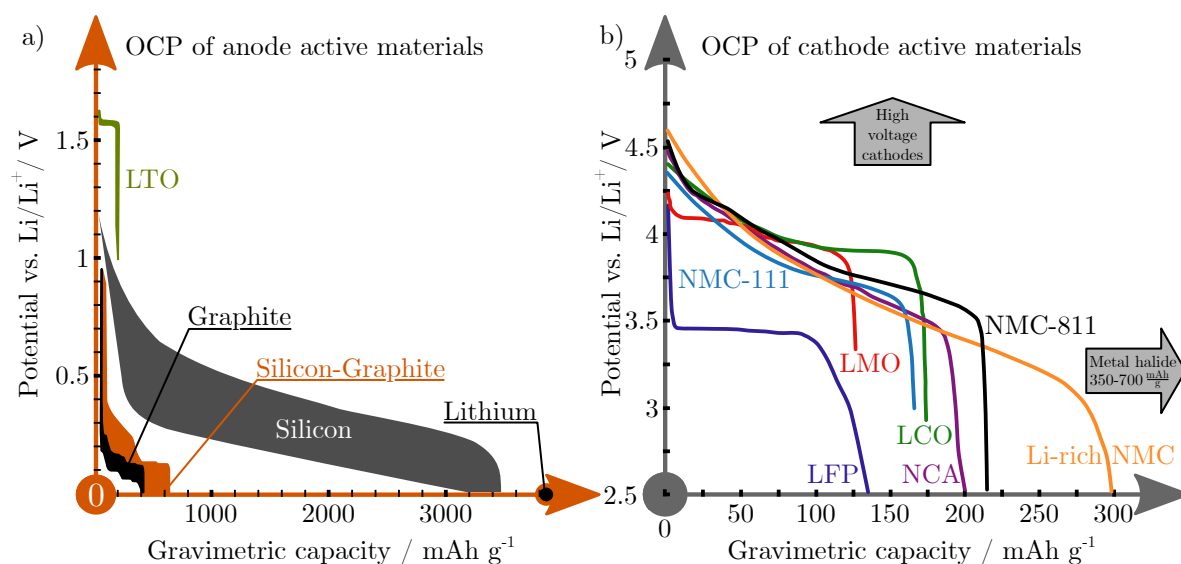

Figure 1.5: Overview of anode and cathode active materials for LIBs. Subplot a) shows the range of half-cell equilibrium potential profiles vs. lithium metal (i.e. Li/Li^+) of current and prospective anode active materials (derived from Ref. [16, 35]). Subplot b) shows explicit half-cell equilibrium potential profiles vs. Li/Li^+ of current and prospective cathode active materials (derived from Ref. [16, 29, 35–37]).

pure graphitic anodes. Using pure lithium metal as anode results in theoretical high capacity beyond $3000 \, \text{mAh} \, \text{g}^{-1}$ [16], but the lithium dissolution and plating reaction reveals shortcomings of inhomogeneous reaction distribution at the interface, high volume changes and possible lithium-dendrite growth [16]. This leads to a poor performance caused by internal resistance increase and severe safety threat caused by possible separator penetration leading to a short-circuit [16]. Silicon appears as a promising candidate offering high theoretical capacities beyond $3000 \, \text{mAh} \, \text{g}^{-1}$ at high lithiation stages (e.g. for $Li_{22}Si_5$ up to $4200 \, \text{mAh} \, \text{g}^{-1}$ [31, 32, 38]), but the critical mechanical expansion of more than 300% [25] due to the de-/alloying reaction restricts the operating window. The depicted range of silicon in Fig. 1.5a refers to $Li_{15}Si_4$ at the lithiated stage [35, 38]. The exceeding mechanical expansion can be partly compensated when silicon is mixed with graphite, which shows a lower expansion around 10% [27]. Current and next-generation anode material in LIBs most-likely utilize compounds of graphite and silicon, where the silicon-graphite compound will dominantly consist of a graphite

host lattice with an insertion of silicon. In general, the gravimetric capacity increases with contents of silicon as indicated in Fig. 1.5a. The insertion is currently achieved in form of a small amount of elemental silicon (< 8 wt.%) or under-stoichiometric silicon oxide (SiO), whereby SiO is available at a lower market price and comes with better manufacturing features than elemental silicon [33]. The issue of high mechanical expansion can be further eased via using nano-sized silicon particles, which is still challenging due to increased electrolyte decomposition, low volumetric density, handling costs and manufacturing costs [33]. Further carbon coatings and pre-lithiation strategies are promising to reduce the electrolyte decomposition and to improve energy density [33].

The anodic active material incorporated in the MJ1 LIB is of a silicon-graphite compound, which was determined to be 3.5 wt.% of silicon in a graphite host lattice [39].

Cathode active materials Standard intercalation type cathodes in LIBs are typically made from layered oxides, such as lithium cobalt oxide (LCO), lithium nickel cobalt aluminum oxide (NCA), or lithium nickel manganese cobalt oxide (NMC), spinels such as lithium manganese oxide (LMO), or polyanion compounds such as lithium iron phosphate (LFP) [35]. The half-cell equilibrium potential vs. Li/Li$^+$ is shown over the gravimetric capacity in Fig. 1.5b, where especially the nickel-rich NCA and NMC-811 cathode active materials represent the current state-of-the-art for high energy LIBs at a capacity around $200 \, \mathrm{mAh \, g^{-1}}$ [16, 28–30]. Both nickel-rich cathode types reveal the highest development stage for application and are already used by car manufacturers today [16]. Further development is heading towards less cobalt and inserting more nickel, which showed promising results in reducing the overall manufacturing costs [40]. As cobalt is one dominant cost driver for manufacturing LIBs, cobalt-free cathodes would significantly lower the costs of the battery cells and thus of the EV [41]. Although high-voltage cathodes as indicated in Fig. 1.5b are expected to achieve around $200 \, \mathrm{mAh \, g^{-1}}$, they come with shortcomings in electrolyte oxidation, cathode dissolution, structural changes, and mechanical stress leading to early energy loss and power fade over lifetime [16]. Indeed, lithium-rich layered oxides (see "Li-rich NMC" in Fig. 1.5b) most likely exceed nickel-rich cathodes in gravimetric capacity [37, 42], but the appearing issues of mechanical failures [16], voltage and capacity decay [42] still hinder an efficient usage in application. Conversion type metal fluoride cathode materials (see "Metal halide" in Fig. 1.5b) theoretically offer higher gravimetric capacity up to $700 \, \mathrm{mAh \, g^{-1}}$ (e.g. $528 \, \mathrm{mAh \, g^{-1}}$ for CuF$_2$ [16]), and further come with lower costs and sufficient availability of the required raw materials [16]. However, the TRL is not advanced enough to solve fundamental issues, such as low electrical conductivity, large hysteresis effects or mechanical degradation [16], and thus hinders a consideration for application.

The cathodic active material incorporated in the MJ1 LIB is of a nickel-rich NMC type, which was measured to a composition of 82 wt.-%, 6.3 wt.-% and 11.7 wt.-% for nickel, manganese and cobalt and is therefore ascribed to the NMC-811 type [39].

Liquid electrolytes In general, a liquid electrolyte should offer high ionic conductivity and diffusivity for the lithium-ion transport and sufficient electrochemical stability towards the anode (i.e. solid electrolyte interphase (SEI)) and cathode (i.e. cathode electrolyte interphase (CEI)) [43]. Moreover, low flammability and high thermal stability, environmental compatibility, sufficient wetting of the porous electrode stack and ideally a certain level of recyclability are required [43]. Typical liquid electrolytes consist of a solute such as lithium hexafluorophosphate (LiPF$_6$) and a solvent, which is typically composed of one or more linear (e.g. diethyl carbonate (DEC), ethylmethyl carbonate (EMC), or dimethyl carbonate (DMC)) or cyclic (e.g. ethylene carbonate (EC)) carbonates [43]. The mixture of solute and solvent results in the dissociation of the solute in anions (PF$_6^-$) and lithium-cations (Li$^+$), which is solvated by solvent molecules. A critical safety issue of these organic electrolytes is their

flammability and is therefore currently addressed via increasing the flash point or use phosphate based flame-retardant additives [43]. However, the use of such additives lowers the ability for surface passivation in graphitic anodes, that leads to a trade-off between safety, energy and power performance [43]. Derived from application scenarios, further developments focus on the capability of fast charging [44]. Following the review of Logan et al. [44], low-viscous solvents (e.g. esters, formates or nitriles) are favored to carbonates to improve the ionic conductivity, but are challenging for the LIB lifetime due to an insufficient built-up of a passivated surface layer. A strong impact on the charging rate capability is also attributed to the transference number of lithium-ions, which could be improved using poly-anionic species regarding the solvent or applying highly concentrated electrolytes ($> 2\,\mathrm{mol\,l^{-1}}$ instead of $1\,\mathrm{mol\,l^{-1}}$ for the solute) resulting in a lower LIB safety [44]. A trade-off between lifetime and rate capability appears and should therefore be a key development goal for future liquid electrolytes in LIBs. Alternative researched electrolytes based on ionic liquids are non-flammable, but expensive, hard to handle in industrial applications due to the required processing under dry conditions [43] and show a low ability of wetting with common separators [45].

The liquid electrolyte of the MJ1 LIB contains $LiPF_6$ as solute and revealed EC, DMC and EMC as solvents [39].

Separators Commercial separators for liquid electrolytes are commonly polyolefin based polymer membranes, which offer chemical and dimensional stability (i.e. shrinkage level $< 5\,\%$), low thickness ($< 25\,\mathrm{\mu m}$) enabling high energy density but maintaining mechanical rupture resistivity [45]. Moreover, optimal porosity ($> 40\,\%$) and tortuosity are required to decrease the internal resistance and to impede lithium dendrite growth as well as a sufficient level of wetting to avoid any dry spots leading to low utilization levels of the electrodes [45]. The separator in the MJ1 LIB was measured to be $12\,\mathrm{\mu m}$ [39], which is a common thickness for polyolefin separators. Mono- or multi-layered micro-porous separators typically consist of polypropylene (PP) and/or polyethylene (PE), whereby current research deals with coating or filling the membrane with ceramics (e.g. aluminum oxide (Al_2O_3) or titanium dioxide (TiO_2)) to improve thermal stability, thermal conductivity and wetting characteristics [45, 46].

After reviewing the advancements for the single components, a comparison of the energy density for LIBs and alternative types of the battery's chemistry is shown in the following.

Battery cells Fig. 1.6 shows an overview of past, current and prospective batteries referring to the single cell level with a comparison of gravimetric and volumetric energy density. Lead-acid ("Pb-acid"), nickel-cadmium ("Ni-Cd"), and nickel-metal-hydride ("Ni-MH") cells were widely outperformed in the last decade by LIBs in terms of volumetric and gravimetric energy density, operating voltage and cycle life [47]. Current LIBs are in the range up to $300\,\mathrm{Wh\,kg^{-1}}$ and $750\,\mathrm{Wh\,l^{-1}}$ [16]. Partly, prospective LIBs are already commercialized as seen for the MJ1, which incorporates a SiC/NMC-811 chemistry and reveals a energy density of $261\,\mathrm{Wh\,kg^{-1}}$ and $678\,\mathrm{Wh\,l^{-1}}$ [39]. Approximately five more years of development will result in a fully-developed technology state of silicon-graphite/nickel-rich LIBs to be used extensively in industrial applications [16]. However, the silicon- and lithium-anode based future concepts are expected to need maybe more than a decade of research due to the aforementioned performance shortcomings of each electrode to achieve an acceptable maturity level, which is suitable for a wide industrial application [16]. Besides, the lithium-air battery (LiO) or the lithium-sulfur battery (LiS) could be considerable alternatives for the future. However, shortcomings for LiOs need to be addressed such as poor reaction kinetics, pore clogging leading to voltage hysteresis and low rate capability [15, 16]. LiSs reveal continuous electrolyte consumption, interfacial side-reactions and shortcomings due to reaction shuttling effects [15, 16]. So far, these issues prevent LiOs and LiSs to become a commercially competitive option on the battery market [15, 16].
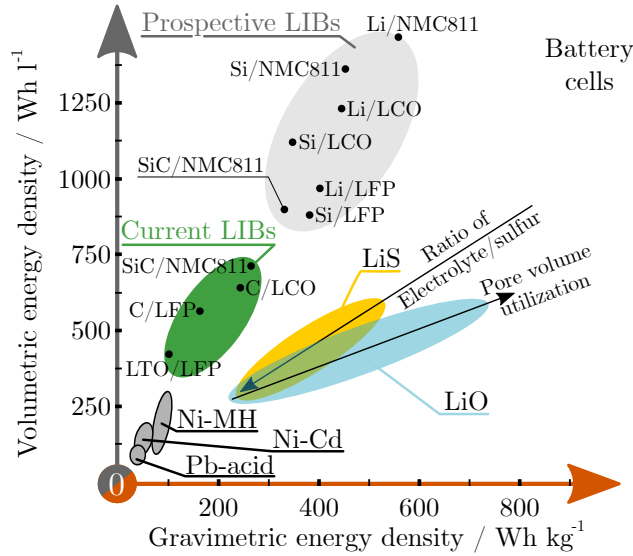
Figure 1.6: Comparison of past, current and prospective battery cells via comparing volumetric and gravimetric energy density of both lithium-ion and alternative battery technologies (figure derived from Ref. [16, 47, 48]).

To conclude, the LIB is assumed to be the technology of choice for electrical energy storage systems within the next decade. The future development of the incorporated components, such as anode and cathode active materials, electrolyte and separator, is expected to result in higher energy densities for the next generation of LIBs compared to state-of-the-art battery technology. With a more and more sophisticated battery technology, the complexity to describe the behavior of these LIBs tends to increase. Therefore, advanced description techniques are required to accurately monitor and control LIBs and to maintain a safe operational state. In applications such as the battery pack in an EV, the BMS monitors and controls the battery system via using state-estimation algorithms, which use measurement and/or model based methods to describe the LIB. In this matter, advanced state-estimation algorithms can incorporate physicochemical models and are most-likely capable to describe the complex mechanisms of current and future battery systems, which can hardly be covered by current approaches such as an equivalent circuit model (ECM). Besides, a more accurate state-estimation enables a better exploitation of the battery's operating window, as safety buffers avoiding safety critical side reactions such as lithium plating can be reduced.

In the following sections, an overview of common BMS architectures and the incorporated state-estimation techniques is presented, to discuss the state-of-the-art and future possibilities of accurately monitoring and controlling LIB systems.

1.2 Features of Battery Management Systems

The required energy and power capabilities of current and future LIBs combined with stressful operations such as fast charging are challenging for the BMS to keep the battery in a safe operational state. The BMS typically monitors and controls current, voltage and temperature of the battery system on different levels: the single cell, the module consisting of several interconnected cells and the entire pack incorporating all modules [49]. Key features of a state-of-the-art BMS are summarized in Fig. 1.7 and are distinguished into seven main tasks [49], which are exemplary discussed on the single cell level.
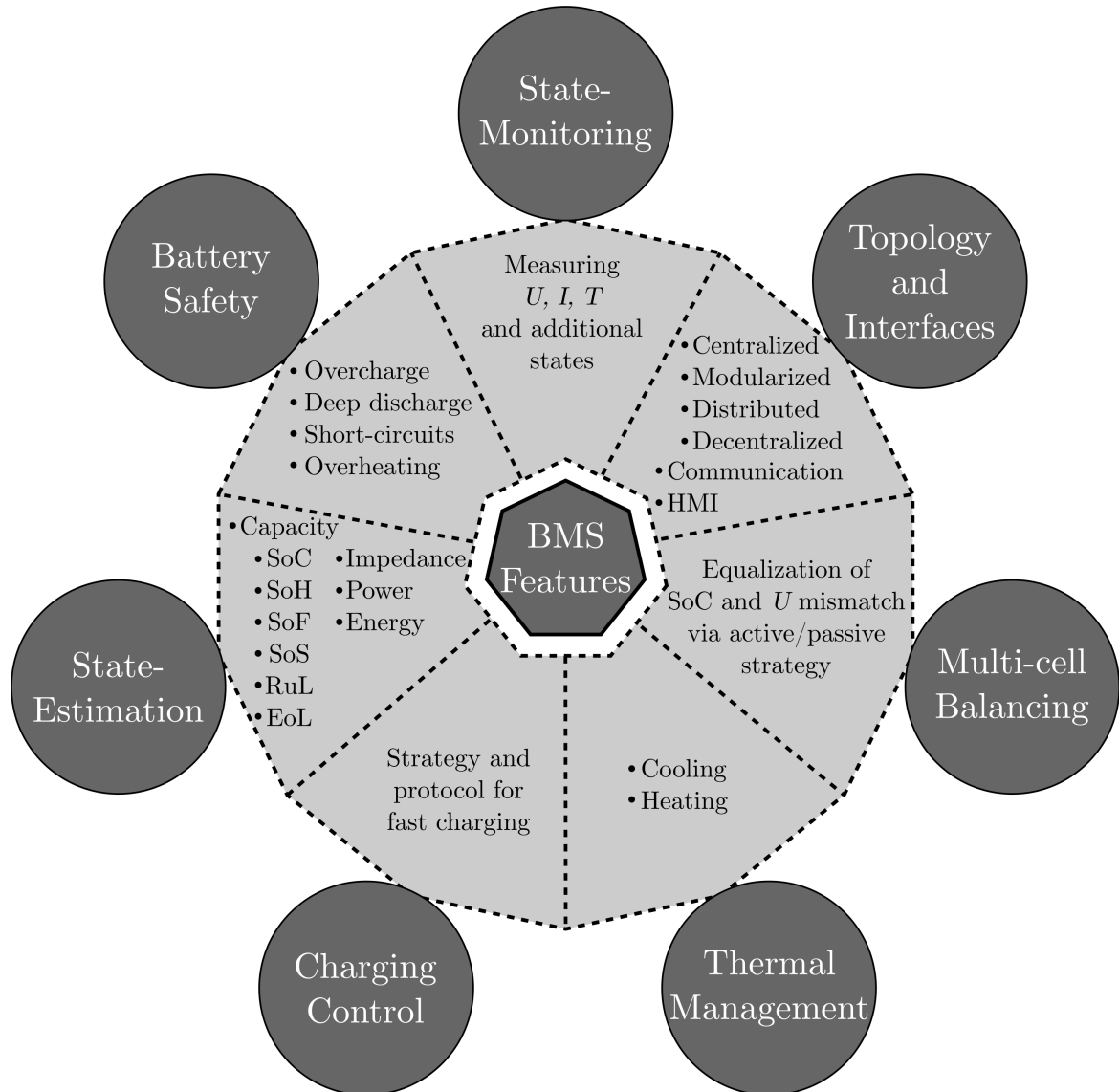
Figure 1.7: Overview of the seven key features in a BMS to monitor and control the operation of a battery system. The figure is based on several works from the research field [49–52].

State-Monitoring The single cell's voltage, current flow and surface temperature are typically measured via various sensor techniques for a single cell. Monitoring techniques in application use specified integrated circuits to process the measured voltage and the current signals from shunt-resistors [53] and the temperature signals from negative temperature coefficient thermistors [54]. Novel techniques in the research field also use strain gauges or load cells to measure the strain or force on the cell's surface [55], which is used to measure the mechanical swelling of LIBs. However, the mechanical swelling state is rarely monitored in application due to the complexity of measurement and evaluation of the force/strain signals compared to the more simple monitoring of terminal voltage, current flow and surface temperature.

State-Estimation The processed signals are typically transferred to a micro-controller (MC), which processes the measured input and estimates the state of a LIB using different state-estimation techniques as presented in the next section. One of the most important states is the SoC representing

the remaining accessible amount of charge in reference to the total capacity of the cell. The state of health (SoH) represents the remaining capacity of a LIB, which is reduced by aging processes such as SEI or lithium plating during lifetime. It is often correlated to the remaining useful life (RuL) and the end of life (EoL) between 70-80 % [56–58] of the initial, nominal capacity. The state of function (SoF), also called state of power, describes to which extent the battery performance meets the actual load demands [59]. The state of safety (SoS) refers to the safe operating window of the battery [60] and can consider various inputs such as limits of the cell voltage, current flow, surface temperature or mechanical swelling. The impedance can be derived from the measured current and voltage signals, which can also be used in terms of estimating the temperature [61–64] without having a temperature signal. As all of the estimated states cannot be measured directly, the state-estimation feature is crucial to correlate the measured signals to physical properties, state functions and to the prior characterized cell behavior. These physical properties and the cell behavior are typically characterized before the actual estimation process takes place via experimental and/or model based methods and are stored in the memory of the MC. With the aid of the estimated and the measured/monitored states the battery system can be controlled within an efficient and safe operational state.

Battery Safety The safe operational state of a LIB is mainly determined by the intrinsic chemical characteristics, which define the upper and lower cell voltage as well as the maximum and minimum charge and discharge current [49]. In terms of the temperature, the chemistry and the environmental conditions define the optimal operating range [49]. A typical operating range as for the MJ1 LIB is defined in a current range up to 1C constant current (CC) charge and 3C CC discharge, a terminal voltage range from 2.5 V to 4.2 V and a temperature range from -20 °C to 60 °C for discharge and 0 °C to 60 °C for charge operation [65]. With the aid of the estimated states of SoC or SoS, hazardous conditions, such as overcharge, under- or deep-discharge as well as overheating, must be avoided through the BMS in any case. Exemplary, the BMS controls the current and if necessary reduces or completely cuts the current flow to ensure a safe state. In case of short-circuit scenarios the emerging high currents must be cut in very limited time spans below 1 ms, which is realized via fuses [66] or pyrotechnical devices [67]. Otherwise, these critical conditions can lead to a thermal runaway coming with possible release of toxic gases, open fire or even explosion [68]. If possible, the safety feature of the BMS includes suitable precursor algorithms to prevent the onset at an early state [69].

Thermal Management The safety of the battery system is not only strongly correlated to the temperature, but the efficiency is also significantly determined by the temperature due to the thermal sensitivity of mass transport properties and electrode kinetics in a LIB [49]. In the BMS, the functionality to homogeneously transfer heat within a battery pack uses heating and cooling subsystems, which typically transfer heat via air or fluid along channels at the bottom or the lateral surface of the single cells [49]. Preheating the battery pack is an essential preconditioning method for fast charging or operation under cold ambient conditions [70]. Cooling is applied to avoid overheating during ongoing fast charging, usual operation and preconditioning under warm ambient conditions [70].

Multi-cell Balancing A battery pack or module typically consists of several LIBs connected in parallel and/or in series to achieve the energy and power density suitable for industrial applications. Manufacturing variations for single cells and/or imbalanced operation conditions such as temperature gradients in the pack/module [71] can evoke inhomogeneity in capacity and/or internal resistance between the single cells. As a result, variances in SoC and SoH appear between the single cells, which lower the overall performance of the battery pack and can lead to unwanted degradation effects and inevitably reduce lifetime of the battery system [71, 72]. A variety of cell balancing systems exists and the different working principles are thoroughly discussed in literature [72], which have all in common to

equalize an imbalance of cell voltage or capacity between the single cells via active or passive balancing procedures [49, 72]. As an example, active methods can incorporate a single DC/DC converter to equalize the charge among cells in a single module or a single bypass resistor is combined with a switch at each cell [49], whereas passive methods can include overcharge procedures which are not suitable for LIBs or fixed shunting resistor methods [72].

Charging Control Fast charging stresses the cell and poses a severe threat to the lifetime of the battery system. Maximizing the charged energy per time can lead to early SoH decay by triggering side reactions such as lithium plating. This aging effect is facilitated at low temperatures [73] or high polarization levels of the cell caused by the increased charging current loads [74]. The charging control feature interacts with the thermal management feature and must guarantee a safe operation between the minimum and maximum temperature to avoid lithium plating as well as overheating. Especially physicochemical model based state-estimation algorithms are promising for the improvement of charging procedures as they consider local electrochemical conditions within a LIB.

Topology and Interfaces A variety of BMS architectures are presented in literature [75] including centralized, modularized, distributed or decentralized topologies. In a centralized topology, a single BMS controls the entire battery pack and the connection to the single cells is implemented via electrical wires or connector plates [75]. A modularized topology incorporates several slave-BMSs and can be implemented for each module of the battery pack, whereby the slave-BMS typically acquires the measurement data and communicates to a master-BMS, which controls the entire battery pack [75]. In application, several slave-BMS are typically connected via an internal isolated controller area network (CAN) to the master-BMS, which is linked to the external CAN bus of an EV and establishes thereby the connection to the human machine interface (HMI) [49, 76]. In a distributed topology, each module or cell can be equipped with a BMS and the single BMS units can communicate among each other, whereby a superimposed control unit manages the communication and the calculation tasks [75]. The decentralized topology consists of autonomously operating BMS units on single cell or module level, which communicate to each other and require no superimposed control unit [75]. To conclude, a distributed or decentralized topology offers more flexibility, scalability and reliability of the BMS as individual modules or single cells can be added, removed or exchanged. The extension of the size of the battery pack is variable and not fixed to the initial layout and failures of individual BMS units have a minor impact on the entire system compared to a centralized or modularized topology [75]. On the other hand, increasing decentralization results in higher costs for embedding a higher number of hardware components.

One of the most important features of a BMS is the state-estimation as it links the measured states from the state-monitoring feature to fundamental characteristics of the LIB, which are crucial to control the battery system within its safe operational range. The inherent correlation of measured signals to physical properties and the prior determined behavior of the battery can be implemented in a variety of techniques ranging from measurement to model based approaches. The next section presents state-of-the-art and prospective state-estimation techniques such as the physicochemical model based approach, which are used in research and application to estimate the states of LIBs.

1.3 State-Estimation Techniques for Lithium-Ion Batteries

One of the most important states during operation of a LIB is the SoC [52, 77–80]. The measured terminal voltage, current flow and surface temperature are usually the input signals for a SoC estimation routine regarding the pack, the module or the single cell level. Focusing on the cell level, various estimation techniques can be applied. Fig. 1.8 shows commonly used techniques in the research and the application field.
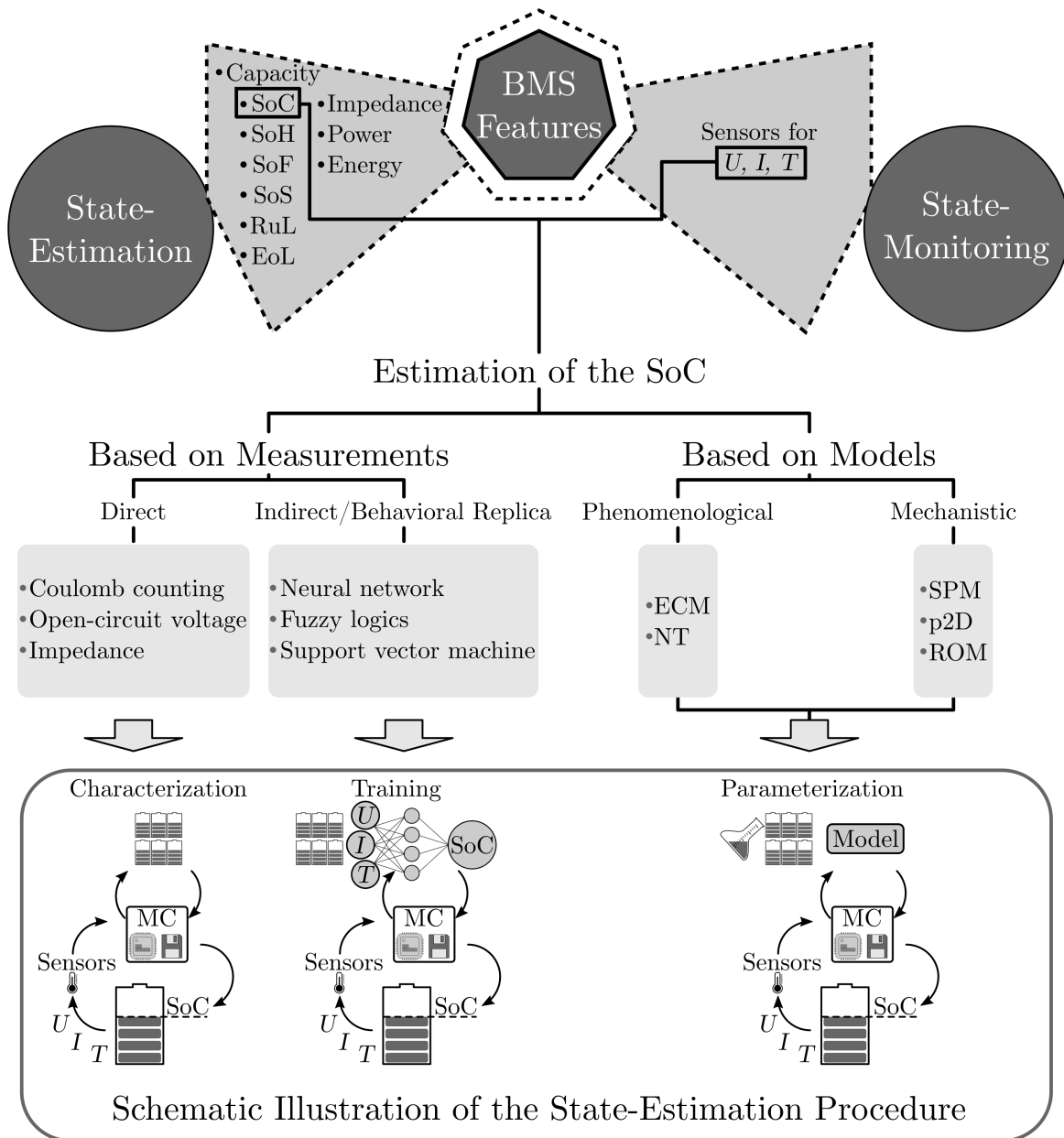

Figure 1.8: Selected techniques to estimate the SoC in a LIB by combining the state-estimation and -monitoring feature in a BMS. The measurement based techniques are further split into direct and indirect/behavioral replica. The model based techniques incorporate phenomenological and mechanistic models. At the bottom, a schematic of the state-estimation routine is shown for the direct and indirect measurement techniques as well as the model based method, where a MC is used for the computation. The figure is based on several works from the research field [51, 78, 80, 81].

A division into measurement and model based estimation techniques appears [51, 78, 80, 81], which is further distinguished into direct and indirect measurement techniques as well as phenomenological and mechanistic models. In this context, the measurement based techniques are called black-box approaches as no physics based model describes the behavior of the actual cell and a dominant dependence on the experimentally measured data exists [81]. If no model is used, the behavior of the cell is correlated to the cell properties, determined through a range of experimental characterization tests, which can easily lead to a tremendous amount of data. The model based techniques describe the behavior of the cell according to their physical structure, which makes e.g. the physicochemical single particle model (SPM) and the p2D rather white-box approaches. The ECM is derived from electrical laws and incorporates more simplifications regarding the real physicochemical behavior of a LIB compared to the more physicochemical structure of the Newman-Tiedemann model (NT) model. Both can be seen as grey-box approaches, which show a strong data-driven structure. There are also grey-box approaches in the form of combining the measurement based approaches, such as impedance measurement [80, 82], with models, which partially fuses behavioral replica and phenomenological models such as the ECM [81].

A choice of well-known and commonly applied measurement and model based techniques is presented and compared in the following section. Further, the accuracy and the computation speed of each state-estimation group is assessed via the predictability of the LIB's SoC and the mathematical complexity of the method.

1.3.1 Comparison of Measurement and Model based Techniques

The measurement and model based state-estimation techniques are depicted in Fig. 1.8 and the estimation of the LIB's SoC is exemplary outlined for each technique in the following.

Techniques based on Measurements Direct measurement and integration of the current flow can calculate the amount of capacity, which can be used to derive the SoC in relation to the total capacity of the cell. This straightforward method is functional and fast to implement. However, the lack of physical insights in the actual LIB's behavior may lead to an inaccurate estimation of cell states, which must be considered for defining the operating window by increasing safety buffers at the operational limits. Therefore, the potential of the battery may not be fully exploited [81]. The correlation of open-circuit voltage of the full-cell (OCV) and SoC can be applied to the measured voltage between the positive and negative terminal, but requires a previous resting phase in the range of several hours [83] (e.g. 20 h [84]) for sufficient relaxation, which is often not suitable for application scenarios [80]. In this matter, empirical extrapolation schemes [84, 85] for the relaxation processes in LIBs are discussed in literature, which can reduce the required rest period. The necessary information about the characteristics, such as the correlation of SoC and OCV, are derived from previous and/or real-time operational data, that are usually stored in the memory of a MC and retrieved if needed. Both terminal voltage and current flow are used within impedance based techniques to correlate the impedance to the cell's SoC [61, 80]. The change of the impedance over lifetime and its thermal sensitivity are challenging and complicate a proper state-estimation [51]. A simplified schematic illustrates the state-estimation routine in Fig. 1.8 for the direct measurement methods. The state-monitoring part transmits the input data from the sensor signals to a MC, where the input is related to the stored characterization data in order to derive an estimate of the cell's SoC.

Indirect or behavioral replica typically incorporate machine learning methods. These methods use experimental data to train general mathematical fitting functions to describe the favored behavior of the

cell [52] without the use of any model based on physical laws [80, 81]. Commonly used techniques for SoC estimation are approaches using artificial neural networks [86, 87], fuzzy logics [88] and support vector machines [89]. Artificial neural networks incorporate an input layer, where terminal voltage, current flow and surface temperature can be fed from experimental training data [81] as illustrated in Fig. 1.8. In the incorporated hidden layers, the input data is mathematically combined to generate the output in form of the SoC [80]. The training process is performed offline and its extent mainly defines the quality of the output [51, 80]. Fig. 1.8 illustrates the simplified estimation routine of a neural network matching voltage, current and temperature to the SoC in the training process.

An insight in the cell's actual behavior is generally not required for most of the measurement based techniques, which makes them easy to apply, but possibly the optimum in operation of a LIB may not be fully achieved [81]. This issue can be addressed with model based techniques, that can offer insights into the cell's behavior and its internal states.

Techniques based on Models   The ECM is the most commonly applied modeling approach and simplifies the major electrochemical processes during operation by means of an equivalent electrical circuit with elements of resistance, capacity and voltage source [51, 81]. The SoC estimation uses the correlation of the OCV characteristics and the measurement of voltage, current and temperature [51]. In general, the model offers fast calculation, simple parametrization and low model complexity. However, the estimation approach is limited to the pre-parametrized operating range and cannot predict a state beyond that [51]. The ECM is often used together with filtering techniques [90, 91] such as a Kalman filter (KF) [92] to increase the accuracy and the robustness of the estimation process [93]. The KF approach basically incorporates a prediction step for a system's state, output, measurement and model error, and a subsequent correction for the current state estimate [51, 80]. In terms of ECM based observer models, the variance between the predicted and the measured terminal voltage is typically used in the KF process to correct the model output such as the SoC [51].

In comparison to the ECM, mechanistic approaches intrinsically offer a description of the SoC within the physicochemical model structure. The physicochemical approaches of SPM, p2D or their reduced order model (ROM) variants, require a large effort in parametrization to characterize the mass and charge transport as well as the electrode kinetics [94], compared to a rather simple parametrization effort for the electrical equations in the ECM. The solving process of the incorporated differential algebraic equation system is complex and often no real-time computation can be achieved. This disadvantage prevents an extensive use of physicochemical model based state-estimation in application. However, applying proper model reduction techniques and suitable implementation for real-time operating systems [95], these models offer a huge potential to optimize the operational range and the overall efficiency of a LIB. Implementing aging mechanisms, the model parametrization can be adapted during the lifetime of a battery. Furthermore, fast charging strategies can avoid lithium plating by using the inherent information of the local anode potential [39, 96]. Fig. 1.8 shows the simplified schematic of the model based state-estimation routine [97–101]. The extension to observer models using filtering techniques as discussed for the ECM is also suitable for the mechanistic models. Implementations in the research field and the results presented in this thesis, show promising results of accurate and robust state-estimation algorithms based on physicochemical models [98, 99].

Another physicochemical, but generally phenomenological model is the NT [102], which is based on a linearization scheme to approximate the polarization behavior of LIBs [103, 104]. It is mainly used in the research field to investigate the cell design of suitable cell formats such as large pouchbag LIB with planar electrodes. It could possibly be of interest for SoC estimation in special applications such as mobile tablet computers, where only a single pouchbag cell is incorporated.

The mechanistic physicochemical models are suitable to be transferred and reused for a similar LIB, which hardly applies for the remaining techniques. As long as the electrode active material, the composition of the electrode materials and the electrolyte remains the same, variations of the cell design such as format, electrode geometry, morphology or different separators can be adopted in the model parametrization. In contrast, the behavioral replica and the phenomenological models must be re-trained or re-parametrized for each particular cell. The direct measurement techniques can thereby partly be re-used (e.g. coulomb counting), but when it comes to cell specific characteristics, for example the temperature dependency of the impedance behavior or the SoC-OCV correlation, the parametrization must be determined for each particular cell as well.

1.3.2 Error Sensitivity of State-Estimation Techniques

The aforementioned state-estimation techniques are compared within this section in terms of both computation speed and accuracy for predicting the SoC to evaluate benefits and drawbacks of each estimation group. Fig. 1.9 shows a qualitative assessment, which is derived from the work of Zheng et al. [78]. The computation speed is inversely correlated to the mathematical complexity of the chosen technique. The optimal technique should guarantee a maximum combined speed and predictability to be most suitable for general application scenarios. A key feature in the application field is the real-time suitability of the carried out calculation in embedded systems, which is depicted in Fig. 1.9 (see red frame) [78].

Each group of estimation techniques includes two trends: Firstly, an increased complexity in the underlying mathematical description of the battery's behavior and, secondly, an increase in complexity of the chosen state-estimation algorithm [78] as described in the legend of Fig. 1.9. The battery description represents the characteristics or the training process in terms of the direct or indirect measurement based techniques or simply the model itself [78] in terms of the model based methods as shown in Fig. 1.8. The chosen algorithm refers to a set of solutions for abstract problems, which is typically used to estimate the actual state based on the underlying mathematical description and to minimize the error of the gained solution [78]. The description in the coulomb counting technique can be described as a tank model [78], where the integrated current flow of the cell is related to the cell's previously determined characteristic capacity. The algorithm itself would be the mathematical integration operation [78]. For the more complex model based techniques, the model is the description part and the algorithm incorporates the extension to an observer model using filtering techniques such as a KF [78]. Using an ECM or a p2D, the algorithm typically tries to reduce the discrepancy between the predicted model output and the measurement input to retrieve a better quality of the state-estimation [98].

The illustrated areas for each of the six estimation groups in Fig. 1.9 and the following discussion of each group is based on the results of Zheng et al. [78] if not indicated otherwise.

Coulomb counting   The coulomb counting method typically incorporates a tank model description, which correlates the charge shift under operation in reference to the cell's capacity [105–108]. The algorithm is typically an integration method [106, 107]. The low complexity offers a high computation speed. Slightly lower computation speed, but a significant improvement of the predictability appears when exemplary high-precision coulometry or self-discharge features are considered as shown in the description trend of Fig. 1.9. Improvements in the chosen integration method significantly enhance the predictability whilst not overly comprising the calculation speed, as described by the algorithm trend in Fig. 1.9.

Open-circuit voltage In comparison to coulomb counting, higher computation speed and predictability appear for OCV techniques, which fundamentally rely on the correlation of SoC and OCV [109] and typically make use of a simple look-up table interpolation as scheme for the underlying algorithm [110]. The more accurate the SoC-OCV correlation, the higher the predictability. A more accurate description could include a temperature dependency of the OCV as a function of the cell's temperature [110]. Improvements of the interpolation scheme only have a minor impact on the computation speed as the required interpolation algorithm is rather lean and, hence, fast in the very
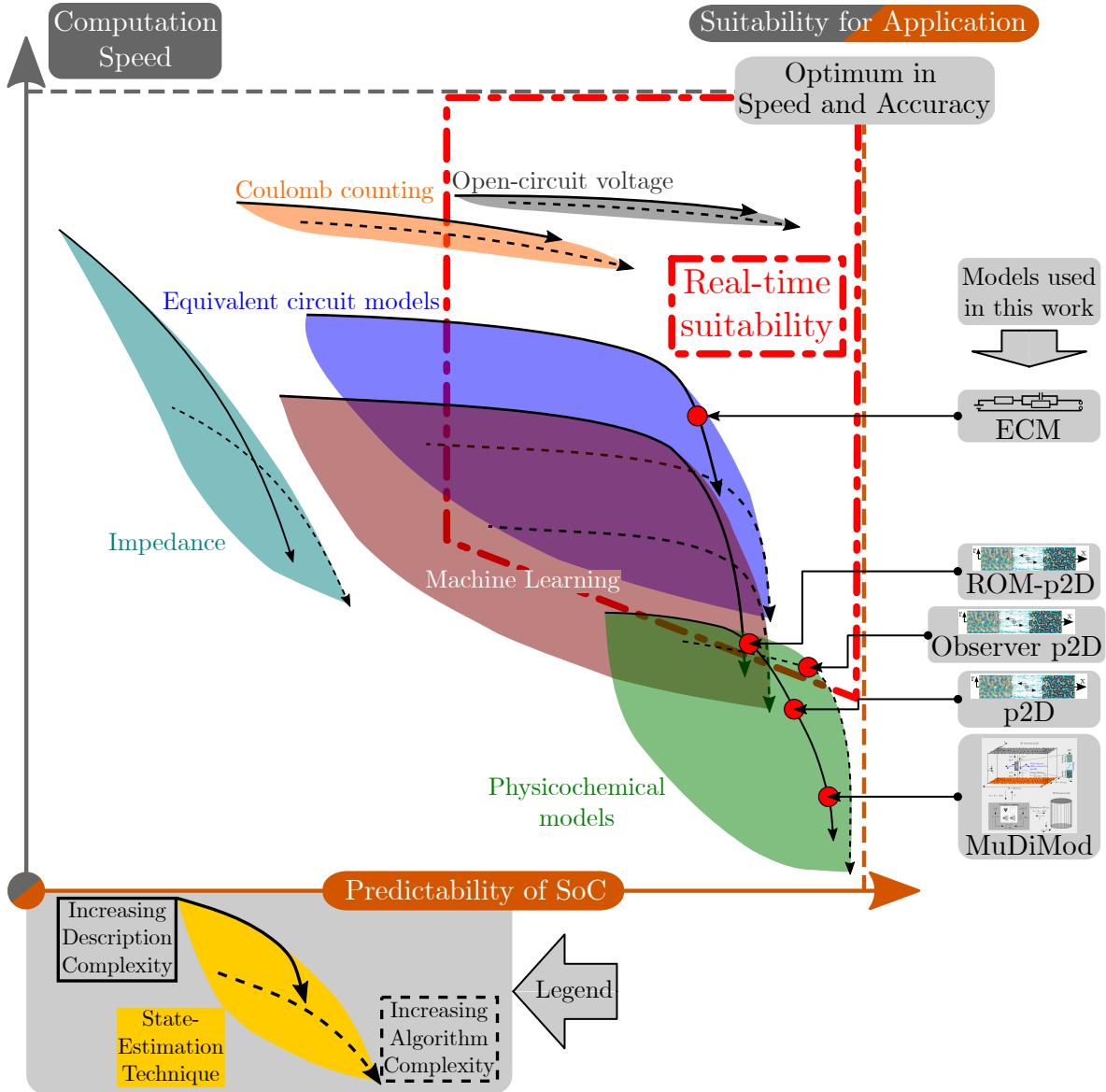

Figure 1.9: Correlation between the predictability of the SoC and the computation speed of selected state-estimation techniques, which were introduced in Fig. 1.8. Each colored area represents a group of estimation techniques, where the solid-line trend indicates the complexity of the description part for the LIB behavior and the dashed-line trend shows the increasing complexity for the state-estimation algorithm. The investigated models used in this work are depicted next to the chart under evaluation of combined predictability and computation speed (see circular marks in "red") for estimating the SoC. The figure is derived from the work of Zheng et al. [78].

first place (see algorithm trend in Fig. 1.9). Overall, a significant improvement of the suitability for application could be achieved by applying the aforementioned empirical extrapolation schemes [84, 85] for the relaxation process in LIBs, which can reduce the required rest periods for the state-estimation process.

Impedance   The complex correlation between the cell's impedance and its SoC [51] results in increased estimation errors coming with a low predictability, even if the complexity of the description and the algorithm is increased. The required gain in predictability at the cost of computational speed makes it rather challenging to meet real-time requirements. However, current research [61, 63, 82] pushes the development of embedded implementations, which are expected to improve the real-time suitability of this method in future.

Machine Learning   Machine learning approaches [88, 111–113] tend to be more complex than model based estimation routines based on an ECM, which inevitably results in lower computational speed. Computationally simplified mathematical descriptions and solver algorithms are partly suitable for real-time estimation of the SoC and with future increasing computational capability of MCs in the BMS, a broader application of this method can be expected. However, increasing the predictability with online operational data remains a big challenge and limits the gain in SoC accuracy for more complex techniques, leading to a deceleration of the underlying calculations.

Equivalent circuit models   The most common model based technique for real-time SoC estimation incorporates an ECM to describe the cell together with a filter [90, 91] such as a KF [90, 114–119]. Increasing the complexity of the model can significantly increase its predictability. However, already complex models, such as an ECM with several resistor and capacity parallel circuits (RCs) show a low gain in predictability whilst slowing down the computation [120, 121]. Sophisticated algorithms can similarly increase the predictability of the estimation technique as shown in Fig. 1.9, but also come with a reduced computation speed.

Physicochemical models   The group of physicochemical models is dominated by the complexity of the model itself [122] and the required extensive parametrization effort [101]. Consequently, the lowest computation speed appears compared to the other groups, whilst showing the highest predictability due to the mechanistic structure of the model. Common research efforts focus on reducing the complexity of the model to increase the computation speed, whereby physically meaningful reduction schemes or numerical reduction approaches are applied. Numerical methods use lean spatial discretizations, entire reformulation methods and/or advanced solving procedures [122, 123]. Increasing computational capacities on MCs in the BMS will further help to allow real-time computation in future. Up to now, little effort has been invested in the actual implementation of physicochemical models in a MC to investigate the performance under field-like computation resources [124], which will be addressed with the presented implementation into an embedded system as part of chapter 3 within this thesis [95]. The algorithm typically incorporates similar filtering techniques [99, 125–128] as for the ECM, but more effort is needed to develop the observer model due to the numerical structure of the physicochemical models. Extending physicochemical models to observer algorithms complicates the implementation and calculation, and makes it more time intense as seen in the trend of Fig. 1.9. The most complex and slowest SoC estimation appears for the physicochemical group, which, however, enables the most accurate prediction of all techniques.

The more accurate the chosen state-estimation technique becomes, the more efficient the operation of LIBs will effectively be, which is why the key motivation is to further study the suitability of physicochemical models for state-estimation purposes within this thesis, focusing on sufficient computation

speed, model accuracy and performance of the observer algorithms. Several physicochemical models are considered for this purpose, including a MuDiMod [39, 96, 129–134] and the original, well known p2D Newman-type model [94], which is widely used in the research field of LIBs [123, 135]. Especially for state-estimation purposes, numerically reduced variants of the p2D are favorable, which is why ROM-p2D approaches are developed via incorporating either physically meaningful simplifications [136, 137] or numerical reformulations [98, 138, 139] of the original p2D. Based on the reduced physicochemical models, recursive state-observer models are developed together with an extended Kalman filter (EKF) [99]. Fig. 1.9 summarizes the investigated models in this thesis and correlates them to the introduced state-estimation groups.

The MuDiMod describes the cell on multiple scales via considering thermal, electrical and electrochemical aspects resulting in higher predictability compared to the original p2D especially for larger-sized, i.e. commercial LIBs. The higher model accuracy is achieved with a more complex, spatially resolved model description, which decelerates the computation speed compared to the p2D. A comparison of the p2D and the MuDiMod approach is outlined in chapter 2 of this thesis. As a perspective, a MuDiMod based state-estimation is most likely not suitable for real-time calculation in MCs, but if sufficient hard- and software resources are available, a possible application could be in a mobile device such as a tablet computer, which typically incorporates only a single large pouchbag LIB. The computational resources could be offered within the operating system and hardware of the tablet computer. A numerically reduced variant of the MuDiMod can further reduce computational limitations [133]. The missing active cooling or heating management together with the geometrical cell size most likely cause a certain inhomogeneity of the lithium-ion concentrations, the potentials and the temperature across the cell's length and height. The cell states could thereby be estimated on multiple scales using a MuDiMod based state-estimation, which are crucial for determining the safety buffers at the boundaries of the operating window. If standard state-estimation techniques are applied, these safety buffers are expected to be oversized due to the model inaccuracy. Using a MuDiMod based state-estimation, smaller safety buffers can be defined at the limits of the operating window due to the increased model accuracy.

The application of reduction or reformulation schemes to the p2D are presented in chapter 3 and the resulting ROM-p2Ds offer real-time computation when embedded and solved on a MC [95] at a slightly lower predictability of the SoC. The computation speed is still significantly lower compared to the ECM as depicted in Fig. 1.9, but offers a valuable increase in predictability.

The extension to an observer p2D further increases the predictability due to the filtering process and is most likely still capable to fulfill real-time computation requirements as the applied extensions are not expected to overly increase the complexity [99]. This results in a deviation from the expected trend for physicochemically based state-estimation algorithms from the work of Zheng et al. [78], as such implementations [98] can meet real-time computation requirements as discussed in this thesis. Chapter 4 deals with the development of the observer p2D and the performance analysis of the physicochemical model based state-estimation process.

1.4 Review of Modeling Approaches for Lithium-Ion Batteries

The common drawback of black- or grey-box estimation approaches is the lack of insights into the occurring physicochemical processes within a LIB, which makes it impossible to fully understand the cell's behavior and, consequently, makes the choice of a suitable operation strategy a very complex task. To understand better and to predict the cell's behavior, model based techniques generally offer such

insights within the definition of their model structure. Within this section, an overview of phenomenological (grey-box) and mechanistic models is presented and discussed in terms of their suitability for state-estimation. Fig. 1.10 shows an assessment of the selected models in terms of computation speed and predictability of the SoC. The trend of decreasing computation speed for increasing predictability of the presented models in Fig. 1.10 is based on the classification of the physicochemial state-estimation group [78], shown in Fig. 1.9. The trend must be seen as an assumption as the correlation between the models and the precise definition of the predictability remain complex to determine. In general, a
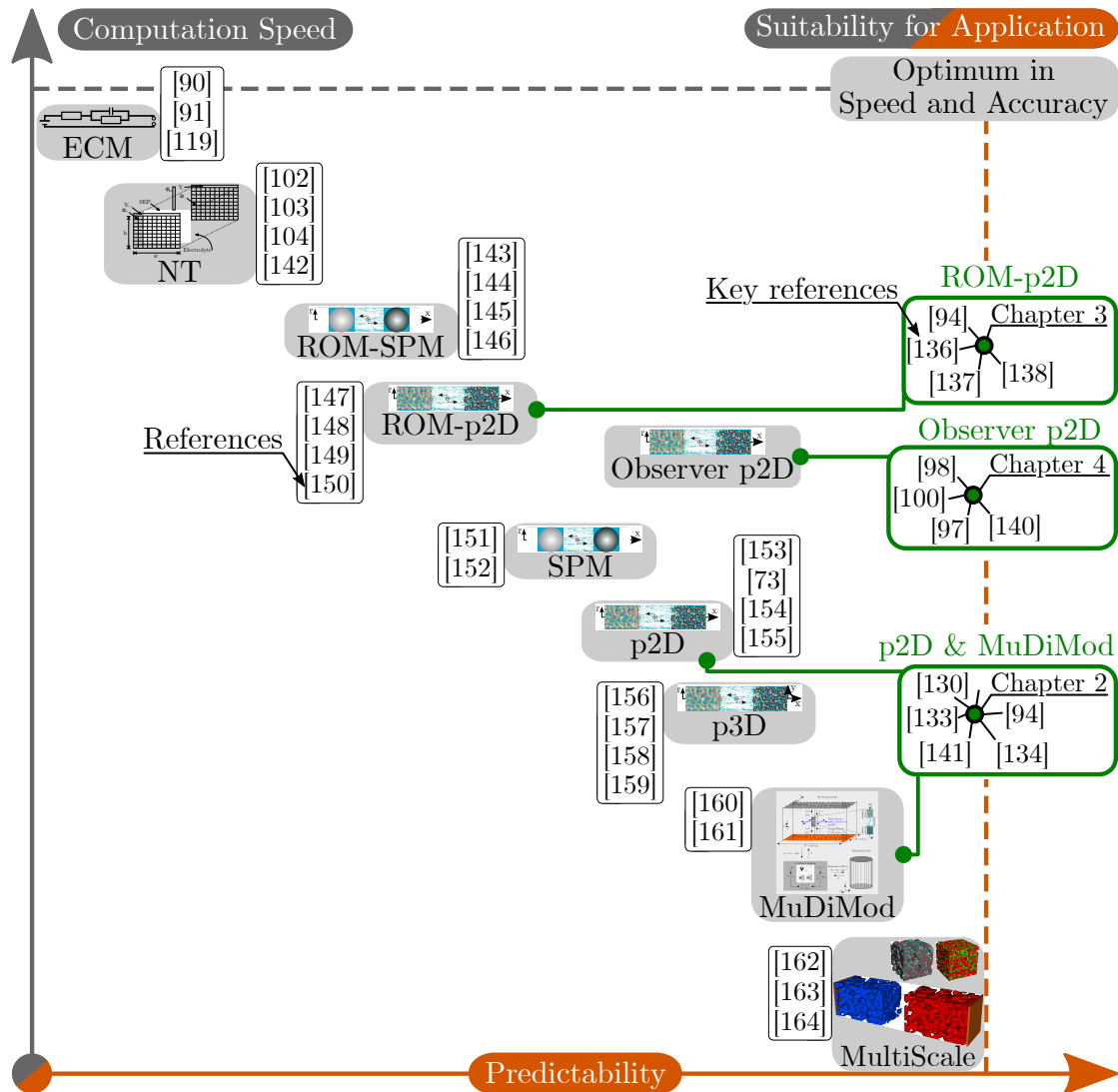

Figure 1.10: Comparison of phenomenological (ECM and NT) and mechanistic (ROM-SPM, SPM, ROM-p2D, p2D, Observer p2D, pseudo three-dimensional model (p3D), MuDiMod and MultiScale) models from literature focusing on the predictability of the cell's behavior and the computation speed. The green boxes on the right-hand side refer to the investigated models in this thesis and the relevant key references from literature. The extension of the p2D to the observer p2D is shown in the upper part on the right-hand side of the graph with its relevant key references from literature. The figure is derived from several works [52, 123] and includes state-of-the-art models from the research field [98] [100] [97] [140] [94] [136] [137] [138] [130] [133] [141] [134] [91] [90] [119] [102] [103] [104] [142] [143] [144] [145] [146] [147] [148] [149] [150] [151] [152] [153] [73] [154] [155] [156] [157] [158] [159] [160] [161] [162] [163] [164].

more complex physical model structure comes with a higher mathematical description resulting in a slowdown of the computation process. In the following, each model depicted in Fig. 1.10 is discussed in terms of predictability of the SoC and computation speed.

ECM The electrically motivated empirical model is the most commonly used approach for state-estimation of LIB applied in the field. The voltage source describes the correlation of OCV and SoC and is typically set in series to RCs [165] to imitate the physicochemical behavior with a purely electrical equivalent circuit structure. Typically, a single resistor is set in series to account for ohmic losses in the LIB. Different quantities of RCs are used in literature, that define both model complexity and parametrization effort [121]. An optimum in predictability and computation speed for state-estimation purposes was found to be an ECM incorporating a single RC element [120]. A typical application uses an ECM together with filtering approaches [90, 91, 118, 166, 167] to improve the estimation accuracy via reducing the variance between the model predicted and measured cell voltage [119, 121]. Compared to the other models shown in Fig. 1.10, the lean mathematical model structure enables a fast solving process, that results in the highest computation speed [95]. The ECM for the MJ1 LIB is presented in chapter 3 of this thesis.

NT The semi-empirical approach based on the work of Newman and Tiedemann [102] is typically used to characterize the current density between two planar electrodes [103], that is used to describe the current density distribution across the active electrode area. The polarization of the cell is approximated by a linear correlation of current flow and overvoltage with respect to a linearized OCV, which is valid for cells showing low ohmic potential drops across the electrodes, such as pouchbag LIBs [103]. The simplicity of the NT and its accuracy to describe the cell's behavior offers over a broad current range fast computation of local imbalances in current density and potential across the electrodes at an acceptable parametrization effort, whereby mainly global states, such as the terminal voltage, the current flow and the surface temperature, are required. The physicochemically meaningful approach can be used for analyzing cell designs in combination with multidimensional model frameworks [104], the effect of the interconnection of several cells on the inhomogeneity of temperature and SoC [142], or as an alternative approach for state-estimation of pouchbag LIBs, as discussed before. However, predictability becomes insufficient, if in-plane voltage losses are non-negligible in comparison to the potential drop through the electrode stack. This is evoked in cylindrical cells, especially for a single-tab design applied to the current collectors [39]. The model structure is not predestined for traditional state-estimation as the ECM, but can be used as a computational efficient and physicochemically meaningful approach to describe the physicochemical behavior of LIBs to a certain extent.

p2D This mechanistic model is based on concentrated solution and porous electrode theory, combined with electrode kinetics [94]. In contrast to the ECM, the fundamental equations of mass transport, solid and liquid potential, charge balance and reaction kinetics are spatially defined along the thickness of both electrodes and the separator, and in the second, pseudo particle domain. The description of the cell's physicochemical behavior along its relevant length scales results in a differential algebraic equation system. This is complex and time intense to solve, compared to the ordinary differential equation system of the ECM. A significant increase in the calculation time [95] appears for the p2D, as shown in Fig. 1.10. However, the benefit in predictability offers not only a more accurate estimation of the inherently incorporated SoC, but also physicochemically meaningful extensions of the model to predict e.g. a cell's aging behavior [73, 74, 153, 168]. Moreover, rate limiting effects under high current scenarios [154, 169] or impacts of mechanical swelling on the inherent transport processes [155, 170] can be investigated. The p2D offers significant potential of accurate state-estimation of LIBs, but the computation process and the parametrization effort with at least 34 parameters is

challenging. Optimized parametrization of the p2D is currently attracting more and more attention in the research field including the usage of artificial neural networks [171], combining a variety of experimental techniques [101, 172] and/or using locally measured potentials from reference electrode signals [173]. The parametrization and validation for the SiC/NMC-811 MJ1 LIB via using a variety of experimental methods is shown in chapter 2. The complexity of the model structure is reduced via physically (see **SPM**) and/or numerically motivated reduction (see **ROM-SPM** and **ROM-p2D**) to enable real-time suitability of physicochemical models.

SPM   In a SPM, to decrease the complexity of the p2D, the active particle domain is reduced to a single particle instead of a spatial distribution of equally sized, spherical particles along the electrode thickness [151]. The concentration distribution within the electrolyte is typically neglected for the standard SPM [151], which gains significant computation speed due to neglecting the complex partial differential equations in the solving process. Albeit the benefit in computation speed, the predictability overly decreases at C-rates higher than 1C, as the transport processes in the electrolyte are becoming more dominant, which are inherently neglected by the SPM approach [152]. Moreover, the description of aging effects such as lithium plating is significantly affected by the state of the electrolyte, which makes the SPM unsuitable to predict an accurate anode potential. Therefore, an extended version of the SPM exists, which considers the concentration distribution within the electrolyte [152]. Nevertheless, the resulting, solid concentration gradients through the thickness of the electrodes are neglected in all variants of the SPM. The SPM performance can be categorized in between the p2D and its ROM variant as shown in Fig. 1.10.

ROM-SPM and ROM-p2D   The most straightforward spatial discretization of the incorporated partial differential equations can be calculated via the finite difference method (FDM) [94, 95, 99]. A variety of more efficient numerical discretization schemes is discussed in literature [135], which aim for a reduction in the mathematical complexity evoked by the non-linear differential algebraic equation system of the p2D. The non-linearity is caused by the dependency of several parameters on the actual solving states, such as the concentration dependency of the equilibrium potentials or the electrolyte diffusivity and conductivity. The solution of single equations can be approximated [136, 137, 147], which is especially useful for the diffusion equation in the solid particle phase, as it dominates the total number of equations to be solved [95, 99]. Other methods reformulate differential algebraic equation system to a mathematically more beneficial form, which is commonly realized with Padé approximations [148, 149], asymptotic reductions [150], or orthogonal decomposition schemes [98, 138, 139]. Two approximation schemes incorporating polynomial [136] or eigenfunction [137] approximation of the solid phase diffusion equation and a reformulation of the differential algebraic equation system using orthogonal collocation [98, 138, 139] are presented and discussed in chapter 3. The numerical reduction schemes applied to the SPM are similar to the p2D, such as polynomial approximations [144] or asymptotic schemes [143, 145, 146]. They show promising results in accuracy and computation speed. However, this model approach is neglected in this thesis as a spatial distribution of lithium-ion concentrations and potentials throughout the electrodes and the electrolyte is expected to have a significant impact on the LIB's behavior in the simulated case studies. As shown in Fig. 1.10, the ROM-SPM calculates faster than the ROM-p2D at the expense of a lower predictability due to the physical reduction of solid and/or liquid mechanisms. Nevertheless, both reduced variants result in significant modeling errors caused by the applied reduction techniques, which reveals a trade-off between modeling error and computation speed. The modeling errors for the ROM-p2Ds are discussed in chapter 3.

Observer p2D   To reduce modeling and parametrization errors and to filter measurement noise [97], observer p2Ds commonly incorporate a ROM-p2D [100] together with a non-linear filtering technique such as an EKF [140]. Different model structures have been discussed in literature, such as the combination of orthogonal collocation for the p2D and an EKF [98], which accounts for both temperature and cell voltage variance in the filtering process. The results suggest a robust state-estimation under various operational conditions and the applied model reduction indicates sufficient computation speed on desktop computers [97, 98]. A performance analysis in embedded systems such as a MC is skipped within that work, which applies to most of the works in this research field. As shown in Fig. 1.10, the use of an observer p2D benefits from using fast calculating ROM-p2Ds and the usage of filtering techniques to limit the loss in predictability. Therefore, a faster computation can be achieved compared to the p2D and the SPM, and a higher predictability appears compared to their reduced variants. Two observer p2D approaches are presented and their estimation results of various fast charging scenarios are discussed in chapter 4. The observer structures include a ROM-p2D with either a polynomial [136] or an eigenfunction [137] approximation for the solid phase diffusion equation, each combined with an EKF [99].

P3D   Extending the p2D domain by either the height [156] or the length [158] of the electrode stack, effects of electrode size on the physicochemical cell behavior can be analyzed, which is typically used for cell design optimization. Single [156] or multiple stacked electrode pairs [157–159] have been modeled to investigate effects of aging [157] or mechanical swelling [158]. Orthogonal collocation is also applied for such a p3D [156], which claims to be robust and sufficiently fast when carrying out the calculation on a desktop computer. However, the implementation on MCs comes with limited memory resources and calculation power, which makes these approaches unfavorable for state-estimation purposes.

MuDiMod   Multidimensional multiphysics models are capable of considering the current flow in the current collector foils and the physicochemical behavior is simulated along both the height and the length of the electrodes. The models are typically used to investigate and to optimize cell design and/or operational strategies for pouchbag [130, 132–134, 141, 160], cylindrical [39, 96, 129, 134, 141, 161] and prismatic [134, 141] cell formats. With the aid of a MuDiMod, size effects of the electrodes [134], the tab design at the current collector foils [39] or thermal cooling conditions, such as tab or localized cooling at the cell's surface [96, 174, 175], can be investigated. The multidimensional model structure can be a continuum [141] or a composition of physicochemical, electrical and thermal submodels [39, 96, 129, 130, 132–134, 160, 161] defined on their relevant length scales in the cell. The usage of submodels comes with a benefit in computation time and orthogonal collocation schemes [133] can be used to accelerate the calculation process. In comparison to the p2D, a significantly enhanced predictability of the cell's behavior can be achieved coming with a significantly reduced computation speed as shown in Fig. 1.10. In contrast to the MuDiMod, the p3D incorporates either the height or the length as additional dimension of the electrodes, whereas the MuDiMod considers both of them. A possible application could be the state-estimation of a LIB within a mobile tablet computer as mentioned before, where the built-in soft- and hardware resources provide sufficient computation capacity. For embedded state-estimation approaches, frameworks such as the MuDiMod are of less interest as the model complexity and computation effort excludes real-time computation on MCs. The parametrization and model structure [39] of the MuDiMod is presented in chapter 2. The MuDiMod approach is used to identify the modeling error of a p2D, which is evoked by spatial inhomogeneity in lithium-ion concentrations, potentials and temperature across a cell's current collectors within a spirally wound configuration. With the aid of the derived modeling error, more accurate limits of the operating window can be estimated for a LIB [39].

MultiScale model   More complex modeling of the physicochemical behavior of a LIB comprises multi-scale approaches, which include a 3D micro-structural domain to describe the geometrical structure of the porous domains. The physicochemical equation system is solved on the complex 3D structure of the electrode stack. Fast charging optimization [164] and design analysis on multiple physical scales [162, 163] are common research topics. This model type offers the highest level of predictability of the selected models, depicted in Fig. 1.10. However, it is not suitable for real-time state-estimation application due to the model complexity and the slow computation speed.

The presented model review emphasizes the p2D as a promising candidate to offer sufficient computation speed and predictability for further development to a physicochemical based state-estimation algorithm for LIBs. The benefits of estimating internal states to describe the battery's inherent condition can be fully exploited as long as the computation of the p2D is fast enough and its model accuracy is not restricted by physical or numerical reduction schemes. Real-time suitable observer p2D are most promising for application in advanced control strategies of the BMS. Multidimensional approaches are rather suitable for design optimization than for state-estimation of LIBs and as well helpful to evaluate the modeling error of the p2D, if local inhomogeneities within the battery can be expected. The p2D is believed to address and solve several of the current and prospective issues of LIB technology such as accelerated aging evoked by fast charging procedures.

Within this thesis, the development of a p2D based state-estimation algorithm is presented and includes the following main development steps: parametrization, validation, model reduction and the extension to an observer model. One of the main obstacles is the computational complexity of the p2D, which is mainly caused by the incorporated differential algebraic equation system presented in the following section. The equation system consists of partial and ordinary differential equations as well as algebraic equations to describe the electrochemical-thermal mechanisms, which is complex to implement and to solve. Model reduction is crucial to simplify the computational complexity and make it applicable for requirements of embedded systems and the extension to an observer model.

1.5 Mechanisms of Physicochemical Modeling and Simulation

The p2D reduces the structure of a LIB to an electrochemical unit cell and describes the main mechanisms along the thickness of a single electrode stack, consisting of anode, separator, and cathode. The first geometrical dimension of the model is defined along these thicknesses and the second geometrical dimension defines the domain of the active material particles in both electrode domains, which are specified to spherical shape [176]. The coupling between the geometrical dimensions is implemented via a scalar describing the electrode kinetics under the assumption, that the solid diffusion process of lithium-ions along the thickness of both electrodes is negligible [94, 176, 177]. As a result, the p2D incorporates two geometrical domains coupled via a scalar, which is why the term "pseudo 2D" is used. The thermal sensitivity can be considered with a 0D temperature submodel, where the temperature is assumed to be uniform in the electrochemical unit cell. Within this section, the fundamental differential algebraic equation system of the p2D is presented together with the extension of a 0D thermal model. The differences between the modeling approach of the p2D and the MuDiMod are discussed in terms of describing the electrochemical behavior along the spatial dimensions of the electrode stack and in terms of modeling the thermal behavior. The explanation of the different modeling perspectives helps to understand better the modeling error of the p2D caused by neglecting spatial imbalances of lithium-ion concentrations, potentials and the temperature in the electrode stack.

1.5.1 Model Structure of the Pseudo Two-Dimensional Model

The structure of the p2D consisting of its differential algebraic equation system is illustrated in Fig. 1.11. If not indicated otherwise, the description within this section is based on the fundamental works of Doyle, Fuller, Newman and Thomas [94, 176–178]. The electrochemical unit cell approach is a volumetric representative of the entire cell, where the main dimension is defined by the x-coordinate along the thickness of anode, separator, and cathode domain. The current collectors are assumed to be of infinite electrical conductivity along the x-coordinate and are therefore not described. A volume averaging approach is applied in the three domains using porous electrode theory. The porous electrodes and separator domain can be modeled by using a superposition of the liquid electrolyte phase and the solid electrode phase including the active material. The reaction at the interface between the electrolyte and the active material is described as a homogeneous reaction in the mass balances using volume superposition and the interfacial area between the solid and liquid phase. The volume share of the electrolyte ε_l is defined in each domain by the porosity of the electrodes and the separator. The solid electrode phase is distinguished into an inert volume share $\varepsilon_{s,na}$, such as binder or conductive additives [23], and an active material volume share ε_s. The active material phase is typically described as spherical particles and incorporates insertion type materials for both electrodes. The volume shares summarize in each domain to

$$\varepsilon_l + \varepsilon_{s,na} + \varepsilon_s = 1 \tag{1.4}$$

The active particle phase in both electrode domains is represented with a second dimension, which is described with the r-coordinate. A geometrical and physical coupling ensures the coherence between the main x- and the r-dimension. The porous separator consists of an non-active solid phase and only mass transport in the liquid electrolyte within the pores is considered. Four main variables are solved in the domains and over time t, such as the concentration of intercalated lithium-ions in the active particles c_s, the concentration of solvated lithium-ions in the electrolyte c_l as well as the corresponding solid phase potential Φ_s and liquid phase potential Φ_l. The molar flux j_n is calculated in the anode and cathode domain to define the physical coupling between the liquid and solid phase. The temperature T is calculated in a separate 0D thermal model.

The transport of solvated lithium-ions in a typically used binary electrolyte consisting of a conductive salt and a solvent is based on the concentrated solution theory, where the local variation of the electrochemical potential of an ionic species (i.e. lithium-cation and solvent-anion) evokes diffusion and migration along the x-coordinate. The partial differential equation can be set with considering the porosity ε_l in each electrode domain as

$$\varepsilon_l \frac{\partial c_l(x,t)}{\partial t} = \frac{\partial}{\partial x}\left(D_l^{\text{eff}} \frac{\partial c_l(x,t)}{\partial x} + \frac{i_l(x,t)\left(1 - t_+^0\right)}{F} \right) \tag{1.5}$$

The equation changes in the separator domain, where no reaction occurs and consequently the second term on the right side equals to zero as shown in Fig. 1.11. In general, the diffusion coefficient D_l, the liquid current density i_l in reference to the cross-sectional area A_{act} of the electrode, and the transference number t_+^0 characterize the transport in the electrolyte. The symbol F represents the Faraday constant. The transference number represents the part of the cationic current density. A relation to the velocity of a reference species in the solution ("0") appears herein, which is typically the solvent [177] and is assumed to be constant within this thesis.
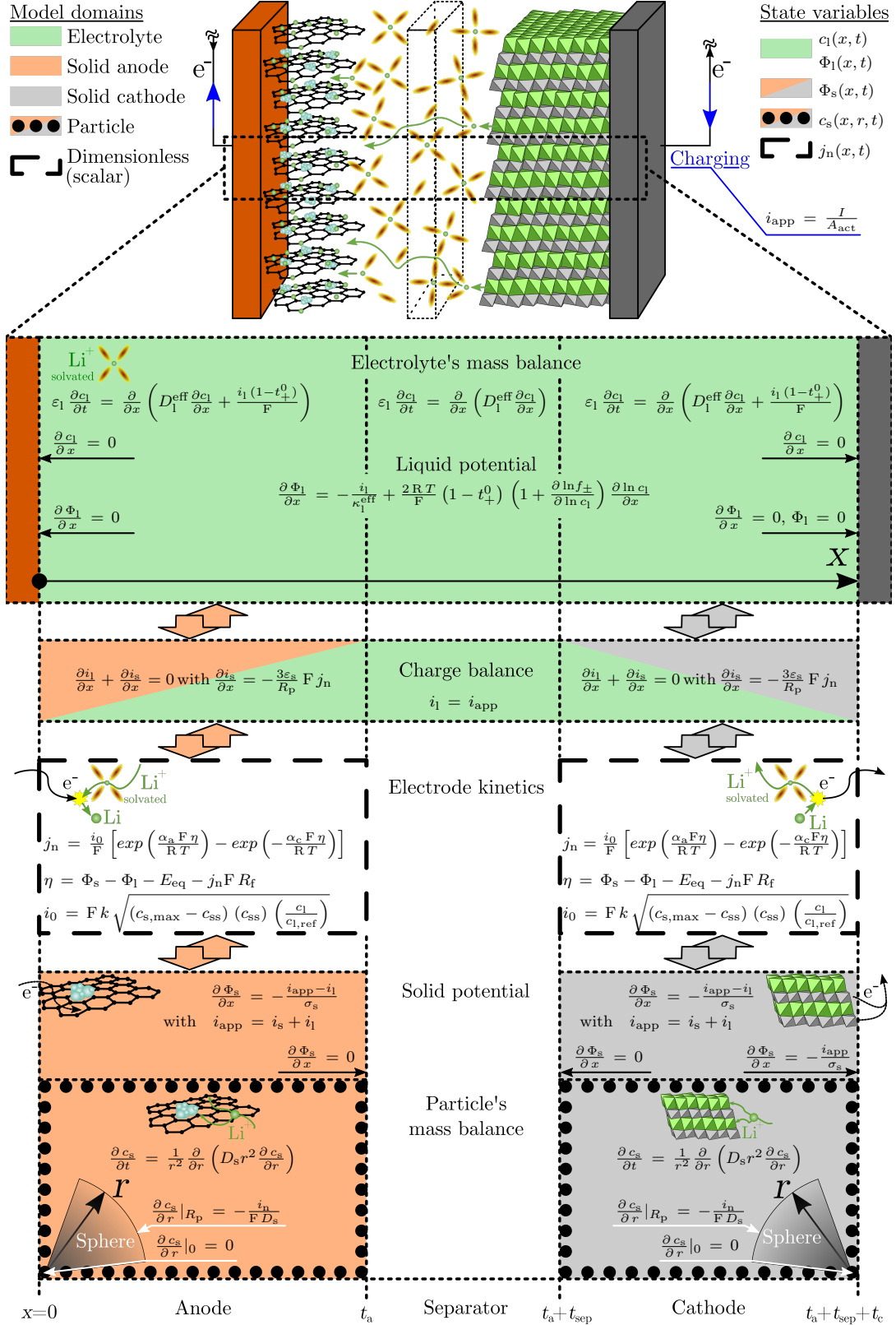
Model domains
- Electrolyte
- Solid anode
- Solid cathode
- Particle
- Dimensionless (scalar)

State variables
- $c_l(x,t)$
- $\Phi_l(x,t)$
- $\Phi_s(x,t)$
- $c_s(x,r,t)$
- $j_n(x,t)$

e^-

Charging

$i_{app} = \dfrac{I}{A_{act}}$

$\text{Li}^+_{\text{solvated}}$

Electrolyte's mass balance

$$\varepsilon_l \frac{\partial c_l}{\partial t} = \frac{\partial}{\partial x}\left(D_l^{\text{eff}} \frac{\partial c_l}{\partial x} + \frac{i_l\,(1-t_+^0)}{\text{F}}\right)$$

$$\varepsilon_l \frac{\partial c_l}{\partial t} = \frac{\partial}{\partial x}\left(D_l^{\text{eff}} \frac{\partial c_l}{\partial x}\right)$$

$$\varepsilon_l \frac{\partial c_l}{\partial t} = \frac{\partial}{\partial x}\left(D_l^{\text{eff}} \frac{\partial c_l}{\partial x} + \frac{i_l\,(1-t_+^0)}{\text{F}}\right)$$

$\frac{\partial c_l}{\partial x} = 0$

$\frac{\partial c_l}{\partial x} = 0$

Liquid potential

$$\frac{\partial \Phi_l}{\partial x} = -\frac{i_l}{\kappa_l^{\text{eff}}} + \frac{2\,\text{R}\,T}{\text{F}}\left(1-t_+^0\right)\left(1+\frac{\partial \ln f_\pm}{\partial \ln c_l}\right)\frac{\partial \ln c_l}{\partial x}$$

$\frac{\partial \Phi_l}{\partial x} = 0$

$\frac{\partial \Phi_l}{\partial x} = 0,\ \Phi_l = 0$

x

Charge balance

$$\frac{\partial i_l}{\partial x} + \frac{\partial i_s}{\partial x} = 0 \text{ with } \frac{\partial i_s}{\partial x} = -\frac{3\varepsilon_s}{R_p}\text{F}\,j_n$$

$i_l = i_{app}$

$$\frac{\partial i_l}{\partial x} + \frac{\partial i_s}{\partial x} = 0 \text{ with } \frac{\partial i_s}{\partial x} = -\frac{3\varepsilon_s}{R_p}\text{F}\,j_n$$

Electrode kinetics

e^- $\quad \text{Li}^+_{\text{solvated}}$ $\quad$ Li

$\text{Li}^+_{\text{solvated}}$ $\quad e^-$ $\quad$ Li

$$j_n = \frac{i_0}{\text{F}}\left[exp\left(\frac{\alpha_a\,\text{F}\,\eta}{\text{R}\,T}\right) - exp\left(-\frac{\alpha_c\,\text{F}\,\eta}{\text{R}\,T}\right)\right]$$

$$\eta = \Phi_s - \Phi_l - E_{eq} - j_n\text{F}\,R_f$$

$$i_0 = \text{F}\,k\sqrt{(c_{s,\max}-c_{ss})\,(c_{ss})\left(\frac{c_l}{c_{l,\text{ref}}}\right)}$$

$$j_n = \frac{i_0}{\text{F}}\left[exp\left(\frac{\alpha_a\text{F}\eta}{\text{R}\,T}\right) - exp\left(-\frac{\alpha_c\text{F}\eta}{\text{R}\,T}\right)\right]$$

$$\eta = \Phi_s - \Phi_l - E_{eq} - j_n\text{F}\,R_f$$

$$i_0 = \text{F}\,k\sqrt{(c_{s,\max}-c_{ss})\,(c_{ss})\left(\frac{c_l}{c_{l,\text{ref}}}\right)}$$

Solid potential

e^-

$$\frac{\partial \Phi_s}{\partial x} = -\frac{i_{app}-i_l}{\sigma_s}$$

$$\text{with}\quad i_{app} = i_s + i_l$$

$\frac{\partial \Phi_s}{\partial x} = 0$

$$\frac{\partial \Phi_s}{\partial x} = -\frac{i_{app}-i_l}{\sigma_s}$$

$$\text{with}\quad i_{app} = i_s + i_l$$

e^-

$\frac{\partial \Phi_s}{\partial x} = 0$

$\frac{\partial \Phi_s}{\partial x} = -\frac{i_{app}}{\sigma_s}$

Particle's mass balance

Li

$$\frac{\partial c_s}{\partial t} = \frac{1}{r^2}\frac{\partial}{\partial r}\left(D_s r^2 \frac{\partial c_s}{\partial r}\right)$$

r

Sphere

$\frac{\partial c_s}{\partial r}\big|_{R_p} = -\frac{i_n}{\text{F}\,D_s}$

$\frac{\partial c_s}{\partial r}\big|_0 = 0$

Li

$$\frac{\partial c_s}{\partial t} = \frac{1}{r^2}\frac{\partial}{\partial r}\left(D_s r^2 \frac{\partial c_s}{\partial r}\right)$$

r

Sphere

$\frac{\partial c_s}{\partial r}\big|_{R_p} = -\frac{i_n}{\text{F}\,D_s}$

$\frac{\partial c_s}{\partial r}\big|_0 = 0$

$x=0$ $\qquad$ Anode $\qquad t_a \qquad$ Separator $\qquad t_a+t_{sep} \qquad$ Cathode $\qquad t_a+t_{sep}+t_c$

Figure 1.11: Overview of the p2D structure showing the three geometrical domains of anode, separator and cathode together with their relevant equations and boundary conditions. The related state variables are the liquid concentration c_l and the active particle concentrations c_s as well as the liquid potential Φ_l and the solid potential Φ_s. The molar flux j_n is evaluated in both electrodes and couples the particle domain and the electrolyte domain. The relevant partial differential equations (i.e. electrolyte's and particle's mass balance), ordinary differential equations (i.e. charge balance, liquid and solid potential) and the algebraic electrode kinetics equation are depicted in their operative domains together with the boundary conditions. The two relevant spatial coordinates are the x-coordinate along the electrode stack's thickness ($x \in [0, t_a+t_{sep}+t_c]$) and the r-coordinate ($r \in [0, R_p]$) in the particle domain beside the dependency in time t to solve non-stationary operation of LIBs. The figure is derived from Ref. [179].

The liquid diffusion coefficient D_l is significantly affected by the concentration of lithium-ions [180] and the temperature [181]. Prolonged transport lengths in porous media are considered via correction [182] in each domain as

$$D_l^{\text{eff}} = D_l \cdot \frac{\varepsilon_l}{\tau} = D_l \cdot N_M^{-1} \tag{1.6}$$

The ratio of tortuosity τ and porosity ε_l is called MacMullin number N_M. The transport correction can be applied with the Bruggeman correlation [183] for ideal spherical particles of identical size as

$$D_l^{\text{eff}} = \varepsilon_l^{1.5} \cdot D_l \tag{1.7}$$

The liquid current density is correlated to the liquid potential, which is defined via a virtual lithium reference electrode in the electrolyte at an arbitrary position along the thickness of the electrode stack to define the variation of the electrical state as

$$\frac{\partial \Phi_l(x,t)}{\partial x} = -\frac{i_l(x,t)}{\kappa_l^{\text{eff}}} + \frac{2\,R\,T}{F}\left(1 - t_+^0\right)\left(1 + \frac{\partial \ln f_\pm}{\partial \ln c_l(x,t)}\right)\frac{\partial \ln c_l(x,t)}{\partial x} \tag{1.8}$$

The electrolyte ionic conductivity κ_l and the activity coefficient $f_\pm$ reveal a significant concentration and temperature dependency, similar to the electrolyte diffusivity [180, 181]. The activity coefficient describes the mean electrostatic interaction between the lithium-cation and the solvent-anion. Transport correction due to the porous structure is applied to the ionic conductivity κ_l^{eff} as discussed before for the electrolyte diffusivity D_l^{eff}. The symbol R describes the universal gas constant.

The definition of the potential in the solid electrode phase follows Ohm's law. Kirchoff's law is used for the liquid current density i_l and the solid current density i_s in the anode and cathode domain as follows

$$\frac{\partial \Phi_s(x,t)}{\partial x} = -\frac{i_{\text{app}}(t) - i_l(x,t)}{\sigma_s} \quad \text{with} \quad i_{\text{app}}(t) = i_s(x,t) + i_l(x,t) \tag{1.9}$$

The parameter σ_s describes the effective electrical conductivity, which is measured for the porous electrode including active material, binder and additives such as conductive carbons. Usually it is not modified using transport correction as discussed for the transport processes in the electrolyte [131]. The solid and liquid current density flowing through the electrolyte and the electrode sums up to the globally applied current density i_{app} throughout the electrode stack, which is calculated from the applied current I and the representative cross-section of the electrode stack A_{act} as shown in Fig. 1.11. The cross-section of the electrode stack is defined perpendicular to the main x-dimension and represents the active electrode area.

The current density in the solid and the liquid phase are coupled via the charge balance as

$$\frac{\partial i_l(x,t)}{\partial x} + \frac{\partial i_s(x,t)}{\partial x} = 0 \tag{1.10}$$

The current flow drained by double layer effects is neglected within this thesis. The de-/intercalation reaction at each electrode's surface can be described as

$$s_- \text{Li}\Theta + s_+ \text{Li}^+ + s_0\Theta \leftrightarrows n \cdot e^- \quad \text{with} \quad s_- = 1,\ s_+ = -1,\ s_0 = -1,\ \text{and } n = 1 \tag{1.11}$$
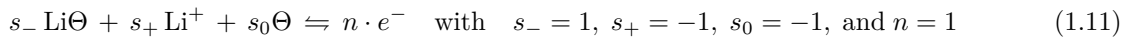
The reaction incorporates the intercalated Li Θ and the solvated Li$^+$ species as well as the host lattice Θ.

The reaction kinetics can be described with the Butler-Volmer equation as

$$j_{\mathrm{n}}(x,t) = \frac{i_0(x,t)}{\mathrm{F}} \left[exp\left(\frac{\alpha_{\mathrm{a}}\, \mathrm{F}\, \eta(x,t)}{\mathrm{R}\, T} \right) - exp\left(-\frac{\alpha_{\mathrm{c}}\, \mathrm{F}\, \eta(x,t)}{\mathrm{R}\, T} \right) \right] \tag{1.12}$$

Within this thesis, symmetric reaction kinetics are assumed, which equals the reactivity of intercalation and de-intercalation for each active material. As a consequence, the charge transfer coefficients $\alpha_{\mathrm{a/c}}$ are both set to 0.5.

The driving force for the reaction is the overpotential η. It is calculated as the potential drop between the electrolyte and the active particle phase in reference to the superficial electrode equilibrium potential E_{eq} and a possible potential drop across a film resistance R_{f} as follows

$$\eta(x,t) = \Phi_{\mathrm{s}}(x,t) - \Phi_{\mathrm{l}}(x,t) - E_{\mathrm{eq}}(x, r = R_{\mathrm{p}}, t) - j_{\mathrm{n}}(x,t)\mathrm{F}\, R_{\mathrm{f}} \tag{1.13}$$

R_{p} represents the radius of the active material particles, which are typically modeled as spheres within the p2D. Film resistances such as the SEI can be included in the p2D at the anode particle surface [168]. Optionally, a surface layer such as CEI [184] at the cathode could be applied, which is neglected within this thesis. The equilibrium potential E_{eq} vs. $\mathrm{Li/Li}^+$ shows a significant concentration and temperature dependency $\frac{\partial E_{\mathrm{eq}}}{\partial T}$, which is also known as entropic coefficient.

The exchange current density i_0 describes the amount of charge, that flows in an equilibrium state at the electrode surface whilst no actual de-/lithiation occurs

$$i_0(x,t) = \mathrm{F}\, k_{\mathrm{c}}^{\alpha_{\mathrm{a}}} \cdot k_{\mathrm{a}}^{\alpha_{\mathrm{c}}} \left(c_{\mathrm{s,max}} - c_{\mathrm{s}}(x, r = R_{\mathrm{p}}, t) \right)^{\alpha_{\mathrm{a}}} \left(c_{\mathrm{s}}(x, r = R_{\mathrm{p}}, t) \right)^{\alpha_{\mathrm{c}}} \left(\frac{c_{\mathrm{l}}(x,t)}{c_{\mathrm{l,ref}}} \right)^{\alpha_{\mathrm{a}}} \tag{1.14}$$

The exchange current density is characterized by the available sites in the host lattice ($c_{\mathrm{s,max}} - c_{\mathrm{s}}(x, r = R_{\mathrm{p}}, t)$), the lithium-ion concentration at the particle surface $c_{\mathrm{s}}(x, r = R_{\mathrm{p}}, t)$ and the available lithium-ions in the electrolyte c_{l}. The surface concentration of the active material particles ($c_{\mathrm{s}}(x, r = R_{\mathrm{p}}, t)$) is often defined as c_{ss}, as shown in Fig. 1.11. The maximum concentration of lithium-ions in the active material is defined as $c_{\mathrm{s,max}}$. The reaction rate constant k is specified into the anodic k_{a} and the cathodic k_{c} path with the corresponding charge transfer coefficients $\alpha_{\mathrm{a/c}}$, which are set to 0.5 (i.e. $\alpha_{\mathrm{a}} = \alpha_{\mathrm{c}} = 0.5$ and $k_{\mathrm{a}} = k_{\mathrm{c}} = k$). In this case, the reaction rate constants reduce to k and the exchange current density reveals a square root characteristic as shown in Fig. 1.11. A temperature dependency is assumed for the reaction kinetics [131] within this thesis, which is implemented via an estimated Arrhenius correlation [185]. The unit of the reaction rate constant is often used to correct the unit of the electrolyte term within the exchange current density [131]. In this thesis, the reference concentration $c_{\mathrm{l,ref}}$ is set to $1\,\mathrm{mol\,m}^{-3}$ to apply a physically meaningful unit of $\mathrm{m\,s}^{-1}$ to the reaction rate constant k.

The physical coupling between the x- and the r-domain incorporates the correlation of the pore wall flux j_{n} to the divergence of the macroscopic current density as

$$\frac{\partial i_{\mathrm{s}}(x,t)}{\partial x} = -\frac{3\,\varepsilon_{\mathrm{s}}}{R_{\mathrm{p}}}\, \mathrm{F}\, j_{\mathrm{n}}(x,t) = -\frac{3\,\varepsilon_{\mathrm{s}}}{R_{\mathrm{p}}} i_{\mathrm{n}}(x,t) \tag{1.15}$$

The geometrical coupling between the x- and the r-domain is set via the ratio of surface to volume of the spherical active particles, which is multiplied by the volume fraction of the active material phase

$$a_{\mathrm{s}} = \varepsilon_{\mathrm{s}} \frac{4\, R_{\mathrm{p}}^2\, \pi}{\frac{4}{3}\, R_{\mathrm{p}}^3\, \pi} = \frac{3\,\varepsilon_{\mathrm{s}}}{R_{\mathrm{p}}} \tag{1.16}$$

Considering the pore-wall flux perpendicular to the active particle surface, the diffusion of the intercalated lithium-ions is defined as mass balance in spherical coordinates as

$$\frac{\partial\, c_{\mathrm{s}}(x,r,t)}{\partial t} \;=\; \frac{1}{r^2}\frac{\partial}{\partial r}\left(D_{\mathrm{s}}r^2\frac{\partial\, c_{\mathrm{s}}(x,r,t)}{\partial r}\right) \quad\text{with}\quad j_{\mathrm{n}} = -D_{\mathrm{s}}\frac{\partial\, c_{\mathrm{s}}(x,r=R_{\mathrm{p}},t)}{\partial r} \qquad (1.17)$$

The spherical shape is justified for a wide range of active material types in LIBs. Typically an average particle radius R_{p} from the particle size distribution in the electrodes is used in simulation studies [39]. The solid diffusion coefficient D_{s} is often defined as a constant, albeit a dependency on the lithium-ion concentration [186, 187] and the temperature [186] is reasonable. Within this thesis, the temperature dependency is included via an estimated Arrhenius correlation [185]. Incorporating a non-linear concentration dependent solid diffusivity would increase the complexity of the model, which is not relevant for this thesis. Important remaining boundary conditions are depicted for each equation in Fig. 1.11. As the potentials in the solid and liquid phase must be defined to a reference, the potential boundary is set to zero for the liquid potential at the interface to the positive current collector [176]. Alternatively, the solid potential could also be set to zero at the interface to the negative current collector [188].

To conclude the electrochemical modeling of LIBs in this section, the differences between the model structure of the p2D and the MuDiMod are explained in the following. The p2D reduces a LIB to an electrochemical unit cell with lithium-ion concentrations and potentials being described along the thickness of anode, separator and cathode. The MuDiMod describes the spatial distribution of lithium-ion concentrations and potentials along the thickness of the electrode stack as well as the length and the height of the electrode stack. Herein, different geometrical structures of the electrode stack such as z-folding [169], spirally [39] or prismatically wound types [169] can be described together with their electrical-thermal interactions [131]. To describe the electrical interaction, Ohm's law is defined in the positive and negative current collector in a 2D electrical model to calculate the electrical potential distribution. The electrode stack domain in between both current collectors is described by several parallel connected p2Ds, which are coupled to the 2D model via the electrical potential and the current flow to include voltage losses along the current collector foils.

1.5.2 Thermal Extension of the Pseudo Two-Dimensional Model

The thermal sensitivity of the properties in a LIB can be described in the p2D with temperature dependent parameters, such as D_{l}, κ_{l}, $f_{\pm}$, $\frac{\partial E_{\mathrm{eq}}}{\partial T}$, k and D_{s} or a direct correlation in the model equations as included in the description of the liquid potential or the Butler-Volmer kinetics. The time constant of thermal processes such as heat conduction lies in a scale of several minutes up to an hour, which reveals a significant inertia compared to diffusion, reaction, and migration effects [81]. Due to the thermal inertia, the temperature calculation can be segregated [99] from solving solid and liquid concentrations and potentials, which implies a converged time step for the main variables of the p2D and a subsequent calculation of the temperature. As a side effect, the subsequent calculation of the temperature reduces the overall complexity of the p2D and accelerates the computation speed. Assuming a homogeneous temperature distribution along the thickness of the electrode stack (as shown in Fig. 1.11) seems valid, as the relevant length scales are in the range of several hundreds of micrometers (e.g. 179 μm for the MJ1 LIB [39]). Regarding the distribution within the entire cell, inhomogeneities can appear as experimental analysis revealed a significant temperature imbalance up to 5 K in cylindrical 18650 high energy LIBs under fast charging conditions [189]. The LIB's format, the applied cooling and operational condition can have a significant influence on the thermal imbalance, which should be well considered

for evaluating the validity of the p2D. A possible validation could be the model-to-model comparison between the p2D and the MuDiMod. Modeling errors caused by spatial imbalances in temperature, concentration and potential can be estimated, which could be used to improve the validity of the p2D. In terms of state-estimation for LIBs, the operational range estimated by a p2D can be corrected by a safety buffer to account for the neglected spatial imbalances, which can be determined by using MuDiMod studies.

The first step to extend the physicochemical p2D for describing thermal effects in LIBs is the calculation of an assumed homogeneous temperature, which is outlined in the following. The ordinary differential equation for calculating the temperature T can be defined as a 0D approach [178, 190].

$$V \, \rho_{\text{stack}} \, c_{\text{p}} \frac{\partial T(t)}{\partial t} \; = \; A_{\text{act}} \, q_{\text{p2D}}(t) - R_{\text{ext}} \, I(t)^2 - A_{\text{surf}} \, q_{\text{rad}}(t) - A_{\text{surf}} \, q_{\text{conv}}(t) - A_{\oslash} \, q_{\text{cond}}(t) \quad (1.18)$$

The mass density ρ_{stack} and the specific heat capacity c_{p} of the electrode stack are derived from a superposition of the single layers in a LIB [39], which are multiplied with the total volume V of the electrode stack to represent the total heat capacity. The heat exchange to the environment is typically described by heat convection q_{conv} and heat radiation q_{rad} at the relevant surface area A_{surf}. Additionally, heat conduction q_{cond} can be included representing heat transport via the electrical connection of the cell, which requires a mechanical contact at a defined cross-sectional area $A_{\oslash}$. The p2D neglects the current collectors and the spatial distribution of the current density along the in-plane dimensions of the electrode stack (i.e. length and height of the current collectors). As a result, the related in-plane heat generation caused by the current flow through the current collectors is not captured by the model. Therefore, an external heat source ($R_{\text{ext}} \cdot I^2$) is accountable for the ohmic resistance R_{ext} along both current collectors and possible electrical contact resistances such as welding seams at the cell terminals.

The heat generation of the electrode stack q_{p2D} refers to the cross-sectional area of the electrode stack A_{act} and can be calculated in a global manner ("g") as $q_{\text{p2D,g}}$ following the definition of Bernardi et al. [190].

$$q_{\text{p2D,g}}(t) \; = \; \left(E_{\text{eq}}(t) \, - \, E(t) \, - \, T(t) \frac{\partial E_{\text{eq}}(t)}{\partial T} \right) \, I(t) \quad (1.19)$$

This global heat generation term incorporates the cell voltage E and the equilibrium potential E_{eq} together with the entropic dependency $T \frac{\partial E_{\text{eq}}}{\partial T}$. The cell voltage and the equilibrium potential are calculated as [134, 154, 190]

$$E \; = \; \Phi_{\text{s}}|_{x=t_{\text{a}}+t_{\text{sep}}+t_{\text{c}}}(t) \, - \, \Phi_{\text{s}}|_{x=0}(t) \quad (1.20)$$

$$E_{\text{eq}} \; = \; \frac{1}{t_{\text{c}}} \int_{x=t_{\text{a}}+t_{\text{sep}}}^{t_{\text{a}}+t_{\text{sep}}+t_{\text{c}}} E_{\text{eq,c}}(\bar{c}_{\text{s}}) \, dx - \frac{1}{t_{\text{a}}} \int_{x=0}^{t_{\text{a}}} E_{\text{eq,a}}(\bar{c}_{\text{s}}) \, dx \quad (1.21)$$

The equilibrium state is evaluated with the average concentration in the active particles $\bar{c}_{\text{s}}$, which is typically included in approximations for the solid phase diffusion equation [94, 136, 137]. The calculation of the average entropic dependency follows the calculation of the equilibrium potential. Alternatively, an integral value $q_{\text{p2D},\int}$ considers the local heat generation in the solid and liquid phase as defined in several published works [39, 98, 188, 191, 192].

$$q_{\text{p2D},\int}(t) \; = \; q_{\text{r}}(t) \, + \, q_{\text{rev}}(t) \, + \, q_{\text{s}}(t) \, + \, q_{\text{l}}(t) \quad (1.22)$$

In detail, the generated heat from the occurring de-/intercalation reaction can be described as

$$q_\mathrm{r} = \frac{3\,\varepsilon_\mathrm{s}\mathrm{F}}{R_\mathrm{p}} \int_{x*} j_\mathrm{n}(x,t)\,\eta(x,t)\,\mathrm{d}x \qquad \text{with} \qquad x* = x \in [0, t_\mathrm{a}] \cup [t_\mathrm{a} + t_\mathrm{sep}, t_\mathrm{a} + t_\mathrm{sep} + t_\mathrm{c}] \quad (1.23)$$

which refers to the particle surface, the molar flux plus the overpotential, which is transferred via the specific surface to the main x-domain. The entropic heat is derived from the entropic coefficient and the molar flux within the same integral boundaries as before.

$$q_\mathrm{rev} = \frac{3\,\varepsilon_\mathrm{s}\,\mathrm{F}}{R_\mathrm{p}} \int_{x*} j_\mathrm{n}(x,t)\,T(t)\,\frac{\partial E_\mathrm{eq}(c_\mathrm{s}(x, r = R_\mathrm{p}, t))}{\partial T}\,\mathrm{d}x \qquad (1.24)$$

The ohmic heat in the solid phase is calculated from the potential drop and the macroscopic solid current density as

$$q_\mathrm{s} = \int_{x*} i_\mathrm{s}(x,t)\,\frac{\partial \Phi_\mathrm{s}(x,t)}{\partial x}\,\mathrm{d}x \qquad (1.25)$$

Similarly the liquid ohmic heat is derived in the electrolyte as

$$q_\mathrm{l} = \int_{x=0}^{t_\mathrm{a}+t_\mathrm{sep}+t_\mathrm{c}} i_\mathrm{l}(x,t)\,\frac{\partial \Phi_\mathrm{l}(x,t)}{\partial x}\,\mathrm{d}x \qquad (1.26)$$

In general, the global and the integral calculation reveal similar results. The integral heat generation enables a more detailed analysis of the overall heat generation and is used in chapter 2 of this thesis [39]. The global calculation is of lower computational complexity and thus easier to implement, which makes it more favorable for embedded systems and is used for the models presented in chapter 3 and 4 [95, 99]. The convective heat transfer is driven by the temperature difference to the environment and under assuming a constant ambient temperature T_∞ and a convective heat transfer coefficient α_conv, the equation can be written as follows [193]

$$q_\mathrm{conv} = \alpha_\mathrm{conv}\,(T(t) - T_\infty) \qquad (1.27)$$

A more detailed explanation and the calculation of the convective coefficient is presented in chapter 2. The radiation of heat is characterized by the emissivity ε_rad and follows a fourth order temperature dependency as follows [193]

$$q_\mathrm{rad} = \varepsilon_\mathrm{rad}\,\sigma_\mathrm{b}\,\left(T^4(t) - T_\infty^4\right) \qquad (1.28)$$

The symbol σ_b represents the Stefan-Boltzmann constant. Heat conduction phenomena are generally neglected within the p2D, but are of significant interest when a heat transfer via a mechanical contact is expected (e.g. electrical connection via copper connectors [39]) at a defined cross-section $A_\oslash$, heat conduction λ and a reference temperature T_ref with respect to the conduction path l [193].

$$q_\mathrm{cond} = \lambda\,\frac{T(t) - T_\mathrm{ref}(t)}{l} \qquad (1.29)$$

To conclude the thermal modeling of LIBs in this section, the differences between the temperature calculation in the p2D and the MuDiMod are explained in the following. The p2D assumes a uniform temperature for a LIB and neglects spatial imbalances, which can be caused by ohmic heating and voltage losses across the current collector foils, localized cooling effects or the anisotropic conduction

of heat within the electrode stack [39]. In contrast, the MuDiMod is able to describe these effects and their thermal interactions. Within the MuDiMod, the local heat generation in the 3D thermal model is superpositioned from the areal specific heat generation of the p2D submodels and the 2D electrical submodel, which are weighted with their volumetric shares at the electrode stack. The temperature distribution is calculated via the Fourier heat equation [193] using the local heat generation, ambient cooling conditions as well as heat conduction in the 3D thermal model. The calculated temperature is transferred from the 3D model back to the 2D model and the p2Ds. A sophisticated coordinate mapping function between the 2D model and the 3D model enables a numerically efficient, geometrical and physical coupling operation, which is capable of describing stacked and spirally wound configurations in pouchbag, cylindrical and prismatic cell formats [39, 134, 169]. A more fundamental explanation of the MuDiMod is given in chapter 2 of this thesis.

1.6 Thesis Outline

LIBs are most promising to fulfill future market needs, especially within the next decade for high energy electrical storage systems. A more efficient usage of current and future LIBs can be achieved by using advanced BMSs, which allow for a more accurate state-estimation with the aim of extending and optimizing the safe operating range whilst maximizing energy and power capability as well as guaranteeing a prolonged lifetime. Model based state-estimation techniques reveal high predictability in estimating the battery states due to their physically motivated structures. Especially physicochemical approaches are capable to predict not only global states, such as terminal voltage, current flow and surface temperature, but also internal states such as lithium-ion concentrations and potentials in the liquid and solid phase. The p2D is a promising approach to enable advanced state-estimation among the reviewed mechanistic models, but must be further adapted to find an optimum between computation speed and predictability.

The motivation of this work is to introduce a suitable state-estimation technique for embedded systems, which uses a properly validated electrochemical-thermal p2D approach with sufficient computation speed and model accuracy. Further predictability improvements are achieved via the extension to an observer model including an EKF and via accounting for the model error caused by neglecting the spatial distribution of concentration, potential and temperature. Furthermore, experimental characterization tests of short-circuit scenarios are analyzed with the aid of the MuDiMod to understand electrochemical rate limiting effects during high current scenarios and to study the impact of locality of the short-circuit event in the electrode stack. In addition, the aging behavior and its correlation to local distribution of mechanical swelling is experimentally investigated, which can be of high interest for an optimized operating range taking the entire lifetime of a LIB into account. In sum, the outline of this thesis is schematically shown in Fig. 1.12.

Within chapter 2, a variety of experimental techniques is presented to properly parametrize and validate the p2D for a high energy LIB. The parametrization is derived for a commercial SiC/NMC-811 LIB with a 18650 cylindrical format. The MuDiMod is parametrized and validated for the same cell to investigate the spatial inhomogeneity of lithium-ion concentration, potential and temperature within a LIB, which are assessed towards the impact of various current collector tab designs. The validity of the p2D to design optimized fast charging protocols is discussed with the model error between the p2D and the MuDiMod. The impact of the cylindrical cell format and the current collector tab design are investigated in the last section of chapter 2. A review of state-of-the-art cylindrical cell designs is presented, which incorporates a variety of commercial cylindrical LIBs. A wide simulation study

Chapter 1: Introduction to State-Estimation of LIBs

Models

Focused Topics

Relevance for BMS

Chapter 2

p2D
vs.
MuDiMod

Parameters & Validation | Fast Charging & Model Error | Format & Tab Design

SoC SoH
SoF SoS

Chapter 3

ECM
vs.
ROM-p2D
vs.
p2D

Real-time vs. Accuracy vs. Memory footprint

Micro-controller Implementation | Driving Cycle Operation

SoC SoH
SoF SoS

Chapter 4

ROM-p2D
&
Observer p2D

Extension to Observer with Filtering Algorithm | Charging Estimation

SoC SoH
SoF SoS

Chapter 5

MuDiMod

Correlation of Internal/Local and External Short-Circuits

SoS

Chapter 6

Correlation of Local Mechanical Swelling to Liftime

SoH

Chapter 7: Summary and Conclusion

Figure 1.12: The thesis outline illustrates the chapters 2 to 6 via the presented modeling and simulation content, the focused topics and the relevance for state-estimation in the BMS. Chapter 7 summarizes the main findings of this thesis in the summary and conclusion part.

of different cylindrical cell formats incorporating various single- and multi-tab designs is described by MuDiMods to investigate the in- and through-plane voltage drops along the current collectors and through the layers of the electrode stack. Optimized fast charging procedures are derived for various configurations of cylindrical formats and tab designs assuming application near cooling conditions. Due to the electrochemical-thermal structure of the p2D and the MuDiMod, the SoC, SoF and SoS can be correlated to the intrinsic model states of concentration, potential and temperature. The SoH is not actually represented via aging mechanisms in the presented models, but an anode potential algorithm is designed to prevent the onset of lithium plating during fast charging.

Chapter 3 presents model reduction and reformulation schemes for the p2D to address the issues of complexity and computation speed. The performances of the ROM-p2Ds are evaluated in terms of real-time computation, simulation accuracy as well as memory footprint and are compared to the performance of a state-of-the-art ECM. The ROM-p2Ds are implemented into a MC instead of using computational powerful desktop computers or work stations to emulate application conditions. Driving cycle operation is simulated and validated by measurement data of the modeled MJ1 LIB.

The development of to state-estimation algorithms based on the ROM-p2Ds and a non-linear EKF is presented in chapter 4. The physicochemically motivated observer p2D is used to describe a LIB under a variety of charging scenarios including CC, a multi-step profile incorporating a boost current (BC) period and pulsed current (PC) profiles. A detailed analysis of accuracy, speed and robustness is presented for the estimation results of global and local states.

Chapter 5 presents an excursion on short-circuit scenarios, as they are one of the most safety critical incidents for LIBs. Critical incidents in the application field show that short-circuits can exemplary be initiated by internal defects, such as separator penetration or external shorting between the battery terminals. To understand better the electrochemical processes during the early stages of the shorting scenario, a variety of experimental studies on single-layer pouchbag LIBs investigates external and internal/local short-circuits in a custom built quasi-isothermal test bench [169]. Thereby, the electrical and the thermal behavior of a LIB during short-circuits can be investigated at the same time. The simulation results of a high current and short-circuit modified MuDiMod helps to correlate the experimental data of both types of short-circuit scenarios and enables a classification of the intensity of the shorting scenario. The applied short-circuit tests do not trigger a thermal runaway, as the test bench guarantees quasi-isothermal conditions. The focus lies on understanding the electrochemical caused rate limiting effects, which occur during the shorting. The findings enable a better understanding of high current effects in LIBs, which are of high interest for the SoS estimation in the BMS.

Chapter 6 presents an aging study of pouchbag LIBs including a test matrix of different applied current rates and ambient temperatures to study their impact on the resulting linear and non-linear aging characteristics. A custom built laser test bench [170] is used to record the reversible and irreversible mechanical swelling of the cells during cyclic aging. The results show a significant correlation of local mechanical swelling across the active electrode area to the SoH decrease and the impedance rise of the LIBs. Possible lithium plating can be correlated to the non-linear aging characteristics, which underlines the importance of sophisticated state-estimation algorithms to avoid excessive aging side reactions. As a perspective, mechanical swelling of a LIB could be used as an alternative state, to estimate the SoH or the SoC of a LIB.

The presented results of the experimental short-circuit and mechanical swelling behavior of LIBs shown in chapter 5 and 6 provide the required insights to understand better the underlying mechanisms and develop suitable physicochemical modeling approaches in future. The resulting extensions of the modeling structure can then be used in advanced state-estimation techniques as well, which was out of

scope for this thesis. The last chapter 7 summarizes the presented content and concludes the main findings as well as closes with an outlook for future works subsequent to this thesis.

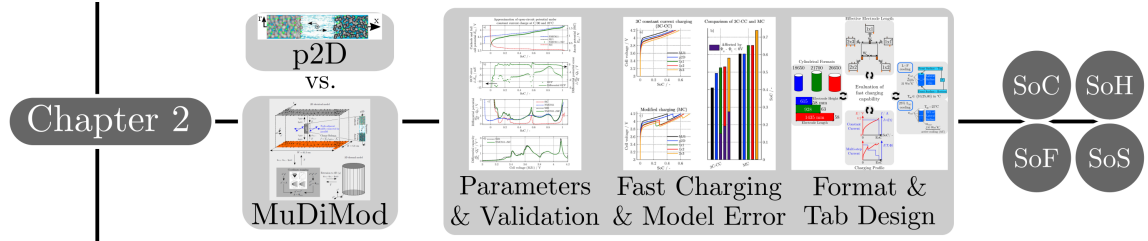# 2 Design of Optimized Operating Strategies using Physicochemical Models

Figure 2.1: Outline of chapter 2.

Within this chapter, the articles titled *Modeling and simulation of inhomogeneities in a 18650 nickel-rich, silicon-graphite lithium-ion cell during fast charging* and *Impact of Electrode and Cell Design on Fast Charging Capabilities of Cylindrical Lithium-Ion Batteries* are presented. First, the underlying model structure of the MuDiMod is presented in section 2.1. In the second section 2.2, the parametrization and experimental validation of the MJ1 LIB for the p2D and the MuDiMod are presented together with the results of optimized fast charging procedures and the error between the two models. In the last section 2.3, the impact of cylindrical formats such as 18650, 21700 and 26650 combined with single- or multi-tab design at the current collector foils are investigated towards the fast charging performance under application near cooling conditions. Fig. 2.1 refers to the thesis outline presented in section 1.6 and summarizes the content of the presented articles.

2.1 Spatial Inhomogeneity in Lithium-Ion Batteries addressed by Multidimensional Physicochemical Models

Increasing the energy density in LIBs comes with larger cell formats, longer or higher electrode sizes, increased coating thickness and an overall more densely packed electrode stack. As a consequence, inhomogeneity of the battery's local states, such as concentration, potential and temperature, tend to increase due to higher voltage losses along the electrode stack thickness, height and length as well as enhanced heat accumulation caused by the thermal inertia. Simulation approaches typically simplify a LIB to a unit cell and neglect local distributions of the inherent states. For example, the simplification for the p2D neglects the dimensions of the electrode length and height. The model validity can be reduced, especially under higher current loads as applied in fast charging scenarios [189]. Therefore, the modeling error of the p2D caused by the simplification can be evaluated using a multidimensional multiphysics model such as the MuDiMod, that intrinsically includes the spatial imbalance of utilization across the active electrode area. In extension to the presented p2D structure in the section 1.5, the fundamental equations of the MuDiMod are briefly outlined in the following.

A 2D electrical submodel accounts for the electrical potential φ_{cc} along the length and height of the current collectors by solving Ohm's law as

$$\boldsymbol{\sigma}_{cc} \nabla^2 \boldsymbol{\varphi}_{cc}(x', y', t) = \pm \frac{i_{p2D}(x', y', t)}{t_{cc}} \tag{2.1}$$

Several p2Ds are connected in parallel between the current collector foils in the 2D electrical model. Each p2D is joint at a single node using finite element method (FEM) for the spatial discretization applied to the 2D geometry. A linear interpolation [133] scheme calculates the 2D distribution of the through-plane current density i_{p2D}. The charge source is implemented by referring the current density to the thickness of each current collector t_{cc}, which is either implemented as source (+) or sink (−) for the positive and the negative current collector [39]. The electrical conductivity σ_{cc} typically describes the copper and aluminum properties for the negative and positive current collector. Both are assumed to show an isotropic behavior. The 2D structure of the model requires a spatial discretization and differentiation, as well as physical properties along the x'- and y'-coordinate along the length and height of the current collectors as

$$\nabla = \left(\frac{\partial}{\partial x'}, \frac{\partial}{\partial y'} \right)^{\mathrm{T}} \qquad \boldsymbol{\sigma}_{cc} = \begin{bmatrix} \sigma_{cc,x'} & 0 \\ 0 & \sigma_{cc,y'} \end{bmatrix} \tag{2.2}$$

The ohmic heating evoked by the current flow through the current collectors can be defined as

$$\boldsymbol{q}_{cc}(x', y', t) = t_{cc}\, \boldsymbol{\sigma}_{cc} \left(\nabla \boldsymbol{\varphi}_{cc}(x', y', t) \right)^2 \tag{2.3}$$

For the p2D, the resistance R_{ext} typically accounts for the ohmic heating in the current collector foils. In terms of the MuDiMod, this heat contribution can be locally resolved via Eq. 2.3.

The 3D thermal submodel calculates the temperature in a 3D geometry of the electrode stack according to the Fourier heat equation as [193]

$$\rho_{stack}\, c_{p} \frac{\partial \boldsymbol{T}(x'', y'', z'', t)}{\partial t} = \boldsymbol{\lambda} \nabla^2 \boldsymbol{T}(x'', y'', z'', t) + \boldsymbol{q}(x'', y'', z'', t) + \boldsymbol{q}_{\infty}(x'', y'', z'', t) \tag{2.4}$$

The 3D structure of the model requires spatial discretization and differentiation as well as physical properties along the x''-, y''- and z''-cartesian coordinates of the electrode stack. In case of a cylindrical format, the definition can use polar coordinates along the radius r'', the azimuthal angle ψ and the height z'' of the spirally wound jelly roll as

$$\nabla = \left(\frac{\partial}{\partial r''}, \frac{\partial}{\partial \psi}, \frac{\partial}{\partial z''} \right)^{\mathrm{T}} \qquad \boldsymbol{\lambda} = \begin{bmatrix} \lambda_{\perp} & 0 & 0 \\ 0 & \lambda_{\parallel} & 0 \\ 0 & 0 & \lambda_{\parallel} \end{bmatrix} \tag{2.5}$$

The heat conduction coefficient λ shows an anisotropic behavior. The heat transport perpendicular ($\perp$) to the single layers of the electrode stack is lower than parallel to the layers ($\parallel$) [39]. Typical values are in the order of magnitude of $1\,\mathrm{W\,m^{-1}K^{-1}}$ for the perpendicular [194–196] and $25\,\mathrm{W\,m^{-1}K^{-1}}$ for the parallel direction [196] of the electrode stack. The heat generation $\boldsymbol{q}$ is calculated from the p2Ds as presented in the section 1.5 and the 2D electrical model and weighted with their thickness shares χ at the total thickness of the electrode stack to gain a volumetric expression for the 3D model as follows

$$\boldsymbol{q} = \frac{\chi_{p2D}}{t_a + t_{sep} + t_c}\, \boldsymbol{q}_{p2D} + \frac{\chi_{cc,+}}{t_{cc,+}}\, \boldsymbol{q}_{cc,+} + \frac{\chi_{cc,-}}{t_{cc,-}}\, \boldsymbol{q}_{cc,-} \tag{2.6}$$

The resulting volumetric shares of the electrode stack, the negative and the positive current collector account to 92.1 %, 3.1 % and 4.8 % for the MJ1 LIB. Referring to the thickness in Eq. 2.6 for each heat generation part enables the calculation of the required 3D volumetric variable for the 3D thermal model. Finally, heat losses to the environment q_∞ can easily be included in the 3D model, such as convective cooling or heat radiation at the surface of the 3D thermal model [39].

With the aid of the MuDiMod, the inhomogeneity in utilization of a LIBs can be investigated on multiple scales, which cannot be offered by the p2D. The derived error of the p2D in reference to the MuDiMod can be used to optimize the model predicted operating range of a LIB. In terms of p2D based state-estimation, a more precise estimation of the SoC, SoF and SoS can be achieved via accounting for spatial imbalances of concentrations, potentials and temperature without actually implementing a computationally complex multidimensional multiphysics model. In terms of the SoH, the simulated anode potential can be used for controlling fast charging to avoid the onset of lithium plating.

2.2 Implementation of Physicochemical Models for a High Energy Lithium-Ion Battery

In the following, the article titled *Modeling and simulation of inhomogeneities in a 18650 nickel-rich, silicon-graphite lithium-ion cell during fast charging* is presented. The commercial high energy MJ1 LIB is investigated using a variety of experimental techniques to characterize the electrochemical-thermal behavior and to derive proper parametrization for the p2D and the MuDiMod, which are validated under both charge and discharge operation. First, the cylindrical 18650 cell is investigated via opening the cell to measure the electrode geometry and to manufacture half-cells vs. lithium metal for each anode and cathode. These half-cells are used to determine the OCP and its temperature dependency in form of the entropic coefficient. Infrared thermography combined with a rate test and accelerating rate calorimetry (ARC) were applied to derive electrical and thermal characteristics of the MJ1 LIB and to validate the models. A differential voltage analysis (DVA) for the full- and half-cells is applied to determine the electrode balancing and correlate the cell's OCV to the stoichiometry in the anode and the cathode. Laser microscopy, inductively coupled plasma-optical emission spectroscopy (ICP-OES) and mercury porosity measurements are applied to characterize the electrode morphology and chemistry. As a result, silicon containing graphite with 3.5 wt.-% of silicon in a highly compacted anode of 21.6 % porosity is combined with a highly densified nickel-rich NMC-811 cathode of 17.1 % porosity, which reveals one of the highest commercially available energy densities of $261\,\mathrm{W\,h\,kg^{-1}}$ for state-of-the-art LIBs. Based on the experimental results, the models are parametrized, which enables for accurate description of the measured electrical-thermal behavior of the MJ1 cell under various charge and discharge operations in an ambient temperature range from 20°C to 40°C. A simulation comparison to a prior parametrized graphite (C)/lithium nickel manganese cobalt oxide $\mathrm{Li(Ni_{0.33}Mn_{0.33}Co_{0.33})O_2}$ (NMC-111) LIB analyzes the fast charging limitations and the onset of hazardous side effects at different electrode loadings of the electrode stack defined by the porosity. A model-to-model comparison analyzes the modeling error of the p2D in reference to the MuDiMod caused by neglecting the electrode dimensions, the tab design and heat transport effects due to the spirally wound jelly roll in the cylindrical 18650 format. Fast charging profiles are developed considering a variety of tab designs in the 18650 format. It is shown how the battery state variables predicted by the p2D diverge from the MuDiMod results, that is caused by the spatially imbalanced concentrations, potentials and temperature within the LIB.

The parametrization and validation of physicochemical-thermal models such as the p2D and the MuDi-Mod is complex and challenging. However, a more accurate description of the LIB behavior offers enormous potential to optimize the operational condition compared to state-of-the-art approaches using an ECM. The modeling error of the p2D estimated from the MuDiMod simulation results can be used to define a safety buffer and limit the operating range for the cell voltage, local anode potential and the temperature. Considering these limitations caused by the spatial imbalances, can extend the validity of the p2D without actually using a multidimensional multiphysics model approach.

Author and co-worker contribution   Johannes Sturm carried out the cell opening and half-cell manufacturing, designed and carried out the OCV measurements, infrared thermography and DVA of full- and half-cells. The model development, parametrization, validation and the simulation studies were done by Johannes Sturm. Calorimetry and entropy measurements were designed and carried out by Ilya Zilberman. Fabian Frie provided the results from the laser microscopy, ICP-OES and mercury porosity measurement. The analysis of the experimental and simulation data was carried out by Johannes Sturm. Alexander Rheinfeld and Simon V. Erhard initiated fundamental ideas of the presented work. Stephan Kosch, Simon V. Erhard and Alexander Rheinfeld provided fundamental modeling work for the MuDiMod prior to this article. The manuscript was written by Johannes Sturm and was edited by Alexander Rheinfeld, Ilya Zilberman, Franz B. Spingler, Stephan Kosch, Fabian Frie and Andreas Jossen. All authors discussed the data and commented on the results.

Publication notes   The article titled *Modeling and simulation of inhomogeneities in a 18650 nickel-rich, silicon-graphite lithium-ion cell during fast charging* is presented in the following and the related supplementary material is shown in the appendix (see section A). The article [39] and the supplementary material [197] are published in the Journal of Power Sources. Parts of the article were presented at the *19th International Meeting on Lithium Batteries* in Kyoto (Japan) in June 2018, at the *16th Symposium on Modeling and Validation of Electrochemical Energy Devices* in Brunswick (Germany) in March 2019 and at the *Oxford Battery Modelling Symposium* in Oxford (UK) in March 2019. A data repository with the most important results of the experiments and the simulation studies is published at the platform 4TU.Centre for Research Data (Netherlands) [198].

Modeling and simulation of inhomogeneities in a 18650 nickel-rich, silicon-graphite lithium-ion cell during fast charging

Johannes Sturm, Alexander Rheinfeld, Ilya Zilberman, Franz Benjamin Spingler, Stephan Kosch, Fabian Frie, Andreas Jossen

Modeling and simulation of inhomogeneities in a 18650 nickel-rich, silicon-graphite lithium-ion cell during fast charging

J. Sturm[a,*], A. Rheinfeld[a], I. Zilberman[a], F.B. Spingler[a], S. Kosch[a], F. Frie[b,c], A. Jossen[a]

[a] *Technical University of Munich (TUM), Institute for Electrical Energy Storage Technology (EES), Arcisstrasse 21, 80333, Munich, Germany*
[b] *Chair for Electrochemical Energy Conversion and Storage Systems, Institute for Power Electronics and Electrical Drives (ISEA), RWTH Aachen University, Jägerstrasse 17-19, 52066, Aachen, Germany*
[c] *Jülich Aachen Research Alliance, JARA-Energy, Germany*

HIGHLIGHTS

- Combined calorimetry, thermography and OCP measurements for model parameterization.
- Charge-rate capability of NMC-111/graphite vs. NMC-811/SiC at varying porosities.
- Tab design correlated to Li-plating at high-rate constant-current charging.
- Accuracy of single p2D vs. multi-dimensional model as a function of tab design.
- Optimum charging current profile as a function of tab and electrode design.

ARTICLE INFO

ABSTRACT

Recent high-energy lithium-ion batteries contain highly densified electrodes, but they are expected to endure fast charging without safety compromises or accelerated aging. To investigate fast charging strategies, we use a multi-dimensional model consisting of several newman-type electrochemical models (p2D) coupled to an electrical-thermal cell domain model. Open-circuit potential, infrared thermography and calorimetry experiments of a high-energy 18650 NMC-811/SiC lithium-ion cell are used for model parameterization and validation. First, a single p2D model is used to compare the charging rate capabilities of NMC-811/SiC and NMC-111/graphite cells. We assess the modeling error of the single p2D model relative to the multi-dimensional model as a function of tab design. The multi-dimensional model is then used to study different tab and electrode designs regarding their susceptibility to lithium plating, which is evaluated based on local anode overpotential and local temperature. High-rate charging current profiles that minimize the risk of lithium plating are derived by implementing an anode potential threshold. We show that a state of charge beyond 60% can be reached in less than 18 min.

1. Introduction

Even if state of the art lithium-ion technologies offer the highest energy and power density among other battery chemistries, the requirements for the next decade [1] of large stationary storage systems and automotive applications exceed available capabilities. Extended operational performance will be required such as offering a range of more than 300 km [2] for a full-electric vehicle while maintaining lifetime and safety [3]. Preliminary estimates target at 300 Wh kg^{-1} on cell level [1,4] to achieve energy densities on battery pack level around 250 Wh kg^{-1}. Referring to the geometrical format and the capacity of the cell, current automotive applications incorporate already larger-sized cells [5] via increasing the width and length of the electrodes and/or the coating thicknesses of the composites with standard chemistries such as Graphite (C), Nickel Manganese Cobalt (NMC) or Nickel Cobalt Aluminum (NCA) oxides [3]. Small formats such as the 18650 cell offer limited geometrical space but higher intrinsic safety due to their thermal behavior compared to large-sized cell formats and higher capacities are achieved through advancements on the electrode level (> 600 Wh kg^{-1}) and active material level (> 700 Wh kg^{-1}) via highly densified electrodes yielding to low porosities (< 20%) and/or employing high-capacity active materials [1].

In order to meet these requirements [3], layered oxide-types such as high-energy NMC, nickel-rich NMC-types (*e.g.* NMC-811) and NCA [1]

---

appear to be the most suitable choice in combination with silicon doped graphite (SiC) anodes [4]. To increase the intrinsic capacity of NMC-type electrodes, the content of nickel, manganese and cobalt is varied from an equalized, standard composition (i.e. NMC-111) to nickel-rich oxides which content nickel beyond 80 wt% [6]. Specific capacities up to 275.5 mAh g^{-1} [7] at a cut-off voltage of 5 V and approximately 200 mAh g^{-1} [6] at 4.3 V are achievable for a NMC-811 cathode and despite the possible capacity fading [7] due to gasing and oxygen release from the host lattice seen above 4 V, nickel-rich active materials turn out to provide high-capacity electrodes.

In terms of the anodic active material, silicon containing graphite compounds offer capacities > 400 mAh g^{-1} [8–11] which exceed the standard graphite anodes (372 mAh g^{-1} [12–14]). Doping graphite with small amounts of silicon (1:93 wt% for Si:C) increases the specific capacity significantly [8]. However, the volumetric expansion of silicon during lithiation is a crucial issue. As the volumetric expansion of pure silicon ($\approx$ 400% [15]) can only partly be accommodated by the graphitic matrix [11], decreasing the size of the particles [16], incorporating silicon nanowires [15] or using coatings with carbon [17] dilute the overall volume expansion [18] and limit the lithiation window of the Si component which makes silicon doped graphite to an appropriate high-capacity active material for anodes.

Considering nickel-rich and silicon doped graphite materials on the electrode level, an increase from $\approx$ 340 Wh kg^{-1} to > 600 Wh kg^{-1} [1] is attainable when the morphology [1], coating thicknesses [5] and the amount of inactive additives [19] are optimized. Standard electrodes reveal porosities of approximately 35% [1], whereas high-energy electrodes reveal porosities even below 20% [20,21], which may enhance unwanted liquid mass transport limitations [22] and lower the charge and discharge-rate capability of the cell.

In short, next generation high-energy electrodes will incorporate high-capacity active materials (e.g. NMC-811/SiC) and low porous electrodes beside thicker coatings or longer electrodes.

In this work, a commercial 3.35 Ah NMC-811/SiC (INR18650-MJ1, LG Chem [23]) lithium-ion battery is characterized via calorimetry, infrared thermography and open-circuit potential (OCP) experiments. Note, that the term OCP is also often referred as open-circuit voltage (OCV). Based on the experimental part, a newman-type [24] pseudo-two dimensional (p2D) model and a Multi-Dimensional Model (MuDiMod) [25–28] are parameterized and validated for a simulation study on the latest, widley discussed field of fast charging [29–32]. In this matter, charge-rate capability and tendency of lithium plating is analyzed for the high-capacity and a standard NMC-111/C material in highly and moderately densified electrodes. The MuDiMod is used to evaluate different tab designs in terms of lithium plating susceptibility for the INR18650-MJ1 (MJ1) cell during high-rate constant-current charging and based on that, cell voltage as well as local anode potential thresholds are used to derive improved fast charging protocols. The charging simulation results are used to evaluate the modeling error of the single p2D model relative to the MuDiMod as a function of tab design.

1.1. Local experimental investigation of lithium-ion cells

Experimental investigation of a cell's local behavior such as changing concentrations or potentials in the electrolyte and the active particles throughout or even along the electrodes requires in-situ or in-operando techniques which are often associated with costly experimental equipment such as X-ray tomography [33], neutron-powder diffraction [34] or focused ion-beam scanning electron microscopy [35]. Using less complex test procedure such as electrochemical impedance spectroscopy (EIS), current density and local potential distribution along the electrode was investigated towards the influence of alternating excitation currents, temperature, tab pattern and frequency for a modified 26650 LFP/C cell with four tabs [36]. Subsequently, a single layered NMC/C pouch cell with several measurement tabs along the electrode

revealed the dependency of local current peaks towards the electrode OCPs and was used to validate the MuDiMod [26], which is used in this work. Cells without multi-tab design can be modified with reference electrodes to measure local potentials and to correlate lithiation levels to the global state of charge (SoC) of the cell [37]. Beside measuring local potentials [38], temperature sensors [39] in the core of the cell or even optical fibres with Bragg Grating [40] are implemented in the cell to measure local temperatures such as the core-temperature.

However, the additional devices may alter the cell's behavior even if model validation could enormously benefit. Generally, these experimental investigations mostly work on a laboratory scale whereas for application purposes, none of these techniques are suitable due to complex measurement techniques and possible altering of the cell's behavior. However, simulation provides an efficient and safe alternative to experimental techniques and may profit through experimental validation in future works.

1.2. Multi-dimensional simulation of lithium-ion cells

Multi-dimensional modeling frameworks reveal reliable results [41,42] to analyze the performance of lithium-ion batteries looking at rate-capability [43], heat generation rate [44] or the non-uniformity of current density along the electrodes related to non-optimized electrical design [45]. These models solve for electrochemical, electrical and thermal mechanisms on their relevant length scales such as particle size and electrode thickness (p2D), current collector length and width (2D) and the total jelly roll/electrode stack (3D). The size and tab pattern of the current collectors mainly influences the gained energy density [46] from the cell and is analyzed in this work via the MuDiMod for a high-energy 18650 cells with an electrode size of 5.8 × 61.5 cm. In literature, electrode sizes of 4.6 × 13.8 cm were analyzed with a 3D electrochemical-thermal model for a NCA/C cell [47] to investigate single- and double-sided cooling for six connected cells and suggested the evaluation of design parameters (i.e. cathode thickness) via the influence on the thermal cell behavior. Model validity is limited as uniform electrode utilization was assumed, which may not be appropriate in case of a single-side cooling condition.

Analysing larger electrode sizes of 11 × 111 cm [48] for a LFP/C cell via a 3D electrochemical-thermal model, the highest risk of lithium plating appeared close to the negative current collector tabs.

Analyzing the electrical configuration via continuum based models [45] for a NCA/C cell, different tab patterns along a 3.23 m electrode revealed an increase of cell impedance and non-uniformity of reaction kinetics, when decreasing the number of tabs.

Large 20.5 × 512 cm electrode sizes were investigated for a NMC/C cell via a 3D electrochemical-thermal model [46] under applying different tab patterns. A correlation of the cell specific energy density and the non-uniformity of the current density was proposed.

Previous works dealt with standard active materials (e.g. NMC-111/C), whereas multidimensional analysis of high-capacity active materials (i.e. NMC-811/SiC) in highly densified electrodes has not been shown before and is presented in this work. Few works are simulating the 3D-thermal and 2D-electrical cell behavior of spirally wound electrodes on local scale, which is presented in this work for a 5.8 × 61.5 cm electrode size and is important especially for high-energy cells as experimental findings of local hot spots [29] indicate.

2. Experimental methods

The measurements in this work comprise calorimetry, infrared thermography and OCP tests of the MJ1 cell which are depicted in Table 1.

In terms of the calorimetry, the heat generation of a pristine MJ1 cell (#1-MJ1) was measured at a 0.2C, 0.5C and 1.0C constant-current (CC) charge- and discharge-rate with an accelerating rate calorimeter (EV-ARC, Thermal Hazard Technology) combined with a cylcer (CTS,

Table 1
Measurement procedure for charge and discharge of half and full cells.

Calorimetry measurement (full cell #1-MJ1)			
Step	Current rate[a]	Termination	Initial Temperature
CC	C/5, C/2, 1C	2.5 V - 4.2 V	
CV	–	until 167.5 mA	25 °C
Thermal relaxation	0	10 h	
Thermography measurement (full cell #2-MJ1)			Ambient Temperature
Preconditioning CC	1C	2.5 V - 4.2 V	
Preconditioning CV	–	until 33.5 mA	
Thermal relaxation I	0	4 h	20, 25
CC	C/5[b], C/2, 1C, 2C[c]	2.5 V - 4.2 V	30 and 40 °C
CV	–	until 33.5 mA	
Thermal relaxation II	–	1 h	
Open-circuit potential measurement (full cell #3-MJ1)			
Preconditioning CC	C/10	2.5 V - 4.2 V	25 °C
Preconditioning CV	–	until 3.35 mA	
Relaxation	0	6 h	
CC	C/30	2.5 V - 4.2 V	
CV	–	until 3.35 mA	
Open-circuit potential measurement for the half cells			
Soaking	0	12 h	25 °C
CC	≈ C/100	0.010–1.7 V (SiC) 3.0 V - 4.3 V (NMC-811)	

[a] $1.0C \equiv 3.35\,A$ [23,49].
[b] Only at 25 °C.
[c] Only discharge at 25 °C.

Basytec). Each charge and discharge step was followed by a constant voltage (CV) period with a termination criterion of 0.05C at 4.2 V and 2.5 V, respectively. After each step the cell was rested for at least 10 h. The total heat capacity of the cell was determined during the adiabatic conditions in the calorimeter and via the thermography measurements during the period 'Thermal relaxation II' (see Table 1).

Regarding the thermography measurements [50], the temperature distribution at the surface of the cell (#2-MJ1) and the adjacent copper connectors (1860C006, Feinmetall [51]) was measured during different charge- (0.2, 0.5 and 1.0) and discharge-rates (0.2, 0.5, 1.0 and 2.0) via an infrared camera (A655sc, FLIR Systems Inc.) with an accuracy of ± 2K at four different ambient temperatures (20, 25, 30 and 40 °C). To increase temperature accuracy, the infrared thermography temperature data is referenced to a four-wire Pt100 sensor with an absolute accuracy of ± 0.15K at 0 °C (DIN/IEC Class A). The optical resolution of 80x480 pixels provides a relative accuracy of ± 30mK between the pixels. Turbulent air-flow at 1.0 and 2.0 m s^{-1} guaranteed convective cooling with a heat transfer coefficient of 22.4 W m^{-2}K and 32.1 W m^{-2}K (see Table A.8) in a custom-built climate chamber [50] combined with a cycler (HPS, Basytec).

OCP-measurements for charge and discharge of the anode (SiC) and cathode (NMC-811) half cells as well as for the full cell (#3-MJ1) were measured in a climate chamber (VT 4021, Vötsch Industrietechnik GmbH) at 25 °C combined with a cycler (CTS, Basytec). The applied current for both half cells was set to 80 μA (≈ 0.01C) and 101 mA (≈ C/30) for the full cell. As the electrodes of the coin cells were extracted from an already utilized cell, no formation cycles were necessary.

2.1. Open-circuit potential measurements

The electrodes for the half cells were extracted from full cell #4-

Table 2
Pressure profile for wetting NMC-811 electrodes.

Step	Pressure/mbar	Duration/s
Vaccum I	10	10
Release I	60	10
Vaccum II	30	10
Release II	80	10
Vaccum III	30	10
Wetting	30	1

MJ1 at 3 V, which was opended inside an argon-filled glove-box (M.Braun Inertgas-Systeme GmbH). Single-side coated electrode samples (⊘14 mm) for the CR2032-type coin cell were gained from a single-coated area at the outer end of the anode and via mechanical abrasion using a scalpel for the continuously double-side coated cathode. The assembly included two aluminum spacers (0.5 mm/ 1 mm), two glasfiber separators each of 250 μm, a single lithium-metal coin (250 μm) and the remaining CR2032-type housing caps, wave spring and insulation ring.

The anode half cells were filled with 90 μL of 1 M LiPF$_6$ in 3:7 (wt:wt) ethylene carbonate (EC)/ethyl methyl carbonate (EMC) electrolyte (99.9% purity, Solvionic) under ambient pressure (≈ 1 bar) in the glove-box.

The assembled NMC-811 half cells did not function, when the electrolyte was inserted under ambient pressure. Wetting cathode samples under vacuum in a pressure chamber (Harro-Höfliger Verpackungsmaschinen GmbH) within the glove-box, the coin cells operated normally. In order to lower capillary effects at the pore [52,53], the pressure profile shown in Table 2 was used for the wetting process.

As the NMC-811 electrode is even more dense with a porosity of 17.1% than the SiC anode (21.6%) (Mercury porosimetry, PASCAL 140/440 with CD3 dilatometer), capillary and wettability effects may inhibit the electrolyte from entering the pore. After this first phase of wetting, another 70 μL of electrolyte are added to the coin cell.

2.2. Entropy measurements

The entropy profiles of the positive and negative electrode were measured using a potentiometric method [54]. The anode and the cathode half cells were initially set to 10 mV and 4.6 V respectively at 0.1C with a subsequent CV period and termination criterion of C/1000. Afterwards the anode was delithiated and the cathode was lithiated with C/30 at SoC steps of 6.25% gaining 17 SoC points in total. After resting for 6 h at 25 °C, a positive temperature pulse of 10 K amplitude and 4 h duration immediately followed by a negative pulse of the same amplitude and duration was applied according to the work of Zilberman et al. [54] at each SoC step with a climate chamber (KT115, Binder), which ensured isothermal test condition at a temperature accuracy of ± 15 mK. PT100 sensors were used to measure the temperature at the surface of each cell. As the half cell voltage was not completely relaxed after 6 h, the voltage response to the temperature profile was corrected using the method presented in Osswald et al. [55].

3. Modeling

In this work, the single p2D model and the MuDiMod incorporating several p2D models, the 2D electrical model of the current collectors and the 3D thermal model of the jelly roll are used. The parameterization of the MJ1 cell is explained more in detail for the high-capacity active materials and additionally, the parameterization for the 2D and 3D model are depicted in Table A.9 and Table A.10.

3.1. Silicon-graphite anode

The dry anode half cell samples were weighed with a total mass of 37.3 mg (Quintix 224-1S, Sartorius Mechatronics) and with the calculated weight of the current collector ($\oslash$14 mm x 11 μm, ρ_{copper}=8.95 g cm^{-3} [56]), the weight of the dry electrode is estimated as 22.1 mg. The current collector thickness was derived from inductively coupled plasma-optical emission spectroscopy (ICP-OES, Varian 7XX-ES ICP-OES Spectrometer, Agilent Technologies), referring to the measured amount of copper and the sample size ($\oslash$20 mm). The total thickness of the electrode was measured via laser microscopy (VK9710K Violet Laser 408 nm, KEYENCE CORPORATION) and micrometer caliper (Micromar 40 EWV, Mahr GmbH), resulting in a coating thickness of 86.7 μm. Mercury porosimetry (PASCAL 140/440 with CD3 dilatometer, PASCAL) revealed porosity values of 21.6% which leads to a total solid volume of 10.1 mm^3 for the coin sample. The fraction of silicon in graphite could be determined via ICP-OES to $\approx$ 3.5 wt%. Specific gravimetric capacities of natural graphite [10] and nano-particle sized silicon [57] can be estimated to 330 mAh g^{-1} and 3600 mAh g^{-1}. Referring to standard compositions of active and inactive material [1,58], 9 wt% are assumed to consist of binder and carbon black (combined density of $\approx$ 1.78 kg m^{-3} [59,60]), resulting in a content of graphite of 87.5 wt%. The maximum theoretical loading (b_g) of the anode is calculated [11] to 415 mAh g^{-1}, which is well in line with comparable gravimetric loadings for SiC [10]. Considering 21.6% porosity and the densities (ρ) of binder, carbon black and 3.5–87.5 wt% SiC (2.24 g cm^{-3}, derived from Ref. [10]), the total volumetric fractions can be calculated [10] to 9% (carbon black/binder) and 69.4% (SiC) from the gravimetric composition. The maximum lithium-ion concentration in the anode is estimated to 34 684 mol m^{-3} according to Eq. (1).

$$c_{smax} = b_g \cdot \rho \cdot F^{-1} \tag{1}$$

The particle radius ($R_{p,\text{D}50}$) was derived from the mercury porosimetry to 6.1 μm. Both lithiation and delithiation paths are considered to estimate the equilibrium potential [61,62] in the single p2D model for charge and discharge simulation of the full cell, as the silicon doped graphite shows distinct hysteresis effects which is well in line with other works [63]. In order to match the measured capacity of the coin cells to the lithiation level, two reference points were considered at 0 mAh and at the transition of LiC$_{12}$ to LiC$_6$ [64], which can be clearly seen in the derivative of the potential vs. capacity. Due to the hysteresis effect, the averaged value in capacity between both peaks in the lithiation and delithiation path was used to match approximately the 50% level [65].

3.2. Nickel-rich cathode

Similar to the anode half cells, the weight of the cathode samples was derived to 37.1 mg with a thickness of 17.3 μm for the aluminum current collector ($\rho_{aluminum}$=2.71 g cm^{-3} [56]). The composition of 82 %-6.3 %-11.7% for nickel, manganese and cobalt was determined via ICP-OES and slightly differs from a strictly 80 %-10 %-10% ratio. Regarding the cathodic porosity of 17.1% and the coating thickness of 66.2 μm, the total solid volume accounts to 8.44 mm^3 for the coin sample. A standard gravimetric composition of 96 wt% to 4 wt% [58] ratio for the active and inactive parts and a crystallographic density of 4.87 g cm^{-3} for NMC-811 [7] is assumed here. Considering the porosity of 17.1%, the volumetric fractions are calculated [10] to 74.5% (NMC-811) and 8.4% (carbon black/binder). The specific gravimetric capacity of the NMC-811 material is assumed to be 275.5 mAh g^{-1} [7]. The particle radius ($R_{p,\text{D}50}$) is derived as 3.8 μm and thus the theoretical maximum concentration is calculated to 50 060 mol m^{-3} (see Eq. (1)).

The lithiation level during both lithiation and delithiation of the OCP is calculated via setting two points at the measured half cell capacity and at 0 mAh in reference to 275.5 mAh g^{-1} [7]. The derived lithiation degrees are well in line with other findings [6].

The determination of the lithiation degree of both electrodes is applied similar for the entropic coefficents. The complete parameterization of the NMC-811/SiC porous electrodes is given in Table 3.

Gas-chromatography combined with mass spectroscopy (Clarus 560/600 GC/MS, PerkinElmer LAS GmbH) of the electrolyte in the MJ1 revealed contents of EC, EMC and dimethyl carbonate (DMC) and the values for a 1 M LiPF$_6$ in polypropylene carbonate (PC)/EC/DMC were used as the most appropriate set available in literature from Valøen and Reimers [69] (see Table A.9). As transport correction for the liquid diffusion coefficient (D_l), the ionic conductivity (κ_l) and the electrical conductivity in the active material (σ_s) [25], the Bruggeman correlation [67] was used with increased coefficients ($\approx$ 23%) for the cathode to account for the low porosity of 17.1%.

To the authors' knowledge, this is the first effort to parameterize a newman-type p2D model for a NMC-811/SiC lithium-ion cell.

3.3. Single p2D and multi-dimensional model

The electrochemical model used in this work is the widely applied newman-type p2D model [24] which is based on porous electrode theory, reaction kinetics and concentrated solution theory [70]. The model equations are summarized in Table A.12 in the appendix.

For the single p2D model, an additional thermal model calculates the volume-averaged cell temperature from heat generation due to ohmic losses in the solid and liquid phase (q_s, q_l), reaction overpotential (q_r), entropy change (q_{rev}) and contact resistance (q_{ext}). Heat transfer to the environment is considered via convection (q_{conv}) and radiation (q_{rad}). In case of the thermography measurements, heat conduction via the connectors is also described (q_{con}). The reference temperature (T_{con}) for the heat conduction was measured on the surface of the connectors.

The MuDiMod consists of several p2D models calculating electrochemical potentials and lithium-ion concentrations perpendicular to the current collectors, the 2D model accounting for the electrical potential along the current collectors and the 3D model calculating the local temperature within the jelly roll of the cylindrical cell. As the basic MuDiMod is already published in previous works [26,27] with an extension of using effective spatial discretization techniques [28], only novel implemented techniques or submodels are outlined here.

An additional charge balance (see Table A.12) guarantees the charge transfer from the p2D models to be in agreement to the total current applied at the cell's tabs in the 2D model in order to avoid slight deviances in the SoC calculation.

Moreover, a fully spatially resolved 3D thermal model for cylindrical cells is incorporated which enables for local coupling of heat generation calculated in the p2D and 2D models and temperature distribution along the electrodes instead of using lumped thermal models [25]. The local coupling enables for analyzing tab pattern influences on heat generation, temperature distribution and local differences in SoC [34].

In general, a computationally efficient mathematical description of the coordinate transformation between a spirally wound domain and its unwound representation is needed for a lean exchange of local states between the related submodels. A variable extrusion algorithm proofed to enable a coupling of a planar 2D and spirally wound 3D model whilst using only 35% of RAM and saving 97% of computation time with sufficient accuracy compared to fully-discretized models [44]. Based on this approach, an extended coupling algorithm transfers the local heat generation of the p2D and the 2D model forward to the 3D thermal model via coordinate mapping, incorporating a lumped finite element methode (FEM) discretization-mesh in the 3D model. By implication, the local temperature is transferred backwards to the 2D model and the p2D models. Further explanation would exceed the scope of this work, therefore the necessary mapping procedure is explained explicitly in the

Table 3
Parameterization of the single p2D model with NMC-811/SiC electrodes.

Geometry		Silicon-graphite	Separator	Nickel-rich
		SiC		NMC-811
Thickness L		86.7 μm[m]	12 μm[m]	66.2 μm[m]
Particle radius R_p		6.1 μm[m,D50]		3.8 μm[m,D50]
Active material fraction ε_s		69.4 %[e]		74.5 %[e]
Inactive fraction $\varepsilon_{s,na}$		9 %[e,*]		8.4 %[e,*]
Porosity ε_l		21.6 %[m]	45 %[e]	17.1 %[m]
Bruggeman coefficient β [VII,**]		1.5	1.5	1.85[e]
Thermodynamics				
Equilibrium potential E_{eq}		see Fig. 2 a[m]		see Fig. 2 b[m]
Entropic coefficient $\frac{\partial E_{eq}}{\partial T}$		see Fig. 2 c[m]		see Fig. 2 d[m]
Stoichiometry	100% SoC	0.852		0.222
	0% SoC	0.002		0.942
Max. theoretical loading b_g		415 mAh g^{-1} [II]		275.5 mAh g^{-1} [II]
Density ρ		2.24 g cm^{-3} [I]		4.87 g cm^{-3} [II]
Concentration $c_{s,max}$		34 684 mol m^{-3} [e]		50 060 mol m^{-3} [e]
Transport				
Solid diffusivity D_s***		5×10^{-14} m^2 s^{-1} [e,V]		5×10^{-13} m^2 s^{-1} [IV,VI]
Specific activation $\frac{E_{a,D_s}}{R}$***		1200 K[e]		1200 K[e]
Solid conductivity σ_s		100 S m^{-1} [IV]		0.17 S m^{-1} [e,IV]
Film resistance R_f		0.0035 Ω m^2 [III]		0 Ω m^2 [e]
Kinetics				
Reaction rate constant k***		3×10^{-11} m s^{-1} [e]		1×10^{-11} m s^{-1} [e]
Specific activation $\frac{E_{a,k}}{R}$***		3600 K[e]		3600 K[e]
Transfer coefficient $\alpha_{a/c}$		0.5[e]		0.5[e]

m = measured e = estimated * PVDF-binder/Carbon black (Ref. [59,60]).
[I] Ref. [10] [II] Ref. [7] [III] Ref. [22] [IV] Ref. [6] [V] Ref. [66] [VI] Ref. [1] [VII] Ref. [67].
** Effective transport correction according to Bruggeman (Ref. [67]): $\Psi_{eff} = \varepsilon^{\beta} \cdot \Psi_0$.
*** Arrhenius law (Ref. [68]): $k = A \cdot \exp\left(\frac{E_{a,i}}{R} \frac{(T - 298[\text{K}])}{T \cdot 298[\text{K}]}\right)$.

supplementary material of this work beside the chosen FEM-mesh for the p2D and the MuDiMod implemented in COMSOL Multiphysics 5.3a.

As the positive (+) and negative (−) current collector tab in the MJ1 cell are located in the center and at the outer end of the jelly roll, electrode utilization is investigated via different tab design to evaluate the electrical configuration on the current collector foils. In this work, the positive/negative tabs are exclusively located at the top/bottom of the electrode. Using several counter-position tabs in different patterns was seen to increase the usable energy density [46] during charge of the cell and following this, possible optimization of the electrical configuration is investigated via three alternative tab patterns (*i.e* 1x1, 1x2 and 2x3), which are depicted in Table 4.

The MuDiMod is used in this work to evaluate the original tab design of the MJ1 cell with the alternative tab pattern during high-rate CC- and improved fast charging protocols in terms of the gained SoC level and the achievable energy density, tendency of lithium plating and local hot spots near the tabs.

Using the single p2D model [71–73], lithium plating can be indicated when the potential drop ($\Phi_s - \Phi_l$) at the particle surface and the anode-separator interface ($x = L_{neg}$) falls below 0 V without implementing actual plating kinetics. Without implementing an actual aging model in this work, an advanced indicator state is calculated over time:

$$\int_t \Phi_s - \Phi_l \, dt \quad \text{if} \quad \Phi_s - \Phi_l < 0V \quad \text{at} \quad x = L_{neg} \tag{2}$$

In terms of the MuDiMod, it can be used to evaluate the likeliness of

lithium plating on local scale near and far from the current collector tabs considering the whole charging scenario instead of evaluating on a single time step. To estimate the amount of charge which is probably affected by lithium plating, a surface integral in the 2D electrical sub-model is calculated for the transfer current density (i_{p2D}) on the electrode area.

$$\int_{x'} \int_{y'} i_{p2D} \, dy' \, dx' \quad \text{if} \quad \Phi_s - \Phi_l < 0V \quad \text{at} \quad x = L_{neg} \tag{3}$$

Table 4
Different tab designs for the 18650 NMC-811/SiC cell.

Tab pattern	Number of tabs		Position of tabs along the electrode (x' /cm)	
	+*	−**	+	−
MJ1 (INR18650-MJ1 reference)	1	1	0	61.5
1x1	1	1	$\frac{61.5}{2}$	$\frac{61.5}{2}$
1x2	1	2	$\frac{61.5}{2}$	0; 61.5
2x3	2	3	$\frac{61.5}{3}$; $\frac{2}{3}$ 61.5	0; $\frac{61.5}{2}$; 61.5

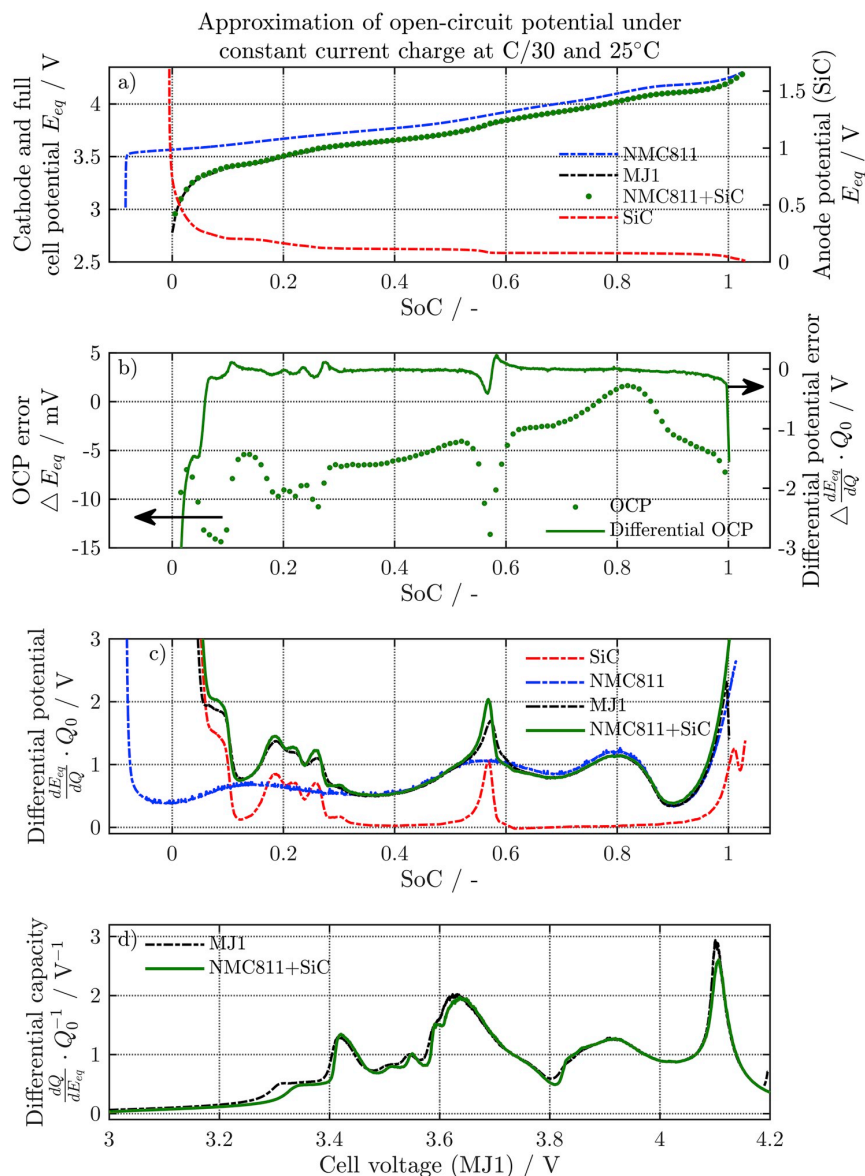* located at $y' = 5.8$ cm ** located at $y' = 0$ cm.

Fig. 1. DVA analysis (c) was used to reconstruct the measured OCP vs. SoC (a) under charge of full cell #3-MJ1 (see 'MJ1') via the delithiation and lithiation path of the respective coin cell (see 'NMC811' and 'SiC'). The approximation errors vs. SoC are shown in subplot b) and the differential capacity vs. full cell voltage together with the reconstruction (see 'NMC811 + SiC') is depicted in subplot d).

4. Results and discussion

4.1. Differential voltage analysis

The discharge capacities gained from the coin cells sum up to 7.96 mAh (5.17 mAh cm^{-2}) and 8.43 mAh (5.48 mAh cm^{-2}) for SiC and NMC-811, respectively. The discharge capacity of the full cell (Q_0) was measured to 3.560 Ah at C/30. The measured OCP data from the half and full cells are used for differential voltage analysis (DVA), which is shown for the charge scenario of the full cell in Fig. 1.

The reconstructed OCP ('NMC811 + SiC') in Fig. 1 a is derived via extending and shifting [74] the measured half cell OCPs towards the full cell capacity level. The residual deviance is shown in Fig. 1 b, which reveals potential errors of less than 15 mV with an average error of 5.7 mV. For the differential potential and differential capacity shown in Fig. 1 c and d, a capacity normalization by multiplying the differential potentials with Q_0 is performed [75]. With the aid of the differential potential, the balancing of the full cell revealed an oversized cathode ($\approx$ 9.4%) and an almost complete use of the anode (> 99%) referring to the specified voltage ranges (see Table 1). The potential differential (see Fig. 1 b) showed slight deviances with a mean deviation of 230 mV Ah^{-1}. The differential capacity vs. cell voltage for charge in Fig. 3 d matches the full cell behavior with marginal deviances. Four characteristic redox peaks can be observed at 3.42, 3.63, 3.91 and 4.1 V attributed to the NMC-811 cathode, which were seen similar in other works [6].

The DVA analysis for the charge scenario revealed accurate reconstruction of the full cell OCP behavior via the custom-built coin
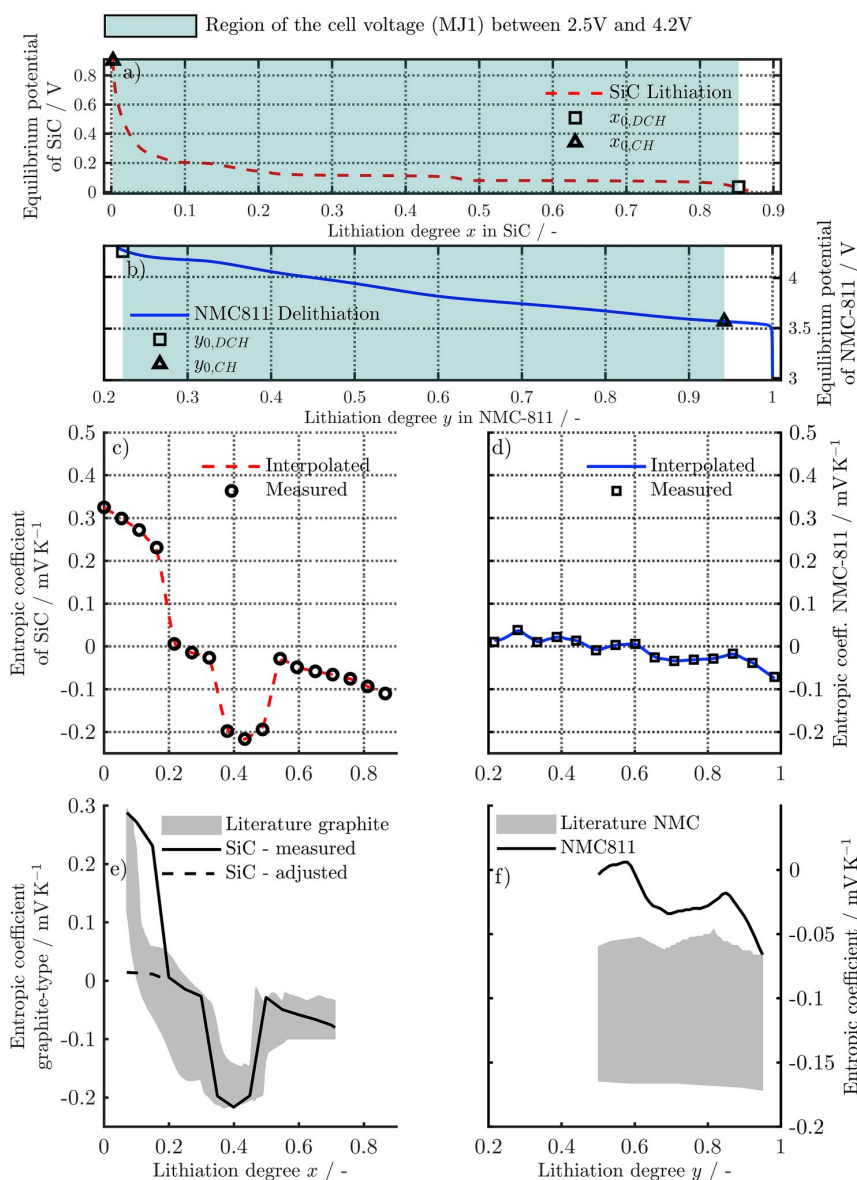
Fig. 2. OCP of the SiC lithiation (a) and NMC-811 delithiation (b) path vs. estimated lithiation degree for the p2D model parameterization with illustration of the full cell voltage range from 2.5 V to 4.2 V and the initial stoichiometric coefficients ($x_{0,i}$, $y_{0,i}$). The measured entropic coefficient vs. estimated lithiation degree referring to the current direction of the full cell is shown for SiC (c) and NMC-811 (d) in comparison to graphite [12,22,64,76–78] (e) and NMC [76,77,79,81] (f) references from literature.

cells. Similar results were gained for the discharge scenario, which is not shown here.

4.2. Half cell potentials and entropic coefficients

Derived from OCP and entropy measurements, the model parameterization is completed via the equilibrium potentials and entropic coefficents shown in Fig. 2 a to d. Regarding the full cell voltage range from 2.5 to 4.2 V (blue-tagged area) in Fig. 2 a and b, the oversized cathode is evident. The initial stoichiometric coefficients are derived from the DVA analysis (see Table 3). The entropic coefficient for SiC in Fig. 2 c is well in line with other measured graphite-type anodes [12,22,64,76–78]. Taking these references into account, Fig. 2 e shows

the range of the entropic coefficient vs. lithiation degree in the grey-tagged area together with the measured entropic profile of this work. At low lithiation levels (< 20%), graphite-type anodes show larger deviances in literature [77,79,80]. The fuzziness of the measured entropic coefficient below the 20% threshold resulted in larger simulation errors for the cell temperature compared to the measurements especially at the beginning of charging. As a consequence, the anode entropic coefficient was adjusted which is still well in line with results from literature as shown in Fig. 2 e.

The entropic coefficient of NMC-811 is shown in Fig. 2 d and resembles NMC-type active materials [76,77,79,81] such as NMC-111. Referring to these works, Fig. 2 f shows the range of the entropic coefficient for the standard NMC-type active materials in the grey-
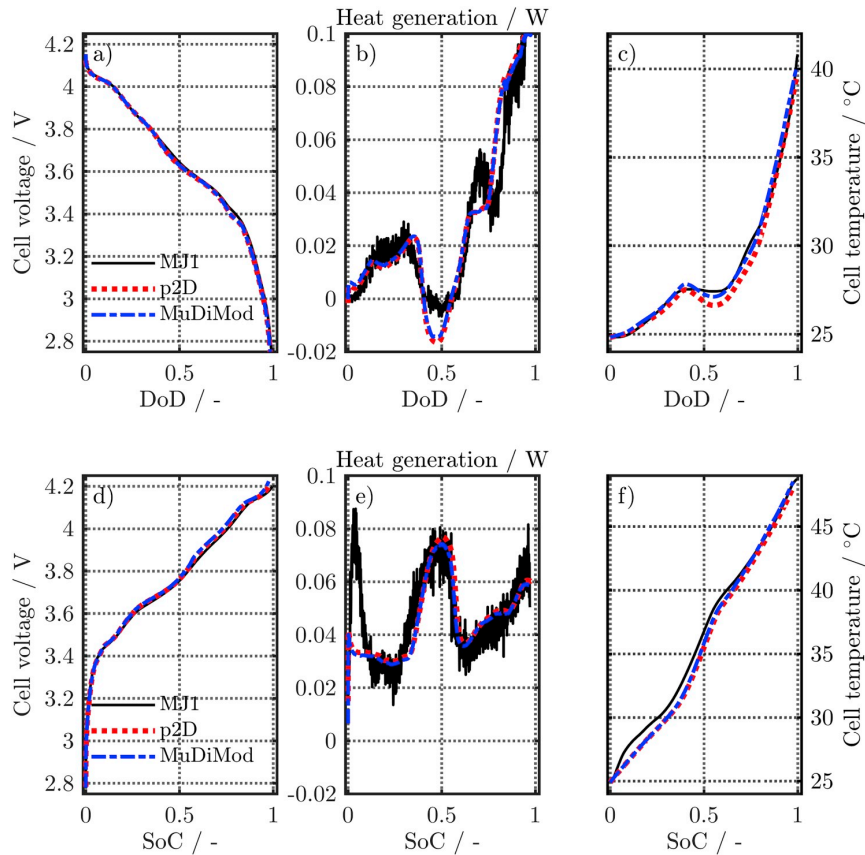
Fig. 3. Calorimetry of the MJ1 cell at C/5 discharge (a, b and c) and charge (d, e and f) to validate the simulated ('p2D' and 'MuDiMod') cell voltage, heat generation rate and surface cell temperature.

tagged area. As seen, the entropic coefficient for NMC-811 slightly exceeds this range for low lithiation degrees. Comparing both entropic coefficients, the entropic heat of the full cell is mainly depending on the anode.

The presented measured data in Fig 2 a to d is implemented in the models via piece-wise cubic interpolation.

At this point, the parameterization of the electrochemical model is completed and in the following, the validation of the single p2D and the MuDiMod is presented via the infrared thermography and the calorimetry measurements.

4.3. Validation via calorimetry

The calorimetry measurements at C/5 discharge and charge are used to validate the simulated cell voltage, heat generation rate and temperature with focus on describing properly the thermal behavior of the cell. Using the calculated heat capacity of $42.1\,\mathrm{J\,K^{-1}}$ of the full cell (see section 2), the simulation results from the single p2D and the MuDiMod are shown in Fig. 3 for discharge and charge at C/5.

The heat dip in Fig. 3 b ($\approx$ 50% DoD) can be explained by the negative entropic heat of the SiC active material. The overall cell behavior is predicted quite accurate by the single p2D and the MuDiMod simulation with an average error of 13.4/11.9 mV and 10.5/16.2 mV for the cell voltage under discharge/charge, respectively. The average temperature errors under discharge/charge resemble the measured temperature with 0.3/0.1 K and 0.8/0.5 K for the single p2D and the MuDiMod. In terms of the C/5 charge simulation, both models show the aforementioned fuzziness of the measured entropic coefficient at low

cell SoC levels (see Fig. 2 e), but the calculated temperature is nevertheless well in line with the measurement with an acceptable deviation below 1 K on average.

The charge and discharge simulation of the calorimetry measurements show an accurate description of the measured electrical and thermal behavior of the MJ1 cell and a proper validation especially for the calculated heat and temperature in the 0D- (single p2D) and 3D-thermal model (MuDiMod) was shown.

4.4. Validation via infrared thermography

Thermography measurements of the full cell are used to validate the simulated cell behavior of both models in terms of varying constant charge- and discharge-rates under varying ambient temperatures and convective cooling conditions [50]. The experimental and simulated cell voltages at 25 °C as well as the residual error are shown in Fig. 4. Following the data sheet [23], a 0.5C charging rate is adviced for the MJ1 while the maximum C-rate during charge is set to 1C. Higher C-rates such as 2C were only applied for discharge. As shown in Fig. 4, the simulated data (a, c and e) matches to the measured cell voltage quite well during charging and discharging. At 1C charging, an average error of 14.5 mV and 13.7 mV and a mean squared error (MSE) of $\approx$ 0.4 $(\mathrm{mV})^2$ is seen for the single p2D model and the MuDiMod. The largest error during charge (see Fig. 4 b, d and f) can be observed at the beginning due to the steep voltage increase referring to the anode OCP at low lithiation degrees (see Fig. 1 c). Similary, the maximum error appears at the end of the discharge. The simulated cell voltages at discharge in Fig. 4 match the measured data quite well and at 1C, an
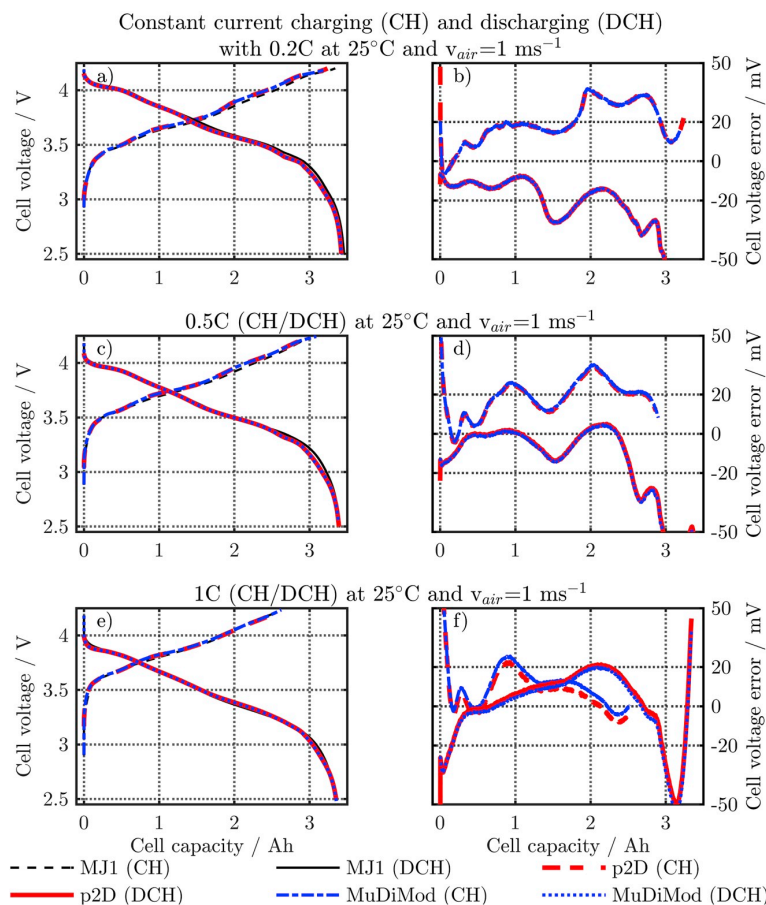
Fig. 4. Thermography measurements of the MJ1 cell to validate the simulated cell voltage (a, c, and e) with the related simulation error (b, d, and f) vs. the usable cell capacity for the p2D model and the MuDiMod.

average error of 13.5 mV and 15.2 mV and a MSE of 0.3 $(mV)^2$ and 0.5 $(mV)^2$ appear for the single p2D and the MuDiMod. Only marginal differences between the single p2D and the MuDiMod can be observed except for 2C, where approximately 20% reduced errors for the mean cell voltage are seen in the MuDiMod simulation results. Regarding the MuDiMod simulation results, current distribution on the current collectors vary ± 5% around the mean value of 9.4 mA cm^{-2}, which cannot be described by a single p2D model assuming homogeneous electrode utilization, resulting in the appearing deviance between the two models.

In terms of the cell voltage, accurate simulation results appeared for both models and the temperature calculation is validated in Fig. 5 at different ambient temperatures for the single p2D model. During charge at 25 °C (see Fig. 5 a), maximum temperature errors of 0.4 K and 0.6 K with a mean deviance of 0.1 K and 0.2 K appear at 0.2C and 0.5C respectively. At 1C, the maximum and mean error account for 1.2 K and 0.34 K, still revealing sufficient accurate simulation results. The highest deviations during discharge shown in Fig. 5 b appear at 2C with 1.4 K and 0.27 K for the maximum and mean error. Regarding the temperature profiles in the ambient temperature range from 20 °C up to 40 °C in Fig. 5 c and f, the simulated temperatures at 1.0C reveal an accurate prediction of the cell behavior with deviances in the range of ± 1 K (see Fig. 5 d and f). The detailed error analysis of the thermography validation at 1 m s^{-1} and 2 m s^{-1} for the single p2D model and the MuDiMod are given in the supplementary part of this work.

The thermography validation under both convective cooling conditions show accurate simulation of the temperature for charge and discharge and reveal errors, which are below 0.5 K on average and thus are in the range of the measurement accuracy.

So far, the parameterization and validation of the single p2D model and MuDiMod were shown for a high-energy NMC-811/SiC 18650 cell. Previous works [25,55] already proofed the validity of the MuDiMod on a similar 26650 cell via local potential measurements along an electrode size of 5.6 × 169 cm with four tabs on both the positive and the negative current collector.

Even if the MJ1 cell reveals a single-tab design and a local evaluation of the electrode potentials is not applicable, compared to the LFP/graphite 26650 cell the slopes of the NMC-811/SiC OCPs are higher and thus the potential and current distribution on the electrode area less critical to simulate.

The following simulation studies aim for evaluating the charge-rate capability and susceptibility of lithium plating of the NMC-811/SiC active material compared to standard NMC-111/graphite [25] (see Table A.11) active material at varying electrode porosities.

4.5. Charge characteristics of NMC-811/SiC and NMC-111/C

Referring to a specified NMC-111/C material [26], electrodes with high-capacity NMC-811/SiC active materials are investigated via the single p2D model towards the influence of morphology and specific capacity on the charge-rate capability and likeliness of lithium plating during CC-charging (1C to 5C) with no additional constant voltage
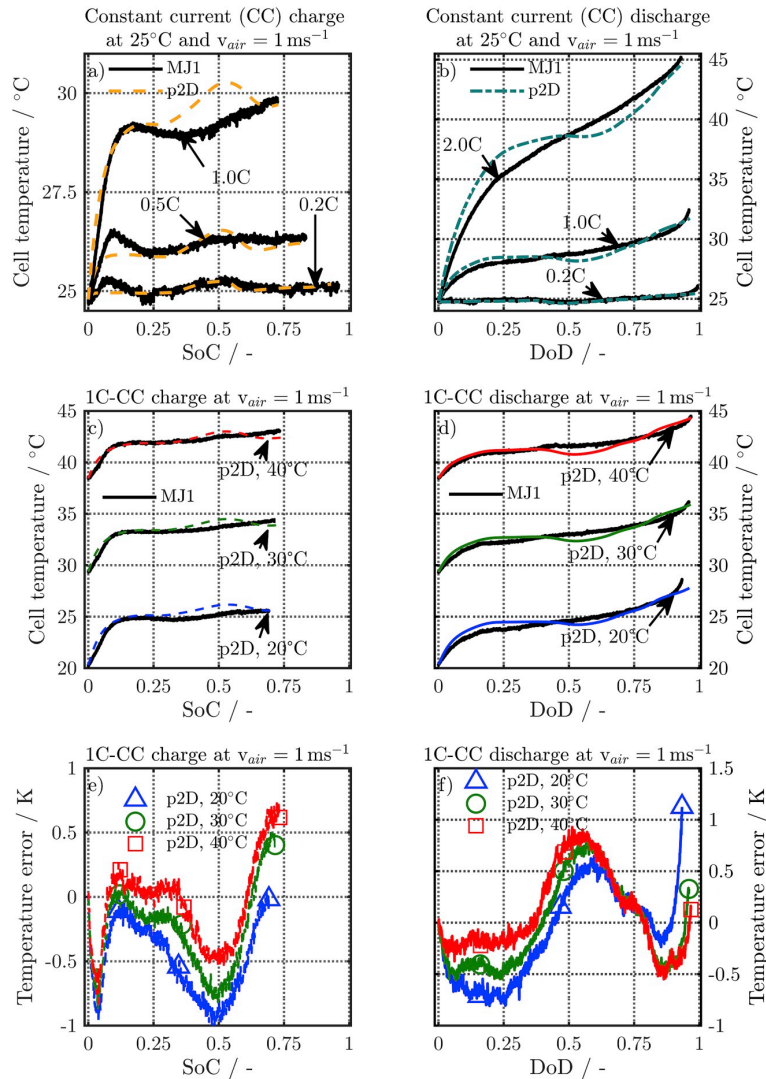
Fig. 5. Thermography measurements of the MJ1 cell to validate the simulated cell temperature at different C-rates for charge (a) and discharge (b) at 25 °C in terms of the single p2D model. 1C-CC charge (c) and discharge (d) validation at different ambient temperatures (20 °C, 30 °C and 40 °C) are shown for the single p2D simulation results together with the related error (e and f).

Table 5
Different porous electrodes with NMC-111/C and NMC-811/SiC ref. to 1C.

Tag		NMC-111/C[a]			NMC-811/SiC		
		high	std	low	high	std	low
Porosity	%	45/50	35/35	17.1/21.6	45/50	35/35	17.1/21.6
Capacity	Ah	1.54	1.95	2.67	2	2.71	3.35
Specific capacity	mAh cm^{-2}	2.2	2.7	3.7	2.8	3.8	4.7
Specific energy	Wh kg^{-1} [b]	122	155	211	159	214	275
density	Wh l^{-1} [c]	339	428	586	440	593	713

[a] P2D parameterization according to Ref. [26,77,82] (see A.11).
[b] Ref. to cell weight of 45.8 g (MJ1).
[c] Ref. exemplarily to a 18650 volume of 16.5 cm^3 and nominal voltage of 3.635 V [23] (MJ1).

phase. Note, as the maximum charge-rate of the MJ1 cell is limited to 1C, no experimental data can be shown beyond 1C. The influence of morphology is analyzed via modeling three different porosities (*i.e.* high, standard (std) and low) and an overview of the simulated cell configurations is shown in Table 5.

The simulation results are shown in Fig. 6 in terms of the gained SoC level at the end-of-charge (EoC) (a) referring to the capacity shown in Table 5, the potential drop ($\Phi_s - \Phi_l$) at the anode-separator interface (b) and its cumulative time-integral (c, see also Eq. (2)). Regarding Fig. 6 a, the expectable decrease of the gained SoC with increasing C-rate and decreasing porosity is well in line with other works [20].

Charge-rate limitation appears beyond 3C for both NMC-111/C and NMC-811/SiC due to mass transport narrowing for lithium-ions in the electrolyte with appearing depletion of the pore, which limits the capability of charge transfer and leads to a premature approach of the cut-off voltage. Regarding the indication of lithium plating in Fig. 6 b, no plating is indicated at 3C except for the NMC-111/C-low simulation results. Analyzing the reaction kinetics during 3C of the NMC-811/SiC-
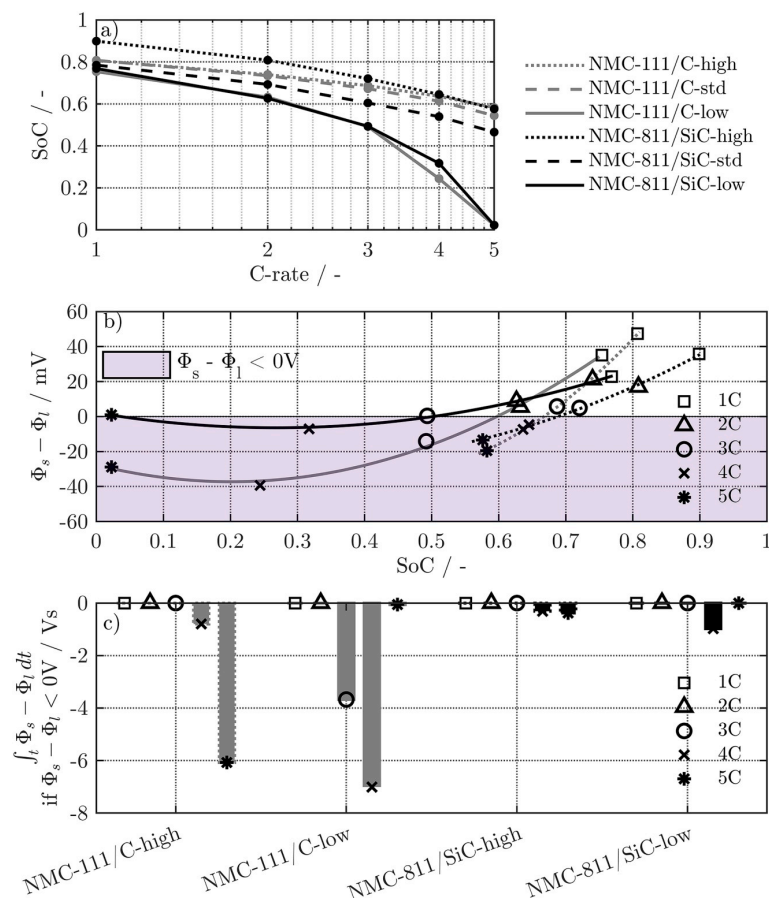
Fig. 6. Single p2D CC-charging simulation results of NMC-111/C and NMC-811/SiC lithium-ion cells with different electrode porosities (high/std/low) from 1C to 5C. The SoC referring to the usable discharge capacity (3.35 Ah) is shown over the applied C-rate in a) and the likelihood of lithium plating is evaluated locally in b) and over time in c).

low and the NMC-111/C-low configuration, reveals larger over-potentials ($\approx$ 36%) due to a lower exchange current density ($\approx$ 40%) on average for the NMC-111/C cell which cause the negative potential drop. The lower exchange current density of the NMC-111/C compared to the NMC-811/SiC cells is caused by the lower maximum concentration ($\approx$ 10%) and the lower heat generation ($\approx$ 25%) and calculated temperature ($\approx$ 13%) resulting in lower reaction kinetics. In the same way lower potential drops are caused for 4C and 5C for the NMC-111/C cells. In this matter, differences in reaction kinetics between natural and silicon-doped graphite were already seen [13] and experimental analysis on the reaction rates of high-capacity and standard NMC-type active materials could further clarify the findings of this work.

Using the indication state given in Eq. (2) of this work, the tendency of lithium plating can be estimated as shown in Fig. 6 c referring to the whole charge process instead of evaluating a single time step as in Fig. 6 b. Gaining approximately the same cell SoC level at 4C, lithium plating is indicated two times more for NMC-111/C compared to NMC-811/SiC for high porous electrodes. Regarding 5C, the ratio increases up to a factor of 16. For low porous electrodes, similar characteristics are seen with even higher indication values of up to -7 Vs for the NMC-111/C-low cell. At 5C, the cut-off voltage is reached at cell SoC levels below 3% and the charge process ends before the onset of lithium plating. The simulation results suggest, that NMC-811/SiC type cells reveal less onset of lithium plating (> -1 Vs) compared to NMC-111/C for the

used parameterizations. To investigate the indicator based findings more, future work will focus on modeling aging mechanisms such as lithium plating/stripping and solid-electrolyte interphase (SEI) growth which will also be compared to other findings on this research field [83–85].

As the single p2D model assumes homogeneous electrode utilization along the electrodes, no lateral electrode effects can be considered, which are induced via the total number [45], position [46] and the geometry of the tabs [41] or the overall thickness of the current collector foils [48,86]. To evaluate lateral electrode effects, the original tab design of the MJ1 cell and three alternative tab patterns are investigated at high-rate CC- and modified fast charging protocols with the MuDiMod.

4.6. Relation between tab design and non-homogeneous electrode utilization

High-rate CC-charging from 1C to 4C is simulated from 2.5 to 4.2 V with the MuDiMod regarding the four different tab designs (see Table 4). The tendency of lithium plating along the electrode is shown at 3C in Fig. 7 according to Eq. (2) together with three reference points, which describe characteristic maxima (*i.e.* near the tabs - P1, P2) and minima (*i.e.* far from the tabs - P3) of local electrode polarization. The MJ1 tab pattern (Fig. 7 a and b) reveals the smallest cell SoC level (41.1%) at EoC due to the longest effective current pathways and related ohmic losses, showing no indication towards lithium plating. In
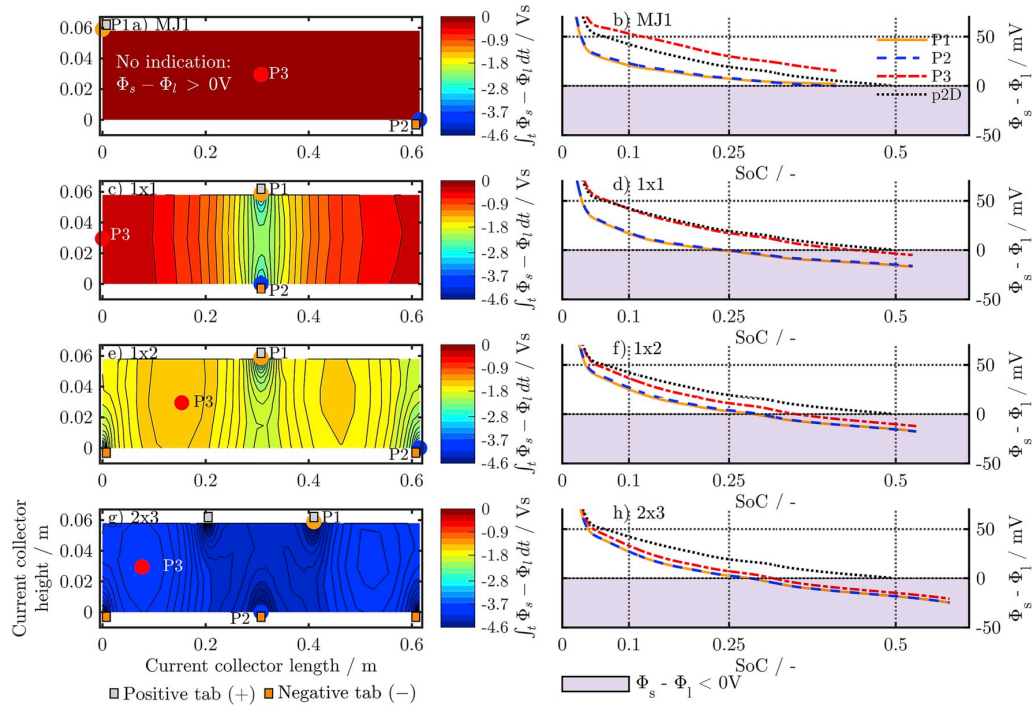
Fig. 7. MuDiMod simulation results for single-tab (MJ1, 1x1) and multi-tab design (1x2, 2x3) electrodes at high-rate 3C-CC charging with the integrated (a, c, e and g, see Eq. (2)) and transient (b, d, f and h) potential drop at the anode-separator interface to evaluate the tendency of lithium plating. As a reference, the single p2D simulation results are depicted as well (see b, d, f and h).

contrast, the remaining configurations (see Fig. 7 c to h) yield to higher SoC levels (52.5%, 53% and 58.1%) at the cost of possible lithium plating, which starts at 43.6%, 34.8% and 31.6% SoC along the entire electrode (*i.e.* P3 < 0V) for the 1x1, 1x2 and 2x3 tab pattern, respectively. Looking at the tab-near regions (P1 and P2) in Fig. 7 d, f and h, the onset of lithium plating appears even earlier at a cell SoC of 23.6%, 28.7% and 28.1%, respectively. Fig. 7 c, e and g illustrate the local onset near the tabs and the penetration depth of the regions far from the tabs for the likelihood of lithium plating. The 2x3 pattern shows the highest risk with an average value of −4.2 Vs compared to −1.93 Vs and −1.95 Vs for the 1x2 and 1x1 configuration. Regarding the temperature distribution on the electrodes at EoC, the maximum spread appears for the MJ1 pattern with 59.7 °C and 67.5 °C at the outer end and the positive tab in the center of the jelly roll, which is well in line with experimental results for high-energy 18650 cells during fast charging [29].

However, a far more uniform temperature distribution with a maximum spread of 2 K and lower average temperatures is seen for the remaining tab patterns. The local temperature distribution at 3C and EoC is shown in the supplementary material of this work.

In sum, the MJ1 tab pattern avoids the onset of lithium plating during 3C-CC thanks to the positive influence on reaction kinetics of its higher average temperature (48.3 °C) as compared to the remaining configurations (45.8 °C (1x1), 45 °C (1x2) and 44.3 °C (2x3)). However, it promotes local overheating close to the tabs which is detrimental to the safety and lifetime of the cell. Reducing the pathway of the electrons along the electrode by 50% via using the 1x1 configuration, higher SoC levels compared to the MJ1 together with the earliest onset of lithium plating compared to the remaining models appears. In case of using the 1x2 or 2x3 tab pattern, the gained SoC level could be increased by further reducing ohmic losses on the current collector foils which is well in line with other works [41,46,48]. However, the simulation results suggest that, the more tabs are used, the more the

potential drop decreases and the highest indication of lithium plating is seen for the 2x3 configuration. In the future, these simulation results shall be investigated experimentally by using lithium reference electrodes to measure local potentials [29,38] during the charging process.

4.7. Relative error between single p2D model and multi-dimensional model

The simulation results of the single p2D model and the multi-dimensional model are shown in Fig. 7 b, d, f and h to evaluate the findings towards a homogeneously utilized electrode and determine the modeling error when using a single p2D. In the case of the MJ1 tab design, the single p2D model predicts a 20% higher cell SoC than the multi-dimensional model. In contrast, the p2D model underestimates the gained SoC level and does not indicate the onset of lithium plating for the alternative tab designs. Hence, neglecting the electrical configuration determines the simulation error of the p2D model. In addition, using a 0D thermal model limits the validity of the temperature calculation. The averaged single p2D simulation errors are summarized in Table 6 for the cell voltage, temperature and the potential drop at the anode-separator interface.

To account for the model limitations when using a single p2D model for indication of lithium plating, the shown discrepancies in Table 6 for the potential drop can be used for adaption in terms of charge control algorithms as presented in Chu et al. [73].

Table 6
Single p2D simulation error on average at 3C-CC.

	MJ1	1x1	1x2	2x3
V_{cell} /mV	42	34	44	88
T_{cell} /K	2.2	2.9	3.8	5.2
$\Phi_s - \Phi_l$ /mV[a]	16	21	16	16

[a] $x = L_{neg}$.

Table 7
Usable energy density and affected SoC range by lithium plating for CC-charging.

Charge-rate	Usable specific energy density/ Wh kg^{-1a}				Affected SoC range by $\Phi_s - \Phi_l < 0$ V/%			
	MJ1	1x1	1x2	2x3	MJ1	1x1	1x2	2x3
1C-CC	211	218	218	222	0	0	0	0
2C-CC	170	186	187	194	0	0	5.6	7
3C-CC	122	154	155	169	0	28.3	36	47.1
4C-CC	22	108	114	138	11.6	86.1	87.1	90.2

[a] Ref. to cell weight of 45.8 g (MJ1).

4.8. Modified CC-charging protocols

To evaluate the CC-charging scenarios from 1C to 4C for all tab designs, the usable specific energy density is calculated from the amount of charge at EoC and the average of cell voltage from the MuDiMod simulation results as shown in Table 7. The usable amount of charge, which is probably affected by lithium plating, is approximated via Eq. (3) and referenced to the amount of charge at EoC. The calculated ratios correspond to the SoC range affected by lithium plating and are shown in Table 7.

Due to its poor electrical configuration, the MJ1 design shows the highest decrease of specific energy with increasing C-rate, but also the lowest indication of lithium plating as the cut-off voltage is reached prematurely. The 1x1 and 1x2 design show quite similar characteristics with lower usable energy loss but increased indication of lithium plating. The highest usable energy densities appear for the 2x3 design together with the highest indication of lithium plating which affects almost half of the usable charge at 3C-CC.

In order to achieve higher cell SoC levels at EoC and to reduce the SoC range affected by lithium plating, the 3C-CC charging process is modified in this work. The modified charging strategies (MC) for all tab designs start with a charging rate of 3C, subsequently switch to 2C and end at 4.2 V. In case of the MJ1 design, the second, lower current stage helps to avoid premature EoC. In case of the other tab configurations (*i.e.* 1x1, 1x2 and 2x3), the first onset of lithium plating can be avoided (see Fig. 7 - P1 and P2). At the switching points, the applied charge rate is lowered and thus the polarization on the electrode is reduced. This results in increased potential drops $\Phi_s - \Phi_l > 0$V and lower the affected SoC range by lithium plating. The switching point for the MJ1 design was set at 40.4% SoC and to 23.1% SoC, 28.6% SoC and 28.1% SoC for the 1x1, 1x2 and 2x3 design, respectively. In case of the 2x3 tab design, a third current stage at 1.5C was implemented at 62.6% SoC since lithium plating was indicated in the second current stage which affected approximately 14% of the SoC range.

The 3C-CC and MC charging strategies for all tab designs are shown in Fig. 8 vs. the cell SoC and the single p2D simulation results as a reference.

Fig. 8 b shows the improvement of SoC at EoC for applying the MC strategy and for all tab designs SoC levels beyond 60% with marginal indication of lithium plating could be achieved compared to the standard 3C-CC. Regarding the single p2D simulation results, the switching point from 3C to 2C was set to 48.8% SoC to avoid premature EoC by reaching the cut-off voltage. If a single p2D is used for evaluating fast charge protocols, adaption referring to the tab design as shown in Table 6 must be considered to avoid falsely predicted switching points.

Comparing standard 3C-CC and MC charging simulation results with different tab designs, reductions of 99.7%, 99.2% and 99.6% of the affected SoC range by lithium plating and SoC increases of +12.7, +12.2 and + 15.8% for the 1x1, 1x2 and 2x3 tab design can be realized. The overall charging times were extended by 349, 406, 367 and 532 s, respectively. Over 19.4% increase of usable capacity compared to 3C-CC could be simulated for the MJ1 configuration in 846 s and no tendency of lithium plating was observed.
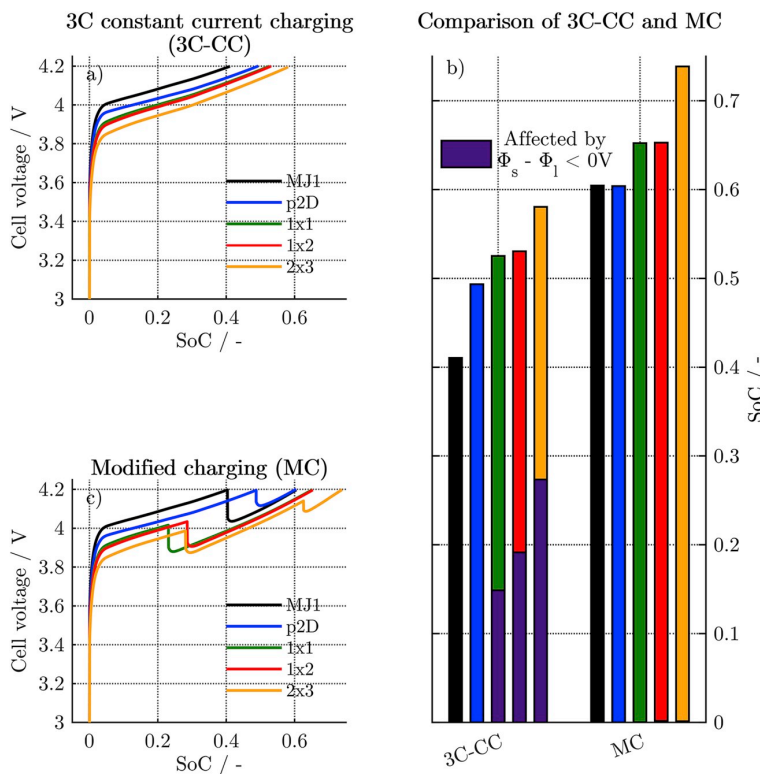

Fig. 8. The 3C-CC (a) and the modified (c) charging strategy are illustrated by the cell voltage vs. the cell SoC (ref. to 3.35 Ah). The comparison of the gained cell SoC levels (b) for both charging strategies is shown with the affected SoC range by lithium plating (see Eq. (3)) in case of all tab designs and the single p2D model as a reference.

In sum, the MC strategy increased the cell SoC at EoC and the simulated indicator states suggests prevention of lithium plating either by applying a global cell voltage or a local anode potential threshold.

5. Conclusion

A full electrochemical-thermal parameterization of a newman-type p2D model for a high-capacity and highly densified NMC-811/SiC electrode pair is presented, including measured open-circuit potentials and entropic coefficients. For both charge and discharge, DVA analysis of full and half cells revealed marginal deviations and simulation results for calorimetry and thermography measurements in a range of 20 °C up to 40 °C ambient temperature showed the validity of the presented parameterization. The charge-rate capability of high and low density electrodes was assessed by means of the single p2D model for both standard NMC-111/C and high-capacity NMC-811/SiC active material. Beyond 3C-CC, liquid transport limitation occurred. A higher tendency of lithium plating could be observed for NMC-111/C, likely due to lower maximum concentrations in the anode and a lower heat generation rate compared to NMC-811/SiC. Depending on the tab design, electrode utilization can be very non-uniform. Comparison of modeling results of the single p2D and the multi-dimensional model made it clear that a more detailed evaluation of the charging behavior should be based on the multi-dimensional model, especially when the onset of lithium plating needs to be estimated accurately. The multi-dimensional model results revealed that, with an effective electrode length of 61.5 cm, a single tab design leads to local overheating and a relatively low end-of-charge SoC at high-rate CC-charging because the cut-off voltage is reached prematurely. However, no indication of lithium plating could be observed until 3C. Increasing the number of tabs or reducing the effective electrode length by 50% leads to a more homogenous temperature distribution, a lower average cell temperature, and increased end-of-charge SoC due to lower ohmic losses in the current collectors. However, more tabs and decreased effective electrode length also result in a higher likelihood of lithium plating. Optimized, two- or three-stage CC-charging protocols were derived from the multi-dimensional model results by defining a switching point either based on cell voltage or on local anode overpotential to account for the onset of lithium plating. The charge protocols allow charging to SoC levels above 60% within 18 min with minimal risk of lithium plating.

In future work, the models presented in this work could be extended by a multi-particle approach to account also for smaller sized particles which may affect the lithium plating characteristic or by locally calculated lithium plating kinetics. We think there are plentiful applications to the presented multi-dimensional model, e. g. the investigation of tab-cooling techniques that have been proposed to reduce local overheating [87].

Appendix A. Supplementary data

Supplementary data to this article can be found online at https://doi.org/10.1016/j.jpowsour.2018.11.043.

Appendix A

Table A.8

Calculation of heat transfer coefficient at convective air-cooling during infrared thermography measurements.

Physical properties[I] of dry air at 25° and 1 bar ambient pressure			
Heat capacity	cp, air	1007 Jkg^{-1} K^{-1}	
Thermal conductivity	λ_{air}	0.0255 Wm^{-1} K^{-1}	
Dynamic viscosity	η_{air}	1.8483×10^{-5} Ns m^{-2}	
Density	ρ_{air}	1.1846 kg m^{-3}	
Prandtl number	Pr	$\eta_{air} \cdot c_{p,air} \cdot \lambda_{air}^{-1} = 0.7299$	
Heat transfer coefficient under forced convective air-flow[II]			
Characteristic length	L	18.7 cm [III]	
Velocity	v_{air}	1 m s^{-1}	2 m s^{-1}
Reynolds number	Re	$\rho_{air} \cdot v_{air} \cdot L \cdot \eta_{air} = 1229.4$	2235.9
Nusselt number	Nu	$0.25 \cdot Re^{0.6} \cdot Pr^{0.38} = 15.8$	22.7
Heat transfer Coefficient	α_{air}	$Nu \cdot \lambda_{air} \cdot L^{-1} = 22.1$ Wm^{-2} K^{-1}	31.7 Wm^{-2} K^{-1}

[I] Ref. [88] [II] Ref. [89] [III] Ref. [23].

Table A.9

Properties of the electrolyte and the current collectors.

Electrolyte	1 M LiPF$_6$ in PC/EC/DMC
Salt diffusivity D_l[I]/m^{2}s^{-1}	$10E\text{-}4 \cdot 10^{-4.43 - \frac{54}{T-229-5c_l} - 0.22c_l}$
Ionic conductivity κ_l[I]/ S m^{-1}	$0.1c_l(-10.5 + 0.668c_l + 0.494c_l^2 + 0.074T - 0.0178c_lT$ $- 8.86 \cdot 10^{-4}c_l^2T - 6.96 \cdot 10^{-5}T^2 + 2.8 \cdot 10^{-5}c_lT^2)$
Activity $\frac{d\,lnf_{\pm}}{d\,lnc_l}$ [I]/-	$(0.601 - 0.24c_l^0.5 + 0.983(1 - 0.0052(T - 294))c_l^{1.5}) \cdot (1 - t_+^0)^{-1} - 1$
Transference t_+^0 [I]/-	0.38

(continued on next page)

Table A.9 (*continued*)

Electrolyte	1 M LiPF$_6$ in PC/EC/DMC	
Ref. concentration c_{ref} [I]/mol m^{-3}	1000	

Current Collector	Copper	Aluminum
Height H/cm	5.8*	5.8*
Length W/cm	61.5*	61.5*
Electrical conductivity σ_{cc} /S m^{-1}	$\frac{5.96 \cdot 10^7}{1 + 3.383 \cdot 10^{-3}(T - 293.15\mathrm{K})}$ S m^{-1} [II]	$\frac{3.78 \cdot 10^7}{1 + 4.290 \cdot 10^{-3}(T - 293.15\mathrm{K})}$ [III]

[I] Ref. [69] [II] Ref. [90] [III] Ref. [91] * Measured and idealized for 2D electrical model.

Table A.10

Thermal parameterization of the single components and the electrode stack.

Properties of single layers		Anode		Separator*	Cathode		Electrolyte
		Copper	SiC		NMC-811	Aluminum	
Thickness	L in μm	11	86.7	12	66.2	17.3	–
Density[I]	ρ in kg m^{-3}	8950 [II]	2242 [III]	1009	4870 [IV]	2710 [II]	1130
Heat capacity[I]	c_p in J kg^{-1}K^{-1}	385	867[V]	1978.2	840.1[VI]	903	2055.1
Heat conductivity[I]	λ in W m^{-1}K^{-1}	398	1.04	0.33	1.58	238	0.6

Properties of electrode stack [I,**]		Effective values
Thickness	L_{stack} in μm	$L_{cc,-} + 2\cdot(L_{neg} + L_{sep} + L_{pos}) + L_{cc,+} = 358$
Density[I]	ρ_{stack} in kg m^{-3}	$\frac{\sum_i L_i \cdot \rho_i}{L_{stack}} = 2761.7$
Heat capacity[I]	c_{stack} in J kg^{-1}K^{-1}	$\frac{\sum_i L_i \cdot \rho_i \cdot c_{p,i}}{L_{stack} \cdot \rho_{stack}} = 918.8$
Heat conductivity[I]	$\lambda_\perp$ in W m^{-1}K^{-1}	$\left(\frac{1}{L_{stack}} \cdot \sum_i \frac{L_i}{\lambda_{p,i}}\right)^{-1} = 2.3$
	$\lambda_\parallel$ in W m^{-1}K^{-1}	$\frac{\sum_i L_i \cdot \lambda_{p,i}}{L_{stack}} = 24.3$

[I] if not indicated otherwise, the properties and calculation are taken from Ref. [92].
[II] Ref. [56] [III] Ref. [10] [IV] Ref. [7] [V] Ref. [93] [VI] Ref. [94].
* Polyolefin ** Porous material superimposed of solid and liquid phase.

Table A.11

Parameterization of the single p2D model with NMC-111/C electrodes.

Geometry		Graphite (C)	Separator	NMC-111
Thickness L		86.7 μm[m]	12 μm[m]	66.2 μm[m]
Particle radius R_p		11 μm[I,D50]		5 μm[II,D50]
Active material fraction ε_s		0.45[I]		0.38[I]
Inactive fraction $\varepsilon_{s,na}$		0.05[I]		0.17[I]
Porosity ε_l		0.5[I]	0.5[I]	0.45[I]
Bruggeman coefficient [IV,*]		1.5	1.5	1.5
Thermodynamics				
Equilibrium potential E_{eq}		Ref. [26]		Ref. [26]
Entropic coefficient $\frac{\partial E_{eq}}{\partial T}$		Ref. [77]		Ref. [77]
Stoichiometry	100% SoC	0.76		0.39
	0% SoC	0.006		0.94
Max. concentration $c_{s,max}$		31 360 mol m^{-3} [II]		52 500 mol m^{-3} [II]
Transport				
Solid diffusivity D_s**		5×10^{-14} m^2 s^{-1}[II]		5×10^{-13} m^2 s^{-1}[II]
Specific activation **		1200 K[e]		1200 K[e]
Solid conductivity σ_s		100 S m^{-1}[II]		3.8 S m[I]
Film resistance R_f		0.0035 Ω m^2 [III]		0 Ω m^{2e}

Table A.11 (*continued*)

Geometry	Graphite (C)	Separator	NMC-111
Kinetics			
Reaction rate constant k**	2.22×10^{-11} m s^{-1} [I]		6×10^{-12} m s^{-1} [I]
Specific activation $\frac{E_{a,k}}{R}$**	3600 K^e		3600 K^e
Transfer coefficient $\alpha_{a/c}$	0.5^e		0.5^e

[I] Ref. [26] [II] Ref. [82] [III] Ref. [22] [IV] Ref. [67] m = measured e = estimated.

* Effective transport correction according to Bruggeman (Ref. [67]): $\Psi_{eff} = \varepsilon^{\beta} \cdot \Psi_0$.

** Arrhenius law (Ref. [68]): $k = A \cdot \exp\left(\frac{E_{a,i}}{R} \frac{(T - 298[\text{K}])}{T \cdot 298[\text{K}]}\right)$.

Table A.12

Equations for the single p2D, 2D electrical and 3D thermal model.

Electrochemical-thermal model (single p2D)	
Mass balance[I]	$\varepsilon_l \frac{\partial c_l(x,t)}{\partial t} = \frac{\partial}{\partial x}\left(D_l^{eff} \frac{\partial c_l(x,t)}{\partial x} + \frac{i_l(x,t)(1-t_+^0)}{F}\right)$
	$\varepsilon_s \frac{\partial c_s(x,t,r)}{\partial t} = \frac{1}{r^2}\frac{\partial}{\partial r}\left(D_s r^2 \frac{\partial c_s(x,t,r)}{\partial r}\right)$
Potentials[I]	$\frac{\partial \Phi_l(x,t)}{\partial x} = -\frac{i_l(x,t)}{\kappa_l^{eff}} + \frac{2RT}{F}(1-t_+^0)\left(1 + \frac{d \ln f_\pm}{d \ln c_l(x,t)}\right)\frac{\partial \ln c_l(x,t)}{\partial x}$
	$\frac{\partial \Phi_s(x,t)}{\partial x} = -\frac{i_{app}(t) - i_l(x,t)}{\sigma_s}$ with $i_{app}(t) = i_s(x,t) + i_l(x,t) \quad \forall\, x, t$
Charge balance[I]	$\frac{\partial i_l(x,t)}{\partial x} + \frac{\partial i_s(x,t)}{\partial x} = 0$ with $\frac{\partial i_s(x,t)}{\partial x} = -\frac{3\varepsilon_s}{R_p} F j_n(x,t)$
Electrode kinetics[I]	$j_n(x,t) = \frac{i_0(x,t)}{F}\left[\exp\left(\frac{\alpha_a F \eta(x,t)}{RT}\right) - \exp\left(-\frac{\alpha_c F \eta(x,t)}{RT}\right)\right]$
	$\eta(x,t) = \Phi_s(x,t) - \Phi_l(x,t) - E_{eq}(x,t) - j_n(x,t)FR_f$
	$i_0(x,t) = F k (c_{s,max} - c_{ss}(x,t))^{\alpha_c} (c_{ss}(x,t))^{\alpha_a} (c_l(x,t))^{\alpha_a}$
Temperature[I,II]	$m\, c_p \frac{\partial T}{\partial t} = A_a \cdot q_{p2D} + Q_{ext} - Q_{conv} - Q_{rad} - Q_{con}$
Heat Sources	$q_r = \frac{3\varepsilon_s F}{R_p}\int_{x*} j_n \cdot \eta\, \mathrm{d}x$
	$q_{rev} = \frac{3\varepsilon_s F}{R_p}\int_{x*} j_n \cdot \frac{\partial E_{eq}}{\partial T}\cdot T\, \mathrm{d}x$
	$q_l = \int_{x=0}^{L_{neg}+L_{sep}+L_{pos}} i_l \cdot \frac{\partial \Phi_l}{\partial x}\, \mathrm{d}x$
	$q_s = \int_{x*} i_s \cdot \frac{\partial \Phi_s}{\partial x}\, \mathrm{d}x$
	$q_{p2D} = q_r + q_{rev} + q_l + q_s$
	$Q_{ext} = i_{app}^2 \cdot R_{ext}$ $\quad\quad Q_{conv} = \alpha_{conv} A_{surf}(T - T_\infty)$
	$Q_{rad} = \varepsilon_{rad}\sigma_b A_{surf}(T^4 - T_\infty^4)$ $\quad Q_{con} = A_{con}\cdot\frac{\lambda_{con}}{L_{con}}(T - T_{con})$

2D electrical model	
	$\nabla = \left(\frac{\partial}{\partial x'}, \frac{\partial}{\partial y'}\right)^T$ $\quad \sigma = \begin{bmatrix} \sigma_{cc,x'} & 0 \\ 0 & \sigma_{cc,y'} \end{bmatrix}$
Charge Balance	$I = \sum_i i_{p2D,i}\cdot A_i$
Potentials	$\sigma_{cc}\nabla^2\phi_{cc} = \pm^{**}\frac{i_{p2D}}{L_{cc}}$
Heat source	$q_{cc} = L_{cc}\cdot\sigma_{cc}\cdot(\nabla\phi_{cc})^2$

3D thermal model	
	$\nabla = \left(\frac{\partial}{\partial r''}, \frac{\partial}{\partial \psi}, \frac{\partial}{\partial z''}\right)^T$ $\quad \lambda = \begin{bmatrix} \lambda_\perp & 0 & 0 \\ 0 & \lambda_\parallel & 0 \\ 0 & 0 & \lambda_\parallel \end{bmatrix}$
Temperature	$\rho_{stack}\, c_p \frac{\partial T}{\partial t} = \lambda\nabla^2 T + q$
Heat source	$q = \frac{\chi_{p2D}}{L_{neg}+L_{sep}+L_{pos}} q_{p2D} + \frac{\chi_{cc,+}}{L_{cc,+}} q_{cc,+} + \frac{\chi_{cc,-}}{L_{cc,-}} q_{cc,-}$ $- q_{conv,\Gamma} - q_{rad,\Gamma} - q_{con,\Gamma}$

[I] Ref. [24] [II] Ref. [95] Γ Only at the surface of the jelly roll.

$x* = x \in [0, L_{neg}] \wedge [L_{neg}+L_{sep}, L_{neg}+L_{sep}+L_{pos}]$ ** < 0 for cc,- and > 0 cc,+.

Table A.13
Nomenclature I.

Greek symbols		
α		Transfer coefficient
α_{conv}	W m^{-2} K^{-1}	Heat transfer coefficient
β		Bruggeman coefficient
ε		Volume fraction
ε_{rad}		Radiation emission coefficient
ε		Numerical tolerance
η	V	Overpotential
κ	S m^{-1}	Ionic conductivity
λ	W m^{-1} K^{-1}	Heat conductivity
Λ	m	Arc length
ρ	kg m^{-3}	Mass density
σ	S m^{-1}	Electrical conductivity
σ_b	5.67×10^{-8} W m^{-2} K^{-4}	Stefan-Boltzmann constant
τ		Tortuosity
Φ	V	Electrical potential
ψ	rad	Azimuthal-coordinate in 3D model
Ψ_{arc}	rad	Azimuthal angle
χ		Thickness ratio

Indices	
a	anodic reaction (oxidation)
c	cathodic reaction (reduction)
cc	current collector
con	Heat conduction
conv	Heat convection
eff	Transport corrected (Bruggeman correlation [67])
ext	External heat (*i.e.* from grid resistance)
l	Liquid phase (*i.e.* Electrolyte)
neg	Negative electrode
pos	Positive electrode
rad	Heat radiation
r	Reaction heat
rev	Reversible heat
s	Solid phase (*i.e.* Active particle)
sep	Separator
ss	Solid phase (*i.e.* Active particle surface)
stack	Electrode stack
surf	Surface
+	Positive current collector
−	Negative current collector

Table A.14
Nomenclature II.

Latin symbols		
a	m^{-1}	Specific surface
b_g	mAh g^{-1}	Maximum theoretical loading
c	mol m^{-3}	Concentration of lithium cations (Li$^+$)
$c_{s,max}$	mol m^{-3}	Maximum theoretical concentration of Li$^+$
c_p	J kg^{-1} K^{-1}	Heat capacity
D	m^2 s^{-1}	Diffusion coefficient
E_{eq}	V	Equilibrium potential vs. Li/Li$^+$
$f_{\pm}$		Mean molar activity coefficient of electrolyte
F	96 485 As mol^{-1}	Faraday's constant
H	m	Height of electrode/current collector
i	A m^{-2}	Current density
I	A	Applied current
i_{app}	A m^{-2}	Applied current density
i_n	A m^{-2}	Current density perpendicular to particle surface

Table A.14 (*continued*)

Latin symbols		
i_{p2D}	A m^{-2}	Current density perpendicular to current collectors
i_0	A m^{-2}	Exchange current density
j_n	mol m^{-2}s^{-1}	Pore-wall flux
k	m s^{-1}	Reaction rate constant
L	m	Thickness
m	kg	Mass of the jelly roll
r	m	Radial-coordinate in active particles of p2D model
r''	m	Radial-coordinate in 3D model
R	8.314 J mol^{-1} K^{-1}	Gas constant
R_{ext}	Ω m^2	Grid resistance
R_f	Ω m^2	Surface-layer resistance
R_p	m	Particle radius
q	W m^{-2}	Heat generation rate per area
Q	W	Heat generation rate
t	s	Time
T	K	Temperature
t_+^0		Transport number of Li$^+$
W	m	Length of electrode/current collector
x	m	x-coordinate in p2D model
x'	m	x-coordinate in 2D model
y'	m	y-coordinate in 2D model
x''	m	x-coordinate in 3D model
y''	m	y-coordinate in 3D model
z''	m	z-coordinate in 3D model

References

[1] D. Andre, S.-J. Kim, P. Lamp, S.F. Lux, F. Maglia, O. Paschos, B. Stiaszny, Future generations of cathode materials: an automotive industry perspective, J. Mater. Chem. A 3 (13) (2015) 6709–6732, https://doi.org/10.1039/C5TA00361J.

[2] A. Chatelain, M. Erriquez, P.-Y. Moulière, P. Schäfer, What a teardown of the latest electric vehicles reveals about the future of mass-market evs, https://www.mckinsey.com/industries/automotive-and-assembly/our-insights/what-a-teardown-of-the-latest-electric-vehicles-reveals-about-the-future-of-mass-market-evs, (2018).

[3] S.-T. Myung, F. Maglia, K.-J. Park, C.S. Yoon, P. Lamp, S.-J. Kim, Y.-K. Sun, Nickel-rich layered cathode materials for automotive lithium-ion batteries: achievements and perspectives, ACS Energy Lett. 2 (1) (2016) 196–223, https://doi.org/10.1021/acsenergylett.6b00594.

[4] T. Liang, Advanced Xev Battery Development at Catl, Aabc Europe - Advanced Automotive Battery Conference, (2017), pp. 1–15.

[5] G.E. Blomgren, The development and future of lithium ion batteries, J. Electrochem. Soc. 164 (1) (2016) A5019–A5025, https://doi.org/10.1149/2.0251701jes.

[6] H.-J. Noh, S. Youn, C.S. Yoon, Y.-K. Sun, Comparison of the structural and electrochemical properties of layered li(ni_xco_ymn_z)o2 (x = 1/3, 0.5, 0.6, 0.7, 0.8 and 0.85) cathode material for lithium-ion batteries, J. Power Sources 233 (2013) 121–130, https://doi.org/10.1016/j.jpowsour.2013.01.063.

[7] R. Jung, M. Metzger, F. Maglia, C. Stinner, H.A. Gasteiger, Oxygen release and its effect on the cycling stability of linixmnycozo2 (nmc) cathode materials for li-ion batteries, J. Electrochem. Soc. 164 (7) (2017) A1361–A1377, https://doi.org/10.1149/2.0021707jes.

[8] Z. Luo, D. Fan, X. Liu, H. Mao, C. Yao, Z. Deng, High performance silicon carbon composite anode materials for lithium ion batteries, J. Power Sources 189 (1) (2009) 16–21, https://doi.org/10.1016/j.jpowsour.2008.12.068.

[9] J.-Y. Li, Q. Xu, G. Li, Y.-X. Yin, L.-J. Wan, Y.-G. Guo, Research progress regarding si-based anode materials towards practical application in high energy density li-ion batteries, Mater. Chem. Front. 1 (9) (2017) 1691–1708, https://doi.org/10.1039/C6QM00302H.

[10] R. Dash, S. Pannala, Theoretical limits of energy density in silicon-carbon composite anode based lithium ion batteries: supplementary information, Sci. Rep. 6 (2016) 27449, https://doi.org/10.1038/srep27449.

[11] N. Dimov, S. Kugino, M. Yoshio, Mixed silicon–graphite composites as anode material for lithium ion batteries, J. Power Sources 136 (1) (2004) 108–114, https://doi.org/10.1016/j.jpowsour.2004.05.012.

[12] H. Zhang, X. Li, H. Guo, Z. Wang, Y. Zhou, Hollow si/c composite as anode material for high performance lithium-ion battery, Powder Technol. 299 (2016) 178–184, https://doi.org/10.1016/j.powtec.2016.05.002.

[13] B. Fuchsbichler, C. Stangl, H. Kren, F. Uhlig, S. Koller, High capacity graphite–silicon composite anode material for lithium-ion batteries, J. Power Sources 196 (5) (2011) 2889–2892, https://doi.org/10.1016/j.jpowsour.2010.10.081.

[14] Z. Du, J. Li, C. Daniel, D.L. Wood, Si alloy/graphite coating design as anode for li-ion batteries with high volumetric energy density, Electrochim. Acta 254 (2017) 123–129, https://doi.org/10.1016/j.electacta.2017.09.087.

[15] C.K. Chan, H. Peng, G. Liu, K. McIlwrath, X.F. Zhang, R.A. Huggins, Y. Cui, High-performance lithium battery anodes using silicon nanowires, Nat. Nanotechnol. 3 (1) (2008) 31–35, https://doi.org/10.1038/nnano.2007.411.

[16] T.D. Hatchard, J.R. Dahn, In situ xrd and electrochemical study of the reaction of lithium with amorphous silicon, J. Electrochem. Soc. 151 (6) (2004) A838, https://doi.org/10.1149/1.1739217.

[17] J.-H. Lee, W.-J. Kim, J.-Y. Kim, S.-H. Lim, S.-M. Lee, Spherical silicon/graphite/carbon composites as anode material for lithium-ion batteries, J. Power Sources 176 (1) (2008) 353–358, https://doi.org/10.1016/j.jpowsour.2007.09.119.

[18] M.-Q. Li, M.-Z. Qu, X.-Y. He, Z.-L. Yu, Effects of electrolytes on the electrochemical performance of si/graphite/disordered carbon composite anode for lithium-ion batteries, Electrochim. Acta 54 (19) (2009) 4506–4513, https://doi.org/10.1016/j.electacta.2009.03.046.

[19] J. Smekens, J. Paulsen, W. Yang, N. Omar, J. Deconinck, A. Hubin, J. van Mierlo, A modified multiphysics model for lithium-ion batteries with a lixni1/3mn1/3co1/3o2 electrode, Electrochim. Acta 174 (2015) 615–624, https://doi.org/10.1016/j.electacta.2015.06.015.

[20] K.G. Gallagher, S.E. Trask, C. Bauer, T. Woehrle, S.F. Lux, M. Tschech, P. Lamp, B.J. Polzin, S. Ha, B. Long, Q. Wu, W. Lu, D.W. Dees, A.N. Jansen, Optimizing areal capacities through understanding the limitations of lithium-ion electrodes, J. Electrochem. Soc. 162 (2) (2016) A138–A149, https://doi.org/10.1149/2.0321602jes.

[21] D. Schmidt, M. Kamlah, V. Knoblauch, Highly densified ncm-cathodes for high energy li-ion batteries: microstructural evolution during densification and its influence on the performance of the electrodes, J. Energy Storage 17 (2018) 213–223, https://doi.org/10.1016/j.est.2018.03.002.

[22] J. Mao, W. Tiedemann, J. Newman, Simulation of temperature rise in li-ion cells at very high currents, J. Power Sources 271 (2014) 444–454, https://doi.org/10.1016/j.jpowsour.2014.08.033.

[23] LG Chem Mobile Battery Division, Technical information of lgc inr18650mj1, http://www.lgchem.com, (2015).

[24] M. Doyle, T.F. Fuller, J. Newman, Modeling of galvanostatic charge and discharge of the lithium/polymer/insertion cell, J. Electrochem. Soc. 140 (6) (1993) 1526–1533.

[25] S.V. Erhard, P.J. Osswald, J. Wilhelm, A. Rheinfeld, S. Kosch, A. Jossen, Simulation and measurement of local potentials of modified commercial cylindrical cells: ii: Multi-dimensional modeling and validation, J. Electrochem. Soc. 162 (14) (2015) A2707–A2719, https://doi.org/10.1149/2.0431514jes.

[26] S.V. Erhard, P.J. Osswald, P. Keil, E. Höffer, M. Haug, A. Noel, J. Wilhelm, B. Rieger, K. Schmidt, S. Kosch, F.M. Kindermann, F. Spingler, H. Kloust, T. Thoennessen, A. Rheinfeld, A. Jossen, Simulation and measurement of the current density distribution in lithium-ion batteries by a multi-tab cell approach, J. Electrochem. Soc. 164 (1) (2017) A6324–A6333, https://doi.org/10.1149/2.0551701jes.

[27] B. Rieger, S.V. Erhard, S. Kosch, M. Venator, A. Rheinfeld, A. Jossen, Multi-dimensional modeling of the influence of cell design on temperature, displacement and stress inhomogeneity in large-format lithium-ion cells, J. Electrochem. Soc. 163 (14) (2016) A3099–A3110, https://doi.org/10.1149/2.1051614jes.

[28] S. Kosch, Y. Zhao, J. Sturm, J. Schuster, G. Mulder, E. Ayerbe, A. Jossen, A computationally efficient multi-scale model for lithium-ion cells, J. Electrochem. Soc. 165 (10) (2018) A2374–A2388, https://doi.org/10.1149/2.1241810jes.

[29] T. Amietszajew, E. McTurk, J. Fleming, R. Bhagat, Understanding the limits of rapid

charging using instrumented commercial 18650 high-energy li-ion cells, Electrochim. Acta 263 (2018) 346–352, https://doi.org/10.1016/j.electacta.2018.01.076.

[30] M.W. Verbrugge, C.W. Wampler, On the optimal sizing of batteries for electric vehicles and the influence of fast charge, J. Power Sources 384 (2018) 312–317, https://doi.org/10.1016/j.jpowsour.2018.02.064.

[31] F.B. Spingler, W. Wittmann, J. Sturm, B. Rieger, A. Jossen, Optimum fast charging of lithium-ion pouch cells based on local volume expansion criteria, J. Power Sources 393 (2018) 152–160, https://doi.org/10.1016/j.jpowsour.2018.04.095.

[32] T.R. Tanim, M.G. Shirk, R.L. Bewley, E.J. Dufek, B.Y. Liaw, Fast charge implications: pack and cell analysis and comparison, J. Power Sources 381 (2018) 56–65, https://doi.org/10.1016/j.jpowsour.2018.01.091.

[33] T. Hutzenlaub, A. Asthana, J. Becker, D.R. Wheeler, R. Zengerle, S. Thiele, Fib/sembased calculation of tortuosity in a porous licoo2 cathode for a li-ion battery, Electrochem. Commun. 27 (2013) 77–80, https://doi.org/10.1016/j.elecom.2012.11.006.

[34] A. Senyshyn, M.J. Mühlbauer, O. Dolotko, M. Hofmann, H. Ehrenberg, Homogeneity of lithium distribution in cylinder-type li-ion batteries, Sci. Rep. 5 (2015) 18380, https://doi.org/10.1038/srep18380.

[35] L. Zielke, T. Hutzenlaub, D.R. Wheeler, C.-W. Chao, I. Manke, A. Hilger, N. Paust, R. Zengerle, S. Thiele, Three-phase multiscale modeling of a licoo 2 cathode: combining the advantages of fib-sem imaging and x-ray tomography, Adv. Energy Mater. 5 (5) (2015) 1401612, https://doi.org/10.1002/aenm.201401612.

[36] P.J. Osswald, S.V. Erhard, A. Noel, P. Keil, F.M. Kindermann, H. Hoster, A. Jossen, Current density distribution in cylindrical li-ion cells during impedance measurements, J. Power Sources 314 (2016) 93–101, https://doi.org/10.1016/j.jpowsour.2016.02.070.

[37] J.R. Belt, D.M. Bernardi, V. Utgikar, Development and use of a lithium-metal reference electrode in aging studies of lithium-ion batteries, J. Electrochem. Soc. 161 (6) (2014) A1116–A1126, https://doi.org/10.1149/2.062406jes.

[38] E. McTurk, T. Amietszajew, J. Fleming, R. Bhagat, Thermo-electrochemical instrumentation of cylindrical li-ion cells, J. Power Sources 379 (2018) 309–316, https://doi.org/10.1016/j.jpowsour.2018.01.060.

[39] G. Zhang, L. Cao, S. Ge, C.-Y. Wang, C.E. Shaffer, C.D. Rahn, In situ measurement of radial temperature distributions in cylindrical li-ion cells, J. Electrochem. Soc. 161 (10) (2014) A1499–A1507, https://doi.org/10.1149/2.0051410jes.

[40] J. Fleming, T. Amietszajew, E. McTurk, D. Greenwood, R. Bhagat, Development and evaluation of in-situ instrumentation for cylindrical li-ion cells using fibre optic sensors, HardwareX 3 (2018) 100–109, https://doi.org/10.1016/j.ohx.2018.04.001.

[41] J.N. Reimers, Accurate and efficient treatment of foil currents in a spiral wound li-ion cell, J. Electrochem. Soc. 161 (1) (2013) A118–A127, https://doi.org/10.1149/2.046401jes.

[42] R. Spotnitz, S. Hartridge, G. Damblanc, G. Yeduvaka, D. Schad, V. Gudimetla, J. Votteler, G. Poole, C. Lueth, C. Walchshofer, E. Oxenham, Design and simulation of spirally-wound, lithium-ion cells, ECS Trans. 50 (26) (2013) 209–218, https://doi.org/10.1149/05026.0209ecst.

[43] J.N. Reimers, M. Shoesmith, Y.S. Lin, L.O. Valoen, Simulating high current discharges of power optimized li-ion cells, J. Electrochem. Soc. 160 (10) (2013) A1870–A1884, https://doi.org/10.1149/2.094310jes.

[44] M. Guo, R.E. White, Mathematical model for a spirally-wound lithium-ion cell, J. Power Sources 250 (2014) 220–235, https://doi.org/10.1016/j.jpowsour.2013.11.023.

[45] K.-J. Lee, K. Smith, A. Pesaran, G.-H. Kim, Three dimensional thermal-, electrical-, and electrochemical-coupled model for cylindrical wound large format lithium-ion batteries, J. Power Sources 241 (2013) 20–32, https://doi.org/10.1016/j.jpowsour.2013.03.007.

[46] W. Zhao, G. Luo, C.-Y. Wang, Effect of tab design on large-format li-ion cell performance, J. Power Sources 257 (2014) 70–79, https://doi.org/10.1016/j.jpowsour.2013.12.146.

[47] F. Bahiraei, A. Fartaj, G.-A. Nazri, Electrochemical-thermal modeling to evaluate active thermal management of a lithium-ion battery module, Electrochim. Acta 254 (2017) 59–71, https://doi.org/10.1016/j.electacta.2017.09.084.

[48] D.A.H. McCleary, J.P. Meyers, B. Kim, Three-dimensional modeling of electrochemical performance and heat generation of spirally and prismatically wound lithium-ion batteries, J. Electrochem. Soc. 160 (11) (2013) A1931–A1943, https://doi.org/10.1149/2.023311jes.

[49] K. h. Lee, Product specification: rechargeable lithium ion battery model: Inr18650 mj1 3500mah, http://www.lgchem.com, (29.07.2016).

[50] A. Rheinfeld, S. Kosch, S.V. Erhard, P.J. Osswald, B. Rieger, A. Jossen, Electro-thermal modeling of large format lithium-ion pouch cells: a cell temperature dependent linear polarization expression, J. Electrochem. Soc. 163 (14) (2016) A3046–A3062, https://doi.org/10.1149/2.0701614jes.

[51] Feinmetall, Product specification - connector 1860c006_de, http://www.feinmetall.de, (2017).

[52] F.B. Spingler, Effective Transport Properties of Gas Diffusion Media in Proton Exchange Membrane Fuel Cells, Diploma Thesis, Technical University of Munich, Munich, 08-21-2014.

[53] J. Gostick, Multiphase Mass Transfer and Capillary Properties of Gas Diffusion Layers for Polymer Electrolyte Membrane Fuel Cells, Ph.D, University of Waterloo, Waterloo, 2008https://uwspace.uwaterloo.ca/bitstream/10012/4236/1/jgostick%20-%20phd.pdf.

[54] I. Zilberman, A. Rheinfeld, A. Jossen, Uncertainties in entropy due to temperature path dependent voltage hysteresis in li-ion cells, J. Power Sources 395 (2018) 179–184, https://doi.org/10.1016/j.jpowsour.2018.05.052.

[55] P.J. Osswald, M. d. Rosario, J. Garche, A. Jossen, H.E. Hoster, Fast and accurate

measurement of entropy profiles of commercial lithium-ion cells, Electrochim. Acta 177 (2015) 270–276, https://doi.org/10.1016/j.electacta.2015.01.191.

[56] J. Christensen, V. Srinivasan, J. Newman, Optimization of lithium titanate electrodes for high-power cells, J. Electrochem. Soc. 153 (3) (2006) A560–A565.

[57] A. Magasinski, P. Dixon, B. Hertzberg, A. Kvit, J. Ayala, G. Yushin, High-performance lithium-ion anodes using a hierarchical bottom-up approach, Nat. Mater. 9 (4) (2010) 353–358, https://doi.org/10.1038/nmat2725.

[58] T. Marks, S. Trussler, A.J. Smith, D. Xiong, J.R. Dahn, A guide to li-ion coin-cell electrode making for academic researchers, J. Electrochem. Soc. 158 (1) (2011) A51, https://doi.org/10.1149/1.3515072.

[59] C.M. Long, M.A. Nascarella, P.A. Valberg, Carbon black vs. black carbon and other airborne materials containing elemental carbon: physical and chemical distinctions, Environ. Pollut. (Barking, Essex : 1987) 181 (2013) 271–286, https://doi.org/10.1016/j.envpol.2013.06.009.

[60] G. Liu, H. Zheng, A.S. Simens, A.M. Minor, X. Song, V.S. Battaglia, Optimization of acetylene black conductive additive and pvdf composition for high-power rechargeable lithium-ion cells, J. Electrochem. Soc. 154 (12) (2007) A1129, https://doi.org/10.1149/1.2792293.

[61] Habib Rahimi-Eichi, Federico Baronti, Mo-Yuen Chow, IEEE International Symposium on Industrial Electronics (ISIE), 2012: 28 - 31 May 2012, Hangzhou Tianyuan Tower Hotel; proceedings, IEEE, Hangzhou, China; Piscataway, NJ, 2012, http://ieeexplore.ieee.org/servlet/opac?punumber=6230783.

[62] M. Mastali, M. Farkhondeh, S. Farhad, R.A. Fraser, M. Fowler, Electrochemical modeling of commercial lifepo 4 and graphite electrodes: kinetic and transport properties and their temperature dependence, J. Electrochem. Soc. 163 (13) (2016) A2803–A2816, https://doi.org/10.1149/2.1151613jes.

[63] W.M. Dose, V.A. Maroni, M.J. Piernas-Muñoz, S.E. Trask, I. Bloom, C.S. Johnson, Assessment of li-inventory in cycled si-graphite anodes using lifepo 4 as a diagnostic cathode, J. Electrochem. Soc. 165 (10) (2018) A2389–A2396, https://doi.org/10.1149/2.1271810jes.

[64] D. Allart, M. Montaru, H. Gualous, Model of lithium intercalation into graphite by potentiometric analysis with equilibrium and entropy change curves of graphite electrode, J. Electrochem. Soc. 165 (2) (2018) A380–A387, https://doi.org/10.1149/2.1251802jes.

[65] T. Ohzuku, Y. Iwakoshi, K. Sawai, Formation of lithium-graphite intercalation compounds in nonaqueous electrolytes and their application as a negative electrode for a lithium ion (shuttlecock) cell, J. Electrochem. Soc. 140 (9) (1993) 2490–2498.

[66] M. Doyle, Y. Fuentes, Computer simulations of a lithium-ion polymer battery and implications for higher capacity next-generation battery designs, J. Electrochem. Soc. 150 (6) (2003) A706, https://doi.org/10.1149/1.1569478.

[67] D.A.G. Bruggeman, Calculation of different physical constants in heterogenous substances, Ann. Phys. 416 (7) (1935) 636–664, https://doi.org/10.1002/andp.19354160705.

[68] S. Arrhenius, About the inversion rate of sucrose caused by acids, Z. Phys. Chem. 4U (1). https://doi.org/10.1515/zpch-1889-0416.

[69] O.V. Valoen, J.N. Reimers, Transport properties of lipf6-based li-ion battery electrolytes, J. Electrochem. Soc. 152 (5) (2005) A882–A891.

[70] K. E. Thomas, R. M. Darling, J. Newman, Mathematical modeling of lithium batteries, in: van Schalkwijk W.A., Scrosati B. (eds) Advances in Lithium-ion Batteries, pp. 345–392. https://doi.org/10.1007/0-306-47508-1_13.

[71] X. Han, M. Ouyang, L. Lu, J. Li, Simplification of physics-based electrochemical model for lithium ion battery on electric vehicle. part ii: pseudo-two-dimensional model simplification and state of charge estimation, J. Power Sources 278 (2015) 814–825, https://doi.org/10.1016/j.jpowsour.2014.08.089.

[72] N. Legrand, B. Knosp, P. Desprez, F. Lapicque, S. Raël, Physical characterization of the charging process of a li-ion battery and prediction of li plating by electrochemical modelling, J. Power Sources 245 (2014) 208–216, https://doi.org/10.1016/j.jpowsour.2013.06.130.

[73] Z. Chu, X. Feng, L. Lu, J. Li, X. Han, M. Ouyang, Non-destructive fast charging algorithm of lithium-ion batteries based on the control-oriented electrochemical model, Appl. Energy https://doi.org/10.1016/j.apenergy.2017.03.111.

[74] P. Keil, Aging of Lithium-ion Batteries in Electric Vehicles, Ph.D, Technical University of Munich, Munich, 04-19-2017http://nbn-resolving.de/urn/resolver.pl?urn:nbn:de:bvb:91-diss-20170711-1355829-1-5.

[75] I. Bloom, J. Christophersen, K. Gering, Differential voltage analyses of high-power lithium-ion cells, J. Power Sources 139 (1–2) (2005) 304–313, https://doi.org/10.1016/j.jpowsour.2004.07.022.

[76] J. Marcicki, X.G. Yang, Model-based estimation of reversible heat generation in lithium-ion cells, J. Electrochem. Soc. 161 (12) (2014) A1794–A1800, https://doi.org/10.1149/2.0281412jes.

[77] R.E. Williford, V.V. Viswanathan, J.-G. Zhang, Effects of entropy changes in anodes and cathodes on the thermal behavior of lithium ion batteries, J. Power Sources 189 (1) (2009) 101–107, https://doi.org/10.1016/j.jpowsour.2008.10.078.

[78] R. Yazami, Y. Reynier, Thermodynamics and crystal structure anomalies in lithium-intercalated graphite, J. Power Sources 153 (2) (2006) 312–318, https://doi.org/10.1016/j.jpowsour.2005.05.087.

[79] V.V. Viswanathan, D. Choi, D. Wang, W. Xu, S. Towne, R.E. Williford, J.-G. Zhang, J. Liu, Z. Yang, Effect of entropy change of lithium intercalation in cathodes and anodes on li-ion battery thermal management, J. Power Sources 195 (11) (2010) 3720–3729, https://doi.org/10.1016/j.jpowsour.2009.11.103.

[80] K.E. Thomas, J. Newman, Heats of mixing and of entropy in porous insertion electrodes, J. Power Sources 119–121 (2003) 844–849, https://doi.org/10.1016/S0378-7753(03)00283-0.

[81] P.A. Linford, Lithium Ion Power Generator: a Novel System for Direct Thermal to Electric Energy Conversion, M.sc. thesis Massachusetts Institute of Technology, Massachusetts, 2017.

[82] S.V. Erhard, Multi-dimensional Electrochemical-thermal Modeling of Lithium-ion Batteries, Ph.D, Technical University of Munich, Munich, 04-20-2017 http://nbn-resolving.de/urn/resolver.pl?urn:nbn:de:bvb:91-diss-20170607-1338266-1-3.

[83] X.-G. Yang, Y. Leng, G. Zhang, S. Ge, C.-Y. Wang, Modeling of lithium plating induced aging of lithium-ion batteries: transition from linear to nonlinear aging, J. Power Sources 360 (2017) 28–40, https://doi.org/10.1016/j.jpowsour.2017.05.110.

[84] X.-G. Yang, C.-Y. Wang, Understanding the trilemma of fast charging, energy density and cycle life of lithium-ion batteries, J. Power Sources 402 (2018) 489–498, https://doi.org/10.1016/j.jpowsour.2018.09.069.

[85] X.-G. Yang, S. Ge, T. Liu, Y. Leng, C.-Y. Wang, A look into the voltage plateau signal for detection and quantification of lithium plating in lithium-ion cells, J. Power Sources 395 (2018) 251–261, https://doi.org/10.1016/j.jpowsour.2018.05.073.

[86] S. Kosch, A. Rheinfeld, S.V. Erhard, A. Jossen, An extended polarization model to study the influence of current collector geometry of large-format lithium-ion pouch cells, J. Power Sources 342 (2017) 666–676, https://doi.org/10.1016/j.jpowsour.2016.12.110.

[87] I.A. Hunt, Y. Zhao, Y. Patel, J. Offer, Surface cooling causes accelerated degradation compared to tab cooling for lithium-ion pouch cells, J. Electrochem. Soc. 163 (9) (2016) A1846–A1852, https://doi.org/10.1149/2.0361609jes.

[88] W. Polifke, J. Kopitz, Heat Transfer: Principles, Analytical and Numerical Methods, second ed., Pearson Studium, Munich, 978-3-8632-6670-7, 2009.

[89] VDI Heat Atlas, eleventh ed., VDI-Buch, Springer Vieweg, Berlin, 2013, https://doi.org/10.1007/978-3-642-19981-3 https://doi.org/10.1007/978-3-642-19981-3.

[90] F.A. Wolff, J.H. Dellinger, The electrical conductivity of commercial copper, Proc. Am. Inst. Elec. Eng. 29 (12) (1910) 1981–2008, https://doi.org/10.1109/PAIEE.1910.6660499.

[91] D.G. Giancoli, Physics: Principles with Application, fourth ed., Prentice Hall College Div, 1995.

[92] S.C. Chen, C.C. Wan, Y.Y. Wang, Thermal analysis of lithium-ion batteries, J. Power Sources 140 (1) (2005) 111–124, https://doi.org/10.1016/j.jpowsour.2004.05.064.

[93] K. Kanari, K. Takano, Y. Saito, Thermal behavior and simulation of a lithium secondary battery, 60 (1996) 65–75.

[94] H. Sun, K. Zhao, Electronic structure and comparative properties of lini x mn y co z o 2 cathode materials, J. Phys. Chem. C 121 (11) (2017) 6002–6010, https://doi.org/10.1021/acs.jpcc.7b00810.

[95] D. Bernardi, A general energy balance for battery systems, J. Electrochem. Soc. 132 (1) (1985) 5, https://doi.org/10.1149/1.2113792.

2.3 Impact of the Cylindrical Cell Format and the Electrode Design on the Suitability for Fast Charging Procedures

Neglecting spatial imbalances of concentrations, potentials and temperature can lead to significant model errors. Besides the 18650 format, even larger formats such as 21700 and 26650 are used in application. This provokes inhomogeneity due to larger electrodes and the amplified heat accumulation due to increased cell diameters. The spatial gradients within a LIB are most likely affected by the selected format and a significant impact of the tab design is expected. The following work complements the investigation of inhomogeneity in cylindrical cells in terms of the size of the cylindrical format and the configuration of the applied current collector tabs.

In the following, the article titled *Impact of Electrode and Cell Design on Fast Charging Capabilities of Cylindrical Lithium-Ion Batteries* is presented and the additionally published supplementary part is shown in the appendix of this thesis. To investigate the impact of cylindrical format and current collector tab design on the spatial imbalance of concentrations, potentials and temperature, a variety of MuDiMods for 18650, 21700 and 26650 formats simulate moderate and fast charging procedures under different cooling conditions and ambient temperatures. An experimental state-of-the-art review of cylindrical cell design helps to determine five application relevant tab designs, which show a certain development delay of high energy 26650 LIBs compared to 18650 and 21700 formats. The models are parametrized for the MJ1 LIB, which revealed the highest gravimetric energy density of commercial LIBs. A novel in- and through-plane voltage drop analysis evaluates the simulated configurations of format and tab design showing a benefit of lower temperature imbalance and less overheating for multi-tab designs. In contrast, single-tab designs are more favorable to avoid lithium plating due to the increased in-plane heat generation in the current collectors, but come with increased in-plane voltage losses and a poorer fast charging performance. Choosing an appropriate tab design can boost the charging efficiency by up to $+23\,\%$ SoC. For each format and tab design configuration, a sophisticated fast charging protocol preventing lithium plating and overheating is presented under application near active cooling conditions.

The insights into spatial inhomogeneity are crucial to profoundly understand the LIB behavior and performance limitations. This helps to apply advanced control strategies to improve the operational conditions. As discussed in the last section 2.2, the results presented next can be used similarly to consider spatial imbalance caused modeling errors of the p2D for model correction purposes.

Author contribution   Johannes Sturm carried out the experimental and simulation work and developed the presented models. Alexander Frank helped with the cell opening study. The analysis of the experimental and simulation data was carried out by Johannes Sturm. Alexander Rheinfeld and Simon V. Erhard initiated fundamental ideas of the presented work. Simon V. Erhard and Alexander Rheinfeld provided fundamental modeling work for the MuDiMod prior to this article. The manuscript was written by Johannes Sturm and was edited by Alexander Frank, Alexander Rheinfeld, Simon V. Erhard and Andreas Jossen. All authors discussed the data and commented on the results.

Publication notes   The article titled *Impact of Electrode and Cell Design on Fast Charging Capabilities of Cylindrical Lithium-Ion Batteries* is presented in the following and the related supplementary material is shown in the appendix (see section B). The article [96] and the supplementary material [199] are published in the Journal of The Electrochemical Society.

Impact of Electrode and Cell Design on Fast Charging Capabilities of Cylindrical Lithium-Ion Batteries

Johannes Sturm, Alexander Frank, Alexander Rheinfeld, Simon Vincent Erhard, Andreas Jossen

Impact of Electrode and Cell Design on Fast Charging Capabilities of Cylindrical Lithium-Ion Batteries

J. Sturm,[1,*,z] A. Frank,[1] A. Rheinfeld,[1] S. V. Erhard,[1] and A. Jossen[1,2]

[1]*Technical University of Munich (TUM), Institute for Electrical Energy Storage Technology (EES), 80333 Munich, Germany*
[2]*Technical University of Munich (TUM), Munich School of Engineering (MSE), 85748 Garching, Germany*

Cylindrical formats for high energy lithium-ion batteries shifted from 18650 to 21700 types offering higher volumetric energy density and lower manufacturing costs. Bigger formats such as 26650 may be of benefit as well, but longer electrodes and increased heat accumulation due to larger cell diameters are challenging for the batterys design and performance. An experimental review of state-of-the-art cylindrical lithium-ion batteries implies a delayed development of high energy 26650 cells. Optimized and prospective tab designs are discussed for high energy 18650, 21700 and 26650 formats using an experimentally-validated multi-dimensional multiphysics model of a silicon-graphite/nickel-rich lithium-ion battery. The model incorporates several 1D electrochemical models combined with a 2D electrical and a 3D thermal model. Novel in- and through-plane voltage-drop analysis reveals a dominant influence of the tab design on the cells total polarization, where a multi-tab instead of a single-tab design can improve the fast charging efficiency by up to +23% SoC. Fast charging profiles are adapted to tab design and cylindrical format, which prevent overheatings and the local onset of lithium plating across the active electrode area. Multi-tab design is recommended for high energy 26650 cells, but imbalances in SoC and temperature suggest alternative formats at slightly reduced cell diameters.

The expanding global market penetration of electric vehicles (EVs)[1] poses performance challenges for the necessary electrical energy storage system incorporating lithium-ion batteries (LIBs) in form of prolonged lifetime, improved safety, enhanced power capability, and higher energy density on battery pack, module, and cell level. Forecasts[2,3] assume a tremendous increase of the required battery production volumes to serve the market demand, which comes with significant pressure on cell price, and thus the need to reduce manufacturing costs of battery cells which cause around 70% of the total costs for a battery pack.[2] The design of high-performance yet low-cost cells is a field of research and development which recently gains substantial attention[4–6] ranging from improving manufacturing processes[7–9] to enhancing overall cell design.[10] On a microscopic scale, cell modifications aim for novel active materials,[11,12] efficient insertion of passive components such as binder,[13,14] modification of liquid electrolytes,[15–17] resilient and fail-safe separators,[17,18] or sophisticated design of electrode coating.[19,20] Macroscopic design modifications focus on electrode geometry such as length and height,[21,22] current collector tab design,[23,24] and final outer cell format (i.e. pouch-type, cylindrical, and prismatic) incorporating either stacked, z-folded, or spirally-wound electrode-pairs.[25,26] In this work, we focus on the macroscopic design aspects, especially on the cylindrical cell format coming with a spirally-wound electrode stack/jelly roll of different sizes and tab designs. Maximizing the volumetric energy density on cell and module level comes with losses in cooling performance compared to pouch-type and prismatic cell formats.[10] In that respect, cylindrical formats such as the 21700 cells offer the highest potential for further development with the expected, lowest manufacturing costs until 2025.[10] Further reduction of the manufacturing costs could possibly be achieved via increasing the cylindrical cell size,[27] which most likely causes safety issues due to a further increased heat generation and accumulation as well as decreased cooling performance. A change from the standard 18650 to the 20700/21700 cylindrical format was observed in the last years[28,29] and the question comes up, if the cylindrical format is suitable for a further dimensional expansion incorporating state-of-the-art and future high-compressed

*Electrochemical Society Member.
zE-mail: johannes.sturm@tum.de

electrodes with high-capacitive active materials. In this matter, macroscopic design aspects such as the electrode length and height as well as the tab design have most likely significant influence on the safety, power capability, and lifetime performance.[24,25,30,31]

In this work, we reflect the state-of-the-art design of cylindrical cell formats via post-mortem analysis and experimental measurements of full and half cell characteristics. Using a multi-dimensional, multiphysics modelling framework (MuDiMod), the presented simulation based work deals with the analysis of power capability, energy efficiency, and safety characteristics under various cooling conditions as well as lifetime predictions of state-of-the-art cylindrical high energy cell formats such as 18650 and 21700 as well as a possibly larger 26650 LIB including five different tab designs.

Experimental and Simulation based Analysis of Cylindrical Battery Behaviour

A battery cell's voltage defined by the potential difference between its terminals/tabs resulting from a certain applied current flow as well as the surface temperature of a battery cell are easy to access. Therefore, it's common practice to measure them when evaluating a battery's rate capability,[32] energy density,[29] safety characteristics,[33] and lifetime.[34] However, these global observations as the cell's voltage, current, and temperature are somewhat misleading in case a considerable variance in spatial distribution of these measures prevails. Therefore, local gradients in electrical potential and current flow,[35] lithium-ion concentration,[36] and temperature[37] within a battery cell need to be considered either via experimental approaches (e.g. local or even in situ sensor placement) or via simulation based methods (e.g. higher dimensional multiphysics models).

The experimental modification of 2.5 Ah 26650 G/LFP cell revealed a direct correlation between the variance in electrical potential along the current collectors[35,38] to local gradients in current density and state of charge (SoC) across the electrodes. This is based on electronic and ionic transport processes which are dominated by the shape of the half cell's open-circuit potential (OCP) vs Li/Li$^+$ as well as local differences in electrode kinetics during constant current (CC) discharge up to 2C. A correlation between decreasing the number of tabs and the temperature increase within the jelly roll is shown for the same cell.[23] The temperature distribution in 18650 and

26650 formats using multiple embedded micro thermocouples[23,39,40] or optical fiber sensors[41–43] revealed around 5 K of temperature spread between the core and the surface during a 2.2C-CC charging operation for a 3 Ah 18650 cell.[41] Using an optical glass as the upper cap of a modified 18650 cell together with infra-red thermography, a 2D, radial temperature analysis[37] shows a similar spread around 5 K at 3C-CC discharge. Using unmodified cells, neutron powder diffraction[36,44] enables for visualizing the distribution of lithiation degrees in graphite and the cell's SoC in common 3.2 Ah 18650 cells, which shows spreads of up to 7% in the fully charged state.[36] As the different modifications cannot exclude a certain impact on the cell's overall behavior and some experimental efforts are expensive and time-intensive, simulation based studies provide a fast and easily accessible alternative for local state analysis without modifying the actual cell. In the overall battery development process these studies are invaluable especially during the early stages of battery design focusing on novel design concepts.

Multi-dimensional multiphysics modelling frameworks describe local battery states along their physical meaningful length scales. In detail, the solid and liquid potentials and concentrations are solved along the thickness t_{stack} of the electrode stack consisting of anode, separator, and cathode.[45] The electrical potentials are defined along the spirally-wound electrode length w_{ele} and height h_{ele}, and the temperature within the jelly roll and the cell's housing (i.e. $r_{cyl}^2 \cdot \pi \times h_{ele}$). An overview of published model frameworks in the research field is shown in Table I focusing on cylindrical cell formats. Regarding the most recent work, a 20 Ah cylindrical cell shows accelerated ageing caused by the substantial electrical heating within the current collector foils and poor intrinsic heat dissipation.[24] Additionally, the local gradients show a strong correlation with the electric path determined by the tab design. It is recommended that the tab design must be optimized for the cylindrical format/electrode size, which is one focus of this work. As shown in Table I, high-capacitive cell chemistries (e.g. SiC/NMC-811) and high volumetric loadings of beyond 150 mAh cm^{-3} are far to little investigated. Considering the aforementioned need of high energy LIBs, our MuDiMod framework[21,25,31,38,46,47] is used in this work with the experimentally validated parametrization from our previous works,[31,48] which describes a SiC/NMC-811 LIB at an volumetric loading of 261 mAh cm^{-3} with respect to the volume of the jelly roll.

In terms of safety, lifetime, and power capability, the suitability for fast-charging has become a key feature for current and prospective LIB technologies[59,60] and will be addressed in this work via analyzing the impact of the cell's format, its tab design, and the prevailing cooling conditions on the local temperature maximum and spread across the electrodes, the overall likeliness of lithium plating, and the charging efficiency.

Multi-Dimensional Multiphysics Modelling Framework

Regarding Fig. 1 our MuDiMod framework incorporates several pseudo-two dimensional (p2D)[45] models to solve for the mass balances of lithium-ions in the electrolyte c_l and the active material particles c_s, the solid Φ_l and liquid Φ_s potentials, and the charge balance ($\nabla i_l = -\nabla i_s$) along the thickness of the electrode stack described by the x-coordinate and separated into Anode (A), Separator (SEP), and Cathode (C) domain. The pseudo active particle domain described by the r-coordinate is coupled to the x-domain via electrode kinetics in form of the pore-wall flux j_n. To account for the in-plane polarization along the current collectors' length and height, a single p2D model per finite element method (FEM) node is connected in parallel over the 2D electrical model described by the x' and y' coordinates, where the electrical potentials $\varphi_{cc,-}$ and $\varphi_{cc,+}$ are solved under the applied current flow I. A charge balance constraint[31] assures identical current flow between the p2Ds and the 2D model. A coordinate mapping from 2D to the 3D model[31] enables for an numerical efficient exchange of the cumulative heat generation rate q_{p2D} from the p2Ds and $q_{cc,\pm}$ from the 2D model. The temperature T is then calculated at the x'', y'', and z'' coordinate in the 3D thermal model and transferred backwards. In this work, we focus on a 18560 ("blue"), 21700 ("green"), and 26650 ("red") format which requires a coordinate mapping as shown in Fig. 1. The resulting differential algebraic equation system is shown in Table VII together with the SiC/NMC-811 parameterization in Tables VIII and IX (see Appendix). Numerical details such as the numerical discretization are discussed in the supplementary material (is available online at stacks.iop.org/JES/167/130505/mmedia). The parametrization of the MuDiMod framework is experimentally validated for the 18650#1 cell as shown in our previous works.[31,48] In this work, we extend our MuDiMod framework in terms of the polarization analysis according to the work of Nyman et al.[61] in order to analyze and evaluate the through-plane polarization $\triangle E_i$ through the electrode stack, caused by mass and charge transport as well as reaction kinetics.[25] Voltage drops caused by diffusion, ohmic losses and Butler-Volmer reaction overpotentials are

Table I. Overview of multi-dimensional multiphysics modelling frameworks focusing on cylindrical cell formats.

Reference	Format[a)]	Chemistry	Volumetric loading[b)] /mAh cm^{-3}	Model approach		
				t_{stack}	$w_{ele} \times h_{ele}$	$r_{cyl}^2 \cdot \pi \times h_{ele}$
49	26–700	G/LMO	57.2[c)]	p2D$_{18}$	2D^E	1D^T
	52–1400		48.4[c)]			
50	46–1350	G/NCA	102	3D-Continuum		
30	32–1150	G/LFP	73[c)]	p2D$_{720}$	2D^E	3D^T
51	20–550[c)]	G/LMO	33	p2D$_{56}$	3D^E	3D^T
52	18–650	G/LMO	13	ESPM$_{n.a.}$	2D^E	3D^T
53	18–650	G/NCA	80	ECM$_{n.a.}$	2D^E	3D^T
54	26–650	G/LFP	84	p2D$_1$	n.a.	3D^T
38	26–650	G/LFP	86	p2D$_{19}$	2D^E	3D^T
55–57	26–650	G/LFP	81	p2D$_7$	n.a.	1D^T
31	18–650	SiC/NMC-811	**261**	p2D$_{197}$	2D^E	3D^T
58	44–1155	G/NMC-532	127	3D-Continuum		
25	26–650	G/NMC-111	99	p2D$_{12}$	2D^E	3D^T
	37–910			p2D$_{36}$	2D^E	3D^T
	53–1290			p2D$_{108}$	2D^E	3D^T

p2D/(E−)SPM/ECM$_x$ Pseudo-two-dimensional/(Extended-)Single-Particle-/Equivalent-Circuit-Model for the electrode-stack thickness used in a total number of x.a) 18-650 = ⌀18 mm and 650 mm of height for the cylindrical format, incorporating a minimum of 5 mm[29] additional height for the top-cap on the jelly roll and 0.2 mm[29] for the housing thickness. b) Considering the nominal capacity (C) and the volume of the electrode stack ($t_{stack} \times w_{ele} \times h_{ele}$). c) Estimated from the given information of the referenced publication.
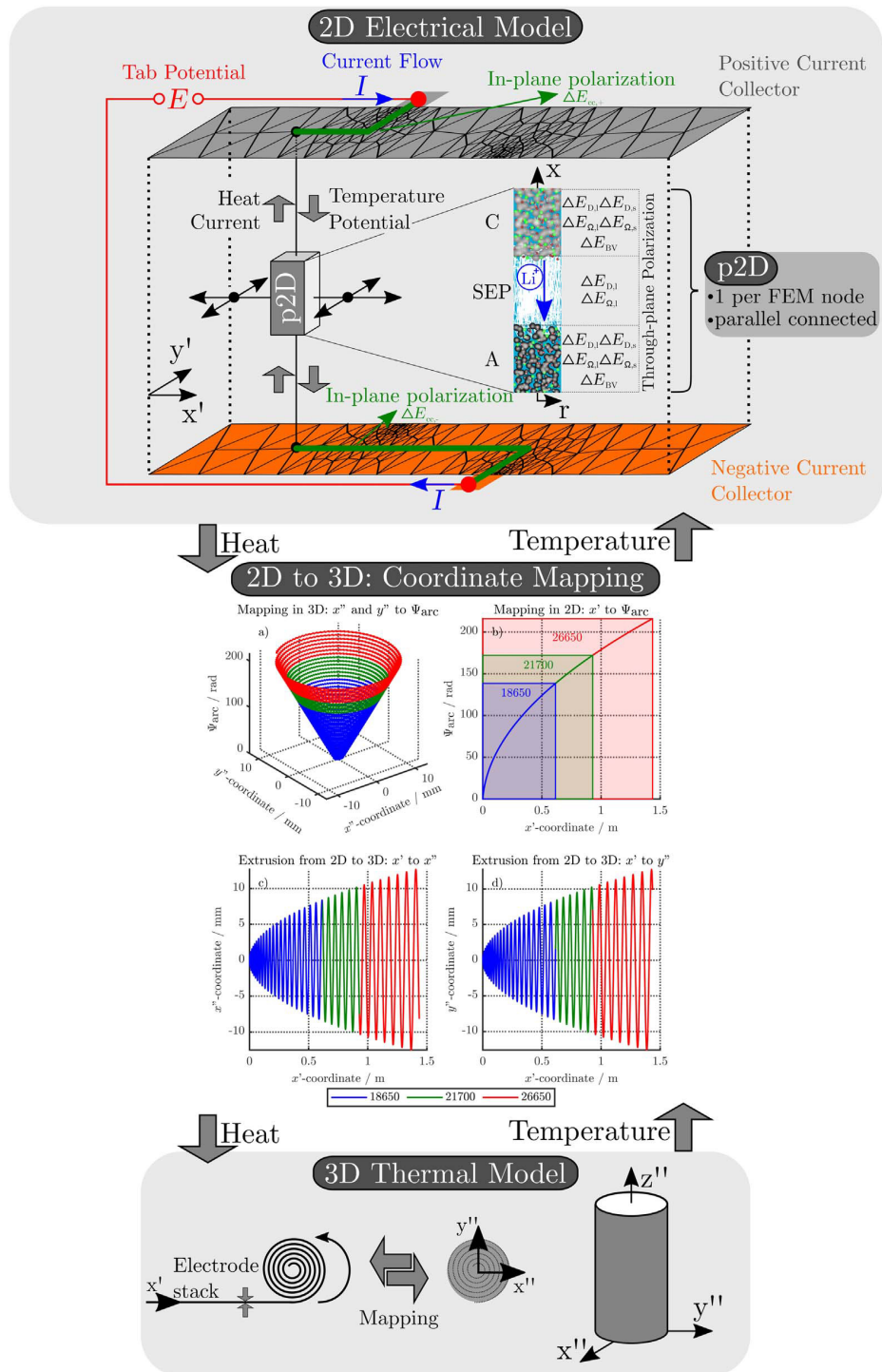
Figure 1. Overview of the MuDiMod framework incorporating several parallel connected p2D models, which are embedded in the 2D electrical model shown for the charging case. The coupling of each p2D is set via the adjacent solid potentials in a single FEM node to each current collector, where the temperature, heat generation, and current flow are exchanged as well. The cumulative heat generation from the p2D and the 2D model are transferred via the coordinate mapping function for cylindrical cells to the 3D thermal model, where the temperature is calculated and transferred backwards.

calculated in each p2D model as shown in Table X (see Appendix) and depicted in Fig. 1. Via the parallel connection in the 2D model, a linear interpolation scheme between the FEM nodes[46] allows calculation of the polarization through the electrode stack at every point along the electrode length and height. The in-plane polarization $\triangle E_{\mathrm{cc},\pm}$ along the current collectors is derived from the variance of the 2D electrical potential field. The differentiation of in- and through-plane polarization within the current collectors and the

electrode stack is only possible via using this extended modelling framework, which helps to understand and evaluate the impact of tab design and cylindrical format on the charging performance of the cell.

State-of-the-art of Cylindrical Cell Formats

Two 18650, a single 20700, four 21700, and three 26650 cylindrical LIBs from well-known cell manufacturers are investigated to review the state-of-the-art of commercial cylindrical cell design. Performance tests applied to three cells of each cylindrical LIB comprise a capacity check-up cycle, a rate-capability test and an open-circuit voltage (OCV) characterization including differential voltage analysis (DVA) at 10 °C, 25 °C, and 40 °C together with an electrochemical impedance spectroscopy (EIS) at 25 °C using a climate chamber (VT 4021, Vötsch Industrietechnik GmbH) together with a battery cycler (CTS, Basytec) and a potentiostat (VMP3, BioLogic Science Instruments). The measurement procedures are summarized in Table XI (see Appendix). The cell design is examined via opening of the cells in an argon-filled glove box (H₂O, O₂ < 0.1 ppm, M.Braun Inertgas-Systeme GmbH) at a discharged state. Using scanning electron microscopy (SEM, JCM-600 JEOL Ltd.), a micrometer calliper (Micromar 40 EWV, Mahr GmbH) and rulers, the in- and through-plane geometry such as thickness, length, and height of the electrode stack are determined together with the weight (Quintix 224-1S, Sartorius Mechatronics) of the entire cell and the dismantled jelly roll. The analyzed tab designs are denoted as "number of positive tabs × number of negative tabs" within this work, which translates "1 × 1" to a single tab at each current collector. Anode and cathode samples are extracted (⌀14 mm, Hohsen Corporation) to manufacture coin cells (CR2032-type, Hohsen Corporation) vs pure lithium metal (⌀15.6 mm × 250 μm, MTI Corporation) with two glass fiber separators (⌀16 mm × 250 μm), two stainless steel spacers (⌀16 mm × 0.5 mm and 1 mm), and 90μl of 1 M LiPF₆ in ethylene-carbonate (EC)/ethyl-methyl-carbonate (EMC) electrolyte (3:7 by weight, Solvionic). The anode and cathode coin cells are cycled at 10 °C, 25 °C, and 40 °C in a climate chamber (KT115, Binder) using a cycler (CTS, Basytec) at 80 μA (0.015C) CC-charge and -discharge both with a constant voltage (CV) phase and a cutoff at 0.001C between either 0.01 V and 1.5 V or 3 V and 4.3 V. Using DVA on the gained open-circuit data of full and half cells, the electrode balancing, anode- and cathode specific peaks are analyzed, which help to compare the different cylindrical formats. Finally, energy-dispersive X-ray (EDX) spectroscopy is applied to the extracted anode and cathode samples to determine the incorporated active material types, which is partly referenced to inductively coupled plasma-optical emission spectroscopy (ICP-OES, Varian 7XX-ES ICP-OES Spectrometer, Agilent Technologies) results.

Cylindrical Formats and Effective Electrode Length

As shown in Fig. 2 five different tab designs are applied to three different cylindrical formats. Each configuration is shown in Table II, which represents a single MuDiMod case. Referring to the total dimensions of a 18650, 21700, and 26650 format, the electrode length w_{ele} and height h_{ele} are calculated[31] assuming a central void/mandrel-space of ⌀ 1 mm, a minimum of 5 mm additional height for the top-cap incorporating the safety vent, and 0.2 mm of thickness for the can.[29] The calculated values refer to the overlap of anode and cathode and represent the active area of one electrode pair in the jelly roll.[48] The five tab designs are derived from the designs of the opened cells. The dimensions of the positive and negative tab are set to 4 mm and 6 mm of length and height in accordance with the results from the opened cells. The applied tab designs result in the effective electrode lengths shown in Table II, which refer to the maximum effective distance a tab addresses within the current collectors. In general, ohmic losses within the current collectors decrease with decreasing effective length due to shorter current pathways along the electrodes. Using the effective electrode lengths facilitates the comparison between different cell formats and tab designs.

The presented simulation study covering the different cell formats and tab designs is used to derive, which configuration is the most favourable in terms of power capability, energy density, avoidance of unwanted side reactions leading to accelerated ageing, and thermal safety. To do so, the rate capability, the gained energy efficiency, and the maximum/minimum temperature rise are evaluated. In terms of lifetime evaluation, the potential drop between the electrolyte and the active material particles at the anode/separator interface describes the likeliness of lithium plating. This potential drop is denoted as anode potential within this work. Integrated over the active area dimensions and analyzed over the charging time,[31] the areal likeliness of lithium plating can be evaluated and enables a quantitative comparison between different formats and tab designs as:

$$A_{act}^{-1} \cdot \int_t \int_{y'} \int_{x'} (\Phi_s(x = t_a, x', y', t)$$
$$- \Phi_l(x = t_a, x', y', t)) dx' \, dy' \, dt$$
$$\text{for } t \in \{0, t_{EoC}\} \wedge x' \in \{0, w_{ele}\} \wedge y' \in \{0, h_{ele}\}$$
$$\text{if } \Phi_s - \Phi_l < 0 \text{ V} \qquad [1]$$

Simulation Cases of Cylindrical Cell Formats

Figure 2 summarizes the MuDiMod cases as shown in Table II and shows the simulated electrical and thermal operation conditions.

First, the tab design study focusses on CC charging conditions ($I \neq f(t)$) from 1C to 4C at 25 °C. The cooling operates at the complete lateral and the two front surfaces, which is denoted as "L + F" case. A convective coefficient of 22 Wm⁻² K⁻¹[31] is applied at the surface of the jelly roll. The ratio between the jelly roll's surface to the housing's surface is used here to correct the smaller cooling surface of the jelly roll. The ratio is complex to be estimated and not sufficiently determined in literature, as it depends on the manufacturing tolerances, redundant separator windings, and the mechanical swelling of the cell, but is of negligible significance for this work as different formats and tab designs are compared to each other under the same thermal assumptions. The CC charging studies range from 3 V to 4.2 V and the performance is evaluated via the gained energy density, rate capability, likeliness of lithium plating, and the temperature rise. Especially the 18650 format is investigated toward in- and through-plane polarization to evaluate the influence of the effective electrode length. Next, only 25% of the cell's lateral surface are applied with an active cooling coefficient of 110 Wm⁻² K⁻¹ to emulate field-like conditions.[62] The so called "25%L$_{AC}$" case is used to evaluate temperature rise and spread in the jelly roll and gained energy density under a multi-step charging scenario ($I(T, \Phi)$), which avoids overheating and critical anode potentials. In all cases heat radiation at an emissivity of 0.75[48] is incorporated at the complete surface and heat dissipation of the tabs in the form of heat conduction to the ambience is neglected.

Results and Discussion

State-of-the-art of experimentally characterized cylindrical cell formats.—Correlating the measured capacity C to the thickness of the electrode stack t_{stack} and the active area A_{act}, the areal C_{act} and volumetric C_{stack} capacity can be compared for the different cylindrical cells and the results are shown in Table III. The maximum areal capacity appears for the 21700#2 cell with 4.74 mAh cm⁻² and the maximum volumetric capacity for the 18650#1 cell with 261 mAh cm⁻³, which is caused by the 49 μm thicker electrode stack of the 21700#2 cell. The moderately-loaded 26650 cells reveal around 3.3 mAh cm⁻² and nearly 200 mAh cm⁻³. The remaining cells are of high energy type such as the 18650#1 cell showing capacities of 4 mAh cm⁻² and 230 mAh cm⁻³ or more. Only cell 21700#3 reveals a lower value around 3.49 mAh cm⁻², which can be correlated to more than 10 cm longer electrodes compared to the remaining 21700 cells. The highest gravimetric energy density appears for the 18650#1 cell with 261 Wh kg⁻¹, whereas the highest volumetric energy appears for the 21700#4 cell
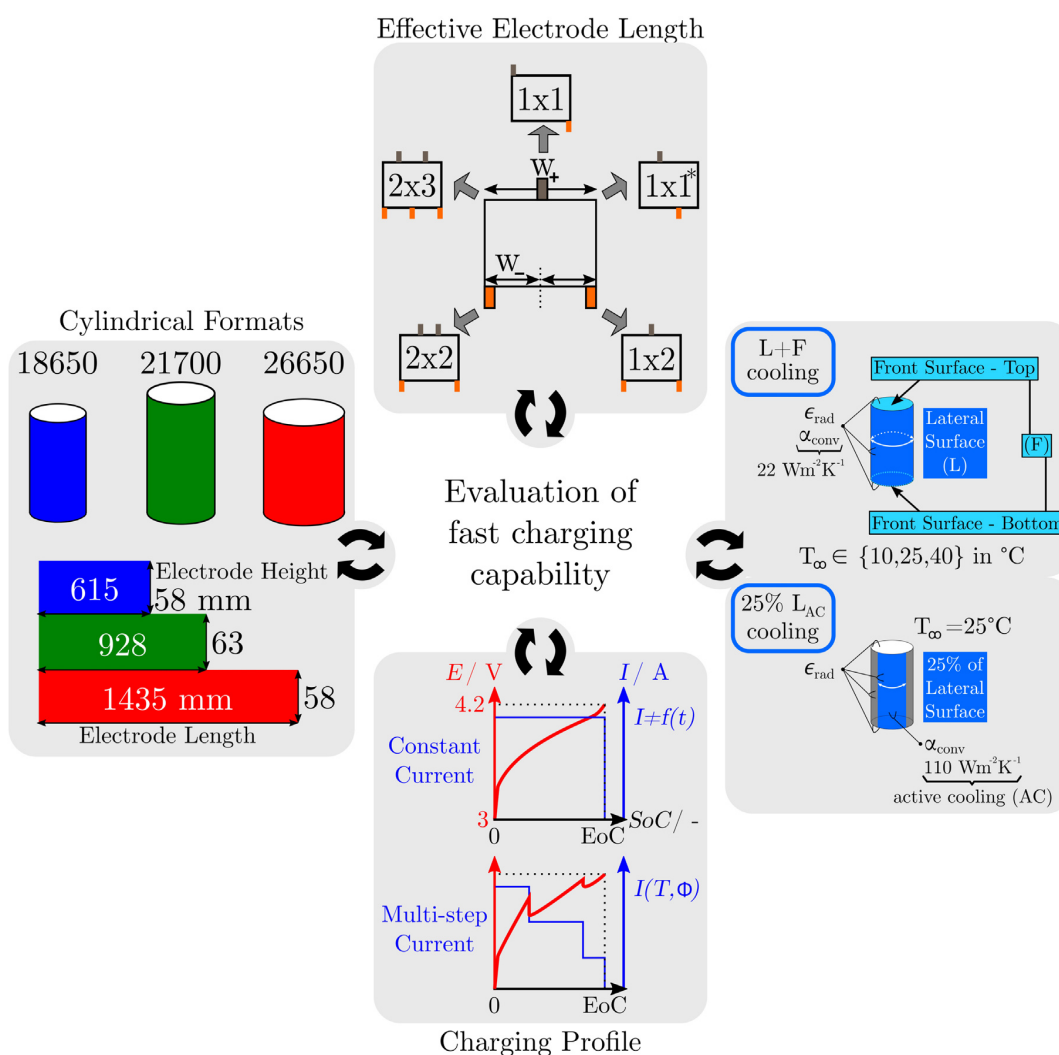
Figure 2. Overview of the simulated MuDiMod cases incorporating three differently sized, cylindrical cell formats (18650, 21700, and 26650) with the related electrode lengths and heights. Each format is applied with five different tab designs resulting in different effective electrode lengths in the 2D electrical model. Two different cooling cases are simulated. First, the ideal cooling scenario "L + F" applies convective heat transfer at 22 $\mathrm{Wm^{-2}\,K^{-1}}$ and heat radiation at the entire surface consisting of the front and bottom surface (F) as well as the lateral surface (L). Three different ambient temperatures (10 °C, 25 °C, 40 °C) are applied within the simulation studies. Second, the active cooling case applies convective heat transfer at 110 $\mathrm{Wm^{-2}\,K^{-1}}$ to 25% of the lateral surface to emulate application near cooling conditions.[62] The heat radiation applies to the entire surface and the ambient temperature is set to 25 °C. The charging scenarios comprise CC and multi-step current profiles, where the latter is set to avoid overheating beyond 60 °C and lithium plating as shown in the last chapter of this work.

at 727 $\mathrm{Wh\,l^{-1}}$. The difference can be correlated to a higher mean cell voltage of the 21700#4 cell. The ratio of the total weight of the cell and the jelly roll is used to derive the share of passive components such as housing, safety vent, insulation plates etc., which should be considered in terms of comparing the gravimetric energy. As a result, the lowest contribution can be observed for the 18650 cells around 15 wt.-% to 16 wt.-%, which implies that the bigger the cells, the higher the share of passive components gets with up to 18 wt.-% and 22 wt.-% for the 21700 and 26650 format, respectively. This is somewhat counter-intuitive as the general perception in lithium-ion battery research and development is that the share of passive components should decrease with increasing cell size. However, this only holds for energy optimized cells with a similar configuration of the electrode stack. The studied 18650 cells offer the maximum of capacity per cell weight, the investigated 21700 formats reveal a slightly better volumetric energy density, and

the exemplary 26650 formats show a roughly 19% lower volumetric energy density due to the highest amount of passive components. The results suggest, that the 26650 format is still not fully optimized compared to the more frequently used 18650 and 21700 formats for high energy applications. A small number of 26650 samples is investigated here and to draw a more profound conclusion, future work could investigate much more 26650 high energy cells.

Various tab designs ranging from 1×1 to 2×2 (e.g. "2×2" incorporates 2 tabs at each electrode) appear and are summarized in the column "Tab design" of Table III. An example of the electrode stack design from the dismantled, unrolled jelly roll of cell 21700#2 is shown in the supplementary material together with an overview of all measured anode and cathode geometries including the tab design at the current collectors foils. Most commonly, a 1×1 tab pattern appears for the 18650 and 21700 formats, where the positive tab is either in the center (18650#1) or approximately at a third of the

Table II. Electrode dimensions and tab design of the MuDiMod frameworks for the 18650, 21700 and 26650 cylindrical formats.

Format	Electrode size[a]		Number of tabs		Position of tabs		Effective lengths	
	Length w_{ele}/cm	Height h_{ele}/cm	+[b]	−[c]	+	−	+ w_+/cm	− w_-/cm
18650[d]								
18650_1 × 1	61.5	5.8	1	1	$\{0\} \cdot w_{ele}$	$\{1\} \cdot w_{ele}$	61.5	61.5
18650_1 × 1*			1	1	$\left\{\frac{1}{3}\right\}$	$\left\{\frac{2}{3}\right\}$	41	41
18650_1 × 2			1	2	$\left\{\frac{1}{2}\right\}$	$\{0, 1\}$	30.8	30.8
18650_2 × 2			2	2	$\left\{\frac{1}{3}, \frac{2}{3}\right\}$	$\{0, 1\}$	20.5	30.8
18650_2 × 3			2	3	$\left\{\frac{1}{4}, \frac{3}{4}\right\}$	$\left\{0, \frac{1}{2}, 1\right\}$	20.5	15.6
21700								
1700_1 × 1	92.8	6.3	1	1	$\{0\}$	$\{1\}$	92.8	92.8
21700_1 × 1*			1	1	$\left\{\frac{1}{3}\right\}$	$\left\{\frac{2}{3}\right\}$	61.9	61.9
21700_1 × 2			1	2	$\left\{\frac{1}{2}\right\}$	$\{0, 1\}$	46.4	46.4
21700_2 × 2			2	2	$\left\{\frac{1}{3}, \frac{2}{3}\right\}$	$\{0, 1\}$	30.9	46.4
21700_2 × 3			2	3	$\left\{\frac{1}{4}, \frac{3}{4}\right\}$	$\left\{0, \frac{1}{2}, 1\right\}$	30.9	23.2
26650								
26650_1 × 1	143.5	5.8	1	1	$\{0\}$	$\{1\}$	143.5	143.5
26650_1 × 1*			1	1	$\left\{\frac{1}{3}\right\}$	$\left\{\frac{2}{3}\right\}$	95.7	95.7
26650_1 × 2			1	2	$\left\{\frac{1}{2}\right\}$	$\{0, 1\}$	71.8	71.8
26650_2 × 2			2	2	$\left\{\frac{1}{3}, \frac{2}{3}\right\}$	$\{0, 1\}$	47.8	71.8
26650_2 × 3			2	3	$\left\{\frac{1}{4}, \frac{3}{4}\right\}$	$\left\{0, \frac{1}{2}, 1\right\}$	47.8	35.9

a) Corresponds to the size of the active area (A_{act}). b) Position at $y' = h$. c) Position at $y' = 0$. d) 18-650 = ⌀18 mm and 650 mm of height for the cylindrical format, incorporating a minimum of 5 mm[29] additional height for the top-cap on the jelly roll and 0.2 mm[29] for the housing thickness. Same assumptions are applied for the 21700 and the 26650 format.

electrode length (18650#2 , 21700#1-4), whereas the negative tab is either at the outer end (18650#1-2, 21700#2) or also approximately at a third of the electrode length. At a maximum, a single tab operates at the entire electrode length of cell 18650#1, which provokes higher, in-plane ohmic losses represented by the highest impedance value of 29.8 mΩ as shown in Table III. Reducing the effective lengths via shifting the position of the tabs either at the cathode (18650#2 and 21700#2), the anode, or both (21700#1 , #3, and #4), consequently reduces the in-plane ohmic losses, which contribute to the measured, lower impedances. Beside, the number of tabs can also be increased leading to a similar effect as mentioned before. The 20700 and the 26650#1 cell show a 1 × 2 design, whereas the remaining 26650 cells show a configuration of 2 × 2. Comparing the performance in the rate test at 25 °C (see supplementary material), the charged capacity at 1C-CC ranges from 65% SoC for the 20700 cell to 87% SoC for the 26650#3 cell. The 26650 and the 21700 cells reach more than 81% SoC except for the 21700#2 cell revealing 75% SoC, whereas a lower performance appears for the 18650 cells with 74% SoC (18650#1) and 78% SoC (18650#2). The observed minimum for the 20700 cell can be explained by increasing rate-limiting effects which can be observed for increasing C-rates. The maximum temperature rise ranges from 3.6 K for the 18650#2 cell to 11.2 K for the 18650#1 cell during 1C-CC charge at 25 °C under free convective cooling. All 21700 cells show an increase between 5 K and 6 K, similar to the 26650 cells. Interestingly, the maximum and minimum in temperature rise can be observed for the 18650 formats and a further increase in C-rate up to 1.7C-CC discharge (maximum range of cycler) show severe overheating of up to 22.6 K for the 18650#1, whereas the 18650#2 cell shows a more than four times lower temperature increase.

Considering the observed differences in the impedance behavior, the capacity gain, and the temperature rise among the cylindrical cells, this work investigates to which extent the current collector design affects the overall cell performance. In order to do so, the properties of the electrode stack are set identically to the parametrization of cell 18650#1 in the modelling framework. A brief summary compares the properties of the analyzed electrode stacks in the following.

Analyzing the EDX results nickel-rich active materials such as NMC-811 (18650#1 and 21700#2) and NCA (20700 and 21700#1 , #3, and #4) are most likely incorporated in the cathode. Single digit wt.-% for the contents of silicon (e.g. 3.5 wt.% for 18650#1) can be estimated in a graphite host-lattice for the anode, which is well in line with supplier information and literature data.[63–65] Compared to pure graphite the presence of silicon in a graphite host-lattice increases the electrochemical potential of the composite electrode vs Li/Li^{+}[66,67] as well as its gravimetric capacity. The analyzed 26650#1 cell suggests a silicon-free graphite anode and a NMC-532 cathode with moderate contents of nickel. The analysis of SEM images reveals anodic flake-like and cathodic spherical shapes of comparable sizes to the 18650#1 cell. A more detailed summary of the measured electrode stack thickness is shown in the supplementary material together with the detailed analysis of the SEM, EDX and DVA results of the half cells. The capacity balancing $\left(\frac{C_a}{C_c}\right)$ of anode and cathode is calculated from the DVA of full and half cells, which similarly reveal an oversized cathode for all cells—ranging from 10% for the 20700 to 1% for the 21700#3 cell as shown in Table III. As an example, the detailed DVA analysis is shown for cell 21700#2 in the supplementary material. To compensate the capacity mismatch and prevent unwanted side reaction at the anode such as

Table III. Experimental analysis of state-of-the-art cylindrical LIBs.

Format Symbol	Number	Capacity				Passive w_{pas} [b]	Energy density [a]		Tab design [d]		Impedance $|Z|$ [e]	Balancing	
		C [a]	A_{act}	C_{act}	C_{stack}		ξ_w [c]	ξ_v	$+$	$-$		$\frac{C_a\,[f]}{C_c}$	$\frac{A_a\,[g]}{A_c}$
Unit		mAh	cm²	mAh cm⁻²	mAh cm⁻³	wt.-%	Wh kg⁻¹	Wh l⁻¹	—	—	mΩ	$\frac{Ah}{Ah}$	$\frac{cm^2}{cm^2}$
18650	#1	3374	722	4.67	261	15	261	678	1_0	1_1	29.8	0.94	1.05
	#2	3322	726	4.58	248	16	258	689	$1_{0.33}$	1_1	25	0.90	1.06
20700		4086	970	4.21	242	18	238	642	$1_{0.33}$	$2_{0.1}$	14.8	0.93	1.06
21700	#1	4823	1192	4.05	242	18	254	690	$1_{0.33}$	$1_{0.33}$	11.5	0.96	1.07
	#2	4826	1019	4.74	232	17	251	674	$1_{0.33}$	1_1	22.1	0.98	1.06
	#3	4677	1342	3.49	234	17	249	696	$1_{0.33}$	$1_{0.33}$	12.4	0.99	1.06
	#4	4903	1161	4.2	249	17	258	727	$1_{0.33}$	$1_{0.33}$	11.9	0.95	1.05
26650	#1	5138	1550	3.31	198	22	193	536	$1_{0.33}$	$2_{0.1}$	17.9	0.97	1.03
	#2	5340	1636	3.26	201	21	203	547	$2_{0.33,0.66}$	$2_{0.1}$	13.6	n.a.	1.09
	#3	5400	1625	3.32	198	20	204	542	$2_{0.33,0.66}$	$2_{0.1}$	13.6	n.a.	1.09

a) Measured in the last CC_{DCH} check-up cycle at 0.5C and 25 °C (see Table XI). b) Derived from the weight ratio of the total cell and the jelly roll. c) Per total weight of the cell. d) The term "$2_{0.33,0.66} \times 2_{0.1}$" translates to two positive tabs at the position of 0.33 and 0.66 · $w_{cc,+}$ and two negative tabs at the position of 0 and 1 · $w_{cc,-}$. e) At 50% SoC, 25 °C, and $|Z|_{Im=0}$. f) Derived from full and half cell DVA using the calculated anode C_a and cathode C_c capacity. g) Derived from measured, geometrical sizes of the coated anode A_a and cathode A_c area.
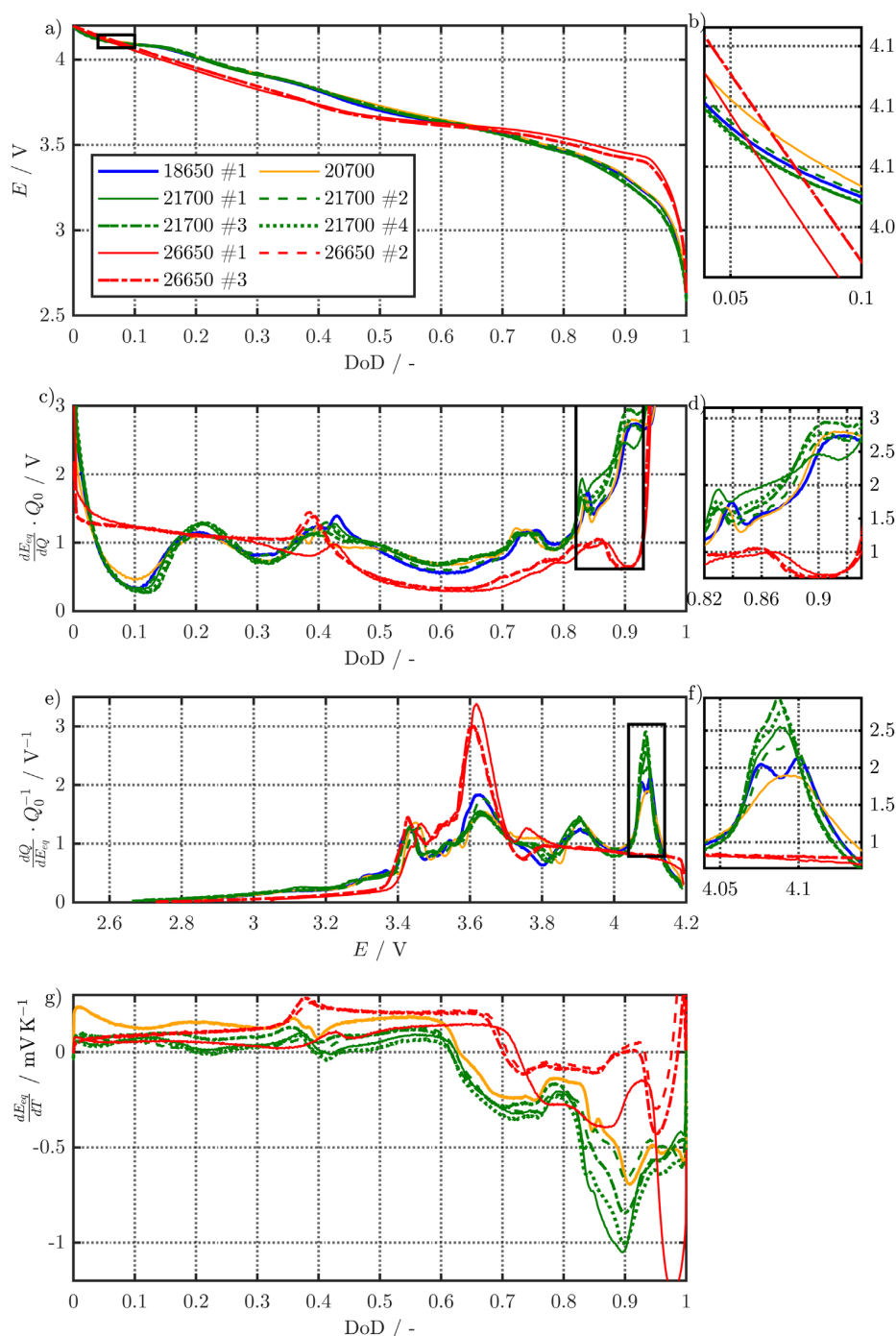
Figure 3. Averaged results from 0.01C-CC charge and discharge OCV measurements at 25 °C for the cell voltage (a), its 1st derivative (c), the differential capacity (e), and the temperature coefficient (g) linearized from measurements at 10 °C, 25 °C, and 40 °C. The magnified subplots (b), (d), and (f) highlight either anode (d) or cathode (b) and (f) specific characteristics.

lithium plating,[68] a geometrical overhang of the anode is chosen for all cells represented by the areal balancing $\left(\frac{A_a}{A_c}\right)$ in Table III, which ranges from 36 cm^2 to 147 cm^2 for the 18650#1 and 26650#2 cell.

To sum up, electrode compositions of graphite anodes without or with low silicon contents and transition metal oxide cathodes with moderate to high nickel contents and comparable electrode thickness for

the composite coatings and current collector foils appear. Similar electrode morphologies as particle size and shape can be observed for all high energy type cylindrical cells, which facilitates the use of one representative set of parameters (e.g. the 18650#1 cell) within this work.

Finally, a brief overview of the carried out OCV measurements, DVA, and thermal analysis is shown in Fig. 3. As shown in Fig. 3a, the OCV levels differ between the high energy 18650, 20700, and 21700
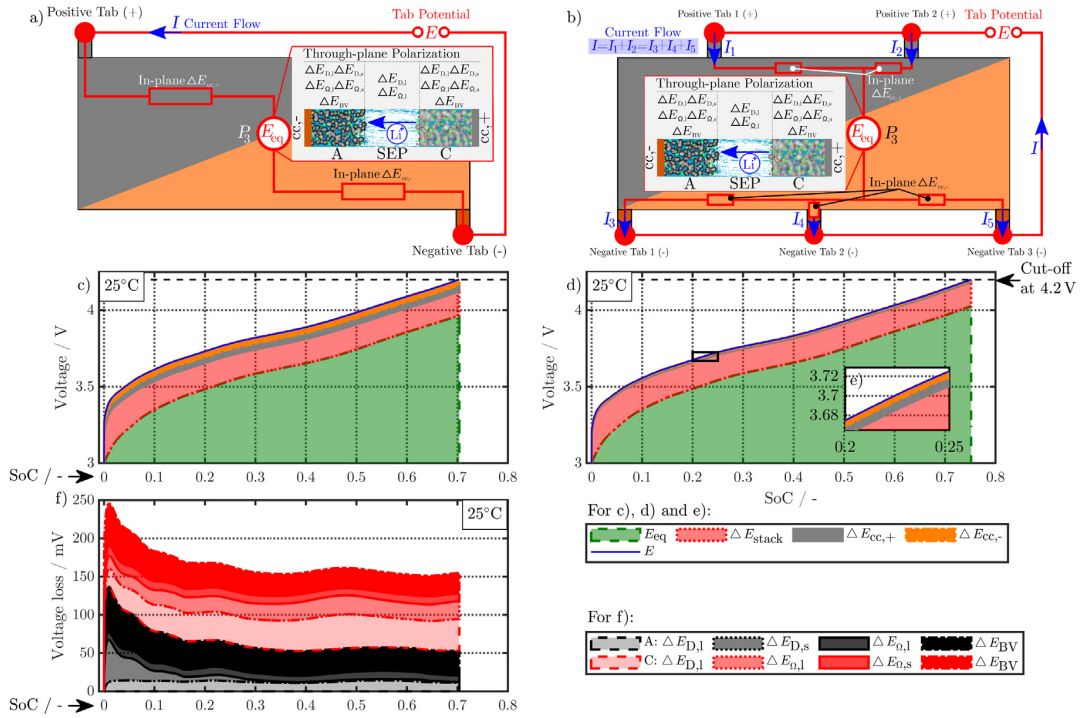
Figure 4. Simulation results at 1C-CC charging (I) from 3 to 4.2 V under L + F cooling at 25 °C for the 18650_1 × 1 and 18650_2 × 3 cell. Subplot (a) and (b) show the schematic composition of the tab potential E composed of in-plane $\triangle E_{cc,\pm}$ polarization within both current collectors, through-plane $\triangle E_{stack}$ polarization in the electrode stack, and the underlying open-circuit potential E_{eq} composed of anode and cathode equilibrium potential. The related electrical potential and polarization profiles are shown in subplot (c) and (d). As a reference point, position P_3 is shown, which carries the lowest current density throughout the charging process. The magnified area in (e) shows the in-plane polarization parts of the 18650_2 × 3 tab design between 20% and 25% SoC. Subplot (f) shows the overall contribution of the dominant through-plane voltage losses at P_3 for the 1 × 1 tab design study.

Table IV. Maximum time-averaged polarization results of the 18650_1 × 1 and the 18650_2 × 3 simulated total cell polarization at 1C-CC and L + F cooling for 10 °C, 25 °C, and 40 °C.

			In-plane	
Symbol	Total $\triangle E_{tot}$	Through-plane $\triangle E_{stack}$	$\triangle E_{cc,+}$	$\triangle E_{cc,-}$
Unit	mV	%	%	%
18650_1 × 1				
10 °C	343 ± 26.7[a]	75.2 ± 7.3	12.9 ± 0.3	11.9 ± 0.3
25 °C	266 ± 25.7	66.3 ± 9.0	17.7 ± 0.4	16.1 ± 0.3
40 °C	226 ± 20.9	57.9 ± 8.4	22.2 ± 0.4	19.9 ± 0.4
18650_2 × 3				
10 °C	267 ± 23.4	94.5 ± 8.7	3.3 ± 0.1	2.3 ± 0.0
25 °C	188 ± 21.6	91.7 ± 11.3	4.9 ± 0.1	3.4 ± 0.1
40 °C	143 ± 16.9	88.4 ± 11.6	6.9 ± 0.1	4.7 ± 0.1
Relative decrease from 10 °C to 40 °C/%				
18650_1 × 1	−34	−49	+14	+11
18650_2 × 3	−46	−50	+13	+11
Relative decrease from 18650_1 × 1 to 18650_2 × 3/%				
10 °C	−22.1	−2.3	|	|
25 °C	−29.4	−2.4	−80.3[b]	−85[b]
40 °C	−36.5	−3.0	|	|

a) Mean deviation. b) Negligible impact of the temperature between the 10 °C, 25 °C, and 40 °C case.

and the rather moderately-loaded 26650 cells underlining a different choice of electrode chemistry for the latter. At the beginning of the discharge operation, a plateau appears around 5% depth of discharge (DoD), which is magnified in Fig. 3b and is characteristic for nickel-rich, cathodic host-lattices[69] and is absent for the 26650 cells. The higher voltages of the high energy cells from 5% to 60% DoD are caused mainly by the cathode OCP (see supplementary material), whereas the shift afterwards is caused both by lower potential values of the cathode due to the nickel-rich type and higher potentials of the anode because of the content of silicon in graphite. The differential

potential $\left(\frac{dE}{dQ} \cdot Q_0\right)$ in Fig. 3c underlines the difference between G/NMC-type and SiC/nickel-rich cells. Looking into the anodic peaks in Fig. 3d between 82% and 93% DoD, a significant divergence appears, which results in higher slopes for the silicon-containing cells. Similar observations can be observed in the differential capacity $\left(\frac{dQ}{dE} \cdot Q_0^{-1}\right)$ vs the cell voltage E in Fig. 3e, where especially the large peak at approximately 4.08 V (see magnification 3f) is also characteristic for nickel-rich cathodes.[69] The thermal analysis focusing on the cell's overall temperature coefficient is shown in Fig. 3g and again underlines a significant difference between cells with a moderate and higher energy density between 82% and 93% DoD.

Commercial state-of-the-art high energy LIBs are available in 18650, 20700, and 21700 cylindrical formats, whereas the larger sized 26650 cells can be mostly found in a rather moderately-loaded configuration. This raises the question, if a high energy 26650 type is favourable or if the geometrical configuration causes issues in terms of power, energy, safety, and lifetime performance despite possible savings in manufacturing costs. Silicon-graphite/nickel-rich chemistries can be often found for high energy LIBs. With the aid of simulation studies, the practicability of 26650 formats comprising such a combination of high energy electrode chemistries is examined. As the 18650#1 cell reveals the maximum energy density in the electrode stack among the exemplary studied cells its parametrization[31,48] is used in the MuDiMod cases. The results of the simulation based work are presented in the following.

Impact of tab design on in- and through-plane polarization as well as current density distribution.—*Moderate charging under various ambient temperature conditions.*—Simulation results of both in- and through-plane polarization during 1C-CC charging whilst applying a convective cooling on all cell surfaces (L+F) at 25 °C is exemplary discussed for both the 1×1 and 2×3 tab designs of the 18650 format, which are shown in Fig. 4. The remaining $1 \times 1^*$, 1×2, and 2×2 simulation results lie in between the maximum (1×1) and minimum (2×3) electrical polarization—in the specified, descending order. The maximum observed temperature in all simulations is well below 60 °C. As the height of the electrode is far smaller than the length of the electrodes, its impact on in-plane polarization is comparably low and almost negligible.

Figures 4a and 4b show a schematic composition of the tab potential E at position P_3, which incorporates the in-plane polarization $\triangle E_{cc,\pm}$ within each current collector, the through-plane polarization $\triangle E_{stack}$ within anode, separator, and cathode domain, and the voltage source E_{eq} composed of anode and cathode equilibrium potentials. The simulated tab potential and its composition under the applied charging condition I is shown in Figs. 4c and 4d at the position P_3 of the minimum current load for the respective tab design. Evaluating the composition of the tab potential on average regarding the entire charging process, a higher tab potential of 3.849 V appears for the 1×1 design compared to the 2×3 design as 3.817 V, which consists of 93.6%/95.1% equilibrium potential, 4.4%/4.5% through- and 1%/0.2% in-plane polarization for the $1 \times 1/2 \times 3$ design. The in-plane polarization decreases by a factor of five within both current collectors, when the 2×3 design is applied. As the overall polarization for the 2×3 design decreases, the contribution of the equilibrium potential slightly increases by 1.5% and +5% SoC at the EoC can be achieved. No significant difference is observed in the through-plane polarization, which is
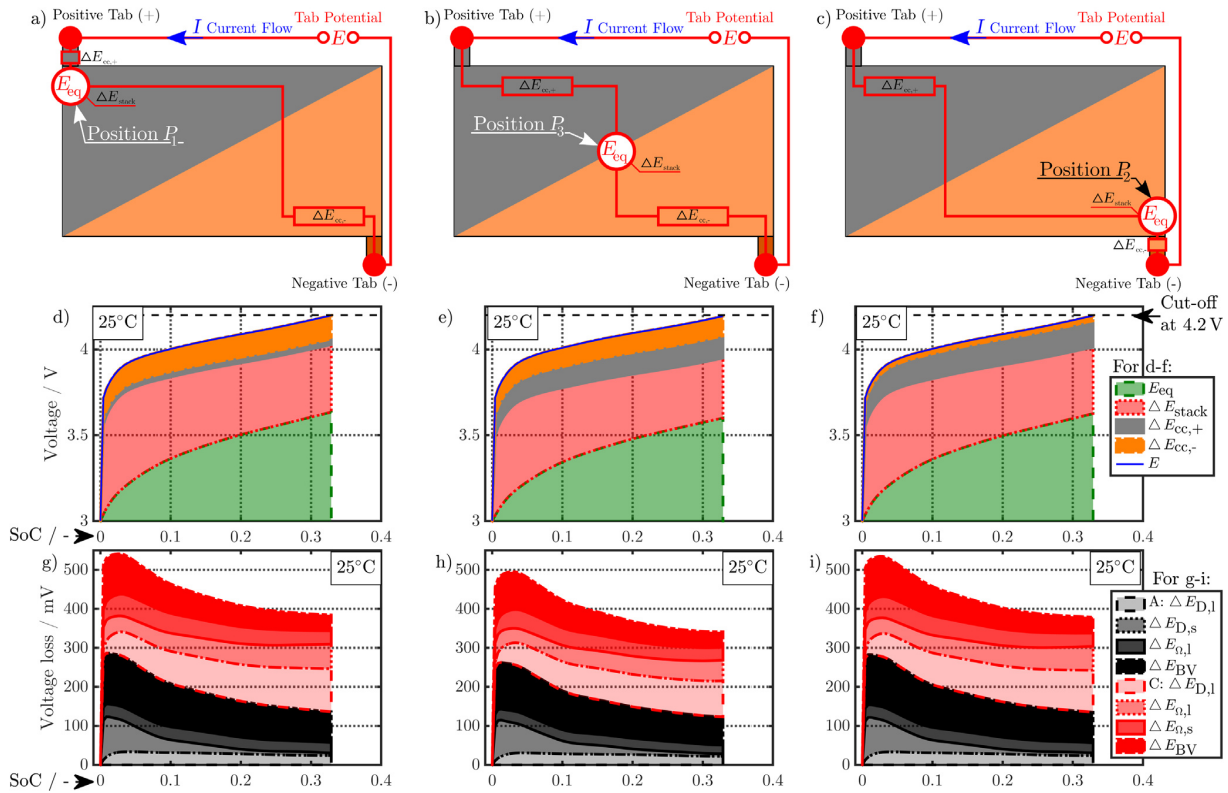
Figure 5. Simulation results at 3C-CC charging (I) from 3 to 4.2 V applying L + F cooling at 25 °C for the 18650_1 $\times$ 1 design. Subplot (a) to (c) show the schematic composition of the tab potential E at three different positions: P_1 near the positive tab (a), (d), (g), P_2 near the negative tab (c), (f), (i), and P_3 in the center of the active area (b), (e), (h). The composition of the tab potential is shown in subplot (d) to (f), which is composed of both in-plane $\triangle E_{cc,\pm}$ and through-plane $\triangle E_{stack}$ voltage losses as well as underlying open-circuit potentials E_{eq} of anode and cathode. The subplots (g) to (i) show the dominating through-plane polarization effects resulting in the overall through-plane voltage loss.

Table V. Maximum time-averaged polarization results of the 18650_1 × 1 and the 18650_2 × 3 simulated total cell polarization under 1C-CC and 3C-CC charging at 25 °C and L + F cooling.

			In-plane	
	Total	**Through-plane**		
Symbol	$\triangle E_{tot}$	$\triangle E_{stack}$	$\triangle E_{cc,+}$	$\triangle E_{cc,-}$
Unit	mV	%	%	%
18650_1 × 1				
1C-CC	266 ± 25.7[a)]	66.3 ± 9.0	17.7 ± 0.4	16.1 ± 0.3
3C-CC	723 ± 105.3	61.6 ± 10.1	20.2 ± 2.4	18.2 ± 2.1
18650_2 × 3				
1C-CC	188 ± 21.6	91.7 ± 11.3	4.9 ± 0.1	3.4 ± 0.1
3C-CC	446 ± 64.6	88.9 ± 13.5	6.6 ± 0.6	4.5 ± 0.4
Relative factor of increase from 1C- to 3C-CC/−				
18650_1 × 1	2.7	2.5	3.1	3.1
18650_2 × 3	2.4	2.3	3.2	3.1
Relative decrease from 18650_1 × 1 to 18650_2 × 3/%				
1C-CC	−29.4	−2.4	−80.3	−85.0
3C-CC	−38.3	−11.1	−79.7	−84.7

a) Mean deviation.
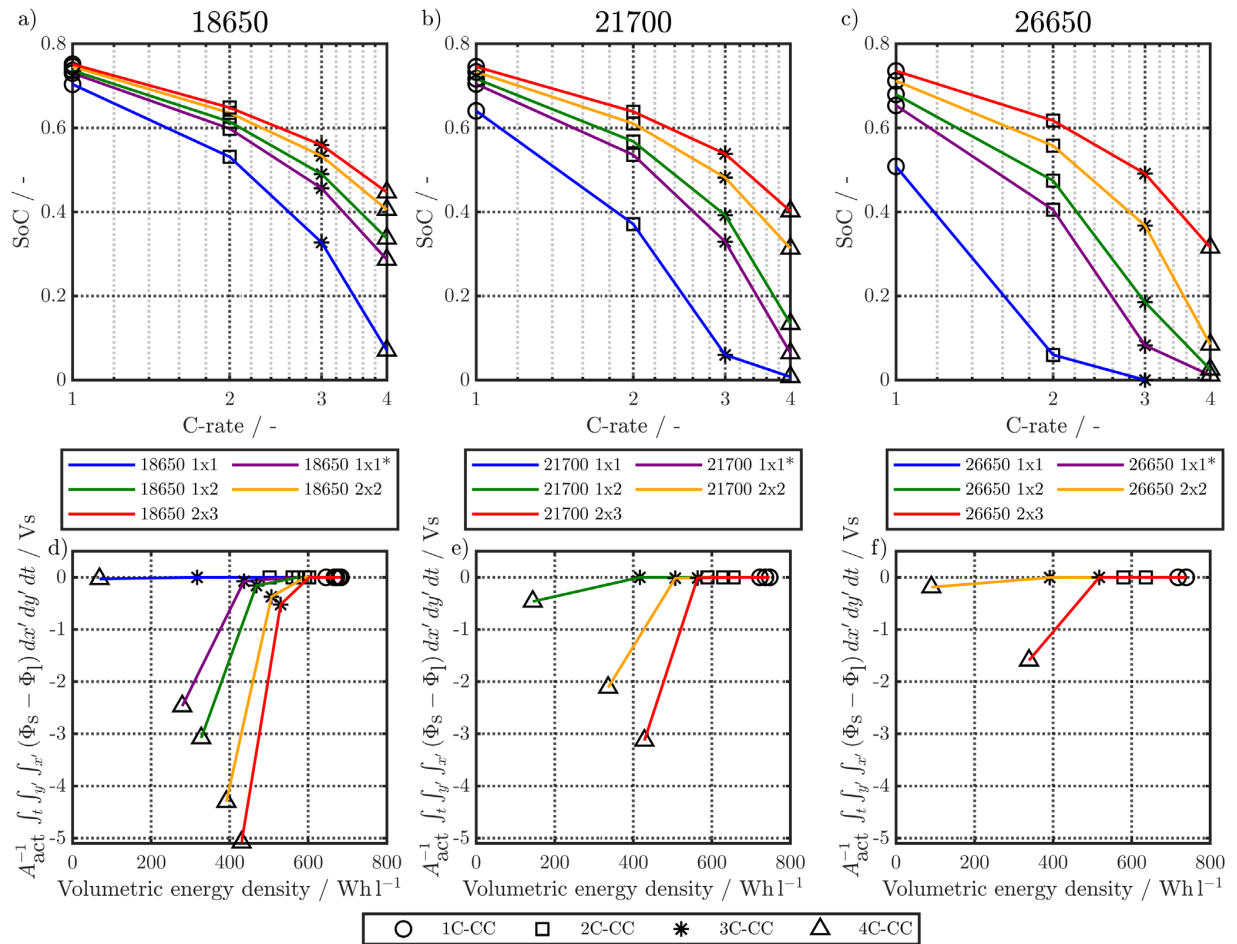
Figure 6. Charging simulation results from 1C to 4C-CC from 3 V to 4.2 V and 25 °C including L + F cooling. The results of the 18650 (a) and (d), 21700 (b) and (e), and 26650 (c) and (f) formats are shown with five different tab designs (1 × 1, 1 × 1*, 1 × 2, 2 × 2, and 2 × 3). The subplots (a) to (c) show the gained SoC at EoC (4.2 V) vs the applied C-rate. The subplots (d) to (f) show the charged volumetric energy density at EoC vs the cumulative plating hazard (see Eq. 1) based on the anode potential across the active area. The lower the value, the higher the likeliness of lithium plating becomes.

why its composition is shown in Fig. 4f only for the 1×1 design. The most relevant parts of the averaged 167 mV on voltage loss compose of 22.7% cathode liquid diffusion limitations $\triangle E_{D,l}$ as well as 21.2% anode and 19% cathode reaction kinetics $\triangle E_{BV}$. The higher ohmic losses within the electrolyte $\triangle E_{\Omega,l}$ for the cathode (12.8%) compared to the anode (5.8%) are most likely caused by the lower cathode porosity (ε_l: 17.1% $<$ 21.6%), which results also in lower liquid diffusion overvoltage within the anode (7.6%). Due to the three orders of magnitude lower solid electrical conductivity[70] in the nickel-rich host-lattice, the solid ohmic polarization $\triangle E_{\Omega,s}$ accounts for 6.4%, whereas the corresponding voltage loss in the anode is almost negligible. The solid diffusion coefficient in the cathode's active material particles is about one order of magnitude higher than in the anode[70–72] (see Table VIII) and together with nearly half the size of the anode's particles ($R_{p,D50}$: 6.1 μm vs 3.8 μm), the solid diffusion overvoltage $\triangle E_{D,s}$ of 4.4% in the cathode is almost negligible compared to the anode. The voltage loss through the separator $\triangle E_{D,l}$ and $\triangle E_{\Omega,l}$ revealed a negligible impact.

Similar simulation studies are carried out at 10 °C and 40 °C ambient temperature to examine the impact of temperature. Referring to P_3, a decrease of 2% in the mean cell voltage can be observed for a temperature rise from 10 °C to 40 °C for both tab designs. The share of the equilibrium potential reveals a marginal increase of around 1% (18650_1×1) and 2% (18560_2×3), whereas the through-plane polarization decreased nearly by a factor of two in both cases. The through-plane polarization composition in the anode decreases around 35% ($\triangle E_{D,s}$), 37% ($\triangle E_{\Omega,l}$), 45% ($\triangle E_{D,l}$), and 55% ($\triangle E_{BV}$). Similar decreases appear within the cathode. This observation is fundamentally based on overall enhanced ionic transport properties within both solid and liquid components as well as an increased reactivity within both electrodes with rising temperatures. In contrast, the in-plane polarization rises about 14% and 11% for the positive and negative current collector, which is well in line with the negative temperature coefficient in the electrical conductivity of copper and aluminum.

Neglecting the local evaluation at P_3 and proceed to a more global analysis, the maximum polarizations across the active area for the yet discussed results are averaged over the charging time. The results are shown in Table IV including the mean deviation to indicate their variance in time. The transient profiles are shown in the supplementary material. The total polarization $\triangle E_{tot}$ of the 2×3 design reveals a slightly higher decrease caused by temperature of 12% from 10 °C to 40 °C compared to the 1×1 design, where the through-plane polarization prevails over the in-plane polarization in both cases. For both designs, the through-plane polarization significantly decreases with elevating temperatures, whilst the in-plane polarization increases. Looking into the difference between the 1×1 and 2×3 tab design in Table IV, can be reduced by 22.1% and 36.5% at 10 °C and 40 °C respectively by choosing a 2×3 tab design instead of a 1×1 tab design. This is mainly caused by a reduced in-plane polarization of 80.3% to 85% for the positive and negative electrode of the 2×3 tab design based on a reduced effective electrode length. The through-plane polarization is marginally reduced by the choice of tab design by 2.3% to 3% from 10 °C to 40 °C. The in-plane polarization is dominated by the tab design and has a significant impact on the mean tab potential and the related charging efficiency. The through-plane polarization is less sensitive to the tab design, but can nearly double with falling temperatures due to being severely affected by temperature-dependent electrode kinetics and the mass transport in the electrolyte. Overall, the maximum, total polarization can be reduced at least by 22% and at most by 36% from 10 °C to 40 °C at 1C-CC charging, when a 2×3 tab design is used instead of a 1×1 design. The general correlation between the tab designs of the 18650 format may most likely be transferable to 21700 and 26650, as the effective lengths increase due to the longer/higher electrodes, but the relative proportion between the tabs remain the same. Consequently, increased in- and through-plane polarizations are expected. The difference in the thermal behavior between the three formats becomes more significant at higher C-rates beyond 1C and non-ideal cooling conditions such as the 25% L_{AC} case, which is both discussed in the multi-step charging section of this work.

Fast charging and variance of local polarization.—Not only an overall increased polarization but also a more inhomogeneous distribution across the active electrode area can be expected at higher C-rates such as 3C-CC charging, which is presented in the following for the 18650_1×1 and 18650_2×3 studies at 25 °C and L + F cooling. For some cases, a local overheating beyond 60 °C can be observed for 3C-CC charging due to insufficient cooling,
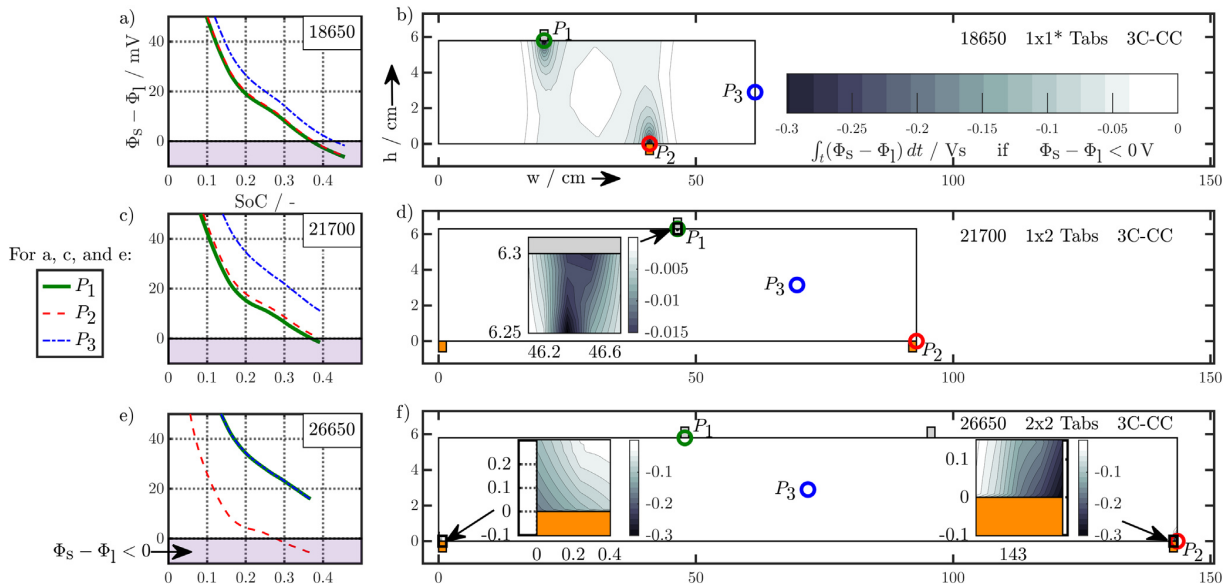

Figure 7. Simulation results for the 18650_1×1*, 21700_1×2, and 26650_2×2 design at 3C-CC charging under L + F cooling and 25 °C. The subplot (a), (c), and (e) show the anode potential at the positions P_1, P_2, and P_3 across the active area. The subplots (b), (d), and (f) show the time-integrated anode potential as an indicator of how long and to which extent the anode is exposed to potential levels, which most likely enhance a lithium plating side reaction. The magnified areas in subplot d and f show the resulting indication near the positive (d, 21700_1×2) and the negative (f, 26650_2×2) current collector tab(s).
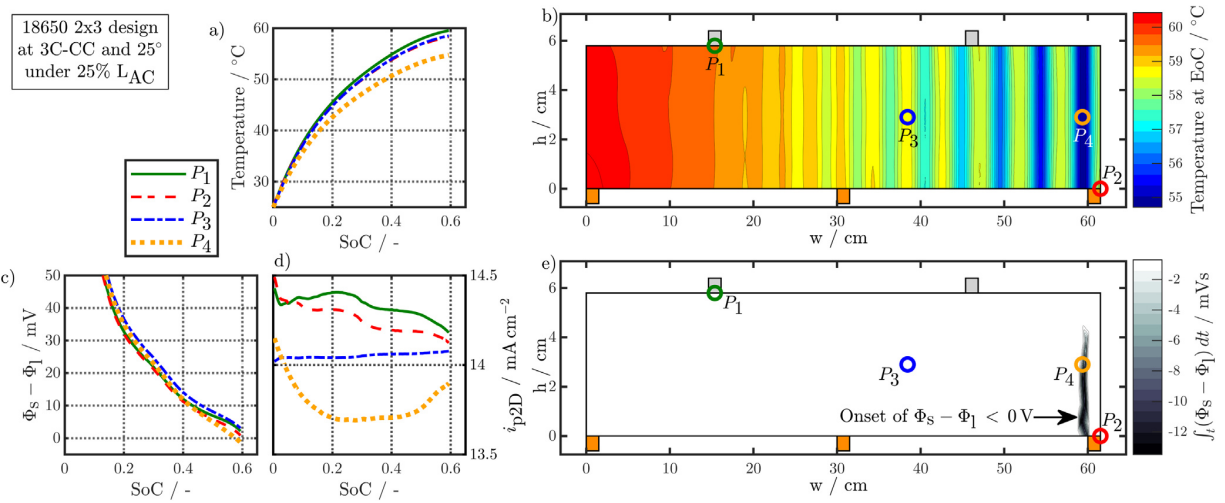
Figure 8. Simulation results of the 18650_2 × 3 design at 3C-CC charging from 3 V to 4.2 V at 25 °C and 25% L$_{AC}$ cooling. Subplot (a) and (b) show the temperature at the local positions P_1 to P_4 over the charged SoC (a) and the areal distribution across the active area at the EoC (b). The anode potential (c) and the current density (i_{p2D}, d) are shown at P_1 to P_4 together with the time-integrated areal evaluation of the likeliness of lithium plating (e).

which is addressed in the last two sections of this work. The simulation results of the maximum-polarizing tab design—the 1 × 1 design—are shown in Fig. 5, which shows a schematic overview of the composition of tab potential at the appearing minimum of current load at P_3, as well as close to the maximum current load near the positive tab at P_1 and the negative tab at P_2. The composition of the tab potential mainly differs in the contribution of in-plane polarization effects along current collectors. Near the positive tab at P_1, 3.3% of the total polarization are based on the negative current collector, whilst only 0.8% arise from the positive current collector. Near the negative tab at P_2 this contribution is almost inverted with the positive current collector dominating the negative current collector. At P_3, a rather balanced contribution of 3% and 2.8% appears for the negative and positive current collector respectively. Considering all three positions, the contributions of equilibrium potential (84.9%, 84.8%, and 84.3%) and through-plane polarization (11%, 10.9%, and 10%) slightly differ, which reveals an increased utilization. This is caused by the higher current density leading to faster lithiation/delithiation and hence increased in- and through-plane polarization effects near the current collector tabs. Regarding Figs. 5g to 5i, no significant difference in the composition of the through-plane polarization appears, but overall the total polarization rises in the vicinity of the current collector tabs. For example, 435 mV and 429 mV of total, time-averaged polarization appear at P_1 and P_2, compared to 393 mV at P_3. Similar trends appear for the 18650_2 × 3 design, only at lower polarizations around 385 mV, 387 mV, and 379 mV at the 1st positive tab, the 2nd negative tab, and at the minimum in current load at P_3. In general, the mean tab potential of the 1 × 1 design accounts to 4.038 V and exceeds the 2 × 3 design by 2%, which results in reduced utilization of −23% SoC.

For both studies, the increase from 1C to 3C evokes an increase of the mean tab potential of ≈5%, where the through-plane polarization increases by a factor of more than two and the in-plane polarizations by a factor of three. The composition of the through-plane polarization for the 1 × 1 design revealed a general increase by at least a factor of two, whereas especially the anode solid diffusion $\triangle E_{D,s}$ and the cathode solid ohmic overvoltage $\triangle E_{\Omega,s}$ increase by a factor of four. As a result, initial onsets of partial rate limitations in the form of anode particle diffusion and cathode electron transport are indicated. Similar trends can be observed for the 2 × 3 design.

A general comparison summarizing the C-rate effect on the 1 × 1 and 2 × 3 tab design is shown in Table V. The maximum total polarizations averaged over time at 3C-CC charge account to 723 mV and 446 mV are caused to nearly 40% by the in-plane

polarization for the 1 × 1 study, whereas only 11% appear for the 2 × 3 study. From 1C to 3C, a similar increase by a factor of 2.7 (18650_1 × 1) and 2.4 (18650_2 × 3) in total appear. Again, an overall lower polarization by 29.4% and 38.3% appear at 1 and 3C for the 2 × 3 tab design. This translates to 2.4%/11.1% lower through-plane, and at least 80.3%/79.7% lower in-plane polarizations at 1C/3C. Regarding the remaining tab design studies for the 18650 format, the polarizations lie in between the two presented cases in the same order as discussed in the section before. The local variance of the through-plane polarization is about five times lower for the 18560_2 × 3 compared to the 18650_1 × 1 study. Around 40% of the total polarization are caused by the ohmic losses along the current collectors at 3C-CC charging for the 1 × 1 study, which lowers by a factor of four in case of the 2 × 3 study. At a maximum, a 38.3% lower polarization can be achieved at 3C using the 2 × 3 tab design which translates to a higher utilization/charge efficiency of +23% SoC at EoC. Again, a transfer of the results to the 21700 and 26650 formats is suitable under the constraint that the increased heat generation due to the higher C-rate may have a more significant impact on the long-term thermal behavior, which is addressed in the last two sections.

Local and time-dependent variance of the current load.—The ohmic drop across the current collector foils has a major impact[21] on the distribution of the current density across the active area. In this matter, it can be distinguished between an instantaneous and a long-term distribution, which refers to the initial state or to the entire charging process. The initial distribution is dominated by the current collector design such as its geometrical dimensions and the tab design. The temperature rise, possible restraints or enhancements of mass transports and alteration of electrode kinetics such as OCP shifts due to the ongoing lithiation/delithiation[21] are crucial on the long-term.

The instantaneous potential drop across the current collector foils is correlated to a local variation of the through-plane potential drop ($\Phi_{cc,+} - \Phi_{cc,-} = E_{eq} + \triangle E_{stack}$ at $P(x', y')$) and defines the local distribution of the current density i_{p2D} across the active area. The instantaneous equilibrium potential level is approximately identical for all analyzed cases, which allows the correlation of the through-plane potential difference ($E_{eq} + \triangle E_{stack}$) to the current density. At 1C-CC charging under L + F cooling and 25 °C, the instantaneous tab potential E calculates to 3.264 V in the 18650_1 × 1 study, which is correlated to a 52 mV, 55 mV, and 74 mV lower potential

Table VI. Overview of the multi-step current charging under 25% L_{AC} cooling at 25 °C whilst avoiding lithium plating.

Identifier	Time	Energy	$\frac{\text{Energy}}{\text{Time}}$	SoC	Δ SoC^c	ΔT	T_{max}
Unit	/s	/Whl^{-1}	Whl^{-1} min^{-1}	/ %		/K	/° C
18650							
$1 \times 1^{3C \to 2C}$	943	547	34.8	57.4	7.4	14.7	60
$1 \times 1^{*3C \to 2C}$	895	610	40.9	63.8	3.6	7.3	60
$1 \times 2^{3C \to 2C}$	940	615	39.2	64.7	3.3	8.5	60
$2 \times 2^{3C \to 2C}$	960	631	39.4	66.7	3.6	8.8	60
$2 \times 3^{3C \to 2C}$	934	646	41.5	68.1	2.8	7.6	58.8
21700							
$1 \times 1^{2C \to 1C}$	2035	675	19.9	65.2	8.1	17.4	60
$1 \times 1^{*3C \to 2C}$	986	597	36.3	57.2	6.1	7.4	54.6
$1 \times 2^{3C \to 2C}$	1040	625	36.1	60.1	5	9.2	56.1
$2 \times 2^{3C \to 2C}$	1110	662	35.8	64.1	5.1	8.8	54
$2 \times 3^{3C \to 2C}$	1145	679	35.6	66	3.1	6.7	50.6
26650							
$1 \times 1^{2C \to 1C}$	1860	546	17.6	52.4	14.4	24.3	56.6
$1 \times 1^{*3C \to 2C \to 1C}$	1820	708	23.4	67.3	9.9	12	60
$1 \times 2^{3C \to 2C \to 1C}$	1915	726	22.7	69.6	6.8	13.2	60
$2 \times 2^{3C \to 2C \to 1C}$	1859	753	24.3	72.6	8.7	13	60
$2 \times 3^{3C \to 2C}$	1135	667	35.3	64.6	4.3	10	56.8
Prospective cylindrical formats							
$22800\_1 \times 1^{*3C \to 2C}$	992	600	36.3	57.5	6	10.9	58.3
$22800\_1 \times 2^{3C \to 2C}$	924	564	36.6	53.7	7.5	8.1	56.1
$23700\_1 \times 2^{3C \to 2C \to 1C}$	1560	763	29.3	72.7	6.2	11.3	60
$23700\_2 \times 2^{3C \to 2C}$	1085	649	35.9	62.6	6.7	11.3	58.7

^{c} Variance in SoC across the active area within the cathode domain.
$^{2C \to 1C}$ 2-step current profile from 2C- to 1C-CC.
$^{3C \to 2C}$ 2-step current profile from 3C- to 2C-CC.
$^{3C \to 2C \to 1C}$ 3-step current profile with initial 3C-, subsequent 2C-, and final 1C-CC phase.

difference at the positions P_1, P_2, and P_3. The local current density appears to be 5.23 mA cm^{-2}, 5.13 mA cm^{-2}, and 4.56 mA cm^{-2}, which reveals a variation of +11%, +9%, and −3% compared to the areal-averaged current density of 4.69 mA cm^{-2}. With rising temperatures from 10 °C to 40 °C, the spread between the maximum and minimum of the current density increases from 10.4% to 15.1%, which is mainly caused by an increased ohmic resistance within the current collectors albeit enhanced electrode kinetics and mass transport properties. With increasing C-rate from 1C to 3C, an increase in the spread between minimum and maximum current density from 8.5% to 11.5% appears due to the evoked higher in-plane ohmic losses, which directly scale with the applied current. Lower in-plane ohmic losses in the 18650_2 × 3 design appear with lower through-plane potential differences of 12 mV and 11 mV near the tabs accompanied with a lower mean tab potential E of 3.209 V and lead to a significantly lower spread in the current density of 2.1% compared to 14% for the 18650_1 × 1 design at 1C-CC charging and 25 °C.

On the long-term, the mean variation in current density appears to be 3.1% between the three positions during a 1C-CC charge for the 18650_1 × 1 study, which indicates a balancing effect across the active area with ongoing charging operation compared to the initial 14% offset. Increasing the ambient temperature from 10 °C to 40 °C causes decreasing mean tab potential E from 3.885 to 3.821 V, which comes with an overall reduction of −1% for the spread in current density. Similarly to other works,[21] higher peaks and amplified local fluctuations of the current density appear at 40 °C compared to 10 °C, but result in a lower, mean current load across the active area. Regarding the C-rate increase, the spread increases from 3.1% at 1C to 11.4% at 3C.

In sum, higher C-rates, longer effective electrode lengths, and higher temperatures increase the instantaneous and long-term spread of the current density, which generally evokes amplified fluctuations across the active area. The instantaneous results are most likely transferable to the 21700 and 26650 formats, where especially long-term, thermal effects are negligible. The higher effective electrode lengths most likely cause an increased spread between the maximum and minimum local current density for the 18650 designs.

Rate capability and local onset of unwanted side reactions during fast charging.—In the following, the charging rate capability from 3 V to 4.2 V is simulated at 1C- to 4C-CC for the 18650, 21700, and 26650 format including each tab design (see Table II). The L + F cooling condition at 25 °C partly revealed insufficient cooling leading to local overheating especially at 4C for 1 × 1 tab designs. Nevertheless, the results are summarized in Fig. 6 to better illustrate the rate-limiting phenomenon coming with a non-linear drop of the charged SoC at higher C-rates coming with a higher probability of lithium plating.

As shown in Figs. 6a to 6c, the larger the cell, the lower the critical C-rate becomes, after which a significant, non-linear drop in SoC can be observed. A significant impact of the tab design on the charging efficiency appears, as the larger the effective electrode lengths, the higher the in-plane polarization becomes and the faster the tab potential increases. This leads to an early approach of the upper cutoff voltage which translates into the shown decreasing SoC trend with increasing C-rate. Consequently, the 1 × 1 tab design reveals the poorest and the 2 × 3 tab design the best charging performance independent of the cell's format. In comparison, the 21700 format has a slight benefit regarding the volumetric energy density compared to the 18650 format, whereas the 26650 format shows the lowest performance. Using more tabs for the 21700 and 26650 format would enhance their performance, but this work focusses on application-near tab designs derived from the studied cylindrical cells, which would most likely be viable for the manufacturing process. Figures 6d to 6f show the likeliness of lithium plating derived from the simulated anode potential across the active area (see Eq. 1). The shorter the effective electrode length is, the higher the risk for lithium plating becomes before the upper cutoff voltage is reached. The aforementioned trend can be clearly
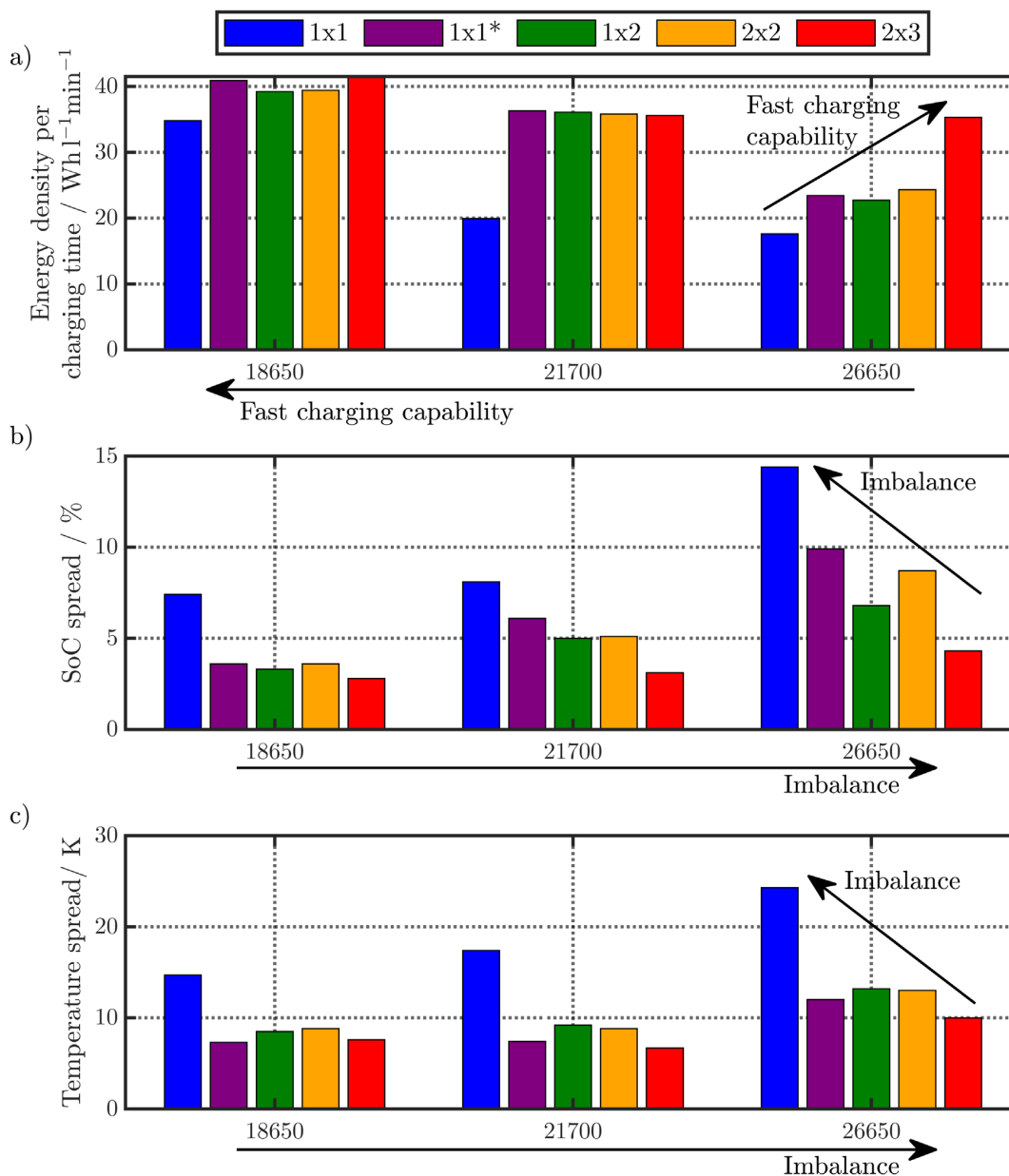
Figure 9. Simulation results of the multi-step fast charging procedure from 3 V to 4.2 V at 25 °C and 25% L_{AC} cooling. Subplot (a) shows the energy density per charging time to evaluate the fast charging capability of all simulated 18650, 21700, and 26650 configurations with the five different tab designs. Subplot (b) and (c) illustrate the corresponding spreads in SoC and temperature, which are used to evaluate the imbalance for each configuration of format and tab design.

seen for the 18650 studies (see Fig. 6d) ranging from a value of −1 mVs for 18650_1 × 1 to −520 mVs for 18650_2 × 3 at 3C-CC charging. Evaluating the earliest onset of negative anode potentials across the active area, the corresponding, with possible lithium plating affected SoC range calculates to 11.3% for 18650_1 × 1 and 40% for 18650_2 × 3 of the charged SoC. The enhanced charging performance of cell designs including multiple tabs comes with a higher risk of lithium plating throughout the charging process especially at higher C-rates. For the 1 × 1 design, the upper cutoff voltage is reached before lithium plating can occur almost independent from the applied C-rate. This is based on a lower SoC at EoC coming with lower degrees of lithiation within the anode and a

higher temperature due to charging losses reducing reaction overpotentials at the anode/separator interface. Both of these effects reduce the likeliness of lithium plating—but also come with a comparably low fast-charging capability including a high demand for cooling performance. This implies that by improving the tab design, fast charging is not primarily limited any more by how quickly the EoC voltage is reached due to voltage losses or if and when the maximum tolerable temperature is exceeded—but by how quickly a lithium plating criterion is violated. In order to avoid lithium plating for multi-tab cells even at higher SoC levels, a multi-step charging profile with reducing the C-rate at higher SoCs can be applied.

With increasing C-rate, the through-plane polarization and the current density increase, which leads to instantaneous and long-term decreasing anode potential and thus the indicated values in Fig. 6d increase up to -5 Vs in case of the 18650_2 $\times$ 3 design. The same findings hold for the 21700 and 26650 studies, where the anode potential increase due to the longer effective electrode lengths and additionally, the delayed heat conduction through the jelly roll increases the mean temperature in the cell. Consequently, the onset shifts to higher C-rates (4C) and multiple-tab designs such as 1 $\times$ 2 (21700) and 2 $\times$ 2 (26650).

In sum, lower in-plane ohmic losses evoked by shorter effective electrode lengths reduce the overall polarization, which lead to lower mean tab potentials and higher SoC levels, but also to a higher likeliness of lithium plating due to the absence of long-term in-plane heating effects and a prolonged charging process. To avoid overheatings and lithium plating on the long-term multi-step current profiles together can be applied in accordance to the tab design,[31] the format, and the cooling condition, which is discussed in the last section.

Focussing further on the locality of negative anode potentials across the active area, the first indication of lithium plating can be observed for the 18650_1 $\times$ 1*, 21700_1 $\times$ 2, and 26650_2 $\times$ 2 designs at 3C-CC charging as shown Fig. 7. At the positions P_1, P_2, and P_3, the anode potential vs the SoC (a, c, and e) is shown together with the time-integrated distribution of negative anode potentials across the active area (b, d, and f). The anode potential falls below 0 V first at either the negative (26650_2 $\times$ 2), the positive (21700_1 $\times$ 2), or both current collector tabs (18650_1 $\times$ 1*). This is caused by the higher current density and the accompanied accelerated lithiation of the anode, which leads to an early drop of the anode equilibrium potential compared to the areas far from the current collectors (see P_3). Interestingly, the 26650_2 $\times$ 2 design reveals no indication at the positive tabs, despite a clear indication at the negative tabs. For the 26650_2 $\times$ 2 design, the effective cathode length is 33% shorter than the anode, which leads to higher current density and accelerated lithiation near the anode's tabs (see magnifications in Fig. 7f) compared to the cathode's tabs. On the contrary, the 21700_1 $\times$ 2 design shows an early onset (see magnification in Fig. 7d) near the positive tab due to the single-tab design compared to double-tab design at the negative collector. For the 18650_1 $\times$ 1* study, the rather balanced effective electrode lengths lead to similar indications at both collector tabs.

The effective electrode lengths at both current collectors majorly affect the current density distribution over the active area and hence the local rate of the anode potential decrease. In general, the longer the effective electrode lengths at each positive or negative current collector becomes, the higher the likeliness for lithium plating appears close to the positive and/or negative tabs.

Impact of active and localized cooling on the battery's charging performance.—The L + F cooling case resulted in partial, local overheating beyond 60 °C at higher C-rates than 3C. Especially for the 1 $\times$ 1 designs this appears in all studied cell formats due to the increased in-plane ohmic losses. Besides, the chosen cooling at both front and lateral surface is not suitable for application in any scenario like EVs.[62] The 25% L_{AC} active cooling case addresses the aforementioned issues and is discussed in the following.

At a maximum 3C-CC could be applied to the temperature limit of 60 °C until reaching 4.2 V in case of the 18650 formats. The maximum uncritical C-rate is 2C for the 21700 and 26650 formats. Chosen temperature distributions across the active area are shown in the supplementary material. Again, the 1 $\times$ 1 design revealed overheating in all three formats. For the remaining tab designs, the localized, active cooling increases the temperature inhomogeneity by nearly a factor of two compared to L + F cooling. At most a spread of 9 K, 8 K, and more than 10 K appear between the maximum and minimum temperature at EoC for the 18650, 21700, and 26650 format. Despite the thermal aspect, the anode potentials close to 0 V

at EOC. The effect of local cooling spots on triggering lithium plating is discussed in the next section with the results of the 2 $\times$ 3 design in the 18650 format.

To keep the LIBs in a safe operating range, unwanted side reactions and overheating must be avoided. By using a multi-step current profile, these charging restrictions can be maintained whilst the charging efficiency can be improved compared to the aforementioned CC profile for each cell format and tab design. The simulation results of the profile presented in the last section initiates at 3C-CC charge and shifts to 2C-CC, when either negative anode potentials across the active area occur or critical temperatures beyond 60 °C throughout the jelly roll appear. Optionally, a second current step can be necessary due to the aforementioned restrictions and then a second step to 1C-CC until EoC is applied.

Cooling spot induced onset of unwanted side reactions.—Localized active cooling revealed local onset of lithium plating, which is discussed for the 18650_2 $\times$ 3 study under 3C-CC charging and 25% L_{AC}. Figure 8a shows the local temperature profiles vs the SoC at positions P_1 to P_4 as marked in Fig. 8b, which illustrates the temperature distribution across the active area at EoC. An obvious influence of the cooling spot appears on the temperature distribution as shown in Fig. 8b, where the minima of approximately 55 °C appear close to the cooling spot and repeat per each winding along the jelly roll from the outer surface at P_4 to the core as a consequence of the heat accumulation—resulting in the maxima at approximately 60 °C. The minimum in temperature, anode potential, and the current density appears just in the cooling spot at P_4. The instantaneous and charging time averaged current density spread between the four points appears to be 3.35% and 3.91%, where the minimum current appears near the cooled surface in the cold spot around P_4. Approximately at 25% SoC, the cooling effect at P_4 noticeably increases the total through-plane polarization compared to the remaining positions. Until EoC, the long-term effect of the cooling spot prevents an overly heating-caused polarization decrease. This results in the maximum 366 mV of through-plane polarization during charging compared to the remaining positions with 361 mV, 364 mV, and 358 mV at P_1, P_2, and P_3. In particular, the increased polarization around the cooling spot can be majorly referred to the higher anodic and cathodic reaction polarization $\triangle E_{BV}$. Together with the ongoing anode equilibrium decrease the increased through-plane polarization leads to the observed early negative anode potentials. Figure 8e shows the affected area. The closer to the negative tab, the higher the likeliness of lithium plating becomes, which correlates to an increased current density closer to the tabs and the accompanied faster lithiation of the anode.

In addition to the prolonged charging and lower in-plane heat generation the local cooling effect further increases the likeliness of lithium plating for the 18650_2 $\times$ 3 design. Only the 18650_2 $\times$ 3 study revealed this effect, as the remaining tab designs and formats are less affected due to the longer effective electrode lengths and/or the higher mean temperatures resulting from the larger formats.

Multi-step fast charging procedure.—Table VI summarizes all simulated multi-step charging simulations under 25% L_{AC} and 25 °C. Regarding the increased in-plane polarization and the resulting in-plane heat generation of the 1 $\times$ 1 tab designs, only the 18650 format could be applied with a prolonged, initial 3C-CC phase, as the appearing overheating due to the delayed radial heat conduction for the 21700 and 26650 formats could not sufficiently be cooled in the following current phases. Therefore, a 2C- to 1C-CC profile is applied in the 21700_1 $\times$ 1 and 26650_1 $\times$ 1 study. Similarly early EoC is avoided for the remaining 21700 and 26650 studies via limiting the first 3C-CC period to 90 s and 60 s, which is derived from preliminary simulations.

In extension to Table VI, Fig. 9 illustrates the results for each simulated configuration of format and tab design. Regarding the 26650 formats, the fast charging capability increases if more tabs are

used and the imbalance of SoC and temeperature can be significantly reduced. As expected, the bigger the cell diameter, the lower the fast charging capability and the higher the imbalance of SoC and temperature. In case of the 18650 formats the 2×3 tab design reveals the best energy per time ratio of 41.5 $Whl^{-1} min^{-1}$ and the maximum SoC of 67.1% and the minimum spread in SoC of 2.8%. The poorest performance appears for the 18650_1×1 design with 34.8 $Whl^{-1} min^{-1}$ accompanied with the lowest SoC of 57.4%, the maximum spread in SoC of 7.4%, and temperature spread around 14.7 K. Similarly, 60 °C appear as a maximum at the transition from 3C to 2C except for the 2×3 design, as negative anode potentials (see Fig. 8) appear before reaching the upper temperature limit.

The bigger the cell radius, the slower the charging. At most 36.3 $Whl^{-1} min^{-1}$ for the 21700_1×1* and 35.3 $Whl^{-1} min^{-1}$ for the 26650_2×3 design appear with increased spreads in SoC around 6.1% and 4.3%, respectively. Again, the 1×1 designs reveal the poorest performance. The 26650 formats reveal the maximum temperature inhomogeneity beyond 10 K in all designs due to the limited radial heat transport based on the largest cell diameter. The resulting heat accumulation leads to overheating in the 2C current phase, which triggers a 2nd current step to 1C in case of the 1×1*, 1×2, and 2×2 tab designs. Consequently, these studies reveal significantly lower energy per time ratios and offer a low capability under 25 $Whl^{-1} min^{-1}$ while fast charging. Compared to the 18650 designs, the 21700 cases reveal a similar temperature spread and a sufficient energy per time ratio at least beyond 35 $Whl^{-1} min^{-1}$—except for the 1×1 tab design. Regarding the 1×1*, 1×2, 2×2, and 2×3 tab design for the 21700 format, the smaller effective electrode lengths lead generally to a lower spread in temperature and SoC, but also to increased charging times and lower energy per time ratios in the multi-step scenario.

To sum up, the 1×1 design for all three formats is critical in terms of overheating, leading to deviation in SoC and temperature, and overall shows the lowest capability toward fast charging. The 26650 format reveals overheating also for the remaining tab designs due to the poor thermal design and only the 2×3 tab design achieved an acceptable energy per time ratio and SoC deviation, but still a temperature spread around 10 K. Comparing the 21700 to the 18650 formats (except for the 1×1 tab design), slightly lower energy per time ratios and higher spread in SoC throughout the jelly roll appear, but a similar thermal performance underlines the benefit of using the 21700 formats.

The correlation between the in-plane heat generation and the tab design/format is shown in Table XII (see Appendix) to evaluate the charging energy efficiency via correlating the charged energy to the accumulated heat generation and cooling flow. The bigger the cell and the longer the effective electrode lengths, the higher the share of in-plane heat generation, but the lower the share of total converted heat from the total charged energy.

Comparing the thermally superior 21700 to the rather unfavourable 26650 format, an improved fast charging performance could possibly be achieved using a mid-sized format. As a prospect for future cylindrical cell formats, exemplary a 22800 ($w_{ele} \times h_{ele} = 102 \times 7.3$ cm) and 23700 (111×6.3 cm) are simulated. Either the jelly roll's diameter ($\oslash 22$ mm) and the height (80 mm) or only the diameter ($\oslash 23$ mm) are increased. The 22800_1×1* and 22800_1×2 designs show similar energy per time ratios as shown in Table VI. A slightly faster charging compared to the respective 21700 formats appears. The 23700_1×2 and 23700_2×2 designs tend to increased heat accumulation coming with higher temperature spread and maximum temperature. Focussing on the 22800_1×2 study, a speed-up of nearly 2 minutes could be achieved compared to the 21700_1×2 study, which offers a similar energy per time ratio at a slightly increased spread in SoC, but reduced temperature spread.

In sum, the thermal design is a key feature when a further increase in cell size from 21700 is favoured. The height can be slightly increased together with the diameter of the cell (22800), otherwise (23700) heat accumulation can become a significant issue to the cell's charging performance and safety.

Conclusions

The experimental analysis of state-of-the-art cylindrical LIBs revealed the highest gravimetric energy density within for a 18650 cell, whereas the highest volumetric energy density could be observed for a 21700 cell. Larger cells, such as the 26650 formats reveal lower gravimetric and volumetric energy density suggesting a delayed development of high-energy 26650 cells compared to the smaller 18650 and 21700 cells. A moderate charging simulation study at 1C-CC of the same three formats revealed a significant influence of the applied tab design on the in-plane polarization and the resulting temperature. The total polarization can be reduced by up to 36% within an ambient temperature range from 10 °C to 40 °C. At 3C-CC fast charging procedures, the local variance of the through-plane polarization across the active area can be similarly lowered by a factor of five and the in-plane polarization by a factor of four, which increases the charged SoC up to +23% at EoC. However, the shorter the effective electrode length is chosen, the lower the in-plane polarization becomes, which eventually increases the likeliness of lithium plating based on lower heat generation throughout the charging procedure and an overall prolonged charging process which comes with higher degrees of lithiation within the anode. Especially the heat accumulation effect in the larger-sized 21700 and 26650 formats tends to inhibit the onset of lithium plating due to the increased temperature rise. The locality of lithium plating onset mainly depends on the current collector tab design and the accompanied current density distribution. Evaluating an application-near multi-step charging profile under local cooling, the 21700 format reveals a comparable thermal behavior to the 18650 formats and less performance losses than the 26650 formats. For high energy 26650 formats overheating can be avoided by using multi tab design and the resulting effective electrode lengths should be long enough to avoid lithium plating in local cold spots. Still, the resulting imbalance of SoC and temperature in the jelly roll suggests more favourable cylindrical formats at lower cell diameters, preferably at slightly increased heights such as 22800 to improve the cooling performance.

In sum, choosing the right tab design for each format should improve rate capability, charging efficiency in form of the gained energy per time ratio, thermal safety, and resistivity toward localized lithium plating. The multi-step profile could be extended by further current steps, to reduce the charging time in total to increase the gained SoC level while maintaining the same thermal and lifetime relevant boundary conditions. In extension to this work, future research work could further investigate the impact of the current collector thicknesses in relation to the applied tab design. Future work could also focus on the economic efficiency for using multi-tab instead of single-tab design, which could investigate the trade-off between the higher expected manufacturing costs for multi-tab designs and the benefits of a more homogeneous utilization.

Acknowledgments

Appendix

Table VII. Differential algebraic equations of the MuDiMod framework.

P2D model
Mass balance[a)]

$$\varepsilon_1 \frac{\partial c_1(x,t)}{\partial t} = \frac{\partial}{\partial x}\left(D_1^{\text{eff}} \frac{\partial c_1(x,t)}{\partial x} + \frac{i_1(x,t)(1 - t_+^0)}{F}\right)$$

$$\varepsilon_s \frac{\partial c_s(x,t,r)}{\partial t} = \frac{1}{r^2}\frac{\partial}{\partial r}\left(D_s r^2 \frac{\partial c_s(x,t,r)}{\partial r}\right)$$

Potentials[a)]

$$\frac{\partial \Phi_1(x,t)}{\partial x} = -\frac{i_1(x,t)}{\kappa_1^{\text{eff}}} + \frac{2RT}{F}(1 - t_+^0)\left(1 + \frac{d \, lnf_\pm}{d \ln c_1(x,t)}\right)\frac{\partial \ln c_1(x,t)}{\partial x}$$

$$\frac{\partial \Phi_s(x,t)}{\partial x} = -\frac{i_{\text{app}}(t) - i_1(x,t)}{\sigma_s} \quad \text{with} \quad i_{\text{app}}(t) = i_s(x,t) + i_1(x,t) \quad \forall x, t$$

Charge balance[a)]

$$\frac{\partial i_1(x,t)}{\partial x} + \frac{\partial i_s(x,t)}{\partial x} = 0 \quad \text{with} \quad \frac{\partial i_s(x,t)}{\partial x} = -\frac{3\varepsilon_s}{R_p}F j_n(x,t) = -\frac{3\varepsilon_s}{R_p}i_n(x,t)$$

Electrode

$$j_n(x,t) = \frac{i_0(x,t)}{F}\left[\exp\left(\frac{\alpha_a F \eta(x,t)}{RT}\right) - \exp\left(-\frac{\alpha_c F \eta(x,t)}{RT}\right)\right]$$

kinetics[a)]

$$\eta(x,t) = \Phi_s(x,t) - \Phi_1(x,t) - E_{\text{eq}}(x,t) - j_n(x,t)F R_f$$

$$i_0(x,t) = F k \sqrt{(c_{s,\text{max}} - c_{ss}(x,t))(c_{ss}(x,t))\left(\frac{c_1(x,t)}{c_{1,\text{ref}}}\right)} \quad \text{with} \quad c_{ss} = c_s|_{r=R_p}$$

Heat Source

$$q_r = \frac{3\varepsilon_s F}{R_p}\int_{x*} j_n \cdot \eta \; dx$$

$$q_{\text{rev}} = \frac{3\varepsilon_s F}{R_p}\int_{x*} j_n \cdot \frac{\partial E_{\text{eq}}}{\partial T} \cdot T \; dx$$

$$q_1 = \int_{x=0}^{t_a + t_{\text{sep}} + t_c} i_1 \cdot \frac{\partial \Phi_1}{\partial x} \; dx$$

$$q_s = \int_{x*} i_s \cdot \frac{\partial \Phi_s}{\partial x} \; dx$$

$$q_{\text{p2D}} = q_r + q_{\text{rev}} + q_1 + q_s$$

2D electrical model

$$\nabla = \left(\frac{\partial}{\partial x'}, \frac{\partial}{\partial y'}\right)^{\text{T}} \qquad \sigma = \begin{bmatrix} \sigma_{cc,x'} & 0 \\ 0 & \sigma_{cc,y'} \end{bmatrix}$$

Charge Balance
Potentials

$$I = \sum_i i_{\text{p2D},i} \cdot A_i$$

$$\sigma_{cc}\nabla^2 \varphi_{cc} = \pm **\frac{i_{\text{p2D}}}{t_{cc}}$$

Heat source

$$q_{cc} = t_{cc} \cdot \sigma_{cc} \cdot (\nabla \varphi_{cc})^2$$

3D thermal model

$$\nabla = \left(\frac{\partial}{\partial r''}, \frac{\partial}{\partial \psi}, \frac{\partial}{\partial z''}\right)^{\text{T}} \qquad \lambda = \begin{bmatrix} \lambda_\perp & 0 & 0 \\ 0 & \lambda_\parallel & 0 \\ 0 & 0 & \lambda_\parallel \end{bmatrix}$$

Temperature

$$\rho_{\text{stack}} c_p \frac{\partial T}{\partial t} = \lambda \nabla^2 T + q$$

Heat source

$$q = \frac{x_{\text{p2D}}}{t_a + t_{\text{sep}} + t_a} q_{\text{p2D}} + \frac{x_{cc,+}}{t_{cc,+}} q_{cc,+} + \frac{x_{cc,-}}{t_{cc,-}} q_{cc,-}$$

$$-q_{\text{conv},\Gamma} - q_{\text{rad},\Gamma}$$

$$q_{\text{conv},\Gamma} = \varepsilon_{\text{rad}} \, \sigma_b(T^4 - T_\infty^4) \qquad q_{\text{rad},\Gamma} = \alpha_{\text{conv}}(T - T_\infty)$$

a) Ref. 45. b) Ref. 73. Γ Only at the surface of the jelly roll.

Table VIII. Parametrization of the MuDiMod framework[31,48]—Part I.

Properties of single layers	Symbol	Unit	Anode Copper	Anode SiC	Separator[P]	Cathode NMC-811	Cathode Aluminum	Electrolyte
Geometry								
Thickness[m]	t	μm	11	86.7	12	66.2	17.3	
Density	ρ	kg m^{-3}	8950[a]	2242[b]	1009[c]	4870[d]	2710[a]	1130[c]
Particle radius[m,D50]	R_p	μm		6.1		3.8		
Active material fraction[e]	ε_s	%		69.4		74.5		
Inactive fraction[e,P/C]	$\varepsilon_\mathrm{s,na}$	%		9		8.4		
Porosity[e]	ε_l	%		21.6[m]	45[e]	17.1[m]		
Tortuosity[B]	τ	—		$\varepsilon_\mathrm{l}^{-0.5}$	$\varepsilon_\mathrm{l}^{-0.5}$	$\varepsilon_\mathrm{l}^{-0.85}$		
Thermodynamics								
Equilibrium potential[m]	E_eq	V		Ref. 48		Ref. 48		
Entropic coefficient[m]	$\frac{\partial E_\mathrm{eq}}{\partial T}$	V K^{-1}		Ref. 48		Ref. 48		
Stoichiometry[m]		100% SoC		0.855		0.267		
		0% SoC		0.031		0.927		
Gravimetric loading	b_g	mAh g^{-1}		415[b]		275.5[e]		
Maximum Concentration[e]	$c_\mathrm{s,max}$	mol m^{-3}		34684		50060		
Transport								
Solid diffusivity[A]	D_s	m^2 s^{-1}		5E-14[f]		5E-13[g,h]		
Solid conductivity	σ_s	S m^{-1}	$\frac{5.96\cdot 10^7}{1+3.383\cdot 10^{-3}(T-293.15\mathrm{K})}$ [i]	100[b]		0.17[b]	$\frac{3.78\cdot 10^7}{1+4.290\cdot 10^{-3}(T-293.15\mathrm{K})}$ [j]	
Film resistance	R_f	Ω m^2		0.0035[k]		0^e		
Kinetics								
Reaction rate constant[e,A]	k	m s^{-1}		3E-11		1E-11		
Transfer coefficient[e]	$\alpha_{a/c}$	—		0.5		0.5		
Ref. concentration	$c_\mathrm{l,ref}$	mol m^{-3}						1
Thermal properties								
Heat capacity	c_p	J kg^{-1} K^{-1}	385[c]	867[j]	1978.2[c]	840.1[e]	903[c]	2055.1[c]
Heat conductivity[c]	λ	W m^{-1} K^{-1}	398	1.04	0.33	1.58	238	0.6
Solid diffusivity[e,A]	$\frac{E_\mathrm{a,Ds}}{R}$	K		1200		1200		
Reaction rate constant[e,A]	$\frac{E_\mathrm{a,k}}{R}$	K		3600^e		3600^e		
Properties of electrode stack [*,S]								
Thickness	t_stack	μm						
Density	ρ_stack	kg m^{-3}						
Heat capacity	c_stack	J kg^{-1} K^{-1}						
Heat conductivity	$\lambda_\perp$	W m^{-1} K^{-1}						
	$\lambda_\parallel$	W m^{-1} K^{-1}						

Effective values

$$t_\mathrm{cc,-} + 2\cdot(t_\mathrm{a} + t_\mathrm{sep} + t_\mathrm{c}) + t_\mathrm{cc,+} = 358$$

$$\frac{\sum_i t_i \rho_i}{t_\mathrm{stack}} = 2761.7$$

$$\frac{\sum_i t_i \rho_i c_{\mathrm{p},i}}{t_\mathrm{stack}/\rho_\mathrm{stack}} = 918.8$$

$$\left(\frac{1}{t_\mathrm{stack}}\cdot\sum_i \frac{t_i}{\lambda_i}\right)^{-1} = 1.1$$

$$\frac{\sum_i t_i \lambda_i}{t_\mathrm{stack}} = 24.6$$

m = measured e = estimated, taken from Ref. 31 S Superposition of solid and liquid phase P/C PVDF-binder/Carbon black (Ref. 74, 75).

B Bruggeman Transport Correction[76]: $\Psi_\mathrm{l,eff} = \varepsilon_\mathrm{l}^{-\beta}\cdot\Psi_0$, estimated within the model validation part of Ref. 31 and adjusted for the cathode in reference to Ref. 77.

A Arrhenius law[78]: $k = A\cdot\exp\left(\frac{E_\mathrm{a,i}}{R}\frac{(T-298\,\mathrm{K})}{T\cdot 298\,\mathrm{K}}\right)$.

* The calculations are adopted from Ref. 79,a) Ref. 80. b) Ref. 81. c) Ref. 79, d) Ref. 69, e) Ref. 82. f) Ref. 71. g) Ref. 70. i) Ref. 83. j) Ref. 84. k) Ref. 85. l) Ref. 86.

Table IX. Parametrization of the MuDiMod framework[31,48]—Part II.

Property	Symbol	Unit	1 M $LiPF_6$ in PC/EC/DMC
Salt diffusivity[a]	D_l	$m^2\,s^{-1}$	$10^{-4} \cdot 10^{-4.43 - \frac{54}{T-229-5c_l} - 0.22c_l}$
Ionic conductivity[a]	κ_l	$S\,m^{-1}$	$0.1c_l(-10.5 + 0.668c_l + 0.494c_l^2 + 0.074T - 0.0178c_lT$ $-8.8610^{-4}c_l^2T - 6.9610^{-5}T^2 + 2.810^{-5}c_lT^2)^2$
Activity[a]	$\frac{d\,lnf_\pm}{d\,lnc_l}$	—	$(0.601 - 0.24c_l^0.5 + 0.983(1 - 0.0052(T - 294))c_l^{1.5}) \cdot (1 - t_+^0)^{-1} - 1$
Transference[a]	t_+^0	—	0.38
Initial concentration	c_0[a]	$mol\,m^{-3}$	1000

a) Ref. 87.

Table X. Calculation of the through-plane polarization[25,61] incorporated in the MuDiMod framework.

Polarization	Symbol	Unit	Anode	Separator	Cathode
Bounds of integration					
Thickness	x_0	μm	0	t_a	$t_a + t_{sep}$
	x_1	μm	t_a	$t_a + t_{sep}$	$t_a + t_{sep} + t_c$
Reference current					
Current flow	i_{tot}	$A\,m^{-2}$	$\int_{x_0}^{x_1}\left(\frac{3\,\varepsilon_s}{R_p} \cdot F\,j_n\right)dx$	n.a.[a]	$\int_{x_0}^{x_1}\left(\frac{3\,\varepsilon_s}{R_p} \cdot F\,j_n\right)dx$
Polarization					
Electrolyte Diffusion	$\triangle E_{D,l}$	V		$-i_{tot}^{-1} \cdot \int_{x_0}^{x_1}\left(i_l\frac{2\,R\,T}{F} \cdot (1 - t_+^0) \cdot \left(1 + \frac{d\,lnf_\pm}{d\,ln\,c_l}\nabla ln\,c_l\right)\right)dx$	
ParticleDiffusion	$\triangle E_{D,s}$	V	$i_{tot}^{-1} \cdot \int_{x_0}^{x_1}\left(\frac{3\,\varepsilon_s}{R_p} \cdot F\,j_n \cdot (E_{eq} - E_{eq,ave})\right)dx$[b]	n.a.	$i_{tot}^{-1} \cdot \int_{x_0}^{x_1}\left(\frac{3\,\varepsilon_s}{R_p} \cdot F\,j_n \cdot (E_{eq} - E_{eq,ave})\right)dx$
Ohmic loss (l)	$\triangle E_{\Omega,l}$	V		$i_{tot}^{-1} \cdot \int_{x_0}^{x_1}\left(\frac{i_l^2}{\kappa_{l,eff}}\right)dx$	
Ohmic loss (s)	$\triangle E_{\Omega,s}$	V	$i_{tot}^{-1} \cdot \int_{x_0}^{x_1}\left(\frac{i_s^2}{\sigma_{s,eff}}\right)dx$	n.a.	$i_{tot}^{-1} \cdot \int_{x_0}^{x_1}\left(\frac{i_s^2}{\sigma_{s,eff}}\right)dx$
Reaction kinetics	$\triangle E_{BV}$	V	$i_{tot}^{-1} \cdot \int_{x_0}^{x_1}\left(\frac{3\,\varepsilon_s}{R_p} \cdot F\,j_n \cdot (\Phi_s - \Phi_l - E_{eq})\right)dx$	n.a.	$i_{tot}^{-1} \cdot \int_{x_0}^{x_1}\left(\frac{3\,\varepsilon_s}{R_p} \cdot F\,j_n \cdot (\Phi_s - \Phi_l - E_{eq})\right)dx$
Superposition	$\triangle E_{tot}$	V		$\sum_i \triangle E_i$	

a) Referred to the total current flow through the cathode. b) $E_{eq,ave}$ calculated from the lithium-ion concentration on average within the particle.

Table XI. Experimental test procedure for the investigated cylindrical LIBs.

Check-up cycles Repetition	Sequence[a]	Feature	Chamber Temperature
1×	R-CC$_{CH}$-R	CC: 0.2C, 4.2 V R: 30 min	5 °C, 25 °C, or 40 °C
5×	CC$_{DCH}$-R-CC$_{CH}$-R	CC$_{DCH}$: 0.5C, 2.5 V R: 30 min CC$_{CH}$: 0.2C, 4.2 V	
1×	CC$_{DCH}$-CV-R	CC$_{DCH}$: 0.2C, 4.2 V CV: <0.015C R: 30 min	
2×	CC$_{CH}$-CV-R-CC$_{DCH}$-CV-R	CC$_{CH}$: 0.2C, 4.2 V CV: <0.015C R: 30 min CC$_{DCH}$: 0.5C, 2.5 V	
1×	CC$_{CH}$-R	CC: 0.2C to 50% SoC R: 30 min	
3×	P$_{CH}$-R-P$_{DCH}$-R	P: 0.33C, 0.66C and 1C for 10 s R: 10 min	
Rate test			
1×	CC$_{CH}$-CV-R	CC: 0.2C, 4.2 V CV: <0.001C R: 3 h	5 °C, 25 °C, or 40 °C

Table XI. (Continued).

Check-up cycles Repetition	Sequence[a]	Feature	Chamber Temperature
3×	CC_{DCH}-CV-R-CC_{CH}-CV-R	CC_{DCH}: 0.2C, 0.5C, 1C 2.5 V CV: <0.001C R: 3 h CC_{CH}: 0.2C, 0.5C, 1C 4.2 V	
3×	CC_{DCH}-CV-R	CC_{DCH}: 5.7 A 2.5 V CV: <0.001C R: 3 h	
OCV test			
1×	CC_{CH}-CV-R	CC: 0.1C, 4.2 V CV: <0.001C R: 6 h	5 °C, 25 °C, or 40 °C
1×	CC_{DCH}-CV-R-CC_{CH}-CV-R	CC_{DCH}: 0.02C 2.5 V CV: <0.001C R: 6 h CC_{CH}: 0.02C 4.2 V	
1×	CC_{DCH}-CV-R-CC_{CH}	CC_{DCH}: 0.5C, 2.5 V CV: <0.015C R: 5 min CC_{CH}: 0.2C to 50% SoC	
EIS test			
1×	R	R: 3 h	

1× **EIS** at 50% SoC with 140 mA excitation current from 10 mHz to 10 kHz[b]

a) CC_{CH} constant current charge CC_{DCH} constant current discharge CV constant voltage R rest period P_{CH} charge pulse current P_{DCH} discharge pulse current.
b) 5, 10, or 13 points per decade and 2, 5, or 10 measurements per frequency between 10 mHz-90 mHz, 100 mHz-990 mHz, or 1 Hz–10 kHz.

Table XII. Energy analysis derived from the cumulated power, heat generation, and cooling conditions during the multi-step current charging.

Identifier	ξ	$\dfrac{Q_{tot}}{\xi}$	$\dfrac{Q_{stack}}{Q_{tot}}$	$\dfrac{Q_{cc,\pm}}{Q_{tot}}$	$\dfrac{Q_{AC}}{\xi}$	$\dfrac{Q_{rad}}{\xi}$
Unit	/Wh	/%	/%	/%	/%	/%
18650[a]						
$1 \times 1^{3C \to 2C}$	7.7	11.4	66.4	33.6	6.3	0.3
$1 \times 1^{*3C \to 2C}$	8.6	9.8	82.9	17.1	5.5	0.3
$1 \times 2^{3C \to 2C}$	8.7	9.7	85.9	14.1	5.6	0.2
$2 \times 2^{3C \to 2C}$	8.9	9.5	90	10	5.5	0.2
$2 \times 3^{3C \to 2C}$	9.1	9.3	94.3	5.7	5.3	0.2
21700[a]						
$1 \times 1^{2C \to 1C}$	14.1	9	53.6	46.4	6.1	0.3
$1 \times 1^{*3C \to 2C}$	12.5	9.3	71.7	28.3	4.6	0.3
$1 \times 2^{3C \to 2C}$	13.1	9.2	75.7	24.3	4.7	0.2
$2 \times 2^{3C \to 2C}$	13.9	8.4	83	17	4.4	0.2
$2 \times 3^{3C \to 2C}$	14.2	7.8	90.8	9.2	4.1	0.2
26650[a]						
$1 \times 1^{2C \to 1C}$	16.3	11	34.4	65.6	6.1	0.3
$1 \times 1^{*3C \to 2C \to 1C}$	21.1	8.7	56	44	5.6	0.2
$1 \times 2^{3C \to 2C \to 1C}$	21.6	8.2	62.2	37.8	5.3	0.2
$2 \times 2^{3C \to 2C \to 1C}$	22.4	7.9	71.6	28.4	4.9	0.2
$2 \times 3^{3C \to 2C}$	19.9	7.8	83.9	16.1	3.6	0.2
Prospective cylindrical formats[a]						
$22800\_1 \times 1^{*3C \to 2C}$	15	9.2	67.5	32.5	4.4	0.2
$22800\_1 \times 2^{3C \to 2C}$	16	9	72	28	4.4	0.2
$23700\_1 \times 2^{3C \to 2C \to 1C}$	19.3	8.5	70.7	29.3	5.5	0.2
$23700\_2 \times 2^{3C \to 2C}$	16.4	8.9	77.7	22.3	4.4	0.2

$^{2C \to 1C}$ 2-step current profile from 2C- to 1C-CC.
$^{3C \to 2C}$ 2-step current profile from 3C- to 2C-CC.
$^{3C \to 2C \to 1C}$ 3-step current profile with inital 3C-, subsequent 2C-, and final 1C-CC phase.a) Cooling surface to volume ratio: 18650 [56 m^{-1}], 21700 [46.7 m^{-1}], 22800 [45.1 m^{-1}], 23700 [42.4 m^{-1}], and 26650 [37.8 m^{-1}].

Table XIII. Nomenclature I.

Greek symbols

α	—	Transfer coefficient
α_{conv}	$\mathrm{W\,m^{-2}\,K^{-1}}$	Heat transfer coefficient
β	—	Bruggeman coefficient
ε	—	Volume fraction
$\varepsilon_{\mathrm{rad}}$	0.75	Radiation emission coefficient
ξ	$\mathrm{Wh\,kg^{-1}}$	Energy density
η	V	Overpotential in Butler-Volmer kinetics
κ	$\mathrm{S\,m^{-1}}$	Ionic conductivity
λ	$\mathrm{W\,m^{-1}\,K^{-1}}$	Heat conductivity
ρ	$\mathrm{kg\,m^{-3}}$	Mass density
σ	$\mathrm{S\,m^{-1}}$	Electrical conductivity
σ_{b}	$5.67 \times 10^{-8}\,\mathrm{W\,m^{-2}\,K^{-4}}$	Stefan-Boltzmann constant
τ	—	Tortuousity
Φ	V	Electrical potential
ψ	rad	Azimuthal-coordinate in 3D model
Ψ_{arc}	rad	Azimuthal angle
χ		Thickness ratio

Indices

a	Negative electrode (Anode)
act	Active area of anode and cathode overlap
app	Globally applied
arc	Arc-length of archimedial spiral
c	Positive electrode (Cathode)
cc	current collector
con	Heat conduction
conv	Heat convection
eff	Transport corrected (Bruggeman correlation[76])
ele	Electrode
eq	Equilibrium
g	Gravimetric
jr	Jelly roll
l	Liquid phase
p	Isobar
pas	Passive
rad	Heat radiation
r	Reaction heat
rev	Reversible heat
s	Solid phase
sep	Separator
ss	Active particle surface
stack	Electrode stack
surf	Surface
+	Positive current collector
−	Negative current collector

Table XIV. Nomenclature II.

Latin symbols

a	$\mathrm{m^{-1}}$	Specific surface
b_{g}	$\mathrm{mAh\,g^{-1}}$	Maximum theoretical loading
c	$\mathrm{mol\,m^{-3}}$	Concentration of lithium-ions ($\mathrm{Li^+}$)
$c_{\mathrm{s,max}}$	$\mathrm{mol\,m^{-3}}$	Maximum theoretical concentration of $\mathrm{Li^+}$
c_{p}	$\mathrm{J\,kg^{-1}\,K^{-1}}$	Heat capacity
D	$\mathrm{m^2\,s^{-1}}$	Diffusion coefficient
E_{eq}	V	Equilibrium potential vs $\mathrm{Li/Li^+}$
$f_{\pm}$	—	Mean molar activity coefficient of electrolyte
F	$96\,485\,\mathrm{As\,mol^{-1}}$	Faraday's constant
h	m	Height of active electrode area
i	$\mathrm{A\,m^{-2}}$	Current density
I	A	Applied current

Table XIV. (Continued).

Latin symbols

i_{app}	A m^{-2}	Applied current density
i_n	A m^{-2}	Current density perpendicular to particle surface
i_{p2D}	A m^{-2}	Current density perpendicular to current collectors
i_0	A m^{-2}	Exchange current density
j_n	$\text{mol m}^{-2}\,\text{s}^{-1}$	Pore-wall flux
k	m s^{-1}	Reaction rate constant
m	kg	Mass of the jelly roll
r	m	Radial-coordinate of particle domain in p2D model
r''	m	Radial-coordinate in 3D model
R	$8.314\ \text{J mol}^{-1}\,\text{K}^{-1}$	Gas constant
R_f	$\Omega\,\text{m}^2$	Surface-layer resistance
R_p	m	Particle radius
q	W m^{-3}	Heat generation rate per volume
Q	W	Heat generation rate
t	s	Time
t_i	m	Thickness of layer i
t_+^0	—	Transference number
T	K	Temperature
w	m	Length of active electrode area
x	m	x-coordinate in p2D model
x'	m	x-coordinate in 2D model
y'	m	y-coordinate in 2D model
x''	m	x-coordinate in 3D model
y''	m	y-coordinate in 3D model
z''	m	z-coordinate in 3D model

Table XV. Nomenclature III.

Abbreviations

DEC	Diethyl carbonate
DMC	Dimethyl carbonate
DoD	Depth of discharge
DVA	Differential voltage analysis
FEM	Finite element method
G	Graphite
E	Electrical model
EC	Ethylene carbonate
ECM	Equivalent-circuit model
ESPM	Extended single particle model
EV	Electric vehicle
LCO	Li_yCoO_2
LFP	Li_yFePO_4
LiPF$_6$	Lithium hexafluorophosphate
LMO	$Li_yMn_2O_4$
MuDiMod	Multidimensional multiphysics modelling framework
NCA	$Li_yNi_{0.8}Co_{0.15}Al_{0.05}O_2$
NMC-111	$Li_yNi_{0.33}Mn_{0.33}Co_{0.33}O_2$
NMC-532	$Li_yNi_{0.5}Mn_{0.3}Co_{0.2}O_2$
NMC-811	$Li_yNi_{0.8}Mn_{0.1}Co_{0.1}O_2$
OCP	Open-circuit potential vs Li/Li$^+$
OCV	Open-circuit voltage
p2D	Pseudo-two dimensional model
PC	Poly-carbonate
PVDF	Polyvinylidene fluoride
SiC	Graphite host lattice with content of silicon
SoC	State of charge
SPM	Single particle model
T	Thermal model

ORCID

J. Sturm https://orcid.org/0000-0001-8876-9989
A. Frank https://orcid.org/0000-0001-8069-2948
A. Rheinfeld https://orcid.org/0000-0003-0995-7266
S. V. Erhard https://orcid.org/0000-0002-5029-7477
A. Jossen https://orcid.org/0000-0003-0964-1405

References

1. J. Eddy, A. Pfeiffer, and J. van de Staaij, (2019), Recharging Economies: The EV Battery Manufacturing Outlook for Europe - McKinsey&Company, https://mckinsey.com/industries/oil-and-gas/our-insights/recharging-economies-the-ev-battery-manufacturing-outlook-for-europe.
2. D. Kuepper, K. Kuhlmann, S. Wolf, C. Pieper, G. Xu, and J. Ahmad, (2018), The Future of Battery Production in Electric Vehicles - The Boston Consulting Group, https://eu-smartcities.eu/sites/default/files/2018-10/BCG-The-Future-of-Battery-Production-for-Electric-Vehicles-Sep-2018%20(1)_tcm81-202396.pdf.
3. P. Hertzke, N. Müller, P. Schaufuss, S. Schenk, and T. Wu, (2019), Expanding Electric-vehicle Adoption Despite Early Growing Pains - McKinsey&Company, https://mckinsey.com/industries/automotive-and-assembly/our-insights/expanding-electric-vehicle-adoption-despite-early-growing-pains.
4. Y. Ding, Z. P. Cano, A. Yu, J. Lu, and Z. Chen, "Automotive li-ion batteries: current status and future perspectives." *Electrochemical Energy Reviews*, **2**, 1 (2019).
5. J. Duan, X. Tang, H. Dai, Y. Yang, W. Wu, X. Wei, and Y. Huang, "Building safe lithium-ion batteries for electric vehicles: a review." *Electrochemical Energy Reviews*, **3**, 1 (2020).
6. Y. Miao, P. Hynan, A. von Jouanne, and A. Yokochi, "Current li-ion battery technologies in electric vehicles and opportunities for advancements." *Energies*, **12**, 1074 (2019).
7. G. Lenze, H. Bockholt, C. Schilcher, L. Froböse, D. Jansen, U. Krewer, and A. Kwade, "Impacts of variations in manufacturing parameters on performance of lithium-ion-batteries." *J. Electrochem. Soc.*, **165**, A314 (2018).
8. F. J. Günter, C. Burgstaller, F. Konwitschny, and G. Reinhart, "Influence of the electrolyte quantity on lithium-ion cells." *J. Electrochem. Soc.*, **166**, A1709 (2019).
9. F. J. Günter, S. Rössler, M. Schulz, W. Braunwarth, R. Gilles, and G. Reinhart, "Influence of the cell format on the electrolyte filling process of lithium-ion cells." *Energy Technology*, **8**, 1801108 (2020).
10. J. Tuebke and K. C. Moeller, (2017), Perspectives on the Developement of Electromobility Related Cell Formats for Lithium-ion Batteries - Fraunhofer-

Allianz Batterien, https://batterien.fraunhofer.de/content/dam/batterien/de/documents/Allianz_Batterie_Zellformate_Studie.pdf.

11. A. Manthiram, "A reflection on lithium-ion battery cathode chemistry." *Nat. Commun.*, **11**, 1550 (2020).

12. M. D. Bhatt and J. Y. Lee, "High capacity conversion anodes in li-ion batteries: a review." *International Journal of Hydrogen Energy*, **44**, 10852 (2019).

13. J. Landesfeind, A. Eldiven, and H. A. Gasteiger, "Influence of the binder on lithium ion battery electrode tortuosity and performance." *J. Electrochem. Soc.*, **165**, A1122 (2018).

14. R. Morasch, J. Landesfeind, B. Suthar, and H. A. Gasteiger, "Detection of binder gradients using impedance spectroscopy and their influence on the tortuosity of li-ion battery graphite electrodes." *J. Electrochem. Soc.*, **165**, A3459 (2018).

15. A. M. Haregewoin, A. S. Wotango, and B.-J. Hwang, "Electrolyte additives for lithium ion battery electrodes: progress and perspectives." *Energy Environ. Sci.*, **9**, 1955 (2016).

16. N. Chawla, N. Bharti, and S. Singh, "Recent advances in non-flammable electrolytes for safer lithium-ion batteries." *Batteries*, **5**, 19 (2019).

17. C. F. J. Francis, I. L. Kyratzis, and A. S. Best, "Lithium battery separators for ionic-liquid electrolytes: a review." *Advanced materials (Deerfield Beach, Fla.)*, **32** (18) e1904205 (2020).

18. M. F. Lagadec, R. Zahn, and V. Wood, "Characterization and performance evaluation of lithium-ion battery separators." *Nat. Energy*, **4**, 16 (2019).

19. J. B. Habedank, J. Kriegler, and M. F. Zaeh, "Enhanced fast charging and reduced lithium-plating by laser-structured anodes for lithium-ion batteries." *J. Electrochem. Soc.*, **166**, A3940 (2019).

20. J. B. Habedank, F. J. Günter, N. Billot, R. Gilles, T. Neuwirth, G. Reinhart, and M. F. Zaeh, "Rapid electrolyte wetting of lithium-ion batteries containing laser structured electrodes: in situ visualization by neutron radiography." *The International Journal of Advanced Manufacturing Technology*, **102**, 2769 (2019).

21. S. V. Erhard et al., "Simulation and measurement of the current density distribution in lithium-ion batteries by a multi-tab cell approach." *J. Electrochem. Soc.*, **164**, A6324 (2017).

22. S. V. Erhard, "Multi-dimensional electrochemical-thermal modeling of lithium-ion batteries." *Ph.D.*, Technical University of Munich, Munich (04-20-2017), http://nbn-resolving.de/urn/resolver.pl?urn:nbn:de:bvb:91-diss-20170607-1338266-1-3.

23. T. Waldmann, G. Geramifard, and M. Wohlfahrt-Mehrens, "Influence of current collecting tab design on thermal and electrochemical performance of cylindrical Lithium-ion cells during high current discharge." *Journal of Energy Storage*, **5**, 163 (2016).

24. H.-K. Kim, J. H. Choi, and K.-J. Lee, "A numerical study of the effects of cell formats on the cycle life of lithium ion batteries." *J. Electrochem. Soc.*, **166**, A1769 (2019).

25. A. Rheinfeld, J. Sturm, A. Frank, S. Kosch, S. V. Erhard, and A. Jossen, "Impact of cell size and format on external short circuit behavior of lithium-ion cells at varying cooling conditions: modeling and simulation." *J. Electrochem. Soc.*, **167**, 013511 (2020).

26. A. Rheinfeld, "Performance and safety of lithium-ion electrodes and cells: modeling, simulation, and validation at elevated temperatures and currents." *Ph. D.*, Technical University of Munich, Munich (07-30-2019), http://nbn-resolving.de/urn/resolver.pl?urn:nbn:de:bvb:91-diss-20190920-1506354-1-9.

27. R. E. Ciez and J. F. Whitacre, "Comparison between cylindrical and prismatic lithium-ion cell costs using a process based cost model." *Journal of Power Sources*, **340**, 273 (2017).

28. S. De-Leon, LIB 18650 Cells New Replacement Cylindrical Cell Sizes (20650, 20700, 21700) Report - Shmuel De-Leon Energy Ltd (2016), https://sdle.co.il/wp-content/uploads/2018/12/15-LIB-18650-Cells-New-Replacement-Cylindrical-Cell-Sizes-20650-20700-21700-Report-ver-3-presentation-for-conferences.pdf.

29. J. B. Quinn, T. Waldmann, K. Richter, M. Kasper, and M. Wohlfahrt-Mehrens, "Energy density of cylindrical li-ion cells: a comparison of commercial 18650 to the 21700 cells." *J. Electrochem. Soc.*, **165**, A3284 (2018).

30. D. A. H. McCleary, J. P. Meyers, and B. Kim, "Three-dimensional modeling of electrochemical performance and heat generation of spirally and prismatically wound lithium-ion batteries." *J. Electrochem. Soc.*, **160**, A1931 (2013).

31. J. Sturm, A. Rheinfeld, I. Zilberman, F. B. Spingler, S. Kosch, F. Frie, and A. Jossen, "Modeling and simulation of inhomogeneities in a 18650 nickel-rich, silicon-graphite lithium-ion cell during fast charging." *Journal of Power Sources*, **412**, 204 (2019).

32. A. M. Colclasure et al., "Electrode scale and electrolyte transport effects on extreme fast charging of lithium-ion cells." *Electrochimica Acta*, **337**, 135854 (2020).

33. S. Ma, M. Jiang, P. Tao, C. Song, J. Wu, J. Wang, T. Deng, and W. Shang, "Temperature effect and thermal impact in lithium-ion batteries: a review." *Progress in Natural Science: Materials International*, **28**, 653 (2018).

34. J. Keil, N. Paul, V. Baran, P. Keil, R. Gilles, and A. Jossen, "Linear and nonlinear aging of lithium-ion cells investigated by electrochemical analysis and in-situ neutron diffraction." *J. Electrochem. Soc.*, **166**, A3908 (2019).

35. P. J. Osswald, S. V. Erhard, A. Noel, P. Keil, F. M. Kindermann, H. Hoster, and A. Jossen, "Current density distribution in cylindrical Li-Ion cells during impedance measurements." *Journal of Power Sources*, **314**, 93 (2016).

36. D. Petz, M. J. Mühlbauer, V. Baran, M. Frost, A. Schökel, C. Paulmann, Y. Chen, D. Garcés, and A. Senyshyn, "Lithium heterogeneities in cylinder-type Li-ion batteries–fatigue induced by cycling." *Journal of Power Sources*, **448**, 227466 (2020).

37. X. Du, Q. Wu, Y.-N. Wang, T.-S. Pan, Y.-M. Wei, H.-S. Chen, W.-L. Song, and D.-N. Fang, "Visualizing two-dimensional internal temperature distribution in cylindrical Li-ion cells." *Journal of Power Sources*, **446**, 227343 (2020).

38. S. V. Erhard, P. J. Osswald, J. Wilhelm, A. Rheinfeld, S. Kosch, and A. Jossen, "Simulation and measurement of local potentials of modified commercial cylindrical cells: II: multi-dimensional modeling and validation." *J. Electrochem. Soc.*, **162**, A2707 (2015).

39. G. Zhang, L. Cao, S. Ge, C.-Y. Wang, C. E. Shaffer, and C. D. Rahn, "In situ measurement of radial temperature distributions in cylindrical li-ion cells." *J. Electrochem. Soc.*, **161**, A1499 (2014).

40. C. Bolsinger and K. P. Birke, "Effect of different cooling configurations on thermal gradients inside cylindrical battery cells." *Journal of Energy Storage*, **21**, 222 (2019).

41. T. Amietszajew, E. McTurk, J. Fleming, and R. Bhagat, "Understanding the limits of rapid charging using instrumented commercial 18650 high-energy Li-ion cells." *Electrochimica Acta*, **263**, 346 (2018).

42. J. Fleming, T. Amietszajew, E. McTurk, D. Greenwood, and R. Bhagat, "Development and evaluation of in situ instrumentation for cylindrical Li-ion cells using fibre optic sensors." *HardwareX*, **3**, 100 (2018).

43. E. McTurk, T. Amietszajew, J. Fleming, and R. Bhagat, "Thermo-electrochemical instrumentation of cylindrical Li-ion cells." *Journal of Power Sources*, **379**, 309 (2018).

44. A. Senyshyn, M. J. Mühlbauer, O. Dolotko, M. Hofmann, and H. Ehrenberg, "Homogeneity of lithium distribution in cylinder-type Li-ion batteries." *Sci. Rep.*, **5**, 18380 (2015).

45. M. Doyle, T. F. Fuller, and J. Newman, "Modeling of galvanostatic charge and discharge of the lithium/polymer/insertion cell." *J. Electrochem. Soc.*, **140**, 1526 (1993).

46. B. Rieger, S. V. Erhard, S. Kosch, M. Venator, A. Rheinfeld, and A. Jossen, "Multi-dimensional modeling of the influence of cell design on temperature, displacement and stress inhomogeneity in large-format lithium-ion cells." *J. Electrochem. Soc.*, **163**, A3099 (2016).

47. S. Kosch, Y. Zhao, J. Sturm, J. Schuster, G. Mulder, E. Ayerbe, and A. Jossen, "A computationally efficient multi-scale model for lithium-ion cells." *J. Electrochem. Soc.*, **165**, A2374 (2018).

48. J. Sturm, S. Ludwig, J. Zwirner, C. Ramirez-Garcia, B. Heinrich, M. F. Horsche, and A. Jossen, "Suitability of physicochemical models for embedded systems regarding a nickel-rich, silicon-graphite lithium-ion battery." *Journal of Power Sources*, **436**, 226834 (2019).

49. J. N. Reimers, M. Shoesmith, Y. S. Lin, and L. O. Valoen, "Simulating high current discharges of power optimized li-ion cells." *J. Electrochem. Soc.*, **160**, A1870 (2013).

50. K.-J. Lee, K. Smith, A. Pesaran, and G.-H. Kim, "Three dimensional thermal-, electrical-, and electrochemical-coupled model for cylindrical wound large format lithium-ion batteries." *Journal of Power Sources*, **241**, 20 (2013).

51. S. Allu, S. Kalnaus, W. Elwasif, S. Simunovic, J. A. Turner, and S. Pannala, "A new open computational framework for highly-resolved coupled three-dimensional multiphysics simulations of Li-ion cells." *Journal of Power Sources*, **246**, 876 (2014).

52. N. Baba, H. Yoshida, M. Nagaoka, C. Okuda, and S. Kawauchi, "Numerical simulation of thermal behavior of lithium-ion secondary batteries using the enhanced single particle model." *Journal of Power Sources*, **252**, 214 (2014).

53. M. Guo and R. E. White, "Mathematical model for a spirally-wound lithium-ion cell." *Journal of Power Sources*, **250**, 220 (2014).

54. J. Li, Y. Cheng, M. Jia, Y. Tang, Y. Lin, Z. Zhang, and Y. Liu, "An electrochemical-thermal model based on dynamic responses for lithium iron phosphate battery." *Journal of Power Sources*, **255**, 130 (2014).

55. C. Hellwig, "Modeling, simulation and experimental investigation of the thermal and electrochemical behavior of a LiFePO4-based lithium-ion battery." *Phd.-Thesis*, University of Stuttgart1 (2013), http://nbn-resolving.de/urn:nbn:de:bsz:93-opus-86858.

56. C. Kupper and W. G. Bessler, "Multi-scale thermo-electrochemical modeling of performance and aging of a LiFePO 4/graphite lithium-ion cell." *J. Electrochem. Soc.*, **164**, A304 (2017).

57. C. Kupper, B. Weißhar, S. Rißmann, and W. G. Bessler, "End-of-life prediction of a lithium-ion battery cell based on mechanistic aging models of the graphite electrode." *J. Electrochem. Soc.*, **165**, A3468 (2018).

58. J. Kim, J. Oh, and H. Lee, "Review on battery thermal management system for electric vehicles." *Applied Thermal Engineering*, **149**, 192 (2019).

59. X.-G. Yang and C.-Y. Wang, "Understanding the trilemma of fast charging, energy density and cycle life of lithium-ion batteries." *Journal of Power Sources*, **402**, 489 (2018).

60. A. Tomaszewska et al., "Lithium-ion battery fast charging: a review." *eTransportation*, **1**, 100011 (2019).

61. A. Nyman, T. G. Zavalis, R. Elger, M. Behm, and G. Lindbergh, "Analysis of the polarization in a li-ion battery cell by numerical simulations." *J. Electrochem. Soc.*, **157**, A1236 (2010).

62. P. T. Tennessen, J. C. Weintraub, and A. H. Weston, United States Patent Application United States patent application US 2011/0212356 A1 (2011), https://patentimages.storage.googleapis.com/pdfs/6f48fe446c12a8e64871/US20110212356A1.pdf.

63. I. Cendoya, 2018 Selection of commercial cells to fit a multiple purpose modular battery pack concept: iModBatt (Grant Agreement No. 770054) (2018), https://cidetec.es/imodbatt/en/wp-content/uploads/2018/12/Selection-of-commercial-cells-06112018v1.pdf.

64. H. Popp, G. Glanz, R. Hamid, N. Zhang, M. A. Martinez, S. Ritz, and I. Cendoya, 2019 Benchmark, aging and ante-mortem of sota cylindrical lithium-ion cells - Eco-Mobility - 14th International A3PS Conference (2019), 10.13140/RG.2.2.10102.96322.

65. H. Popp, N. Zhang, M. Jahn, M. Arrinda, S. Ritz, M. Faber, D. U. Sauer, P. Azais, and I. Cendoya, "Ante-mortem analysis, electrical, thermal, and ageing testing of state-of-the-art cylindrical lithium-ion cells." *e & i Elektrotechnik und Informationstechnik*, **104**, 8 (2020).

66. M. Klett, J. A. Gilbert, K. Z. Pupek, S. E. Trask, and D. P. Abraham, "Layered oxide, graphite and silicon-graphite electrodes for lithium-ion cells: effect of electrolyte composition and cycling windows." *J. Electrochem. Soc.*, **164**, A6095 (2017).

67. M. Otero, C. Heim, E. P. M. Leiva, N. Wagner, and A. Friedrich, "Design-considerations regarding silicon/graphite and tin/graphite composite electrodes for lithium-ion batteries." *Sci. Rep.*, **8**, 15851 (2018).

68. B. Son, M.-H. Ryou, J. Choi, S.-H. Kim, J. M. Ko, and Y. M. Lee, "Effect of cathode/anode area ratio on electrochemical performance of lithium-ion batteries." *Journal of Power Sources*, **243**, 641 (2013).

69. R. Jung, M. Metzger, F. Maglia, C. Stinner, and H. A. Gasteiger, "Oxygen release and its effect on the cycling stability of LiNixMnyCozO2 (NMC) cathode materials for li-ion batteries." *J. Electrochem. Soc.*, **164**, A1361 (2017).

70. H.-J. Noh, S. Youn, C. S. Yoon, and Y.-K. Sun, "Comparison of the structural and electrochemical properties of layered Li(Ni_xCo_yMn_z)O2 (x = 1/3, 0.5, 0.6, 0.7, 0.8 and 0.85) cathode material for lithium-ion batteries." *Journal of Power Sources*, **233**, 121 (2013).

71. M. Doyle and Y. Fuentes, "Computer simulations of a lithium-ion polymer battery and implications for higher capacity next-generation battery designs." *J. Electrochem. Soc.*, **150**, A706 (2003).

72. D. Andre, S.-J. Kim, P. Lamp, S. F. Lux, F. Maglia, O. Paschos, and B. Stiaszny, "Future generations of cathode materials: an automotive industry perspective." *J. Mater. Chem. A*, **3**, 6709 (2015).

73. D. Bernardi, "A general energy balance for battery systems." *J. Electrochem. Soc.*, **132**, 5 (1985).

74. C. M. Long, M. A. Nascarella, and P. A. Valberg, "Carbon black vs black carbon and other airborne materials containing elemental carbon: Physical and chemical distinctions." *Environmental pollution (Barking, Essex : 1987)*, **181**, 271 (2013).

75. G. Liu, H. Zheng, A. S. Simens, A. M. Minor, X. Song, and V. S. Battaglia, "Optimization of acetylene black conductive additive and PVDF composition for high-power rechargeable lithium-ion cells." *J. Electrochem. Soc.*, **154**, A1129 (2007).

76. D. A. G. Bruggeman, "Calculation of different physical constants in heterogenous substances." *Ann. Phys.*, **416**, 636 (1935).

77. J. Landesfeind, J. Hattendorff, A. Ehrl, W. A. Wall, and H. A. Gasteiger, "Tortuosity determination of battery electrodes and separators by impedance spectroscopy." *J. Electrochem. Soc.*, **163**, A1373 (2016).

78. S. Arrhenius, "About the inversion rate of Sucrose caused by acids." *Zeitschrift für Physikalische Chemie*, **4**U(1), 226-248 (1889).

79. S. C. Chen, C. C. Wan, and Y. Y. Wang, "Thermal analysis of lithium-ion batteries." *Journal of Power Sources*, **140**, 111 (2005).

80. J. Christensen, V. Srinivasan, and J. Newman, "Optimization of lithium titanate electrodes for high-power cells." *J. Electrochem. Soc.*, **153**, A560 (2006).

81. R. Dash and S. Pannala, "Theoretical limits of energy density in silicon-carbon composite anode based lithium ion batteries: supplementary information." *Sci. Rep.*, **6**, 27449 (2016).

82. H. Sun and K. Zhao, "Electronic structure and comparative properties of LiNi x Mn y Co z O 2 cathode materials." *The Journal of Physical Chemistry C*, **121**, 6002 (2017).

83. F. A. Wolff and J. H. Dellinger, "The electrical conductivity of commercial copper." *Proceeding of the American Institute of Electrial Engineers* **29**, 1981 (1910).

84. D. G. Giancoli, *Physics: Principles with Application* (Prentice Hall College Div, Englewood Cliffs, New Jersey, USA) 4th ed. (1995).

85. J. Mao, W. Tiedemann, and J. Newman, "Simulation of temperature rise in Li-ion cells at very high currents." *Journal of Power Sources*, **271**, 444 (2014).

86. K. Kanari, K. Takano, and Y. Saito, "Thermal behavior and simulation of a lithium secondary battery." *Denshi Gijutsu Sogo Kenkyusho Iho/Bulletin of the Electrochenical Laboratory*, **60**, 65 (1996).

87. O. V. Valoen and J. N. Reimers, "Transport properties of lipf6-based li-ion battery electrolytes." *J. Electrochem. Soc.*, **152**, A882 (2005).

3 Model Reduction and Embedded Implementation of Physicochemical Models
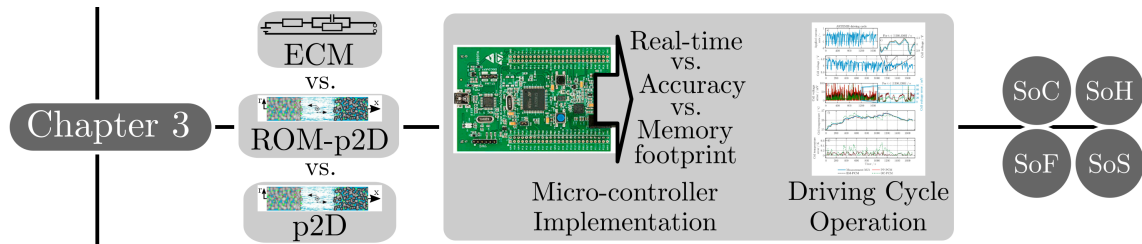
Figure 3.1: Outline of chapter 3.

Within this section, the article titled *Suitability of physicochemical models for embedded systems regarding a nickel-rich, silicon-graphite lithium-ion battery* is presented. Fig. 3.1 refers to the thesis outline shown in section 1.6 and summarizes the content of the presented article in this section.

3.1 Challenges of Embedded Implementation

After presenting the parametrization, validation and the spatial imbalance caused limitations of the p2D, the question if and under which restrictions such a model can be used in embedded systems is discussed in this section. Typically the efficiency of model reduction and its gained computation speed-up is discussed with implementations in sophisticated mathematical software tools such as MATLAB [200], Mathematica [201] or Maple [202] and even more computational complex framework tools such as ANSYS [203] or COMSOL Multiphysics [204]. The tools typically run on a desktop computer, which is oversized in terms of calculation and memory resources compared to hardware near systems like a MC. To evaluate model reduction schemes, a suitable mathematical and computational environment must be chosen to emulate embedded software and hardware resources as used for BMS application. Therefore, the implementation in embedded software codes such as C and the usage of lean computational resources as found in MCs is recommended to derive a reliable conclusion of the suitability of physicochemical models in embedded systems, which is sparsely discussed in literature [124]. The implementation in embedded systems is more challenging as no operating system, no mathematical framework tool with standardized functionality such as interpolation schemes, solver routines or matrix inversion operation are available and must be defined prior to the actual implementation of the model structure. Using a MC comes with limitations such as memory size to store and solve the model, which remain unseen if powerful desktop computers are used.

In the following article, a MC programmed with C-code versions of three differently reduced or reformulated p2Ds is presented enabling a valuable assessment of the real-time computation. The three presented ROM-p2Ds incorporate either FDM together with a polynomial approximation [136] or an eigenfunction method [137] for the solid diffusion equation, or a complete reformulation using an

orthogonal collocation scheme [98, 138, 139] for the entire differential algebraic equation system.

3.2 Computational Simplification and Micro-Controller Application for Physicochemical Models

The three *C*-code p2Ds are first evaluated on a desktop computer using MATLAB [200] to determine possible *C*-code implementation errors. The MC offers computational resources of 168 MHz, 192 kB of random access memory (RAM) and 1 MB of flash memory. Computation efficiency and model accuracy are additionally referenced to a numerically rigorous p2D implemented in COMSOL Multiphysics [204] and calculated on the same desktop computer. To have a benchmark to state-of-the-art models used in the BMS, an ECM is used and solved on the desktop computer. Each of the presented models is parametrized for the MJ1 LIB. The performance on the MC is evaluated for various charge and discharge operations including a driving cycle. The impact of processor frequency and hardware acceleration schemes on the computation performance are elaborated. The model performance is evaluated towards real-time computation, accuracy of the simulation results in reference to measurement data of the MJ1 LIB and the required memory footprint for the entire implementation of the model structure, including the parametrization data. As a result, ROM-p2Ds are able to calculate at least 37 % faster than real-time at a mean cell voltage error below 20 mV and require at most 213 kB of memory of the MC. The accuracy of the *C*-code ROM-p2D is in the same range as the faster calculating ECM.

The implementation of physicochemical models is a challenging task, but suitable model reduction can ease the computational complexity and increase the computation speed. Implementing such ROM-p2Ds in embedded systems reveals additional issues, such as memory limitations or the lack of basic mathematical functionality, but enable for a valuable assessment of physicochemical model based state-simulation in hardware near embedded systems without the influences of a computational oversized hard- and software.

Author and coworker contribution   Johannes Sturm initiated and developed the idea to implement different ROM-p2Ds in a MC and to investigate the real-time computation of physicochemical models in hardware near environments. Sebastian Ludwig enabled the implementation of the model codes into the MC and supervised together with Johannes Sturm the transfer of the model structure into a *C*-code, which was elaborated by Benedikt Heinrich and Conrado Ramirez-Garcia. Julius Zwirner and Hassen Ennifar developed the fundamental model structures in MATLAB codes prior to this article. Sebastian Ludwig and Max F. Horsche provided a well parametrized ECM for the MJ1 LIB as a reference for the computation speed of the p2Ds. The experimental and simulation based results were analyzed and interpreted by Johannes Sturm. The manuscript was written by Johannes Sturm and edited by Sebastian Ludwig, Julius Zwirner, Conrado Ramirez-Garcia, Benedikt Heinrich, Max F. Horsche and Andreas Jossen. All authors discussed the data and commented on the results.

Publication notes   The article titled *Suitability of physicochemical models for embedded systems regarding a nickel-rich, silicon-graphite lithium-ion battery* is presented in the following and the related supplementary material is shown in the appendix (see section C). The article [95] and the supplementary material [205] are published in the Journal of Power Sources. Parts of the results were presented at the *16th Symposium on Modeling and Validation of Electrochemical Energy Devices* in Brunswick

(Germany) in March 2019. A data repository with the most important experimental and simulation based results is published at the platform 4TU.Centre for Research Data (Netherlands) [206].

Suitability of physicochemical models for embedded systems regarding a nickel-rich, silicon-graphite lithium-ion battery

Johannes Sturm, Sebastian Ludwig, Julius Zwirner, Conrado Ramirez-Garcia, Benedikt Heinrich, Max Ferdinand Horsche, Andreas Jossen

Suitability of physicochemical models for embedded systems regarding a nickel-rich, silicon-graphite lithium-ion battery

J. Sturm [*], S. Ludwig, J. Zwirner, C. Ramirez-Garcia, B. Heinrich, M.F. Horsche, A. Jossen

Technical University of Munich (TUM), Institute for Electrical Energy Storage Technology (EES), Arcisstrasse 21, 80333, Munich, Germany

HIGHLIGHTS

- Collocation-reformulation compared to FDM with solid-approximation for the p2D model.
- Maximum of 115 kB to solve and 213 kB to store the p2D models on a microcontroller.
- P2D and ECM experimentally validated for CC CH/DCH and drive cycle of NMC-811/SiC LIB.
- Microcontroller-p2D offers 37% speed-up at 20 mV mean voltage error for drive cycle.
- FDM paired with eigenfunction approximation as best option for p2D in embedded system.

GRAPHICAL ABSTRACT
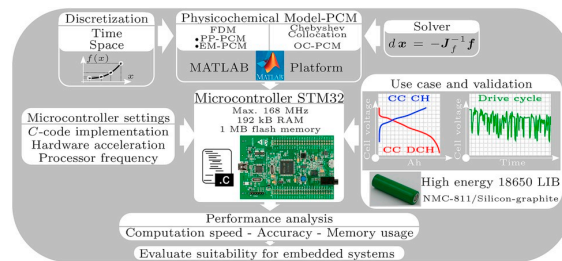
ARTICLE INFO

ABSTRACT

Local inhomogeneous electrode utilization in recent lithium-ion batteries tends to increase due to larger sizes and/or higher densification, which poses a challenge for accurate, model-based monitoring. Pseudo-two dimensional (p2D) physicochemical models (PCM) can offer such locality via calculating local potentials and concentrations through the thickness of the electrode stack and are numerically reduced for implementation in a microcontroller in this work. Finite difference method combined with solid-diffusion approximations and orthogonal collocation reformulation are applied to generate three MATLAB- and three microcontroller-suitable *C*-code p2D-PCMs, which are experimentally validated towards constant current charge/discharge and driving cycle loads on a high-energy NMC-811/SiC-18650 lithium-ion battery. Benchmarking to an equivalent circuit model reveals similar mean cell voltage errors below 20 mV for the driving cycle. Reducing spatial elements reveals errors below 1% for local (*i.e.* concentrations/potentials) and global states (*i.e.* cell voltage/temperature) and is applied to speed-up the *C*-code p2D-PCMs in the microcontroller (max. 168 MHz with 192 kB RAM) to calculate at least 37% faster than real-time. Real-time computability is investigated via varying processor frequencies and using hardware acceleration schemes. The memory allocation to solve and store the p2D-PCMs on the microcontroller require 115 kB and 213 kB at a maximum, respectively.

* Corresponding author.
  E-mail address: johannes.sturm@tum.de (J. Sturm).

1. Introduction

Recent achievements in higher energy density of lithium-ion batteries (LIBs) promote inhomogeneous usage [1] either along the electrodes or through the thickness of the cell stack [2]. Therefore, monitoring and controlling of the battery's states on local scale are necessary to guarantee efficient utilization and safety during both dynamic (*i.e.* driving cycle) or rather static loads (*i.e.* fast charging).

Beside larger electrodes, thicker composite coatings, higher densification (*i.e.* porosity <20%) and high capacitive active materials such as nickel-rich cathodes (*e.g.* NMC-811) and graphite-silicon composite anodes (SiC) are applied to increase the energy density. The resulting increase of capacity can lead to local current densities along the electrodes exemplarily up to 4.91 mA cm^{-2} at 1C for a 3.35 Ah 18560 LIB (INR18650-MJ1, LGChem) incorporating low electrode porosities of 21.6% and 17.1% for the SiC anode and NMC-811 cathode [2]. As a result, inhomogeneous utilization through the cell stack and along the electrodes appears [1].

Beside the global states such as cell voltage, applied current and surface temperature, proper LIB monitoring should estimate also the local states such as potentials and concentrations in the electrolyte and the active material to ease harmful side-reactions such as lithium plating [3,4] or solid-electrolyte-interphase (SEI) growth and cracking [5] or to avoid critical hot spots [1]. State-of-the-art model-based monitoring incorporate equivalent circuit models (ECMs) as it offers fast calculation and easy parameterization. However, only global states can be simulated. Physicochemical models (PCMs) such as the pseudo-two dimensional (p2D) model [6] offer simulated local states based on porous electrode, concentrated solution theory and electrode kinetics through the thickness of the cell stack. However, this model comes with computational complexity due to solving its differential algebraic equation (DAE) system, which significantly slows down the calculation. Together with the complex parameterization, application in battery management system (BMS) outside the research field is hindered.

In this matter, we want to investigate the suitability of the p2D model in embedded systems (*i.e.* microcontroller) via evaluating the computational performance and simulation accuracy of p2D-PCMs using different spatial and time discretizations, approximation schemes for the particle domain and solvers. Three different p2D-PCMs are parameterized for a 18650 NMC-811/SiC LIB (INR18650-MJ1 [2]) and implemented first in MATLAB® and second transferred into a stand-alone *C*-code for microcontroller implementation. Errors of parameterization, model reduction, transfer into the microcontroller and validation via measurements are outlined for constant current (CC) charge and discharge and a driving cycle scenario to evaluate the suitability of the p2D-PCMs for real-time simulation in embedded systems.

2. Model reduction of the p2D physicochemical model

To ease the computational inefficiency, model reduction can be applied to the p2D-PCM [6], which is summarized in fundamental reviews [7,8]. In this work, its actual implementation in the STM32F407VGT6 microcontroller (STM32, STMicroelectronics [9]) is evaluated towards computation speed and simulation accuracy, coming with crucial limitations in computation power (max. 168 MHz in a 32-bit ARM® Cortex®-M4 core) and memory ressources offering only a maximum of 1024 kB flash memory to store and a maximum of 192 kB static random accessible memory (RAM) to solve the model. These limitations are often not considered in research as reductions are investigated on desktop computers.

In this matter, low spatial discretizations with sufficient accuracy are favored as the total number of spatial elements defines the size of the DAE, the related memory requirements and thus the computational effort. Spatial discretization of the particle domain (*i.e.* 'pseudo'-domain, *r*-coordinate) can cause a large DAE system via discretizing the solid-diffusion partial differential equation (PDE). At every node in the

electrolyte domain (*x*-coordinate), this PDE is solved for the concentration c_s of lithium-ions, which tremendously raises the allocated memory. As only the particle-surface concentration $c_{s,s}$ is needed for the kinetics, its numerical reduction is feasible. Approximation methods for the concentration profile in the particle were implemented in literature via volume averaging together with a parabolic profile (PP) [10–21] or diffusion length approaches [22–24], which suggests linearity between surface- and average-concentration $c_{s,ave}$. Sufficient accuracy and computation efficiency appeared via using an eigenfunction method (EM) [25–28], where the solution is derived from a truncated, analytical solution of an infinite series of eigenfunctions. Maintaining a spatial discretization of the PDE, reformulations to an ordinary differential equation (ODE) in time via spectral methods (*e.g.* orthogonal collocation (OC)) [29–35] showed an enormous calculation acceleration while guaranteeing sufficient accuracy. Also standard discretization schemes such as finite volume methods (FVM) (*e.g* finite difference method (FDM) or finite element method (FEM)) [30,36–38] were investigated next to integral methods such as the duhamel superposition integral (DSI) [6,39–42]. Reducing the entire solid phase to a single particle (SPM, [16,43–45]) revealed promising computational efficiency, but is not regarded in the following as the original p2D-PCM [6] is focussed in this work.

Referring to real-time computability and sufficient simulation accuracy as seen in our previous work [46], we focus on a FDM discretization for the electrolyte domain accompanied with two different approximation schemes (*i.e.* PP- [11] and EM [25]) for the particle domain. For comparison, the third p2D-PCM uses orthogonal collocation and thus maintains a spatial discretization of the particle domain.

As the PP- [47] and EM-approximation are adopted from the corresponding original work, which have already shown its validity, accuracy and computational efficiency, the reader is referred to these works [13–15,17,26,27,48] for more information. The OC-method was used as well in literature before [31,49] and a single work [34] investigated the performance on a microcontroller (ATMEL 32UC3A1512 at 16 MHz and 512 kB RAM [34]) including 21 DAE which could be solved in at least 190 ms under 1C CC discharge. Unfortunately, no description of the actual implementation on this microcontroller is shown [34] and the work misses implementation recommendations, detailed computational performance analysis and application-near load scenarios.

According to literature, the PP-, EM- and OC-PCM offer significant computation speed, reduction of DAE size and maintain sufficient accuracy to be implemented in the STM32 [9] used in this work. Far to little work [34] had focussed on an actual microcontroller implementation of the p2D-PCM in the past, which is one of the main objectives of this work together with evaluating the most suitable discretization/approximation scheme to gain real-time computation and low simulation error in embedded systems.

Table 1
Model overview.

Model	Spatial discretization		Framework	Thermal **model**
	x-domain	r-domain		
PP-PCM	FDM	Parabolic [I]	MATLAB [III] & *C*-code [IV]	√
EM-PCM	FDM	Eigenfunction [II]		√
OC-PCM	Orthogonal collocation			√
COMSOL-PCM	FDM		COMSOL [V]	√
ECM	n.a.		MATLAB/Simulink [III]	√

[I] Ref. [11]. [II] Ref. [25]. [III] Ref. [50]. [IV] for STM32 microcontroller. [V] Ref. [51].

3. Modeling of a 18650 NMC-811/SiC lithium-ion battery

As shown in Table 1, three different p2D-PCMs are investigated incorporating different spatial discretizations/approximations and two benchmark models (COMSOL-PCM and ECM) are used to simulate a 18650 NMC-811/SiC LIB [2].

The three p2D-PCMs are used as stand-alone MATLAB®- and *C*-code to simulate on a desktop computer and the STM32 microcontroller, respectively. The MATLAB®-codes are used for model parameterization and validation, determining the simulation error via reducing spatial discretization and evaluate the implementation error for the *C*-code equivalents in the microcontroller. As benchmarks, the COMSOL-PCM uses COMSOL Multiphysics® and the ECM is implemented in MAT-LAB/Simulink to simulate on a desktop computer. The PP- and EM-PCM revealed different suitability in terms of constant and dynamic loads [46] and are chosen in this work for evaluating a standard, equidistant spatial FDM discretization paired with different solid-approximations on a microcontroller instead of hardware and software oversized desktop PCs, which are not suitable to evaluate embedded system applicability. The OC-PCM uses no solid-approximation and no standard FDM-dicsretization, but a reformulation of the p2D-PCM equations to exclusively ODEs in time via Chebyshev orthogonal collocation, which revealed distinct speed-up on desktop PCs compared to models like the PP- and EM-PCM. However, this reformulation must be evaluated in a microcontroller to evaluate its suitability for embedded systems, which is investigated here.

The DAE system of the p2D-PCM is shown in Table A.14 and the parameterization [2] is shown in Table A.12 and A.13.

3.1. Equivalent circuit model

The ECM consists of a single capacitor/resistor network R_1 and C_1 ('RC'), an ohmic resistance R_i and an open-circuit voltage V_{OCV}. As the temperature has significant influence on the cell behavior [52], the parameterization tests of the ECM were proceeded at 25 and 40 °C beside the state of charge (SoC) dependency. This first-order model [26] offers the best compromise of accuracy and complexity [53] incorporating the fundamental equations as

$$I_{cell} = C_1 \cdot \frac{d V_1}{d t} + \frac{V_1}{R_1}$$

$$V_{cell} = V_{OCV} + V_1 + I_{cell} \cdot R_i$$

$$m\, c_p \frac{d T_{cell}}{d t} = \left(V_{OCV} - V_{cell} - \frac{d V_{OCV}}{d T} \cdot T \right) \cdot I_{cell} - I_{cell}^2 R_i - \alpha_\infty A_{surf} (T_{cell} - T_\infty)$$

with $I_{cell} > 0$ for charge and $I_{cell} < 0$ for discharge.

The resistance R_i represents the ohmic resistance on the current collector foils, the RC network accounts for any transient dynamics referring to electrochemical processes [54] and the voltage source V_{OCV} represents the equilibrium state. To parameterize the ECM variables (*i.e.* V_{OCV}, R_i, R_1, C_1, $\frac{d V_{OCV}}{d T}$), three different INR18650-MJ1 cells were tested and the generated data was averaged and interpolated in 1% SoC steps. The tests included CC, constant voltage (CV), pulse current (PC) and electrochemical impedance spectroscopy (EIS) periods as summarized in Table 2.

In terms of V_{OCV}, the charge and discharge measurement were averaged to compensate cell polarization effects. The entropic coefficient $\frac{d V_{OCV}}{d T}$ was derived from accelerated rate calorimetry (ARC) [2] and validated via the potentiometric method according to Zilberman et al. [55]. The passive components R_i, R_1 and C_1 were parameterized by pulse fitting as depicted in Table 2. 88 pulses for each temperature were used and a graphical illustration of the ECM and its parameters is shown in our supplementary part. The input variable is the applied current I_{cell} from which the SoC variable is integrated over time. The ECM is

Table 2
Measurements for parameterizing the ECM.

Parameter	Measurement	Voltage	Current	Temperature
V_{OCV}	CC charge/discharge	2.5–4.2 V	0.033C	25°C
	CV	2.5/4.2 V	+0.01C/-0.01C [I]	
$\frac{d V_{OCV}}{d T}$	CC charge/discharge	2.5–4.2 V	0.2C	ARC[Ref. [55]]
	Potentiometric method according to Zilberman et al. [55]			
R_1, C_1	PC	2.5–4.2 V	±0.5/1C for 10/20s [II]	25°C / 40°C
R_i	PC/EIS [III]	2.5–4.2 V	±0.5/1C for 10/20s [II]	25°C / 40°C

[I] Measurement equipment (BaSyTec CTS) defines charge > 0 and discharge < 0.
[II] 1 h rest before PC, applied in 10% SoC steps from 2.5 to 4.2 V and vice versa. [III] EIS at 0.042C before PC and zero-crossing at Re{Z} = 0 as initial point for the fitting algorithm of.R_i

implemented in MATLAB®/Simulink and solved via the *ode14x* [56] solver at a step-size of 1s.

The solving process and the necessary parameterization files are expected neither to overload the RAM and flash memory nor to exceed the computation power of the STM32 and other works [57–59] have already shown the actual implementation in microcontrollers. As this work focusses on the implementation and solving of the p2D-PCM, the ECM is not transferred into the microcontroller but used as a benchmark for state-of-the-art model-based monitoring of LIBs in real-time operating systems and is referenced for computation speed and simulation accuracy of the MATLAB®-code PCMs.

3.2. PP- and EM-PCM using FDM and solid-diffusion approximation

The PP- and EM-PCM were already presented in our previous work [46] in terms of steady-state representation together with a non-linear Kalman Filter [60–62] for state estimation of a $LiCoO_2/LiC_6$ LIB. In this work, the MATLAB®-code PP- and EM-PCM are parameterized for a NMC-811/SiC LIB and transferred into stand-alone *C*-codes for the microcontroller.

Fig. 1 shows the flow chart of the PP- and EM-PCM, which differ in the approximation of the solid-diffusion PDE ('Mass Balance (solid)').

The MATLAB® codes start with the parameterization (see Table A.12 and A.13) and calculate the initial states by assuming an equilibrium state [42]. In the main part, a new time period $\triangle t$ is added until a stop condition as t_{max}, V_{min} or V_{max} is met. The initial state vector for the iterative time step k is set to the previous, consistent solution $k - 1$ and the model is run to compute a new consistent solution of the state variables x_k. The iterative approximation i of the model equations refers to every node j in the electrolyte domain and calculates the model equations g (see Table A.14) and the corresponding jacobian J [46]. The Crank-Nicolson method [40] is used for first order time derivatives [46] and the time step is set to 1 s. Next, the matrix inversion [63] (A/b, MATLAB®) is used to generate the state update dx. Note, that the temperature is calculated afterwards [46] according to heat generation q and heat loss to the ambience q_∞. The heat calculation proposed from COMSOL Multiphysics® and other works [49] revealed similar results with small deviations up to 0.2/0.7% on average for 1C CC charge/discharge as the computational less expensive calculation [52,64,65] used in this work (see Table A.14).

To conclude, the PP- and EM-PCM use FDM together with solid-diffusion approximation and in this work we want to evaluate, if such standard techniques are sufficient to gain real-time computability of the p2D-PCM in the STM32 microcontroller.

3.3. OC-PCM using orthogonal collocation on Chebyshev nodes

The OC-PCM uses a spectral method to reformulate the spatial dis-
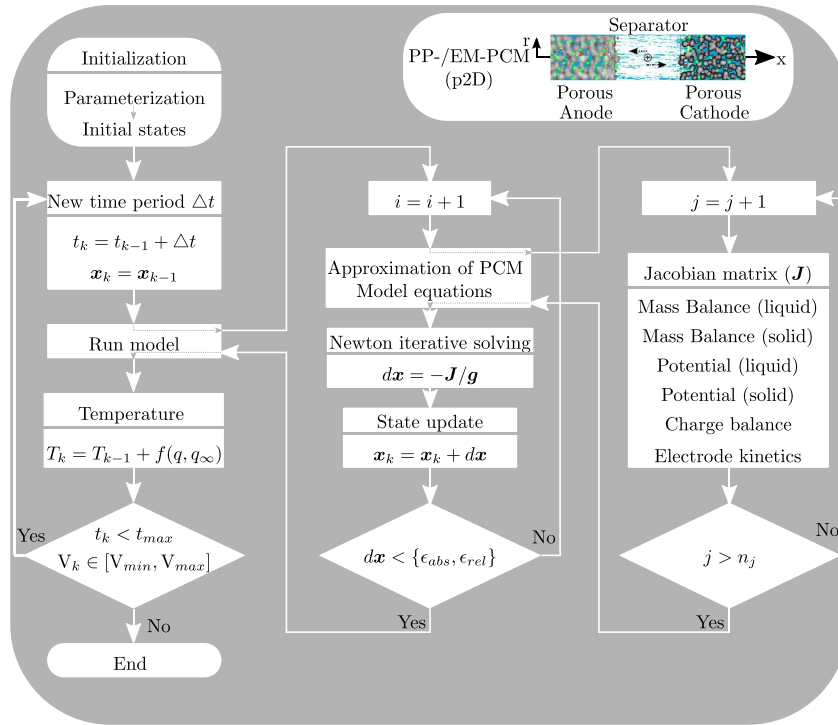
Fig. 1. Simplified flow chart of the stand-alone-codes of PP- and EM-PCM implemented in MATLAB®2017b. The approximation of the solid-diffusion PDE ('Mass balance (solid)') is either implemented via the polynomial profile (PP) [11] or an eigenfunction method (EM) [25] for the PP- and EM-PCM, respectively.
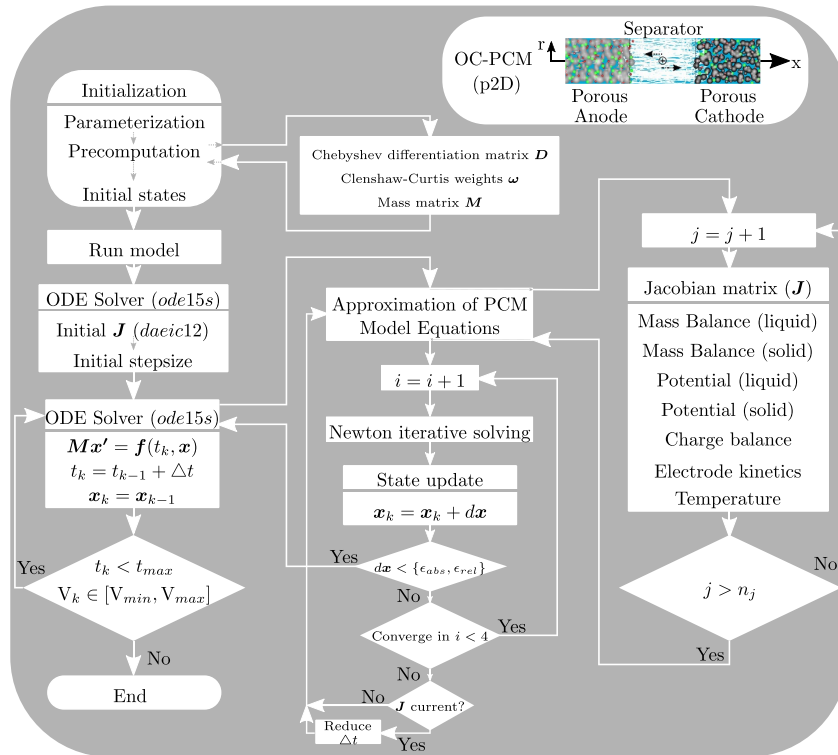
Fig. 2. Simplified flow chart of the stand-alone-code of the OC-PCM implemented in MATLAB®2017b. The spatial discretization is reformulated using Chebyshev orthogonal collocation [49] and the resulting DAE system is solved using an ODE solver (*ode15s* [66–68]) of MATLAB®.

cretization on Chebyshev collocation nodes [49] of the DAEs in both the x and r domain. The resulting ODEs in time and algebraic equations (AEs) form a DAE system as

$$M x' = f(t_k, x)$$

which is solved via the *ode15s* [66–68] solver of MATLAB$^{®}$. In terms of the reformulation, an unknown continuous function is approximated by a polynomial, which is determined by its values at the so called Chebyshev nodes (*i.e.* $x_j = cos\left(\frac{\pi j}{n_j}\right)$) for a given number of nodes j after rescaling each domain into $[-1,1]$ [49]. In contrast to other work [49], the electrolyte potential Φ_l accounts for activity formulation $f_{\pm}$ [6] as

$$\frac{\partial \Phi_l(x,t)}{\partial x} = -\frac{i_l(x,t)}{\kappa_l^{eff}} + \frac{2RT}{F}\left(1-t_+^0\right)\cdot\left[1+\frac{d\,ln\,f_{\pm}}{d\,ln\,c_l(x,t)}\right]\cdot\frac{\partial\,ln\,c_l(x,t)}{\partial x}$$

and the temperature calculation is identical to the PP- and EM-PCM [52, 64,65]. Fig. 2 shows the flow chart of the OC-PCM.

It starts with the calculation of the required Chebyshev differentiation matrix D, which is calculated once together with the mass matrix M and the Clenshaw quadrature weights ω to evaluate the sum of finite integrals to determine the jacobian matrix J. Next, the initialization of the ODE solver (*ode15s* [66–68]) is defined via calculating an initial jacobian (*daeic12* [69]) and a first time step is estimated. The following Newton iterative solving uses the same thresholds for the tolerances ε_{abs} and ε_{rel} within the cell voltage range and the time span as given for the PP- and EM-PCM. If four iterations offer no convergence, the solver updates the jacobian and respectively the iteration matrix M_i and the process starts again. If the jacobian is current and no convergence is expected, the step-size is decreased [66]. The solver itself uses a linearly implicit, one-step method based on numerical differentiation formulas (NDFs) implemented in backward differences [66,67,70], which uses an iteration matrix M_i as

$$M_i = M - \frac{\triangle t}{(1-k)\gamma_k}\cdot J$$

to generate the state update dx. The term γ_k represents the coefficients of the NDFs [66], k the order of the NDF and κ is a scalar factor [70]. At this point, the reader is referred to the original work [66,67] for more information about the solver itself and the iterative state update is outlined in more detail in our supplementary part.

Note, the jacobian is calculated analytically at every spatial node j for every derivative $\frac{\partial f}{\partial y}$ and passed directly to the solver instead of using the incorporated *ode15s* FDM. Thus, a discretization of 10–10-10-30 (*i.e.* 'anode-separator-cathode-particle' domain) reveals approximately a 20 times faster calculation as seen in this work. Further improvement was achieved by using sparse structure (*sparse* [69]) of the jacobian and the mass matrix. Even if the used spectral method leads to full differentiation matrices while the jacobian for the DAE system is still sparse ($\approx$4% are non-zero), using sparse linear algebra reduces the computational cost by a factor of 4 (referring to 10-10-10-30), which tends to increase for finer discretizations.

In sum, the OC-PCM uses reformulation, which shows significant computational acceleration of the solving process on a desktop computer. In this work we evaluate the transfer of the OC-PCM into a standalone *C*-code including the ODE solver and the real-time ability of simulating a LIB on a microcontroller.

3.4. Rigorous COMSOL-PCM

As a benchmark, the *liion*-model [51] of COMSOL Multiphysics$^{®}$ is used and run via the LiveLink [44] application using MATLAB$^{®}$2017b. The approximation functions are set to linear and a total 53, 8 and 40 of spatial nodes in the anode, separator and cathode domain are used with 20 nodes in the particle domain. The temperature is calculated with a single ODE (see Table A.14). The DAE system is solved with the 'Multifrontal massively parallel sparse direct solver' (MUMPS) [71] at a fixed step-size of 1 s.

3.5. Spatial configuration and DAE size of the PCMs

The spatial discretization for the PP- and EM-PCM is denoted as n_{neg} - n_{sep} - n_{pos}, which corresponds to the respective number of nodes in the anode, separator and cathode domain. The total number of DAEs calculates as

$$n_{DAEs} = \left(n_{neg} + n_{pos} + 2\right)\cdot 6 + \left(n_{sep} - 1\right)\cdot 3$$

referring to the boundary interfaces ('$+ 2$') and electrode domains ('$n_{neg} + n_{pos}$') with six (c_l, c_s, i_l, j_n, Φ_l, Φ_s) and three DAEs (c_l, i_l, Φ_l) at the internal nodes of the separator ('$n_{sep} - 1$'), respectively. In terms of the OC-PCM, the spatially discretized particle domain ('n_P') must be included as well as the calculation of the temperature ('$+ 1$'):

$$n_{DAEs} = \left(n_{neg} + n_{sep} + n_{pos} - 2\right)\cdot 2 + \left(n_P + 3\right)\cdot\left(n_{neg} + n_{pos}\right) + 1$$

Again, the term '$- 2$' is referring to the boundary interfaces of the electrodes and the separator, which are implemented in a common node for the definition of c_l and i_l. The term '$n_P + 3$' refers to the solid-concentration c_s and the molar flux j_n/ionic current density i_l as well as the solid-potential Φ_s.

Table 3 summarizes the spatial discretizations used in this work for the p2D-PCMs with the corresponding number of DAEs.

4. Microcontroller implementation

Primarily the small-sized RAM of microcontrollers and low processor frequencies imply challenges for solving the p2D-PCM, which poses no challenge for a standard desktop computer equipped exemplarily with 16 GB RAM at 3.2 GHz as used in this work for the MATLAB$^{®}$-code PCMs. 192 kB of RAM and a maximum of 168 MHz are offered by the chosen microcontroller to solve the *C*-code p2D-PCMs in this work.

Beside working without an operating system and with hardware modules like universal asynchronous reciever transmitter (UART) for data transmission, the transfer from the scripting language MATLAB$^{®}$ to the programming language *C* is a significant step as some framework related options such as matrix inversion (*A/b* [63]), linear algebra operations (*sparse* [69]) or solvers (*ode15s* [66–68]) are not available and must be transferred without overloading the memory. Note, that most of these specific functions cannot be exported via the *MATLAB$^{®}$ to C* export option [72] and even if, they would not be necessarily runnable on a microcontroller.

Table 3
Spatial discretizations of the PCMs.

Model	Indices	Number of spatial nodes				Number of DAEs
		Anode	Separator	Cathode	Particle	
PP-PCM	1-1-1	1	1	1	PP^{I}	24
	2-1-2	2	1	2		36
	5-3-5	5	3	5		78
	10-5-10	10	5	10		144
EM-PCM	1-1-1	1	1	1	EM^{II}	24
	2-1-2	2	1	2		36
	5-3-5	5	3	5		78
	10-5-10	10	5	10		144
OC-PCM	5-3-5-2	5	3	5	2	73
	5-3-5-3	5	3	5	3	83
	5-3-5-5	5	3	5	5	103
	20-10-20-25	20	10	20	25	1217
COMSOL-PCM	53-8-40-20	53	8	40	20	2338^{III}

^{I} Ref. [11]. ^{II} Ref. [25]. ^{III} referring to linear element order.

Basically, the hardware abstraction layer (HAL) library (Cortex Microcontroller Software Interface Standard (CMSIS), ARM [73]) and the STM32 CubeMX software [74] were used to configure the system clock, peripherals and an initial code structure. The flow chart of both stand-alone *C*-codes (PP-/EM-PCM and OC-PCM) are shown in Fig. 3.

Via running the *C*-code PCMs on the STM32 and sending the simulation results (UART-to-USB converter) to a desktop computer, computation efficiency and simulation accuracy can be analyzed and compared to the corresponding MATLAB®-code PCMs. The analysis using the MATLAB®-code PCMs on a desktop computer is not useful to evaluate the performance in low-hardware/software environment, as multi-threading calculation, oversized memory capacities, the comprehensive operating system and the framework MATLAB® itself would distort the results.

4.1. PP- and EM-PCM stand-alone C-code

After power up (see Fig. 3, left), global variables with fixed memory allocation are set, which are accessible in any case whilst the remaining variables are allocated and freed with every function call. Next, the processor calls the main function to configure the system clock, initialize the peripherals, load the parameterization including analytical functions, look-up tables and single parameters, set the stop conditions and call the initialization. Via UART the messages to be transmitted are initialized and the initial states are sent to the desktop computer using the UART-to-USB converter. The main loop is entered next and the time simulation is started. It ends as soon as a stop condition is met (see Fig. 1). Note, that only the current state k and the previous state $k-1$ are stored on the STM32 - otherwise the microcontroller's memory would be exceeded after a short time period. The main loop runs the PCM as depicted in Fig. 1 and transmits the current states to the desktop computer at every converged time step.

In detail, the interpolation of the look-up tables E_{eq} and $\frac{\partial E_{eq}}{\partial T}$ are defined on the STM32 via spline interpolation at the junction nodes, which offers differentiability compared to piece-wise linear approximation. Based on a MATLAB® structure (*spline* [75]), the implementation includes the coefficients c, number of pieces s, order of polynomials l, range of the measured data and a pointer to the array of single intervals to define a spline as [50,76]:

$$f(x) = c_{0,s}(x - x_s)^{l-1} + c_{1,s}(x - x_s)^{l-2} + \cdots + c_{l-1,s}(x - x_s) + c_{l,s}$$

where the coefficients differ in each knot interval of

$$x \in [x_s, x_{s+1}]$$

Not only the value of two adjacent intervals are matched but also their derivatives, which is a crucial point when calculating the jacobian. To reduce memory allocation, the coefficients are stored in an array and evaluated via pointer function. Using double precision [77], a total of 751 and 41 knots are used for E_{eq} and $\frac{\partial E_{eq}}{\partial T}$ allocating 6008 and 328 Byte, respectively.

The matrix inversion to calculate the inverse of the jacobian J^{-1} uses a MATLAB® function (A/b [63]) in the MATLAB®-code PCMs. As standard *C*-algorithms (*e.g.* CMSIS) failed, the Gauss-Jordan (GJ) algorithm
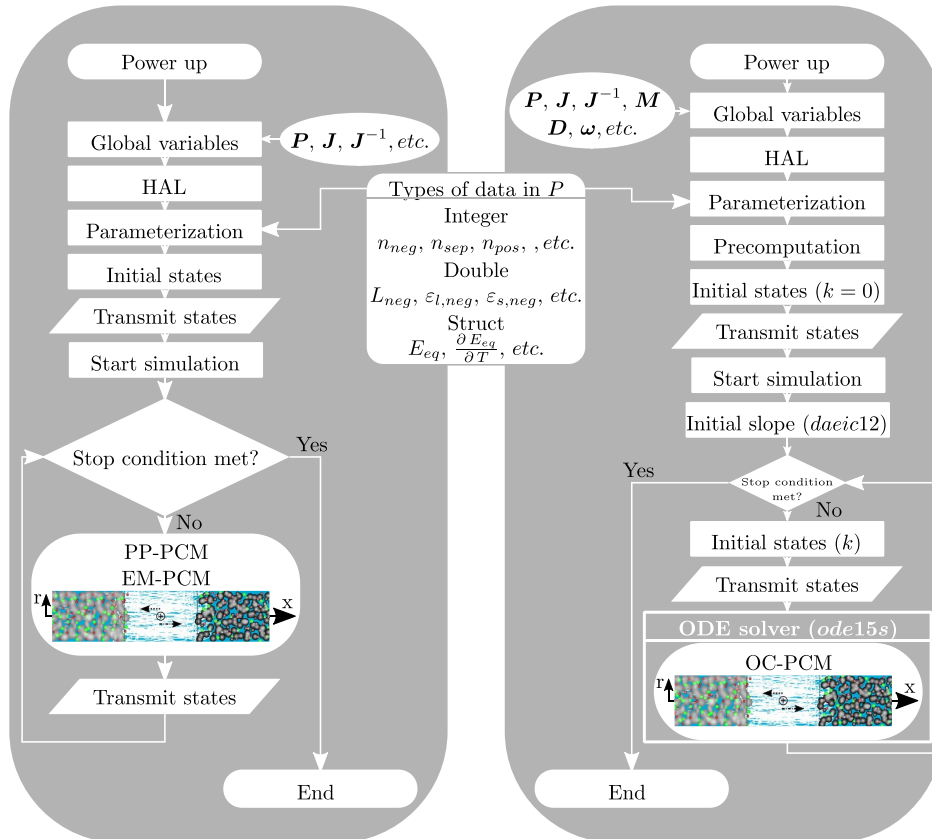
Fig. 3. Flow chart of the stand-alone *C*-codes of the PP-/EM-PCM (left) and the OC-PCM (right) implemented in the microcontroller (STM32F407VGT6, STMicroelectronics [9]). The PP-/EM-PCM and OC-PCM routines refer to the p2D-PCM models shown in Figs. 1 and 2. The generated simulation results are sent per converged time step via an UART-to-USB converter to a desktop computer and evaluated in terms of computation performance and simulation accuracy.

[78] was implemented, which is not a matrix-type specified algorithm like existing, tridiagonal-block-type algorithms (*e.g.* BAND(j), [79]). As floating point numbers are used in the processor, the highest accuracy is gained at low absolute values. In order to minimize the error caused by performing floating point operations during the matrix inversion, the concept of pivoting [80] is applied, which leads to lower absolute values and thus higher accuracy. In addition, the STM32 provides a floating point unit (FPU) of single precision [77]. Before the inversion starts, the matrix-entries are converted into single precision, next the inversion takes place on the FPU and the results are converted into double precision in the end. The related loss of accuracy and computation speed up is discussed in this work.

The 'Transmit states' action (see Fig. 3) uses a virtual COM port between the STM32 and the desktop computer and a UART-to-USB converter (115200 bit·s^{-1}), where the COM port is evaluated via a MATLAB® script.

In terms of RAM, the size of n_x ($= 6$) state variables x, both the jacobian J and its inverse J^{-1} as well as the calculation of the solid-diffusion approximation x_s determine the total size in Byte:

$$\text{size}(J, J^{-1}) = 2 \cdot (n_j \cdot n_x)^2 \cdot 8 \text{ Byte}$$

$$\text{size}(x) = (n_j \cdot n_x) \cdot 2 \cdot 8 \text{ Byte}$$

$$\text{size}(x_s) = (n_j \cdot n_s) \cdot 2 \cdot 8 \text{ Byte}$$

with a total number of nodes:

$$n_j = n_{neg} + n_{sep} + n_{pos} + 1$$

The multiplication with '2' for x and x_s is necessary for the current and previous state. The additional states n_s are two [11] for the PP- and six [25] for the EM-PCM. Table 4 shows exemplarily the possible discretizations and RAM/flash memory usage in the STM32 for the PP- and the EM-PCM.

The maximum runnable spatial configuration included 14 nodes in total as enough memory space for the variables and the solving process must be reserved. The minimum converging setup was found to be 2-1-2. The increase in memory by using the EM-approximation is negligible regarding x_s in reference to the PP-approach. The major influence is seen in the increase of spatial discretization as the jacobian size increases as well and the overall RAM usage increases quadratically.

In sum, the PP-/EM-PCM on the microcontroller need at least $\approx$ 10 kB up to a maximum of 115 kB during calculation and the maximum flash memory allocation consumed around 174/178 kB of the maximum 1024 kB flash memory ($\approx$ 17/17.4%).

Table 4
Memory usage of the stand-alone *C*-code PP- and EM-PCM.

Model	PP-PCM			EM-PCM		
Discretization	1-1-1	2-1-2	5-3-5	1-1-1	2-1-2	5-3-5
size (J, J^{-1}) in Byte	9216	20736	112896	9216	20736	112896
size (x) in Byte	384	576	1344	384	576	1344
size (x_s) in Byte	128	192	448	384	576	1344
RAM						
Total size in Byte	9728	21504	114688	9984	21888	115584
Memory allocation in %[I]	5.1	11.2	58.8	5.2	11.4	60.2
Flash memory						
Total size in kB	173.66	173.95	174.58	177.61	177.88	178.55
Memory allocation in %[II]	$\approx$ 17%			$\approx$ 17.4%		

[I] Referring to the STM32 with 192 kB of RAM. [II] Referring to the STM32 with 1024 kB flash memory.

4.2. OC-PCM stand-alone C-code

The structure of parameters, interpolation schemes and communication to the desktop computer of the *C*-code OC-PCM is similar to the *C*-code PP-/EM-PCM. A specified version of the *ode15s* solver [66–68] is developed in *C* offering main functionalities as.

- Calculation of initial jacobian (*daeic12* [68])
- Initial step estimation $k = 0$
- Calculation of iteration matrix M_i
- Iteration with simplified Newton method using GJ-inversion for M_i
- Calculating new jacobian J
- Adjusting step-size $\triangle t$

For calculating an initial jacobian, *daeic12* [68] was extracted from the *ode15s* solver and transferred into *C* right after setting the initial values (see Fig. 3). The *sparse* function [69] was adopted to gain a sparse jacobian via neglection of any zeros and the non-zero entries are stored in an array $\frac{df}{dx}$ together with the respective index coordinate pair $\frac{df}{dx}\big|_{index}$ to save memory. The estimation of the initial step-size is performed according to Curtis et al. [81]. The iteration matrix M_i is obtained at every iteration and uses the previously calculated jacobian (see Fig. 2). The main loop integrates from the previous state $k - 1$ to the current state k and uses simplified Newton method [67,82] incorporating the GJ-inversion [78] for inversing M_i to generate the state update dx. Step-size reduction and new jacobian calculation are implemented as described in section 3.3.

Regarding the memory allocation, the iteration matrix M_i contributes as

$$\text{size}(M_i) = \left\{ (n_{neg} + n_{pos})(m + 5) + 2n_{sep} - 3 \right\}^2 \cdot 8 \text{ Byte}$$

Similar to the jacobian of the PP-/EM-PCM, the memory usage of the M_i increases quadratically and the spatial discretization in the particle domain m is here the main driver. The analytical calculation of the jacobian $\frac{df}{dx}$ is stored as array of the non-zero entries as

$$\text{size}\left(\frac{df}{dx}\right) = \left\{ n_{neg}(5n_{neg} + 3m + 6) + n_{sep}(3n_{sep} - 2) + n_{pos}(5n_{pos} + 3m + 6) - 5 \right\} \cdot 8 \text{ Byte}$$

Therefore, the indices $\frac{df}{dx}\big|_{index}$ of the position in the jacobian (*i.e.* row and column) are stored as integers with 4 Byte each

$$\text{size}\left(\frac{df}{dx}\Big|_{index}\right) = 2 \cdot \left\{ n_{neg}(5n_{neg} + 3m + 6) + n_{sep}(3n_{sep} - 2) + n_{pos}(5n_{pos} + 3m + 6) - 5 \right\} \cdot 4 \text{ Byte}$$

Improvement using unsigned 16 bit integer is optional but not considered in this work. The mass matrix M is stored as integer to

$$\text{size}(M) = \left\{ (n_{neg} + n_{pos})(m + 5) + 2n_{sep} - 3 \right\} \cdot 4 \text{ Byte}$$

and the backward differences for the NDFs [66,70] are crucial to find a consistent solution and their memory usage amounts to

$$\text{size}(\nabla^m) = 7 \cdot \left\{ (n_{neg} + n_{pos})(m + 5) + 2n_{sep} - 3 \right\} \cdot 8 \text{ Byte}$$

The factor '7' is required by the integration order and two additional states are saved for following iterations [66,70]. The variable x stores the states

$$\text{size}(x) = 2 \cdot \left\{ (n_{neg} + n_{pos})(m + 5) + 2n_{sep} - 3 \right\} \cdot 8 \text{ Byte}$$

and the factor '2' accounts for the previous stored iteration. The maximum runnable spatial configuration 5-3-5-5 is in the same memory range as for the PP-/EM-PCM, whereas the most coarse configuration 5-

3-5-2 offering sufficient accuracy needs at least five resp. three nodes in the electrode resp. separator domain for the NMC-811/SiC parameterization. Note, that the minimum converging configuration appears to 3-2-3-2, but was neglected due to insufficient simulation accuracy. Table 5 shows the range of runnable *C*-code OC-PCMs on the STM32.

In sum, the OC-PCM on the microcontroller needs at least 54 kB RAM during calculation and the maximum allocates around 100 kB. The overall model size uses around 212 kB of the maximum 1024 kB flash memory ($\approx 20.7\%$).

5. Results and discussion

5.1. Validation and computational efficiency under constant load scenarios

The experimental validation of the three PCMs and the benchmark models is shown via thermographic measurements of the INR18650-MJ1 LIB at different CC charge (0.2/0.5/1C) and discharge (0.2/0.5/1/1.5/2C) rates at 25 °C ambient temperature under convective cooling as presented in previous work [2]. A desktop computer equipped with an Intel(R) Core(TM) i5-6500 CPU at 3.20 GHz processor and 16 GB of RAM was used for calculation.

The mean cell voltage error (a, b), temperature error (c, d), overall simulation time (e, f) and averaged calculation time per step (g, h) are shown in Fig. 4. Regarding CC charging in Fig. 4 a and c, the mean cell voltage error ranges from 10 mV for the ECM up to 20 mV for the OC-PCM until 0.5C and increases for the ECM at 1C up to 29 mV while a decreasing trend can be seen for all PCMs. The mean temperature error appears below 0.6 K for all models. Regarding discharge, the ECM matches quite well the measurements with errors on average below 21 mV and 0.1 K until 2C while all PCMs show increasing errors for higher C-rates (*e.g.* max. 68 mV for the PP-/EM-PCM and max. 1.5 K for the OC-PCM at 2C CC). The ECM shows increased modeling errors at 1C charging, which may be linked to limitations in the pore of the porous electrodes [2] and improvements can be achieved via using physically more meaningful, distributed-parameter ECMs [83] or adaptive, online-parameter estimation [84].

In general, all PCMs show increasing errors with higher applied C-rates ($> 1C$) as inhomogeneities along the electrodes (61.5×5.8 cm, width $\times$ height) increase as shown in our previous work [2], which cannot be modeled with a single-PCM as the electrode utilization is assumed to be homogeneous. Nevertheless, certain differences appear between the MATLAB®-code PCMs compared to the COMSOL-PCM. The temperature calculation is included in the jacobian of the OC-PCM,

Table 5
Memory usage of the stand-alone *C*-code OC-PCM.

Discretization	OC-PCM		
	5-3-5-2	5-3-5-3	5-3-5-5
size (M_i) in Byte	42632	55112	84872
size ($\frac{df}{dx}$) in Byte	3088	3328	3808
size ($\frac{df}{dx}\big|_{index}$) in Byte	3088	3328	3808
size (M) in Byte	292	332	412
size (∇^m) in Byte	4088	4648	5768
size (x) in Byte	1168	1328	1648
RAM			
Total size in Byte	54356	68076	100316
Memory allocation in %[I]	28.3	35.5	52.2
Flash memory			
Total size in kB	212.08	212.27	212.95
Memory allocation in %[II]		$\approx 20.7\%$	

[I] Referring to the STM32 with 192 kB RAM. [II] Referring to the STM32 with 1024 kB flash memory.
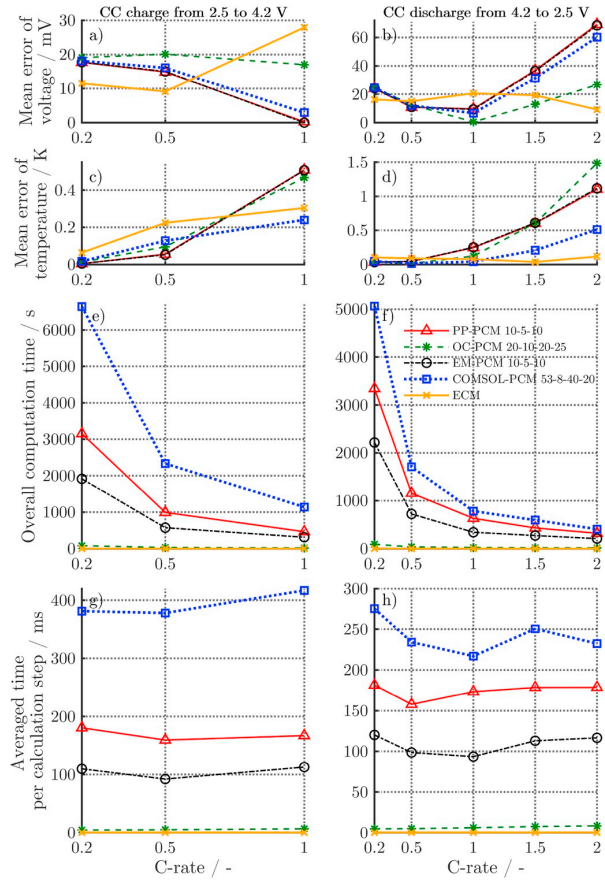
Fig. 4. Experimental validation with the INR18650-MJ1 NMC-811/SiC LIB of the simulation results including the ECM, the MATLAB®-code PCMs ('PP-PCM 10-5-10', 'OC-PCM 20-10-20-25' and 'EM-PCM 10-5-10') and the rigorous benchmark PCM ('COMSOL-PCM 53-8-40-20'). The mean cell voltage error (a, b) and temperature error (c, d) are shown together with the overall computation time (e, f) and averaged calculation time per converged time step (g, h) for the different CC charge (a, c, e and g) and discharge (b, d, f and h) tests at 25 °C ambient temperature and convective cooling conditions [2].

which is not implemented for the remaining PCMs and may have a significant influence on the cell voltage and temperature calculation beside the different spatial discretization and approximation schemes.

The reformulation and solving of the solid-diffusion PDE in the OC-PCM instead of using approximations contributes to the different cell voltages compared to the PP- and EM-PCM. The error for the OC-PCM remains at ≈ 22 mV for all scenarios, whereas the used approximations (PP [11] and EM [25]) lead to increased errors for 1.5 and 2C discharge (≈ 68 mV at 2C). As the *liion*-module [51] for the COMSOL-PCM offers only the particle concentration at the center, the surface and on average, an approximation may be used here as well, which may explain the appearing deviations.

In sum, all MATLAB®-code PCMs reveal sufficient accurate simulation of the electrochemical-thermal behaviour throughout the thickness of the NMC-811/SiC electrode stack under CC charge and discharge scenarios compared to the measured electrical-thermal behaviour of the INR18650-MJ1 LIB. Increasing errors appear, when inhomogeneities of the current density [2] along the electrodes are expected to increase for high applied C-rates ($> 1C$).

The computation times in Fig. 4 e and f of the COMSOL-PCM appear to be the slowest and the fastest appear for the ECM, as expected. The

same trend can be seen for the averaged calculation time per step (see Fig. 4 g and h). Approximately 6.3 ms per step are needed at 1C CC discharge for the OC-PCM, while the ECM needs only 0.2 ms. This results in an approximately 32, 470, 865 and 1085 times faster computation for the ECM compared to the OC-, EM-, PP- and COMSOL-PCM, respectively. The benefit of using explicit functions of state and input variables to solve the ECM [83] instead of solving the DAE system of the PCM is not questioned here. Even if large frameworks are used, lean computational costs confirm that implementation in the microcontroller would lead to similar results. Therefore, the ECM is used as benchmark only and not implemented in the microcontroller.

Around 16, 67 and 26% of the desktop computer's CPU and approximately 660, 670 and 793 MB RAM for the PP-/EM-, OC- and COMSOL-PCM are used at a full 1C CC discharge. Considering also the computation time, the OC-PCM may be most suitable for fast computation but preferring low memory usage and CPU load, the PP- or the
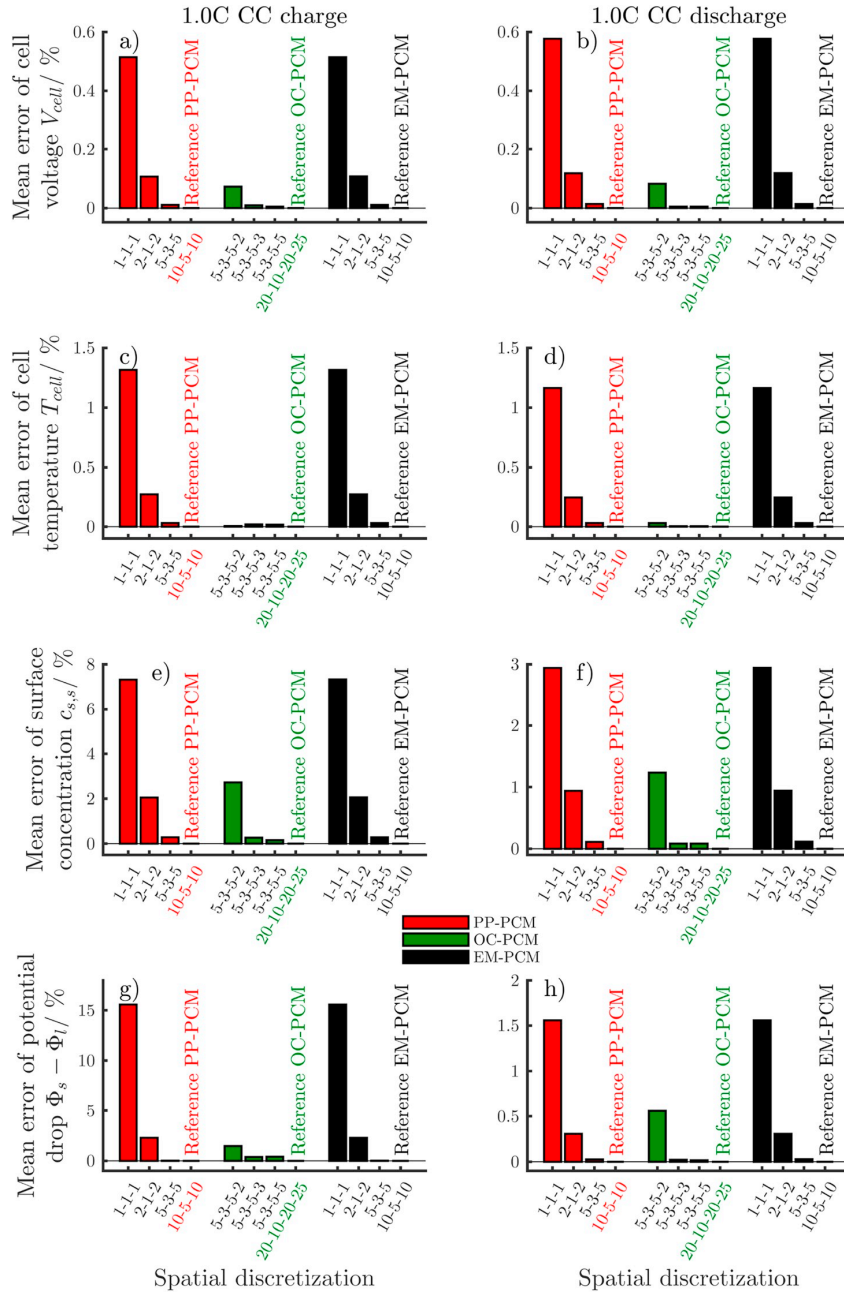
Fig. 5. The relative (%) increase of modeling error for the cell voltage (a, b), the cell temperature (c, d), the surface concentration (e, f) and the potential drop $\Phi_s - \Phi_l$ (g and h) both located at the anode-separator interface $x = L_{neg}$ is shown for gradually reducing the total number of spatial nodes in the MATLAB®-code PCMs (PP-, EM- and OC-PCM) in reference to the experimentally validated PCMs shown in Fig. 4('PP-PCM 10-5-10', 'EM-PCM 10-5-10' and 'OC-PCM 20-10-20-25').

even faster calculating EM-PCM seem more suitable. The ECM allocates ≈ 1400 MB at $\approx 10\%$ CPU, which is mainly caused by using the MAT-LAB/Simulink framework.

The simulation results are run on a desktop computer offering sufficient computation ressources of 3.20 GHz and 16 GB RAM. The STM32 offers maximum 168 MHz and 192 kB RAM and evaluating the most suitable PCM for embedded systems must be based on adequate conditions as proposed in control devices for a BMS, which are similar to the microcontroller of this work and offer similar no commercial framework tool or a sophisticated operating system.

5.2. Reducing memory allocation via coarser spatial discretizations

For implementation in the microcontroller, the number of spatial elements in the PP-/EM-PCM and the OC-PCM is gradually reduced to save RAM and decrease computation time. The related increase of modeling error for the cell voltage V_{cell}, temperature T_{cell}, surface concentration $c_{s,s}$ and the potential drop $\Phi_s - \Phi_l$ both at the anode-separator interface is analyzed in reference to the validated MATLAB®-code PCM configurations shown in Fig. 4. Fig. 5 shows the increase of error exemplarily for the 1C CC charge and discharge scenario.

Regarding the global cell variables V_{cell} and T_{cell}, similar error increase appears for charge and discharge for all PCMs. The PP- and EM-PCM show mean cell voltage error increase of $\approx 0.6\%$ for the minimum configuration (1-1-1), whereas the OC-PCM shows errors below 0.1% in all cases. The deviance for the cell temperature is around 1.2% for the PP- and EM-PCM, whereas nearly no deviance could be seen for the reduced configurations of the OC-PCM. Note, a minimum of 5 and 3 nodes for the electrodes and separator domain in the OC-PCM appeared for guaranteeing convergence.

Regarding the internal variables $c_{s,s}$ and $\Phi_s - \Phi_l$, higher deviances for the charge than for the discharge scenario appear with the chosen parameterization, which differs between charge and discharge to account for hysteresis effects of the open-circuit potentials [2]. Regarding the most coarse discretization, errors up to 7.3/3% compared to 2.7/1.2% for charge/discharge of the PP-/EM-PCM and the OC-PCM respectively appeared for $c_{s,s}$. In terms of $\Phi_s - \Phi_l$, the errors increase up to 16% for charging regarding PP-/EM-PCM, whereas lower errors appear for the OC-PCM ($\approx 1.4\%$).

The results indicate no distinct difference between the PP- and EM-PCM, when lean spatial discretization is chosen even at the lowest configuration of 1-1-1. The OC-PCM shows less error with decreasing number of nodes when mainly the spatial discretization in the particle is reduced - which reduces the overall size of the DAE enormously. In general, the error on global variables such as cell voltage and temperature seems acceptable but when internal variables are used such as the potential drop at the anode-separator interface to indicate the onset of lithium plating [4,85], distinct errors due to a lean spatial discretization must be considered for interpreting the results correctly.

In terms of the microcontroller, spatial configurations of 2-1-2 and 5-3-5 are used for the PP- and EM-PCM as similar mean errors regarding 2-1-2 of 4 mV (0.12%), 7E-2 K (0.25%), 84 mol m^{-3} (0.94%) and 0.8 mV (0.3%) are expected due to modeling error at 1C CC charge and discharge, which offer still sufficient accuracy to describe accurately the NMC-811/SiC INR18650-MJ1 LIB. In terms of the OC-PCM, the 5-3-5-3 and 5-3-5-5 are used which show maximum averaged errors regarding 5-3-5-3 of 0.25 mV (5E-3%), 2E-3 K (2E-3%), 6.7 mol m^{-3} (8E-2%) and 6E-2 mV (2E-2%).

5.3. Stand-alone C-code models on the microcontroller under constant load scenario

The CC charge and discharge loads as shown in section 5.1 are simulated on the STM32 using the stand-alone C-codes of the PP-, EM- and OC-PCM. The simulations incorporate the coarse 2-1-2, 2-1-2 and 5-3-5-3 and the maximum 5-3-5, 5-3-5 and 5-3-5-5 spatial discretizations,
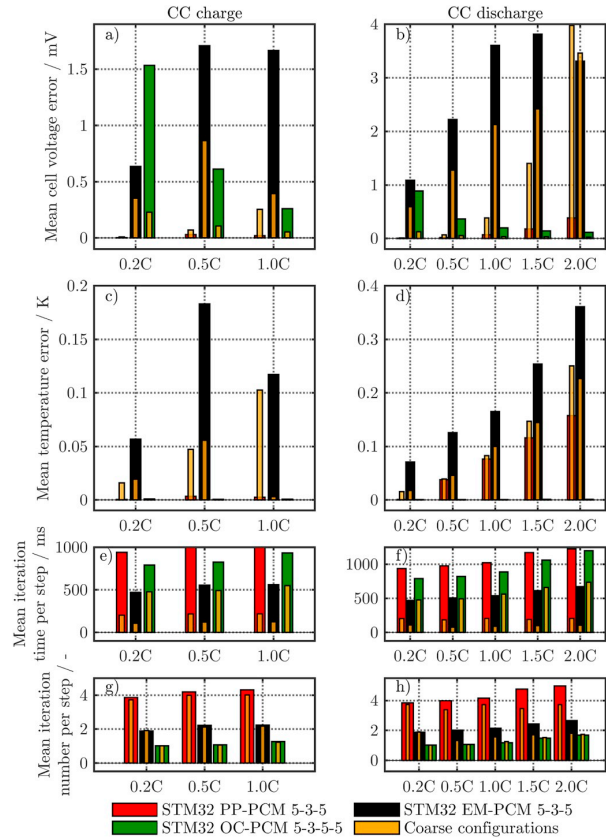
Fig. 6. Evaluation of the simulation accuracy (a, b, c and d) and computational efficiency (e, f, g, and h) of the stand-alone C-code PP-, EM- and OC-PCM under constant current charge (0.2, 0.5, and 1C) and discharge (0.2, 0.5, 1, 1.5 and 2C) scenarios. The mean cell voltage (a, b) and temperature error (c, d) is shown in reference to the corresponding MATLAB®-code PCM for the coarse (2-1-2, 2-1-2 and 5-3-5-3 for PP-, EM- and OC-PCM, 'Coarse configurations') and maximum spatial configuration. The computational efficiency is shown similar in form of the iteration time (e, f) and the mean number of iteration per 1 s step (g, h).

respectively. Fig. 6 shows the mean cell voltage and temperature error in reference to the corresponding MATLAB®-code. The computational performance is analyzed via the mean iteration time and total number of iterations per 1 s time step on the STM32 processor at 168 MHz. Table 6 summarizes the analysis at 1C CC charge and discharge. The lowest mean cell voltage error for charge and discharge appears for the PP-PCM (< 0.4 mV) and the highest appears up to 3.8 mV for the EM-PCM. Reducing the number of spatial nodes (see 'Coarse configurations' in Fig. 6), leads to higher deviations regarding the PP-PCM whereas the EM- and OC-PCM reveal less deviations. In terms of the cell temperature for charge and discharge, similar trends can be seen except for the lowest temperature error, which is seen for the OC-PCM.

In sum, all C-code PCMs on the STM32 show sufficient accuracy below 4 mV of cell voltage and 0.4 K of cell temperature error, which is mainly caused by approximations and rounding errors. The analysis of the internal states such as concentrations and potentials is neglected here as similar low error ranges appear.

Regarding the computational performance in Fig. 6 e and f, the fastest computation appears for the EM-PCM (max. 560 ms per step with min. 2 iterations) whereas the slowest is seen for the PP-PCM (max. 1052 ms per step with min. 4 iterations). When the coarse discretization

Table 6
Performance of *C*-code PCMs on the microcontroller at 1C CC.

Model Discretization	PP-PCM		EM-PCM		OC-PCM	
	2-1-2	5-3-5	2-1-2	5-3-5	5-3-5-3	5-3-5-5
1C CC *charging*						
Mean ΔV_{cell} /mV[I]	0.255	0.019	0.3956	1.665	0.053	0.262
Mean ΔT_{cell} /K[I]	0.103	0.003	0.003	0.117	<1E-3	<1E-3
Mean number of iterations per step/-	4.02	4.31	2.17	2.23	1.22	1.26
Mean iteration time per step/ms	219	1052	124	560	550	932
1C CC *discharging*						
Mean ΔV_{cell} /mV[I]	0.388	0.069	2.126	3.603	0.032	0.195
Mean ΔT_{cell} /K[I]	0.08	0.08	0.10	0.17	<1E-3	<1E-3
Mean number of iterations per step/-	3.72	4.17	1.56	2.14	1.25	1.18
Mean iteration time per step/ms	205	1021	90	540	563	887

[I] in reference to the corresponding MATLAB®-code PCM with the same discretization.

is used, the OC-PCM reveals the slowest calculation (max. 563 ms per 1 s step). For the OC-PCM, the 1 s time step is set as a maximum as the solver routine is implemented with the option, to reduce the step-size if no convergence appears (see Fig. 2) and the OC-PCM is thus more susceptible to prolong the overall computation time. Thus, the minimal number of iterations appears for the OC-PCM and the PP-PCM needs the most iterations. The spatial discretization has less significant influence and only slightly reduces the number of iterations.

In sum, the EM-PCM is the fastest calculating model with 90 respectively 540 ms per 1 s time step for an entire 1C CC discharge using coarse respectively maximum spatial discretization in the STM32. The OC-PCM offers still calculation times below the real-time threshold even if the solver routine reduces the stepsize during runtime. The PP-PCM is most likely to require the longest calculation time and number of iterations. Under CC load scenarios, the most appropriate choice for simulating the INR18650-MJ1 LIB in real-time on the microcontroller would be the EM-PCM.

5.3.1. Influence of the processor frequency

In application, lower processor frequency results in lower energy consumption and reducing the computation power can thus pose a challenge for the *C*-code p2D-PCMs to hold real-time computability. The 32-bit ARM Cortex M4 processor [9] of the STM32 offers a frequency range up to 168 MHz and three different configurations at 50, 109 and 168 MHz are used to simulate 1C CC charge and discharge with all *C*-code PCMs to evaluate the influence on the computation speed. The UART transfer time reveals negligible influence herein.

Fig. 7 a and b show the total computation time versus the simulated time and for all frequencies, the EM-PCM shows the fastest computation, whereas the PP-PCM the slowest. A more detailed analysis of the computation performance is shown in Table 7. As the simulation accuracy and iteration number (see Table 6) are not influenced by the processor frequency, only the mean iteration and total calculation time versus the simulated time (see 'Time reduction') are shown in Table 7. Similarly to Fig. 7 a and b, Fig. 7 c and d illustrate the average iteration time per 1 s step. The blue horizontals in Fig. 7 mark the real-time suitability, when the calculation time equals the simulated time (see 'Time factor' in Table 7). At 168 MHz, the PP-PCM is slightly atop the threshold with +8%/+6%, whereas the OC- and the fastest calculating EM-PCM show time reductions of 6%/10% and 41%/43% during 1C CC
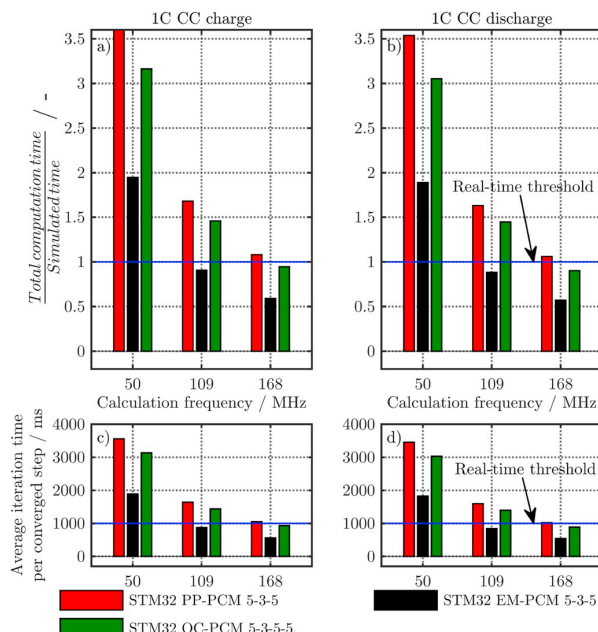
Fig. 7. Computational performance of the *C*-code PP-, EM- and OC-PCM for simulating 1C CC charge (a and c) and discharge (b and d) on the STM32 at 50, 109 and 168 MHz. The horizontal line depicted in 'blue' marks the real-time threshold when the simulated time equals the total computation time (see 'Time factor = 1' in a and b) and the average iteration time per converged step equals the simulation step-size of 1 s (see '1000 ms' in c and d). (For interpretation of the references to colour in this figure legend, the reader is referred to the Web version of this article.)

Table 7
Computational performance of *C*-code PCMs at different processor frequencies.

Model Load[I]	PP-PCM 5-3-5		EM-PCM 5-3-5		OC-PCM 5-3-5-5	
	CH	DCH	CH	DCH	CH	DCH
Frequency of 168 MHz						
Mean iteration time per step/ms [II]	1052	1021	560	540	932	887
Time factor [III]	1.08	1.06	0.59	0.57	0.94	0.90
Frequency of 109 MHz						
Mean iteration time per step/ms [II]	1639	1592	872	841	1436	1394
Time factor [III]	1.68	1.63	0.91	0.88	1.46	1.45
Frequency of 50 MHz						
Mean iteration time per step/ms [II]	3555	3452	1889	1823	3132	3031
Time factor [III]	3.63	3.55	1.95	1.89	3.16	3.05

[I] at 1C constant current charge (CH) and discharge (DCH). [II] referring to a 1 s step-size. [III] $\dfrac{Total\ calculation\ time}{Simulated\ time}$ = Time factor

charge/discharge. Only the EM-PCM reveals sufficient computation speed (max. 872 ms for 1C CC charge) at 109 MHz, whereas at 50 MHz none of the PCMs can simulate in real-time. A minimum increase of 89% (1890 ms for 1 s at 1C CC discharge) is seen for the EM-PCM and over 3 times longer computation times than the actual simulated time appar for the PP- and OC-PCM.

In sum, real-time suitability poses a challenge for the *C*-code PCMs

on the microcontroller and under CC loads, the necessary speed-up can be achieved via using coarser spatial discretizations (*e.g.* 2-1-2 resp. 5-3-5-3 for the PP-/EM-PCM and OC-PCM). As seen in Table 6, reducing the spatial configuration reveals the EM-PCM as fastest-calculating *C*-code PCM. As the accuracy is not distorted by the frequency, the most appropriate choice at low frequencies is the EM-PCM.

5.3.2. Influence of the microcontroller's accuracy

To reduce computation time, the jacobian/iteration matrix inversion is calculated using the FPU of single precision. The transfer needs two extra arrays of single precision for a current copy of the matrix and for storing the inverse. The coarse configurations 2-1-2 and 5-3-5-3 for the PP-/EM- and OC-PCM are used to avoid RAM overloads. 1C CC charge and discharge at 168 MHz are simulated and the results are shown in Table 8.

The maximum mean cell voltage error accounts to 1.862 mV for 1C CC discharge using the EM-PCM in reference to the corresponding MATLAB®-code PCM. The lowest error is seen for the OC-PCM below 0.12 mV. Negligible errors for the cell temperature (see Table 8) appear.

Comparing the results between single- (see Table 8) and double-precision (see Table 6), a trend of decreasing iterations appears ($\approx$ 19% less) for the EM-PCM at 1C CC charge.

The benefit can be seen in the average iteration times per step in Table 8. The EM- and OC-PCM show calculation times around 80 ms and the PP-PCM up to 156 ms. For constant loads, minimum reduction of 29%, 23% and 86% for the PP-, EM- and OC-PCM appears when the FPU is used. The mean error of the PCMs may slightly increase while using FPU, but still sufficient accuracy is offered. Regarding the maximum calculation times, single time steps are simulated in $\approx$ 600 ms for a 1 s time step at a total iteration number up to 9 for the OC-PCM. This may be critical, when real-time computation must be guaranteed. The PP- and EM-PCM show lower maximum iteration numbers and computation times, where the PP-PCM appears as the overall slowest converging model.

In sum, the most benefit in using the FPU is gained with the OC-PCM but certain overshoots in calculation time and iteration number may be a problem for real-time suitability. The EM- and PP-PCM show a more stable calculation with slightly increased errors for the EM-PCM and slower computation speed for the PP-PCM. Comparing the total calculation time to the simulated times for 1C charge and discharge, a minimum reduction of 84%, 92% and 92% appears at constant load simulations for the PP-, EM- and OC-PCM, respectively.

5.4. Validation and computational efficiency under driving cycle scenario

Referring to application of LIBs in EVs, the ARTEMIS [86] drive cycle was adapted to the INR18650-MJ1 LIB current range as seen in Fig. 8 a.

Table 8
Computational performance of *C*-code PCMs using FPU for 1C CC charge and discharge.

Model Load [I]	PP-PCM 2-1-2		EM-PCM 2-1-2		OC-PCM 5-3-5-3	
	CH	DCH	CH	DCH	CH	DCH
Mean ΔV_{cell} /mV [II]	1.343	0.416	1.683	1.862	0.055	0.115
Mean ΔT_{cell} /K [II]	<1E-2	0.08	0.12	0.09	<1E-3	<1E-3
Mean number of iterations per step/-	3.90	3.33	1.75	1.59	1.17	1.30
Mean iteration time per step/ms	156	134	75	69	76	80
Time reduction [III]	29%	35%	40%	23%	86%	86%

[I] at 1C constant current charge (CH) and discharge (DCH) [II] in reference to the corresponding MATLAB®-code PCM with identical spatial discretization [III] compared to the calculation time without using the FPU on the STM32.
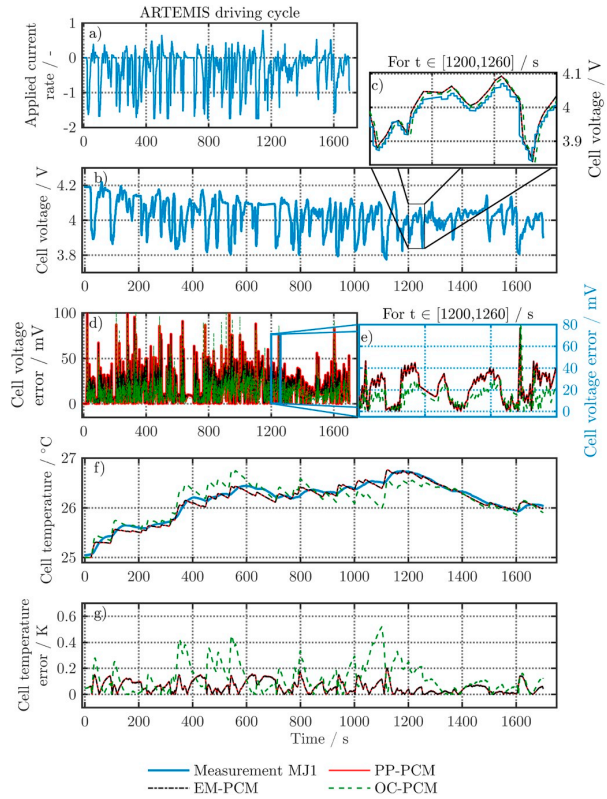
Fig. 8. Measurement results of the INR18650-MJ1 LIB ('Measurement MJ1') for the applied current (a), cell voltage (b) and temperature (f) under the adapted ARTEMIS [86] driving cycle. The subplot (c) shows a magnified part from 1200 to 1260 s for the measured and simulated (MATLAB®-code 'PP-PCM 5-3-5′, 'EM-PCM 5-3-5′ and 'OC-PCM 5-3-5-5′) cell voltages in (b). The resulting error profiles for the PCMs are shown for the cell voltage (d) with a magnified part similar to (c). Subplot (g) shows the temperature error.

Table 9
Validation of MATLAB®-code PCMs under the adapted ARTEMIS driving cycle.

Model Load	PP-PCM		EM-PCM		OC-PCM	
	ARTEMIS driving cycle (see Fig. 8 a)					
Discretization	**2-1-2**	**5-3-5**	**2-1-2**	**5-3-5**	**5-3-5-3**	**5-3-5-5**
Mean ΔV_{cell} /mV [I]	19.3	18.7	19.3	18.7	12.4	12.4
RMSE ΔV_{cell} /mV [I]	23.8	23.1	23.8	23.1	16.6	16.6
Mean ΔT_{cell} /K [I]	0.07	0.06	0.07	0.06	0.13	0.13
RMSE ΔT_{cell} /K [I]	0.09	0.07	0.09	0.07	0.17	0.17

[I] in reference to the experimentally measured data of the INR18650-MJ1 cell.

For the experiments, a cycler (CTS, BaSyTec) paired with a climate chamber (VT 4021, Vötsch Industrietechnik GmbH) at 25 °C was used at initial 100% SoC of the LIB. Fig. 8 b illustrates the measured cell voltage together with a magnified region (Fig. 8 c) showing the simulation results. The temperature profile (see Fig. 8 f) and both voltage and temperature error (Fig. 8 d, e and g) of the MATLAB®-code PP-, EM- and OC-PCM are shown. Table 9 summarizes the related simulation accuracy for the MATLAB®-code PCMs.

In this case, averaged open-circuit potentials (E_{eq}, see supplementary part) of lithiation and delithiation [2] were used to ease the effect of

measurement-related polarization and improve the simulation of dynamic loads.

The mean cell voltage error for the PP- and EM-PCM appear to be around 18.7 mV on average with a root mean squared error (RMSE) of 23.1 mV. Reducing the spatial nodes, the error slightly increases but remain below 20 mV. The OC-PCM shows no distinct difference between the coarse and the maximum configuration and reveals the most accurate simulation with a mean error of 12.4 mV at a RMSE of 16.6 mV. The temperature error for all MATLAB®-code PCMs are below 0.15 K (RMSE<0.2), which is in the range of the measurement accuracy (*i.e.* Pt100 sensor with ±0.15 K at 0 °C, DIN/IEC Class A). For comparison, the ECM simulation results calculated on the same desktop computer revealed a mean cell voltage error of 13.7 mV at a RMSE of 17.5 mV and a mean temperature error of 0.22 K.

The PCMs are in the same range of accuracy as the ECM and choosing the appropriate discretization or reformulation to gain real-time operability, a competitive alternative appears for model-based monitoring of LIBs.

The benefit of using a PCM lies in the simulated local concentrations and potentials, which can be used to develop sophisticated control algorithms such as avoiding lithium plating during fast charging [85].

Finally, the performance of simulating the ARTEMIS profile with the *C*-code PCMs on the STM32 is evaluated. Table 10 summarizes the simulation accuracy in reference to the MATLAB®-code PCM (see Table 9) together with the computation speed.

The mean cell voltage deviation is below 0.4 mV for all PCMs, where the OC-PCM shows the most accurate implementation and the EM-PCM the maximum deviation to the corresponding MATLAB®-code PCM. Again, the temperature deviances are in the range of measurement accuracy. Regarding the computational performance, the OC-PCM is not able to simulate in real-time due to the step-size reduction option in the solver. The EM-PCM shows the fastest calculation and for a step-size of 250 ms, only the coarse configuration is able to simulate with a time reduction of 37% under real-time requirements. The PP-PCM required at least 190 ms on average, which corresponds to a time reduction of 24%.

To conclude, the EM-PCM shows the most promising results for simulating an application-near scenario with fulfilling real-time requirements.

6. Conclusion

Trending towards high-energy LIBs, physicochemical model based monitoring can help to account for inhomogeneties on local scales and improve the state-estimation process. Efficiently reduced p2D-PCMs are evaluated on a microcontroller using either FDM together with solid-diffusion approximations or Chebyshev orthogonal collocation to reformulate particle and electrolyte domain. Experimental validation with CC charge and discharge, ARTEMIS [86] driving cycle and benchmarking to ECM and rigorous COMSOL p2D-PCM showed accurate simulation for a NMC-811/SiC LIB. In sum, the average cell voltage error of the p2D-PCMs can be summarized as modeling and parameter uncertainties, errors from spatial reduction and errors from implementation in the STM32 as shown in Table 11.

At low processor frequencies down to 50 MHz, crucial limitations appear for the p2D-PCMs to calculate in real-time. Using hardware acceleration such as the FPU, computation acceleration up to 86% appeared, which can be recommended at low processor frequencies to gain real-time computability again. Computation analysis under CC and

Table 10
Computational performance of *C*-code PCMs simulating the adapted ARTEMIS driving cycle.

Model	PP-PCM		EM-PCM		OC-PCM	
Load	ARTEMIS driving cycle (see Fig. 8 a)					
Discretization	**2-1-2**	**5-3-5**	**2-1-2**	**5-3-5**	**5-3-5-3**	**5-3-5-5**
Mean ΔV_{cell} /mV[I]	0.153	0.148	0.361	0.330	0.030	0.065
Mean ΔT_{cell} /K[I]	0.15	0.07	0.16	0.15	<1E-3	<1E-3
Mean number of iterations per step/-	3.46	4.12	2.68	3.31	3.15	3.15
Mean iteration time per step/ms	190	1009	157	838	1250	2072
Time reduction [II]	24%	n.a.	37%	n.a.	n.a.	n.a.

[I] in reference to the corresponding MATLAB®-code PCM with the identical discretization [II] for a step-size of 250 ms

Table 11
Summary of average cell voltage error for MATLAB®- and *C*-code PCMs.

Model	PP-PCM	EM-PCM	OC-PCM	Code
Error from modeling and parameters/mV[I]	Compared to experimental data from 3.35 Ah NMC-811/SiC INR18650-MJ1 LIB			MATLAB
1C CC CH/DCH	<1/9.7	<1/9.3	17/<1	
Driving cycle	18.6	18.6	12.4	
Error from spatial reduction/mV[II]	4.1/4	4.1/4	<1/<1	
Error from microcontroller/mV	STM32 with max. 168 MHz @32-bit ARM® Cortex®-M4 max. 1024 kB flash memory and max. 192 kB RAM [9]			*C*
1C CC CH/DCH	<0.5/<0.5	0.5/2.1	<0.5/<0.5	
Driving cycle	<0.5			

[I] for PP-PCM 10-5-10, EM-PCM 10-5-10 and OC-PCM 20-10-20-25. [II] for PP-PCM 10-5-10 → 2-1-2, EM-PCM 10-5-10 → 2-1-2 and OC-PCM 20-10-20-25 → 5-3-5-3.

driving cycle loads revealed the EM-PCM as best choice for simulating a single LIB at least 37% faster than real-time, which consumes 21.9 kB RAM for solving and 175 kB flash memory for storing the model on the microcontroller.

Future work can investigate more robust solver in terms of the OC-PCM to improve the performance on a microcontroller and test the *C*-code EM-PCM model-based monitoring for estimating a LIB online and develope local-anode potential based fast charging profiles to avoid lithium plating.

Appendix A

Table A12
Properties of the electrolyte [2].

Electrolyte	1 M LiPF6 in PC/EC/DMC
Salt diffusivity D_l^{I}/m^{2}s^{-1}	$10E-4\cdot10^{-4.43-\dfrac{54}{T-229-5c_l}-0.22c_l}$
Ionic conductivity κ_l^{I}/ S m^{-1}	$0.1c_l(-10.5+0.668c_l+0.494c_l^2+0.074T-0.0178c_lT$ $-8.8610^{-4}c_l^2T-6.9610^{-5}T^2+2.810^{-5}c_lT^2)$
Activity $\dfrac{d\,lnf_{\pm}\mathrm{I}}{d\,ln\,c_l}$/-	$(0.601-0.24c_l^0.5+0.983(1-0.0052(T-294))c_l^{1.5})$ $\cdot(1-t_+^0)^{-1}-1$
Transference $t_+^{0\,\mathrm{I}}$/-	0.38
Ref. concentration c_{ref}^{I}/mol m^{-3}	1000

$^{\mathrm{I}}$ Ref. [87].

Table A13
Parameterization of the p2D-PCM for a NMC-811/SiC LIB [2].

Geometry		Silicon-graphite (SiC)	Separator	Nickel-rich (NMC-811)
Thickness L		86.7 μm $^{\mathrm{m}}$	12 μm $^{\mathrm{m}}$	66.2 μm$^{\mathrm{m}}$
Particle radius R_p		6.1 μm $^{\mathrm{m,D50}}$		3.8 μm $^{\mathrm{m,D50}}$
Active material fraction ε_s		69.4% $^{\mathrm{e}}$		74.5% $^{\mathrm{e}}$
Inactive fraction $\varepsilon_{s,na}$		9% $^{\mathrm{e,*}}$		8.4% $^{\mathrm{e,*}}$
Porosity ε_l		21.6% $^{\mathrm{m}}$	45%$^{\mathrm{e}}$	17.1% $^{\mathrm{m}}$
Bruggeman coefficient $\beta^{\mathrm{VI,**}}$		1.5	1.5	1.85 $^{\mathrm{e}}$
Thermodynamics				
Equilibrium potential E_{eq}		Ref. [2] $^{\mathrm{m}}$		Ref. [2] $^{\mathrm{m}}$
Entropic coefficient $\dfrac{\partial E_{eq}}{\partial T}$		Ref. [2] $^{\mathrm{m}}$		Ref. [2] $^{\mathrm{m}}$
Stoichiometry	100% SoC	0.852		0.222
	0% SoC	0.002		0.942
Max. theorectical loading b_g		415 mAh g$^{-1\,\mathrm{I}}$		275.5 mAh g$^{-1\,\mathrm{II}}$
Density ρ		2.24 g cm$^{-3\,\mathrm{I}}$		4.87 g cm$^{-3\,\mathrm{II}}$
Concentration $c_{s,max}$		34684 mol m$^{-3\,\mathrm{e}}$		50060 mol m$^{-3\,\mathrm{e}}$
Transport				
Solid diffusivity D_s^{***}		5E-14 m^2 s$^{-1\,\mathrm{e,IV}}$		5E-13 m^2 s$^{-1\,\mathrm{III,V}}$
Specific activation $\dfrac{E_{a,D_s}^{***}}{R}$		1200 K $^{\mathrm{e}}$		1200 K $^{\mathrm{e}}$
Solid conductivity σ_s		100 S m$^{-1\,\mathrm{III}}$		0.17 S m$^{-1\,\mathrm{e,III}}$
Kinetics				
Reaction rate constant k^{***}		3E-11 m s$^{-1\,\mathrm{e}}$		1E-11 m s$^{-1\,\mathrm{e}}$
Specific activation $\dfrac{E_{a,k}^{***}}{R}$		3600 K $^{\mathrm{e}}$		3600 K $^{\mathrm{e}}$
Transfer coefficient $\alpha_{a/c}$		0.5$^{\mathrm{e}}$		0.5$^{\mathrm{e}}$

m = measured. e = estimated. * PVDF-binder/Carbon black (Ref. [88,89]).
$^{\mathrm{I}}$ Ref. [90]. $^{\mathrm{II}}$ Ref. [91]. $^{\mathrm{III}}$ Ref. [92]. $^{\mathrm{IV}}$ Ref. [93]. $^{\mathrm{V}}$ Ref. [94]. $^{\mathrm{VI}}$ Ref. [95].
** Effective transport correction according to Bruggeman (Ref. [95]): $\Psi_{eff}=\varepsilon^{\beta}\cdot\Psi_0$

*** Arrhenius law (Ref. [96]): $k=A\cdot\exp\left(\dfrac{E_{a,i}}{R}\dfrac{(T-298[\mathrm{K}])}{T\cdot298[\mathrm{K}]}\right)$

Table A14
Differential algebraic equations of the p2D-PCM

Mass balance$^{\mathrm{I}}$	$\varepsilon_l\,\dfrac{\partial c_l(x,t)}{\partial t}=\dfrac{\partial}{\partial x}\left(D_l^{eff}\dfrac{\partial c_l(x,t)}{\partial x}+\dfrac{i_l(x,t)\,(1-t_+^0)}{F}\right)$
	$\varepsilon_s\,\dfrac{\partial c_s(x,t,r)}{\partial t}=\dfrac{1}{r^2}\dfrac{\partial}{\partial r}\left(D_s r^2\dfrac{\partial c_s(x,t,r)}{\partial r}\right)$
Potentials$^{\mathrm{I}}$	$\dfrac{\partial\,\Phi_l(x,t)}{\partial x}=-\dfrac{i_l(x,t)}{\kappa_l^{eff}}+\dfrac{2\,R\,T}{F}(1-t_+^0)\left(1+\dfrac{d\,lnf_{\pm}}{d\,ln\,c_l(x,t)}\right)\dfrac{\partial\,ln\,c_l(x,t)}{\partial x}$
	$\dfrac{\partial\,\Phi_s(x,t)}{\partial x}=-\dfrac{i_{app}(t)-i_l(x,t)}{\sigma_s}\quad\text{with}\quad i_{app}(t)=i_s(x,t)+i_l(x,t)\quad\forall\,x,t$
Charge balance$^{\mathrm{I}}$	$\dfrac{\partial i_l(x,t)}{\partial x}+\dfrac{\partial i_s(x,t)}{\partial x}=0\quad\text{with}\quad\dfrac{\partial i_s(x,t)}{\partial x}=-\dfrac{3\varepsilon_s}{R_p}\,Fj_n(x,t)$
Electrode kinetics$^{\mathrm{I}}$	$j_n(x,t)=\dfrac{i_0(x,t)}{F}\left[exp\left(\dfrac{\alpha_a\,F\,\eta(x,t)}{RT}\right)-exp\left(-\dfrac{\alpha_c\,F\,\eta(x,t)}{RT}\right)\right]$
	$\eta(x,t)=\Phi_s(x,t)-\Phi_l(x,t)-E_{eq}(x,t)$
	$i_0(x,t)=F\,k\,(c_{s,max}-c_{ss}(x,t))^{\alpha_c}\,(c_{ss}(x,t))^{\alpha_a}\,(c_l(x,t))^{\alpha_a}$
Temperature$^{\mathrm{I,\,II}}$	$\dfrac{m\,c_p}{A_{act}}\dfrac{\partial\,T_{cell}}{\partial\,t}=-i_{app}\cdot V_{cell}+q-q_{ext}-q_{\infty}$

(continued on next page)

Table A14 (*continued*)

$$q = \frac{3\varepsilon_s F}{Rp} \int_{x*} j_n \cdot \left(E_{eq}\left(\frac{c_s(x,r_p)}{c_{s,max}}\right) - \frac{\partial E_{eq}\left(\frac{c_s(x,r_p)}{c_{s,max}}\right)}{\partial T} \cdot T \right) \mathrm{d}x$$

$$q_{ext} = i_{app}^2 \cdot R_{ext} \qquad\qquad q_\infty = \alpha_\infty^* \frac{A_{surf}}{A_{act}}(T_{cell} - T_\infty)$$

[I] Ref. [6]. [II] Ref. [52,64,65]. $x* = x \in [0, L_{neg}] \wedge [L_{neg} + L_{sep}, L_{neg} + L_{sep} + L_{pos}]$ $\alpha_\infty^* = 44.3 \mathrm{W\,m^{-2}K^{-1}}$, simplified for combining heat radiation, conduction and convection [2].

Table A15
Nomenclature I

Greek symbols		
α		Transfer coefficient
α_∞	W m^{-2} K^{-1}	Ambient heat transfer coefficient
β		Bruggeman coefficient
ε		Volume fraction
ε		Numerical tolerance
η	V	Overpotential
κ	S m^{-1}	Ionic conductivity
ρ	kg m^{-3}	Mass density
σ	S m^{-1}	Electrical conductivity
Φ	V	Electrical potential
Ψ		Variable
ω		Clenshaw-Curtis weights

Indices		
a		Anodic reaction (oxidation)
act		Active area
app		Applied (*i.e.* current density)
c		Cathodic reaction (reduction)
eff		Transport corrected (Bruggeman correlation [95])
ext		External heat (*i.e.* from grid resistance)
l		Liquid phase (*i.e.* electrolyte)
max		Maximum
neg		Negative electrode (*i.e.* SiC)
pos		Positive electrode (*i.e.* NMC-811)
s		Solid phase (*i.e.* active particle)
sep		Separator
s,s		Solid phase (*i.e.* active particle surface)
surf		Surface

Table A16
Nomenclature II

Latin symbols		
a	m^{-1}	Specific surface
b_g	mAh g^{-1}	Maximum theoretical loading
c	mol m^{-3}	Concentration of lithium cations (Li$^+$)
$c_{s,max}$	mol m^{-3}	Maximum theoretical concentration of Li$^+$
c_p	J kg^{-1} K^{-1}	Heat capacity
D	m^2 s^{-1}	Diffusion coefficient
$\boldsymbol{D}$		Differentiation matrix
E_{eq}	V	Equilibrium potential vs. Li/Li$^+$
$\frac{\partial E_{eq}}{\partial T}$	V/K	Entropic coefficient
$f_\pm$		Mean molar activity coefficient of electrolyte
F	96 485 A mol^{-1}	Faraday's constant
g		Non-linear equations of p2D-PCM
i	A m^{-2}	Current density
i_{app}	A m^{-2}	Applied current density
i_n	A m^{-2}	Current density perpendicular to particle surface
i_0	A m^{-2}	Exchange current density
j_n	mol m^{-2} s^{-1}	Pore-wall flux
$\boldsymbol{J}$		Jacobian matrix
k	m s^{-1}	Reaction rate constant
L	m	Thickness
m	kg	Mass of cell
$\boldsymbol{M}$		Mass matrix
$\boldsymbol{M}_i$		Iteration matrix
r	m	r-coordinate particle domain of p2D-PCM
R	8.314 J mol^{-1} K^{-1}	Gas constant

(*continued on next page*)

Table A16 (*continued*)

Latin symbols		
R_{ext}	$\Omega\,m^2$	Grid resistance
R_p	m	Particle radius
q	$W\,m^{-2}$	Heat generation rate per area
t	S	Time
T	K	Temperature
t_+^0		Transport number of Li^+
x	m	x-coordinate in electrolyte domain of p2D-PCM

Appendix B. Supplementary data

Supplementary data to this article can be found online at https://doi.org/10.1016/j.jpowsour.2019.226834.

References

[1] T. Amietszajew, E. McTurk, J. Fleming, R. Bhagat, Understanding the limits of rapid charging using instrumented commercial 18650 high-energy li-ion cells, Electrochim. Acta 263 (2018) 346–352, https://doi.org/10.1016/j.electacta.2018.01.076.

[2] J. Sturm, A. Rheinfeld, I. Zilberman, F.B. Spingler, S. Kosch, F. Frie, A. Jossen, Modeling and simulation of inhomogeneities in a 18650 nickel-rich, silicon-graphite lithium-ion cell during fast charging, J. Power Sources 412 (2019) 204–223, https://doi.org/10.1016/j.jpowsour.2018.11.043.

[3] C. von Lüders, V. Zinth, S.V. Erhard, P.J. Osswald, M. Hofmann, R. Gilles, A. Jossen, Lithium plating in lithium-ion batteries investigated by voltage relaxation and in situ neutron diffraction, J. Power Sources 342 (2017) 17–23, https://doi.org/10.1016/j.jpowsour.2016.12.032.

[4] C. von Lüders, J. Keil, M. Webersberger, A. Jossen, Modeling of lithium plating and lithium stripping in lithium-ion batteries, J. Power Sources 414 (2019) 41–47, https://doi.org/10.1016/j.jpowsour.2018.12.084.

[5] F.M. Kindermann, J. Keil, A. Frank, A. Jossen, A sei modeling approach distinguishing between capacity and power fade, J. Electrochem. Soc. 164 (12) (2017) E287–E294, https://doi.org/10.1149/2.0321712jes.

[6] M. Doyle, T.F. Fuller, J. Newman, Modeling of galvanostatic charge and discharge of the lithium/polymer/insertion cell, J. Electrochem. Soc. 140 (6) (1993) 1526–1533.

[7] V. Ramadesigan, P.W.C. Northrop, S. De, S. Santhanagopalan, R.D. Braatz, V. R. Subramanian, Modeling and simulation of lithium-ion batteries from a systems engineering perspective, J. Electrochem. Soc. 159 (3) (2012) R32–R45.

[8] A. Jokar, B. Rajabloo, M. Désilets, M. Lacroix, Review of simplified pseudo-two-dimensional models of lithium-ion batteries, J. Power Sources 327 (2016) 44–55, https://doi.org/10.1016/j.jpowsour.2016.07.036.

[9] STMicroelectronics, Stm32f4discovery Microcontroller, STM Technical Data, 2018. https://www.st.com/en/evaluation-tools/stm32f4discovery.html.

[10] V.R. Subramanian, J.A. Ritter, R.E. White, Approximate solutions for galvanostatic discharge of spherical particles: 1. constant diffusion coefficient, J. Electrochem. Soc. 148 (11) (2001) 444–449.

[11] V.R. Subramanian, V.D. Diwakar, D. Tapriyal, Efficient macro-micro scale coupled modeling of batteries, J. Electrochem. Soc. 152 (10) (2005) 2002–2008.

[12] S. Santhanagopalan, Q. Guo, P. Ramadass, R.E. White, Review of models for predicting the cycling performance of lithium ion batteries, J. Power Sources 156 (2) (2006) 620–628, https://doi.org/10.1016/j.jpowsour.2005.05.070.

[13] V.R. Subramanian, V. Boovaragavan, V.D. Diwakar, Toward real-time simulation of physics based lithium-ion battery models, Electrochem. Solid State Lett. 10 (11) (2007) A255, https://doi.org/10.1149/1.2776128.

[14] V.R. Subramanian, V. Boovaragavan, V. Ramadesigan, M. Arabandi, Mathematical model reformulation for lithium-ion battery simulations: galvanostatic boundary conditions, J. Electrochem. Soc. 156 (4) (2009) A260–A271.

[15] V. Boovaragavan, V. Ramadesigan, M.V. Panchagnula, V.R. Subramanian, Continuum representation for simulating discrete events of battery operation, J. Electrochem. Soc. 157 (1) (2010) A98–A104.

[16] R. Klein, N.A. Chaturvedi, J. Christensen, J. Ahmed, R. Findeisen, A. Kojic, State estimation of a reduced electrochemical model of a lithium-ion battery, in: American Control Conference, 2010, pp. 6618–6623.

[17] V. Ramadesigan, K. Chen, N.A. Burns, V. Boovaragavan, R.D. Braatz, V. R. Subramanian, Parameter estimation and capacity fade analysis of lithium-ion batteries using reformulated models, J. Electrochem. Soc. 158 (9) (2011) A1048–A1054.

[18] T.S. Dao, C.P. Vyasarayani, J. McPhee, Simplification and order reduction of lithium-ion battery model based on porous-electrode theory, J. Power Sources 198 (1) (2012) 329–337.

[19] R. Klein, N.A. Chaturvedi, J. Christensen, J. Ahmed, R. Findeisen, A. Kojic, Electrochemical model based observer design for a lithium-ion battery, IEEE Trans. Control Syst. Technol. 21 (2) (2013) 289–301, https://doi.org/10.1109/TCST.2011.2178604.

[20] C. Zou, C. Manzie, S. Anwar, Control-oriented modeling of a lithium-ion battery for fast charging, IFAC Proc. Vol. 47 (3) (2014) 3912–3917, https://doi.org/10.3182/20140824-6-ZA-1003.00829.

[21] R. Masoudi, T. Uchida, J. McPhee, Parameter estimation of an electrochemistry-based lithium-ion battery model, J. Power Sources 291 (2015) 215–224. https://doi.org/10.1016/j.jpowsour.2015.04.154.

[22] C.Y. Wang, W.B. Gu, Micro-macroscopic coupled modeling of batteries and fuel cells: model development, J. Electrochem. Soc. 145 (10) (1998) 3407–3417.

[23] W.B. Gu, Micro-macroscopic coupled modeling of batteries and fuel cells, J. Electrochem. Soc. 145 (10) (1998) 3418, https://doi.org/10.1149/1.1838821.

[24] W.B. Gu, C.Y. Wang, Thermal-electrochemical coupled modeling of a lithium-ion cell, Proc. ECS 99 (2000) 1–16.

[25] M. Guo, R.E. White, An approximate solution for solid-phase diffusion in a spherical particle in physics-based li-ion cell models, J. Power Sources 198 (2012) 322–328, https://doi.org/10.1016/j.jpowsour.2011.08.096.

[26] X. Hu, S. Stanton, L. Cai, R.E. White, A linear time-invariant model for solid-phase diffusion in physics-based lithium ion cell models, J. Power Sources 214 (2012) 40–50, https://doi.org/10.1016/j.jpowsour.2012.04.040.

[27] X. Hu, S. Stanton, L. Cai, R.E. White, Model order reduction for solid-phase diffusion in physics-based lithium ion cell models, J. Power Sources 218 (2012) 212–220, https://doi.org/10.1016/j.jpowsour.2012.07.007.

[28] S. Khaleghi Rahimian, S. Rayman, R.E. White, Extension of physics-based single particle model for higher charge–discharge rates, J. Power Sources 224 (2013) 180–194, https://doi.org/10.1016/j.jpowsour.2012.09.084.

[29] L. Cai, R.E. White, Reduction of model order based on proper orthogonal cecomposition for lithium-ion battery simulations, J. Electrochem. Soc. 156 (3) (2009) A154–A161.

[30] V. Ramadesigan, V. Boovaragavan, J.C. Pirkle, V.R. Subramanian, Efficient reformulation of solid-phase diffusion in physics-based lithium-ion battery models, J. Electrochem. Soc. 157 (7) (2010) A854, https://doi.org/10.1149/1.3425622.

[31] P.W.C. Northrop, V. Ramadesigan, S. De, V.R. Subramanian, Coordinate transformation, orthogonal collocation, model reformulation and simulation of electrochemical-thermal behavior of lithium-ion battery stacks, J. Electrochem. Soc. 158 (12) (2011) A1461–A1477, https://doi.org/10.1149/2.058112jes.

[32] B. Suthar, V. Ramadesigan, P.W.C. Northrop, B. Gopaluni, S. Santhanagopalan, R. D. Braatz, V.R. Subramanian, Optimal control and state estimation of lithium-ion batteries using reformulated models, in: American Control Conference, 2013, pp. 5350–5355.

[33] C.G. Mayhew, W. He, C. Kroener, R. Klein, N.A. Chaturvedi, A. Kojic, Investigation of projection-based model-reduction techniques for solid-phase diffusion in li-ion batteries, Am. Contr. Conf. (2014) 123–128.

[34] P.W.C. Northrop, B. Suthar, V. Ramadesigan, S. Santhanagopalan, R.D. Braatz, V. R. Subramanian, Efficient simulation and reformulation of lithium-ion battery models for enabling electric transportation, J. Electrochem. Soc. 161 (8) (2014) E3149–E3157, https://doi.org/10.1149/2.018408jes.

[35] M.T. Lawder, P.W.C. Northrop, V.R. Subramanian, Model-based sei layer growth and capacity fade analysis for ev and phev batteries and drive cycles, J. Electrochem. Soc. 161 (14) (2014) A2099–A2108, https://doi.org/10.1149/2.1161412jes.

[36] K. Smith, C.-Y. Wang, Solid-state diffusion limitations on pulse operation of a lithium ion cell for hybrid electric vehicles, J. Power Sources 161 (1) (2006) 628–639, https://doi.org/10.1016/j.jpowsour.2006.03.050.

[37] Y. Zeng, P. Albertus, R. Klein, N. Chaturvedi, A. Kojic, M.Z. Bazant, J. Christensen, Efficient conservative numerical schemes for 1d nonlinear spherical diffusion equations with applications in battery modeling, J. Electrochem. Soc. 160 (9) (2013) A1565–A1571, https://doi.org/10.1149/2.102309jes.

[38] P.C. Urisanga, D. Rife, S. De, V.R. Subramanian, Efficient conservative reformulation schemes for lithium intercalation, J. Electrochem. Soc. 162 (6) (2015) A852–A857, https://doi.org/10.1149/2.0061506jes.

[39] T.F. Fuller, M. Doyle, J. Newman, Simulation and optimization of the dual lithium ion insertion cell, J. Electrochem. Soc. 141 (1) (1994) 1–9.

[40] M. Doyle, Design and Simulation of Lithium Rechargeable Batteries, Ph.d. thesis, University of California, Berkeley, 08/1995.

[41] K.E. Thomas, J. Newman, R.M. Darling, Mathematical modeling of lithium batteries, in: W.A. van Schalkwijk, B. Scrosati (Eds.), Advances in Lithium-Ion Batteries, Springer US, Boston, MA, 2002, pp. 345–392, https://doi.org/10.1007/0-306-47508-1_13.

[42] J. Newman, Fortran Programs for the Simulation of Electrochemical Systems: dualfoil5.2.F, 2014. http://www.cchem.berkeley.edu/jsngrp/.

[43] D. Zhang, B.N. Popov, R.E. White, Modeling lithium intercalation of a single spinel particle under potentiodynamic control, J. Electrochem. Soc. 147 (3) (2000) 831, https://doi.org/10.1149/1.1393279.

[44] B. Rajabloo, M. Désilets, Y. Choquette, Parameter estimation of single particle model using comsol multiphysics and matlab optimization toolbox, in: Proceedings of the 2015 COMSOL Conference in Boston, 2010, pp. 1–6.

[45] M. Guo, G. Sikha, R.E. White, Single-particle model for a lithium-ion cell: thermal behavior, J. Electrochem. Soc. 158 (2) (2011) A122, https://doi.org/10.1149/1.3521314.

[46] J. Sturm, H. Ennifar, S.V. Erhard, A. Rheinfeld, S. Kosch, A. Jossen, State estimation of lithium-ion cells using a physicochemical model based extended kalman filter, Appl. Energy 223 (2018) 103–123, https://doi.org/10.1016/j.apenergy.2018.04.011.

[47] V.R. Subramanian, J.A. Ritter, R.E. White, Approximate solutions for galvanostatic discharge of spherical particles i. constant diffusion coefficient, J. Electrochem. Soc. 148 (11) (2001) E444, https://doi.org/10.1149/1.1409397.

[48] V. Boovaragavan, S. Harinipriya, V.R. Subramanian, Towards real-time (milliseconds) parameter estimation of lithium-ion batteries using reformulated physics-based models, J. Power Sources 183 (1) (2008) 361–365, https://doi.org/10.1016/j.jpowsour.2008.04.077.

[49] A.M. Bizeray, S. Zhao, S.R. Duncan, D.A. Howey, Lithium-ion battery thermal-electrochemical model-based state estimation using orthogonal collocation and a modified extended kalman filter, J. Power Sources 296 (2015) 400–412, https://doi.org/10.1016/j.jpowsour.2015.07.019. http://arxiv.org/pdf/1506.08689v1.

[50] The MathWorks, Matlab Function Reference. https://de.mathworks.com/?s_tid=gn_logo 2017.

[51] COMSOL Multiphysics, The Batteries & Fuel Cells Module User's Guide, 2017. https://www.comsol.com/.

[52] D. Bernardi, E. Pawlikowski, J. Newman, A general energy balance for battery systems, J. Electrochem. Soc. 132 (1985) 5–12.

[53] C. Campestrini, T. Heil, S. Kosch, A. Jossen, A comparative study and review of different kalman filters by applying an enhanced validation method, J. Energy Storage 8 (2016) 142–159, https://doi.org/10.1016/j.est.2016.10.004.

[54] Z. Wei, T.M. Lim, M. Skyllas-Kazacos, N. Wai, K.J. Tseng, Online state of charge and model parameter co-estimation based on a novel multi-timescale estimator for vanadium redox flow battery, Appl. Energy 172 (2016) 169–179, https://doi.org/10.1016/j.apenergy.2016.03.103.

[55] I. Zilberman, A. Rheinfeld, A. Jossen, Uncertainties in entropy due to temperature path dependent voltage hysteresis in li-ion cells, J. Power Sources 395 (2018) 179–184, https://doi.org/10.1016/j.jpowsour.2018.05.052.

[56] The MathWorks, Mathworks' Documentation on the Mkpp Function. https://de.mathworks.com/help/matlab/ref/mkpp.html 2018.

[57] F. Zhang, M.M.U. Rehman, H. Wang, Y. Levron, G. Plett, R. Zane, D. Maksimovic, State-of-charge estimation based on microcontroller-implemented sigma-point kalman filter in a modular cell balancing system for lithium-ion battery packs, in: 2015 IEEE 16th Workshop on Control and Modeling for Power Electronics (COMPEL), 2015, pp. 1–7, https://doi.org/10.1109/COMPEL.2015.7236525.

[58] J. Li, Adaptive Model-Based State Monitoring and Prognostics for Lithium-Ion Batteries, Dissertation, University of Ulm, Ulm, 05.08.2016.

[59] Jorge V Barreras, Federico Ferrari, David A Howey, Development of Diagnosis Algorithms for Li-Ion Batteries, Implementation in a Microcontroller and Testing in an Hardware-In-The-Loop Simulator, University of Oxforddoi:10.13140/RG.2.2.26819.09768.

[60] R.E. Kalman, Kalman, (1960) - contributions to the theory of optimal control, Bol. Soc. Mat. Mex. 1 (5) (1960) 102–119.

[61] R.E. Kalman, A new approach to linear filtering and prediction problems, J. Basic Eng. 82 (1) (1960) 35, https://doi.org/10.1115/1.3662552.

[62] R.E. Kalman, R.S. Bucy, New results in linear filtering and prediction theory, J. Basic Eng. 83 (1) (1961) 95, https://doi.org/10.1115/1.3658902.

[63] The MathWorks, Solvers for Real-Time Simulation. https://www.mathworks.com/help/physmod/simscape/ug/solvers-for-real-time-simulation.html?searchhighlight=ode14x&s_tid=doc_srchtitle.

[64] J. Mao, W. Tiedemann, J. Newman, Simulation of temperature rise in li-ion cells at very high currents, J. Power Sources 271 (2014) 444–454, https://doi.org/10.1016/j.jpowsour.2014.08.033.

[65] J. Mao, W. Tiedemann, J. Newman, Simulation of li-ion cells by dualfoil model under constant-resistance load, ECS Trans. 58 (48) (2014) 71–81, https://doi.org/10.1149/05848.0071ecst.

[66] L.F. Shampine, M.W. Reichelt, The matlab ode suite, SIAM J. Sci. Comput. 18 (1) (1997) 1–22, https://doi.org/10.1137/S1064827594276424.

[67] L.F. Shampine, M.W. Reichelt, J.A. Kierzenka, Solving index-1 daes in matlab and simulink, SIAM Rev. 41 (3) (1999) 538–552, https://doi.org/10.1137/S003614459933425X.

[68] The MathWorks, Mathworks' Documentation on 'solve Stiff Differential Equations and Daes — Variable Order Method'. https://www.mathworks.com/help/matlab/ref/ode15s.html 2018.

[69] The MathWorks, Mathworks' Documentation on Sparse Matrix Creation. https://de.mathworks.com/help/matlab/ref/sparse.html 2018.

[70] W. Klopfenstein, Numerical differentiation formulas for stiff systems of ordinary differential equations, RCA Rev. 32 (1971) 447–462.

[71] P. Amestoy, A. Buttari, A. Guermouche, J.-Y. L'Excellent, B. Ucar, Mumps: Multifrontal Massively Parallel Sparse Direct Solver - Version 5.1.2, 2017. http://mumps.enseeiht.fr/.

[72] The MathWorks, Mathworks' Documentation on the A/b Function. https://de.mathworks.com/help/matlab/ref/mldivide.html 2018.

[73] ARM, Cortex Microcontroller Software Interface Standard (Cmsis) Library. https://developer.arm.com/embedded/cmsis.

[74] STMicroelectronics, Stm32cubemx for Stm32 Configuration and Initialization C Code Generation, STM Technical Data, 2018. https://www.st.com/content/ccc/resource/technical/document/user_manual/10/c5/1a/43/3a/70/43/7d/dm00104712.pdf/files/dm00104712.pdf/jcr:content/translations/en.dm00104712.pdf.

[75] The MathWorks, Mathworks' Documentation on Spline Interpolation Functionality. https://de.mathworks.com/help/matlab/ref/spline.html 2018.

[76] The MathWorks, Mathworks' Documentation on the C-Code Export Function. https://www.mathworks.com/help/ecoder/examples/exporting-functions.html 2018.

[77] IEEE, Ieee Standard for Floating-point Arithmetic. doi:10.1109/IEEESTD.2008.4610935.

[78] M. Neher, Descriptive Higher Mathematics for Engineers and Scientists, Lehrbuch, Springer Vieweg, Wiesbaden, 2018. http://www.springer.com/de/book/9783658194192.

[79] J. Newman, Numerical solution of coupled, ordinary differential equations, Ind. Eng. Chem. Fundam. 7 (3) (1968) 514–517, https://doi.org/10.1021/i160027a025.

[80] G. Peters, J.H. Wilkinson, On the stability of gauss-Jordan elimination with pivoting, Commun. ACM 18 (1) (1975) 20–24, https://doi.org/10.1145/360569.360653.

[81] A.R. Curtis, The Facsimile Numerical Integrator for Stiff Initial Value Problems, Atomic Energy Research Establishment (AERE-R-9352), 1979, pp. 1–42.

[82] T. Arens, F. Hettlich, C. Karpfinger, U. Kockelkorn, K. Lichtenegger, H. Stachel, Mathematics, second ed., Spektrum Akad. Verl., Heidelberg, 2010.

[83] Y. Li, M. Vilathgamuwa, T. Farrell, S.S. Choi, N.T. Tran, J. Teague, A physics-based distributed-parameter equivalent circuit model for lithium-ion batteries, Electrochim. Acta 299 (2019) 451–469, https://doi.org/10.1016/j.electacta.2018.12.167.

[84] Z. Wei, C. Zou, F. Leng, B.H. Soong, K.-J. Tseng, Online model identification and state-of-charge estimate for lithium-ion battery with a recursive total least squares-based observer, IEEE Trans. Ind. Electron. 65 (2) (2018) 1336–1346, https://doi.org/10.1109/TIE.2017.2736480.

[85] Z. Chu, X. Feng, L. Lu, J. Li, X. Han, M. Ouyang, Non-destructive fast charging algorithm of lithium-ion batteries based on the control-oriented electrochemical model, Appl. Energy. doi:10.1016/j.apenergy.2017.03.111.

[86] M. André, The artemis european driving cycles for measuring car pollutant emissions, Sci. Total Environ. 334–335 (2004) 73–84, https://doi.org/10.1016/j.scitotenv.2004.04.070.

[87] L.O. Valoen, J.N. Reimers, Valoen_transport properties of lipf6-based li-ion battery electrolytes, J. Electrochem. Soc. 152 (5) (2005) A882–A891.

[88] C.M. Long, M.A. Nascarella, P.A. Valberg, Carbon black vs. black carbon and other airborne materials containing elemental carbon: physical and chemical distinctions, Environ. Pollut. 181 (2013) 271–286, https://doi.org/10.1016/j.envpol.2013.06.009.

[89] G. Liu, H. Zheng, A.S. Simens, A.M. Minor, X. Song, V.S. Battaglia, Optimization of acetylene black conductive additive and pvdf composition for high-power rechargeable lithium-ion cells, J. Electrochem. Soc. 154 (12) (2007) A1129, https://doi.org/10.1149/1.2792293.

[90] R. Dash, S. Pannala, Theoretical limits of energy density in silicon-carbon composite anode based lithium ion batteries, Sci. Rep. 6 (2016) 27449, https://doi.org/10.1038/srep27449.

[91] R. Jung, M. Metzger, F. Maglia, C. Stinner, H.A. Gasteiger, Oxygen release and its effect on the cycling stability of lini x mn y co z o 2 (nmc) cathode materials for li-ion batteries, J. Electrochem. Soc. 164 (7) (2017) A1361–A1377, https://doi.org/10.1149/2.0021707jes.

[92] H.-J. Noh, S. Youn, C.S. Yoon, Y.-K. Sun, Comparison of the structural and electrochemical properties of layered li[nixcoymnz]o2 (x = 1/3, 0.5, 0.6, 0.7, 0.8 and 0.85) cathode material for lithium-ion batteries, J. Power Sources 233 (2013) 121–130, https://doi.org/10.1016/j.jpowsour.2013.01.063.

[93] M. Doyle, Y. Fuentes, Computer simulations of a lithium-ion polymer battery and implications for higher capacity next-generation battery designs, J. Electrochem. Soc. 150 (6) (2003) A706, https://doi.org/10.1149/1.1569478.

[94] D. Andre, S.-J. Kim, P. Lamp, S.F. Lux, F. Maglia, O. Paschos, B. Stiaszny, Future generations of cathode materials: an automotive industry perspective, J. Mater. Chem. 3 (13) (2015) 6709–6732, https://doi.org/10.1039/C5TA00361J.

[95] D.A.G. Bruggeman, Calculation of different physical constants in heterogenous substances, Ann. Phys. 416 (7) (1935) 636–664, https://doi.org/10.1002/andp.19354160705.

[96] S. Arrhenius, About the reaction rate during acid induced inversion of sucrose, Z. Phys. Chem. 4 (1). doi:10.1515/zpch-1889-0116.

4 State-Estimation of Lithium-Ion Batteries using Physicochemical Models
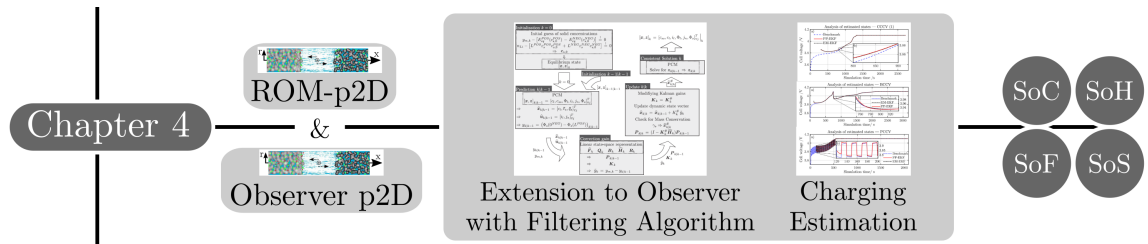

Figure 4.1: Outline of chapter 4.

The article titled *State estimation of lithium-ion cells using a physicochemical model based extended Kalman filter* is presented within this section. Fig. 4.1 refers to the thesis outline shown in section 1.6 and summarizes the content of the presented paper within this section.

4.1 State-Estimation Methods combining Model and Filtering Approaches

After discussing the suitability of physicochemical models to accurately describe the behavior of LIBs and showing the suitability for embedded systems, the extension of ROM-p2Ds to observer models is presented as a last step for the physicochemical model based state-estimation process. For observer models, a recursive formulation of the p2D is required, which calculates the inherent state of the LIB based on input signals such as cell voltage, current flow and surface temperature derived from the physically motivated model structure. Uncertainties in the p2D parametrization, modeling approach, such as neglecting inhomogeneity within a LIB, and the noise of the measured input signals typically lead to a discrepancy between the model predicted and the monitored/measured states of the battery. To ease the deficiency between prediction and measurement, filtering approaches are typically used to correct the predicted state in reference to the input signal. Most commonly KF approaches are used for model based state-estimation of LIBs [114, 121]. In the following section, the extension of suitable ROM-p2Ds to observer models including a linear state-space representation is presented together with an EKF approach to enable a physicochemical model based state-estimation of LIBs.

4.2 Extension of Physicochemical Models to Observer Algorithms

Two different reduction methods are chosen to develop two variants of ROM-p2Ds to limit the computational effort and to enable for a recursive formulation for developing the observer models. The reduction methods incorporate either a polynomial profile [136] or an eigenfunction method [137] to approximate the partial differential equation of the solid diffusion process. The solid diffusion equation dominates the computational complexity due to the node wise calculation in each electrode and its numerical reduction or approximation is typically used to develop a computationally efficient ROM-p2D. The emerging model errors – via applying the reduction schemes – are referenced to the original p2D using the Duhamel Superposition Integral [94] as approximation of the solid diffusion equation. The evaluation for an exemplary graphite type mesocarbon microbeads (MCMB)/LCO LIB revealed benefits for the polynomial approach under CC loads and in general a faster calculation than the eigenfunction method, which shows a higher accuracy under dynamic current loads. The extension to observer models requires a linearized state-space representation, which is based on the fully-spatially-resolved ROM-p2D. The combination with an EKF algorithm incorporates the conservation of lithium mass to increase the estimation accuracy and conserves the states physical interpretation along with their spatial distribution. Initialization issues are addressed via an iterative solving to match the input and the predicted cell voltage under conserving lithium mass in the electrodes and the electrode specific equilibrium potential states. As a result, robust and fast reduction of residual errors of cell voltage and SoC appear under a variety of charging scenarios incorporating CC, multi-step BC and PC loads. Exemplary, the estimation process is capable of reducing the cell voltage error below $1\,\text{mV}$ within $30\,\text{s}$ at an initial error of $42.2\,\%$ SoC in the 4C-CC charging scenario at $25\,°\text{C}$ ambient temperature. Overall, fast and robust regression of the SoC error appears and the proper estimation of the anode potential can be used for fast charging strategies to avoid unwanted lithium plating and prevent an early decay of SoH on the long term. Using both global and local estimated states enables a more precise estimation of SoF and SoS, which is not possible with state-of-the-art state-estimation techniques such as ECM based methods.

The presented observer models are implemented in MATLAB and calculated on a desktop computer. As the extension including the linearized state-space representation and the EKF are of lower mathematical complexity compared to the p2D structure, an implementation into embedded systems is most likely suitable and should neither overload the memory nor exceed the computational resources of a MC. The embedded implementation of the observer models should be the content of future work as the necessary fundamental model structure have already been developed within this thesis.

Author contribution   Johannes Sturm initiated and developed the idea to compare two different observer p2Ds and correlated their suitability towards the operational scenario via the gained accuracy and the computation speed. Hassen Ennifar developed the MATLAB codes for the p2Ds and their extension to the observer models including an EKF. Simon V. Erhard initiated the idea of using physicochemical models for state-estimation purposes, supported the development of the observer models, and helped to set a suitable storyline for the presented article. Alexander Rheinfeld helped to derive the key findings of the presented work and Stephan Kosch helped with the review of different numerical reduction methods for the p2D. The simulation data was analyzed and interpreted by Johannes Sturm. The manuscript was written by Johannes Sturm and edited by Hassen Ennifar, Simon V. Erhard, Alexander Rheinfeld, Stephan Kosch and Andreas Jossen. All authors discussed the data and commented on the results.

Publication notes   The article [99] titled *State estimation of lithium-ion cells using a physico-chemical model based extended Kalman filter* is published in the Journal Applied Energy and parts of the article were presented at the *15th Symposium on Modeling and Experimental Validation of Electrochemical Energy Devices* in Aarau (Switzerland) in April 2018. A data repository with the most important experimental and simulation based results is published at the platform 4TU.Centre for Research Data (Netherlands) [207].

State estimation of lithium-ion cells using a physicochemical model based extended Kalman filter

Johannes Sturm, Hassen Ennifar, Simon Vincent Erhard, Alexander Rheinfeld, Stephan Kosch, Andreas Jossen

Permanent weblink:
https://doi.org/10.1016/j.apenergy.2018.04.011
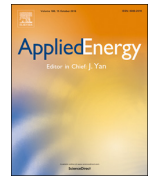
State estimation of lithium-ion cells using a physicochemical model based extended Kalman filter

J. Sturm*, H. Ennifar, S.V. Erhard, A. Rheinfeld, S. Kosch, A. Jossen

Technical University of Munich (TUM), Institute for Electrical Energy Storage Technology (EES), Arcisstr. 21, 80333 Munich, Germany

HIGHLIGHTS

- Two different recursive state-observer models using reduced p2D.
- Influence of reduction schemes analyzed for estimation process.
- Adjusted finite volume method for improved robustness.
- Modified EKF uses improved initialization and mass conservation.
- Estimation accuracy analyzed for both global and local states.

ARTICLE INFO

ABSTRACT

Two time-varying linear state-space representations of the generally accepted physicochemical model (PCM) of a lithium-ion cell are used to estimate local and global states during different charging scenarios. In terms of computational speed and suitability towards recursive state observer models, the solid-phase diffusion in the PCM of an exemplaric MCMB/LiCoO$_2$ lithium-ion cell is derived with the aid of two different numerical reduction methods in the form of a Polynomial Profile and an Eigenfunction Method. As a benchmark, the PCM using the original Duhamel Superposition Integral approximation serves for the comparison of accuracy and computational speed. A modified spatial discretization via the finite volume method improves handling of boundary conditions and guarantees accurate simulation results of the PCM even at a low level of spatial discretization. The Polynomial Profile allows for a significant speed-up in computational time whilst showing a poor prediction accuracy during dynamic load profiles. The Eigenfunction Method shows a comparable accuracy as the benchmark for all load profiles whilst resulting in an even higher computational effort. The two derived observer models incorporate the state-space representation of the reduced PCM applying both the Polynomial and Eigenfunction approach combined with an Extended Kalman Filter algorithm based on a novel initialization algorithm and conservation of lithium mass. The estimation results of both models show robust and quick reduction of the residual errors for both local and global states when considering the applied current and the resulting cell voltage of the benchmark model, as the underlying measurement signal. The carried out state estimation for a 4C constant charge current showed a regression of the cell voltage error to 1 mV within 30 s with an initial SOC error of 42.4% under a standard deviation of 10 mV and including process noise.

1. Introduction and literature review

The high energy and power density compared to other battery chemistries [1] established the lithium-ion battery as the state of the art technology for electrical energy storage systems for a wide application field, ranging from small electronic devices up to large scale applications such as stationary storage systems or automotive battery packs [2]. However, the manufacturing costs are still challenging [3], which slows down a market penetration to an economically competitive energy storage system especially in the automotive sector [3].

To address this circumstance, current efforts [4] aim to push the price below US$200 per kW h or even lower for lithium-ion cells [2] within the next few years. Other estimations are cautiously optimistic and presume lower reduction of the production costs [5]. Besides the development of enhanced battery materials such as the active materials, the electrolyte, the metal collector foils and the separator [6] as well as the economical factors through increased production volumes [7], the size of lithium-ion cells [2] is regarded to be a substantial factor in

---

order to decrease the production costs. The size of the cell is enlarged either by longer electrodes or by thicker coatings of composite material. Compared to small-sized cells, the application of large-sized (*i.e.* >10 Ah) [8] cells offers potential towards the reduction of cost per kW h [3]. This comes along with an influence on the cell performance based on dynamics [9] and inhomogeneity effects [10] within the cell. With increasing the cell's size, safety hazards may also rise as the convertable amount of energy during a failure scenario of a single cell correlates directly to the cell size. Maximizing the efficiency and minimizing safety threats [1] for a single cell or a whole battery pack consisting of larger sized cells, brings up new challenges for battery management systems (BMS). Battery monitoring algorithms mainly focus on an accurate prediction of the state of charge (SOC), the state of health (SOH), the capacity and impedance of a cell in order to ensure all operations within its safe operating area (SOA) by means of BMS control strategy [11]. Size effects must be considered for an accurate observing and controlling of cells such as increased inhomogeneities for the local current, concentration, potentials and temperature within the cell. Since state of the art model-based monitoring algorithms incorporate non-physicochemical models such as the equivalent circuit model (ECM), besides the cell's voltage, surface temperature and applied current, no information on the local scale can be incorporated for state estimation purposes. Falsely predicted SOC of a lithium-ion cell increases the threat of using the cell out of the SOA and local harming processes [12] may occur during operation. Considering electric vehicles, a more simple but very meaningful worst-case scenario would be a falsely predicted available range based on SOC and temperature estimation considering no local effects within large-sized cells, which would compound the issue of range anxiety of the customer. A more profound and mechanistic model for the lithium-ion cell which offers information on the local scale is the physicochemical model (PCM), commonly known as pseudo two-dimensional model [13]. The generally more complex and also more inaccurate model compared to the strictly empirical ECM offers great potential to ease the problems accompanied with inhomogeneities in large sized cells. By reformulating the underlying equations, state observer models can be derived, which are able to incorporate information on the local scale to enhance the accuracy of monitoring lithium-ion cell performance during challenging tasks such as fast charging.

In this work, the PCM is used for implementation of two different recursive state observer models to show the suitability for accurate state monitoring of lithium-ion batteries under varying load scenarios. To the author's best knowledge, the presented work is the first attempt to estimate local states of a fully-spatially-resolved PCM solved via the finite volume method (FVM) using a modified extended Kalman filter (EKF) which conserves lithium mass and the states' physical interpretation along with their spatial distribution.

1.1. Models for monitoring lithium-ion batteries

The literature review reveals plenty of models to describe and predict the behaviour of lithium-ion batteries. In the following part, the decision for the PCM model is outlined in comparison to other, widely used models of lithium-ion batteries in the application field of battery monitoring algorithm.

Artificial neural networks (ANN) models incorporate mathematical models which reduce the error between input and output signal using weighting and cost functions, which are adjusted by training data. To parameterize an ANN, all battery operation areas need to be covered and the training process becomes a time and cost-intensive task. The work of Cai et al. [14] deals with a model for a nickel-metal hydride battery and uses the applied current and the cell voltage as input signals. Since a trial of different functions of these input signals is needed, a dramatical increase of the computational costs is seen. The authors aspire to a more computationally efficient model incorporating a mechanistic description of the electrochemical behaviour of a lithium-ion

cell and thus neglect this type of model for this work.

Besides ANN models, the equivalent circuit model (ECM) is widely used in research and application field of the BMS for monitoring the global states of a lithium-ion battery. The work of Hu et al. [15] presents a variety of different ECMs and the reader is referred to this publication for more profound information. In short, the ECM is an empirical, mathematical approach which requests little computational power [11], therefore less simulation time and can be easily parameterized via experimental data of the cell [9]. The main drawback of this approach is its limited validity beyond the chosen parameterization window as the model parameters are fitted to experimental data under specific operating conditions [9] and the model itself is not based on general physical or chemical principles governing the performance of electrochemical cells. In automotive applications, the extending operating window in terms of temperature, voltage and applied current may lead to false predictions and subsequent reduction of lifetime, safety and performance. Since the efforts of Plett et al. which firstly used a non-linear Kalman filter (*i.e.* EKF) [16] to estimate the cell's SOC and subsequently a Sigma-Point Kalman Filter [17] to further increase the accuracy of the estimated global states of the cell, the application of filter and observer techniques is widely used in order to gain accurate monitoring of lithium-ion batteries via the ECM. Other works focussing on the same problem such as Zhang et al. [18] fitted the ECM parameters based on electrochemical properties and showed a distinct improvement compared to commonly used parameterization methods.

Most recent work of Wei et al. [19] seem to further ease the inaccuracy as well via data-driven, online adapted ECM parameterization. Nevertheless, since the ECM still lacks of a mechanistic description of the cell's electrochemical behaviour and no local states in the lithium-ion battery can be estimated, this model is not suitable for this work.

The newman-type PCM [13] – often referenced as pseudo two-dimensional model – correlates the fundamental principles of transport phenomena, thermodynamics and electrochemistry on a macroscopic (*i.e.* electrolyte domain) and microscopic (*i.e.* particle domain) scale for a lithium-ion battery [9]. Compared to the strictly empirical ECM, the mechanistic PCM not only consumes more computational time based on its complexity but also requires vast parameterization effort due to the amount of more than 30 parameters and the nature of the parameters such as transport properties, electrode's morphology or reaction rate constants. The comparably high computational demand and parameterization effort results in a model which then shows superior validity over a wider range of applications and offers the incorporation of further physics-based processes such as aging phenomena [20], volume expansion [21] and safety related effects [22]. Large-sized cells and increased coating thicknesses of the electrodes inevitably promote gradients in potential and concentration, which can be simulated by the PCM. Based on the growing importance of localized cell utilization, the PCM is the model of choice in order to describe the performance of future cell generations accurately enough.

1.2. Recursive state observer models using PCM

The complexity of the parameterization for a PCM recommends an application of filter techniques to iteratively reduce the deviance between simulated and measured states of a lithium-ion battery. Only a few research efforts [23–25] are dealing with recursive state observer models using the PCM [26], which shows the necessity of our work.

Smith et al. [23] reduced the PCM to a single input multiple output model, which is linearized at 50% SOC. Based on this model, a linear Kalman filter was implemented for the estimation of local potentials, concentration gradients and the SOC from the applied current and cell voltage measurements. The estimation for a 6 Ah lithium-ion cell shows good performance within a SOC range from 30% to 70% by using 2 A and 25 mV process noise for the applied current and the cell voltage. The computational efficiency is comparable to the performance of ECMs [23], however, the filter performance beyond 70% SOC could be

improved. In this work, we show a robust and accurate estimation results of two state observer models until the fully charged state of a lithium-ion cell.

In the work of Domenico et al. [24], a simplified PCM was combined with an EKF. The simplification yields to significant loss of representativity of a lithium-ion cell but was investigated in this publication towards its feasibility in observer applications. Regarding the cell voltage as measured value, the focus lied on the estimation of the SOC which revealed excellent performance under various test scenarios. However, this work lacks an investigation of local states such as the potential drop between the electrolyte and the electrodes, which is an indicator for aging phenomena [27].

Regarding aging phenomena such as lithium-plating during charging processes, the work of Klein et al. [28] showed a PCM based observer model to identify the optimal charging strategy referring to the local side-reaction overpotential in the anode and the cell temperature. Since the electrolyte concentration was constant a certain loss of accuracy has to be considered. In this work, the electrolyte concentration is calculated via the fundamental mass balance equation of the PCM and gains a more accurate state-estimation for the lithium-ion battery. The publication of Bizeray et al. [25] was the first approach dealing with a fully-spatially-resolved PCM incorporating Chebyshev orthogonal collocation method using an EKF algorithm. The local states are corrected via measured values of cell voltage, applied current and surface temperature. The error in measured cell voltage and surface temperature is set to 10 mV and 0.5 K, respectively. The approach showed robust behavior regarding falsified initialization of SOC (30%) and less than 1% error for the anode bulk SOC after 185 s estimation time for a 4C constant current discharge scenario. The publication lacks a detailed analysis of the spatial distribution of the local states and the total number of differential algebraic equations (DAEs) was not outlined. Since the microscopic domain is discretized with 15 nodes, the number of the overall DAE increases and conservation of lithium mass [29] is missing in the EKF algorithm in order to gain a more robust and more accurate state-estimation.

In this work, the authors present the first approach of a fully-spatially-resolved PCM solved by the FVM using a modified EKF algorithm accounting for conservation of lithium mass. This allows for conserving all the properties of the modeled dynamics over a wide operating window with no further assumptions such as constant concentration in the electrolyte [28]. Particular attention lies on the numerical reduction of the microscopic particle domain to limit the total number of DAEs and the modification of the FVM in terms of accurate handling of boundary conditions of the PCM with a low number of discretization elements.

1.3. Application of observer models for charging scenarios

The charging time is majorly affecting the customers' experience of any battery powered device. Improved battery monitoring algorithms will further help to correctly estimate not only global but also local states of the cell which is believed to allow for maximizing the charging current whilst monitoring and controlling accompanied safety risks. Hazardous processes inside the cell during charging scenarios were indentified to be lithium-plating [12] at the interface of anode and separator. With the aid of the estimated local states in the PCM, the overpotential for this side reaction can be described as follows:

$$\eta_{lithium-plating} = (\Phi_s - \Phi_l)_{x=L^{NEG}, t_k} \leqslant 0 \tag{1}$$

The potential drop $(\Phi_s - \Phi_l)$ between the solid (i.e. electrode) and the liquid phase (i.e. electrolyte) at the anode-separator interface ($x = L^{NEG}$) at a certain time (t_k) holds as indicator for possible lithium plating when the state is 0 or becomes even negative [27]. The aforementioned publication of Klein et al. [28] uses an algebraic constraint for the side-reaction overpotential within the anode, which could be

estimated with a residual error of 15 mV. In contrast to the observer model of Klein et al. [28], the concentration within the electrolyte is not assumed to be constant and improved accuracy of the gained simulation results is expected in this work. The two observer models in this work focus on the estimation accuracy and speed especially for the local states such as the characteristic potential drop in Eq. (1) in order to enable for a more precise indication of critical side reactions during charging such as lithium plating.

2. Methodology

2.1. Physicochemical model

The PCM describes the lithium-ion cell on the macroscopic scale (i.e. x-dimension) via two porous insertion electrodes, a single insulating porous separator and the electrolyte. The porous electrodes are composed of active material, additives (e.g. carbon black) and binder, coated on a current collector foil [30], whereby the latter is neglected for the modeling approach in this work due to its in orders of magnitude higher electrical conductivity compared to the remaining materials. The additional dimension on microscopic scale (i.e. r-dimension) describes the particles of the active material, which is often referenced as "pseudo" dimension of the PCM. In Fig. 1, the electrochemical cell with MCMB/LiCoO$_2$ as active material pairing is schematically shown with the adjacent copper/aluminium current collector foils.

The underlying processes of charge and mass transport as well as electrode kinetics are mathematically described by the model in accordance with Doyle et al. [13]. The active material in the solid phase is modeled via symmetric, identically-sized spheres where the diffusion equation is implemented. The liquid phase describes the electrolyte. The coupling between the phases is implemented via mass and charge balances as well as the electrode kinetics, which results in a potential drop between the two phases [30]. A more precise description of the PCM is presented elsewhere [31] and the reader is referred to this work for more information, but for the readers' convenience the governing equations are summarized in the appendix (see Table 10). In addition, the related boundary conditions are depicted in Table 11 included in the appendix. In this work, the temperature dependency of the reaction kinetics, thermodynamics and the transport parameters in solid and liquid phase of the PCM is implemented and the temperature is calculated via the fundamental energy balance according to the work of Bernardi et al. [32]. For all simulations in this work, the ambient temperature was set to 25°C. The temperature of the cell is not included in the dynamic state vector but calculated at every time step. In sum, the PCM reduces the thermal-electrochemical performance of a lithium-ion cell to a dynamic state vector of

$$\mathbf{x}(x,t) = [\, c_l(x,t) \quad c_{ss}(x,t) \quad \Phi_l(x,t) \quad i_l(x,t) \quad j_n(x,t) \quad \Phi_s(x,t)\,]^T \tag{2}$$

The state vector includes the concentrations (c_l, c_{ss}) and potentials (Φ_l, Φ_s) in solid and liquid phase, the macroscopic current density in the electrolyte (i_l) and the molar flux (j_n). One objective of this work is the development of a robust discretization of the PCM in time and space and the reduction of the solid-phase diffusion partial differential equation (PDE) in a form, which enables for a computational efficient and accurate model of a lithium-ion battery using a low number of spatial discretization elements and can be used for recursive state observer models.

2.1.1. Parameterization

The parameterization of the PCM includes thermodynamic, kinetic, transport and geometrical parameters [30]. The basic parameters were adopted from the publications of Mao et al. [33], which included a MCMB/LiCoO$_2$ cell with 1 M LiPF$_6$ in 1:1 EC/DMC electrolyte. The film resistance accounting for deposit layers on the surface of the MCMB particles was included in the PCM setup. The activity coefficient was
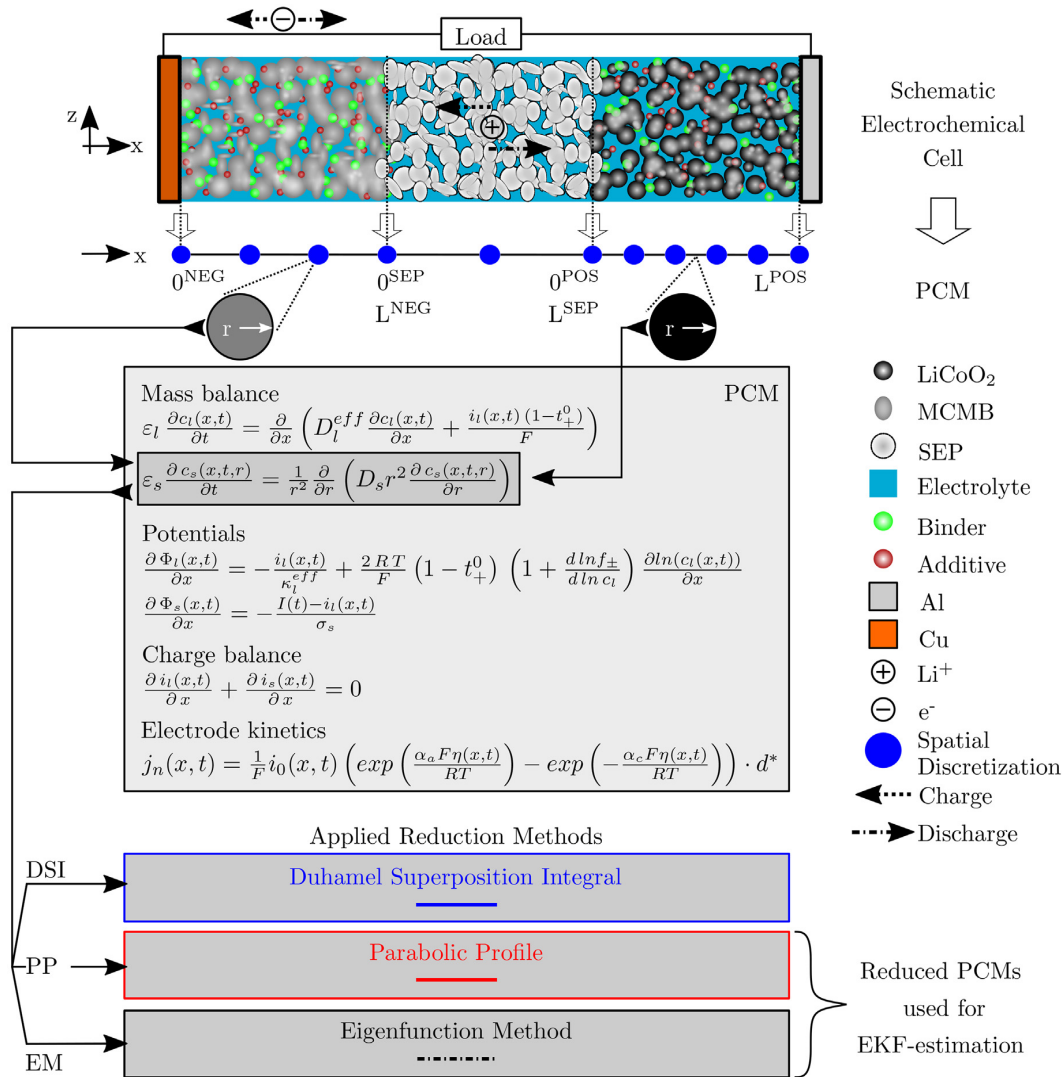
Fig. 1. Schematic representation of a MCMB/LiCoO$_2$ lithium-ion cell shown in the upper part with the subsequent pseudo two-dimensional reduction to the PCM [13]. The fundamental model equations are depicted for the solid (*i.e.* active material) and liquid (*i.e.* electrolyte) phase, including three different numerical approximation methods (*i.e.* DSI, PP and EM) for the solid-phase diffusion. The PP- and EM-approach are used for the development of the recursive state observer models using the EKF-algorithm.

adopted from the parameter set of Mao et al. [33] and thus set to zero. The temperature dependency is applied to the parameters of the diffusion coefficient in the active materials and the electrolyte, the reaction rate constants, the ionic conductivity and the film resistance at the anode surface. In the appendix of this work, the summary of the basic PCM parameters is given in Table 12 and the thermal parameters are depicted in Table 13. In terms of the lithium mass conservation in the EKF used in the observer models, the total lithium in the solid phase is calculated to 1.7040 mol m^{-2}. The initial concentrations are defined as the reference concentration (c_{ref}) for the electrolyte and according to the stoichiometric coefficient for the active materials depending on the regarded charge or discharge scenario. Note, that the initial stoichiometric coefficients for the charging scenarios were set to 0.1 and 0.96 in the anode and cathode domain, respectively.

2.1.2. Discretization via FVM

The DUALFOIL model is taken as reference for the PCM in developed in this work, which was the latest release [22] of the PCM embedded in FORTRAN of the Newman research group [34]. The fundamental equations (see Table 10) and the boundary conditions (see Table 11) of the PCM form a non-linear DAE system with the six aforementioned state variables (see Eq. (2)). The DAE consists of the two PDEs for the mass balances in solid and liquid phase, three ordinary differential equations (ODEs) for the charge balance and the definition of the potentials as well as a single algebraic equation for the electrode kinetics. The non-linearity is caused by the Butler-Volmer equation to describe the electrode kinetics as well as the temperature and concentration dependent physical properties of the cell components [30]. As the non-linear DAE cannot be solved analytically, numerical

Table 1
Spatial discretization for the non-linear DAE of the PCM using FDM with FVM formulation [34].

Equation	Phase	Domain	Orientation
Mass balance	solid	MCMB/LiCO$_2$	[a]
	liquid	MCMB/SEP/LiCO$_2$	Central Diff.
Potential	solid	MCMB	Backward Diff.
		LiCO$_2$	Forward Diff.
	liquid	MCMB/SEP/LiCO$_2$	Forward Diff.
Charge balance	liquid	MCMB	Forward Diff.
		SEP	Conservation
		LiCO$_2$	Backward Diff.
Electrode kinetics	solid + liquid	MCMB/LiCO$_2$	[b]

Diff. = Difference.
  [a] Numerical reduction method.
  [b] Algebraic equation.

Table 2
Linearization of Kalman Filter algorithm [42].

Extension for *non-linear* DAE
$\mathbf{f}(x_k, z_k, u_k) \approx \mathbf{f}(\hat{x}_k, z_k, u_k) + \hat{\mathbf{F}}_k (x_k - \hat{x}_k)$
$\mathbf{h}(x_k, z_k, u_k) \approx \mathbf{h}(\hat{x}_k, z_k, u_k) + \hat{\mathbf{H}}_k (x_k - \hat{x}_k)$
$\hat{\mathbf{F}}_k = \dfrac{\partial \mathbf{f}(x_k, z_k, u_k)}{\partial x_k}\bigg|_{x_k = \hat{x}_k}$
$\hat{\mathbf{H}}_k = \dfrac{\partial \mathbf{h}(x_k, z_k, u_k)}{\partial x_k}\bigg|_{x_k = \hat{x}_k}$

approximations in form of linearization schemes are used which include discretization methods in time and space. For all state variables, the time discretization is implemented by the Crank-Nicolson formulation [30]. The spatial discretization over the three domains differs for each equation and is explained more in detail. The numerical approximation within both electrode and the separator domain is based on the FVM, which uses Gauss' theorem to approach a state variable within a specified control volume [35]. The implementation itself uses the finite difference method (FDM) with differently oriented discretization directions. Regarding the associated boundary conditions within each domain and the type of the equation, the chosen approximation method and its orientation for each equation is depicted in Table 1. The number of discretization elements were set to 3, 2 and 5 in the anode, separator and cathode domain, respectively. This corresponds to characteristic spatial discretization lengths of 24, 12.5 and 10 µm. In this work, we used only equidistant distribution for the 3-2-5 discretization and thus the spatial discretization length is constant in each domain. Table 14 is attached in the appendix for the readers' convenience, which shows the FDM implementation using the FVM formulation of the mass balance in the liquid phase and the related three ODEs for the definition of the potentials as well as the charge balance at the anode-separator interface ($x = L^{NEG}$) (see Table 2).

An approximation via FDM for the mass balance in the solid phase would increase the number of DAE since at every node in the electrode domains, a single discretized solid phase diffusion PDE must be taken into account. In order to save computational time and to limit the number of the DAE, this equation is approximated via three different numerical reduction methods and will be discussed later in this work. Note that the total number of DAE (n_{DAE}) is defined by the chosen number of spatial discretization elements (n_j) in each domain and summarizes to

$$n_{DAE} = (n^{NEG} + n^{POS} + 2) \cdot 6 + (n^{SEP} - 1) \cdot 3 \qquad (3)$$

Looking into the discretization scheme for solving the ionic current density, the internal boundary conditions at the separator interfaces to the anode and cathode are already occupied (see Table 11 – "Charge

Balance") and the discretization orientation is set to forward and backward, respectively. Note, that the adjacent boundary conditions at the current collector interface set the macroscopic ionic current density to zero and are fully respected by the chosen discretization scheme. To the authors' best knowledge, the referenced PCM embedded in FORTRAN includes similar boundary conditions at the interfaces and the adjacent boundaries. In addition, a second model to compare the simulation results was taken into account, namely the lithium-ion battery interface embedded in the commercial FEM-solver COMSOL Multiphysics®. As this model is based on the DUALFOIL model as well, the same boundary conditions are implemented in this model.

In this work the robustness of the developed models is shown, guaranteeing accurate handling of these internal and external insulating boundary conditions with a low number of spatial discretization elements (3-2-5) and the accuracy of the gained simulation results in comparison to the FORTRAN and the COMSOL model.

2.1.3. Approximation of the solid-phase diffusion equation

As mentioned before, the spatial discretization of the microscopic particle domain incorporates no FDM, but is approximated via three different reduction schemes in this work. For instance, an arbitrarily chosen number of 5 nodes in each electrode and 2 nodes in the separator within the macroscopic electrolyte domain would lead to a total number of 100 nodes only to discretize the solid-phase diffusion PDE, if 10 nodes in the particle domain are chosen as well. The aforementioned total number of DAE would significantly increase when the FDM is used for the spatial discretization of the particle domain, which comes along with a larger computational time. The necessary memory space seems not critical for desktop PCs or workstations, but for microcontroller environments the size of the linearized DAE is crucial as typically, low memory space (*i.e.* in the range of Kilobytes) for the calculation is available. The total number of DAEs defines the size of the system matrix which needs to be solved for the simulation and a low number of DAE is important in the models presented in this work, as future work of the authors will be dealing with the implementation on a microcontroller, which is out of the scope of this paper but briefly discussed in the following. For instance, the chosen 3-2-5 discretization generates 63 DAEs according to Eq. (3), which leads to a 66 × 66 jacobian matrix as the entries for the dynamic and algebraic states of the solid phase have to be considered in the separator domain as well. On a standard microcontroller equipped with 192 kB available RAM, the allocated memory for this jacobian matrix accounts for 19.3% of the total RAM available, when the values are stored with double precision (8 kB). Since the solving process needs also the inverted matrix, the allocated memory rises to 38.6%. This shows, that the number of DAEs is crucial for the real application as the size of the jacobian matrix allocates the major part of the memory space.

Therefore, one of the main objectives in this work is a lean DAE which generates still accurate simulation results. The numerical approximation schemes in this work are adopted from other research groups and account for the calculation of the surface concentration as it is the relevant state for the PCM needed from the microscopic domain. As the original DUALFOIL model from the Newman group [13] serves as the reference for this work, the first approximation scheme is its inbuilt Duhamel Superposition Integral (DSI). The PCM incorporating this approximation is further used as a benchmark. Since the DSI is not suitable for recursive state observer models as it takes into account all previous concentration states in the solid phase, two other approximations were chosen which allow a recursive implementation only depending on the previous solid concentration states. The first approximation is a Polynomial Profile (PP) adopted from the work of Subramanian et al. [36] and the second approximation is an Eigenfunction Method (EM) adopted from the work of Guo et al. [37]. As the reduction schemes are only adopted from these works, the reader is referred to the original works for more detailed information.

In short, with the aid of the three approximation schemes in the

microscopic particle domain, the total number of the linearized DAE could be efficiently reduced for using the FDM in the macroscopic electrolyte domain. The Polynomial and the Eigenfunction approximation are used for the two models implemented in MATLAB (*i.e.* PP- and EM-PCM) beside the benchmark model, which uses the DSI approach. The PP- and EM-PCM are crucial for enabling the implementation of the recursive state observer models using the steady-state representation of the fully-spatially-resolved PCM, which is of high interest for battery management system applications.

2.1.4. Solving of the linearized DAE

The linearized DAE is solved via the Newton-Raphson formula [38]. Let **f** be the vector summarizing all system equations of number *n*, by computing the Jacobian (J_f) of **f**, the system equations can be linearized around a trial function. The solution state vector ($\mathbf{x}^{(i+1)}$) can be gained by iterating for *i*-times until the required convergence is reached [39] as

$$\mathbf{x}^{(i+1)} = \mathbf{x}^{(i)} - \mathbf{J}_f^{-1}(\mathbf{x}^{(i)}) \cdot \mathbf{f}(\mathbf{x}^{(i)}) \tag{4}$$

In terms of the convergency criteria [38], the absolute (ϵ_{abs}) and relative tolerance (ϵ_{rel}) are defined as [40]

$$\epsilon_{abs} = \max |\mathbf{x}^{(i+1)} - \mathbf{x}^{(i)}| = \max |\Delta \boldsymbol{x}_{i|i+1}| \qquad \epsilon_{rel} = \max \left| \frac{\Delta \boldsymbol{x}_{i|i+1}}{\mathbf{x}^{(i+1)}} \right| \tag{5}$$

In this work, the relative tolerance was set to 1×10^{-4} and the absolute tolerance was set to 1×10^{-10}. The discrete time step is set to 25 ms up to 1 s of simulation time and subsequently increased to 1 s. The most computational effort is caused by generating and inverting the jacobian matrix. The linearized DAE considered in this work, is forming a block-tridiagonal matrix [31] when using the FDM. Thus, the system equations can be defined as

$$\boldsymbol{g}_j(\boldsymbol{x}_{j-1}, \boldsymbol{x}_j, \boldsymbol{x}_{j+1}) = \boldsymbol{0} \tag{6}$$

with $\boldsymbol{g}_j$ representing the model equations evaluated at the node *j* with the unknowns $\boldsymbol{x}_j$. The block-tridiagonal matrix is set of the matrices $\boldsymbol{A}_j$, $\boldsymbol{B}_j$ and $\boldsymbol{D}_j$ which represent the Jacobians of the model equations at the node (*j*) and its adjacent ones (*i.e.* *j*−1 and *j* + 1) as

$$\boldsymbol{A}_j = \frac{\partial \boldsymbol{g}_j}{\partial \boldsymbol{x}_{j-1}}\bigg|_{(i)} \qquad \boldsymbol{B}_j = \frac{\partial \boldsymbol{g}_j}{\partial \boldsymbol{x}_j}\bigg|_{(i)} \qquad \boldsymbol{D}_j = \frac{\partial \boldsymbol{g}_j}{\partial \boldsymbol{x}_{j+1}}\bigg|_{(i)} \tag{7}$$

and thus the solving procedure can be depicted as

$$\Delta \mathbf{x}_{i|i+1} = -\mathbf{J}_g^{-1}(\mathbf{x}^{(i)}) \cdot \mathbf{g}(\mathbf{x}^{(i)}) \tag{8}$$

according to the Newton-Raphson formula shown in Eq. (4). The matrix inversion uses a MATLAB® 2016b in-built function [40], which adjust the solving algorithm according to the sparsity of the current constitution of the jacobian matrix. In short, only the matrix inversion was implemented via an MATLAB in-built function. The whole solving process is reduced to a simple matrix inversion. In terms of real applications, this function can be easily embedded by Gauß-Jordan [41] matrix inversion schemes in order to transfer the solving routine into compiled languages such as C which is used in microcontrollers.

2.2. Recursive state observer model

In order to enable for the recursive state estimation of a lithium-ion cell and to overcome parameterization uncertainties such as deviations for the reaction rate constants which increase the error of the simulated states, filter algorithms like the EKF are useful model-enhancements to reduce the residual error between measurement and simulation. Since the work of Plett et al. [42], this has been a widely used method in terms of state estimation for the lithium-ion battery.

As the state observer models need a recursive formulation, only the PP- and EM-PCM models are suitable for implementation. The benchmark-PCM using the DSI approach generates the targeted states of the

lithium-ion cell in this work to enable the analysis of the estimation accuracy and speed of local states within the lithium-ion cell. *In-situ* measurements of local states in a lithium-ion battery are difficult and not available for this work, nevertheless the analysis of the local estimated states by the observer models can be evaluated by using the presimulated, noise corrupted states of the DSI-PCM.

In short, the application of a Kalman Filter [43] on a DAE system is performed by the prediction and the update step. First, the prediction step generates estimates of the current state variables including all its uncertainties. Second, the update step corrects the predicted states via the noise corrupted measurement values. For the readers' convenience, the authors attached the basic steps of the Kalman Filter briefly in the appendix (see Table 15) based on the works of Kalman et al. [43–45]. As the DAE of the PP- and EM-PCM is non-linear, the extended version of the Kalman Filter (*i.e.* EKF) must be used in this work. Following the general introduction of the Kalman filter and its extended version [46] the linearized state-space representation is defined as

$$\widehat{\boldsymbol{x}}_k = \widehat{\mathbf{F}}_k \, \widehat{\boldsymbol{x}}_{k-1} + \mathbf{B}_k \, \widehat{\boldsymbol{u}}_k + \boldsymbol{\omega}_k \tag{9}$$

$$\boldsymbol{y}_k = \widehat{\mathbf{H}}_k \, \widehat{\boldsymbol{x}}_k + \boldsymbol{v}_k \tag{10}$$

where Eq. (9) and (10) represent the process and the measurement model, respectively. The algorithm steps of the Kalman Filter and the EKF are the same except that the transition ($\mathbf{F}_k$) and observation matrix ($\mathbf{H}_k$) are *linearized* (*i.e.* $\widehat{\mathbf{F}}_k$ and $\widehat{\mathbf{H}}_k$). Note, that the vectors $\widehat{\boldsymbol{x}}_k$ and $\widehat{\boldsymbol{u}}_k$ refer to the state (*i.e.* most recent estimate) and input vector of the linearized state-space model. The algebraic states ($\boldsymbol{z}_k$) are not regarded for the process model, as the EKF focuses on the dynamic states only. The vectors $\boldsymbol{\omega}_k$ and $\boldsymbol{v}_k$ represent the Gaussian white process and measurement noise, which corrupt the process and the measurement model with independent uncorrelated continuous random variables with zero mean. The covariances of the noise vectors $\boldsymbol{\omega}_k$ and $\boldsymbol{v}_k$ are defined as $\mathbf{Q}_k$ and $\mathbf{R}_k$.

The *linearized* transition and observation matrix are derived as follows:

The functions **f** and **h** are mapping functions for the differential and state-output equations. The symbols $\boldsymbol{x}_k$, $\boldsymbol{z}_k$ and $\boldsymbol{u}_k$ are the vectors of the dynamic state, algebraic state and the input variables, respectively.

The linearized matrices $\widehat{\mathbf{F}}_k$ and $\widehat{\mathbf{H}}_k$ represent the Jacobians referring to the dynamic states in case of our PP- and EM-PCM. The linearized DAE of the PP- and EM-PCM is thus reformulated to a linearized state-space representation around the most recent estimate $\widehat{\boldsymbol{x}}_k$ for every time step *k*.

To the authors' best knowledge, this is the first time the linear state-space representation of the fully-spatially-resolved PCM is derived by using the FDM with control volume formulation (*i.e.* FVM). The implemented FDM of this work rectifies the insulting boundary conditions in the electrolyte and is suitable for a low number of chosen discretization elements, which leads to a lean DAE of the PCM and its state-space representation which makes it a suitable approach for microcontroller application, as discussed in the section before.

2.2.1. EKF with PP-PCM

The dynamic state vector for the PP-PCM based observer model is defined as

$$\widehat{\boldsymbol{x}}_{j,k} = [\, c_l(x_j, t_k) \quad \bar{c}_s(x_j, t_k) \quad \bar{q}_s(x_j, t_k) \,]^T \tag{11}$$

where $\bar{c}_s$ and $\bar{q}_s$ represent the volume-averaged concentration in the solid phase and the volume-averaged concentration flux, respectively. These can be calculated at each node *j* and at each discrete time step *k* referring to the previous time step by using the formulation according to Subramanian et al. [36] as

$$\begin{pmatrix} \bar{c}_s(x_j,t_k) \\ \bar{q}_s(x_j,t_k) \end{pmatrix} = \begin{bmatrix} 1 & 0 \\ 0 & 1-30\Delta t \frac{D_s}{R_p^2} \end{bmatrix} \begin{pmatrix} \bar{c}_s(x_j,t_{k-1}) \\ \bar{q}_s(x_j,t_{k-1}) \end{pmatrix} + \begin{pmatrix} -3\frac{\Delta t}{R_p} \\ -\frac{45\Delta t}{2R_p^2} \end{pmatrix} j_n(t_k) \tag{12}$$

Accounting for all spatial discretization nodes, an overall representation can be defined for the concentration in the liquid phase as

$$\mathbf{M}_l \mathbf{c}_{l,k} = \mathbf{A}_l \mathbf{c}_{l,k-1} + \mathbf{b}_l \mathbf{i}_{l,k} \quad \rightarrow \quad \mathbf{c}_{l,k} = \mathbf{M}_l^{-1}\mathbf{A}_l \mathbf{c}_{l,k-1} + \mathbf{M}_l^{-1}\mathbf{b}_l \mathbf{i}_{l,k} \tag{13}$$

where a matrix inversion allows for a definition, which relates the electrolyte concentration to its previous state and the ionic current density. For the reader's convenience we attached an example of the spatial discretization in the appendix (see Table 14), where the FDM for the mass balance in the electrolyte with central orientation combined with the Crank-Nicolson formulation over time is shown at the interface between the anode and the separator. To the author's best knowledge, the linear state-space representation using the FDM including both the solid and liquid concentration states was not shown before in literature. Note, that the vectors of concentration ($\mathbf{c}_{l,k}$) and ionic current density ($\mathbf{i}_{l,k}$) include every node at a discrete time step (t_k). The derived equations in Eqs. (12) and (13) yield to the linearized versions of the transition matrix (*i.e.* $\widehat{\mathbf{F}}_k$) and the input matrix (*i.e.* $\mathbf{B}_k$). For instance, the aforementioned discretization of 3-2-5 would lead to 31 equations, which lead to a system matrix of 33x33 since zero-entries of the solid dynamic states must be regarded in the separator as well. This would lead to an allocated memory space (*i.e.* RAM) on the aforementioned microcontroller of around 8.7 kB with double precision of the stored variables, which corresponds to 4.5% of the available memory space. This shows, that the implementation of the observer model in this microcontroller is possible since the implementation is based on a lean DAE which generates accurate states even at a low chosen number of discretization elements. The input vector can be defined as

$$\widehat{\boldsymbol{u}}_{j,k} = [\, i_l(x_j,t_k) \quad j_n(x_j,t_k) \,]^T \tag{14}$$

The process noise covariance matrix $\mathbf{Q}_k$ is of diagonal shape and dependent on the applied current in case of a pulsed charge or discharge scenario. In terms of the electrolyte concentration, the process noise variance refers to the amount of total lithium in the electrolyte within the pore of the anode domain, which is consumed or generated (*i.e.* charge or discharge scenario) for the estimated step (Δt_k) as follows

$$\sigma_{Q,cl}^2 \bigg|_{\forall j} = \left[\frac{\Delta t_k (1-t_+^0)}{L^{NEG} \, \varepsilon_l^{NEG}} \cdot \frac{I(t_k)}{F} \right]^2 \tag{15}$$

The process noise variance of the averaged concentration in the solid phase is set to the amount of total lithium which enters or leaves the microscopic particle domain of the anode and can be written as follows

$$\sigma_{Q,\bar{c}_s}^2 \bigg|_{\forall j \in \{NEG,POS\}} = \left[\frac{3\Delta t_k}{R_p^{NEG}} \cdot \frac{I(t_k)}{F} \right]^2 \tag{16}$$

In case of an applied pulsed current of 53.75 A m^{-2} (*i.e.* 2.5 C-rate) and a time step of 1 s, the process noise variances would exemplarily calculate to $75.7665 (\text{mol m}^{-3})^2$ and $4.3642 \times 10^4 (\text{mol m}^{-3})^2$ which corresponds to a standard deviation of 8.7 mol m^{-3} and 208.9 mol m^{-3} for the liquid and averaged solid concentration, respectively. In case of a constant applied current, the process noise variance is set to 10 and $100\,(\text{mol m}^{-3})^2$ for the liquid and averaged solid concentration. The corruption for the volume-averaged concentration flux $\bar{q}_s$ is set to zero for both the constant and pulsed applied current to avoid violations of the mass conservations, which is explained later in this section.

The measurement noise covariance matrix $\mathbf{R}_k$ is set to 1×10^{-4} V^2 which corresponds to a standard deviation of 10 mV and accounts for sensor noise of the measured cell voltage.

The Kalman gain matrix ($\mathbf{K}_k$) and the approximation error covariance matrix ($\mathbf{P}_k$) are calculated as shown in the appendix (see Table 15). The initialization of the approximation covariance matrix is set equal to the initial values of the process noise matrix. For more profound information about the meaning and impact of the filter specific matrices, the reader is referred to the work of Campestrini et al. [47]. The linearized observation matrix $\widehat{\mathbf{H}}$ is determined by the voltage of the cell V_{cell}, which is derived from the potential difference in solid phase between the external boundaries of the model.

$$V_{cell}(t_k) = y_{k|k-1} = \Phi_s(L^{POS},t_k) - \Phi_s(0^{NEG},t_k) \tag{17}$$

Therefore, the potential in the solid phase is expressed via the dynamic states, the inversion of the electrode kinetics and the insertion of the overpotential as

$$\Phi_s(x_j,t_k) = \Phi_l(x_j,t_k) + E_{eq}(c_{ss}\bigg|_{x_j,t_k}) + \frac{2\,R\,T}{F} \sinh^{-1}\left[\frac{F\,j_n(x_j,t_k)}{2 \cdot i_0(c_{ss},c_l)|_{x_j,t_k}} \right] \tag{18}$$

whereas the surface concentration can be directly related to the dynamic states in Eq. (11) using the PP-approximation of the work of Subramanian et al. [36]. The term E_{eq} represents the equilibrium potential in each electrode, i_0 describes the exchange current density outlined in Table 14 and F and R represent Faraday's constant and the gas constant (see Table 17).

The linearized observation matrix is defined with respect to the external nodes according to the partial derivatives of the dynamic states as

$$\widehat{\mathbf{H}}_k = \begin{bmatrix} \frac{\partial \Phi_s}{\partial c_l} & \frac{\partial \Phi_s}{\partial \bar{c}_s} & \frac{\partial \Phi_s}{\partial \bar{q}_s} & 0 & \cdots & 0 & \frac{\partial \Phi_s}{\partial c_l} & \frac{\partial \Phi_s}{\partial \bar{c}_s} & \frac{\partial \Phi_s}{\partial \bar{q}_s} \end{bmatrix}_k \tag{19}$$

Due to the non-observability of the reformulated PCM, lithium-mass conservation according to the work of Klein et al. [48] is included in the EKF algorithm. In contrast to this work, the mass conservation is included in an EKF algorithm and the linear state-space representation does not assume a constant electrolyte concentration, but the fully-spatially-resolved mass balance in the liquid phase of the PCM solved by the FVM. Referring to the initial concentration within the electrodes at the fully charged or discharged state of the cell, the total amount of cycleable lithium is predefined. For all times, the total amount of lithium is calculated within both electrodes and separately within the electrolyte. Both in the solid and liquid phase, the conservation of lithium referring to the predefined amount of cycleable lithium must hold at any time, as no aging effects or other side reactions are considered in this work. In this work, the EKF was modified to improve the estimation of the estimated solid-phase concentrations in the anode. The chosen MCMB active material shows open circuit potential (OCP) areas with low gradients referring to the lithiation level, which may cause the estimation to fail. Therefore, the Kalman gains at the nodes within the LiCoO$_2$ domain are used in the anode for the concentration in the solid phase due to the relatively higher slope of the OCP. Thus, a better estimation of the solid states can be achieved. The mass conservation is subsequently used to correct the solid states in the negative electrode via a correction factor (γ_s).

2.2.2. EKF with EM-PCM
The dynamic state vector for the EM-PCM based observer model using the EKF is truncated in terms of the volume-averaged concentration flux $\bar{q}$ to the form of

$$\widehat{\boldsymbol{x}}_{j,k} = [\, c_l(x_j,t_k) \quad \bar{c}_s(x_j,t_k) \,]^T \tag{20}$$

to reduce the computational effort and limit the computational time. Hence, the reformulated model regards only the first row of Eq. (12) and incorporates Eq. (13) as already presented for the PP-PCM based observer model for determining the linear state-space representation. The implementation of the EM-PCM based observer model is similar to the aforegiven definition in Section 2.2.1, except that the dynamic state

vector only incorporates two states. The linearization output matrix is hence defined as

$$\widehat{\mathbf{H}}_k = \begin{bmatrix} \dfrac{\partial \Phi_s}{\partial c_l} & \dfrac{\partial \Phi_s}{\partial \bar{c}_s} & 0 & \cdots & 0 & \dfrac{\partial \Phi_s}{\partial c_l} & \dfrac{\partial \Phi_s}{\partial \bar{c}_s} \end{bmatrix}_k \quad (21)$$

as the volume-averaged concentration flux is neglected.

The EM-PCM is reformulated to a novel linear state-space representation using the fully spatially resolved PCM solved by the FVM, which needs only a 22×22 jacobian matrix with the chosen 3-2-5 discretization. As a consequence, the observer model would only allocate around 5.8kByte (*i.e.* 3.0% of the total RAM) for the calculation process on a microcontroller.

2.2.3. Initialization of the state estimation

Small derivatives of the OCP lead to several possible states at the beginning ($k = 0$), due to the missing prior state ($k-1$) for the state estimation algorithm. To overcome this initialization problem, a novel iterative Newton-Raphson method [40] is implemented, which solves for the initial solid concentrations ($c_{s,0}$) of each electrode.

$$y_{m,k} = E_{eq}^{POS}(c_{s,0}^{POS}) - E_{eq}^{NEG}(c_{s,0}^{NEG}) \quad (22)$$

$$n_{Li} = \mathrm{L}^{NEG} \varepsilon_s^{NEG} c_{s,0}^{NEG} + \mathrm{L}^{POS} \varepsilon_s^{POS} c_{s,0}^{POS} \quad (23)$$

The cell voltage is calculated in Eq. (22) from the OCPs of each electrode. The total amount of lithium in the solid phase is calculated in Eq. (23) from the volumetric fraction of active material in each electrode. As a first rough estimate, equilibrium is assumed and the current

measured cell voltage is set as boundary condition in Eq. (22) and the second boundary condition in Eq. (23) takes into account the defined total amount of lithium in the solid phase. The iterative solving algorithm solves the non-linear system of Eqs. (22) and (23) until the relative and absolute tolerance criteria are fulfilled (see Eq. (5)). As a result, the initial concentrations in the solid phase are estimated and the approach offers great potential to ease the issue of the initialization for this kind of state observer models.

2.2.4. Process of the state estimation

The state estimation procedure used in this work is shown in Fig. 2 and shortly summarized in the following section. The initialization step calculates the initial dynamic and algebraic state vectors. In case of $k = 0$, the routine described in Section 2.2.3 proceeds, otherwise the previous estimated states are used ($k-1$).

In the prediction step, the PCM simulates a *priori* state estimate ($k|k-1$) from the initialization step ($k-1|k-1$).

In the following correction gain, the linearized transition ($\widehat{\mathbf{F}}_k$) and observation ($\widehat{\mathbf{H}}_k$) matrix are derived from the linear state-space representation of the PCM using the *priori* estimated dynamic states and the input vector. The approximate error covariance matrix $\mathbf{P}_{k-1|k-1}$ from the previous time step is propagated in time using the transition and the process noise matrix, to gain its *priori* estimate ($\mathbf{P}_{k|k-1}$). The Kalman gain matrix $\mathbf{K}_k$ is calculated depending on $\widehat{\mathbf{H}}_k, \mathbf{R}_k$ and $\mathbf{P}_{k|k-1}$.

In the following update step, the Kalman gain matrix is updated with the constant gain of the positive electrode in both porous domains. The *posteriori* state estimate $\widehat{\mathbf{x}}_{k|k}$ is derived from the residual cell voltage
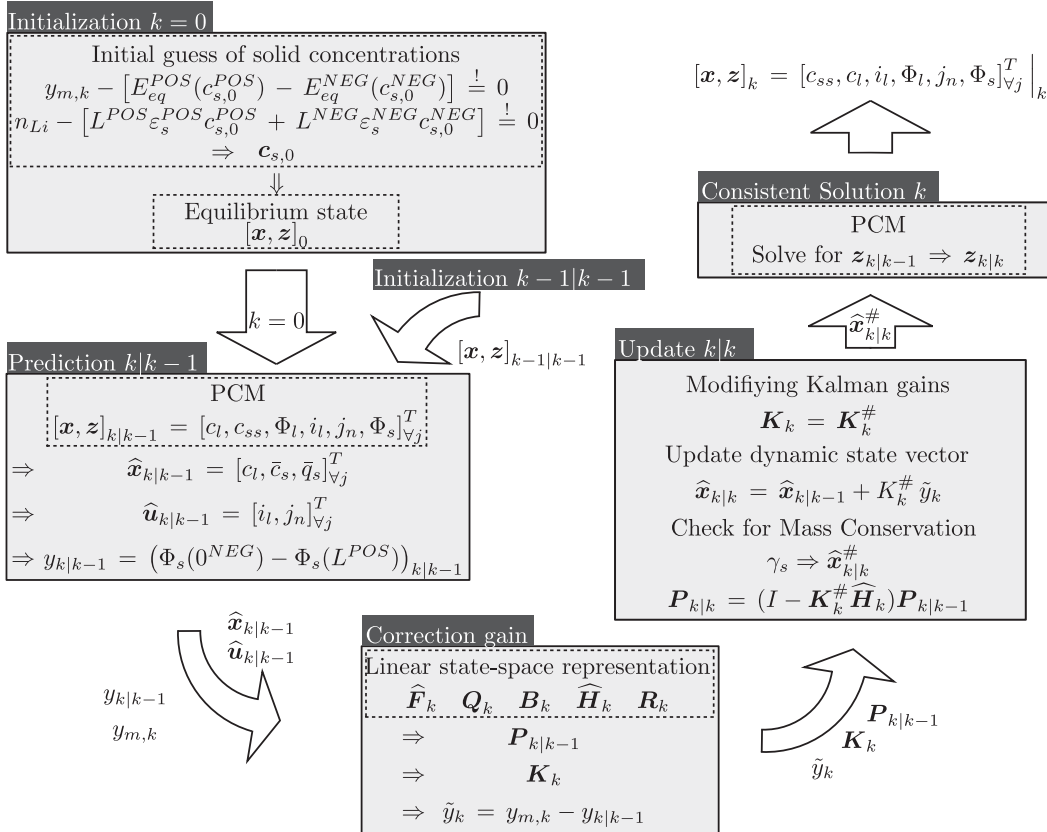
Fig. 2. Overview of the state-estimation process using the PP-PCM with an EKF. The dynamic state vector ($\widehat{\mathbf{x}}$) differs for the EM-PCM based observer model in terms of neglecting the volume-averaged concentration flux ($\bar{q}_s$).

error ($\tilde{y}_k$) and the updated Kalman gain matrix $\mathbf{K}_k^\#$. To proof the consistency of the updated states, the mass conservation is checked and adjusts deviations of the solid states within the negative electrode. According to this modification, the *posteriori* states are corrected as well ($\hat{\mathbf{x}}_{k|k}^\#$). The *posteriori* approximation error covariance matrix $\mathbf{P}_{k|k}$ is calculated at the end of the update step.

To find a consistent solution for all states ($\mathbf{x}_k$) using the already estimated dynamic states ($\hat{\mathbf{x}}^\#$), the *priori* estimated algebraic states ($\mathbf{z}_{k|k-1}$) are propagated to find a consistent solution via applying the iterative Newton-Raphson method to the algebraic equations ($\mathbf{g}$) of the PCM only.

In a nutshell, the presented recursive state observer models use the fully-spatially-resolved PCM for the definition of the linear state-space representation. The EKF algorithm is able to conserve lithium mass and incorporates a robust initialization routine solved by the Newton-Raphson formula which enables the observer-models to conserve the states' physical interpretation along with their spatial distribution. The implementation focussed on a lean DAE for the PCM and the observer models with no restrictions of the physical validity even for a low chosen number of discretization elements, which makes it a suitable approach for low computational environment such as microcontrollers.

3. Simulation results and discussion

3.1. Simulation results of the PCM

The first part of the result section analyzes the computational speed and the error of the simulated local and global states of the PP-PCM and the EM-PCM with reference to the benchmark, which is the PCM incorporating the original DSI approach. In particular, the accurate handling of the internal and external boundary conditions of the PCM compared to two reference models implemented in FORTRAN and COMSOL Multiphysics® is outlined. The second part shows the estimation results of the two observer models, which are designated with "PP-EKF" and "EM-EKF". The detailed analysis focusses on the time-constants for accurately estimated global and local states, the computational speed and the possible application of the gained observer models in real application scenarios. Both the PCMs and the observer models are implemented in MATLAB® 2016b whereas the DUALFOIL model is embedded in FORTRAN and the COMSOL model uses the commercial FEM-solver COMSOL Multiphysics®. All simulations run on a desktop computer equipped with a Intel(R) Core(TM) i5-6500 CPU @ 3.20 GHz processor and 16 Gigabyte of RAM.

3.1.1. Constant discharge simulation

Four models are compared in the first analysis to show the accurate handling of the internal and external boundary conditions especially with a low chosen number of discretization elements (*i.e.* 3-2-5) for the PCMs in this work. The first PCM model is embedded in FORTRAN [31] (*i.e.* FORTRAN-PCM (3-2-5)), the second in COMSOL Multiphysics® (*i.e.* COMSOL-PCM (3-2-5)) and the third model is the implementation in MATLAB presented here, using the DSI-approach for the solid-phase diffusion (*i.e.* DSI-PCM (benchmark, 3-2-5)). An additional COMSOL model with a different, much larger number of discretization elements by choosing the in-built mesh configuration "physics-controlled" and "extremely fine" serves as additional reference (*i.e.* COMSOL-PCM ("extremely fine")). The simulation results for the current density in the electrolyte for a 8C discharge simulation at 210 s is shown in Fig. 3a. In terms of the COMSOL-PCM (3-2-5), the ionic current density is overestimated above the applied current in the narrow region close to the separator within the electrode domains. Slight deviances are seen at the external boundaries where the current density equals not exactly 0 A m^{-2}. The FORTRAN-PCM (3-2-5) underestimates the current density
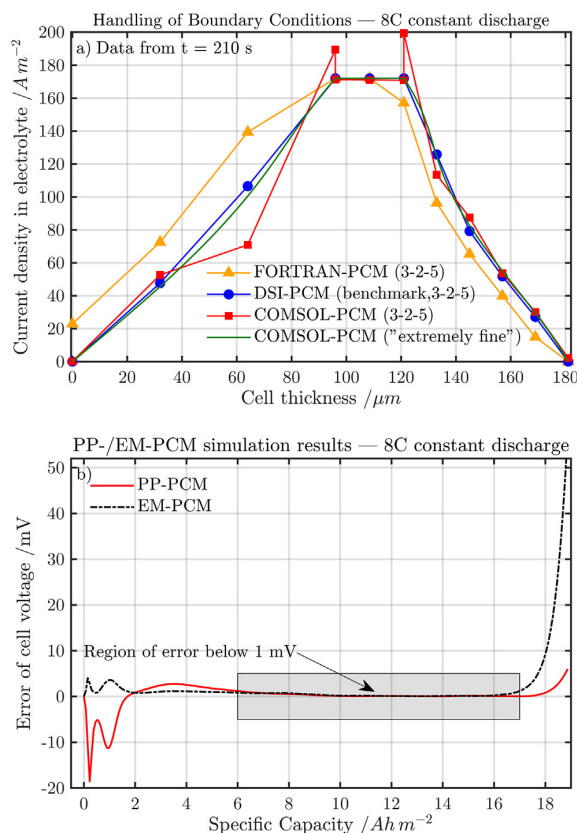
Fig. 3. The subplot (a) shows the ionic current density in the electrolyte for a 8C constant current discharge simulation at 210 s of the PCM embedded in FORTRAN, COMSOL and MATLAB in order to analyze the handling of the boundary conditions with a low spatial discretization. For each model, the spatial discretization is indicated in the legend. The subplot (b) shows the simulation error for the cell voltage of the PP- and EM-PCM compared to the benchmark model for the 8C constant current discharge scenario.

near the separator interface of the cathode domain. Within the electrode domains, the current density is permanently under- or overestimated compared to the extremely fine discretized reference COMSOL-PCM ("extremely fine"). At the external boundary to the adjacent copper current collector, the current density is overestimated and the zero flux condition is not conserved. In contrast to that, the DSI-PCM of this work (*i.e.* benchmark model) can handle the boundary conditions accurately at both the internal and external interfaces and shows marginal deviances compared to the extremely fine reference COMSOL model within the electrode domains. Note, that for a higher number of discretization elements all models generate very accurate simulation results and only marginal differences are seen.

After showing the suitability of our PCM implementation in MATLAB for simulating accurate states of a lithium-ion cell with a low number of discretization elements, the difference between the chosen approximation schemes for the solid-phase diffusion is analyzed in the following. The simulation results of three different constant current discharge scenarios (*i.e.* 0.2C-, 2C- and 8C-rate) using the PP- and the EM-approach are compared to the benchmark model in the range from 4.1 and 3.0 V. In Fig. 3b, the error of the simulated cell voltage for the 8C discharge scenario is shown. The error of the cell voltage reveals a slightly higher deviance of up to 20 mV at the beginning of the

Table 3
Computational time and accuracy for constant discharge scenario.

Model	Benchmark			PP-PCM			EM-PCM		
C-rate	0.5C	2C	8C	0.5C	2C	8C	0.5C	2C	8C
A/ms	30.5	31.2	8.2	8.6	8.3	11.1	72	50.7	23.4
B/–	3.87	3.74	3.96	3.87	3.67	3.77	9.03	5.70	5.47
C/mV		Ref.		0.15	0.09	0.1	0.90	0.64	2
D/mV		Ref.		4	1.8	6	2.4	16.8	52.6

A = Average time per step B = Average iterations per step.
C = Average voltage error D = Maximum voltage error.

Table 4
Computational time and accuracy for pulsed discharge scenario.

Model	Benchmark	PP-PCM	EM-PCM
Max. time per step/ms	36.3	8.6	60.8
Av. time per step/ms	29.9	11.9	46.3
Max. iterations per step	5	4	9
Av. iterations per step	4.6	4.2	7.2
Av. voltage error/mV	Ref.	12.6	2.1
Max. voltage error/mV	Ref.	123.1	50.7

Av. = Average Max. = Maximum Min. = Minimum.

discharge simulation for the PP-PCM. In a wide range from six up to 17 Ah m^{-2} no significant difference can be seen between the PP- and the EM-PCM and the error falls below 1 mV. However, at the end of the discharge scenario the EM-PCM shows a cell voltage error up to 52.6 mV which is more than 8 times higher compared to the PP-PCM. The detailed analysis in terms of computational demand per time step and the simulation error compared to the benchmark model in each discharge scenario are shown in Table 3. The fastest computational time and the lowest number of iterations to reach convergency is observed for the PP-PCM. This computation is approximately 3.5 times faster than the benchmark needing roughly the same number of iterations. At 8C, the benchmark shows a reduced computational time and is even faster than the PP-PCM. This may be caused by the DSI approximation, which is working much faster for short simulation times as the number of previous stored states [49] is kept low. The EM-PCM requires both the highest number of iterations and the longest time on average for solving a single time step. This behavior improves for increasing C-rates compared to the PP-PCM. Compared to the benchmark, the EM-PCM shows an approximately 2.5 times higher computational time for each discharge rate. Regarding the average and maximum voltage error in Table 3, the PP-PCM generally provides a lower mean voltage error for the discharge scenarios compared to the EM-PCM.

To sum up the constant discharge simulations, the PP-PCM shows fast computational time and high accuracy up to 4C compared to the benchmark. For high discharge rates like 8C, the accuracy and computational speed is reduced, but still provides sufficient results. The EM-PCM generally consumes more computational time and the average voltage error is at least six times larger compared to the PP-PCM. Despite the different performances of the PP- and EM-PCM, both models reveal the same accurate handling of the internal and external boundary conditions as the benchmark model with a low number of discretization elements and thus guarantee sufficient accurate simulation of a lithium-ion cell with a lean DAE system.

3.1.2. Pulsed discharge simulation

The performance of the PP- and EM-PCM are further investigated under a dynamic load profile in the form of a 10C discharge pulse for 10 s followed by a 10 s resting phase. The cell voltage limits are kept as for the constant load scenario. The performance results including the average and maximum iteration steps and calculation times per single time step as well as the cell voltage error compared to the benchmark are shown in Table 4. Similar to the constant load profile, the PP-PCM shows the fastest computational time, followed by the benchmark model and again - as the slowest converging model - the EM-PCM takes the longest computational time. A similar characteristic can be observed for the maximum and average number of iterations. In terms of numerical accuracy, the benefit of the EM-PCM for dynamic profiles becomes apparent. The average voltage error is approximately six times smaller compared to the PP-PCM and the maximum voltage error is roughly 2.5 times lower. This shows the drawback of the PP approach

for the solid-phase diffusion PDE. When it comes to dynamic load profiles, the prediction for the concentration profile is not accurate enough due to overshoots at the beginning of each pulse period caused by the parabolic approximation method. In addition to Table 4, Fig. 4 shows the impact of the chosen approximation method on the simulated SOC (see Fig. 4a) and the cell voltage (see Fig. 4b) in form of the deviance to the benchmark. Regarding the SOC, which is derived from the average lithiation level of the limiting cathode for the used parameter set, the simulation error shown in Fig. 4a reveals more instable calculation by the PP-PCM with a maximum error of 0.15% compared to the EM-PCM. The simulated deviance of the EM-PCM shows a rather stable deviance of around 0.06%. In sum, the deviances for both approaches
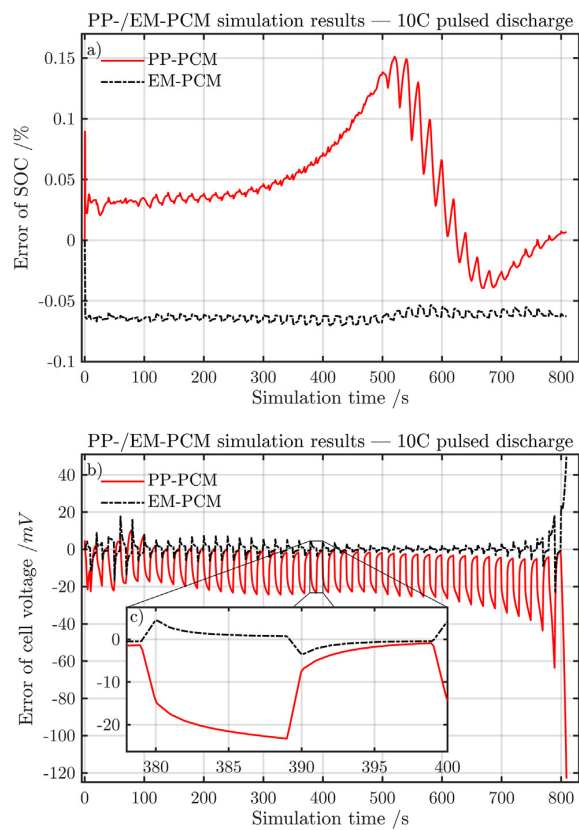
Fig. 4. The upper plot (a) shows the SOC error derived from the deviance between the benchmark and the PP-/EM-PCM. The bottom plot (b) shows the error of the simulated cell voltage with a magnified section (c) between 378 and 400 s, emphasizing the differences between the PP- and the EM-PCM during the pulse and the resting period.

Fig. 5. Error of the simulated surface concentration in reference to the benchmark model under a 10C pulsed discharge load for 10 s extracted from the interface between the cathode and the aluminium current collector for the PP-(a) and the EM-PCM (b).

Table 5
Suitability for constant and dynamic load profiles.

		PP-PCM	EM-PCM
Constant Load	Accuracy	+	+
	Speed	+	−
Dynamic Load	Accuracy	−	+
	Speed	+	−

PCM ($-18.7 \, \text{mol} \, \text{m}^{-3}$) is more than 15 times higher compared to the PP-PCM ($-283.1 \, \text{mol} \, \text{m}^{-3}$).

To sum up, the first part of the results in this work proofed the accurate handling of the chosen FVM spatial discretization for the fully-spatially-resolved PCM for constant load scenarios, which holds also for the pulsed load scenario. The detailed analysis of the computational speed and the generated error for the PP- and the EM-approximation schemes revealed their suitability for both constant and pulsed load scenario, which is summed up in Table 5.

As automotive applications include dynamic profiles while driving as well as mainly constant load profiles during charging, a load-scenario distinction and the derived choice for either the PP- or the EM-approximation routine could help to minimize the error of cell voltage and SOC estimation. Since the PP- and the EM-approach require low computational effort, less memory space compared to the remaining solved equations and offer a recursive formulation, the implementation of both approaches in parallel is suitable even on a microcontroller and depending on the load scenario, the most appropriate approximation for the solid-phase diffusion can be selected whereas the other approach remains redundant.

The computational performance and accuracy was analysed for the PP- and EM-PCM for a pulsed and constant discharge load scenario at this point. The same performance applies for charging scenarios and when it comes to control algorithms in the BMS, state observer models are used in order to monitor the states of a lithium-ion cell for guaranteeing the SOA for charging and discharging, calculating the maximum available power and energy as well as predicting the SOH. In the following, the estimation results of the presented two observer models using the linear state-space representation based on the PP- or the EM-PCM combined with an EKF are evaluated for three different charging scenarios.

3.2. Recursive state estimation results

Knowing about the strengths and weaknesses of the PP- and EM-PCM, the second part of the results deals with the performance of the recursive state observer models and analyzes to which extent the chosen approximation scheme influences the state estimation of local and globals states within a lithium-ion battery, the regression speed of the related errors and the robustness towards constant and dynamic load scenarios.

The simulation results of the PP- and EM-EKF are presented for three different charging scenarios, including a constant current scenario (CCCV) at 2.5C current rate, a boost charging scenario with a high (4C) and low (0.1C) constant current rate (BCCV) and finally a pulsed current scenario (PCCV) at 10C for 10 s. Note, that for each charging scenario an additional constant voltage period at 4.1 V with a limiting applied current of 0.01C is added to avoid harming high potentials in the active material within the LiCoO$_2$-electrode [2]. The presimulated states of the cell were set by the benchmark model which holds as the measurement input for the filter algorithm.

The state estimation started at 300 s and 120 s, for the CCCV and

referring to the benchmark are acceptable. In Fig. 4b, the simulated cell voltage error illustrates the aforementioned more accurate calculation of the EM-PCM which results in a lower maximum and average error. The magnified section (see Fig. 4c) shows the pulse and resting period from 378 to 400 s. The pulse period from 379 to 389 s reveals the much higher deviance of the PP-PCM from the benchmark compared to the EM-PCM. During the resting period from 389 to 399, the PP-PCM recovers its accuracy to a certain extent, but still remains less accurate than the EM-PCM. In short, a certain deviation of the predicted SOC and cell voltage is seen for both reduced PCM models, which is more distinct in terms of the PP-PCM. The PP-PCM approximately might gain a factor of 2.5 and 4 on average in terms of computational speed compared to the benchmark and the EM-PCM, but calculates a 6 times less accurate cell voltage compared to the EM-PCM at the same time. This finding supports the reported drawback of the parabolic profile for simulating dynamic load-scenarios [50] which implies choosing the EM-PCM in this case.

Since the surface concentration is the most important state from the microscopic domain for the macroscopic domain of the PCM, Fig. 5 shows its error for the PP- (see Fig. 5a) and the EM-PCM (see Fig. 5b) at the cathode-current collector interface. The cathode-current collector interface is important for calculating the cell voltage, since the solid potential at this node directly influences its calculation. In accordance to Fig. 4a, the PP-PCM shows a more instable behavior in simulating surface concentration than the EM-PCM. The mean error for the EM-
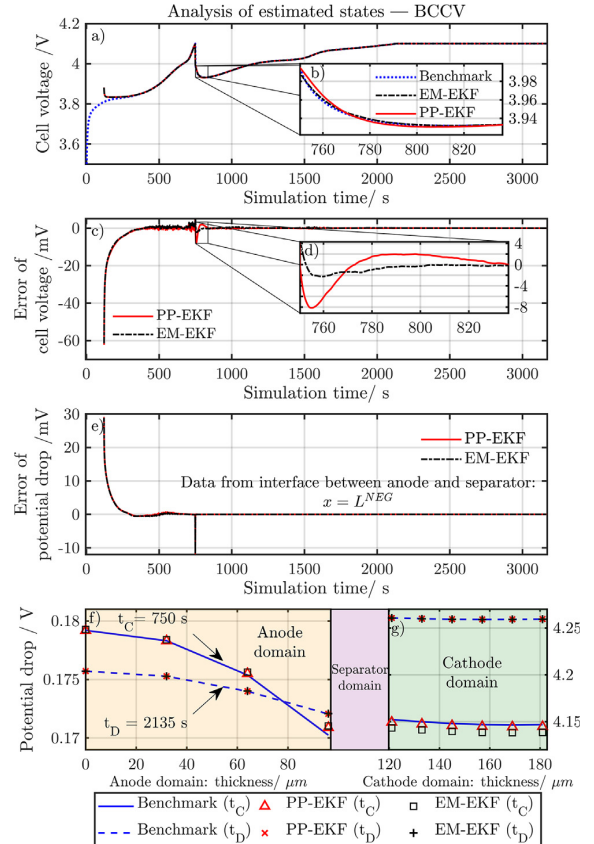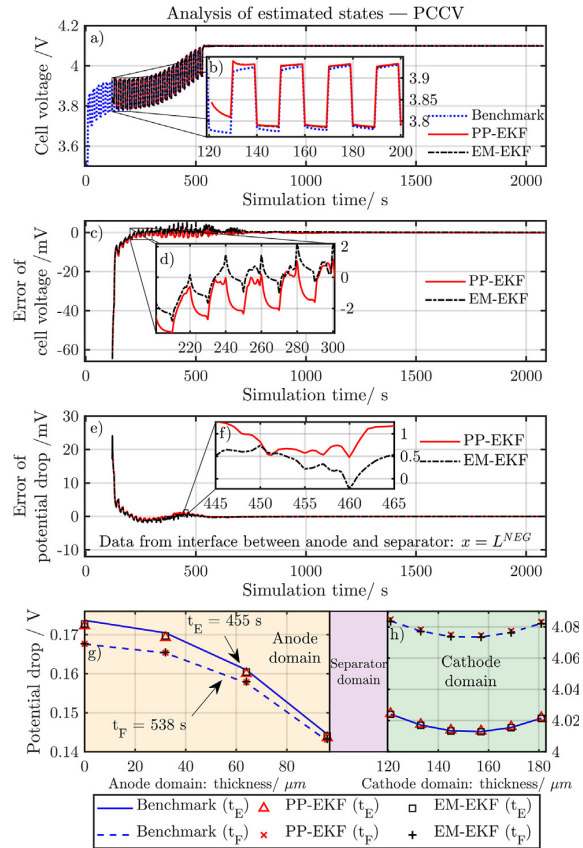
Fig. 6. Estimation results for the CCCV charging scenario. The subplot (a) shows the presimulated cell voltage from the benchmark model and the estimated cell voltages of the PP- and EM-EKF. The magnified region in subplot (b) illustrates the regression of the residual cell voltage error between 800 and 900 s. The subplot (c) shows the related error of the cell voltage and the subplot (d) illustrates the error in the same limits as in subplot (b). The subplot (e) shows the error regression of the potential drop (*i.e.* $\Phi_s - \Phi_l$, see Eq. (1)) at the interface between anode and separator.

both for the BCCV and PCCV scenario, respectively. The error of the initial SOC based on the averaged concentrations states of the limiting cathode is arbitrarily set to 36.1%, 42.4% and 35.2% for the CCCV, BCCV and PCCV, respectively. The specific initial errors depend on the elapsed time between the start of the charging and the estimation process. The initial error for the electrolyte concentration at the start of the state estimation depends on the local position within the cell and the applied charging scenario as well. For the CCCV, the minimum and maximum error was 15.4% and 31.4%, with reference to the current state when the state estimation started. In case of the BCCV and the PCCV, the error ranged from 32.0% to 38.1% and from 44.8% to 48.7%, respectively.

3.2.1. Constant current charging

In general, the estimation of the CCCV scenario shows comparable results for both observer models with a slight tendency of quicker estimation for the EM-EKF. In Fig. 6,the simulation results of the benchmark and the estimation results of the PP- and the EM-EKF are shown in terms of the cell voltage, the estimation error of the cell

Table 6
Computational time and accuracy for the CCCV estimation.

States[a]	PP-EKF			EM-EKF		
	α_e	$t_{\leqslant 10\%}$	$t_{\leqslant 1\%}$	α_e	$t_{\leqslant 10\%}$	$t_{\leqslant 1\%}$
Φ_l	100	27	509	100	28	515
c_{ss}	67	193	993	67.0	194	985
j_n	100	625	-	100	622	1903[b]
Φ_s	10.3	1	463	10.8	1	451
η	100	625	746	100	622	737
V_{cell}	2.1	1	191	2.1	1	187

α_e = Initial deviance after EKF initialization/%.

$t_{\leqslant 10\%}$, $t_{\leqslant 1\%}$ = Estimation time for error threshold of 10% and 1% referring to $t = 300$ s.

  [a] 1 CC period at $x = \mathrm{L}^{\mathrm{NEG}}$.

  [b] 2 CV period at $x = \mathrm{L}^{\mathrm{NEG}}$.

voltage and the error of the estimated potential drop between solid and liquid phase according to Eq. (1), which will be referenced as "potential drop" in this work. As seen in Fig. 6a, the estimation process starts at 300 s with a 36.1% error in the SOC and shows a deviation of less than 1% for the cell voltage error after 191 s and 187 s for the PP- and EM-EKF. The magnified subplot (b) illustrates the regression of both observer models between 800 and 900 s. Fig. 6c shows the regression of the related cell voltage error and the magnified subplot d) reveals the marginal differences of approximately 1 mV between both observer models in the same time limits as shown in subplot (b). In accordance to Fig. 6, the numerical analysis is presented for the cell voltage and various local states in Table 6. The relative error values are related to the targeted present value of each state (*i.e.* predefined by the benchmark model) and the given time is related to the start of the estimation process (*i.e.* 300 s). Comparing local and global states of both observer-models, the potential in solid phase at the anode-separator interface takes approximately 4 times longer reaching the 1%-threshold than the cell voltage. The surface concentration takes approximately twice the time of the local solid potential to fall below the 1% threshold. The pore-wall flux converges far slower and even avoids a convergency to the 1%-threshold for the PP-EKF.

In sum, the CCCV estimation results show the fast and robust regression of the initial error regarding the cell voltage, but an accurate estimation of the global cell voltage is not bound to a proper estimation of the internal states. This results raises the question, to which extent the internal states deviate over the thickness of the electrodes. Looking into Fig. 6e, the residual error of the potential drop at the anode separator interface shows a stable regression below 1 mV after 700 s. Lithium plating most likely occurs at this location due to the largest overpotential within the anode [12] and thus a control strategy in the BMS could consider a lower limit of 0 V for this side-reaction overpotential (see Eq. (1)) in order to reduce the applied charging current if the limit is exceeded. The time to gain accurate values for this indicator – in this case 700 s – must be known to evaluate the readiness for use of this control algorithm.

The recovery of local states from only the measured current and the cell voltage need further analysis of the spatial gradients over the thickness of the cell to proof the functionality of the presented observer models. To do so, Fig. 7 shows the estimated local states such as the concentrations in both liquid and solid phase, the pore-wall flux and the potential drop at two discrete times of 1315 (t_A) and 1900 s (t_B). These times were chosen in accordance with the threshold between CC and CV period (t_A) and close to the 1% residual error for the pore-wall flux during the CV period (t_B). The concentration of the electrolyte in Fig. 7a
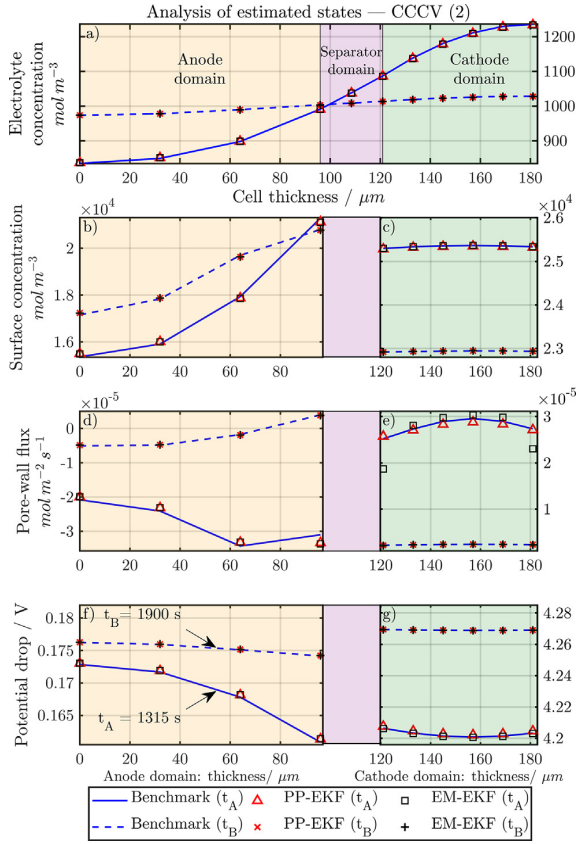
Fig. 7. The estimation results of local states at two different times (*i.e.* t_A and t_B) are shown in terms of the distribution over the cell thickness. The first subplot shows the concentration within the electrolyte (a) over the whole cell thickness. The plots b-g only depict the anode and cathode domain with the surface concentration (see (b) and (c)), the pore-wall flux (see (d) and (e)) and the potential drop (see (f) and (g)) over the related thicknesses.

shows the lowest deviation across the cell thickness at both times. Keeping in mind the initial errors ranged between 15.4 and 31.4%, the estimation error shows maximum values of 0.13% in the anode at the reference time t_A, which equals approximately a full recovery for the liquid concentration. The differences between the PP- and EM-EKF are negligible with a maximum deviation of 0.2% in the anode domain.

Regarding the surface concentration in Fig. 7b, the highest deviation of around 0.85% occurs at the anode-separator interface at t_B and differences of less than 0.01% for the mean error over the electrode thickness between both observer models can be seen.

The largest error is observed for the pore-wall flux (see Fig. 7c) whereas the potential drop (see Fig. 7d) shows marginal deviances over the thickness of the electrodes.

To sum up, both observer models show a fast regression of the residual error below 1% of the cell voltage from an initial SOC error of 35.2% in less than 200 s. Similar performance can be seen for the PP- and the EM-EKF with only marginal differences in estimation accuracy and regression speed. In terms of the surface concentration, it takes up to 5 times longer to reach similar residual errors compared to the global cell voltage. The SOC estimation is derived on the averaged solid concentrations and thus needs about 5 times longer for accurate estimation

Fig. 8. Estimation results for the BCCV charging scenario. The subplot (a) shows the presimulated cell voltage from the benchmark model and the estimated cell voltages of the PP- and EM-EKF. The magnified region in subplot (b) illustrates the regression of the residual cell voltage error after changing the boundary condition. The subplot (c) shows the related error of the cell voltage and the subplot (d) illustrates the error in the same limits as in subplot (b). The subplot (e) shows the error regression of the potential drop (*i.e.* $\Phi_s - \Phi_l$ see Eq. (1)) and subplots (f) and (g) show its spatial distribution for the times t_C and t_D.

results. The error of local states over the cell thickness appeared to be marginal, which proofs the functionality of the presented observer models. In terms of the potential drop, accurate estimation below 1 mV after 700 s enables to evaluate the readiness of the estimation process which is crucial for application of control algorithms especially for fast-charging scenarios.

3.2.2. Boost current charging

The BCCV scenario aims to proof the suitability of the two observer models towards varying boundary conditions in the form of changing the applied current. The BCCV simulation included a constant current rate of 4C during the boost period which was switched a 0.1C rate for the following low period at 750 s (t_C) to avoid an increase of the cell voltage above 4.1 V within the first period. The additional constant voltage period took place at 2135 s (t_D). The estimation results for the cell voltage, the error of the cell voltage and the potential drop at the anode-separator interface as well as its spatial distribution within the anode and the cathode at t_C and t_D are shown in Fig. 8.

As seen in Fig. 8a and c, the observer-models show a very quick

Table 7
Computational time and accuracy for the BCCV estimation.

States[a]	PP-EKF			EM-EKF		
	α_e	$t_{\leqslant 10\%}$	$t_{\leqslant 1\%}$	α_e	$t_{\leqslant 10\%}$	$t_{\leqslant 1\%}$
Φ_l	100	23	332	100	23	348
c_{ss}	100	96	545	100	94	350
j_n	100	340	514	100	337	482
Φ_s	9.2	1	227	9.4	1	233
η	100	344	491	100	338	466
V_{cell}	1.9	1	5	1.9	1	5

$\alpha_e/\%$ = Initial deviance after EKF initialization.
$t_{\leqslant 10\%}, t_{\leqslant 1\%}$ = Estimation time for error threshold of 10% and 1% referring to $t = 120$ s.
  [a] Boost period at $x = L^{NEG}$.

regression of the cell voltage recovery below 1% error within the first 5 s after the state estimation started at 120 s. Regarding the initial SOC error of 42.4%, this proofs the robustness of the presented models incorporating the novel initialization process against large initial failures. Again, the overall performance of the PP- and the EM-EKF show low deviances with a tendency of quicker estimation for the EM-EKF. Looking into Table 7, this can be seen especially in terms of the surface concentration at the anode-separator interface falling below the 1% error threshold 1/3 times faster than the PP-EKF. The slowest convergency below the 1% error threshold is seen for the surface concentration (545 s) and the pore-wall flux (482 s) for the PP- and EM-EKF, respectively. The cell voltage falls approximately after 150 s below the 0.1% error threshold which is approximately 3–4 times faster than the slowest estimated local state.

The magnified sections from 750 to 828 s in Fig. 8b and c show the fast recovery of the cell voltage with a comparably similar behavior for both observer-models at t_C and emphasize, that the estimation is robust for changing boundary conditions. As seen in Fig. 8e, the maximum error of the potential drop at the anode-separator interface is around 12 mV at t_C, but recovers very fast afterwards. Looking at the local states at t_C and t_B in Fig. 8f and g, also its estimated spatial distribution reveal sufficient accurate results for both observer models even at the change of the boundary condition. In short, the analysis of the BCCV estimation revealed a very quick regression of the cell voltage error and similar to the CCCV, longer estimation time is needed for accurate local states. The analysis of the changing boundary conditions showed the robustness of the presented observer models against an abrupt change of the applied current.

3.2.3. Pulsed current charging

The last estimated charging scenario aims to proof the suitability of the two observer models towards a pulsed input current. The PCCV estimation results are shown in Fig. 9 and the related numerical analysis is depicted in Table 8. Looking into Fig. 9a, the whole charging scenario is shown where the magnified subplot (see Fig. 9b) shows the approximation behavior of both models and no significant difference in terms of the cell voltage is seen between them. Both models converge below 1% error after approximately 8 s. At this time, the voltage error is around 39 mV. After 71 s, the error for both models falls below 4 mV. Regarding the error of cell voltage in Fig. 9c, the quick regression is shown and the magnified subplot (see Fig. 9d) between 205 and 300 s shows the characteristic error progression during the pulse and the resting period in the range of ±2 mV. Contrary to the charging scenarios discussed before, both observer-models do not converge below

Fig. 9. Estimation results for the PCCV charging scenario. The subplot (a) shows the presimulated cell voltage from the benchmark model and the estimated cell voltages of the PP- and EM-EKF. The magnified region in subplot (b) illustrates the initial approximation process. The subplot (c) shows the related error of the cell voltage and the subplot (d) illustrates the error between 210 and 300 s. The subplot (e) shows the error regression of the potential drop with a magnified section between 445 and 465 s. The subplots (g) and (h) show its spatial distribution for the times t_E and t_F.

Table 8
Computational time and accuracy for the PCCV estimation.

States[a]	PP-EKF				EM-EKF			
	α_e	$t_{\leqslant 10\%}$	$t_{\leqslant 5\%}$	$t_{\leqslant 1\%}$	α_e	$t_{\leqslant 10\%}$	$t_{\leqslant 5\%}$	$t_{\leqslant 1\%}$
c_l	5.5	21	43	352	5.5	21	61	351
Φ_l	100	29	63	303	100	29	80	363
c_{ss}	5.5	32	50	–	5.4	32	120	–
j_n	100	349	388	–	100	329	368	–
Φ_s	12.4	1	13	255	12.6	1	15	260
η	100	347	–	–	100	308	–	–
V_{cell}^1	1.7	–	1	8	1.7	–	1	7

α_e = Initial deviance after EKF initialization/%.
$t_{\leqslant 10\%}, t_{\leqslant 5\%}, t_{\leqslant 1\%}$ = Estimation time for error threshold of 10%, 5% and 1% referring to $t = 120$ s.
2 = CV period.
  [a] Pulse period at $x = L^{NEG}$.

Table 9
Error regression of cell voltage for the observer models.

	CCCV	BCCV		PCCV	
Initial SOC error	36.1%	42.4%	–	35.2%	
Current rate	2.5C	4C	0.1C	10C – pulse	
Error of V_{cell} = 1 mV	650 s	67 s	210 s	130 s[a]	PP-EKF
	630 s	30 s	200 s	90 s[a]	EM-EKF

[a] Error of V_{cell} = 4 mV.

1% for all local states such as the surface concentration, the over-potential and the pore-wall flux as seen in Table 8. This is caused by the pulsed load and gives the estimation process not enough time for convergency during the pulse period. Therefore, an additional 5% error threshold was added for the estimation performance in Table 8. In general, the performance of both models is similar with a slight tendency of faster convergency for the PP-EKF. In Fig. 9f, the potential drop at the anode-separator interface is magnified between 445 and 465 s which reveals the slight better accuracy of the EM-EKF. Looking into the spatial distribution of the potential drop over thickness of the electrodes, sufficient accuracy can be seen for both observer models exemplarily shown in Fig. 9g and h at 455 (t_E) and 538 s, which depicts the beginning of the CV-period (t_F).

To sum up, both observer models showed a quick regression of the cell voltage error below 1% in less than eight seconds with an initial SOC error of 35.2%. Both the PP- and the EM-EKF showed robust regression under the pulsed current with a slight tendency for better accuracy for the EM-EKF. The analysis of the potential drop over time and spatially within the electrodes at two different times revealed an accurate estimation of the indicator state for lithium-plating.

3.2.4. Comparison of the state estimation performance

In general, the observer models gain comparable results in terms of accuracy and computational speed for all charging scenarios regarded in this work. The robustness against varying boundary conditions was shown and the quick regression of the residual error was seen in all charging scenarios. The regression speed is summarized for the three charging scenarios referring to the initial SOC error, the remaining cell voltage error of 1 mV and the related estimation time in Table 9. Regarding only the cell voltage, the EM-EKF shows slightly faster regression compared to the PP-EKF. Particular interest is laid on the potential drop at the anode-separator interface and its spatial distribution within both electrodes. The observer models proofed the accurate recovery of this local indicator state for lithium plating from the measured current and cell voltage. As the observer models gain an accurate and robust estimation for local states, these could be used for control strategies in fast charging algorithms for controlling the applied current to the cell based on this indicator. In Fig. 10, the regression of the SOC error of the limiting cathode based on the average lithium concentration is shown for all charging scenarios. Marginal differences are seen for the CCCV and BCCV scenario, whereas the pulsed current charging revealed a slightly quicker regression for the EM-EKF than for the PP-EKF, which is well in line with the suitability for dynamic and constant discharge load scenarios shown in the simulation results. Looking at the overall charging times in Fig. 10, a reduction of 24.3%, 13.5% and 42.3% could be reached for the CCCV, BCCV and PCCV scenario, compared to a constant charge process comprising a 1C charging rate whilst avoiding possible lithium plating, which was monitored via the indicator state.
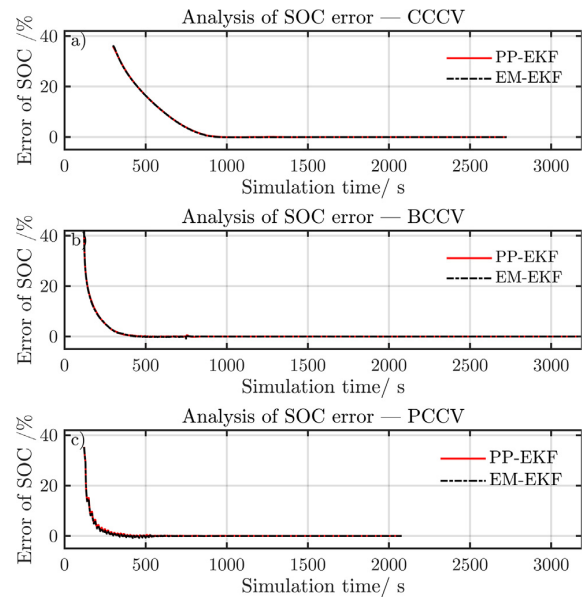
Fig. 10. The regression of the SOC error based on the average lithium concentration within the cathode domain is shown for the CCCV (a), BCCV (b) and the PCCV (c) scenario for both observer models.

4. Conclusion

The generally accepted pseudo two-dimensional physicochemical model (PCM) for lithium-ion batteries is used in this work for the simulation of constant and dynamic load scenarios. The non-linear differential algebraic equations were discretized in time via Crank-Nicolson formulation and the finite difference method with finite volume formulation was used for the fully-spatially-resolved PCM. Particular interest lied on the handling of boundary conditions with a low number of spatial discretization elements and the validity of the model was checked via comparison to reference models implemented in FORTRAN and COMSOL Multiphysics®. Further reducing the computational effort and enabling for a recursive formulation, the solid-phase diffusion equation was numerically approximated via a Polynomial Profile and an Eigenfunction Method. The simulation results confirmed the computational efficiency of the Polynomial Profile under constant current load and the Eigenfunction Method under dynamic load scenarios. The two computationally efficient PCMs were further used for implementation of two different linear state-space representations of the PCM using an Extended Kalman Filter algorithm which conserves lithium mass. To the authors best knowledge, this is the first approach using the PCM solved by finite volume method together with a non-linear Kalman Filter which accounts for lithium mass conservation and incorporates a robust Newton-Raphson initialization routine to ease the initial value problem. The state-estimation results showed a quick recovery of the cell's state for the measured cell voltage and the applied current together with robustness against changing boundary conditions and pulsed current signals. The models were able to reduce the residual cell voltage error to 2 mV with an initial SOC error of 35.2% in less than 90 s for a 10C pulsed charging scenario. Current and future work of the authors deals with the implementation of these two models on

microcontrollers, as first implementations proofed the suitability of the models presented in this work in low computational hardware environment. With the aid of this hardware-based implementation and a further development of the presented observer models towards constraints on the local battery states, novel fast charging strategies will be investigated to reduce charging time whilst avoiding lithium plating. The state estimation process will also be extended in terms of integrating temperature effects. Further development of the presented observer models can focus on the implementation of side-reactions such as lithium-plating and solid-electrolyte interphase to account for aging phenomena.

Acknowledgement

Appendix A. PCM

See Table 10.

Table 10
Equation system of the PCM.

Mass balance[a]	$\varepsilon_l \frac{\partial c_l(x,t)}{\partial t} = \frac{\partial}{\partial x}\left(D_l^{eff}\frac{\partial c_l(x,t)}{\partial x} + \frac{i_l(x,t)(1-t_+^0)}{F}\right)$
	$\varepsilon_s \frac{\partial c_s(x,t,r)}{\partial t} = \frac{1}{r^2}\frac{\partial}{\partial r}\left(D_s r^2 \frac{\partial c_s(x,t,r)}{\partial r}\right)$
Potentials[a]	$\frac{\partial \Phi_l(x,t)}{\partial x} = -\frac{i_l(x,t)}{\kappa_l^{eff}} + \frac{2RT}{F}(1-t_+^0)\left(1 + \frac{d\,lnf_\pm}{d\,ln\,c_l(x,t)}\right)\frac{\partial\,ln\,c_l(x,t)}{\partial x}$
	$\frac{\partial \Phi_s(x,t)}{\partial x} = -\frac{I(t)-i_l(x,t)}{\sigma_s}$ with $I(t) = i_s(x,t) + i_l(x,t) \quad \forall\ x,t$
Charge balance[a]	$\frac{\partial i_l(x,t)}{\partial x} + \frac{\partial i_s(x,t)}{\partial x} = 0$ with $\frac{\partial i_s(x,t)}{\partial x} = -3\frac{\varepsilon_s}{R_p}Fj_n(x,t)$
Electrode kinetics[a,b]	$j_n(x,t) = \frac{i_0(x,t)}{F}\left[exp\left(\frac{\alpha_a F \eta(x,t)}{RT}\right)-exp\left(-\frac{\alpha_c F \eta(x,t)}{RT}\right)\right]d^*$
	$\eta(x,t) = \Phi_s(x,t)-\Phi_l(x,t)-E_{eq}(x,t)-j_n(x,t)FR_f$
	$i_0(x,t) = F\,k\,(c_{s,max}-c_{ss}(x,t))^{\alpha_c}\,(c_{ss}(x,t))^{\alpha_a}\,(c_l(x,t))^{\alpha_a}$
Temperature[a,c]	$M\,C_p\frac{\partial T}{\partial t} = \left(U_0-V-T\frac{\partial U_0}{\partial T}\right)\cdot I-R_{ext}I^2-h_{conv}(T-T_\infty)$

[a] Ref. [13].
[b] Ref. [22].
[c] Ref. [32].

A.1. Boundary conditions

See Table 11.

Table 11
Internal and external boundary conditions of the PCM.

Model equation	Phase	Boundary conditions
Mass balance	solid	$\frac{\partial c_s(x,r,t)}{\partial r}\bigg|_{r=0} = 0$
		$\frac{\partial c_s(x,r,t)}{\partial r}\bigg|_{r=R_p} = -\frac{1}{D_s}j_n(x,t)$
	liquid	$\frac{\partial c_l(x,t)}{\partial x} = 0$,$\forall\ x \in \{0,L^{POS}\}$
		$D_l^{eff}\frac{\partial c_l(x,t)}{\partial x}\bigg|_{x=L^{NEG}} = D_l^{eff}\frac{\partial c_l(x,t)}{\partial x}\bigg|_{x=0^{SEP}}$
		$D_l^{eff}\frac{\partial c_l(x,t)}{\partial x}\bigg|_{x=L^{SEP}} = D_l^{eff}\frac{\partial c_l(x,t)}{\partial x}\bigg|_{x=0^{POS}}$
		$c_l(x,t)|_{x=L^{NEG}} = c_l(x,t)|_{x=0^{SEP}}$
		$c_l(x,t)|_{x=L^{SEP}} = c_l(x,t)|_{x=0^{POS}}$
Potentials	solid	$\Phi_s(x,t) = 0$,$\forall\ x \in\ ]0^{SEP},L^{SEP}[$
	liquid	$\Phi_l(L^{POS},t) = 0$
Charge balance	liquid	$i_l(0^{NEG},t) = 0$
		$i_l(x,t) = I$,$\forall\ x \in [0^{SEP},L^{SEP}]$
		$i_l(L^{POS},t) = 0$

A.2. Parameterization

See Tables 12 and 13.

Table 12
Parameterization I.

Geometry	MCMB	Separator	LiCoO$_2$
Thickness L	96 μm [a]	25 μm [a]	60 μm [a]
Particle radius R_p	8 μm [a]		5 μm [a]
Active material fraction ε_s	0.536 [a]		0.534 [a]
Porosity ε_l	0.40[a]	0.40[a]	0.36[a]
Thermodynamics			
Equilibrium potential E_{eq}	*analytic term*[a,b]		*analytic term*[a,b]
Entropic coefficient $\frac{\partial E_{eq}}{\partial T}$	*analytic term*[a,b]		*analytic term*[a,b]
Stoichiometric coefficient	0.8[a,d]		0.47[e,d]
Max. concentration $c_{s,max}$	24 984 mol m^{-3} [e]		51 219 mol m^{-3} [e]
Kinetics			
Reaction rate constant k	3.0×10^{-9} m s^{-1} [a]		3.0×10^{-9} m s^{-1} [a]
Transfer coefficient $\alpha_{a/c}$	0.5[a]		0.5[a]
Denominator d^*	1[a]		1[a]
Transport			
Solid diffusivity D_s	7×10^{-14} m^2 s^{-1} [a]		3×10^{-14} m^2 s^{-1} [a]
Solid conductivity σ_s	100 S m^{-1} [a]		0.5 S m^{-1} [a]
Film resistance R_f	3.5×10^{-3} Ω m^2 [a]		0 Ω m^2 [a]
Electrolyte (1 M LiPF$_6$ in 1:1 EC/DMC)			
Salt diffusivity D_l^{eff}	$5.34 \times {}^{-10} \frac{m^2}{s} \varepsilon_l^{1.5} \exp\left(\frac{-0.65\,c_l}{c_{ref}}\right)$[a,c]		
Ionic conductivity κ_l^{eff}	$\varepsilon_l^{1.5}\left[0.0911 + \frac{1.9101\,c_l}{c_{ref}} - 1.052\left(\frac{c_l}{c_{ref}}\right)^2 + 0.1554\left(\frac{c_l}{c_{ref}}\right)^3\right]\frac{S}{m}$[a,c]		
Activity $\frac{d\,lnf_{\pm}}{d\,lnc_l}$	0 [a]		
Transference t_+^0	0.4 [a]		
Ref. concentration c_{ref}	1000 mol m^{-3} [a]		
Global			
Grid resistance R_{ext}	2×10^{-4} Ω m^2 [a]		

[a] Ref. [33].
[b] Ref. [34].
[c] Ref. [51].
[d] Discharge scenario ($k = 0$)
[e] estimated

Table 13
Parameterization II.

Thermal Parameters I – Activation energy $\frac{E_A}{R}$ [c]	
Reaction rate constants $k_{a/c}$	1800 K[a]
Film resistance R_f	-1800 K[a]
Solid diffusivity $D_{s,a}$	200 K[a]
Solid diffusivity $D_{s,c}$	900 K[a]
Salt diffusivity D_l^{eff}	2000 K[a]
Ionic conductivity κ_l^{eff}	1690 K[a]
Thermal Parameters II – Cell specifications	
Specific mass M	0.4932 kg m^{-2a}
Heat capacity C_p	1000 J kg^{-1} K^{-1a}
Heat transfer Coefficient h_{conv}	1 W m^{-2} K^{-1b}

[a] Ref. [33].
[b] Estimated.
[c] Arrhenius law [52]: $k = A \cdot \exp\left(-\frac{E_A \cdot (T - 298)}{R\,T \cdot 298}\right)$.

A.3. Spatial discretization using FDM with FVM formulation

See Table 14.

Table 14
FDM-discretization for DAE of the PCM at $x = \mathrm{L}^{\mathrm{NEG}}$

Mass balance in liquid phase

$$-\frac{\varepsilon_l^{\mathrm{NEG}}\,h^{\mathrm{NEG}}}{\Delta t\,8}[c_l(x_{j-1},t_k) - c_l(x_{j-1},t_{k-1}) + 3c_l(x_j,t_k) - 3c_l(x_j,t_{k-1})]\cdots$$
$$-(\varepsilon_l^{\mathrm{NEG}})^{1.5}\frac{1}{2}(D_l(x_j) - D_l(x_{j-1}))\frac{1}{h^{\mathrm{NEG}}}(c_l(x_j,t_k) - c_l(x_{j-1},t_k))\cdots$$
$$-\left[1 - \frac{1}{2}(t_+^0(x_j) + t_+^0(x_{j-1}))\right]\frac{1}{2F}(i_l(x_j,t_k) - i_l(x_{j-1},t_k))\cdots$$
$$-\frac{\varepsilon_l^{\mathrm{SEP}}\,h^{\mathrm{SEP}}}{\Delta t\,8}[c_l(x_{j+1},t_k) - c_l(x_{j+1},t_{k-1}) + 3c_l(x_j,t_k) - 3c_l(x_j,t_{k-1})]\cdots$$
$$+ (\varepsilon_l^{\mathrm{SEP}})^{1.5}\frac{1}{2}(D_l(x_{j+1}) - D_l(x_j))\frac{1}{h^{\mathrm{SEP}}}(c_l(x_{j+1},t_k) - c_l(x_j,t_k))\cdots$$
$$+ \left[1 - \frac{1}{2}(t_+^0(x_j) + t_+^0(x_{j+1}))\right]\frac{1}{2F}(i_l(x_j,t_k) + i_l(x_{j+1},t_k))$$

Potential in liquid phase

$$\Phi_l(x_{j+1},t_k) - \Phi_l(x_j,t_k) + \frac{h^{\mathrm{SEP}}}{2(\varepsilon_l^{\mathrm{SEP}})^{1.5}}\left[\frac{i_l(x_j,t_k)}{\kappa_l(x_j)} + \frac{i_l(x_{j+1},t_k)}{(\kappa_l(x_{j+1})}\right] - \frac{R\,T}{F}\left[\left(\frac{1}{c_l(x_j,t_k)}\cdots\right.\right.$$
$$\left.+ \frac{dlnf_\pm}{d\,c_l}\bigg|_{x_j}\right)(1 - t_+^0(x_j)) + \left(c_l(x_{j+1},t_k)^{-1} + \frac{dlnf_\pm}{d\,c_l}\bigg|_{x_{j+1}}\right)(1 - t_+^0(x_{j+1}))\right]\cdots$$
$$\cdot(c_l(x_{j+1},t_k) - c_l(x_j,t_k))$$

Potential in solid phase

$$-(\Phi_s(x_j,t_k) - \Phi_s(x_{j-1},t_k)) - h^{\mathrm{NEG}}\frac{I(t_k)}{\sigma(x_j)} + \frac{h^{\mathrm{NEG}}}{2\,\sigma(x_j)}(i_l(x_j,t_k) + i_l(x_{j-1},t_k))$$

Charge balance

$$I(t_k) - i_l(x_j,t_k)$$

Appendix B. Linear Kalman filter algorithm

See Table 15.

Table 15
Kalman Filter algorithm [43–45].

Vectors	Discrete State-Space Model of DAE
x = Dynamic state z = Algebraic state u = Measured input y = Measured Output v_k, ω_k = Noise	$x_k = f(x_{k-1}, z_{k-1}, u_k) + \omega_k \quad 0 = g(x_{k-1}, z_{k-1}, u_k)$ $y_k = \mathbf{h}(x_k, z_k, u_k) + v_k$
	Filter Algorithm
Linear state-space representation [46] Prediction Correction gain	$\mathbf{x}_k = \mathbf{F}_k\, x_{k-1} + \mathbf{B}_k\, u_k + \omega_k$ $y_k = \mathbf{H}_k\, x_k + v_k$ $x_{k|k-1} = \mathbf{F}_k\, x_{k-1|k-1} + \mathbf{B}_k\, u_k$ $\mathbf{P}_{k|k-1} = \mathbf{F}_k\, \mathbf{P}_{k-1|k-1}\, \mathbf{F}_k^T + \mathbf{Q}_k$ $\mathbf{K}_k = \mathbf{P}_{k|k-1}\, \mathbf{H}_k^T [\mathbf{H}_k\, \mathbf{P}_{k|k-1}\, \mathbf{H}_k^T + \mathbf{R}_k]^{-1}$ $\widetilde{y}_k = y_k - \mathbf{H}_k\, x_{k|k-1}$
Update	$\mathbf{x}_{k|k} = \mathbf{x}_{k|k-1} + \mathbf{K}_k\, \widetilde{y}_k$ $\mathbf{P}_{k|k} = (\mathbf{I} - \mathbf{K}_k\, \mathbf{H}_k)\mathbf{P}_{k|k-1},$

Appendix C. Symbols

See Tables 16 and 17.

Table 16
Symbols I.

Greek symbols		
α		Transfer coefficient
ε		Volume fraction
ϵ		Numerical tolerance
η	V	Overpotential
κ	$S\,m^{-1}$	Ionic conductivity
σ	$S\,m-1$	Electrical conductivity
τ		Tortuosity
Φ	V	Electrical potential
Indices		
0		Reference state
a		anodic
c		cathodic
eff		Transport corrected
i		Discrete iteration step
j		Discrete node
k		Discrete time step
l		Liquid phase
NEG		Negative electrode (MCMB)
POS		Positive electrode (LiCoO$_2$)
s		Solid phase - Active particle
ss		Solid phase - Active particle surface
SEP		Separator

Table 17
Symbols II.

Latin symbols		
a	m^{-1}	Specific surface
$\mathbf{B}$		Input matrix
c	$\mathrm{mol\,m}^{-3}$	Concentration of lithium cations (Li^{+})
$c_{s,max}$	$\mathrm{mol\,m}^{-3}$	Maximum concentration of Li^{+}
C_p	$\mathrm{J\,kg}^{-1}\mathrm{K}^{-1}$	Heat capacity
E_{eq}	V	Equilibrium potential vs. $\mathrm{Li/Li}^{+}$
$f_{\pm}$		Mean molar activity coefficient of electrolyte
F	$96\,485.33\,\mathrm{As\,mol}^{-1}$	Faraday's constant
$\mathbf{F}$		Transition matrix
h	$\mathrm{W\,m}^{-2}\mathrm{K}^{-1}$	Convective heat transfer coefficient
$\mathbf{H}$		Observation matrix
i	$\mathrm{A\,m}^{-2}$	Current density
i_n	$\mathrm{A\,m}^{-2}$	Current density normal to particle surface
I	$\mathrm{A\,m}^{-2}$	Applied current density
j_n	$\mathrm{mol\,m}^{-2}\mathrm{s}^{-1}$	Pore-wall flux
$\mathbf{K}$		Kalman gain matrix
L	m	Thickness
M	$\mathrm{kg\,m}^{-2}$	Specific mass of the cell
n_{Li}	$\mathrm{mol\,m}^{-2}$	Total amount of cycleable lithium
$\mathbf{P}$		Approximate error covariance matrix
$\mathbf{Q}$		Process noise covariance matrix
r	m	Dimension within active particles
R	$8.314\,\mathrm{J\,mol}^{-1}\mathrm{K}^{-1}$	Gas constant
R_p	m	Particle radius
$\mathbf{R}$		Measurement noise covariance matrix
t	s	Time
Δt	s	Discrete time step
T	K	Temperature
t_+^0		Transport number of Li^{+}
U_0	V	Open circuit voltage of the cell
x	m	Dimension through thickness of electrodes

References

[1] Languang L, Xuebing H, Jianqiu L, Jianfeng H, Minggao O. A review on the key issues for lithium-ion battery management in electric vehicles. J Power Sources 2013;226:272–88.

[2] Blomgren GE. The development and future of lithium ion batteries. J Electrochem Soc 2016;164(1):A5019–25. http://dx.doi.org/10.1149/2.0251701jes.

[3] Ciez RE, Whitacre JF. Comparison between cylindrical and prismatic lithium-ion cell costs using a process based cost model. J Power Sources 2017;340:273–81.

[4] Vehicle Technologies Office, Battery; 2012. < https://energy.gov/eere/electricvehicles/about-electric-vehicles > .

[5] Lazard. Lazards's levelized cost of storage – version 2.0; 2016. < https://www.lazard.com/media/438042/lazard-levelized-cost-of-storage-v20.pdf > .

[6] Luo X, Wang J, Dooner M, Clarke J. Overview of current development in electrical energy storage technologies and the application potential in power system operation. Appl Energy 2015;137:511–36. http://dx.doi.org/10.1016/j.apenergy.2014.09.081.

[7] Nykvist B, Nilsson M. Rapidly falling costs of battery packs for electric vehicles. Nat Clim Change 2015;5(4):329–32. http://dx.doi.org/10.1038/nclimate2564.

[8] Orendorff J. The role of separators in lithium-ion cell safety. Electrochem Soc Interface 2012:61–5.

[9] Ramadesigan V, Northrop PWC, De S, Santhanagopalan S, Braatz RD, Subramanian VR. Modeling and simulation of lithium-ion batteries from a systems engineering perspective. J Electrochem Soc 2012;159(3):R32–45.

[10] Lee K-J, Smith KA, Pesaran A, Kim G-H. Three dimensional thermal-, electrical-, and electrochemical-coupled model for cylindrical wound large format lithium-ion batteries. J Power Sources 2013;241:20–32. http://dx.doi.org/10.1016/j.jpowsour.2013.03.007.

[11] Waag W, Fleischer C, Sauer DU. Critical review of the methods for monitoring of lithium-ion batteries in electric and hybrid vehicles. J Power Sources 2014;258:321–39. http://dx.doi.org/10.1016/j.jpowsour.2014.02.064.

[12] Hein S, Latz A. Lithium plating and stripping in the framework of a 3d electrochemical model. ECS Trans 2015;69(1):3–5. http://dx.doi.org/10.1149/06901.0003ecst.

[13] Doyle M, Fuller TF, Newman J. Modeling of galvanostatic charge and discharge of the lithium/polymer/insertion cell. J Electrochem Soc 1993;140(6):1526–33.

[14] Cai C-H, Du D, Liu Z-Y, Zhang H. Modeling and identification of ni-mh battery using dynamic neural network. IEEE Mach Learn Cybernet 2002;3:1594–600.

[15] Hu X, Li S, Peng H. A comparative study of equivalent circuit models for li-ion batteries. J Power Sources 2012;198:359–67. http://dx.doi.org/10.1016/j.jpowsour.2011.10.013.

[16] Plett GL. Extended Kalman filtering for battery management systems of LiPB-based HEV battery packs. J Power Sources 2004;134(2):277–92. http://dx.doi.org/10.1016/j.jpowsour.2004.02.033.

[17] Plett GL. Sigma-point Kalman filtering for battery management systems of LiPB-based HEV battery packs. J Power Sources 2006;161(2):1369–84. http://dx.doi.org/10.1016/j.jpowsour.2006.06.004.

[18] Zhang X, Lu J, Yuan S, Yang J, Zhou X. A novel method for identification of lithium-ion battery equivalent circuit model parameters considering electrochemical properties. J Power Sources 2017;345:21–9. http://dx.doi.org/10.1016/j.jpowsour.2017.01.126.

[19] Wei Z, Zou C, Leng F, Soong BH, Tseng K-J. Online model identification and state-of-charge estimate for lithium-ion battery with a recursive total least squares-based observer. IEEE Trans Industr Electron 2018;65(2):1336–46. http://dx.doi.org/10.1109/TIE.2017.2736480.

[20] Prada E, Di Domenico D, Creff Y, Bernard J, Sauvant-Moynot V, Huet F. A simplified electrochemical and thermal aging model of LiFePO4-graphite li-ion batteries: power and capacity fade simulations. J Electrochem Soc 2013;160(4):A616–28. http://dx.doi.org/10.1149/2.053304jes.

[21] Rieger B, Erhard SV, Kosch S, Venator M, Rheinfeld A, Jossen A, et al. displacement and stress inhomogeneity in large-format lithium-ion cells. J Electrochem Soc 2016;163(14):A3099–110. http://dx.doi.org/10.1149/2.1051614jes.

[22] Mao J, Tiedemann W, Newman J. Simulation of li-ion cells by dualfoil model under constant-resistance load. ECS Trans 2014;58(48):71–81. http://dx.doi.org/10.1149/05848.0071ecst.

[23] Smith KA, Rahn CD, Wang C-Y. Model-based electrochemical estimation and constraint management for pulse operation of lithium ion batteries. IEEE Trans Control Syst Technol 2010;18(3):654–63. http://dx.doi.org/10.1109/TCST.2009.2027023.

[24] Domenico DD, Fiengo G, Stefanopoulou A. Lithium-ion battery state of charge estimation with a kalman filter based on a electrochemical model. In: [CCA]; San Antonio, TX, 3–5 september 2008; [part of 2008 IEEE multi-conference on systems and control (MSC)]. IEEE Multi-conference on systems and control, vol. 17; 2008. p. 702–7.

[25] Bizeray AM, Zhao S, Duncan SR, Howey DA. Lithium-ion battery thermal-electrochemical model-based state estimation using orthogonal collocation and a modified extended Kalman filter. J Power Sources 2015;296:400–12. http://dx.doi.org/10.1016/j.jpowsour.2015.07.019. Available from: 1506.08689v1.

[26] Jokar A, Rajabloo B, Désilets M, Lacroix M. Review of simplified pseudo-two-dimensional models of lithium-ion batteries. J Power Sources 2016;327:44–55. http://dx.doi.org/10.1016/j.jpowsour.2016.07.036.

[27] Ning G, White RE, Popov BN. A generalized cycle life model of rechargeable li-ion batteries. Electrochim Acta 2006;51(10):2012–22. http://dx.doi.org/10.1016/j.electacta.2005.06.033.

[28] Klein R, Chaturvedi NA, Christensen J, Ahmed J, Findeisen R, Kojic A. Optimal charging strategies in lithium-ion battery. Am Control Conf 2011:382–7.

[29] Klein R, Chaturvedi NA, Christensen J, Ahmed J, Findeisen R, Kojic A. State estimation of a reduced electrochemical model of a lithium-ion battery. Am Control Conf 2010:6618–23.

[30] Thomas KE, Newman J, Darling RM. Mathematical modeling of lithium batteries. In: van Schalkwijk WA, Scrosati B, editors. Advances in lithium-ion batteries Boston, MA: Springer US; 2002. p. 345–92. http://dx.doi.org/10.1007/0-306-47508-1_13.

[31] Newman J, Thomas-Alyea KE. Electrochemical systems, 3rd ed. Berkeley, CA: Wiley-Interscience; 2004. 94720-1462.

[32] Bernardi D, Pawlikowski E, Newman J. A general energy balance for battery systems. J Electrochem Soc 1985;132:5–12.

[33] Mao J, Tiedemann W, Newman J. Simulation of temperature rise in li-ion cells at very high currents. J Power Sources 2014;271:444–54. http://dx.doi.org/10.1016/j.jpowsour.2014.08.033.

[34] Newman J. Fortran programs for the simulation of electrochemical systems: dualfoil5.2.f; 2014. < http://www.cchem.berkeley.edu/jsngrp/ > .

[35] Katz VJ. The history of stokes' theorem. Math Mag 1979;52(3):146–56 < http://www.jstor.org/page/info/about/policies/terms.jsp > .

[36] Subramanian VR, Diwakar VD, Tapriyal D. Efficient macro-micro scale coupled modeling of batteries. J Electrochem Soc 2005;152(10):2002–8.

[37] Guo M, White RE. An approximate solution for solid-phase diffusion in a spherical particle in physics-based li-ion cell models. J Power Sources 2012;198:322–8. http://dx.doi.org/10.1016/j.jpowsour.2011.08.096.

[38] Brenan KE, La Campbell SV, Petzold LR, editors. Numerical solution of initial-value problems in differential-algebraic equations. Classics in applied mathematics. Society for Industrial and Applied Mathematics, Philadelphia, vol. 14; 1996. http://dx.doi.org/10.1137/1.9781611971224.

[39] Newman J. Numerical solution of coupled, ordinary differential equations. Industr Eng Chem Fund 1968;7(3):514–7. http://dx.doi.org/10.1021/i160027a025.

[40] The MathWorks. Matlab function reference; 2017. < https://de.mathworks.com/help/matlab/ref/mldivide.html?requestedDomain=www.mathworks.com > .

[41] Arens T, Hettlich F, Karpfinger C, Kockelkorn U, Lichtenegger K, Stachel H.

[42] Plett GL. Extended Kalman filtering for battery management systems of LiPB-based HEV battery packs. J Power Sources 2004;134(2):252–61. http://dx.doi.org/10.1016/j.jpowsour.2004.02.031.

[43] Kalman RE. Contributions to the theory of optimal control. Bol Soc Mat Mexicana 1960(5):102–19.

[44] Kalman RE. A new approach to linear filtering and prediction problems. J Basic Eng 1960;82(1):35. http://dx.doi.org/10.1115/1.3662552.

[45] Kalman RE, Bucy RS. New results in linear filtering and prediction theory. J Basic Eng 1961;83(1):95. http://dx.doi.org/10.1115/1.3658902.

[46] Haykin SS, editor. Kalman filtering and neural networks. Adaptive and learning systems for signal processing, communications, and control. New York NY, u.a.: Wiley; 2001.

[47] Campestrini C, Heil T, Kosch S, Jossen A. A comparative study and review of different Kalman filters by applying an enhanced validation method. J Energy Storage 2016;8:142–59. http://dx.doi.org/10.1016/j.est.2016.10.004.

[48] Klein R, Chaturvedi NA, Christensen J, Ahmed J, Findeisen R, Kojic A. Electrochemical model based observer design for a lithium-ion battery. IEEE Trans Control Syst Technol 2013;21(2):289–301. http://dx.doi.org/10.1109/TCST.2011.2178604.

[49] Doyle M. Design and simulation of lithium rechargeable batteries [Ph.d. thesis]. Berkeley: University of California; 08/1995.

[50] Ramadesigan V, Boovaragavan V, Pirkle JC, Subramanian VR. Efficient reformulation of solid-phase diffusion in physics-based lithium-ion battery models. J Electrochem Soc 2010;157(7):A854. http://dx.doi.org/10.1149/1.3425622.

[51] Bruggeman DAG. Berechnung verschiedener physikalischer konstanten von heterogenen substanzen. III. die elastischen konstanten der quasiisotropen mischkörper aus isotropen substanzen. Ann Phys 1937;421(2):160–78. http://dx.doi.org/10.1002/andp.19374210205.

[52] Arrhenius S. Über die reaktionsgeschwindigkeit bei der inversion von rohrzucker durch säuren. Z Phys Chem 4(1). http://dx.doi.org/10.1515/zpch-1889-0116.

Mathematik, 2nd ed. Spektrum Akad. Verl. Heidelberg; 2010.

5 Safety-Critical Short-Circuit Scenarios of Lithium-Ion Batteries
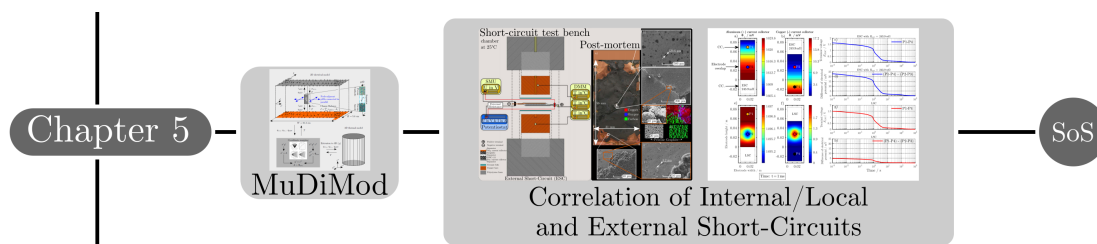
Figure 5.1: Outline of chapter 5.

Within this section, the article titled *On The Impact of the Locality on Short-Circuit Characteristics: Experimental Analysis and Multiphysics Simulation of External and Local Short-Circuits Applied to Lithium-Ion Batteries* is presented. Fig. 5.1 refers to the thesis outline shown in section 1.6 and summarizes the content of the article in this section.

5.1 Emulating and Analyzing the Short-Circuit Behavior

A key feature of the BMS is to keep the LIB in a safe operating range and to guarantee a sufficient SoS all the time. A short-circuit is one of the most critical safety issues, which can occur during operation of a LIB. To mitigate safety issues, the understanding of the physical processes during a short-circuit is crucial, when fail-safe or precursor/early detection methods [69] are developed for the BMS to counter abuse scenarios and eventually avoid a thermal runaway [134, 169]. Combining experimental and simulation based studies on short-circuit events offers huge potential to increase the understanding of the occurring electrochemically caused rate limiting behavior of a LIB, which defines the characteristics of the short-circuit and are rather sparsely discussed in literature [169]. To profoundly investigate electrochemically caused rate limiting effects during a short-circuit, thermal effects such as overheating or a thermal runaway should be excluded. This can be realized via a quasi-isothermal test bench and the usage of small capacitive pouchbag LIBs [154, 208]. Emulating field-like short-circuits with experimental techniques is challenging with mostly unsatisfactory outcome due to the unpredictability of the actual trigger mechanisms and the recreation of application conditions. Internal short-circuits are complex as often failures are triggered on the long term due to aging effects or manufacturing impurities, which typically initiate a shorting through the penetration of the separator in the electrode stack. Nevertheless, nail-penetration techniques are suitable to trigger at least a similar high current load across the active electrode area by mechanically penetrating the electrode stack at a single spot. This can be described as a local short-circuit scenario emulating an internal short-circuit. External short-circuits are less complex, more reproducible and can be emulated with an external resistance between the terminals of a LIB to control the current flow during the actual shorting, which

correlates well to the intensity of the short-circuit event. The current flow is complex to measure for the internal/local short-circuits, which complicates the assessment of the shorting intensity. However, a suitable alternative uses the experimental results of both short-circuits to validate a high current modified physicochemical model [134]. The current flow in case of the internal/local short-circuit can be simulated and the intensity of the shorting scenario can be correlated to the external short-circuit. Furthermore, the model based analysis can be used to explain the occurring electrochemically caused rate limiting effects during the short-circuit event.

In the following section, the experimental characterization of internal/local and external short-circuits is presented together with a high current and short-circuit modified MuDiMod, which enables the correlation of the intensity between the two shorting scenarios.

5.2 Correlating Local and External Short-Circuits

Within the following article, short-circuit tests were applied to single- and double-layered pouchbag C/NMC-111 LIBs in a quasi-isothermal calorimetric test bench. The focus of this experimental work lies on investigating the potentiostatic and calorimetric behavior of a short-circuit scenario and identifying electrochemically caused rate limiting behavior. With the aid of the measured terminal voltage, current flow and heat generation the transient short-circuit behavior can be characterized in terms of its intensity. The applied external short-circuits appear to be most reproducible and their intensity correlates with the external resistance, used between the terminals to control the short-circuit current. The internal short-circuit is emulated by a local short-circuit applied with nail-penetration in the center of the active electrode area and reveals a lower reproducibility. Nevertheless, a clear correlation between the used nail diameter and the shorting intensity appears. The potentiostatic correlation between external and local short-circuits is complex, as the terminal voltage profile cannot directly be compared due to different electrical potential fields across the active electrode area evoked by the locality of the shorting. A correction of the measured terminal voltage for the local short-circuit can be derived from simulation results using MuDiMod studies, which can describe the voltage drops across the active electrode area for both short-circuit scenarios. As a result, the local short-circuit reveals a comparable shorting intensity to external short-circuit tests, which are conducted at an external resistance in the range from $5\,\mathrm{m\Omega}$ to $50\,\mathrm{m\Omega}$. Post-mortem analysis reveals in both cases significant copper dissolution from the negative current collector, which dominantly increases the discharge capacity under short-circuit events by more than $25\,\%$ SoC.

The experimental and simulation based results of the following article provide the required insights to understand better the underlying electrochemical mechanisms during a short-circuit event, which help to develop high current suitable physicochemical modeling approaches in future. The resulting extensions of the physicochemical modeling structure can then be used in advanced state-estimation techniques as well, which was out of scope for this thesis.

Author contribution Johannes Sturm carried out, analyzed and interpreted all experimental tests. The MuDiMod was extended to simulate internal short-circuits by Johannes Sturm, who also carried out and interpreted together with Alexander Rheinfeld the simulation data. Alexander Rheinfeld developed the idea of the quasi-isothermal short-circuit, developed the custom built test bench and initiated the idea of correlating the internal/local to the external short-circuit. The manuscript was written by Johannes Sturm and edited by Alexander Rheinfeld, Didier Buzon and Andreas Jossen.

All authors discussed the data and commented on the results.

Publication notes   The article titled *On The Impact of the Locality on Short-Circuit Characteristics: Experimental Analysis and Multiphysics Simulation of External and Local Short-Circuits Applied to Lithium-Ion Batteries* is presented in the following and the related supplementary material is shown in the appendix (see section D). The article [209] and the supplementary material [210] are published in the Journal of The Electrochemical Society. The extension of the MuDiMod to simulate internal/local short-circuits in LIBs was presented at the *14th Symposium on Fuel Cell and Battery Modeling and Experimental Validation* in Karlsruhe (Germany) in March 2017.

On The Impact of the Locality on Short-Circuit Characteristics: Experimental Analysis and Multiphysics Simulation of External and Local Short-Circuits Applied to Lithium-Ion Batteries

Johannes Sturm, Alexander Rheinfeld, Didier Buzon, Andreas Jossen

On The Impact of the Locality on Short-Circuit Characteristics: Experimental Analysis and Multiphysics Simulation of External and Local Short-Circuits Applied to Lithium-Ion Batteries

J. Sturm,[1,z] A. Rheinfeld,[1] D. Buzon,[2,3] and A. Jossen[1,4]

[1]*Institute for Electrical Energy Storage Technology (EES), Technical University of Munich (TUM), 80333 Munich, Germany*
[2]*Univ. Grenoble Alpes, 38000 Grenoble, France*
[3]*CEA, Liten, 38054 Grenoble, France*
[4]*Munich School of Engineering (MSE), Technical University of Munich (TUM), 85748 Garching, Germany*

Emulating true, field-like internal short-circuits (ISCs) by experimental methods is a complex task with mostly unsatisfactory outcome. However, understanding the evolution and impact of ISCs is crucial to mitigate safety issues related to lithium-ion batteries. Local short-circuit (LSC) conditions are applied to single-layered, small-sized (i.e. <60 mAh), and single-side coated graphite/NMC-111 pouch-type cells in a quasi-isothermal test bench using the nail/needle penetration approach. The cell's impedance, capacity, and the contact resistance at the penetration site mainly define the short-circuit current and, hence, the terminal voltage and heat generation rate associated with polarization effects and electrochemical rate limitations, which are correlated to the cell's behavior during external short-circuits (ESCs) at various short-circuit resistances. Measuring the electrical potential between the needle and the cell's negative tab allows to evaluate the polarization across the electrodes and to estimate the short-circuit intensity. LSC simulation studies are used to correlate current flux and resistance to ESC conditions. Double-layered cells are penetrated to create short-circuit conditions within either a single or both electrode stacks to study the difference between multiple LSCs (e.g. during a nail penetration test) and a single LSC (e.g. due to a particle/dendrite). Post-mortem analysis reveals copper dissolution/deposition across both electrodes.

Recent reports[1] summarizing critical incidents involving lithium-ion batteries (LIBs) revealed similar characteristics of initial overheating, followed by smoke[2–4] and/or spark emission,[1] and, in case of a self-accelerating heat generation, leading to explosions[5] and/or fire and flames released by the battery.[6,7] Unless the safety of LIBs cannot be maintained under all conditions to minimize or even exclude any harm to the environment/individuals, the current trend toward optimizing cost[8] and performance of LIBs involving higher energy densities[9,10] and/or an improved rate capability[11] may impede the market penetration for mobile, automotive, and stationary energy storage applications.

Safety issues of LIBs can be caused by a variety of internal and external triggers related to manufacturing issues, shortcomings in design, and/or operation strategy,[7] as well as mechanical,[8] electrical, and thermal abuse conditions,[12,13] which can lead to external and internal short-circuit scenarios. Hence, there is a strong need for relevant test scenarios simulating such triggers, which help understanding the underlying mechanisms in order to derive suitable means to mitigate or even rule out safety issues related to LIBs (e.g. shutdown separators,[14] integrated circuits,[15] pyrotechnical safety systems,[16] etc.) by increasing the battery's tolerance toward ESCs and ISCs.

On the one hand, ESC tests revealing a good reproducibility[17] and relevance for simulating realistic high current and abusive short-circuit conditions applied via the terminals of a LIB. On the other hand, simulating ISCs within a LIB by experimental means is a more complex task. As an example for a typical, field-like ISC failure, metallic particle contamination, followed by dissolution and deposition including dendrite growth can lead to a local penetration of the separator and initiate a short-circuit.[18–20] In order to reproduce such a field-like shorting scenario, the test must trigger the shorting only at a single site, set a low ohmic resistance, form over time/operation of the LIB, and should reveal sufficient reproducibility. Adjusting

the locality of the short-circuit seems to be viable regarding the range of already existing test procedures including a complete or partial penetration the LIB with a nail or needle[21] or the insertion of local defects during assembly of the battery,[22] whereas controlling the shorting resistance may only be partly viable due to the variety of possible materials and contact conditions between the electrodes and current collectors[23] as well as possible changes during the shorting scenario.[24] The formation over time can hardly be recreated by experimental methods as the aforementioned defects form over the lifetime of LIBs and exceed practical operation times of safety tests by far. As a result, existing tests such as nail penetration[21,24–29] or the more complex modification of LIB via insertion of local defects in the electrode stack/jelly roll[22,30] cannot satisfactorily simulate a real, field-like ISC scenario but at least approximate similar high current scenarios with a strong local heat generation.

The insertion of local defects such as low-melting temperature alloys[22] require a modification of the electrode stack/jelly roll which may alter the battery's behavior beside time- and cost-intensive efforts to manufacture these prototype cells. In comparison, a nail penetration test can be applied easier using similar cells as used for ESC tests. Investigating both short-circuit conditions applied to the same cells enables for a comparison/correlation to understand the electrical and thermal behavior of locally applied short-circuits.

In sum, so far there is no test that can satisfactorily recreate a realistic, field-like ISC in LIBs. Based on its straightforward applicability, a nail or needle penetration technique was applied to create not field-like ISCs but local short circuits (LSCs) within a cell. In addition to studying the cell's LSC characteristics, ESC tests were applied in accordance with our previous work.[31] The influence of the electrical electrode design was minimized by using the same single-side coated electrodes, with a counter-tab design throughout all tests. By further studying cells with one or two electrode stacks within a quasi-isothermal calorimetric test bench, effects related to the cell's thermal design or the locality of heat generation were minimized. In this work, we investigate the influence of the locality of the shorting scenario via triggering the short-circuit in the center of the electrodes

[z]E-mail: johannes.sturm@tum.de

using the nail/needle penetration technique and eventually compare the cell's local short-circuit characteristics to its external short-circuit behavior. As the external resistance directly correlates to both the current flux and heat generation rate and, hence, defines the intensity of the ESC, a low-ohmic resistance range as expected for the LSC tests was investigated, which enables for a comparison/correlation of the terminal voltage and the heat generation rate in order to evaluate the intensity of the applied LSC scenario. As the locality of the shorting affects local electrode polarization during the LSC tests, a correction of the terminal voltage based on a multi-dimensional simulation study must be applied in order to allow for a direct comparison of LSC and ESC test results, which eventually allows estimating the shorting resistance evoked via nail/needle penetration. Using the quasi-isothermal, calorimetric test bench, the short-circuit proceeds without triggering a high local heat generation rate, which may lead to thermal, self-accelerating processes such as a thermal runaway scenario. Usually, this applies when local particle insertion procedure or nail penetration tests are applied for emulating ISC scenarios in LIBs. By applying our technique, we can mitigate the influence of these thermal effects and study the pure electrical short-circuit behavior at the beginning of the short-circuit (i.e. <1 s) and the subsequent, various electrochemical rate limitation effects (i.e. >1 s),[31,32] which are caused by either the anode or the cathode within the tested cells. To further study various LSC conditions in a stacked electrode configuration, nail/needle penetration were further applied to cells with two electrode stacks with and without a hole within one of the electrode stacks. This allows for applying either a LSC across both electrode stacks representing a complete penetration during a common nail penetration test or a LSC within only one of the two electrode stacks representing a local piercing of a separator such as occurring within the final stage of an ISC. Various diameters of the needle were used during the penetration resulting in differently sized penetration sites and consequently, different short-circuit resistances. To increase the understanding of the electrical and thermal behavior during the ESC and LSC scenario, the characteristic current, electrical potential and heat rate signals of all tests are analyzed toward significant plateau and transitionzones[31,33] referring to the cell's polarization and rate limiting electrochemical processes within the electrodes. The observed overdischarge occurring during all tests can be correlated to severe copper dissolution of the negative current collector including copper deposition throughout and across both electrodes using *post-mortem* analysis.

Experimental

Calorimetric test bench for short-circuit tests.—The calorimetric setup for the ESC and LSC test is schematically shown in Fig. 1. In our previous work, the test bench was used for applying ESC tests[31] and is modified in this work for applying LSC tests (i.e. nail/needle penetration tests) as well. For the potentiostatic measurements of current flux and electrical potential, a potentiostat (SP-300, Bio-Logic Science Instruments) and a source measurement unit (SMU, B2901A, Keysight Technologies) were used. In terms of ESC tests, a 10 A/5 V amplifier (SP-300, Bio-Logic Science Instruments) extends the current range to apply the expected current peaks around 10 A in the very beginning of the short-circuit. Besides applying a 0 V condition at the cell's terminals via the potentiostat, an external resistance (i.e. 5, 50, and 500 mΩ) was used to vary the intensity of the ESC condition[31,33] as depicted in Fig. 1 (left) whereas the SMU measures the cell's voltage (E_{sc}) at the cell's terminals. The current flux at the tabs (I_{sc}) can only be measured in case of ESC tests, and not for the LSC tests. Regarding the LSC tests, only the terminal voltage is measured via the potentiostat without the amplifier. The SMU is used to measure the electrical potential (Φ_{sc}) at the penetration site in the center of the active electrode area (i.e. needle) vs the cell's negative tab (see Fig. 1, right). The stainless steel needles (2R2, Unimed) are electrically connected to measure the expected potential drop across the electrodes because of the current flux, geometrical configuration, and contact resistance, and may be correlated to the polarization of the cell. For the

calorimetric measurement, three digital multimeters (DMM, 34 470A, Keysight Technologies) measure the cell's temperature at the positive current collector tab/terminal (T_{tab}), the bottom ($T_{cu,1}$), and the upper ($T_{cu,2}$) copper bar (45 × 45 × 90 mm, CW004A) which mechanically clamp the tested cell. The clamping pressure is expected not to distort the electrical-thermal behavior of the cell. The temperature signals during ESC and LSC tests are used to calculate the heat generation rate from the short-circuit scenario. The upper and bottom copper bar exhibit a narrow through-hole and a shallow-hole for the penetration needle, which requires a new calibration similarly to our previous work.[31] Pt100 sensors at an accuracy of ±0.15 C at 0 C (DIN/IEC Class A) centrally measure the temperature of the copper bars (installed with a thermal adhesive). To reduce the thermal contact resistance between the copper bars and the cell, ceramic foils (86/600 Softtherm, Kerafol Keramische FolienGmbH) of 0.5 mm thickness and 6 W m^{-1} K^{-1} were used at the interface as shown in Fig. 1. The measurement device is embedded in a 12 cm extruded polystyrene foam (XPS) at a thermal conductivity of 0.04 W m^{-1} K^{-1} to impede the heat exchange to the surrounding climate chamber. The whole setup is placed in a custom built climate chamber[34] incorporating resistive heating and Peltier-cooling to set the ambient temperature to 25 C. Reference measurements with a thermometer (1524, Fluke Corporation) revealed a temperature accuracy of ±0.03 C.

As shown in Fig. 1, the LSC is triggered via rotation of the short-circuit device (1) formed of a an indexing plunger[35] with a plastic rod attachment (PEEK) which incorporates the needle, subsequent forward movement (2) via a linear spring of △x = 9.7 mm displacement at a spring rate of 7.861 N mm^{-1} (1 × 6 × 18 mm, Febrotec), and finally penetration (3) of the tested cell with the needle.

In sum, the adaption of the calorimetric test bench incorporated the insertion of the short-circuit device to apply the nail penetration for the LSC test and the adjustment of the copper bars, which requires a re-calibration of the setup.

Calibration of the calorimetric test bench.—The calibration procedure is used for the temperature sensors, the determination of heat capacities, and losses to the environment. The calibration of the three Pt100 sensors uses a reference thermometer (1524, Fluke Corporation) equipped with a platinum resistance thermometer (5662, Fluke Corporation).[31] To determine the calorimetric constant (i.e. heat capacity and losses to the environment), a single-layered pouch-type cell (i.e. calibration cell)[31] similar to the cells of this work is equipped with two resistive heaters connected in series (1218.4 Ω, Thermo Technologies) and using the SMU, three different heat rates (0.1, 5, and 10 W) were applied for different durations (7200, 144, and 72 s) resulting in an overall applied amount of heat around 720 J. The measured temperature increase of the two copper bars $\left(\frac{d\bar{T}_{cu,i}}{dt}\right)$ and the calibration cell $\left(\frac{d\bar{T}_c}{dt}\right)$ multiplied with their heat capacities ($C_{p,i}$) can be correlated to the applied heat rate ($\dot{Q}_{tot}^*$) whilst accounting for heat exchange ($\alpha_{cu,i}$) of the copper bars to the climate chamber (T_∞) as follows:[31]

$$\dot{Q}_{tot}^* = C_{p,1}\frac{d\bar{T}_{cu,1}}{dt} + C_{p,2}\frac{d\bar{T}_{cu,2}}{dt} + C_{p,c}\frac{d\bar{T}_c}{dt}$$
$$+ \alpha_{cu,1}(\bar{T}_{cu,1} - T_\infty) + \alpha_{cu,2}(\bar{T}_{cu,2} - T_\infty) \quad [1]$$

Correcting the measured copper temperatures with the heat losses to the ambience, the adiabatic temperatures ($\bar{T}_{ad,i}$) of the copper bars and the measured cell temperature ($\bar{T}_c$) are used together with applying an iterative linear fit[31] of their effective heat capacities ($C_{p,i}$) to fit the applied heat rate as:[31]

$$\dot{Q}_{tot}^* = C_{p,1}\frac{d\bar{T}_{ad,1}}{dt} + C_{p,2}\frac{d\bar{T}_{ad,2}}{dt} + C_{p,c}\frac{d\bar{T}_c}{dt} \quad [2]$$

Finally, the thermal inertia of the test bench must be considered to derive the total heat rate ($\dot{Q}_{tot}$) and dissipated heat (Q_{tot}) via
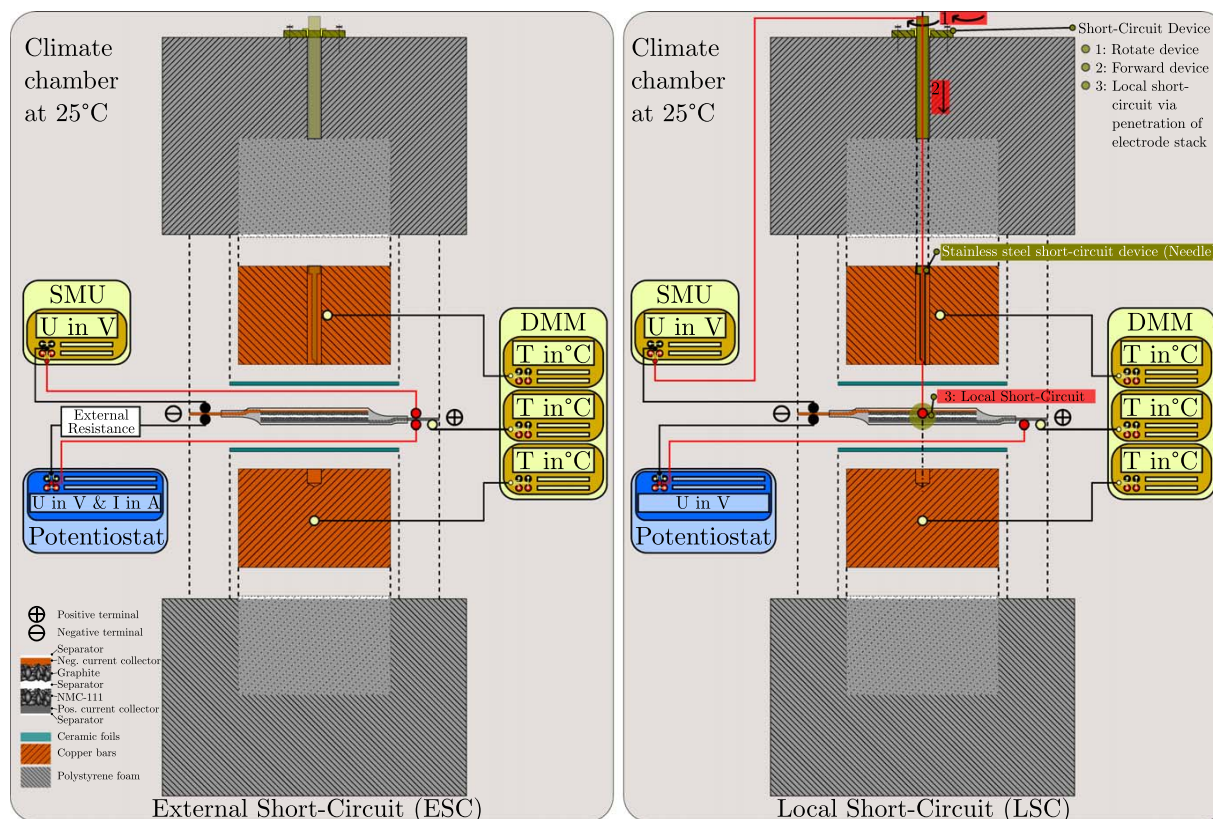
Figure 1. Schematic view of the calorimetric test bench for ESC (left) and LSC (right) tests applied to the pouch-type cells depicted in the center of each configuration. The test bench is placed inside of a climate chamber at 25 °C and the potentiostatic (Potentistat, SMU) and calorimetric (DMM) measurement devices are depicted with their respective sensor locations. For the LSC tests, the penetration procedure (see steps 1, 2, and 3) using the short-circuit device with the penetration needle is shown in the upper right part.

accounting for a certain time lag ($\triangle t_\infty$) and an approximately linear[31] heat offset ($\triangle Q_\infty$) as:

$$Q_{tot} = Q_{tot} + \triangle t_\infty \cdot \dot{Q}_{tot} \cdot \left(1 - \exp\left(-\frac{t}{\triangle t_\infty}\right)\right)$$

$$\dot{Q}_{tot} = \dot{Q}_{tot}\left(1 + \exp\left(-\frac{t}{\triangle t_\infty}\right)\right) \qquad [3]$$

A more detailed description of the calibration and the processing of the measured data is given in the supplementary material of this work at (stacks.iop.org/JES/167/090521/mmedia).

The heat capacities ($C_{p,i}$) are calculated to 660.6 J K^{-1} (407.8 J kg^{-1} K^{-1}) and 659.8 J K^{-1} (407.2 J kg^{-1} K^{-1}) for the bottom and the upper copper bar. The heat capacity of the pouch-type cell ($C_{p,c}$) is iteratively determined to approximately 900 J kg^{-1} K^{-1} (5.9 J K^{-1}), which is well in line with comparable pouch-type cells.[36,37] The time lag ($\triangle t_\infty$) accounts to 5.9 s and the linearized heat offset ($\triangle Q_\infty$) is depicted in the supplementary material.

To conclude, the modification of the calorimetric test bench for LSC tests reveal a shorter time lag due to shorter maintenance intervals for the ceramic foils and slightly increased mechanical clamping, and comparable calorimetric constants as shown in our previous work.[31]

Pouch-type lithium ion cells for short-circuit tests.—19 custom built (Custom Cells Itzehoe GmbH), pouch-type LIBs were investigated under quasi-isothermal external (4 cells) and local (15 cells)

short-circuit conditions. The four different pouch-type LIBs (i.e. configuration P1, P2, P3, and P4) studied within this work mainly differ in their stacking sequence of electrode and separator layers which is schematically shown in Fig. 2. The stacking sequence of separator (SEP), graphite anode (A) and NMC-111 cathode (C) from configuration P1 to P4 are as follows:

- **P1**: SEP/A/SEP/C/SEP
- **P2**: SEP/A/SEP/C/SEP/C/SEP/A/SEP
- **P3**: SEP/A*/SEP/C*/SEP/C/SEP/A/SEP
- **P4**: SEP/C*/SEP/A*/SEP/A/SEP/C/SEP

A polyolefin separator (SEP) of 20 μm electronically insulates the electrode pairs and is wrapped around the entire electrode stack to ensure its position. 1 M of LiPF$_6$ solved with ethylene carbonate (EC) and dimethyl carbonate (DMC) at a weight ratio of 1:1 and 2 wt% vinylene carbonate (VC) was used as electrolyte. Configuration P2 (double-layered) differs from P1 (single-layered) only in the total number of electrode pair. Configuration P3 (double-layered) differs from P2 as the upper electrode pair (see Fig. 2) includes a centered hole ($\oslash$ 5 mm) through the anode (A*) and the cathode (C*) to enable penetration only in the bottom stack in order to initiate an LSC, which subsequently applies an ESC in the upper stack via the current collector paths. Configuration P4 (double-layered) differs from P3 only in the sequence of the layers as the anodes are facing each other in the middle part to investigate if the sequence of electrode penetration influences the short-circuit behavior in terms of varying shorting resistances. All electrodes were single-side coated to guarantee comparability between the resulting cell polarization in the ESC and LSC tests.
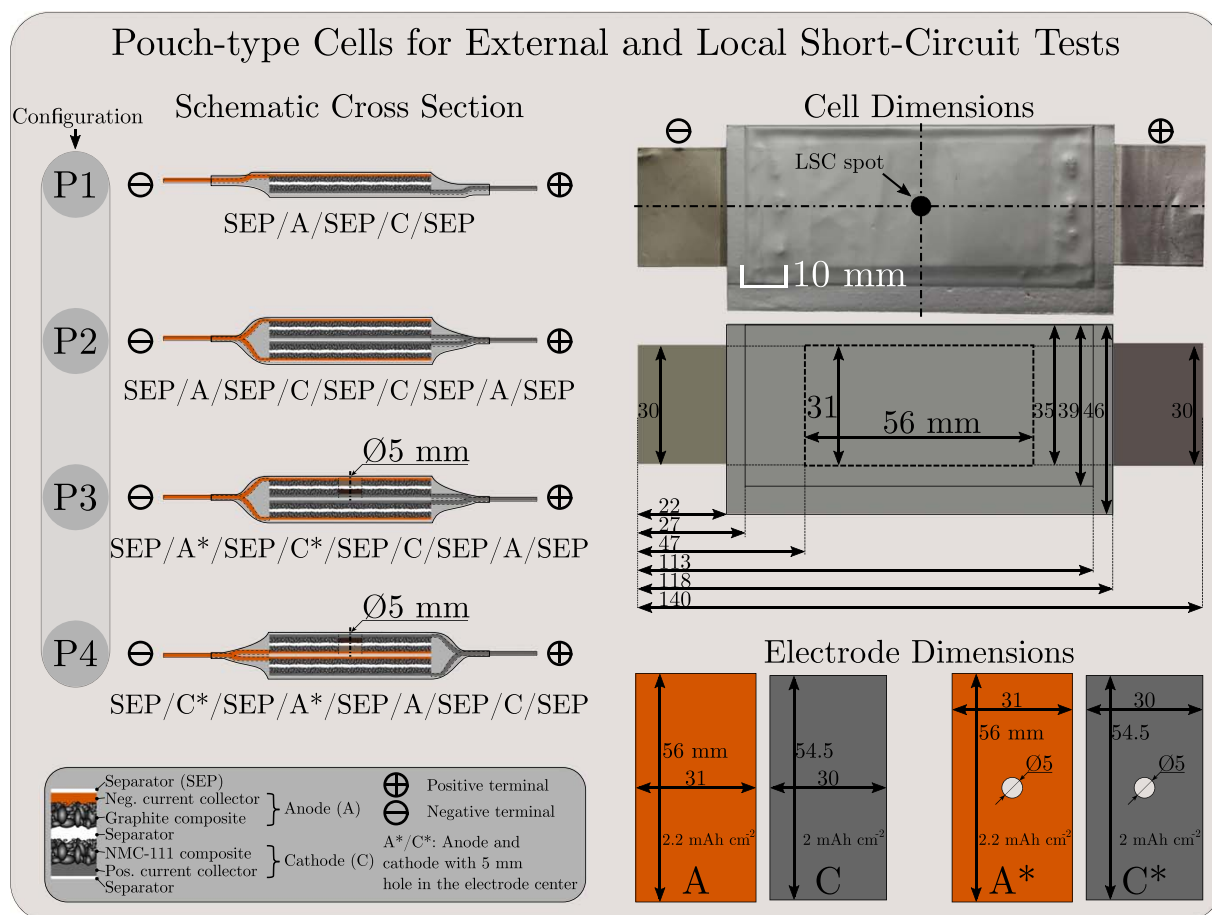
Figure 2. Schematic cross-section of the single- (i.e. P1-type) and double-layered (i.e. P2-, P3-, and P4-type) pouch-type LIBs showing the electrode and separator stacking sequence (left). Despite various stacking sequence chosen for the configuration P3 and P4, the main difference to P2 is that the upper electrode pair comprises a 5 mm hole to enable LSC tests based on the penetration of only one electrode stack (see "Electrode Dimensions"). The geometrical size of the test cells is depicted under "Cell Dimensions" with the centered position for the nail penetration site used for the LSC test.

All tests carried out in this work are summarized in Table I showing the initial cell voltage, state of charge (SoC), initial cell temperature/ambient temperature (T_∞), and the shorting condition for the ESC (0 V as well as 5, 50, and 500 mΩ, Power Metal Strip, Vishay Intertechnology Inc.) and the LSC tests with varying nail/needle diameters ($\oslash d$ of 0.5, 1, and 2 mm, 2R2, Unimed), respectively.

In order to determine the balancing and analyze the expected overdischarge,[31] differential voltage analysis (DVA) was applied to cell P2#10 and self-built CR2032-type half cells of pristine anode and cathode samples ($\oslash$ 14 mm, Custom Cells Itzehoe GmbH) vs lithium metal ($\oslash$ 15.6 mm × 250 μm, MTI Corporation). Based on the supplier's information and our measurements, 96 wt.-% of graphite combined with each 2 wt.-% of binder and conductive carbon form the anode composite at a final thickness of 67 μm on a 12 μm copper foil which results in an areal capacity of 2.2 mAh cm^{-2} and a gravimetric loading of 350 mAh g^{-1}. The cathode contains 86 wt.-% of NMC-111 (i.e. equal proportion of nickel, manganese, and cobalt) combined with 6 wt.-% of binder and 8 wt.-% conductive carbon at 79 μm on a 18 μm aluminum foil which results in an areal capacity of 2 mAh cm^{-2} (145 mAh g^{-1}). For the DVA, the full cell (P2#10) was charged and discharged at a constant current (CC) at 600 μA ($\approx$0.01 C) using a battery cycler (CTS, Basytec GmbH) in a climate chamber (VT 4021, Vötsch Industrietechnik GmbH) at 25 C. The half cells were assembled in an argon-filled glove box (H$_2$O, O$_2$ < 0.1 ppm,

M.Braun Inertgas-Systeme GmbH) using two glassfiber separators ($\oslash$16 mm × 250 μm), two stainless steel spacers ($\oslash$16 mm × 0.5 and 1 mm), the CR2032-type housing caps, wave spring, insulation ring and 90 μl of 1 M of LiPF$_6$ EC:DMC (1:1 by weight) and 2 wt.-% VC. Formation of the coin cells included an initial 33.9/30.7 μA ($\approx$0.01 C) lithiation from 2.789/3.172 V to 10 mV/3 V and 6 subsequent cycles at 30 μA CC charge and discharge (between 1.7 V and 10 mV/3 V and 4.3 V) with constant voltage (CV) periods until ±6.8/6.1 μA for the anode and cathode half cell with the same measurement equipment. Finally an anodic delithiation and cathodic lithiation profile was used after stable capacity retention appeared (<0.01 %).

In sum, LSC tests were applied to the P1-type cells to correlate the electrical-thermal characteristics to the P1-type ESCs at various external resistances. The set of experiments proposed on single-layered ("P1-LSC") and double-layered cells ("P2-LSC" and "P3/P4 —coupled LSC/ESC") give the opportunity to investigate and decouple the different phenomena occurring in a stacked, pouch-type LIB during LSC tests.

Measurement procedure for ESC and LSC tests.—Table II shows the procedure for the ESC and LSC test, starting with "Initial cycles" using a battery cycler (CTS, Basytec GmbH) and a climate chamber at 25 C (KT115, Binder) to exclude any influence of formation processes. Pulse measurements at 50% SoC were applied to characterize the dynamic electrical behavior at different C-rates.

Table I. Overview of ESC and LSC Tests Applied to the Studied Cells.

Scenario	$E_{sc,0}$/V	SoC_0/—	T_∞/K	R_{ext}/mΩ
ESC tests				
P1#5[b]	4.2 V	100%	25 °C	0 ($\equiv$"0 V")
P1#10[b]				5
P1#6[b]				50
P1#7[b]				500
LSC tests				$\oslash\ d_{Needle}$
P1—LSC				
P1#2[b]	4.2 V	100%	25 °C	1 mm
P1#3[b]				
P1#9				
P2—LSC				
P2#1[b]	4.2 V	100%	25 °C	1 mm
P2#10[a]				
P3/P4—coupled LSC/ESC				
P3#1	4.2 V	100%	25 °C	1 mm
P3#2				
P3#4[b]				
P4#1[b]				
P4#2				
Varying needle diameter				
P2#3	4.2 V	100%	25 °C	2 mm
P2#4				
P2#5	4.2 V	100%	25°C	0.5 mm
P2#6				
P2#7				

a) Used for DVA. b) Used for *post-mortem* analysis.

A single "Capacity check-up" was used to determine the initial capacity (C_0) at 0.5 C CC discharge from 4.2 to 3 V and in the subsequent "Preconditioning" 0.2 C CC charge with a CV period until 0.01 C prepares the cells at 4.2 V (=100% SoC). Afterwards, the cells were embedded in the calorimetric test bench (see Fig. 1), electrochemical impedance spectroscopy (EIS, see Table II) determined the cell's impedance ($R_{i,0}$) and the setup was rested for 12 h to allow for thermal equalization.

The "Quasi-isothermal short-circuit scenarios at 25° C" initiates after a resting period and subsequently differs for the ESC and LSC tests in terms of the potensiostatic sampling (see Table II). In case of the ESC, a constant voltage phase (4.2 V) to precondition the measurement device is applied and after 5 s, a 0 V condition is set in reference to the cell's terminals. The sampling rate is subsequently reduced to sufficiently but not excessively record the dynamic behavior and limit memory allocation. The ESC is terminated, when the current measured by the potentiostat falls below 100 μA and finally a resting phase of 17 h records relaxation. In case of the LSC, the short-circuit device is triggered right after the resting period (10 s) and the sampling rates are continually reduced as well. The cells tested in the LSC tests are exposed to a longer discharge than those tested in the ESC tests as the LSC test was terminated after $\approx$20 h. Simultaneously to the potentiosatic measurements, the calorimetric measurement includes the temperatures of the cell and the upper/bottom copper bar. Finally, EIS was applied to determine the cell's impedance ($R_{i,sc}$) and the terminal voltage ($E_{sc,end}$) after the short-circuit event.

As possible investigations toward the influence of initial state of charge and ambient temperature have been thoroughly discussed for ESCs,[31] similar influences are expected for the studied LSCs and the tests are consequently carried out at 100% SoC and 25 C without exception.

Correlation of ESC and LSC tests.—Local variations in electrode polarization (i.e. along the electrodes' thicknesses, widths, and lengths) are expected between the external and the local short-circuit

scenario and, hence, different spatial distribution of the current flux. Assuming the same shorting current (i.e. the same shorting intensity) from an ESC and LSC test applied to identical cells, a certain offset of the resulting terminal voltages can be expected simply due to the spatial distribution of current flux. To correlate the resulting terminal voltages from the ESC and the LSC tests, the local variations of the electrode polarization should be considered. Therefore, multidimensional multiphysics simulation studies investigate exemplary ESC and LSC scenarios for the P1-type cells corresponding to an ESC test at an external short-circuit resistance of 243.9 mΩ, which lies in the range of the cells' initial impedances. The simulative work is outlined in the supplementary material as it exceeds the experimental focus of this work. Both short-circuit simulations reveal nearly the same shorting current over time whilst the local polarization effects (i.e. along the electrodes' thicknesses, widths, and lengths) reveal significantly differing local current flux and potential distribution. As a result, the offset between the terminal voltages is calculated and normalized with respect to the ESC results. Extrapolation from the external short-circuit resistance applied in the ESC case, reveals a high prediction accuracy of the local short-circuit resistance with errors below 2% until 100 ms.

Regarding the measured terminal voltages from the P1-LSC cells, a simulation-derived correction factor of 0.062 at 100 ms was used in this work to account for the aforementioned local polarization effects and enable for the comparison to the P1-type ESC test results. The corresponding external resistance for the shorting scenario can be calculated for the LSC tests, which must have been applied to gain the same current flux/shorting intensity resulting from a P1-type ESC test. The calculation itself uses the electrical potential difference to the P1-type ESC results showing a higher (i.e. 50 mΩ ESC test) and a lower terminal voltage (i.e. 5 mΩ ESC test) at 100 ms. By further interpolating the calculated effective external short-circuit resistances, the short-circuit resistance of the LSC tests can be estimated.

Post-mortem analysis.—*Post-mortem* analysis is used to qualitatively study effects such as active material degradation and/or copper dissolution/deposition occurring during the short-circuit tests. The cells were opened in an argon-filled glove box (H$_2$O, O$_2$ < 0.1 ppm, M.Braun Inertgas-Systeme GmbH) for a first visual inspection and $\oslash$ 14 mm samples were subsequently extracted for scanning electrode microscopy (SEM) and energy-dispersive X-ray spectroscopy (EDX) measurements. The samples were washed with diethyl carbonate (DEC) and dried before applying SEM/EDX (JCM-600, JEOL Ltd.) where a MP-00040EDAP detector at 15 kV acceleration voltage offered magnifications levels from 150 to 2000 of the electrodes.

Results and Discussion

Beginning with the DVA analysis, Fig. 3a shows the open circuit potentials (OCPs) of the coin cells together with their superposition ("Graphite + NMC-111 coin cells") as a function of full cell SoC (i.e. P2#10). The superposition reveals marginal errors (see Fig. 3b) around 10 mV with increased deviations at low SoCs due to the steep rise of the anode potential at low lithiation levels. The overcharge and overdischarge zone are depicted beyond the safe operation window between 0 to 100% SoC referring to 3 and 4.2 V. Regarding the 1st derivative in Fig. 3c, the balancing of the anode and cathode in reference to the full cell is shown with similar deviations. The ESC and LSC tests considerable result in an overdischarge of the tested cells, which most likely provokes side reactions besides a highly delithiated anode and a highly lithiated cathode. In this context, the differential capacities are shown in Figs. 3d and 3e, where the capacity gain from de-/intercalation reaction during overdischarge approaches zero. As a result, the overdischarged capacity may not be related to de-/intercalation reaction within the active materials but most likely to side reactions such as copper dissolution/deposition occurring at $\gtrsim$3.2 V vs

Table II. Test Procedures

Initial cycles

Repetition	Sequence[a)]	Feature	Chamber Temperature
2×	CC_{CH}-CV-R-CC_{DCH}-R	CC: 0.1 C, 3 V–4.2 V CV: <0.01 C R: 15 min	25°C
8×	CC_{CH}-CV-R-CC_{DCH}-CV-R	CC: 0.5 C, 3 V–4.2 V CV: < ± 0.01 C R: 15 min	
1×	CC_{CH}-R	CC: 0.5 C to 50% SoC R: 30 min	
1×	P_{CH}-R-P_{DCH}-R	P: 0.3, 1 and 2 C for 10 s R: 10 min	

Capacity check-up

1×	CC_{CH}-CV-R-CC_{DCH}-R	CC: 0.5 C, 3 V–4.2 V CV: <0.01 C R: 15 min	25° C

Preconditioning

1×	CC_{CH}-CV-R	CC: 0.2 C, 3 V–4.2 V CV: <0.01 C R: 2 h	25° C

EIS at 4.2 V with 1 mA excitation current from 100 mHz to 10 kHz[b)]

Quasi-Isothermal short-circuit scenarios at 25 °C

Termination and measurement conditions of the calorimetric test bench (see Fig. 1)

Resting for 12 h

Potentiostatic duration phase and measurement sampling frequency

ESC		**LSC**	
R	10 s at 1 Hz		
CV	5 s at 10 Hz	R	10 s at 1 Hz
ESC	10 s at 10 kHz	**LSC**	30 s at 10 kHz
	100 s at 100 Hz		120 s at 100 Hz
	$I_{sc} < 0.1$ mA at 10 Hz		20 h at 10 Hz
R	17 h at 1 Hz		

Calorimetric duration phase and measurement sampling frequency

20 s at 1 kHz

100 s at 100 Hz

880 s at 10 Hz

150 min at 1 Hz

until end at 0.5 Hz

EIS with 1 mA excitation current from 100 mHz to 10 kHz[b)]

a) CC_{CH} constant current charge CC_{DCH} constant current discharge CV constant voltage R rest/relaxation period P_{CH} charge pulse current P_{DCH} discharge pulse current. b) 6 points per decade and 2 measurements per frequency.

Li/Li$^+$.[38] The ESC and LSC test conditions lead to high anodic overpotentials (>1.6 V)[31] and together with the low lithiation stages in the graphite anode resulting in potentials >1.7 V vs Li/Li$^+$ (see Fig. 3a), oxidation of the copper current collector is most likely triggered, which is indicated here via DVA analysis and will be verified in the *post-mortem* section. Table III summarizes the potentiostatic measurement data for all cells studied by means of ESC and LSC tests. The initial (C_0) and overdischarged (C_{sc}) capacity is only shown in case of the ESC tests via the current flux measurement and the cells are overdischarged $\left(\frac{C_{sc} - C_0}{C_0}\right)$ to 34.9, 28.6, 30.8, and 26.1% for the 0 V, 5, 50, and 500 mΩ condition. Regarding the cell's impedance increase $\left(1 + \frac{R_{i,sc} - R_{i,0}}{R_{i,0}}\right)$, manufacturing tolerances of the tested cells most likely cause the various initial impedances and capacities. The resulting overdischarge, impedance rise and maximum current peak are hereby affected. Similar variations of the initial capacity and the impedance appear for the cells applied with the LSC tests. Additionally, the various contact conditions[23] at the penetration site may affect the resulting impedance increase and the final terminal voltage. Maximum impedance increases by a factor of 1.98, 1.64, 1.72, and 1.53 appear

for the P1-LSC, P2-LSC, P3/P4-coupled LSC/ESC and the varying needle diameter LSC tests, which are in the range of the ESC test results. After the end of each test, the higher terminal voltages of the ESC tests ($E_{sc,end} > 800$ mV, see Table III) are caused by the aforementioned shorter short-circuit exposure compared to the LSC tests, which is also reflected in a lower, local copper deposition across the electrodes shown in the *post-mortem* part (see *Post-mortem* analysis).

Potentiostatic correlation of ESC and LSC tests.—The difference in applying the ESC conditions compared to the LSC using nail penetration raises the question, if and to which extent the resulting electrical and thermal behavior differs and how the intensity of the shorting scenario (i.e. hard or soft) can be compared/correlated from the resulting current flux, potential, and temperature measurements. Evaluation toward various ESC tests, which vary in their intensity and the appearing onset of electrochemical limitation mechanisms caused by the applied external condition (i.e. 0 V as well as 5, 50, and 500 mΩ), are using the terminal voltage for a first, simple correlation as the current flux is not measureable for the LSC tests. As shown in our previous works[31,32] investigating P1-type ESC tests, the cell's polarization correlates to the electrochemical
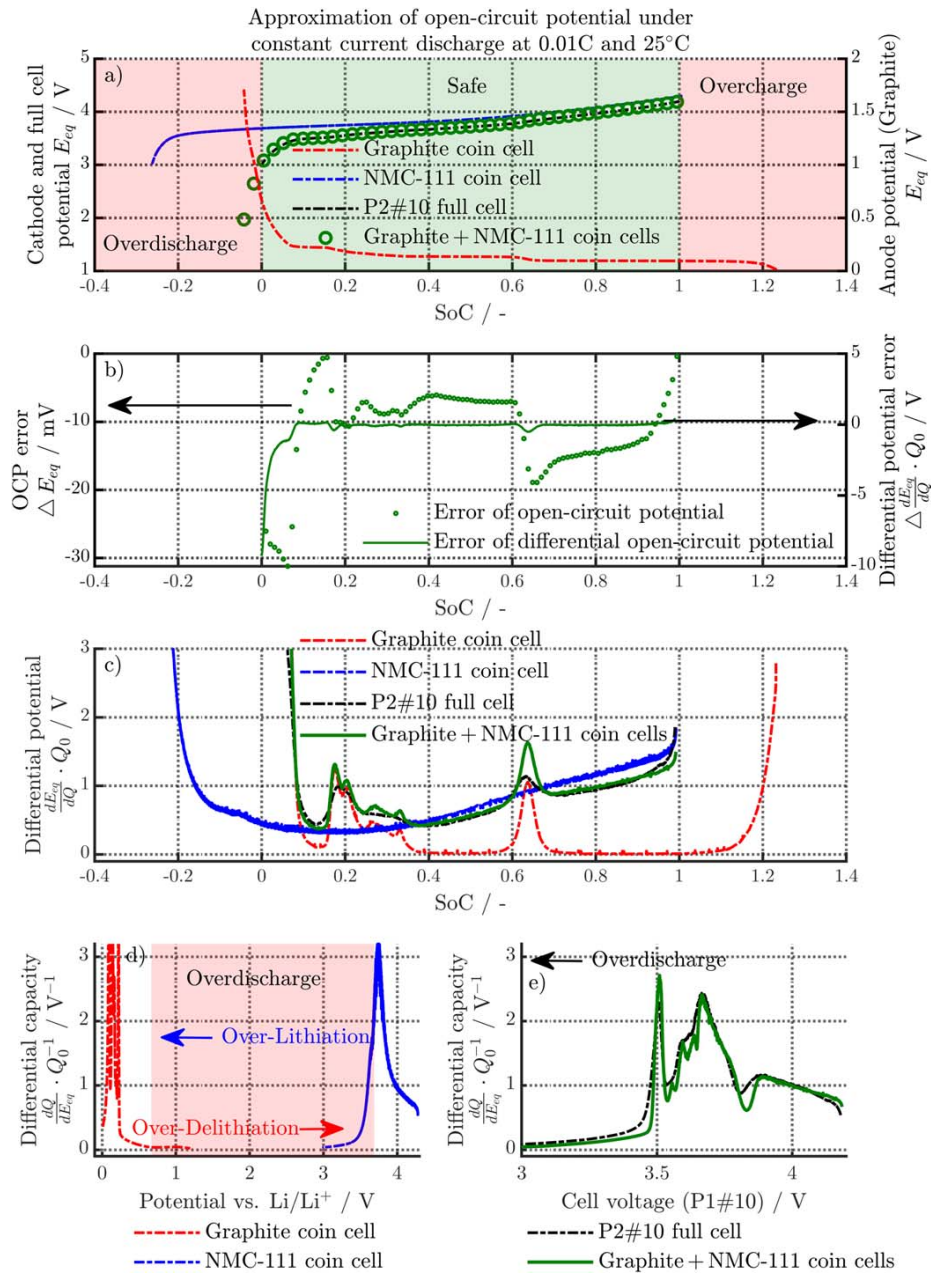
Figure 3. DVA using the measured potentials of full (double-layered pouch-type cell "P2#10") and half cells ("Graphite coin cell" and "NMC-111 coin cell") vs lithium metal and its superposition ("Graphite + NMC-111 coin cells") under OCP CC discharge (≈0.01 C) conditions. Subplot a) shows the measured and calculated potentials and subplot c) shows the corresponding 1st derivative. The calculated superposition of both half cells is compared to the full cell in both cases showing the resulting errors in subplot b). Subplot d) and e) show the differential capacity of the half (d) and full cell (e) together with the superposition to emphasize the potentials vs Li/Li$^+$, the terminal voltage and the marginal capacity gain during overdischarge from the de-/intercalation reaction.

limitations and the resulting plateau/transition zones of the current flux, terminal voltage, and heat generation rate can be interpreted as follows:

• **Plateau zone I**: Polarization dominated by ohmic losses in the electrolyte throughout the entire electrode stack and most likely limiting delithiation kinetics in the graphite electrode
• **Transition zone I-II**: Increasing polarization due to liquid phase depletion within the cathode and possible solid phase depletion within the anode leading to current and electrical potential drop

• **Plateau zone II**: Second plateau zone with solid (i.e. saturation of Li-ions due to solid-phase diffusion limitation near the separator) and liquid (i.e. depletion of Li-ions in the electrolyte near the current collector) mass transport limitations at the cathode surface throughout the entire electrode (stage "a") followed by a saturation at the cathode particle (stage "b")
• **Transition zone II-III**: Depletion of anode particles' surfaces lead to polarization increase with further current and potential drop, as well as possible copper dissolution/deposition from the negative current collector

Table III. Potentiostatic Results of ESC and LSC Tests Applied to the Studied Cells.

Scenario	C_0/mAh	C_{sc}/mAh	$R_{i,0}$/mΩ	$R_{i,sc}$/mΩ	$1 + \frac{R_{i,sc} - R_{i,0}}{R_{i,0}}$/—	$E_{sc,end}$/V	I_{max}/A	R_{ext}/mΩ
ESC tests								
P1#5[b]	23.3	35.8	214.7	372.2	1.73	0.810	9.9496	0 (i.e. "0 V")
P1#10[b]	25.6	35.9	226.6	517.7	2.28	0.864	10.0822	5
P1#6[b]	24.5	35.4	207.1	376.9	1.82	0.800	9.2152	50
P1#7[b]	26.9	36.4	201.4	309.0	1.53	0.854	4.9635	500
LSC tests								$\oslash d_{Needle}$
P1—LSC								
P1#2[b]	17.1	n.a.	359.7	587.8	1.63	0.038	n.a.	1 mm
P1#3[b]	19.1		357.4	547.8	1.53	0.074		
P1#9	28.2		298.7	592.4	1.98	0.234		
P2—LSC								
P2#1[b]	59.9	n.a.	222.6	365.4	1.64	0.061	n.a.	1 mm
P2#10[a]	49.9		276.7	418.6	1.51	0.005		
P3/P4—coupled LSC/ESC								
P3#1	53.2	n.a.	285.5	428.4	1.50	0.020	n.a.	1 mm
P3#2	55.5		277.9	480.5	1.72	0.590		
P3#4[b]	57.9		236.7	384.2	1.62	0.149		
P4#1[b]	49.6		242.2	357.2	1.47	0.043		
P4#2	52.4		257.9	423.7	1.64	0.026		
Varying needle diameter								
P2#3	50.6	n.a.	289.6	443.2	1.53	0.276	n.a.	2 mm
P2#4	45.5		307	468.9	1.52	0.581		
P2#5	51.9	n.a.	397.5	560	1.40	0.022	n.a.	0.5 mm
P2#6	50		285.4	407.6	1.42	0.057		
P2#7	51.4		292	412.9	1.41	0.009		

a) Used for DVA. b) Used for *post-mortem* analysis.

• **Plateau zone III**: Continuing de-/intercalation and copper dissolution/deposition with attenuation of the overall physical processes

Analyzing the current flux and terminal voltage profiles of the P1-type ESC tests of this work, similar zones appear as shown in Figs. 4a and 4b. Table IV summarizes the test duration until each plateau and transition zone ends (i.e. t_{end}).

High current rates appear during stage I (see Figs. 4a and 4b) starting at 9.95 ($\approx$427 C), 10.1 (394 C), 9.2 (376 C), and 4.96 A (185 C) for the 0 V, 5, 50, and 500 mΩ condition, respectively. Subplot b magnifies the transition zone I-II and illustrates the higher the external resistance, the later the transition begins and the softer the short-circuit becomes. Zone II reaches around 10 C in all cases. The transition of zone II a and II b appears similarly around 73 s for all ESC tests. Beyond 500 s, zone III initiates and lasts until the end of the test (i.e. $I_{sc} < 0.1$ mA). For the 0 V and 5 mΩ ESC test, control limitations of the measurement equipment cause the observed fluctuations between 20 and 200 ms.

Regarding the terminal voltage in Fig. 4c, the different stages appear similarly for the P1-LSC results. The terminal voltages lie in between the 5 and 50 mΩ ESC test and the zones I, I-II, and II can be determined as shown in Table IV. Comparing the ESC and LSC results in the very beginning of the short-circuit (i.e. zone I, <3 ms), the lowest voltage values appear for the LSC cases which indicate a very high intensity or a so called hard short. As soon as electrochemical rate limitation effects initiate (i.e. zone I-II), the electrical behavior shows subsequently (i.e. zones I-II to III) similar damping/attenuation characteristics as the ESC cases. To conclude, the locality of the short-circuit defines the electrical behavior in the very beginning (i.e. <1 s, zone I), but the subsequent electrical short-circuit behavior is similar to the ESC scenarios and is mainly defined by electrochemical rate limitation effects. Regarding the comparison of the terminal voltages in Fig. 4c, one could simply estimate the intensity of the LSC tests in between the 5 and 50 mΩ ESC test. The noisy signals appearing for the LSC cases are most likely caused via

marginal mechanical oscillation by the shorting device in stage I and caused by the measurement equipment in the following zones.

Figure 4d is used to compare the terminal voltage (E_{sc}) to the electrical potential measured between the cell's negative tab and the needle (Φ_{sc}) in order to evaluate the local polarization effects during the P1-LSC tests. The locally measured potentials show a higher ohmic drop just at the beginning and proceed similarly to the tab potential at lower electrical potentials. Comparing the P1-LSC tests, the P1#3 tests shows a higher potential offset to the terminal voltage as the P1#2 test. As the cell's initial impedances are approximately the same (see Table III), a lower ohmic resistance in the penetration site is expected resulting in the overall lower electrical potentials and the higher spread between them. A certain measurement fuzziness is expected such as the contact condition[23] may change in the penetration site, the ohmic drop due to the current flux through the needle, and the polarization along the negative current collector. Nevertheless, the measured lower potentials at the penetration site indicate that the locality of the LSC (i.e. short-circuit in the center of the electrode stack) complicates the correlation to ESC tests when the measured terminal voltages are compared. As a result, simply correlating ESC and LSC via the terminal voltages as mentioned before may incorporate a certain error due to the different polarization effects across the electrodes caused by the ESC and LSC condition. In the following part, simulation studies help to evaluate the electrical potential fields across the electrodes for P1-type ESC and P1-LSC tests, which simulate the same current flux during the shorting scenario. The correlation uses the resulting terminal voltage difference and the derived correction factor is applied to the measured terminal voltages of the P1-LSC tests in order to estimate the current flux and shorting resistance by interpolating between the P1-type ESC results.

Correction of LSC polarization effects.—As discussed before, comparing the terminal voltages may incorporate a certain error due to the expected high local polarization around the penetration site in the LSC tests as indicated by the local potential measurements (see
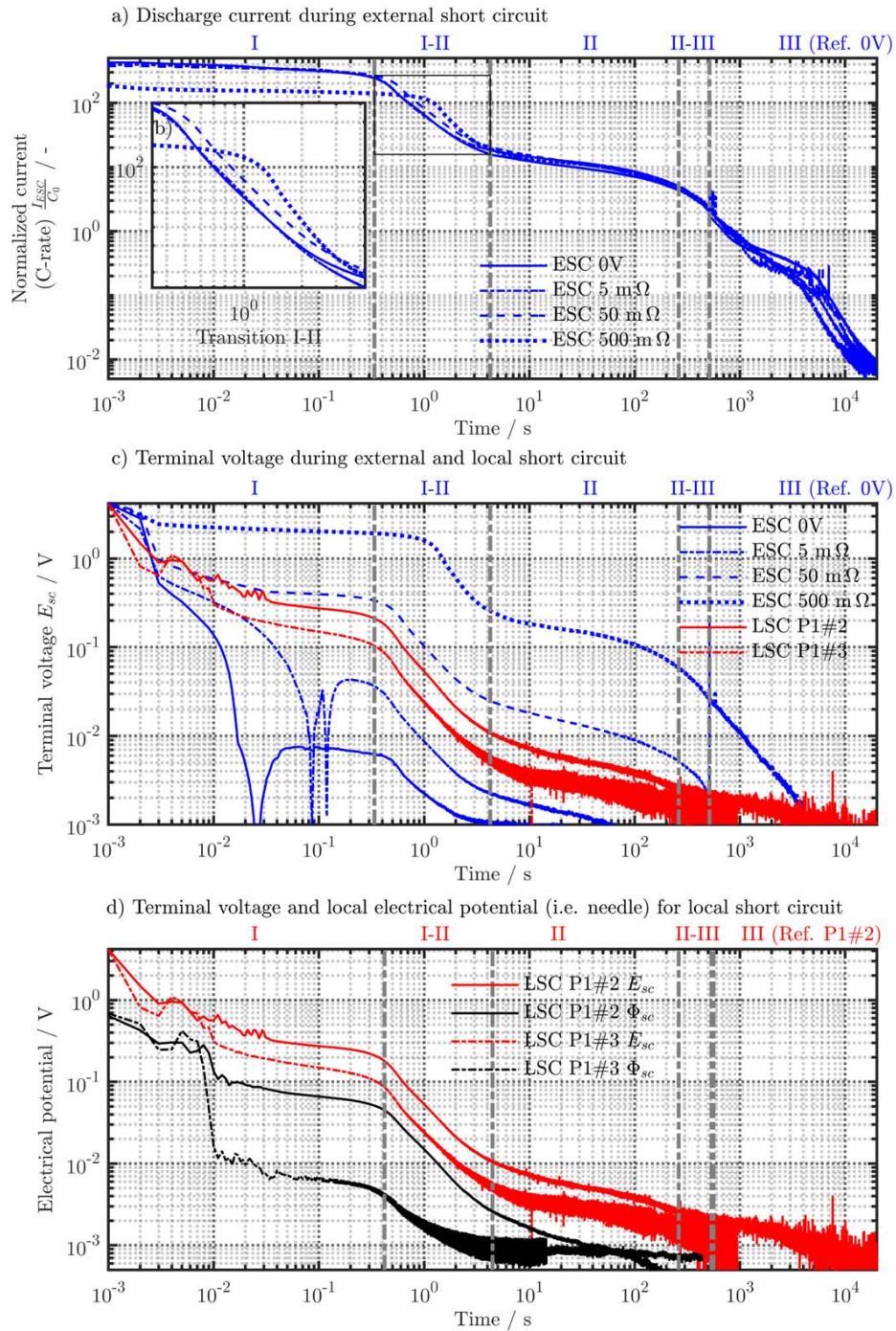
Figure 4. Normalized current (a), (b) and electrical potential (c), (d) measurement results of external (0 V as well as 5, 50, and 500 mΩ) and local (1 mm needle for P1#2 and #3) short-circuit tests applied to single-layered pouch-type cells (i.e. P1-LSC). Plateau and transition zones (I, I-II, II, II-III and III) are depicted referring to our previous works[31,32] for the 0 V ESC (a), (b), and (c) and the P1#2 LSC case (d). The electrical potential measured between the negative tab and the needle is depicted in subplot d) in reference to the terminal voltage between the positive and negative current collector tab.

Fig. 5c). To estimate the polarization/intensity for the P1-LSC cells, insights in the local potential distribution across the electrode would help to evaluate the measured potentials and to determine the difference of an externally (ESC) or locally (LSC) induced shorting on the local potential distribution.

To do so, a multidimensional multiphysics model[39–44] previously validated for the P1-type cells[32] is presented in the supplementary material and used to simulate an exemplary ESC and LSC case, which reveal a similar current flux either through the tabs or the internally shorted area in the simulation model. As the same current

Table IV. Plateau and Transition Zones of P1-type ESC and P1-LSC Tests.

Cell	Stage ESC	I	I-II	II	II-III	III
				t_{end}/s		
P1#5	0 V	0.34	4.24	262	514	end of test
P1#10	5 mΩ	0.37	4.42		537	
P1#6	50 mΩ	0.45	4.85		560	
P1#7	500 mΩ	1.03	5.47		580	
	P1—LSC					
P1#2	1 mm	0.42	4.46	between 5 and		end of test
P1#3		0.40	4.44	50 mΩ of ESC test		

flux is simulated, similar shorting resistances are expected and most likely both scenarios occur at the same short-circuit condition and shorting intensity. The resulting difference of electrical potential distribution across the electrode results in different terminal voltages, which overall occur under similar short-circuit conditions. Using the terminal voltage difference from the P1-LSC to the P1-type ESC simulation, a correction factor for the terminal voltage is derived, which accounts for the local polarization effect in the P1-LSC case and enables for its correlation to the P1-type ESC test in terms of current flux and shorting resistance.

The ESC shorting scenario simulates an external shorting of 243.9 mΩ which corresponds approximately to the P1-type cells' impedance range (see Table III) and the LSC scenario corresponds to a nail penetration similarly to the P1-LSC tests using the 1 mm needle. The resulting potential fields and transient voltage drops are shown in the supplementary material. Using the resulting correlation factor of 0.062 from the simulation results at 100 ms, the measured terminal voltage of the P1-LSC tests is corrected and the offsets to the 5 and 50 mΩ ESC tests (see Fig. 5b) are used for interpolation of the estimated shorting resistance ($R_{LSC,est}$) as shown in Table V. The 5 and 50 mΩ case were used, as the corrected P1-LSC terminal voltages from zone I to III lie in between theses cases similar as seen for the uncorrected signals in Fig. 5. The estimated shorting resistance and the corrected terminal voltage can now be used to calculate the expected current flux ($I_{LSC,est}$) at 100 ms as shown in Table V and lie in between the 5 and 50 mΩ ESC case.

A more profound analysis and discussion of the modelling and simulation part will be addressed in future as it would exceed the content of this work, but is used here to emphasize the local polarization differences, which makes a correction of the overall measured signals such as the terminal voltage necessary in order to gain a physically meaningful correlation between ESC and LSC scenarios.

To summarize, the P1-LSC test results revealed a rather hard short (see Table V and Fig. 4c) and show a very similar electrical behavior compared to the ESC tests, especially after the onset of electrochemical rate limitations (i.e. zone I-II to III). Considering the aforementioned correction for local electrode polarization, most likely an ESC test with an appropriately chosen external short-circuit resistance (see Table V) could emulate a LSC test.

Calorimetric correlation of ESC and LSC tests.—Beneficially, the actual measurement signal (i.e. temperature) for calculating the heat rate is not directly affected of the local polarization effects due to the expected thermal uniformity in the copper bars as shown in our previous works.[31,32] Hence, the P1-type ESC and P1-LSC shorting scenarios can be analyzed regarding the plateau and transition zones of the heat rate, which appears similarly to the current flux, terminal voltage, and local electrical potential (see Figs. 4a–4c) only with a certain delay in time[31] due to the inertia of heat transport phenomena and the calorimetric test bench. Figure 5 shows the calorimetric results of the P1-type ESC and P1-LSC tests after 1 s. The total heat ranges from 450 to 353 J depending on the highest to lowest capacitive cell (i.e. P1#7 and P1#2, see Fig. 5a). As the cell's capacity defines the total amount of heat,[31] the heat rate

(see Fig. 5b) is related to the cell's capacity in order to enable for a better correlation between the cells. The capacity related heat rate vs SoC of the ESC tests is shown in Fig. 5c, which helps to estimate the onset of overdischarge as shown at 100% SoC. Figure 5d magnifies the spread of heat rate where the highest external resistance shows the lowest intensity as expected. The maximum, capacity related heat rates in zone I-II can be observed for the 50 mΩ condition and the 0 V as well as the 5 mΩ case appear slightly below due to the aforementioned deviances in the cells' capacity and initial impedance (see Table III). Most interestingly, the ESC and LSC condition result in similar characteristics as shown in Fig. 5e, which allows for a correlation in the zones I-II to III exemplarily shown for the 0 V case (see also Fig. 4a). Looking into Fig. 5f, the P1-LSC results lie initially in between the 5 and 500 mΩ ESC cases and the current flux may be in between as well. The initial current flux is most likely defined by the shorting resistance (i.e. either external or at the penetration site) and the cell's impedance. For the P1-LSC, cell P1#2 indicates a lower shorting resistance due to a lower offset between the potential at the tabs and the penetration site (i.e. E_{sc} vs Φ_{sc}) and an overall slower terminal voltage decay compared to cell P1#3. As their impedances are approximately the same (see Table III), the expected higher shorting current for P1#3 results in the observed higher heat rates. Regarding stage II in Fig. 5e, the P1-LSC cases reveal lower heat rates compared to all ESC cases, which indicates higher mass transport limitations and/or variation of the short-circuit resistance. The local polarization effects (i.e. E_{sc} vs Φ_{sc}) coming with very high local currents around the penetration site or the variation[23] of the contact condition may cause the observed earlier onset of mass transport limitations, accompanied with a stronger current drop, and, consequently lower heat rates for the P1-LSC cases. Again, cell P1#2 shows a lower plateau than cell P1#3 due to the aforementioned difference in shorting resistance and resulting current flux.

Comparing all P1-LSC tests, the initial impedances (see Table III) vary in the range from 298.7 (P1#9) to ≈360 mΩ (P1#2 and #3) as well as the cell's capacities (28.1, 17.1, and 19.1 mAh). Regarding the resulting heat generation rate profiles, the higher the impedance and the lower the capacity, the lower the initial current in zone I-II, and the higher the subsequent mass transport limitations accompanied with lower heat rates in zone II. Note, that also the altering contact condition during the short-circuit may most likely affect the heat generation rate profile. Unfortunately, none of the tested P1-LSC cells revealed a similar, initial impedance as the P1-type ESC cells. Most likely, the applied pressure condition between

Table V. Estimated Shorting Resistance and Current Flux for P1-LSC Tests at 100 ms.

$t = 100$ ms	Resistance $R_{LSC,est}$/mΩ	Current $I_{LSC,est}$/A
P1#2	38.7	7.5
P1#3	24.5	6.4
P1#9	40.9	7.6

est = estimated.
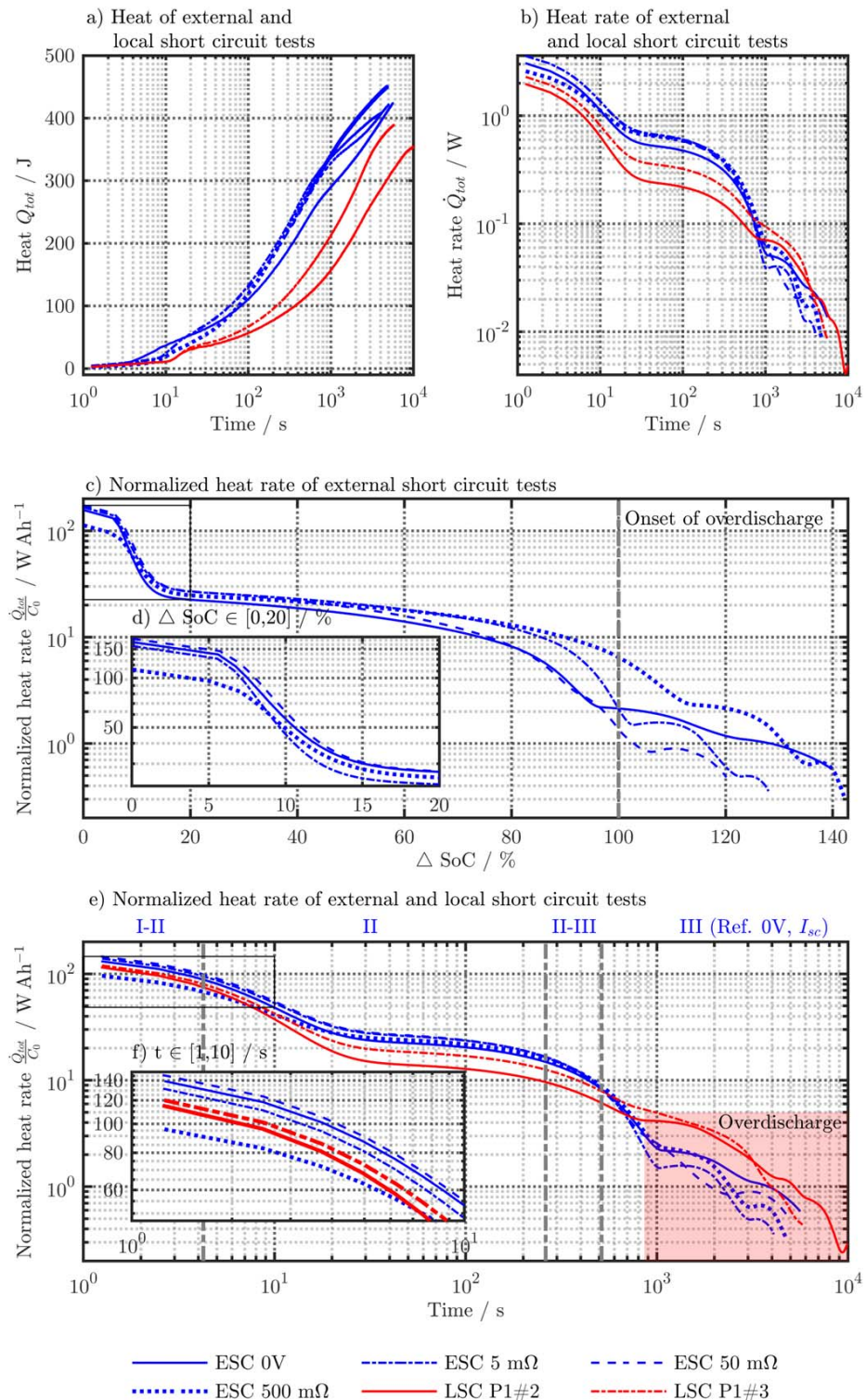
Figure 5. Calorimetric measurements of ESC and LSC applied to single-layered pouch-type cells (i.e. P1-LSC). Subplot (a) and (b) show the total amount of heat (Q_{tot}) and the heat rate ($\dot{Q}_{tot}$). Subplot (c) shows the heat rate related to the cell's capacity vs the SoC with a magnified area (d) between 0 and 20% for all ESC tests. Subplot (e) shows the related heat rates vs time with a magnified area (f) between 1 and 10 s. For comparison, the zones I-II to III are depicted as shown in Fig. 4a for the 0 V case, referring to the measured current flux (I_{sc}).

Table VI. Nomenclature.

Latin symbols

C_p	J K^{-1}	Heat capacity
C_0	Ah	Initial capacity at 0.5 C CC discharge
C_{sc}	Ah	Discharged capacity after the ESC test
d	m	Diameter of nail (i.e. stainless steel needle)
E_{eq}	V	Equilibrium potential vs Li/Li$^+$
E_{sc}	V	Terminal voltage
$E_{sc,end}$	V	Terminal voltage after the short-circuit test
F	96 485 As mol^{-1}	Faraday's constant
I_{sc}	A	Current flux during short-circuit scenario
$I_{LSC,est}$	A	Estimated current flux for LSC test
I_{max}	A	Maximum current flux for ESC test
m	kg	Mass of cell
R	8.314 J mol^{-1} K^{-1}	Gas constant
R_{ext}	Ω	External resistance for ESC test
$R_{i,0}$	Ω	Initial impedance from EIS measurement
$R_{i,sc}$	Ω	Final impedance from EIS measurement after the short-circuit test
$R_{LSC,est}$	Ω	Estimated shorting resistance of LSC test
$\dot{Q}_{tot}^*$	W	Uncorrected heat generation rate
$\dot{Q}_{tot}$	W	Calorimetric-corrected heat generation rate
Q_{tot}^*	W	Uncorrected total amount of heat
Q_{tot}	W	Calorimetric-corrected total amount of heat
t	s	Time
T	K	Temperature
Greek symbols		
Φ_{sc}	V	Electrical potential between the penetration site vs the cell's negative tab

the copper bars during the short-circuit experiments influenced the impedance of the cells, which will be investigated in the future. Regarding zones II-III (see Fig. 6d) and III, similar heat rate decays for the ESCs and the P1#9 LSC case appear due to the lower potential, heat rate and expected current flux plateau during zone II compared to the cells P1#2 and #3. Interpreting the P1-LSC tests using the calorimetric results may reveal a slightly more inaccurate correlation to the P1-type ESC tests (i.e. between 5 and 500 mΩ), but helps to better understand the correlation of the cell's initial impedance, initial capacity and the shorting resistance at the penetration site during the short-circuit scenario.

LSC applied to double-layered pouch-type cells.—To investigate LSCs occurring simultaneously in multiple electrode layers, nail penetration is applied in the P2-LSC tests to trigger short-circuits in both electrode stacks. In comparison, only a single electrode stack is penetrated with the nail in the P3/P4-coupled LSC/ESC tests and the second one undergoes an ESC via the current collector path.

Figure 7 shows the resulting terminal voltages of the P2-LSC and P3/P4-LSC/ESC in reference to the P1-type ESC and P1-LSC cases. After the attenuation of mechanical oscillations of the short-circuit device, all LSC tests (P2, P3, and P4) lie in between the 50 and 500 mΩ ESC case (i.e. from zone I to II-III ref. to the 50 mΩ case) until the onset of zone III. At the transition I-II, the P2-LSC shows faster voltage decrease compared to the P3/P4-LSC/ESC tests, which more or less show no significant difference in their electrical behavior. From zone II until III, the P3/P4-LSC/ESC test approach the 500 mΩ ESC case, which indicates a higher ohmic resistance behavior caused by lower mass transport limitations during zone II. The P2-LSC shows increased mass transport limitations during zone II and a faster voltage decay, and remains in between the aforementioned ESC cases.

Ideally, similar contact conditions in both penetration sites of the P2-LSC test should be achieved and the terminal voltage should

assimilate the P1-LSC test. At the very beginning ($\approx$2 ms), the lower initial impedance and the higher capacity of P2#1 (see Table III) compared to the P1#2 cell leads to a lower onset of the terminal voltage during zone I and a higher initial current peak is expected. During zone I, the contact condition in both electrode layers most likely forms/alters and results in a higher ohmic resistance behavior, which leads to the subsequent offset from zone I-II to III. As a result, non-ideal penetration may lead to a higher ohmic contact condition in one or both electrode stacks, when two stacks are penetrated at once.

The P3- and P4-type cells' impedances differ (see Table III), which leads to the appearing marginal lower voltage plateau of P4#1 compared to P3#2 in zone I, but overall no significant difference in the electrical behavior appears. The higher ohmic resistance behavior during the transition zone I-II is probably correlated to the simultaneous ESC in the second electrode stack. As no difference between the P3 and P4 case were observed, penetrating first the anode or the cathode has negligible influence on the resulting shorting behavior.

The total amount of heat is shown in Fig. 8a and totals of 874, 821, and 799 J for the P2-LSC, the P3, and P4-LSC/ESC test appear. Relating the heat rates shown in Fig. 8b to the cell capacity, Fig. 8c allows to evaluate the shorting scenarios as discussed for the P1-type cells. Beside the contact condition at the penetration site, higher capacity and lower impedances (see Table IIId) most likely lead to higher initial currents in stage I-II compared to the P1-type cells. Similar mass transport limitations appear for the P2- and P4-type cell shown in Fig. 8e, which assimilate the 50 mΩ ESC case until zone II-III. The P3-type LSC test shows slightly increased mass transport limitations resulting in a marginal lower heat rate plateau in zone II, similar to the P1-type LSC test. Analyzing the electrical potential at the penetration site for the P3-type cell, a slightly higher offset to the terminal voltage appeared compared to the P2- and P4-type cells, which indicates an increased local polarization across the electrodes
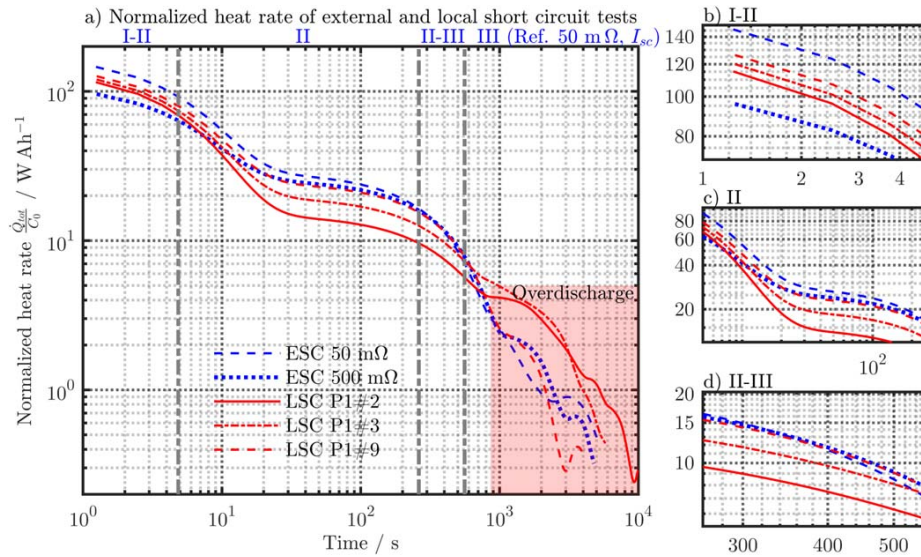
Figure 6. Capacity related heat generation rate of the P1-type ESC (50 and 500 mΩ) and P1-LSC tests. Subplot (a) shows the related heat rates of ESC and LSC tests over time with magnified areas (b)–(d) referring to the zones I-II, II, and II-III of the 50 mΩ case (I_{sc}).
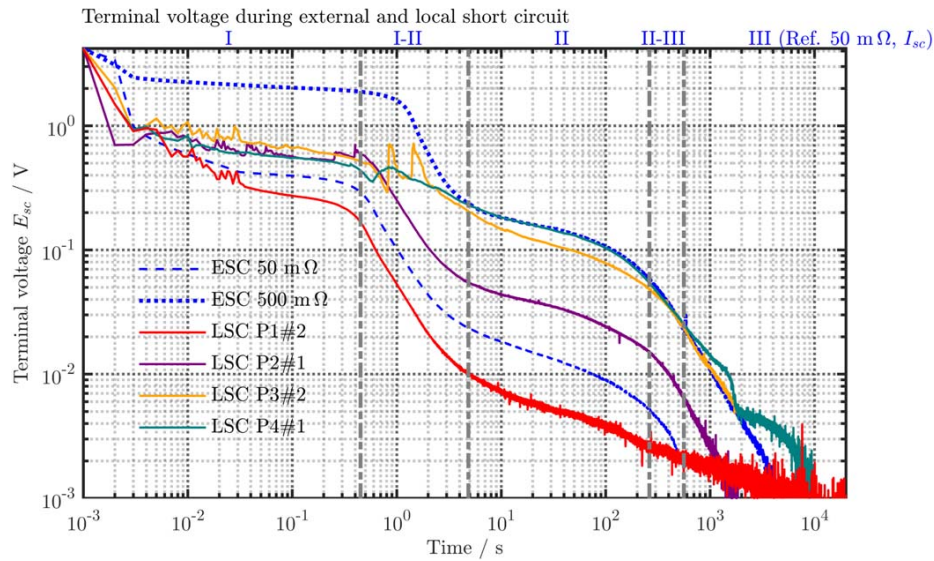
Figure 7. Measurement results showing the terminal voltage of ESC (50 and 500 mΩ, only configuration P1) and LSC (1 mm needle) tests applied to single-(P1#2) as well as double-layered (P2# 1, P3#2, and P4#1) pouch-type cells. Plateau and transition zones (I, I-II, II, II-III and III) are depicted referring to the 50 mΩ ESC case.

and therefore increases the limitation behavior as discussed before. This corresponds to the slightly lower terminal voltage plateau of the P3-type cell shown in zone II (see Fig. 7). As the current flux during zone II is most likely higher for all double-layered cells compared to the P1-LSC cells, faster discharge/voltage decay appears in zone II-III (see Fig. 8f) similar to the P1-type 50 mΩ ESC case. From zone I-II to II-III, the P2-LSC cell shows higher heat rates than the P3/P4-type cells which corresponds to the terminal voltage profiles in Fig. 7, and ends in zone III with the fastest discharge/limitation of the P2-LSC cell. To conclude, the results of the P2-LSC test revealed an unexpected offset to the P1-LSC test, which is most likely caused by non-similar contact condition in one or both penetrated electrode stacks. Penetrating both (P2-LSC) or only a

single electrode stack (P3/P4-coupled LSC/ESC) in a double-layered test cell, revealed significant differences for the terminal voltage profile after the transition zone I-II, which corresponds to the observed capacity related heat rate profile. The actual local shorting conditions (i.e. either LSC applied to all electrode stacks or a single LSC in one electrode stack leading to a subsequent ESC in the remaining one) must therefore be considered, when the results of a nail/needle penetration test are interpreted in terms of emulating ISC scenarios in LIBs.

LSC applied to double-layered pouch-type cells using various needle diameter.—P2-type LSCs are applied with a needle of 0.5, 1, and 2 mm to analyze the correlation of penetration size, the resulting
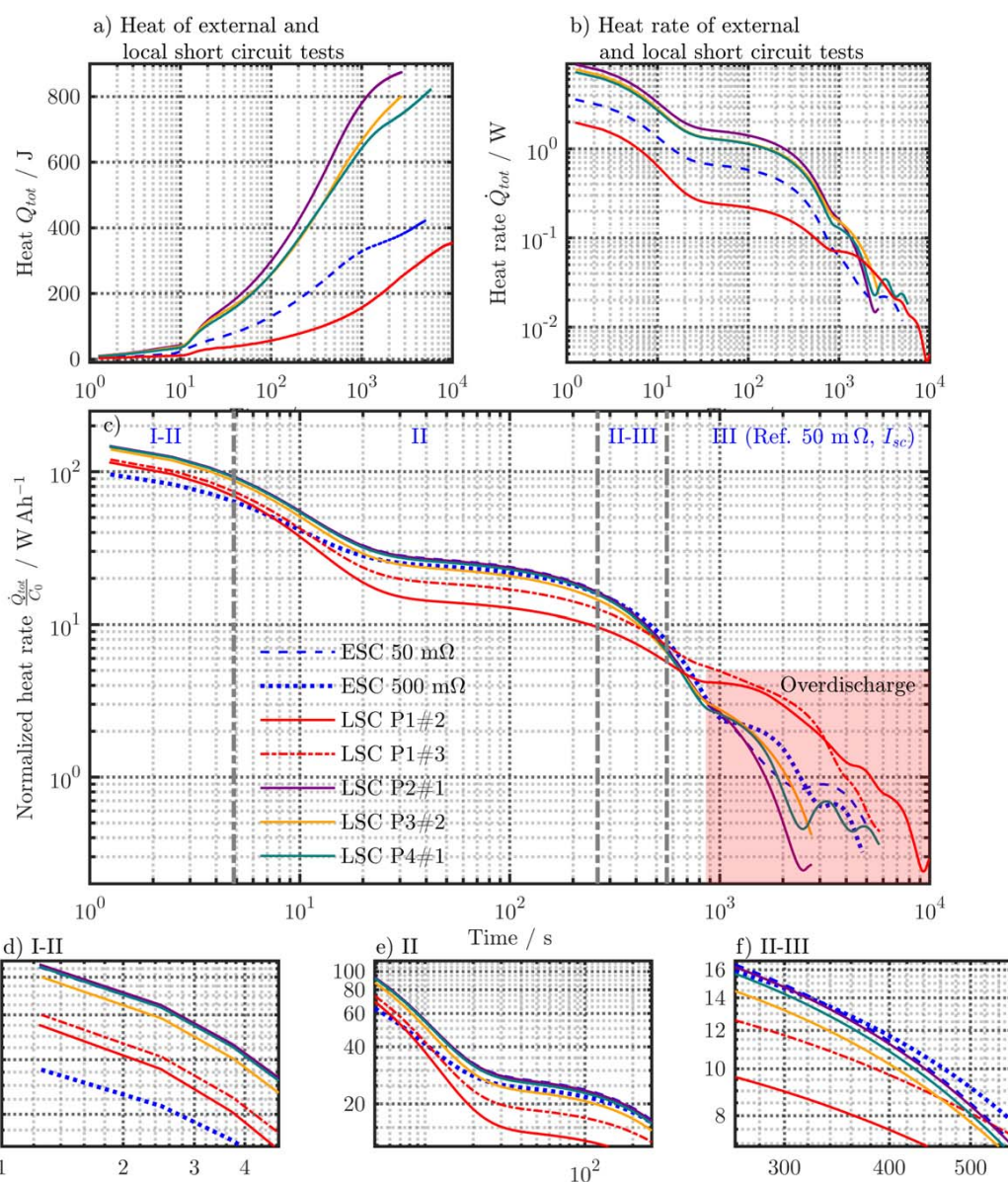
Figure 8. Calorimetric measurements of the P2-LSC and P3/P4-coupled LSC/ESC tests in comparison to the P1-type ESC and P1-LSC tests. Subplot a) and b) show the total amount of heat (Q_{tot}) and the heat rate ($\dot{Q}_{tot}$). Subplot c) shows the capacity related heat generation rates $\left(\frac{\dot{Q}_{tot}}{C_0}\right)$ with magnifications for zone I-II (d), II (e), and II-III (f). The zones I-II to III are depicted as shown in Fig. 4 for the 50 mΩ case, referring to the measured current (I_{sc}).

contact condition, and the appearing short-circuit intensity. Figure 9 shows the capacity related heat rates in comparison to the P1-type ESC and P1-LSC cases.

Regarding zone I-II in Fig. 9b, the 2 mm case reveals the highest (>160 W Ah^{-1}) heat rate, the 0.5 mm case the lowest ($\approx$120 W Ah^{-1}) heat rate but higher than the 500 mΩ ESC as well as the P1-LSC cases, and the 1 mm case lies in between these two cases, assimilating the 50 mΩ case as discussed before. Considering the cells' impedances and the capacities (see Table III), most likely the resulting maximum heat rates in zone I-II correlate well with the diameter of the needle as: The larger the diameter of the needle, the higher the heat rate and the underlying shorting intensity. Regarding zone II in Fig. 9c, increased mass transport limitations are seen for the 2 mm case, which shows the lowest heat rates compared to the 1 and 0.5 mm case, and the lowest mass transport limitation are seen for the 0.5 mm case. Due to the

highest capacity, the cell applied with 1 mm shows the slowest heat rate decay in zone II-III (see Fig. 9d) compared to the 0.5 and 2 mm case. As a conclusion, the intensity of the LSC test is directly affected by the shorted area in the penetration site, which correlates well with the chosen needle diameter.

Post-mortem analysis.—*Post-mortem* analysis by means of visual inspection, SEM, and EDX is applied to cells used in the ESC and the LSC tests in order to evaluate the degradation of the graphite and NMC-111 electrodes. Similar results were observed for all studied cells depicted in the supplementary material and the results of cell P1#10 (ESC at 5 mΩ) and P1#2 (LSC with 1 mm) are presented in the following.

Figure 10 shows the opened cell P1#10 revealing partly delamination of the graphite composite electrode (a) and a
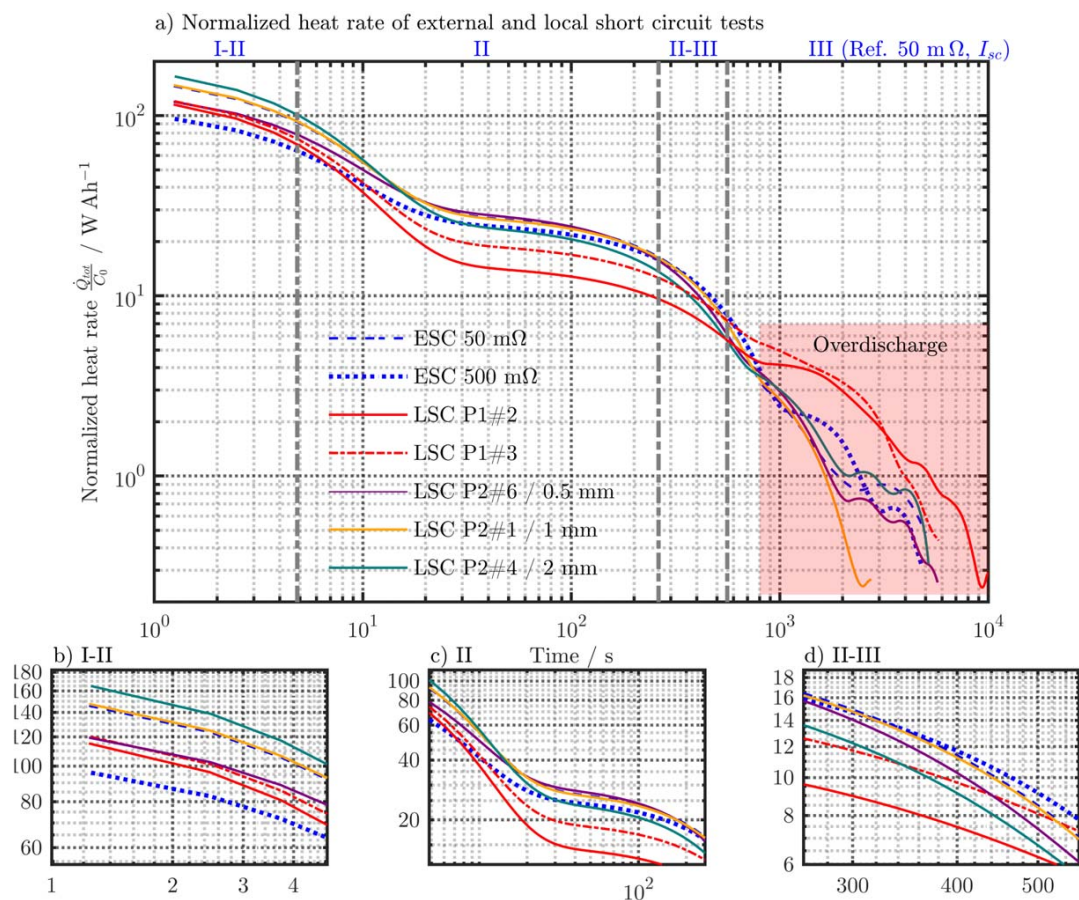
Figure 9. Capacity related heat rate of the varying needle diameter tests applied to P2-type cells. Diameters of 0.5, 1, and 2 mm tests are shown in comparison to the P1-type ESC (50 and 500 mΩ) and P1-LSC tests using a 1 mm needle applied to P1-type cells. The plateau and transition zones are shown in reference to 50 mΩ ESC case (I_{sc}).

mechanically rather intact NMC-111 cathode (b). Magnifications (see Figs. 10c and 10d) at a factor of 1000 show SEM images of the electrode surface revealing depositions on the anode and cracked or even burst NMC-111 active material particles on the cathode as discussed in our previous work.[31] Applying EDX measurements at these positions (e to h) indicates significant amounts of copper on both electrodes, which is not the case for the pristine materials (i to l) before the ESC. Low lithiation levels and high overpotentials in the anode most likely cause copper dissolution from the negative current collector during the ESC and subsequent deposition across the electrodes as impurities during disassembly, handling and preparation during the *post-mortem* analysis could be excluded. Most likely, the deposition of copper in the anode is caused by significant potential differences through the thickness of the graphite coating during the short-circuit and in the cathode by its higher potential levels. The amount of oxygen is most likely caused by handling the samples outside the argon-filled glove box and the carbon content is referred to the actual active material (f, i) and the content of binder (h, l). Regarding the P1-LSC test of cell P1#2 shown in Figs. 11 and 12, the graphite anode in Fig. 11a clearly shows delamination of its composite material and looking into the magnifications near the tab (b, x50) and near the bottom (h, x500), entire holes (≈⌀ 129.6 μm) or partly surficial dissolutions (≈⌀ 3.2 μm) appear (see 11i) where copper is completely or partly dissolved. Magnifications near the penetration site (c) reveal deep radial cracks through the thickness of the graphite composite, which indicates significant amounts of copper (d and e) compared to the pristine material (f and g).

Around the penetration site, all cells showed complete dissolution of the copper foil, which indicates the highest current densities and overpotentials and thus maximum local intensity of the shorting scenario. Similar to the ESC analysis, copper dissolution and deposition could be observed at strongly delaminated spots across the anode, where the coating came off during disassembly. Beside cracked or burst active material particles of the NMC-111 cathode shown in Fig. 12, no delamination but deep cracks were observed throughout the coating (SEM x150 and x1000, h and i) near the penetration site, which underlines a higher local intensity of the shorting scenario. The magnification in b (SEM × 40) shows the penetration site itself with clear marks of cutting and crumpling of the cathode caused by the needle penetration. A magnification (SEM x500, c) offers a cross view analysis through the coating thickness as shown in Fig. 12e (SEM × 1000, see d). Compared to the pristine material (f and g), contents of copper are significantly indicated not only on the surface of the electrode, but also throughout the entire thickness of the cathode as well as near the aluminum current collector. Overall, significantly increased indications of copper dissolution and deposition can be observed throughout the coating thickness as well as across both anode and cathode. As the LSC tests result in a deeper discharge condition compared to the ESC test (i.e. ESC stops at $I_{sc} < 0.1$ mA), the observed increased intensity of copper dissolution and deposition seems justified. The expected intense locality appearing in the LSC scenario was shown by complete dissolution of the copper current collector around the penetration site and increased degradation signs in the NMC-111 cathode.
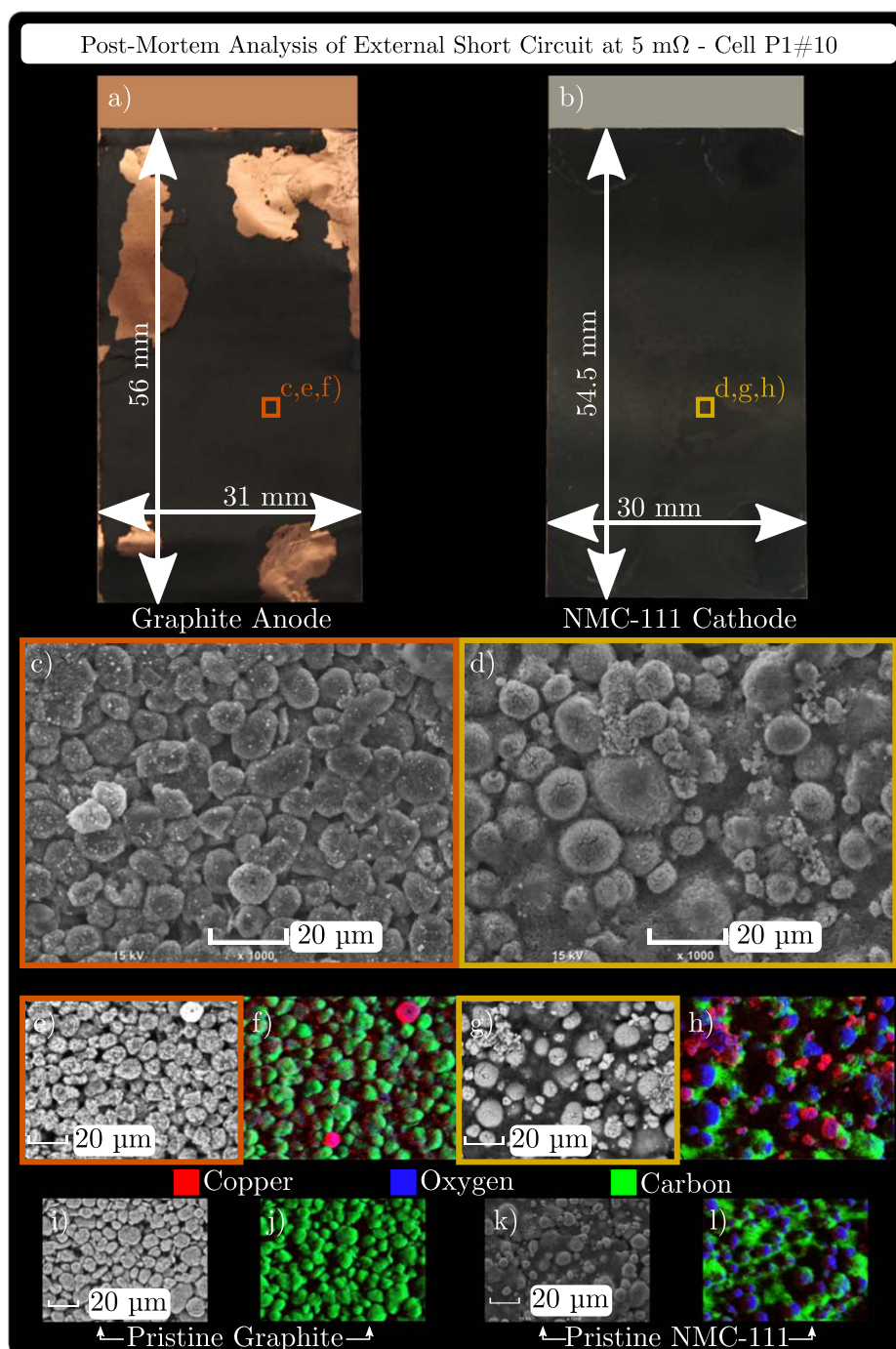
Figure 10. *Post-mortem* analysis of cell P1#10 after the applied ESC at 5 mΩ showing images of the entire anode (a) and cathode (b), magnified (SEM × 1000) spots (marked in orange and gold) on each electrode (e to h), and their EDX analysis in comparison to the pristine electrodes (i to l) showing contents of copper (red), oxygen (blue), and carbon (green).

Conclusions

The electrical and thermal short-circuit behavior of externally and locally applied short-circuits (i.e. needle/nail penetration) was investigated on single or double-layered graphite/NMC-111 pouch-type LIBs using a quasi-isothermal, calorimetric test bench. The quasi-isothermal short-circuit conditions enable for analyzing the electrical and thermal short-circuit behavior without triggering a high local heat generation rate, which may lead to thermal, self-accelerating processes such as a thermal runaway scenario. By applying our technique, we can mitigate the influence of such local, thermal effects and analyze the pure electrical short-circuit behavior in the very beginning (i.e. zone I) until various current rate limitation effects (i.e. zones I-II to III) appear,
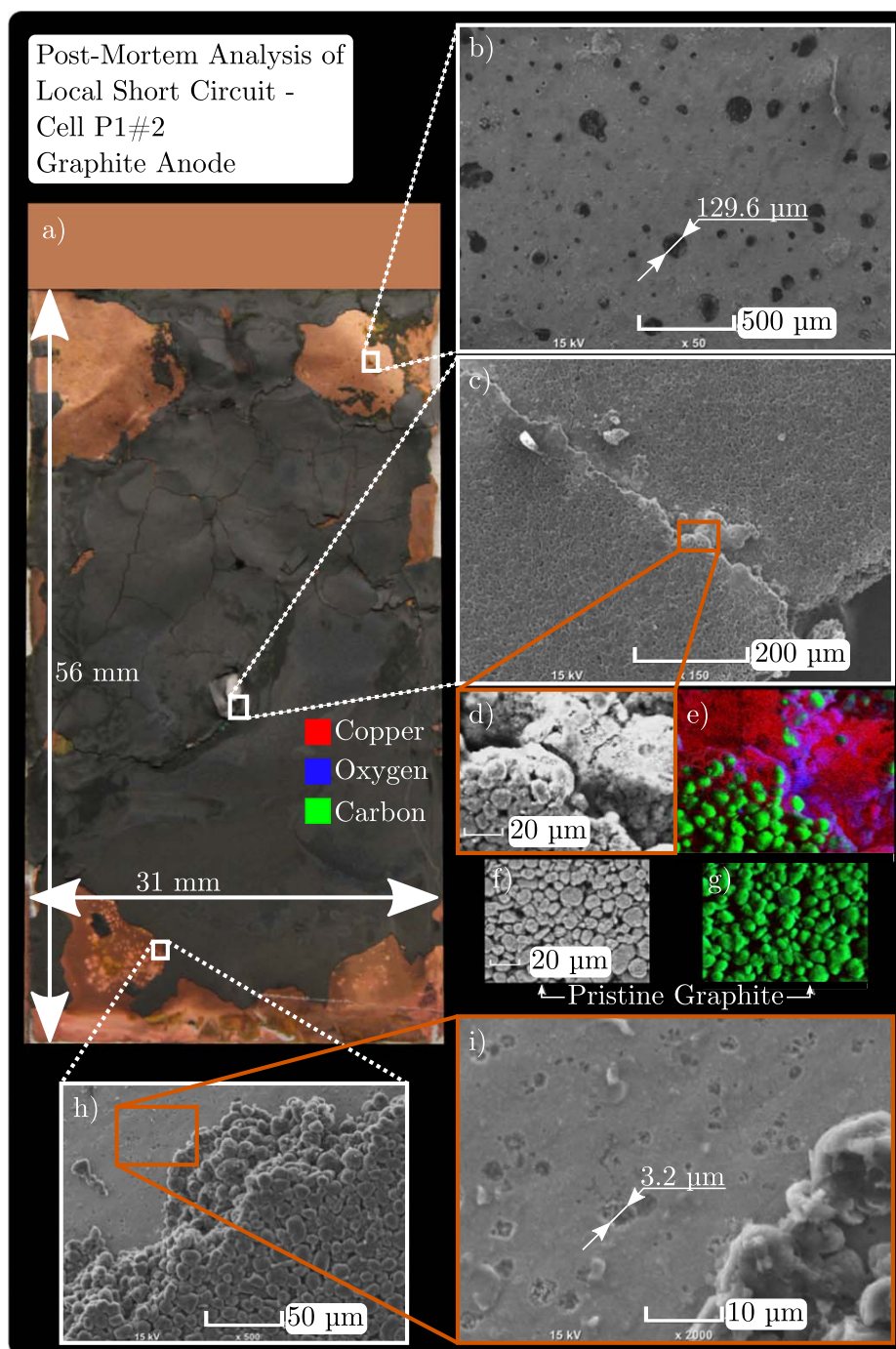
Figure 11. *Post-mortem* analysis of cell P1#2 after the P1-LSC test showing the entire graphite anode (a) and magnified sites near the tab (SEM x50, b), the penetration site (SEM × 150, c), and at the bottom (SEM x500, h) depicting holes in the copper current collector, cracks through the electrode or initially dissolved copper sites (SEM x2000, i), respectively. The crack shown in c) is magnified (SEM x2000, f) for EDX analysis (e) revealing significant contents of copper compared to the pristine material shown in f) and g) before the P1-LSC test.

which are caused by either the anode or the cathode within the tested cells. Comparing the P1-type ESC and LSC results in the very beginning of the short-circuit (i.e. zone I), differences in the electrical behavior were seen but as soon as electrochemical rate limitation effects within both the anode and the cathode initiate (i.e. from zone I-II to III), the electrical behavior shows similar damping characteristics. As a result, the locality of the short-circuit defines the electrical behavior in the very beginning (i.e. <1 s, zone I), but the subsequent rate limitation effects proceed similarly for the ESC and the LSC test. The observed hard short-circuit conditions caused by the needle penetration can thus be emulated by an ESC test with an appropriately chosen external short-circuit resistance for the very beginning (i.e. zone I), which also accounts for the discussed terminal voltage variance calculated from the presented simulation results. The measured local
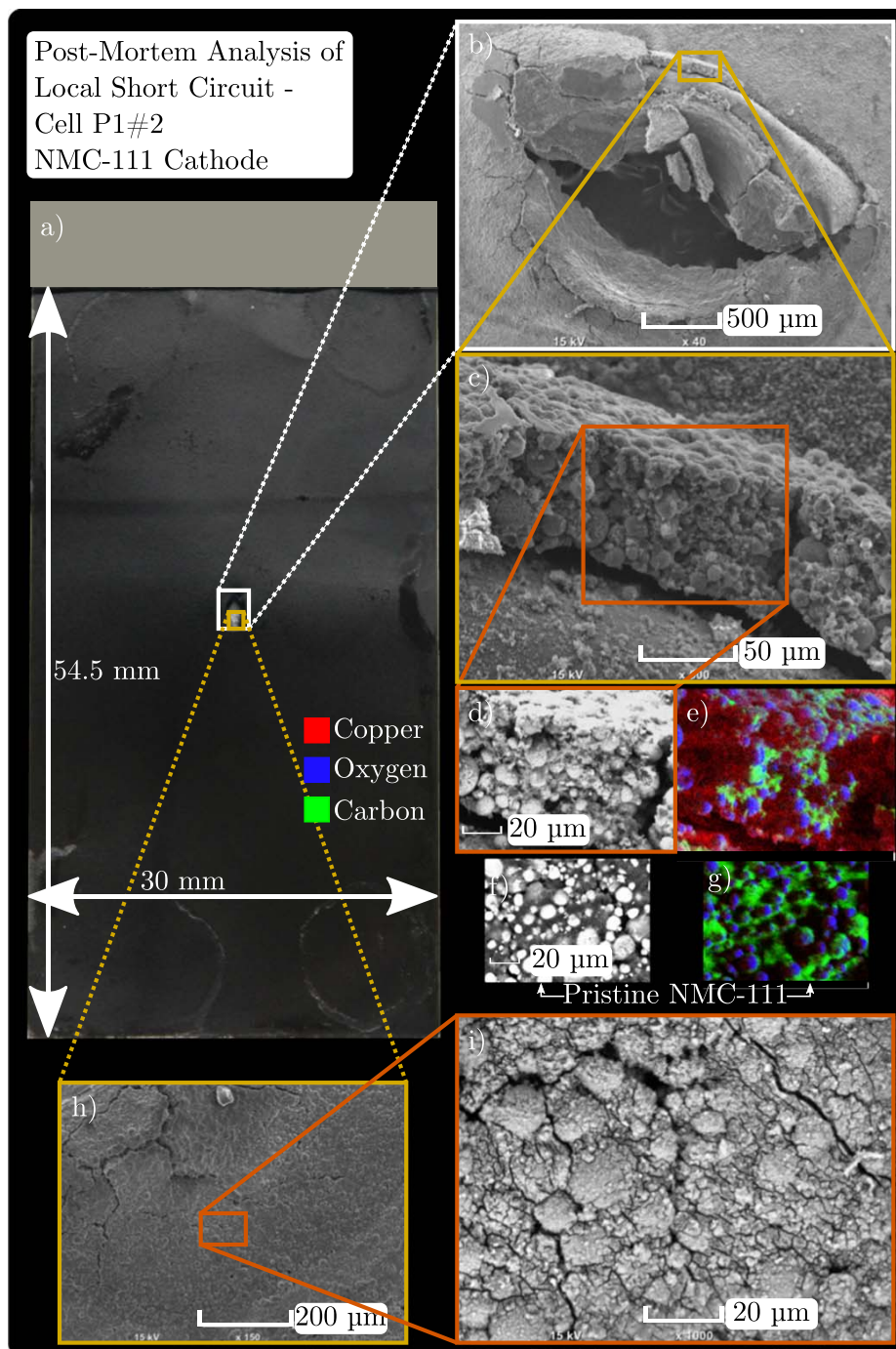
Figure 12. *Post-mortem* analysis of cell P1#2 after the P1-LSC test showing the entire NMC-111 cathode (a) and magnified sites near the penetration area (SEM x150/x1000 in h/i and SEM x40 in c). The penetration site in b) reveals cut (bottom) and crumpled (top) areas (SEM x40) and EDX applied over the coating thickness (SEM x500/x1000, c/d) indicates significant copper content (e) compared to the pristine cathode (SEM x1000, f and g) before the P1-LSC test.

potential at the penetration site via the electrically connected needle vs the cell's negative tab shows the same characteristics as the measured terminal voltage, only with a significant potential offset caused by electrode polarization, current flux over the needle, and the altering short-circuit contact condition. Most likely, the differently appearing potential offsets in the P1-LSC tests may be correlated to a higher or lower current flux around the penetration site and may indicate higher

or lower polarization effects in the cell and thus can be used to evaluate the local short-circuit intensity at the penetration site. Overall, a cells' initial impedance, initial capacity and the electrical contact condition at the penetration site mainly determine the electrical and thermal LSC behavior resulting in a higher or lower current rate limitation behavior. The ESC test offers higher reproducibility, practicability of the actual measurement, and can emulate a LSC scenario in terminal voltage and

heat rate profile. Based on these results, the presented ESC test method is recommended not only to emulate external short-circuits, but also local/internal short-circuit scenarios in LIBs.

Applying needle penetration to both electrode stacks in double-layered cells (i.e. P2-LSC), only marginal differences were observed for the electrical behavior in the very beginning (i.e. <1 s, zone I) compared to a short-circuit applied to a single electrode stack, which triggers an external short-circuit on the second one (i.e. P3/P4—coupled LSC/ESC). However, a significant difference in the electrochemical rate limitation behavior was observed subsequently (i.e. >1 s, zone I-II to III), which indicates reduced rate limitation effects for a coupled LSC/ESC case. Increasing the shorting area investigated via various needle diameters (i.e. 0.5, 1, and 2 mm) leads to higher heat generation rates, which correlates well to a more intensive short-circuit or so called harder short. Similar to the single-layered cells, capacity, impedance, and contact condition determine the short-circuit intensity where the latter shows severe dependency on the used needle diameter as well as the number of penetrated electrode stacks as seen from the results of the double-layered cells.

Overdischarge of the cells appeared in all tests as indicated via initial DVA and finally correlated to copper dissolution/deposition across both active areas of the electrodes analyzing the results of SEM and EDX measurements. Regarding the LSC tests, increased local degradation around the penetration site appeared and a deeper discharge resulting in more intense copper detection indicate the highly local polarization and longer exposure to high current conditions compared to the ESC tests.

Future work will focus on statistical relevance of the presented LSC tests regarding the variance of contact conditions within the penetration site and multidimensional multiphysics simulation studies of LSC and ESC scenarios in order to investigate the difference in local polarization effects throughout and across the electrodes.

Acknowledgments

Appendix

ORCID

J. Sturm https://orcid.org/0000-0001-8876-9989
A. Rheinfeld https://orcid.org/0000-0003-0995-7266

References

1. FAA Office of Security and Hazardous Materials Safety, *Lithium Batteries & Lithium Battery-Powered Devices*, FAA Office of Security and Hazardous Materials Safety - United States Department of Transportation, Federal Aviation Administration (2019), https://faa.gov/hazmat/resources/lithium_batteries/media/Battery_incident_chart.pdf.
2. M. J. Kolly, J. Panagiotou, and B. A. Czech, *The Investigation of a Lithium-Ion Battery Fire Onboard a Boeing 787 by the US National Transportation Safety Board*, National Transportation Safety Board (2013), https://ntsb.gov/investigations/pages/boeing_787.aspx.
3. M. P. Huerta, *Safety Recommendation A-14-032 through -036*, National Transportation Safety Board (2014), https://ntsb.gov/investigations/pages/boeing_787.aspx.
4. D. A. P. Hersman, *Investigative Update of Battery Fire Japan Airlines B-787*, National Transportation Safety Board (2013), https://ntsb.gov/investigations/pages/boeing_787.aspx.
5. S. Tobishima, *Encyclopedia of Electrochemical Power Sources*, ed. J. Garche and C. K. Dyer (Academic Press and Imprint of Elsevier, Amsterdam and Boston) (2009), https://elsevier.com/books/encyclopedia-of-electrochemical-power-sources/garche/978-0-444-52093-7.
6. K. White, *Samsung Recall Support Note7 Investigation*, Exponent—Engineering and Scientific Consulting (2017), https://news.samsung.com/global/wp-content/themes/btr_newsroom/download.php?id=E0RaV5Kg8MHmLtmcg%2BD%2BJXcIe2h9FIPFzKNa3EsW0Ao%3D.
7. Samsung Electronics, *Galaxy Note7 What we discovered*, Samsung Electronics (2017), https://news.samsung.com/us/Samsung-Electronics-Announces-Cause-of-Galaxy-Note7-Incidents-in-Press-Conference.
8. S. Abada, G. Marlair, A. Lecocq, M. Petit, V. Sauvant-Moynot, and F. Huet, *Journal of Power Sources*, **306**, 178 (2016).
9. G. E. Blomgren, *J. Electrochem. Soc.*, **164**, A5019 (2017).
10. D. Andre, S.-J. Kim, P. Lamp, S. F. Lux, F. Maglia, O. Paschos, and B. Stiaszny, *Journal of Materials Chemistry A*, **3**, 6709 (2015).
11. J. B. Habedank, L. Kraft, A. Rheinfeld, C. Krezdorn, A. Jossen, and M. F. Zaeh, *J. Electrochem. Soc.*, **165**, A1563 (2018).
12. V. Ruiz, A. Pfrang, A. Kriston, N. Omar, P. van den Bossche, and L. Boon-Brett, *Renew. Sustain. Energy Rev.*, **81**, 1427 (2018).
13. A. Rheinfeld, *Performance and Safety of Lithium-Ion Electrodes and Cells: Modeling, Simulation, and Validation at Elevated Temperatures and Currents*, Technical University of Munich, Department of Electrical and Computer Engineering, Institute for Electrical Energy Storage Technology (2019), Ph.D.-Thesis http://nbn-resolving.de/urn/resolver.pl?urn:nbn:de:bvb:91-diss-20190920-1506354-1-9.
14. C. J. Orendorff, "The Role of Separators in Lithium-Ion Cell Safety." *The Electrochemical Society Interface*, **21**, 2 (2012) .
15. J. A. Jeevarajan, J. Collins, and J. S. Cook, *Safety Evaluation of two commercial lithium-ion batteries for space applications*, NASA-Johnson Space Center (2004), https://ntrs.nasa.gov/archive/nasa/casi.ntrs.nasa.gov/20050217484.pdf.
16. R. Bisschop, O. Willstrand, F. Amon, and M. Rosengren, *Fire Safety of Lithium-Ion Batteries in Road Vehicles 2019:50*, RISE Research Institutes of Sweden AB (2019), http://diva-portal.org/smash/get/diva2:1317419/FULLTEXT02.
17. A. Abaza, S. Ferrari, H. K. Wong, C. Lyness, A. Moore, J. Weaving, M. Blanco-Martin, R. Dashwood, and R. Bhagat, *Journal of Energy Storage*, **16**, 211 (2018).
18. C. T. Love, O. A. Baturina, and K. E. Swider-Lyons, *ECS Electrochem. Lett.*, **4**, A24 (2014).
19. Y. Zhu et al., *Nat. Commun.*, **10**, 2067 (2019).
20. B. Barnett, D. Ofer, S. Sriramulu, and R. Stringfellow, *Encyclopedia of Sustainability Science and Technology*, ed. R. A. Meyers (Springer, New York and London) p.6097 (2012).
21. T. Yokoshima, D. Mukoyama, F. Maeda, T. Osaka, K. Takazawa, and S. Egusa, *J. Electrochem. Soc.*, **166**, A1243 (2019).
22. C. J. Orendorff, E. P. Roth, and G. Nagasubramanian, *Journal of Power Sources*, **196**, 6554 (2011).
23. S. Santhanagopalan, P. Ramadass, and J. Zhang, *Journal of Power Sources*, **194**, 550 (2009).
24. C.-S. Kim, J.-S. Yoo, K.-M. Jeong, K. Kim, and C.-W. Yi, *Journal of Power Sources*, **289**, 41 (2015).
25. D. P. Finegan, B. Tjaden, T. M. M. Heenan, R. Jervis, M. Di Michiel, A. Rack, G. Hinds, D. J. L. Brett, and P. R. Shearing, *J. Electrochem. Soc.*, **164**, A3285 (2017).
26. T. D. Hatchard, S. Trussler, and J. R. Dahn, *Journal of Power Sources*, **247**, 821 (2014).
27. P. Poramapojana, *Experimental investigation of internal short circuits in lithium-ion batteries*, The Pennsylvania State University (2015), Ph.D.-Thesis https://etda.libraries.psu.edu/files/final_submissions/11020.
28. T. R. Tanim, M. Garg, and C. d. Rahn, *An Intelligent Nail Design for Lithium Ion Battery Penetration Test. ASME 2016 X International Conference on Energy Sustainability collocated with the ASME 2016 Power Conference and the ASME 2016 XIV International Conference on Fuel Cell Science, Engineering and Technology*, New York, N.Y. p. V002T01A001 (2016).
29. T. Yokoshima, D. Mukoyama, F. Maeda, T. Osaka, K. Takazawa, S. Egusa, S. Naoi, S. Ishikura, and K. Yamamoto, *Journal of Power Sources*, **393**, 67 (2018).
30. T. Volck et al., *Batteries*, **2**, 8 (2016).
31. A. Rheinfeld, A. Noel, J. Wilhelm, A. Kriston, A. Pfrang, and A. Jossen, *J. Electrochem. Soc.*, **165**, A3427 (2018).
32. A. Rheinfeld, J. Sturm, A. Noel, J. Wilhelm, A. Kriston, A. Pfrang, and A. Jossen, *J. Electrochem. Soc.*, **166**, A151 (2019).
33. A. Kriston, A. Pfrang, H. Döring, B. Fritsch, V. Ruiz, I. Adanouj, T. Kosmidou, J. Ungeheuer, and L. Boon-Brett, *Journal of Power Sources*, **361**, 170 (2017).
34. A. Rheinfeld, S. Kosch, S. V. Erhard, P. J. Osswald, B. Rieger, and A. Jossen, *J. Electrochem. Soc.*, **163**, A3046 (2016).
35. Otto Ganter GmbH & Co. KG, (2018), Indexing plunger https://ganternorm.com/de/produkte/3.1-Rasten-Arretieren-Sperren-mit-Bolzen-und-Kugeln/Rastbolzen-Arretierbolzen/GN-817.9-Rastbolzen-demontierbar-mit-und-ohne-Rastsperre.
36. H. Maleki, *J. Electrochem. Soc.*, **146**, 947 (1999).
37. J.-S. Hong, *J. Electrochem. Soc.*, **145**, 1489 (1998).
38. L. D. Ellis, J. P. Allen, L. M. Thompson, J. E. Harlow, W. J. Stone, I. G. Hill, and J. R. Dahn, *J. Electrochem. Soc.*, **164**, A3518 (2017).
39. B. Rieger, S. V. Erhard, S. Kosch, M. Venator, A. Rheinfeld, and A. Jossen, *J. Electrochem. Soc.*, **163**, A3099 (2016).
40. S. V. Erhard, P. J. Osswald, J. Wilhelm, A. Rheinfeld, S. Kosch, and A. Jossen, *J. Electrochem. Soc.*, **162**, A2707 (2015).
41. S. V. Erhard et al., *J. Electrochem. Soc.*, **164**, A6324 (2017).
42. S. Kosch, Y. Zhao, J. Sturm, J. Schuster, G. Mulder, E. Ayerbe, and A. Jossen, *J. Electrochem. Soc.*, **165**, A2374 (2018).
43. J. Sturm, A. Rheinfeld, I. Zilberman, F. B. Spingler, S. Kosch, F. Frie, and A. Jossen, *Journal of Power Sources*, **412**, 204 (2019).
44. A. Rheinfeld, J. Sturm, A. Frank, S. Kosch, S. V. Erhard, and A. Jossen, *J. Electrochem. Soc.*, **167**, 013511 (2020).

6 Correlation of Mechanical and Aging Behavior in Lithium-Ion Batteries
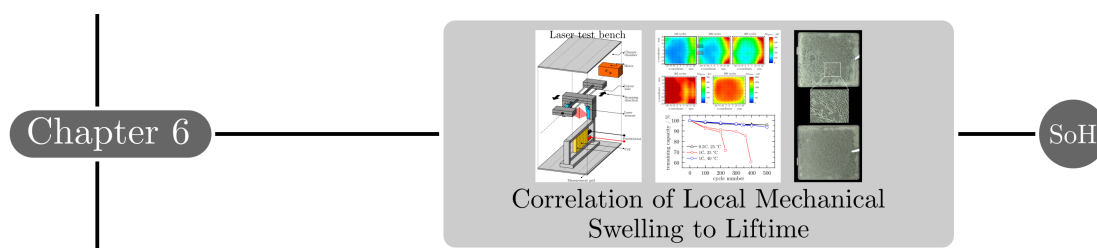

Figure 6.1: Outline of chapter 6.

The article titled *Non-Destructive Detection of Local Aging in Lithium-Ion Pouch Cells by Multi-Directional Laser Scanning* is presented within this section. Fig. 6.1 refers to the thesis outline shown in section 1.6 and summarizes the content of the article in this section.

6.1 Mechanical Swelling during Operation

Beside the traditional measurable states of a LIB, such as terminal voltage, current flow and surface temperature, the mechanical swelling behavior can be alternatively traced to evaluate the state of the battery. Albeit a significant correlation between the thickness of the cell measured by strain gauges or mechanical load cells with the SoC exists [55], a widespread application of mechanics based state-estimation is not expected due to the additional measurement equipment and challenging estimate errors compared to common measurement or model based techniques. Nevertheless, the mechanical behavior of a LIB comes with significant reversible and irreversible thickness changes [211] during operation and lifetime. Therefore, it is crucial to develop an optimal mechanically motivated design of single cells, modules and entire battery packs [170]. Especially during fast charging, significant over-shoots in mechanical swelling [212] can apply mechanical stress on LIBs and lead to accelerated aging. Insights into the correlation of SoH and mechanical swelling behavior during lifetime of a LIB help to better understand the aging from a mechanical point of view and provide mechanically motivated design guidelines for next generation LIBs. Regarding the current development trend towards higher energy density in LIBs, silicon-graphite compounds with increased contents of silicon or even pure silicon anodes are herein of high significance, which result in an overall increased mechanical swelling caused by the volume expansion of silicon [25]. In this context, the mechanical behavior most likely becomes more significant for next generation of LIBs.

6.2 Imbalance of Local Utilization and Aging visualized by Mechanical Swelling

In the following article, an aging study using C/LCO pouchbag LIBs is analyzed towards the correlation of SoH and local mechanical swelling at different charging loads and ambient temperatures. The reversible and irreversible thickness change over lifetime is recorded with a 3D laser scanning method across the active electrode area. The custom built laser test bench was developed and presented in the previous work of Bernhard Rieger [170]. The insights in the local distribution of the mechanical swelling near and further away from the current collector tabs are used to estimate the local utilization of the electrode stack during aging. In a previous work, the correlation of local utilization and reversible thickness change across the electrode was shown using a mechanically extended version of the MuDiMod [132]. The observed local thickness overshoots initiate first near the current collector tabs. This was expected as the current density [132] near the tabs is higher than in the center or the bottom part of the cell – further away from the tabs. With ongoing aging, the local thickness overshoots shift to the center/bottom as the higher utilized region near the tabs most likely reveal a lower SoH due to the prior higher utilization. The imbalance of the mechanical degradation could be observed in post-mortem analysis as a highly non-uniform surface layer deposition across the electrodes. A non-linear SoH decay as seen for the highest applied charging rate at 25 °C is correlated to an exceeding reversible and irreversible thickness change across the entire active electrode area. The final irreversible mechanical swelling accounted for more than 30 % of the initial height of the LIB, which reveal the important role of mechanical restraints during operation to counter degradation effects, such as mechanical cracking or delamination of the coatings, as seen in the post-mortem analysis. As a result, the mechanical swelling behavior reveals a significant correlation to the capacity fade, the increase of the internal resistance and the indication of local utilization and aging across the active electrode area.

Mechanically motivated state-estimation of LIBs most likely remains an optional method in the future, which cannot replace common and prospective state-estimation techniques. Nevertheless, the presented experimental results of the mechanical behavior in the following article can be used to adapt and optimize future state-estimation and operational strategies to further exploit the potential of LIBs. The results help to better understand the mechanical behavior of LIBs, which is the basis to develop suitable mechanical extensions for physicochemical modeling approaches in future. The resulting extensions of the modeling structure can then additionally be used in advanced state-estimation techniques as well, which was out of scope for this thesis.

Author contribution   Bernhard Rieger initiated and carried out the experimental aging study and analyzed the aging behavior via correlating the SoH to the reversible and irreversible mechanical swelling of a LIB. The experimental data was analyzed and interpreted by Bernhard Rieger and Johannes Sturm. The post-mortem analysis was carried out by Johannes Sturm. The manuscript was written by Johannes Sturm and edited by Bernhard Rieger, Franz B. Spingler, Alexander Rheinfeld and Andreas Jossen. All authors discussed the data and commented on the results.

Publication notes   The article titled *Non-Destructive Detection of Local Aging in Lithium-Ion Pouch Cells by Multi-Directional Laser Scanning* is presented in the following. The article [211] is published in the Journal of The Electrochemical Society. Parts of the article were presented at the

Kraftwerk Batterie in Aachen (Germany) in March 2017. A data repository with the most important experimental and simulation based results is published at the platform 4TU.Centre for Research Data (Netherlands) [213].

Non-Destructive Detection of Local Aging in Lithium-Ion Pouch Cells by Multi-Directional Laser Scanning

Johannes Sturm, Franz Benjamin Spingler, Bernhard Rieger, Alexander Rheinfeld, Andreas Jossen

Permanent weblink:
`https://doi.org/10.1149/2.0161707jes`

Non-Destructive Detection of Local Aging in Lithium-Ion Pouch Cells by Multi-Directional Laser Scanning

Johannes Sturm,*,z F. B. Spingler, B. Rieger,* A. Rheinfeld,* and Andreas Jossen

Technical University of Munich, Institute for Electrical Energy Storage Technology, Munich, Germany

Understanding the mechanical activity of lithium-ion cells during cycling and its connection with aging phenomena is essential to improve cell design and operation strategies. Previous studies of lithium-ion pouch cells [B. Rieger et al., *Journal of Energy Storage*, **8**, 1 (2016)] have shown non-uniform swelling with local displacement overshoots during charging. In this experimental work, a novel three-dimensional laser scanning method is used to investigate local reversible and irreversible thickness changes of six commercial LiCoO$_2$/graphite cells during a cyclic aging experiment. Three cycle scenarios were included and two cells each were exposed to a specific temperature and charging rate. The cells showing local displacement overshoots also exhibit non-uniform distributions of irreversible thickness change. Post-mortem analysis showed largely inhomogenously degraded surfaces of the single anode layers. It is shown that the cells' irreversible thickness change correlates with capacity fade and internal resistance increase monitored via electrochemical impedance spectroscopy.

Lithium-ion batteries have become the most promising energy storage technology for small electronic devices such as smartphones or laptops as well as for battery packs in electric vehicles. Although their relatively high density in power and energy make Li-ion batteries the technology of choice for many applications, its aging and degradation behavior likewise limits their use in applications that require extreme safety standards and cycle life.[2] In order to quantify the decay of batteries, the *state of health* (SOH)[3] is used which refers to the capacity fade by relating the current capacity of the cell to its initial capacity. This relation can be seen as an overall concept introducing a measurable quantity of aging effects occurring during battery lifetime.

Detecting the cell's SOH by measuring external stress and strain on the surface of the cell's housing[2,4] is a recent method based on the mechanical behavior of Li-ion batteries in form of volume change effects during charge and discharge processes. These are largely caused by electrode swelling,[5–8] polymer deformation[5,9] and film growth.[10,11]

Estimating the cell's SOH by a single point measurement implies a homogeneous stress and strain distribution over the housing of the cell. Hence, the utilization of the cell would need to be homogeneous. Local variations in current density and electrode potential occurring during cell operation along the current collector foils[12–15] object this assumption. Considering an inhomogeneous utilization of the electrodes described by local variations in *state of charge* (SOC),[15] an overall estimation of SOH seems inappropriate to gain a deeper understanding of aging mechanisms occurring in commercial Li-ion cells. Consequently, there is a need for local detection of aging mechanisms to account for design specific inhomogeneous load across the cell.

As already presented in previous work,[1] extending the measurement of strain or stress to a local resolution allows for local analysis of lithium-ion cell aging. This information may provide a more profound data basis for explaining displacement overshoots near the end of the charging process under constant current which were described in detail in several previous works[1,7,16] and were ascribed to failure mechanisms.

Continuous analysis of cell aging during cycling requires an appropriate method which is able to monitor the local state of the cell without damaging it. For analyzing local aging effects, post-mortem analysis such as disassembling methods enable to investigate local degradation phenomena but are cost and time consuming.[17–19]

Beside non-destructive methods such as electrochemical impedance spectroscopy (EIS),[20] differential voltage analysis (DVA)[21] or neutron diffraction (ND),[22–25] measuring the cell's thickness proved to be a reliable method for determining intercalation stages in the electrodes[7,26,27] and the corresponding electrode specific SOC, to monitor irreversible swelling effects during aging[4] and to detect lithium plating.[16,28] ND[22–25] is not readily available as the experimental setup is highly complex and expensive which makes it inappropriate in our case. Even though EIS and DVA are frequently used to describe overall cell aging,[29–31] these characterization methods do not provide information about local cell aging.

Placing tactile high precision fiber optic sensors on the cell's surface is challenging due to space restrictions, only a few positions[6–8,32,33] can be measured simultaneously. In another work[16] a single tactile dial-indicator was placed on the surface of a lithium-ion cell in order to investigate the formation of lithium plating. However, the measurements only considered a single measurement point assuming a homogeneous distribution of the formed deposit layer. The work of Birkenmaier et al.[28] dealt with the detection of the spatial distribution of lithium plating by point-laser sensor measurements. Measurements are gathered from one side of the cell requiring an initial data set in order to correct the recorded thicknesses at each point. Hence process time increase and displacement results are always dependent on the initial state.

The multidirectional laser scanning technique described in our previous work[1] combines several advantages compared to the measurement methods mentioned above. This method provides an in-operando, non-destructive measurement and the variable number of measurement points ensures an adequate covering of the entire cell-stack related surface area of the cell. Owing to the application of linear laser sensors placed on both sides of the cell, no correction referring to the initial state of the recorded thicknesses has to be performed which reduces the effort in post-processing and ensures robustness toward spatial displacements of the whole cell within the measurement area.

Experimental

Experimental setup.—Six 2.28 Ah Enertech SPB655060 pouch cells with a LiCoO$_2$/graphite cell chemistry were used for the cyclic aging experiments. In Table I, the basic parameters of the studied cell are outlined. More detailed electrode and cell data are provided in our previous work.[26]

In a previous study of the same cell,[1] an overshoot in the thickness change near the tabs was observed at a 1 C charging rate and 25°C chamber temperature, which was not observed anymore when the temperature was increased to 40°C. To investigate the impact of this phenomenon on reversible and irreversible thickness change as well as capacity fade and impedance response, three cycling scenarios were chosen for the experiments. Six cells were considered, two cells

*Electrochemical Society Student Member.
zE-mail: johannes.sturm@tum.de

Table I. Enertech SPB655060 pouch cell specifications.[26]

Name	Value
Capacity	2.28 Ah
Maximum charging rate	1 C
Maximum discharging rate	2 C
Cell length	60 mm
Cell width	50 mm
Cell height	6.4 mm
Anode electrode length	52 mm
Cathode electrode length	51 mm
Anode electrode width	46.4 mm
Cathode electrode width	45.4 mm
Anode coating thickness	$77 \pm 0.5 \,\mu$m
Cathode coating thickness	$68 \pm 0.5 \,\mu$m
Double-coated anode layers	17
Double-coated cathode layers	16
Single-coated cathode layers	2

Table II. Cycling conditions for the studied cells.

Cell	Charging rate	Temperature	Displ. overshoot
#80	0.5 C	25°C	no
#82	0.5 C	25°C	no
#83	1 C	25°C	yes
#84	1 C	25°C	yes
#85	1 C	40°C	no
#86	1 C	40°C	no

each were exposed to a specific combination of charging rate and cell temperature. The cycling conditions for each pair of cells are shown in Table II. The scenarios with 0.5 C charging rate at 25°C and 1 C charging rate at 40°C are denoted as *homogeneous* charging scenarios, as the displacement during charging was uniform across the cell and no local overshoot was observed.[1] The scenario with 1 C charging rate at 25°C is denoted as *inhomogeneous* charging, as a displacement overshoot was observed near the tabs.[1]

The same discharge rate was used for all cells to assure that the observed effects are caused by either charging rate or temperature. The detailed experimental procedure for cycling and check-up are given in Table III. Cycling was conducted inside a temperature chamber. Every 100 cycles, the cell was charged to 100% SOC and left for relaxation for at least 20 h to assure reliable impedance measurements.[34] The impedance was measured at 25°C using a VMP3 potentiostat (Bio-

Table III. Procedure for cycling and check-up.

Parameter	Value
Cycling	
Charging rate	see Table II
Temperature	see Table II
Charge	CC to 4.2 V - CV until I<0.1 C
Pause	30 min
Discharge	1 C CC to 3.0 V
Pause	30 min
Check-up	
Charge	0.5 C CC to 4.2 V - CV until I<0.05 C
Pause	20 h
Location	Temperature chamber at 25°C
EIS	100 kHz to 45 mHz
Location	Laser test bench at 25°C
Discharge	0.5 C CC to 3.0 V - CV until I<0.05 C
Pause	30 min
Charge	0.1 C CC to 4.2 V - CV until I<0.05 C
Pause	30 min
Discharge	0.1 C CC to 3.0 V - CV until I<0.05 C
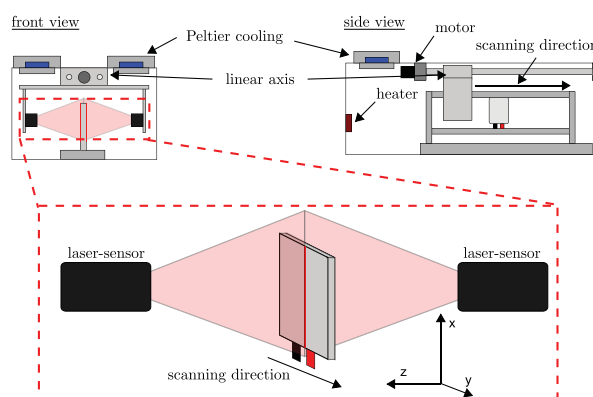
Figure 1. Experimental structure of the laser test bench.

Logic SAS, France). Next, a laser check-up to detect the local reversible and irreversible thickness changes of the cell was conducted. In Fig. 1 the structure of the laser test bench is shown. The procedure in the laser test bench was repeated up to five times depending on the capacity fade of the respective cell. The scanning process caused no heat generation on the cell itself and the cell behavior was therefore not influenced by the measurement equipement. For the check-up inside the laser test bench, which was also kept at 25°C, the local thickness of the cell at 99 positions was recorded every 60 s during the full cycle at 0.1 C charging and discharging rate. This cycle at low current also serves for the capacity measurement and differential voltage analysis.

The reversible thickness change was measured between the fully charged and fully discharged state. At the end of this phase the irreversible thickness change of the cell was detected. A calibration of the laser test bench was conducted before every check-up by using a calibration bar, and preliminary experiments showed that the resulting uncertainty at a given position is no more than $\pm 5 \,\mu$m for a single measuring process, which is much smaller than displacement effects during cycling. For further information about the two test environments and the post processing procedure, the reader is referred to our previous work.[1]

Mechanical activity of lithium-ion cells.—There are several works dealing with the absolute thickness change of cells during charging and discharging based on temperature effects, intercalation stages within the electrodes as well as mechanical inhomogeneities in cells.[22,35,36]

The effect of thermal expansion is negligible in the present study, as the thickness measurement is conducted at a low current rate of 0.1 C, leading to a thermal expansion which is below the laser scanner resolution.[1]

The intercalation induced volume expansion within the graphite electrode was estimated to more than 10%,[67] referring to the fully deintercalated state. However, the deintercalation induced volume expansion of $LiCO_2$ electrodes was determined to be around 2.3%[67], referring to the fully intercalated state. More information about the intercalation induced volume expansion is given in previous work[67]. The intercalation induced thickness change of lithium-ion cells is strongly related to intercalation stages of lithium in graphite.[6,26,27] As the lithiation degree of graphite changes with aging,[22,23] a variation of the reversible thickness change is expected. The reversible thickness change $\triangle t_{rev}$ induced by intercalation and deintercalation[26] can be defined as follows:

$$\triangle t_{rev} = t_{cell,SOC=1,k} - t_{cell,SOC=0,k} \qquad [1]$$

For a check-up after cycle quantity k, the reversible thickness change is derived from the local thickness values between fully charged (SOC = 1) and completely discharged (SOC = 0) state of the cell, see Fig. 2.
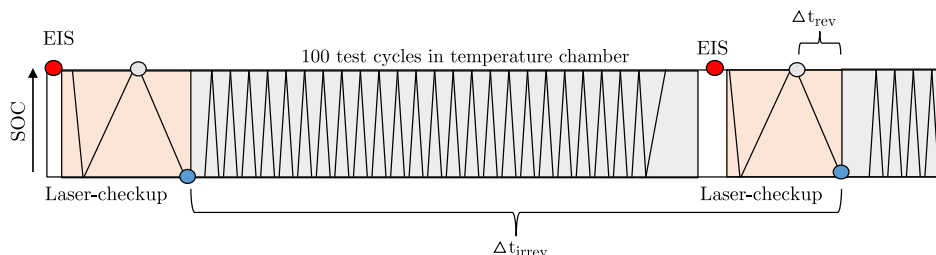
Figure 2. Cycling procedure in the aging experiment. After every 100 cycles in the temperature chamber, an EIS and a check-up is performed via laser scanning to determine the irreversible and reversible thickness change.

The irreversible part of the thickness change can be related to solid electrolyte interphase (SEI) growth[37] in the form of a deposit layer on the particles of the graphite electrode, new crystal arrangement within the particles,[38] increasing porosity of the electrodes due to continuous volume change[39] as well as particle size increase caused by void formation.[40] The parameter $\triangle t_{irrev}$ is determined by subtracting the initial thickness ($k = 0$) from the thickness at the end of check-up after cycle quantity k. Both thickness values are measured in the fully discharged state of the cell (SOC = 0).

$$\triangle t_{irrev} = t_{cell,SOC=0,k} - t_{cell,SOC=0,k=0} \qquad [2]$$

In addition to the causes mentioned above for reversible and irreversible thickness changes, lithium plating at the graphite anode needs to be considered.[16,24] Lithium plating describes the precipitation of metallic lithium on the surface of the solid particles. This deposit layer causes a higher volume change than intercalation into the host lattice.[41,42] This process is partly reversible as some of the plated lithium intercalates after the charging process is finished.[24] The lithium remaining on the surface is considered to be irreversibly deposited.[37,43] The irreversibly deposited lithium causes a permanent thickness change.[16,28] Experimental measurements in the work of Agubra et al.[37] determined the irreversible thickness change per electrode layer to be between 21 μm and 53 μm depending on the local SOC and the affected area of the anode. These measurements were gained from an accelerated aging cycle (4 C) involving 600 cycles applied to a NMC/graphite pouch cell which was analyzed by means of a destructive post-mortem method. In another work of Agubra et al.,[43] the same cell was subjected to 600 cycles at different current rates (2 C, 3 C, 4 C) and the irreversible thickness change was determined to range from 1 μm to 37 μm for 2 C and from 27 μm to 56 μm for 4 C. This supports the assumption that higher charging rates result in a stronger formation of deposit layers at the anode.[44] Burow et al.[45] analyzed the formation of plated lithium for the same cell chemistry in a prismatic cell format. Using an accelerated aging process via pulse charging (8 C), the irreversible thickness increment was determined to range from 11 μm to 31 μm for a single anode sheet after 500 cycles in a post-mortem analysis.

In the work presented here, the investigation of local reversible and irreversible thickness changes under the aforementioned homogeneous and inhomogeneous charging scenarios is investigated by using a novel 3D laser scanning characterization method.

Correlation of aging effects.—As introduced in another work,[46] EIS can be a helpful tool for characterization of aging effects, such as SEI. The formation of SEI is caused by irreversible electrochemical decomposition of the electrolyte at the surface of the active material particles.[10] The growth of SEI implies a certain loss of cycleable lithium[11,30] and the additional layer causes a rising resistance of the cell.[11,47] The increment of internal resistance can be detected by EIS[48] in the form of impedance buildup during aging. In this work, EIS data of the cycled cells at 1 kHz and 45 mHz were analyzed to quantify the growth of pure ohmic and DC-resistance, respectively.

Recent research deals with the estimation of SOC[49] and SOH/capacity fade[4,50] by measuring the pressure evolution in me-chanically restricted cells. Considering homogeneous aging behavior of the cell, a linear dependency between the measured pressure and SOH was found, which does not hold for strongly aged cells.[9] In continuation of these studies, this work focuses on the correlation of internal resistance, irreversible thickness change and capacity fade.

Results and Discussion

Firstly, the capacity fade during the cyclic aging tests is discussed. Further on, the reversible and irreversible thickness changes are analyzed and the correlation between displacement, capacity fade and internal resistance is investigated. Finally, the observed capacity fade is correlated to the DVA-results to identify electrode specific degradation.

Capacity fade.—During each check-up phase, the capacity of the cells was determined according to Table III. In Fig. 3 the capacity fade is shown as a function of cycle number for all studied cells. The capacities are normalized to their initial state (fresh cell). The results indicate a nearly linear decrease of capacity with growing cycle number for the cells which showed no displacement overshoot (see Table II). The cells showing a local overshoot in displacement are characterized by a distinct capacity loss of up to 30% and 40% at cycle number 230 and 396, respectively. The significant decay of these cells points at a distinct aging process which will be further analyzed in the following chapters.

Spatial distribution of reversible and irreversible thickness changes.—The development of the local reversible thickness change from the initial state to 500 cycles is shown in Fig. 4 for cell #80. At the beginning of the cycling experiment, no significant displacement inhomogeneities were detected across the cell. The average reversible thickness change between discharged and charged state was about 160 μm. From 100 to 500 cycles, however, a greater reversible thickness change could be found near the edges of the cell. It was shown in previous works[28,36] that lithium plating initiates in areas close to the edges of the electrodes due to manufacturing tolerances and edge effects. Furthermore, ND analysis showed an accelerated aging behavior
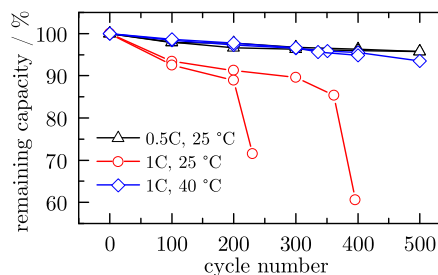
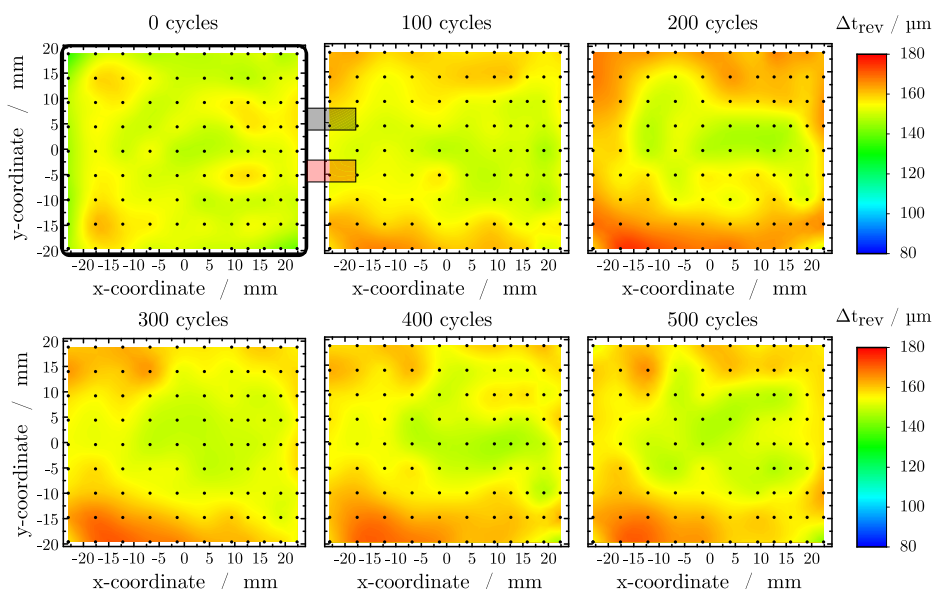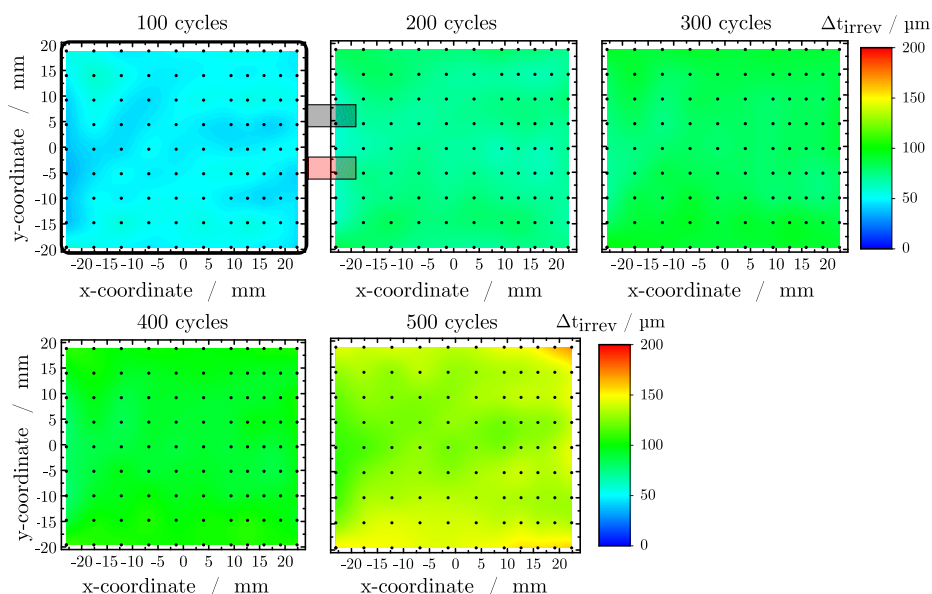**Figure 3.** Capacity fade of the six cells considered in this aging experiment.

Figure 4. Development of the local reversible thickness change Δt_{rev} for a cell cycled at a charging rate of 0.5 C at 25°C (#80). The 99 measurement points of the laser sensors are denoted by the black dots within each depicted surface plot.

in these regions.[22] Bearing in mind these observations and accounting for a stronger fixation of the electrode stack near the edges due to the seam of the pouch-foil, the higher reversible thickness change seems to be justifiable. The mean value of Δt_{rev} was estimated to be 160 μm in our previous work[1] which is in good agreement with the values presented in this work. The irreversible thickness changes for cell #80 upon cycling are shown in Fig. 5. The thickness of the cell increased continuously without the occurrence of distinct inhomogeneities. Within the first 100 cycles, the irreversible thickness increase was around 50 μm. The following check-ups showed a lower increase of approximately 30 μm per 100 cycles with a final displace-

ment of about 140 μm after 500 cycles. The irreversible thickness increase is expected to be caused by swelling of polymer components such as separator and binder in the electrodes[51] as well as SEI growth, and was therefore mainly attributed to the anode in previous publications.[4,52,53] Gas evolution may also be a contributing factor to the overall thickness change as CO_2-gas evolves during cycling.[54] However, based on the thickness change during cycling of a punctured and a gastight pouch cell, Cannarella et al.[4] state that the effect of gas evolution on irreversible thickness change can be neglected. The second cell (#81) cycled at a charging rate of 0.5 C at 25°C showed nearly the same behavior for reversible and irreversible thickness change.

Figure 5. Development of the local irreversible thickness change Δt_{irrev} for a cell cycled at a charging rate of 0.5 C at 25°C (#80). The check-up results at cycle 0 are not shown here because no significant irreversible thickness changes could be detected.
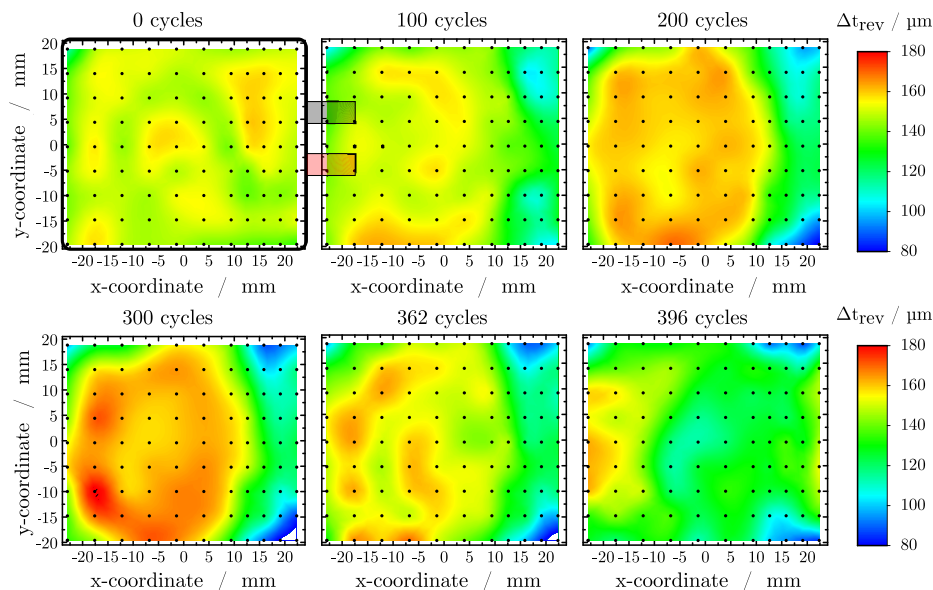
Figure 6. Development of the local reversible thickness change $\triangle t_{rev}$ for the cell cycled at a charging rate of 1 C at 25°C with longer cycle life (#83).

The cells cycled at a charging rate of 1 C and 40°C showed similar behavior to the cells cycled at a charging rate of 0.5 at 25°C and are not discussed in detail here.

At a charging rate of 1 C at 25°C, not only severe capacity fade was observed at cycle 230 and 396 (see Fig. 3) but also distinct inhomogeneities in reversible and irreversible thickness change appeared in cells showing a displacement overshoot. In the following, the local reversible and irreversible thickness changes of cell #83 cycled at a charging rate of 1 C at 25°C are presented and discussed. The authors chose this cell due to the longer cycle life compared to cell #84 and because both cells showed very similar reversible and irreversible thickness changes in the cyclic aging experiment.

The local reversible thickness change of cell #83 is presented in Fig. 6. Initially, the cell showed a rather homogeneous reversible displacement. In contrast to the cells cycled at 40°C and at a charging rate of 0.5 C at 25°C, a lower reversible displacement in the area near the tabs could be observed after 100 cycles. This phenomenon may indicate that the electrode's active material is damaged. With increasing cycle number, the magnitude in reversible displacement remained nearly constant in this specific area whereas it reached higher values in the other parts of the cell. These observations led to the conclusion that the undamaged areas of the cell were more utilized. This non-linear aging behavior was investigated in more detail between the 362nd and the 396th cycle. For this purpose, the cycling procedure in the climate chamber was interrupted in order to perform 34 cycles inside the laser chamber with simultaneous thickness measurement. Regarding the difference between the results of the check-ups after the 362nd and the 396th cycle, the formerly pronounced reversible thickness change in the area opposite to the tabs decreased while close to the tabs no significant changes were seen. The decreasing reversible thickness changes at cycle 396 may also refer to the distinct capacity fade at cycle 396 (see Fig. 3) which is linked to a certain loss of cycleable lithium. Consequently the lithiation range of both electrodes during a full cycle is narrowed and the overall reversible cell displacement, which is directly related to the lithiation stages of the electrodes, is reduced in the same amount. Again, the reader is referred to the work of Rieger et al.[67] for more information about the lithiation induced volume change of the LiCO$_2$/graphite electrodes.

The irreversible thickness changes of cell #83 are shown in Fig. 7. An increased irreversible thickness change could be observed in the area close to the tabs after 100 cycles. The mean irreversible thickness increase of around 300 μm in this region was even higher than the largest irreversible thickness change after 500 cycles of the cells cycled at 40°C and at a charging rate of 0.5 C at 25°C. The remaining cell area showed an irreversible thickness increase which is comparable to cells operated at a 0.5 C charging rate at the same temperature (#80 and #82). After 200 cycles, the irreversible thickness change near the tabs reached values of up to 500 μm whereas the remaining cell area only showed a moderate increase of around 100 μm. The irreversible thickness changes for 300 cycles indicated no significant degradation in the major part of the cell but after 362 cycles an enormous increase was detected. The damaging effect took place also in the remaining part and after 396 cycles displacements of up to 1500 μm were seen.

Comparing the local reversible and irreversible thickness changes, it seems that larger reversible thickness changes in a given area lead to larger irreversible thickness change in the same area. At first, the area close to the tabs showed as large reversible thickness changes as the center part of the cell, probably due to relatively low ohmic losses and resulting good utilization of the active material.[12,15,55] For all follwing check-ups, however, decreasing local reversible thickness change resulted in larger irreversible thickness increase in the area near to the tabs. The lower reversible thickness change indicates a lower utilization and perhaps that the material is damaged, which is in agreement with the dramatic increase in irreversible thickness change shown in Fig. 7. Interestingly, this is followed by an onset of large reversible thickness changes in the center of the cell at cycle 200 and 300, respectively, which may indicate that these areas compensate for the damaged material close to the tabs. At cycle 362, in a similar way to the area close to the tabs, reversible thickness change of the center area decreased while irreversible thickness change increased dramatically. This trend culminated at cycle 396, where most of the cell area showed relatively small reversible thickness changes and the irreversible thickness change reached values of up to 1500 μm. At this point, the SOH of the cell was as low as 60%. Considering these large irreversible thickness increases, lithium plating may play a major role in this process, which is in line with the severe capacity fade[45,47] of these cells, see Fig. 3. This raises the question how utilization and lithium plating are connected. Generally, a high local utilization is equivalent to a high current density of lithium ions. This leads to
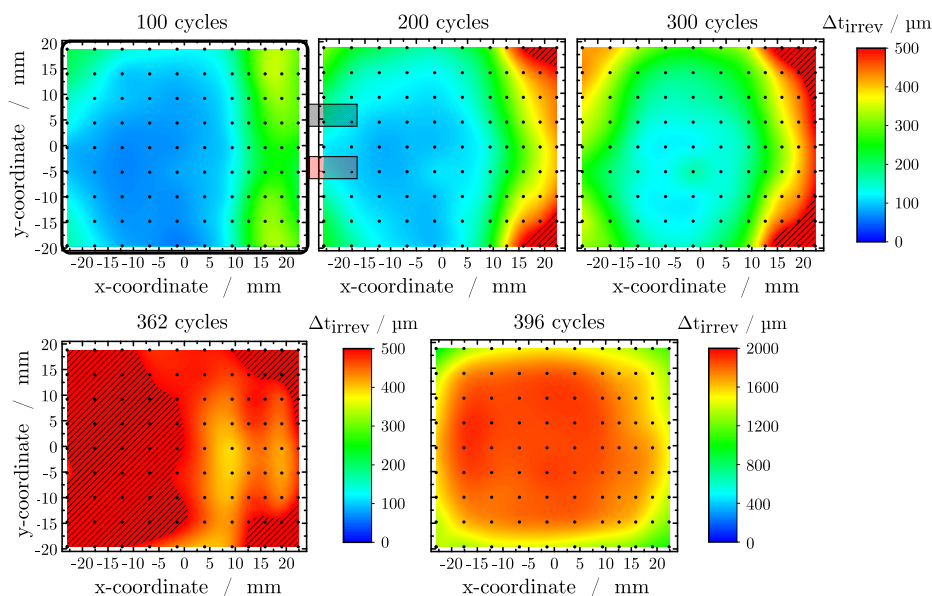
Figure 7. Development of local irreversible thickness changes $\triangle t_{irrev}$ for the cell cycled at a charging rate of 1 C at 25°C with longer cycle life (#83).

high overpotentials in the anode which, during charging, may promote lithium plating to a certain extent.[16,56,57]

Cell #84, which showed a steeper capacity decrease in the inhomogeneous charging scenario, was opened for measuring the thickness of the individual electrodes. Each double side coated anode sheet showed a deposit layer on both sides resulting in a thickness increase ranging between 15 and 40 μm on each side which was measured by using a micrometer screw. These values are comparable to findings by other groups.[37,43,45] The sum of the thicknesses of all deposit layers on the 34 anode sheets agrees with the observed overall thickness increase of the cell. Regarding the irreversible thickness changes from cycle number 362 to 396, the mean value across the measurement area was found to be 1.0911 mm which translates into a relative thickness increase of 17% for the whole cell. The active area of the cell is restricted to the dimensions of the double side coated cathode sheet as it is the smaller one of the two electrodes (see Table I). Considering a corresponding active area of 2315.4 mm², a total volume change of 2526.33 mm³ was determined. The total loss of capacity between the 362nd and 396th cycle amounts to 0.5768 Ah. Considering a molar volume of 13.1 cm³ mol⁻¹ of metallic lithium,[58] the volume of the lost cycleable lithium inventory when in the metallic state is estimated to be 281.93 mm³. The measured volume change, however, is approximately 9 times larger. But it is unlikely that the plated lithium forms a homogeneous layer. The deviation may be explained by mossy and dendritic deposition of lithium, which takes up more volume than a film of solid lithium.[28,59] In order to validate this assumption, a post-mortem analysis of cell #83 was conducted to investigate possible damages on the electrode sheets. As shown in Fig 8, anode sheets were largely covered with inhomogeneously distributed deposit layers. It may be assumed that these mossy layers of all anode sheets combined caused the greater part of the enormous thickness increase. On the cathode sheets no deposit layer or other damages could be seen directly. Severe inhomogeneously distributed deposit layers could be seen on every anode layer and no significant differences were found between the 17 sheets. In summary, prominent mossy deposit layers were observed on the anode, however, there is no clear proof that they correlate with the amount of lost cycleable lithium.

Breaking down the thickness increment per single sided anode sheet from the full cell measurement, each of the 34 coated layers would have grown by 32.1 μm within the last 34 cycles. This cor-
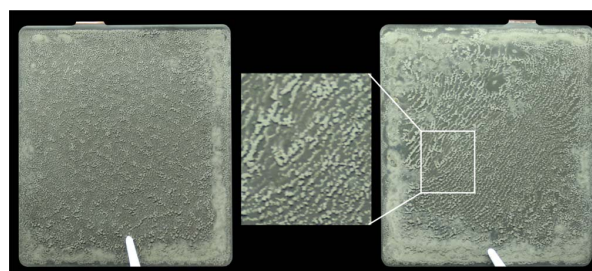
Figure 8. Deposit layers on both sides of the graphite anode of cell #83 after opening in an argon filled glove box. The inhomogeneous structure of the deposit layers is shown in the magnified area. The tweezers used for clamping the sheets are visible at the bottom of the picture.

responds to a growth of 41.7% of the coating thickness. The overall thickness change per layer between the cell's initial state prior to the applied cycling procedure and its final state after cycling can be found to be 47.3 μm which corresponds to a relative thickness increase of 61.4%. In the work of Burow et al.,[45] the initial layer thickness of the graphite coated copper foil was 60 μm and the minimal thickness increase was 51.7% since the thickness of the copper foil is unknown here. Gallagher et al.[60] estimated the increase for 58 μm and 97 μm initial coating thickness to be 12.1% and 72.2%, respectively. Comparing our results with these works, the relative increase seems justifiable.

Correlation of capacity fade, thickness increase and impedance data.—The measurements of capacity fade, irreversible thickness change and impedance of the studied cells are shown in Fig. 9 for all check-ups. The depicted values are normalized to the initial state of the check-up at 0 cycles. The irreversible thickness change is derived as a mean value from the 99 measured points distributed across the surface area of each cell. At cycle 230 and 396 in Fig. 9b, the excessive increase of irreversible thickness change up to 20% and 25% was subjected to the cells cycled at a charging rate of 1 C at 25°C,
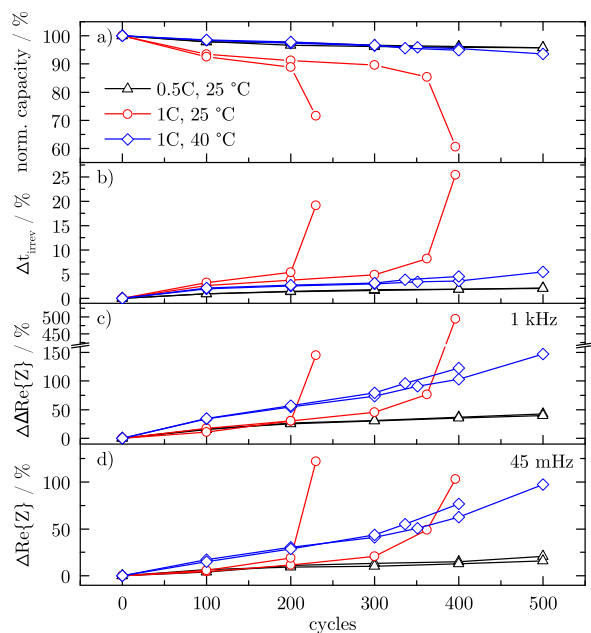
Figure 9. Comparison of a) normalized capacity fade, b) mean irreversible cell thickness change and normalized impedance rise at c) 1 kHz and at d) 45 mHz.

respectively. During the whole aging test in this study, a steeper increase and higher values of the irreversible thickness change for these cells were found compared to the remaining four cells. At a charging rate of 1 C at 40°C both cells showed irreversible thickness changes from 3% up to 5% after 400 cycles. The measurements of the cells at a charging rate of 0.5 C at 25°C exhibited the lowest irreversible thickness changes (2%) of all studied cells.

Comparing Fig. 9a to Fig. 9b, a correlation between normalized capacity loss and irreversible thickness increase may be assumed for all cells. The higher the capacity fade, the higher the irreversible thickness change. The rapid increase of capacity fade between the last two check-ups (200th/230th and 362th/396th) of the cells cycled at a charging rate of 1 C at 25°C is comparable to the findings of other researchers for cylindrical cells.[29,47] In this context the correlation has been denoted as non-linear aging effect. The correlated excessive thickness increase in Fig. 9b confirms the assumed correlation for these cells. None of the cells cycled at a charging rate of 0.5 C at 25°C and 1 C at 40°C showed such a non-linear behavior in this study. The difference between these cells exhibited a higher capacity fade and a greater irreversible thickness increase for the latter ones. This may reveal a certain charging rate or temperature influence which was not investigated in further detail here.

The real parts of the measured cell impedances are shown in Figs. 9c and 9d for a high (1 kHz) and a low (45 mHz) excitation frequency, respectively. At cycle 100 and 200 in Fig. 9c, the values for the impedance rise at 1 kHz exhibit no significant differences for the four cells cycled at 25°C and were estimated to be around 10%. At this point, both cells cycled at 40°C already showed an increase of up to 30%. At cycle 230, the last check-up of one cell (#84) cycled at a charging rate of 1 C at 25°C revealed an excessive impedance increase up to 150%. The second cell (#83) of this charging scenario, showed a steeper impedance rise after cycle 300 and 362 compared to the two cells cycled at a charging rate of 0.5 C at 25°C. Again at cycle 396, this cell (#83) revealed an excessive impedance rise of 500% at 1 kHz. The impedance of the cells cycled at 0.5 C at 25°C was steadily increasing by up to 45% at cycle 500 without an excessive increase

during the whole aging test. The final impedance rises for the cells cycled at a charging rate of 1 C at 40°C were estimated to be 125% and 150% at cycle 400 and 500, respectively.

All studied cells show a distinct increase of the measured impedance for increasing cycle number which can be related to the formation of a SEI-layer.[10] Steeper impedance rise of the cells cycled at 40°C compared to the cells cycled at 25°C may be related to an accelerated SEI growth at higher temperatures for both excitation frequencies.[61] The cells cycled at a charging rate of 1 C at 25°C show excessive impedance rise at the final check-ups which probably may not be justified by SEI-growth alone. The authors conclude, that the greater part is caused by the progressive loss of lithium due to the formation of deposit layers which correlates with the increasing mean irreversible thickness change of the cell at the same time (see Fig. 9b).

As seen in Fig. 9c until cycle 200, the four cells cycled at 25°C showed almost identical values for the impedance rise whereas a significant capacity fade (see Fig. 9a) has already occurred. As the local distribution of reversible and irreversible thickness change presented in Figs. 6 and 7 indicates distinctly localized damaged areas, it is concluded that EIS at this high frequency is not capable to detect the observed inhomogeneities in enough detail for the cells studied in this work. Hence, the penetration depth of the excitation signal seems to be limited and its significance may assumed to be limited[62] for detecting local aging effects.

In Fig. 9d, the values for the cell impedance measured at 45 mHz showed a similar characteristic for all studied cells except for the cells cycled at a charging rate of 1 C at 25°C. At cycle 200, a significantly higher impedance was measured for cell #84 than for #83.

Comparing the values of the impedance rise in Fig. 9c and Fig. 9d of cell #83 and #84 at cycle 200, a significant deviation at 45 mHz for cell #84 appears which is missing at 1 kHz. At a low excitation frequency of 45 mHz, this impedance rise seems to be capable for detecting the already decreased capacity of the cell which is caused by the local damaged areas. Interestingly, the excitation frequency may have an influence on the quality of the gained EIS-data of the cell. Lower excitation frequency may increase the penetration depth and is therefore more suitable for detecting local damaging effects within the cell.[62]

The normalized irreversible thickness change is correlated to the impedance rise at 45 mHz in Fig. 10 and also to the normalized capacity fade in Fig. 11.

The irreversible thickness change in Fig. 10a shows an increased slope for both cells cycled at a charging rate of 1 C at 25°C compared to the remaining four which almost show identical characteristics (see Fig. 10b). At the second check-up after 100 cycles, the impedance rise for the four cells cycled at 25°C was determined to be around 5%, while the impedance increases for the cells cycled at 40°C were determined to be around 16%.

Comparing the four cells cycled at 25°C, the cells cycled at a charging rate of 1 C showed a greater thickness increase for nearly the same impedance rise compared to the ones cycled at a charging rate of 0.5 C. This coincides with the finding, that a certain capacity fade for the cells at 1 C occurred and hence the irreversible thickness change has already increased, which was already discussed in Figs. 9a and 9b. At 100 cycles, the temperature influence revealed in an higher value of the impedance for the cells cycled at 40°C compared to the cells cycled at 25°C. This phenomenon may be caused by temperature dependent aging effects like binder expansion,[63,64] enhanced SEI growth[10,48] or possible gas evolution.[54]

In Fig. 11a, the normalized irreversible thickness change and the capacity fade of all studied cells are shown. The normalized capacity fade (1-SOH) for the cells cycled at a charging rate of 1 C at 25°C was estimated to be around 30% and 40%, respectively. Regarding Fig. 11b, the cells at a charging rate of 0.5 C at 25°C were used in this aging test until 4.2% and the cells at 40°C until 6.4% of normalized capacity fade. Latter cells exhibited a steeper increase of irreversible thickness change at the same normalized capacity fade compared to the cells cycled at 25°C. A linear correlation (see Fig. 11a) can be approximated between the normalized capacity fade and the
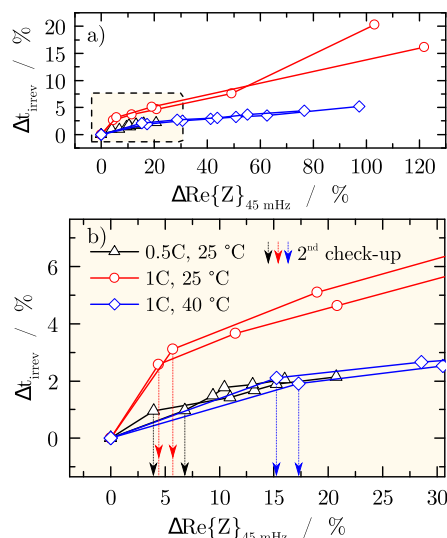
Figure 10. a) Normalized irreversible thickness increase and normalized impedance rise at 45 mHz. b) Magnified region marked in a) up to 7% irreversible thickness increase and 30% impedance rise. The range of the measured real parts at 45 mHz is depicted by the arrows referring to the second check-up after 100 cycles.

thickness increase for the cells cycled at a charging rate of 1 C at 25°C. This finding is confirmed by other researches which dealt with the correlation of stress increase during cyclic aging tests.[4] This phenomenon may indicate the continuous consumption of cycleable lithium due to the formation of deposited lithium on the surface of the active material. For the remaining cells the measured capacity fade in this study is too small for assuming a linear correlation.

The temperature influence on the relation between irreversible thickness change and capacity fade may be indicated by the steeper slope of the cell cycled at 40°C (see Fig. 11b). Enhanced SEI formation does not quite explain the increased slope as this process is regarded to consume lithium in the same amount and therefore no significant
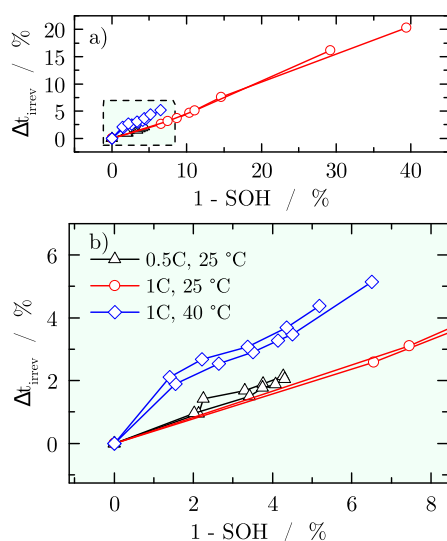
Figure 11. a) Normalized irreversible thickness increase correlated to normalized capacity fade (1-SOH) including all measurements. b) Magnified region marked in a) up to 7% normalized thickness increase and 8% capacity fade.
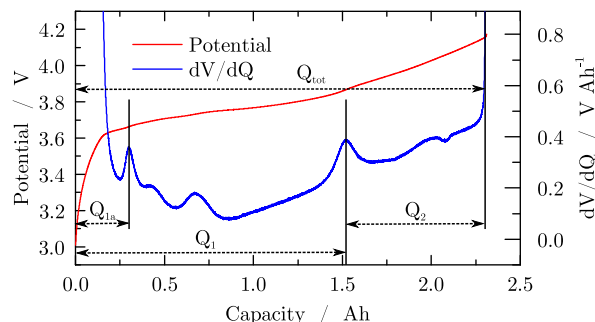
Figure 12. Cell potential V and its derivative $\frac{dV}{dQ}$ for cell #83 at a discharge rate of 1 C for cycle 0.

deviation for the slopes of all cells should be detectable.[11,65] Again, an explanation for this behavior may be additional gas evolution due to electrolyte decomposition[54] or binder degradation,[63,64,66] leading to a steeper electrode thickness increase and resistance rise at the same SOH. Since the cycling conditions included also different charging rates, a clear separation of temperature and charging rate induced effects cannot be conducted in this work and the authors assume, that the resulting characteristic is influenced by both effects at the same time.

Electrode specific capacity fade.—DVA according to the work of Keil et al.[31] was performed during the check-up to analyze the contributions of anode and cathode, respectively, to the overall capacity fade of the cell.[30] The results were compared to the displacement data in order to further elucidate the degradation mechanisms in this study. In Fig. 12 the measured cell potential and its derivative $\frac{dV}{dQ}$ related to the capacity of the cell is shown for cell #83 at cycle 0. Q_{tot} represents the total capacity of the cell. The part from zero up to Q_{1a} denotes the first graphite peak in the differential graphite potential at the transition from a lower Li loading to LiC_{12}. Q_1 represents the charge difference between the fully discharged state of the cell (SOC=0) and the central peak of the differential graphite potential at the transition of LiC_{12} to LiC_6. The remaining part Q_2 between Q_1 and Q_{tot} represents the distance between the fully charged state (SOC=1) and the central graphite peak and can be seen as an indicator for shifts in the electrode balancing which changes the total amount of cycleable lithium.[31]

The DVA analysis for all studied cell are shown in Fig. 13. For cells cycled at a charging rate of 1 C at 25°C (#83, #84) a significant
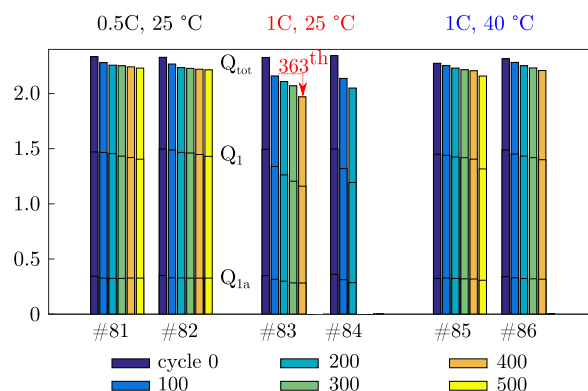
Figure 13. Differential voltage analysis (DVA) for all cells at all conducted check-ups. Cycling of cells #83 and #84 was stopped at cycle number 230 and 396, respectively, due to excessive capacity fade.

decrease of Q_1, while Q_2 stayed approximately constant, was derived from the check-ups at 0, 100 and 200 cycles, which points at a degradation mainly taking place within the anode. The authors assume that the greater part of the excessive capacity fade of the cell was caused by the degradation of the anode. This assumption is confirmed by the post-mortem analysis shown in Fig. 8 where deposit layers were only seen on the anode layers and no obvious degradation mechanism could be seen directly on the cathode layers. The DVA-analysis of the last check-ups at the 230th and 396th cycle, respectively, are missing in Fig. 13 because the peaks of the differential graphite potential could not be determined exactly for the highly degraded states of these cells (#83, #84).

The cells cycled at a charging rate of 0.5 C at 25°C and 1 C at 40°C showed a slightly decreasing capacity fade at higher cycle numbers which indicates that they were far from reaching their end of life.

Conclusions

Measuring the local thickness of lithium-ion pouch cells via laser-scanning was used to correlate reversible and irreversible thickness change to cell degradation during cyclic aging experiment. For cells showing a non-linear aging behavior, locally distributed damage was indicated by an initial reversible thickness change increase, followed by a decrease as soon as the irreversible thickness change increased dramatically within these cells. These effects were first seen in the area near the tabs and subsequently in the center of the cells, accompanied by excessive capacity fade. Post-mortem analysis and DVA-analysis revealed that the larger part of the cell degradation can be ascribed to the anode. The correlation of irreversible thickness increase, impedance rise and capacity fade provides helpful insights into the aging mechanisms of lithium-ion cells. But it also raises the question which mechanisms contribute to the irreversible thickness increase and to which extent, e.g. lithium plating, SEI formation, binder degradation or gas evolution. Further work will focus on the combination of thickness measurements with coulometric measurements and a more detailed investigation of the thermal influence on the aging behavior of lithium-ion cells. Overall, the presented method is a viable means of investigating dynamic thickness changes of lithium-ion cells and provides an interesting perspective on cell aging.

Acknowledgment

References

1. B. Rieger, S. F. Schuster, S. V. Erhard, P. J. Osswald, A. Rheinfeld, C. Willmann, and A. Jossen, *Journal of Energy Storage*, **8**, 1 (2016).
2. X. M. Liu and C. B. Arnold, *Journal of The Electrochemical Society*, **163**, A2501 (2016).
3. T. Okoshi, K. Yamada, T. Hirasawa, and A. Emori, *Journal of Power Sources*, **158**, 874 (2006).
4. J. Cannarella and C. B. Arnold, *J. Power Sources*, **269**, 7 (2014).
5. B. Rieger, S. Schlueter, S. V. Erhard, J. Schmalz, G. Reinhart, and A. Jossen, *J. Energy Storage*, **6**, 213 (2016).
6. L. W. Sommer, A. Raghavan, P. Kiesel, B. Saha, J. Schwartz, A. Lochbaum, A. Ganguli, C.-J. Bae, and M. Alamgir, *J. Electrochem. Soc.*, **162**, A2664 (2015).
7. L. W. Sommer, P. Kiesel, A. Ganguli, A. Lochbaum, B. Saha, J. Schwartz, C.-J. Bae, M. Alamgir, and A. Raghavan, *J. Power Sources*, **296**, 46 (2015).
8. K.-Y. Oh, J. B. Siegel, L. Secondo, S. U. Kim, N. A. Samad, J. Qin, D. Anderson, K. Garikipati, A. Knobloch, B. I. Epureanu, C. W. Monroe, and A. Stefanopoulou, *J. Power Sources*, **267**, 197 (2014).
9. J. Cannarella and C. B. Arnold, *Journal of Power Sources*, **245**, 745 (2014).
10. M. B. Pinson and M. Z. Bazant, *Journal of the Electrochemical Society*, **160**, A243 (2012).
11. A. J. Smith, J. C. Burns, X. Zhao, D. Xiong, and J. R. Dahn, *Journal of The Electrochemical Society*, **158**, A447 (2011).
12. U. S. Kim, C. B. Shin, and C.-S. Kim, *Journal of Power Sources*, **180**, 909 (2008).
13. U. S. Kim, C. B. Shin, and C.-S. Kim, *Journal of Power Sources*, **189**, 841 (2009).
14. B. Wu, Z. Li, and J. Zhang, *Journal of the Electrochemical Society*, **162**, A181 (2014).
15. G.-H. Kim, K. Smith, K.-J. Lee, S. Santhanagopalan, and A. Pesaran, *Journal of The Electrochemical Society*, **158**, A955 (2011).
16. B. Bitzer and A. Gruhle, *J. Power Sources*, **262**, 297 (2014).
17. M. Klett, R. Eriksson, J. Groot, P. Svens, K. Ciosek Högström, R. W. Lindström, H. Berg, T. Gustafson, G. Lindbergh, and K. Edström, *Journal of Power Sources*, **257**, 126 (2014).
18. B. Markovsky, A. Rodkin, Y. Cohen, O. Palchik, E. Levi, D. Aurbach, H.-J. Kim, and M. Schmidt, *Journal of Power Sources*, **119–121**, 504 (2003).
19. K. Jalkanen, J. Karppinen, L. Skogström, T. Laurila, M. Nisula, and K. Vuorilehto, *Applied Energy*, **154**, 160 (2015).
20. A. Barai, G. H. Chouchelamane, Y. Guo, A. McGordon, and P. Jennings, *Journal of Power Sources*, **280**, 74 (2015).
21. S. Schindler, M. Bauer, M. Petzl, and M. A. Danzer, *J. Power Sources*, **304**, 170 (2016).
22. L. Cai, K. An, Z. Feng, C. Liang, and S. J. Harris, *J. Power Sources*, **236**, 163 (2013).
23. S. Shiotani, T. Naka, M. Morishima, M. Yonemura, T. Kamiyama, Y. Ishikawa, Y. Ukyo, Y. Uchimoto, and Z. Ogumi, *Journal of Power Sources*, **325**, 404 (2016).
24. V. Zinth, C. V. Lüders, M. Hofmann, J. Hattendorff, I. Buchberger, S. Erhard, J. Rebelo-Kornmeier, A. Jossen, and R. Gilles, *J. Power Sources*, **271**, 152 (2014).
25. S. C. Nagpure, B. Bhushan, and S. S. Babu, *Journal of the Electrochemical Society*, **160**, A2111 (2013).
26. B. Rieger, S. Schlueter, S. V. Erhard, and A. Jossen, *Journal of The Electrochemical Society*, **163**, A1595 (2016).
27. Z. J. Schiffer, J. Cannarella, and C. B. Arnold, *Journal of The Electrochemical Society*, **163**, A427 (2015).
28. C. Birkenmaier, B. Bitzer, M. Harzheim, A. Hintennach, and T. Schleid, *J. Electrochem. Soc.*, **162**, A2646 (2015).
29. S. F. Schuster, T. Bach, E. Fleder, J. Müller, M. Brand, G. Sextl, and A. Jossen, *J. Energy Storage*, **1**, 44 (2015).
30. P. Keil and A. Jossen, *Journal of The Electrochemical Society*, **164**, A6066 (2016).
31. P. Keil, S. F. Schuster, J. Wilhelm, J. Travi, A. Hauser, R. C. Karl, and A. Jossen, *Journal of The Electrochemical Society*, **163**, A1872 (2016).
32. K.-Y. Oh, B. I. Epureanu, J. B. Siegel, and A. G. Stefanopoulou, *J. Power Sources*, **310**, 118 (2016).
33. K.-Y. Oh and B. I. Epureanu, *J. Power Sources*, **303**, 86 (2016).
34. F. M. Kindermann, A. Noel, S. V. Erhard, and A. Jossen, *Electrochimica Acta*, **185**, 107 (2015).
35. M. Fleischhammer, T. Waldmann, G. Bisle, B.-I. Hogg, and M. Wohlfahrt-Mehrens, *J. Power Sources*, **274**, 432 (2015).
36. M. Tang, P. Albertus, and J. Newman, *J. Electrochem. Soc.*, **156**, A390 (2009).
37. V. A. Agubra, J. W. Fergus, R. Fu, and S.-Y. Choe, *J. Power Sources*, **270**, 213 (2014).
38. N. Zhang and H. Tang, *Journal of Power Sources*, **218**, 52 (2012).
39. R. S. Rubino, H. Gan, and E. S. Takeuchi, *Journal of The Electrochemical Society*, **148**, A1029 (2001).
40. K. Dai, Z. Wang, G. Ai, H. Zhao, W. Yuan, X. Song, V. Battaglia, C. Sun, K. Wu, and G. Liu, *Journal of Power Sources*, **298**, 349 (2015).
41. M. Petzl, M. Kasper, and M. A. Danzer, *J. Power Sources*, **275**, 799 (2015).
42. R. Mukherjee, A. V. Thomas, D. Datta, E. Singh, J. Li, O. Eksik, V. B. Shenoy, and N. Koratkar, *Nat Comms*, **5** (2014).
43. V. A. Agubra, J. W. Fergus, R. Fu, and S.-Y. Choe, *Electrochim. Acta*, **149**, 1 (2014).
44. T. Waldmann, M. Kasper, and M. Wohlfahrt-Mehrens, *Electrochimica Acta*, **178**, 525 (2015).
45. D. Burow, K. Sergeeva, S. Calles, K. Schorb, A. Börger, C. Roth, and P. Heitjans, *Journal of Power Sources*, **307**, 806 (2016).
46. U. Tröltzsch, O. Kanoun, and H.-R. Tränkler, *Electrochimica Acta*, **51**, 1664 (2006).
47. T. C. Bach, S. F. Schuster, E. Fleder, J. Müller, M. J. Brand, H. Lorrmann, A. Jossen, and G. Sextl, *J. Energy Storage* (2016).
48. I. Buchberger, S. Seidlmayer, A. Pokharel, M. Piana, J. Hattendorff, P. Kudejova, R. Gilles, and H. A. Gasteiger, *J. Electrochem. Soc.*, **162**, A2737 (2015).
49. S. Mohan, Y. Kim, J. B. Siegel, N. A. Samad, and A. G. Stefanopoulou, *Journal of the Electrochemical Society*, **161**, A2222 (2014).
50. N. A. Samad, Y. Kim, J. B. Siegel, and A. G. Stefanopoulou, *Journal of The Electrochemical Society*, **163**, A1584 (2016).
51. J. H. Lee, H. M. Lee, and S. Ahn, *Journal of Power Sources*, **119–121**, 833 (2003).
52. A. Mukhopadhyay, A. Tokranov, X. Xiao, and B. W. Sheldon, *Electrochimica Acta*, **66**, 28 (2012).
53. D. Liu, Y. Wang, Y. Xie, L. He, J. Chen, K. Wu, R. Xu, and Y. Gao, *Journal of Power Sources*, **232**, 29 (2013).
54. B. B. Berkes, A. Jozwiuk, H. Sommer, T. Brezesinski, and J. Janek, *Electrochemistry Communications*, **60**, 64 (2015).
55. G. Zhang, C. E. Shaffer, C.-Y. Wang, and C. D. Rahn, *Journal of the Electrochemical Society*, **160**, A610 (2013).
56. B. V. Ratnakumar and M. C. Smart, *ECS Transactions*, **25**, 241 (2010).
57. W. Lu, C. M. López, N. Liu, J. T. Vaughey, A. Jansen, and D. W. Dees, *Journal of The Electrochemical Society*, **159**, A566 (2012).
58. S. Smiles and R. O. Herzog, *Chemische Konstitution und Physikalische Eigenschaften*; Springer Berlin Heidelberg and Imprint and Springer: Berlin, Heidelberg, 1914.
59. C.-Y. Tang and S. J. Dillon, *Journal of The Electrochemical Society*, **163**, A1660 (2016).
60. K. G. Gallagher, S. E. Trask, C. Bauer, T. Woehrle, S. F. Lux, M. Tschech, P. Lamp, B. J. Polzin, S. Ha, B. Long, Q. Wu, W. Lu, D. W. Dees, and A. N. Jansen, *Journal of The Electrochemical Society*, **163**, A138 (2015).
61. Y. Xie, J. Li, and C. Yuan, *Journal of Power Sources*, **248**, 172 (2014).

62. P. J. Osswald, S. V. Erhard, A. Noel, P. Keil, F. M. Kindermann, H. Hoster, and A. Jossen, *Journal of Power Sources*, **314**, 93 (2016).
63. Z. Zhang, T. Zeng, Y. Lai, M. Jia, and J. Li, *Journal of Power Sources*, **247**, 1 (2014).
64. W. Wu, X. Xiao, M. Wang, and X. Huang, *Journal of the Electrochemical Society*, **161**, A803 (2014).

65. T. Bond, J. Zhou, and J. Cutler, *Journal of The Electrochemical Society*, **164**, A6158 (2016).
66. E. K. Rahani and V. B. Shenoy, *Journal of the Electrochemical Society*, **160**, A1153 (2013).
67. B. Rieger, S. V. Erhard, K. Rumpf, and A. Jossen, *J. Electrochem. Soc.*, **163**, A1566 (2016).

7 Summary and Conclusion

The recent, worldwide growth in EV market share underlines the importance of electrified mobility for realizing the transition towards a carbon free society. However, a sustainable market penetration requires further development of the LIB technology, which forms a key component of today's battery and plug-in hybrid electric vehicles. An advanced BMS offers a significant potential to improve the overall efficiency of battery systems. Together with enhanced battery components, an overall improved performance of the battery systems can be achieved in future. In this matter, a prospective BMS can use physicochemical model based state-estimation paired with a profound experimental parametrization and characterization of LIBs. It appears to be a helpful method to monitor and control important battery states such as the anode potential, to guarantee safe and durable operation in application scenarios such as fast charging. A properly designed BMS can therefore help to satisfy the market demand of battery features, such as high energy density, sufficient power capability, safe operation and prolonged lifetime.

The functionality of current and prospective LIB technology must be well understood in order to develop sophisticated models. Therefore, the inherent structure is analyzed and characterized, which is exemplary shown for the investigated MJ1 LIB in this thesis. A silicon-graphite compound was found to be the anode active material, which is a common and prospective active material incorporated in high energy LIBs. A nickel-rich NMC-811 cathode active material is used in the MJ1 LIB. As a result, the investigated cell incorporates one of the highest energy densities, which are commercially available today. In general, nickel-rich types are state-of-the-art and possibly also future materials for high energy cathodes. The LIB is expected to remain the technology of choice for electrical energy storage systems with continuing improvement of its components. The more advanced the individual components in LIBs become, the more difficult it gets to describe a battery's behavior, which emphasizes the importance of sophisticated software algorithms to be able to fully exploit the technology's potential. State-estimation of LIBs is one of the main tasks a BMS performs to ensure a beneficial and safe operational state. All estimation methods have in common that they correlate the measured signals, such as terminal voltage, current flow and surface temperature, to physical properties or behavioral cell characteristics. Sophisticated model based methods using physicochemical models can inherently correlate the measured global states to apparent cell-internal local states, such as concentrations and potentials. Current application demands such as fast charging protocols would significantly profit from using such approaches as the estimated anode potential can be used to control the applied current in order to avoid lithium plating and thus to trigger early capacity fade of the battery system.

Moreover, physicochemical models are able to describe similar cells with a low re-parametrization effort compared to phenomenological models such as the ECM or behavioral replica such as neural network approaches. The discussed black- and grey-box approaches may overly restrict the operating range of LIBs due to the inaccuracy in describing the cell behavior. However, mechanistic approaches such as the physicochemical model can describe the necessary insights into the cell's behavior.

State-of-the-art measurement based techniques using OCV or coulomb counting offer the fastest estimation of the SoC at a sufficient accuracy level, but may require oversized safety buffers at the operational limits. ECM based methods are state-of-the-art when using model based state-estimation

techniques due to the inherently simple parametrization, fast computation and robustness of the calculation. Once a physicochemical model is properly parametrized, an extended operating range can be covered via using additional mechanisms such as aging, high current or mechanical swelling features. However, the structure of the physicochemical model becomes more complicated when including such adaptations and it must be evaluated, if the real-time capability of the modeling approach is affected. By applying physical reduction schemes, numerical reduction or reformulation for the physicochemical p2D, a sufficient speed-up and real-time performance can be achieved. Multidimensional physicochemical models such as the MuDiMod are less favorable for state-estimation purposes due to their complexity and slow computation, but are crucial to better understand the battery behavior and to determine an optimal operating range especially for larger-sized (e.g. automotive) battery cells. The modeling error of the p2D can be determined with a model-to-model comparison to the MuDiMod. For application, the modeling error of the p2D in reference to the MuDiMod can be used to correct operational limits of a LIB via using a specified safety buffer to account for the non-considered spatial inhomogeneity of concentration, potential and temperature states. As long as the computation of the p2D is fast enough and its model accuracy is not overly restricted by physical or numerical reduction schemes, the benefits of estimating internal states to give insights in the battery's intrinsic condition can be fully exploited for control strategies in the BMS. Within this thesis, a suitable way is presented which aims at achieving this task by using a proper parametrization and validation approach for a specified LIB, estimating the inhomogeneity within the cell with the aid of the MuDiMod, reducing the p2D for embedded systems and extending it to an observer model for BMS applications, which can correct the model error of the p2D caused by neglecting spatial inhomogeneities along the electrodes of the battery cell.

The main part of this thesis starts with the presentation of a comprehensive model parametrization for the electrochemical-thermal p2D and the MuDiMod in section 2.2 for a state-of-the-art high energy SiC/NMC-811 LIB. Model validation comprised DVA, infrared thermography, calorimetry, various charge and discharge scenarios from 20°C to 40°C ambient temperature, which revealed a high quality of the models in predicting the electrical-thermal behavior of the studied MJ1 LIB. Effects of using silicon containing graphite compounds instead of pure graphite together with nickel-rich cathodes instead of e.g. NMC-111 are discussed in terms of their suitability for fast charging scenarios when being integrated in electrodes with high, moderate and low porosity. The electrode design significantly affects the fast charging behavior of the investigated 18650 LIB, where a single-tab design at each electrode shows local overheating and low energy per time ratios due to increased in-plane voltage losses along the current collector foils. The best fast charging efficiency and the most balanced thermal behavior was observed for a multi-tab design as the in-plane voltage losses decrease. However, the shorter the effective electrode length or the more tabs are used, the higher the risk of lithium plating becomes. Optimized charging profiles considering the tab design of the studied 18650 formats are presented via using the MuDiMod approach, which enable charging up to 60 % SoC in less than 18 min at no indication of lithium plating, which showed a significant difference to the charging behavior predicted by the p2D. The model-to-model comparison revealed errors in the range of several tens of millivolts for the cell voltage and the local anode potential. The identified model error can be considered, if a p2D is to be used for state-estimation purposes including safety buffers at the predicted operational limits.

In the last section 2.3 of chapter 2, a state-of-the-art review of cylindrical cell designs revealed a delayed development of high energy 26650 formats compared to the higher gravimetric and volumetric energy density for 18650 and 21700 types. Favorable cylindrical formats for high energy LIBs are

investigated using a wide MuDiMod simulation study parametrized for the MJ1 LIB with varying formats and tab designs. In- and through-plane voltage drop analysis reveal benefits for multi-tab designs to avoid overheating due to the lower in-plane heat generation along the current collector's height and length. However, optimized fast charging profiles with field-like localized cooling conditions revealed a certain threat of lithium plating in the cold spots, if the effective electrode lengths are too short. The onset of lithium plating across the active electrode area shows a significant correlation to the tab design applied to each current collector. Moreover, the tab design revealed a dominant impact on the LIB's rate capability, fast charging capability and resistivity towards accelerated aging. As a result, a multi-tab design is required for 26650 formats to enable a sufficient level of fast charging (i.e. $> 35\,\mathrm{Whl^{-1}min^{-1}}$), but still reveals the lowest charging performance compared to 18650 and 21700 formats. Single tab design results in long effective electrode lengths and lead to high in-plane voltage losses as well as overheating, whereas small formats applied with multi-tab design can cause lithium plating under localized cooling conditions. The observed local imbalance varies with the configuration of cylindrical format and tab design and should be considered, when a p2D based state-estimation algorithm is applied, which is inherently not capable to simulate in-plane inhomogeneity of concentration, potential and temperature.

To investigate the suitability of physicochemical models for embedded systems in chapter 3, model reduction is applied to the p2D either using FDM paired with physical meaningful approximation of the solid diffusion equation or applying orthogonal collocation reformulation in order to decrease the computational complexity and gain computation speed. A comparison to a numerically rigorous p2D and a state-of-the-art ECM approach shows accurate simulation results and significant speed-up of the calculation process, under evaluating experimental data of a driving cycle scenario of the investigated MJ1 LIB. The errors caused by uncertainties in the model's parametrization, the application of reduction methods and the implementation into embedded systems are analyzed. Embedding a ROM-p2D into a MC is crucial for a field-like emulation of computational resources, which cannot be simulated on desktop computers or workstations as commonly used in this research field. Three different *C*-code implementations are evaluated and compared to an state-of-the-art ECM, which reveal comparable accuracy of simulating the cell voltage and surface temperature during the driving cycle. At most 168 MHz, 192 kB of RAM and 1 MB of flash memory are available on the MC and the performance of the best ROM-p2D implementation revealed at least a 37 % faster calculation than real-time, where 21.9 kB RAM to solve and 175 kB flash memory to store the model are allocated under simulating the driving cycle. Following these results, the best *C*-code implementation is the ROM-p2D incorporating FDM and the eigenfunction method approximation, which offers an optimum of model accuracy, memory footprint and real-time computation. The results emphasize the suitability of physicochemical models in embedded systems under the right choice of model reduction, a proper parametrization and *C*-code suitable implementation of the model structure.

For developing the state-estimation algorithm in chapter 4, variants of the ROM-p2Ds are chosen, which show improved accuracy and robustness via enhanced handling of inherent boundary conditions. The chosen models are benchmarked to the original Dualfoil model [94] and a numerically rigorous model in COMSOL Multiphysics [188]. The two discussed reduction schemes of the solid diffusion equation showed significant benefits for either simulating constant or dynamic load profiles, which is of high interest for selecting the right reduction for the applied load scenario. Two linearized state-space representations based on the ROM-p2Ds are presented to develop recursive observer models to estimate the state of a LIB, which is combined with an EKF algorithm. A sophisticated initialization algorithm and the conservation of lithium mass during the estimation process increase the robustness of the physic-

ochemical model based state-estimation. The terminal voltage is used as input signal for the filtering algorithm and robustness of the observer models appears towards changing boundary conditions and dynamic current loads, which are typical for application scenarios. Fast charging estimation at 4C-CC revealed a quick error regression below 1 mV within 30 s at an initial error of more than 42 % SoC. PC charging at 10C revealed regression of the terminal voltage error below 2 mV within 90 s at an initial error of more than 35 % SoC. Compared to the estimate of the terminal voltage, the delayed time constants for achieving a similar accuracy of the internal states of concentrations, potentials, and reaction kinetics is discussed. This is crucial to evaluate the applicability for using internal states as design guidelines in fast charging protocols. The feasibility of incorporating the observer models into an embedded system is content of future work, which is most promising as the necessary extension of the observer p2D is of less complexity compared to the actual p2D structure and most likely does not overload calculation or memory resources of embedded systems. An adaptation of the physicochemical model structure and parametrization to account for aging effects in a LIB is not considered within this thesis. Future work should use suitable aging mechanisms [73, 168] for the p2D to extend the presented models and algorithms of this thesis and to increase their validity with describing also the aging behavior of LIBs.

Additional experimental investigations on the safety of LIBs are presented in chapter 5, where external and local short-circuits applied to single- and double-layered pouchbag C/NMC-111 LIBs are characterized in terms of their electrical and thermal behavior. Therefore, a quasi-isothermal short-circuit test bench is used, which analyzes terminal voltage, heat generation, shorting current or local shorting potential without triggering a thermal runaway. The short-circuit scenarios pass through transition and plateau zones for all measured signals, which are correlated to effects of electrochemically based rate limitations. External short-circuits are triggered via an external resistance, whereas internal short-circuits are emulated with locally applied nail penetration in the center of the active electrode area. The intensity of internal short-circuits can be approximated by using the external and local short-circuit data and simulation results of a modified MuDiMod, which lies in the range of $5 \, \mathrm{m\Omega}$ to $50 \, \mathrm{m\Omega}$ of a comparable external short-circuit. The appearing over discharge of at least 25 % SoC could be correlated to copper dissolution from the negative current collector during the short-circuit condition. The fundamental understanding of the electrochemically caused rate limiting behavior of external and internal/local short-circuits is of high interest, if fail-safe strategies or precursor techniques are developed in a BMS to counter abusive scenarios and eventually avoid a possible thermal runaway [134, 169].

In the last chapter 6, reversible and irreversible thickness changes caused by various cyclic aging studies applied to C/LCO pouchbag LIBs are studied via a 3D laser scanning method. The local distribution of thickness change across the active electrode area correlates well with the expected current load distribution, which is first enhanced near the current collector tabs and shifts to regions with lower utilization further away from the tabs with ongoing aging. Considering the non-linear decay of the SoH, this shift can be correlated to a prior aging near the current collector tabs triggering possibly SEI growth, lithium plating, gassing or binder degradation and with ongoing local decay, the aging spot shifts towards the center/bottom part of the battery, which is less degraded in the beginning. The aging study revealed a measurable mechanical state, which clearly indicates the imbalance of local utilization in the electrode stack and emphasizes the importance and consideration of spatial inhomogeneity in LIBs. The mechanical swelling behavior of LIBs has a significant influence on the performance and lifetime of a LIB, which should be regarded in the development and design of the battery technology on the single cell, the module and the battery pack level [170].

Key steps for realizing a physicochemical model based state-estimation for LIBs are presented within this thesis. The suitability of the p2D for state-estimation purposes is outlined, starting with a proper parametrization and validation of the model, presenting a further model order reduction as well as an implementation of the model within embedded systems and finally showing ways of extending the model to a robust observer model. The inherent modeling error towards imbalanced utilization along the electrode stack can be considered with the help of the MuDiMod, which revealed to be a useful tool to examine the inhomogeneity in concentration, potential, and temperature accounting for a cell's format and tab design. Safety and lifetime issues have been addressed with sophisticated experimental methods to better understand the electrochemical-thermal-mechanical behavior of a LIB, which is crucial for determining optimized operational conditions. Remaining open topics and issues are addressed in the following.

Further improvement of the parametrization process of physicochemical models is crucial, which incorporates experimental studies on single-layered pouchbag LIBs instead of coin-cells for half-cell DVA. The improved internal resistance would enable to emulate rate and aging tests of LIBs on half-cell level, which could improve the electrodes' parametrization incorporated in the p2D, beside a useful correlation of the results to the full-cell level. Another benefit of using pouchbag cells for the parametrization process could be the incorporation of reference electrodes, which could enable a validation of the local potentials in the model. A follow-up work of the presented short-circuit tests is currently in progress at the Institute for Electrical Energy Storage Technology at the Technical University of Munich dealing with manufacturing of silicon-graphite/nickel-rich LIBs and analyzing their short-circuit characteristics. The investigated single-layered pouchbag cells incorporate partly lithium reference electrodes to track the internal potentials of anode and cathode during short-circuit events. Further experimental characterization of fast charging capability under controlled cooling conditions for the presented cylindrical LIBs can be used to extend the MuDiMod validation and discuss the simulation based conclusions of the impact of format and tab design on the fast charging capability, which is also currently in progress at the Institute for Electrical Energy Storage Technology. Based on the MuDiMod results, the safety buffer at the operational limits for the p2D can be further specified for cylindrical cells and further applied to pouchbag and prismatic LIB formats, which were not the focus of this thesis. Current model development of the MuDiMod at the Institute for Electrical Energy Storage Technology focuses on describing the electrical behavior in a stacked electrode configuration as found in pouchbag and prismatic formats. In terms of the physicochemical model based state-estimation, the fundamental modeling work is done and presented within this thesis. The actual implementation of the observer p2D into embedded systems together with a wide experimental validation of the state-estimation technique should be the focus of follow-up work. Herein, the implementation of aging mechanisms [73, 168] to adapt the model structure and parametrization of the p2D will be a crucial feature for the physicochemical state-estimation technique, especially when safe fast charging procedures for the entire lifetime of a LIB are developed.

References

[1] J. Buss. *Automakers Need A Global Timetable For Phasing Out Internal-Combustion Engines.* Ed. by Forbes. 2018. URL: `https://www.forbes.com/sites/oliverwyman/2018/03/27/automakers-need-a-global-timetable-for-phasing-out-internal-combustion-engines/#2b15c91f23c3` (visited on 09/18/2020).

[2] A. Vartmann and A. Stumpf. *The number of electric vehicles globally increases from 5.6 to 7.9 million cars.* Ed. by Zentrum für Sonnenenergie und Wasserstoff-Forschung Baden-Württemberg - ZSW. 2020. URL: `https://www.zsw-bw.de/fileadmin/user_upload/pi03-2020-ZSW-WeltweiteZahlenElektroautos.pdf` (visited on 09/18/2020).

[3] ACEA. *New passenger car registrations by fuel type in the european union.* Ed. by European Automobile Manufacturers Association ACEA. 2020. URL: `https://www.acea.be/uploads/press_releases_files/20200512_PRPC_fuel_Q1_2020_FINAL.pdf` (visited on 09/18/2020).

[4] T. Gersdorf, P. Hertzke, P. Schaufuss, and S. Schenk. *McKinsey Electric Vehicle Index: Europe cushions a global plunge in EV sales.* Ed. by McKinsey & Company. 2020. URL: `https://www.mckinsey.com/~/media/McKinsey/Industries/Automotive%20and%20Assembly/Our%20Insights/McKinsey%20Electric%20Vehicle%20Index%20Europe%20cushions%20a%20global%20plunge%20in%20EV%20sales/McKinsey-Electric-Vehicle-Index-Europe-cushions-a-global-plunge-in-EV-sales-vF.pdf` (visited on 09/18/2020).

[5] T. Gersdorf, R. Hensley, P. Hertzke, P. Schaufuss, and A. Tschiesner. *The road ahead for e-mobility.* Ed. by McKinsey & Company. 2020. URL: `https://www.mckinsey.com/industries/automotive-and-assembly/our-insights/the-road-ahead-for-e-mobility` (visited on 09/18/2020).

[6] Kraftfahrtbundesamt. *Annual record of passenger cars at the first of january 2020.* Ed. by Kraftfahrtbundesamt. 2020. URL: `https://www.kba.de/DE/Statistik/Fahrzeuge/Bestand/b_jahresbilanz.html?nn=644526` (visited on 09/18/2020).

[7] ACEA. *ACEA Report Vehicles in use-Europe 2019.* Ed. by European Automobile Manufacturers Association ACEA. 2020. URL: `https://www.acea.be/uploads/publications/ACEA_Report_Vehicles_in_use-Europe_2019.pdf` (visited on 09/18/2020).

[8] K. Y. Bjerkan, T. E. Nørbech, and M. E. Nordtømme. "Incentives for promoting Battery Electric Vehicle (BEV) adoption in Norway". In: *Transportation Research Part D: Transport and Environment* 43 (2016), pp. 169–180. DOI: `10.1016/j.trd.2015.12.002`.

[9] N. Hill, I. Skinner, G. Zazias, P. Siskos, A. Petropoulos, K. Fragkiadakis, and L. Paroussos. *Assessing the impacts of selected options for regulating CO2 emissions from new passenger cars and vans after 2020.* Ed. by Ricardo Energy&Environment. 2018. URL: `https://ec.europa.eu/clima/sites/clima/files/transport/vehicles/docs/ldv_post_2020_co2_en.pdf` (visited on 09/18/2020).

[10] European Union. *REGULATION (EU) 2019/631*. 2020. URL: `https://eur-lex.europa.eu/legal-content/EN/TXT/PDF/?uri=CELEX:02019R0631-20200121&from=EN` (visited on 09/18/2020).

[11] Bundesregierung Deutschland. *Climate policy, Energy Revolution, Mobility - What are the actions of the federal government for the protection of the climate?* Ed. by Bundesregierung Deutschland. 2020. URL: `https://www.bundesregierung.de/breg-de/themen/klimaschutz/bundesregierung-klimapolitik-1637146` (visited on 09/18/2020).

[12] Tesla. *Technical Data of Model 3 - Driving range under WLTP*. Ed. by Tesla. 2020. URL: `https://www.tesla.com/de_DE/inventory/new/m3` (visited on 09/18/2020).

[13] IONITY GmbH. *IONITY - European Charging Infrastructure*. Ed. by IONITY GmbH. 2020. URL: `https://ionity.eu/de` (visited on 09/18/2020).

[14] H. A. Bonges and A. C. Lusk. "Addressing electric vehicle (EV) sales and range anxiety through parking layout, policy and regulation". In: *Transportation Research Part A: Policy and Practice* 83 (2016), pp. 63–73. DOI: `10.1016/j.tra.2015.09.011`.

[15] T. Kim, W. Song, D.-Y. Son, L. K. Ono, and Y. Qi. "Lithium-ion batteries: outlook on present, future, and hybridized technologies". In: *Journal of Materials Chemistry A* 7.7 (2019), pp. 2942–2964. DOI: `10.1039/C8TA10513H`.

[16] F. Wu, J. Maier, and Y. Yu. "Guidelines and trends for next-generation rechargeable lithium and lithium-ion batteries". In: *Chemical Society reviews* 49.5 (2020), pp. 1569–1614. DOI: `10.1039/c7cs00863e`.

[17] The Mobility House AG. *Energy Storage*. Ed. by The Mobility House AG. Zürich, 2020. URL: `https://www.mobilityhouse.com/int_en/energy-storage` (visited on 09/18/2020).

[18] M. Woodward, J. Hamilton, H. Wu, G. Alberts, J. Hooper, and B. Walton. *New market. New entrants. New challenges. Battery Electric Vehicles*. Ed. by Deloitte. 2019. URL: `https://www2.deloitte.com/content/dam/Deloitte/uk/Documents/manufacturing/deloitte-uk-battery-electric-vehicles.pdf` (visited on 09/18/2020).

[19] Horizon 2020 research and innovation projects. *Electric Vehicle Enhanced Range, Lifetime And Safety Through INGenious battery management (EVERLASTING)*. Ed. by Innovation and Networks Executive Agency (INEA) - European Commission. 2020. URL: `https://ec.europa.eu/inea/en/horizon-2020/projects/h2020-transport/green-vehicles/everlasting` (visited on 09/18/2020).

[20] E. Helmers, J. Dietz, and M. Weiss. "Sensitivity Analysis in the Life-Cycle Assessment of Electric vs. Combustion Engine Cars under Approximate Real-World Conditions". In: *Sustainability* 12.3 (2020), p. 1241. DOI: `10.3390/su12031241`.

[21] E. Emilsson and L. Dahllöf. *Lithium-Ion Vehicle Battery Production*. Ed. by Swedish Energy Agency. 2019. URL: `https://www.ivl.se/download/18.14d7b12e16e3c5c36271070/1574923989017/C444.pdf` (visited on 09/18/2020).

[22] R. Hausbrand, G. Cherkashinin, H. Ehrenberg, M. Gröting, K. Albe, C. Hess, and W. Jaegermann. "Fundamental degradation mechanisms of layered oxide Li-ion battery cathode materials: Methodology, insights and novel approaches". In: *Materials Science and Engineering: B* 192 (2015), pp. 3–25. DOI: `10.1016/j.mseb.2014.11.014`.

[23] A. van Nguyen and C. Kuss. "Review—Conducting Polymer-Based Binders for Lithium-Ion Batteries and Beyond". In: *Journal of The Electrochemical Society* 167.6 (2020), p. 065501. DOI: 10.1149/1945-7111/ab856b.

[24] X. Zhao, C. M. Hayner, M. C. Kung, and H. H. Kung. "In-Plane Vacancy-Enabled High-Power Si-Graphene Composite Electrode for Lithium-Ion Batteries". In: *Advanced Energy Materials* 1.6 (2011), pp. 1079–1084. DOI: 10.1002/aenm.201100426.

[25] L. David, R. Bhandavat, U. Barrera, and G. Singh. "Silicon oxycarbide glass-graphene composite paper electrode for long-cycle lithium-ion batteries". In: *Nature communications* 7 (2016), p. 10998. DOI: 10.1038/ncomms10998.

[26] H. Sun and K. Zhao. "Electronic Structure and Comparative Properties of LiNi x Mn y Co z O 2 Cathode Materials". In: *The Journal of Physical Chemistry C* 121.11 (2017), pp. 6002–6010. DOI: 10.1021/acs.jpcc.7b00810.

[27] J. Wu, Y. Cao, H. Zhao, J. Mao, and Z. Guo. "The critical role of carbon in marrying silicon and graphite anodes for high–energy lithium–ion batteries". In: *Carbon Energy* 1.1 (2019), pp. 57–76. DOI: 10.1002/cey2.2.

[28] K. Märker, P. J. Reeves, C. Xu, K. J. Griffith, and C. P. Grey. "Evolution of Structure and Lithium Dynamics in LiNi 0.8 Mn 0.1 Co 0.1 O 2 (NMC811) Cathodes during Electrochemical Cycling". In: *Chemistry of Materials* 31.7 (2019), pp. 2545–2554. DOI: 10.1021/acs.chemmater.9b00140.

[29] T. Li, X.-Z. Yuan, L. Zhang, D. Song, K. Shi, and C. Bock. "Degradation Mechanisms and Mitigation Strategies of Nickel-Rich NMC-Based Lithium-Ion Batteries". In: *Electrochemical Energy Reviews* 3.1 (2020), pp. 43–80. DOI: 10.1007/s41918-019-00053-3.

[30] T. Wang, K. Ren, W. Xiao, W. Dong, H. Qiao, A. Duan, H. Pan, Y. Yang, and H. Wang. "Tuning the Li/Ni Disorder of the NMC811 Cathode by Thermally Driven Competition between Lattice Ordering and Structure Decomposition". In: *The Journal of Physical Chemistry C* 124.10 (2020), pp. 5600–5607. DOI: 10.1021/acs.jpcc.0c00720.

[31] D. Ma, Z. Cao, and A. Hu. "Si-Based Anode Materials for Li-Ion Batteries: A Mini Review". In: *Nano-micro letters* 6.4 (2014), pp. 347–358. DOI: 10.1007/s40820-014-0008-2.

[32] K. Roy, M. Wahid, D. Puthusseri, A. Patrike, S. Muduli, R. Vaidhyanathan, and S. Ogale. "High capacity, power density and cycling stability of silicon Li-ion battery anodes with a few layer black phosphorus additive". In: *Sustainable Energy & Fuels* 3.1 (2019), pp. 245–250. DOI: 10.1039/C8SE00476E.

[33] J. Asenbauer, T. Eisenmann, M. Kuenzel, A. Kazzazi, Z. Chen, and D. Bresser. "The success story of graphite as a lithium-ion anode material – fundamentals, remaining challenges, and recent developments including silicon (oxide) composites". In: *Sustainable Energy & Fuels* 100 (2020), p. 101. DOI: 10.1039/D0SE00175A.

[34] R. Schmuch, R. Wagner, G. Hörpel, T. Placke, and M. Winter. "Performance and cost of materials for lithium-based rechargeable automotive batteries". In: *Nature Energy* 3.4 (2018), pp. 267–278. DOI: 10.1038/s41560-018-0107-2.

[35] N. Nitta, F. Wu, J. T. Lee, and G. Yushin. "Li-ion battery materials: present and future". In: *Materials Today* 18.5 (2015), pp. 252–264. DOI: 10.1016/j.mattod.2014.10.040.

[36] L. Wang, B. Chen, J. Ma, G. Cui, and L. Chen. "Reviving lithium cobalt oxide-based lithium secondary batteries-toward a higher energy density". In: *Chemical Society reviews* 47.17 (2018), pp. 6505–6602. DOI: 10.1039/c8cs00322j.

[37] T. Placke. *Progress and Challenges: Generation 3b.* Brussels, 2018. URL: https://europa.eu/sinapse/webservices/dsp_export_attachement.cfm?CMTY_ID=0C46BEEC-C689-9F80-54C7DD45358D29FB&OBJECT_ID=230DABFD-90AB-8F7D-083EF5BD909DD025&DOC_ID=9C5B921B-D269-C275-41EAC7B11885EA47&type=CMTY_CAL (visited on 09/18/2020).

[38] T. D. Hatchard and J. R. Dahn. "In Situ XRD and Electrochemical Study of the Reaction of Lithium with Amorphous Silicon". In: *Journal of The Electrochemical Society* 151.6 (2004), A838. DOI: 10.1149/1.1739217.

[39] J. Sturm, A. Rheinfeld, I. Zilberman, F. B. Spingler, S. Kosch, F. Frie, and A. Jossen. "Modeling and simulation of inhomogeneities in a 18650 nickel-rich, silicon-graphite lithium-ion cell during fast charging". In: *Journal of Power Sources* 412 (2019), pp. 204–223. DOI: 10.1016/j.jpowsour.2018.11.043.

[40] H. Li, M. Cormier, N. Zhang, J. Inglis, J. Li, and J. R. Dahn. "Is Cobalt Needed in Ni-Rich Positive Electrode Materials for Lithium Ion Batteries?" In: *Journal of The Electrochemical Society* 166.4 (2019), A429–A439. DOI: 10.1149/2.1381902jes.

[41] J. Morris. *Tesla's Shift To Cobalt-Free Batteries Is Its Most Important Move Yet.* Ed. by Forbes. 2020. URL: https://www.forbes.com/sites/jamesmorris/2020/07/11/teslas-shift-to-cobalt-free-batteries-is-its-most-important-move-yet/#5740958546b4 (visited on 09/18/2020).

[42] W. Hu, Y. Zhang, L. Zan, and H. Cong. "Mitigation of voltage decay in Li-rich layered oxides as cathode materials for lithium-ion batteries". In: *Nano Research* 13.1 (2020), pp. 151–159. DOI: 10.1007/s12274-019-2588-0.

[43] E. Quartarone and P. Mustarelli. "Review—Emerging Trends in the Design of Electrolytes for Lithium and Post-Lithium Batteries". In: *Journal of The Electrochemical Society* 167.5 (2020), p. 050508. DOI: 10.1149/1945-7111/ab63c4.

[44] E. R. Logan and J. R. Dahn. "Electrolyte Design for Fast-Charging Li-Ion Batteries". In: *Trends in Chemistry* 2.4 (2020), pp. 354–366. DOI: 10.1016/j.trechm.2020.01.011.

[45] C. F. J. Francis, I. L. Kyratzis, and A. S. Best. "Lithium-Ion Battery Separators for Ionic-Liquid Electrolytes: A Review". In: *Advanced materials (Deerfield Beach, Fla.)* 32.18 (2020), e1904205. DOI: 10.1002/adma.201904205.

[46] J. Nunes-Pereira, C. M. Costa, and S. Lanceros-Méndez. "Polymer composites and blends for battery separators: State of the art, challenges and future trends". In: *Journal of Power Sources* 281 (2015), pp. 378–398. DOI: 10.1016/j.jpowsour.2015.02.010.

[47] Y. Liang et al. "A review of rechargeable batteries for portable electronic devices". In: *InfoMat* 1.1 (2019), pp. 6–32. DOI: 10.1002/inf2.12000.

[48] A. El Kharbachi, O. Zavorotynska, M. Latroche, F. Cuevas, V. Yartys, and M. Fichtner. "Exploits, advances and challenges benefiting beyond Li-ion battery technologies". In: *Journal of Alloys and Compounds* 817 (2020), p. 153261. DOI: 10.1016/j.jallcom.2019.153261.

[49] H. Rahimi-Eichi, U. Ojha, F. Baronti, and M.-Y. Chow. "Battery Management System: An Overview of Its Application in the Smart Grid and Electric Vehicles". In: *IEEE Industrial Electronics Magazine* 7.2 (2013), pp. 4–16. DOI: 10.1109/MIE.2013.2250351.

[50] L. Lu, X. Han, J. Li, J. Hua, and M. Ouyang. "A review on the key issues for lithium-ion battery management in electric vehicles". In: *Journal of Power Sources* 226 (2013), pp. 272–288. DOI: `10.1016/j.jpowsour.2012.10.060`.

[51] W. Waag, C. Fleischer, and D. U. Sauer. "Critical review of the methods for monitoring of lithium-ion batteries in electric and hybrid vehicles". In: *Journal of Power Sources* 258 (2014), pp. 321–339. DOI: `10.1016/j.jpowsour.2014.02.064`.

[52] M.-F. Ng, J. Zhao, Q. Yan, G. J. Conduit, and Z. W. Seh. "Predicting the state of charge and health of batteries using data-driven machine learning". In: *Nature Machine Intelligence* 2.3 (2020), pp. 161–170. DOI: `10.1038/s42256-020-0156-7`.

[53] G. Zhou. *Simplify current and voltage monitoring with isolated SPI and I2C in your BMS.* Ed. by Texas Instruments. 2018. URL: `http://www.ti.com/lit/an/slla411/slla411.pdf?ts=1591432941876` (visited on 09/18/2020).

[54] G. Zhou. *Temperature Monitoring in HEV and EV Traction Inverter Systems Using ADS795x-Q1.* Ed. by Texas Instruments. 2018. URL: `http://www.ti.com/lit/an/sboa267/sboa267.pdf?ts=1591432930888` (visited on 09/18/2020).

[55] T. Poloni, M. A. Figueroa-Santos, J. B. Siegel, and A. G. Stefanopoulou. "Integration of Non-monotonic Cell Swelling Characteristic for State-of-Charge Estimation". In: *2018 Annual American Control Conference (ACC)*. IEEE, 27.06.2018 - 29.06.2018, pp. 2306–2311. DOI: `10.23919/ACC.2018.8431237`.

[56] C. Kupper, B. Weißhar, S. Rißmann, and W. G. Bessler. "End-of-Life Prediction of a Lithium-Ion Battery Cell Based on Mechanistic Aging Models of the Graphite Electrode". In: *Journal of The Electrochemical Society* 165.14 (2018), A3468–A3480. DOI: `10.1149/2.0941814jes`.

[57] G. Harper et al. "Recycling lithium-ion batteries from electric vehicles". In: *Nature* 575.7781 (2019), pp. 75–86. DOI: `10.1038/s41586-019-1682-5`.

[58] L. C. Casals, B. Amante García, and C. Canal. "Second life batteries lifespan: Rest of useful life and environmental analysis". In: *Journal of environmental management* 232 (2019), pp. 354–363. DOI: `10.1016/j.jenvman.2018.11.046`.

[59] P. Shen, M. Ouyang, L. Lu, and J. Li. "State of Charge, State of Health and State of Function Co-Estimation of Lithium-Ion Batteries for Electric Vehicles". In: *2016 IEEE Vehicle Power and Propulsion Conference (VPPC)*. IEEE, 17.10.2016 - 20.10.2016, pp. 1–5. DOI: `10.1109/VPPC.2016.7791782`.

[60] E. Cabrera-Castillo, F. Niedermeier, and A. Jossen. "Calculation of the state of safety (SOS) for lithium ion batteries". In: *Journal of Power Sources* 324 (2016), pp. 509–520. DOI: `10.1016/j.jpowsour.2016.05.068`.

[61] X. Wang, X. Wei, H. Dai, and Q. Wu. "State Estimation of Lithium Ion Battery Based on Electrochemical Impedance Spectroscopy with On-Board Impedance Measurement System". In: *2015 IEEE Vehicle Power and Propulsion Conference (VPPC)* (2015), pp. 1–5. DOI: `10.1109/VPPC.2015.7353021`.

[62] L. H. J. Raijmakers, D. L. Danilov, J. P. M. van Lammeren, T. J. G. Lammers, H. J. Bergveld, and P. H. L. Notten. "Non-Zero Intercept Frequency: An Accurate Method to Determine the Integral Temperature of Li-Ion Batteries". In: *IEEE Transactions on Industrial Electronics* 63.5 (2016), pp. 3168–3178. DOI: `10.1109/TIE.2016.2516961`.

[63] X. Wang, X. Wei, Q. Chen, J. Zhu, and H. Dai. "Lithium-ion battery temperature on-line estimation based on fast impedance calculation". In: *Journal of Energy Storage* 26 (2019), p. 100952. DOI: 10.1016/j.est.2019.100952.

[64] H. Beelen, K. Mundaragi Shivakumar, L. Raijmakers, M. Donkers, and H. J. Bergveld. "Towards impedance–based temperature estimation for Li–ion battery packs". In: *International Journal of Energy Research* 44.4 (2020), pp. 2889–2908. DOI: 10.1002/er.5107.

[65] K. H. Lee. *Product specification - Rechargeable Lithium Ion Battery - INR18650-MJ1 3500 mAh.* Ed. by LG Chem. 2016. URL: https://www.lgchem.com/main/index (visited on 09/18/2020).

[66] Pacific Engineering Corporation. *Automotive Fuse Catalogue.* Ed. by Pacific Engineering Corporation. 2019. URL: https://www.pecj.co.jp/fuse/files/PEC_Fuse_Catalogue_en.pdf (visited on 09/18/2020).

[67] Autoliv B.V. & Co. KG. *Pyroswitches – normally closed NC.* Ed. by Autoliv B.V. & Co. KG. 2020. URL: https://www.pyroswitch.com/products/pss-overview/ (visited on 09/18/2020).

[68] P. Sun, R. Bisschop, H. Niu, and X. Huang. "A Review of Battery Fires in Electric Vehicles". In: *Fire Technology* 56.4 (2020), pp. 1361–1410. DOI: 10.1007/s10694-019-00944-3.

[69] S. Koch, K. Birke, and R. Kuhn. "Fast Thermal Runaway Detection for Lithium-Ion Cells in Large Scale Traction Batteries". In: *Batteries* 4.2 (2018), p. 16. DOI: 10.3390/batteries4020016.

[70] BMW EfficientDynamics. *BMW i3. Quick Start Guide.* Ed. by BMW Group. 2016. URL: https://www.bmw.co.uk/bmwi (visited on 09/18/2020).

[71] I. Zilberman, S. Ludwig, M. Schiller, and A. Jossen. "Online aging determination in lithium-ion battery module with forced temperature gradient". In: *Journal of Energy Storage* 28 (2020), p. 101170. DOI: 10.1016/j.est.2019.101170.

[72] J. Gallardo-Lozano, E. Romero-Cadaval, M. I. Milanes-Montero, and M. A. Guerrero-Martinez. "Battery equalization active methods". In: *Journal of Power Sources* 246 (2014), pp. 934–949. DOI: 10.1016/j.jpowsour.2013.08.026.

[73] J. Keil and A. Jossen. "Electrochemical Modeling of Linear and Nonlinear Aging of Lithium-Ion Cells". In: *Journal of The Electrochemical Society* 167.11 (2020), p. 110535. DOI: 10.1149/1945-7111/aba44f.

[74] J. Keil, N. Paul, V. Baran, P. Keil, R. Gilles, and A. Jossen. "Linear and Nonlinear Aging of Lithium-Ion Cells Investigated by Electrochemical Analysis and In-Situ Neutron Diffraction". In: *Journal of The Electrochemical Society* 166.16 (2019), A3908–A3917. DOI: 10.1149/2.1271915jes.

[75] A. Reindl, H. Meier, and M. Niemetz. "Scalable, Decentralized Battery Management System Based on Self-organizing Nodes". In: *Architecture of Computing Systems – ARCS 2020.* Ed. by A. Brinkmann, W. Karl, S. Lankes, S. Tomforde, T. Pionteck, and C. Trinitis. Vol. 12155. Lecture Notes in Computer Science. Cham: Springer International Publishing, 2020, pp. 171–184. DOI: 10.1007/978-3-030-52794-5_13.

[76] X. Huang, X. Sui, D.-I. Stroe, and R. Teodorescu. "A Review of Management Architectures and Balancing Strategies in Smart Batteries". In: *IECON 2019 - 45th Annual Conference of the IEEE Industrial Electronics Society* (2019), pp. 5909–5914. DOI: 10.1109/IECON.2019.8926687.

[77] J. Rivera-Barrera, N. Muñoz-Galeano, and H. Sarmiento-Maldonado. "SoC Estimation for Lithium-ion Batteries: Review and Future Challenges". In: *Electronics* 6.4 (2017), p. 102. DOI: `10.3390/electronics6040102`.

[78] Y. Zheng, M. Ouyang, X. Han, L. Lu, and J. Li. "Investigating the error sources of the online state of charge estimation methods for lithium-ion batteries in electric vehicles". In: *Journal of Power Sources* 377 (2018), pp. 161–188. DOI: `10.1016/j.jpowsour.2017.11.094`.

[79] Q. Zhang, B. Liu, F. Zhou, Q. Wang, and J. Kong. "State-of-charge estimation method of lithium-ion batteries based on long-short term memory network". In: *IOP Conference Series: Earth and Environmental Science* 208 (2018), p. 012001. DOI: `10.1088/1755-1315/208/1/012001`.

[80] A. M. S. M. H. S. Attanayaka, J. P. Karunadasa, and K. T. M. U. Hemapala. "Estimation of state of charge for lithium-ion batteries - A Review". In: *AIMS Energy* 7.2 (2019), pp. 186–210. DOI: `10.3934/energy.2019.2.186`.

[81] U. Krewer, F. Röder, E. Harinath, R. D. Braatz, B. Bedürftig, and R. Findeisen. "Review— Dynamic Models of Li-Ion Batteries for Diagnosis and Operation: A Review and Perspective". In: *Journal of The Electrochemical Society* 165.16 (2018), A3656–A3673. DOI: `10.1149/2.1061814jes`.

[82] J. Sihvo, T. Roinila, T. Messo, and D.-I. Stroe. "Novel online fitting algorithm for impedance-based state estimation of Li-ion batteries". In: *IECON 2019 - 45th Annual Conference of the IEEE Industrial Electronics Society* (2019), pp. 4531–4536. DOI: `10.1109/IECON.2019.8927338`.

[83] J. Yang et al. "Rapid Prediction of the Open-Circuit-Voltage of Lithium Ion Batteries Based on an Effective Voltage Relaxation Model". In: *Energies* 11.12 (2018), p. 3444. DOI: `10.3390/en11123444`.

[84] L. Pei, T. Wang, R. Lu, and C. Zhu. "Development of a voltage relaxation model for rapid open-circuit voltage prediction in lithium-ion batteries". In: *Journal of Power Sources* 253 (2014), pp. 412–418. DOI: `10.1016/j.jpowsour.2013.12.083`.

[85] L. Pei, C. Zhu, and R. Lu. "Relaxation model of the open-circuit voltage for state-of-charge estimation in lithium-ion batteries". In: *IET Electrical Systems in Transportation* 3.4 (2013), pp. 112–117. DOI: `10.1049/iet-est.2013.0020`.

[86] G. Chuangxin, Y. Gen, Z. Chengzhi, W. Xueping, and C. Xiu. "SoC Estimation for Lithium-Ion Battery Using Recurrent NARX Neural Network and Genetic Algorithm". In: *IOP Conference Series: Materials Science and Engineering* 486 (2019), p. 012076. DOI: `10.1088/1757-899X/486/1/012076`.

[87] A. G. Kashkooli, H. Fathiannasab, Z. Mao, and Z. Chen. "Application of Artificial Intelligence to State-of-Charge and State-of-Health Estimation of Calendar-Aged Lithium-Ion Pouch Cells". In: *Journal of The Electrochemical Society* 166.4 (2019), A605–A615. DOI: `10.1149/2.0411904jes`.

[88] L. Gan, F. Yang, Y. F. Shi, and H. L. He. "Lithium-ion battery state of function estimation based on fuzzy logic algorithm with associated variables". In: *IOP Conference Series: Earth and Environmental Science* 94 (2017), p. 012133. DOI: `10.1088/1755-1315/94/1/012133`.

[89] J. C. Alvarez Anton, P. J. Garcia Nieto, C. Blanco Viejo, and J. A. Vilan Vilan. "Support Vector Machines Used to Estimate the Battery State of Charge". In: *IEEE Transactions on Power Electronics* 28.12 (2013), pp. 5919–5926. DOI: `10.1109/TPEL.2013.2243918`.

[90]   M. Zhang, K. Wang, and Y.-t. Zhou. "Online State of Charge Estimation of Lithium-Ion Cells Using Particle Filter-Based Hybrid Filtering Approach". In: *Complexity* 2020 (2020), pp. 1–10. DOI: 10.1155/2020/8231243.

[91]   N. Chen, P. Zhang, J. Dai, and W. Gui. "Estimating the State-of-Charge of Lithium-Ion Battery Using an H-Infinity Observer Based on Electrochemical Impedance Model". In: *IEEE Access* 8 (2020), pp. 26872–26884. DOI: 10.1109/ACCESS.2020.2971002.

[92]   R. E. Kalman and R. S. Bucy. "New Results in Linear Filtering and Prediction Theory". In: *Journal of Basic Engineering* 83.1 (1961), pp. 95–108. DOI: 10.1115/1.3658902.

[93]   R. Zhang, B. Xia, B. Li, L. Cao, Y. Lai, W. Zheng, H. Wang, and W. Wang. "State of the Art of Lithium-Ion Battery SOC Estimation for Electrical Vehicles". In: *Energies* 11.7 (2018), p. 1820. DOI: 10.3390/en11071820.

[94]   M. Doyle, T. F. Fuller, and J. Newman. "Modeling of Galvanostatic Charge and Discharge of the Lithium/Polymer/Insertion Cell". In: *Journal of The Electrochemical Society* 140.6 (1993), pp. 1526–1533. DOI: 10.1149/1.2221597.

[95]   J. Sturm, S. Ludwig, J. Zwirner, C. Ramirez-Garcia, B. Heinrich, M. F. Horsche, and A. Jossen. "Suitability of physicochemical models for embedded systems regarding a nickel-rich, silicon-graphite lithium-ion battery". In: *Journal of Power Sources* 436 (2019), p. 226834. DOI: 10.1016/j.jpowsour.2019.226834.

[96]   J. Sturm, A. Frank, A. Rheinfeld, S. V. Erhard, and A. Jossen. "Impact of Electrode and Cell Design on Fast Charging Capabilities of Cylindrical Lithium-Ion Batteries". In: *Journal of The Electrochemical Society* 167.13 (2020), p. 130505. DOI: 10.1149/1945-7111/abb40c.

[97]   R. Klein, N. A. Chaturvedi, J. Christensen, J. Ahmed, R. Findeisen, and A. Kojic. "Electrochemical Model Based Observer Design for a Lithium-Ion Battery". In: *IEEE Transactions on Control Systems Technology* 21.2 (2013), pp. 289–301. DOI: 10.1109/TCST.2011.2178604.

[98]   A. M. Bizeray, S. Zhao, S. R. Duncan, and D. A. Howey. "Lithium-ion battery thermal-electrochemical model-based state estimation using orthogonal collocation and a modified extended Kalman filter". In: *Journal of Power Sources* 296 (2015), pp. 400–412. DOI: 10.1016/j.jpowsour.2015.07.019.

[99]   J. Sturm, H. Ennifar, S. V. Erhard, A. Rheinfeld, S. Kosch, and A. Jossen. "State estimation of lithium-ion cells using a physicochemical model based extended Kalman filter". In: *Applied Energy* 223 (2018), pp. 103–123. DOI: 10.1016/j.apenergy.2018.04.011.

[100]   Z. Chu, G. L. Plett, M. S. Trimboli, and M. Ouyang. "A control-oriented electrochemical model for lithium-ion battery, Part I: Lumped-parameter reduced-order model with constant phase element". In: *Journal of Energy Storage* 25 (2019), p. 100828. DOI: 10.1016/j.est.2019.100828.

[101]   Z. Chu, R. Jobman, A. Rodríguez, G. L. Plett, M. S. Trimboli, X. Feng, and M. Ouyang. "A control-oriented electrochemical model for lithium-ion battery. Part II: Parameter identification based on reference electrode". In: *Journal of Energy Storage* 27 (2020), p. 101101. DOI: 10.1016/j.est.2019.101101.

[102]   J. Newman and W. Tiedemann. "Potential and Current Distribution in Electrochemical Cells: Interpretation of the Half–Cell Voltage Measurements as a Function of Reference–Electrode Location". In: *Journal of The Electrochemical Society* 140.7 (1993), pp. 1961–1968. DOI: 10.1149/1.2220746.

[103] A. Rheinfeld, S. Kosch, S. V. Erhard, P. J. Osswald, B. Rieger, and A. Jossen. "Electro-Thermal Modeling of Large Format Lithium-Ion Pouch Cells: A Cell Temperature Dependent Linear Polarization Expression". In: *Journal of The Electrochemical Society* 163.14 (2016), A3046–A3062. DOI: 10.1149/2.0701614jes.

[104] S. Kosch, A. Rheinfeld, S. V. Erhard, and A. Jossen. "An extended polarization model to study the influence of current collector geometry of large-format lithium-ion pouch cells". In: *Journal of Power Sources* 342 (2017), pp. 666–676. DOI: 10.1016/j.jpowsour.2016.12.110.

[105] K. S. Ng, C.-S. Moo, Y.-P. Chen, and Y.-C. Hsieh. "Enhanced coulomb counting method for estimating state-of-charge and state-of-health of lithium-ion batteries". In: *Applied Energy* 86.9 (2009), pp. 1506–1511. DOI: 10.1016/j.apenergy.2008.11.021.

[106] D. I. Stroe, V. Knap, and E. Schaltz. "State-of-Health Estimation of Lithium-Ion Batteries Based on Partial Charging Voltage Profiles". In: *ECS Transactions* 85.13 (2018), pp. 379–386. DOI: 10.1149/08513.0379ecst.

[107] D. N. T. How, M. A. Hannan, M. S. Hossain Lipu, and P. J. Ker. "State of Charge Estimation for Lithium-Ion Batteries Using Model-Based and Data-Driven Methods: A Review". In: *IEEE Access* 7 (2019), pp. 136116–136136. DOI: 10.1109/ACCESS.2019.2942213.

[108] C. P. Lin, J. Cabrera, D. Y. W. Yu, F. Yang, and K. L. Tsui. "SOH Estimation and SOC Recalibration of Lithium-Ion Battery with Incremental Capacity Analysis & Cubic Smoothing Spline". In: *Journal of The Electrochemical Society* 167.9 (2020), p. 090537. DOI: 10.1149/1945-7111/ab8f56.

[109] Z. Liu, X. Dang, and B. Jing. "A Novel Open Circuit Voltage Based State of Charge Estimation for Lithium-Ion Battery by Multi-Innovation Kalman Filter". In: *IEEE Access* 7 (2019), pp. 49432–49447. DOI: 10.1109/ACCESS.2019.2910882.

[110] Y. Xing, W. He, M. Pecht, and K. L. Tsui. "State of charge estimation of lithium-ion batteries using the open-circuit voltage at various ambient temperatures". In: *Applied Energy* 113 (2014), pp. 106–115. DOI: 10.1016/j.apenergy.2013.07.008.

[111] Z. Chen, M. Sun, X. Shu, R. Xiao, and J. Shen. "Online State of Health Estimation for Lithium-Ion Batteries Based on Support Vector Machine". In: *Applied Sciences* 8.6 (2018), p. 925. DOI: 10.3390/app8060925.

[112] H. B. Sassi, F. Errahimi, N. Es-Sbai, and C. Alaoui. "A comparative study of ANN and Kalman Filtering-based observer for SOC estimation". In: *IOP Conference Series: Earth and Environmental Science* 161 (2018), p. 012022. DOI: 10.1088/1755-1315/161/1/012022.

[113] M. A. Hannan, M. S. H. Lipu, A. Hussain, P. J. Ker, T. M. I. Mahlia, M. Mansor, A. Ayob, M. H. Saad, and Z. Y. Dong. "Toward Enhanced State of Charge Estimation of Lithium-ion Batteries Using Optimized Machine Learning Techniques". In: *Scientific reports* 10.1 (2020), p. 4687. DOI: 10.1038/s41598-020-61464-7.

[114] Dipl.-Ing. Univ. Christian Campestrini. "Practical feasibility of Kalman filters for the state estimation of lithium-ion batteries". PhD thesis. Munich: Technical University of Munich, 5.11.2017. URL: http://nbn-resolving.de/urn/resolver.pl?urn:nbn:de:bvb:91-diss-20180122-1362581-1-2 (visited on 09/18/2020).

[115] Y. Fang, R. Xiong, and J. Wang. "Estimation of Lithium-Ion Battery State of Charge for Electric Vehicles Based on Dual Extended Kalman Filter". In: *Energy Procedia* 152 (2018), pp. 574–579. DOI: 10.1016/j.egypro.2018.09.213.

[116]   X. Yu, J. Wei, G. Dong, Z. Chen, and C. Zhang. "State-of-charge estimation approach of lithium-ion batteries using an improved extended Kalman filter". In: *Energy Procedia* 158 (2019), pp. 5097–5102. DOI: 10.1016/j.egypro.2019.01.691.

[117]   X. Ma, D. Qiu, Q. Tao, and D. Zhu. "State of Charge Estimation of a Lithium Ion Battery Based on Adaptive Kalman Filter Method for an Equivalent Circuit Model". In: *Applied Sciences* 9.13 (2019), p. 2765. DOI: 10.3390/app9132765.

[118]   W.-Y. Kim, P.-Y. Lee, J. Kim, and K.-S. Kim. "A Nonlinear-Model-Based Observer for a State-of-Charge Estimation of a Lithium-Ion Battery in Electric Vehicles". In: *Energies* 12.17 (2019), p. 3383. DOI: 10.3390/en12173383.

[119]   S. Wang, D.-I. Stroe, C. Fernandez, C. Yu, C. Zou, and X. Li. "A novel energy management strategy for the ternary lithium batteries based on the dynamic equivalent circuit modeling and differential Kalman filtering under time-varying conditions". In: *Journal of Power Sources* 450 (2020), p. 227652. DOI: 10.1016/j.jpowsour.2019.227652.

[120]   X. Hu, S. Li, and H. Peng. "A comparative study of equivalent circuit models for Li-ion batteries". In: *Journal of Power Sources* 198 (2012), pp. 359–367. DOI: 10.1016/j.jpowsour.2011.10.013.

[121]   C. Campestrini, T. Heil, S. Kosch, and A. Jossen. "A comparative study and review of different Kalman filters by applying an enhanced validation method". In: *Journal of Energy Storage* 8 (2016), pp. 142–159. DOI: 10.1016/j.est.2016.10.004.

[122]   S. Kolluri, S. V. Aduru, M. Pathak, R. D. Braatz, and V. R. Subramanian. "Real-time Nonlinear Model Predictive Control (NMPC) Strategies using Physics-Based Models for Advanced Lithium-ion Battery Management System (BMS)". In: *Journal of The Electrochemical Society* 167.6 (2020), p. 063505. DOI: 10.1149/1945-7111/ab7bd7.

[123]   V. Ramadesigan, P. W. C. Northrop, S. De, S. Santhanagopalan, R. D. Braatz, and V. R. Subramanian. "Modeling and Simulation of Lithium-Ion Batteries from a Systems Engineering Perspective". In: *Journal of The Electrochemical Society* 159.3 (2012), R31–R45. DOI: 10.1149/2.018203jes.

[124]   P. W. C. Northrop, B. Suthar, V. Ramadesigan, S. Santhanagopalan, R. D. Braatz, and V. R. Subramanian. "Efficient Simulation and Reformulation of Lithium-Ion Battery Models for Enabling Electric Transportation". In: *Journal of The Electrochemical Society* 161.8 (2014), E3149–E3157. DOI: 10.1149/2.018408jes.

[125]   D. Di Domenico, G. Fiengo, and A. Stefanopoulou. "Lithium-ion battery state of charge estimation with a Kalman Filter based on a electrochemical model". In: *17th IEEE International Conference on Control Applications* (2008), pp. 702–707. DOI: 10.1109/CCA.2008.4629639.

[126]   A. Tulsyan, Y. Tsai, R. B. Gopaluni, and R. D. Braatz. "State-of-charge estimation in lithium-ion batteries: A particle filter approach". In: *Journal of Power Sources* 331 (2016), pp. 208–223. DOI: 10.1016/j.jpowsour.2016.08.113.

[127]   B. Liu, X. Tang, and F. Gao. "Joint estimation of battery state-of-charge and state-of-health based on a simplified pseudo-two-dimensional model". In: *Electrochimica Acta* 344 (2020), p. 136098. DOI: 10.1016/j.electacta.2020.136098.

[128]   F. Ringbeck, M. Garbade, and D. U. Sauer. "Uncertainty-aware state estimation for electrochemical model-based fast charging control of lithium-ion batteries". In: *Journal of Power Sources* 470 (2020), p. 228221. DOI: 10.1016/j.jpowsour.2020.228221.

[129] S. V. Erhard, P. J. Osswald, J. Wilhelm, A. Rheinfeld, S. Kosch, and A. Jossen. "Simulation and Measurement of Local Potentials of Modified Commercial Cylindrical Cells". In: *Journal of The Electrochemical Society* 162.14 (2015), A2707–A2719. DOI: 10.1149/2.0431514jes.

[130] S. V. Erhard et al. "Simulation and Measurement of the Current Density Distribution in Lithium-Ion Batteries by a Multi-Tab Cell Approach". In: *Journal of The Electrochemical Society* 164.1 (2017), A6324–A6333. DOI: 10.1149/2.0551701jes.

[131] S. V. Erhard. "Multi-dimensional electrochemical-thermal modeling of lithium-ion batteries". PhD thesis. Munich: Technical University of Munich, 7.06.2017. URL: http://nbn-resolving.de/urn/resolver.pl?urn:nbn:de:bvb:91-diss-20170607-1338266-1-3 (visited on 09/18/2020).

[132] B. Rieger, S. V. Erhard, S. Kosch, M. Venator, A. Rheinfeld, and A. Jossen. "Multi-Dimensional Modeling of the Influence of Cell Design on Temperature, Displacement and Stress Inhomogeneity in Large-Format Lithium-Ion Cells". In: *Journal of The Electrochemical Society* 163.14 (2016), A3099–A3110. DOI: 10.1149/2.1051614jes.

[133] S. Kosch, Y. Zhao, J. Sturm, J. Schuster, G. Mulder, E. Ayerbe, and A. Jossen. "A Computationally Efficient Multi-Scale Model for Lithium-Ion Cells". In: *Journal of The Electrochemical Society* 165.10 (2018), A2374–A2388. DOI: 10.1149/2.1241810jes.

[134] A. Rheinfeld, J. Sturm, A. Frank, S. Kosch, S. V. Erhard, and A. Jossen. "Impact of Cell Size and Format on External Short Circuit Behavior of Lithium-Ion Cells at Varying Cooling Conditions: Modeling and Simulation". In: *Journal of The Electrochemical Society* 167.1 (2020), p. 013511. DOI: 10.1149/2.0112001JES.

[135] A. Jokar, B. Rajabloo, M. Désilets, and M. Lacroix. "Review of simplified Pseudo-two- Dimensional models of lithium-ion batteries". In: *Journal of Power Sources* 327 (2016), pp. 44–55. DOI: 10.1016/j.jpowsour.2016.07.036.

[136] V. R. Subramanian, J. A. Ritter, and R. E. White. "Approximate Solutions for Galvanostatic Discharge of Spherical Particles I. Constant Diffusion Coefficient". In: *Journal of The Electrochemical Society* 148.11 (2001), E444–E449. DOI: 10.1149/1.1409397.

[137] M. Guo and R. E. White. "An approximate solution for solid-phase diffusion in a spherical particle in physics-based Li-ion cell models". In: *Journal of Power Sources* 198 (2012), pp. 322–328. DOI: 10.1016/j.jpowsour.2011.08.096.

[138] L. Cai and R. E. White. "Reduction of Model Order Based on Proper Orthogonal Decomposition for Lithium-Ion Battery Simulations". In: *Journal of The Electrochemical Society* 156.3 (2009), A154. DOI: 10.1149/1.3049347.

[139] L. Cai and R. E. White. "Lithium ion cell modeling using orthogonal collocation on finite elements". In: *Journal of Power Sources* 217 (2012), pp. 248–255. DOI: 10.1016/j.jpowsour.2012.06.043.

[140] K. D. Stetzel, L. L. Aldrich, M. S. Trimboli, and G. L. Plett. "Electrochemical state and internal variables estimation using a reduced-order physics-based model of a lithium-ion cell and an extended Kalman filter". In: *Journal of Power Sources* 278 (2015), pp. 490–505. DOI: 10.1016/j.jpowsour.2014.11.135.

[141] H.-K. Kim, J. H. Choi, and K.-J. Lee. "A Numerical Study of the Effects of Cell Formats on the Cycle Life of Lithium Ion Batteries". In: *Journal of The Electrochemical Society* 166.10 (2019), A1769–A1778. DOI: 10.1149/2.0261910jes.

[142]   Y. Liu, Y. G. Liao, and M.-C. Lai. "Transient Temperature Distributions on Lithium-Ion Polymer SLI Battery". In: *Vehicles* 1.1 (2019), pp. 127–137. DOI: 10.3390/vehicles1010008.

[143]   S. G. Marquis, V. Sulzer, R. Timms, C. P. Please, and S. J. Chapman. "An Asymptotic Derivation of a Single Particle Model with Electrolyte". In: *Journal of The Electrochemical Society* 166.15 (2019), A3693–A3706. DOI: 10.1149/2.0341915jes.

[144]   Z. Cen and P. Kubiak. "Lithium-ion battery SOC/SOH adaptive estimation via simplified single particle model". In: *International Journal of Energy Research* (2020). DOI: 10.1002/er.5374.

[145]   G. Richardson, I. Korotkin, R. Ranom, M. Castle, and J. M. Foster. "Generalised single particle models for high-rate operation of graded lithium-ion electrodes: Systematic derivation and validation". In: *Electrochimica Acta* 339 (2020), p. 135862. DOI: 10.1016/j.electacta.2020.135862.

[146]   A. Aitio, S. G. Marquis, P. Ascencio, and D. Howey. *Preprint - Bayesian Parameter Estimation Applied to the Li-ion Battery Single Particle Model with Electrolyte Dynamics.* Ed. by University of Oxford, Department of engineering Science. 2019. URL: http://arxiv.org/pdf/2001.09890v1.

[147]   A. Subramaniam, S. Kolluri, C. D. Parke, M. Pathak, S. Santhanagopalan, and V. R. Subramanian. "Properly Lumped Lithium-ion Battery Models: A Tanks-in-Series Approach". In: *Journal of The Electrochemical Society* 167.1 (2020), p. 013534. DOI: 10.1149/2.0342001JES.

[148]   N. T. Tran, M. Vilathgamuwa, T. Farrell, S. S. Choi, Y. Li, and J. Teague. "A Padé Approximate Model of Lithium Ion Batteries". In: *Journal of The Electrochemical Society* 165.7 (2018), A1409–A1421. DOI: 10.1149/2.0651807jes.

[149]   J. Xu, T. Wang, L. Pei, S. Mao, and C. Zhu. "Parameter identification of electrolyte decomposition state in lithium-ion batteries based on a reduced pseudo two-dimensional model with Padé approximation". In: *Journal of Power Sources* 460 (2020), p. 228093. DOI: 10.1016/j.jpowsour.2020.228093.

[150]   M. G. Hennessy and I. R. Moyles. "Asymptotic reduction and homogenization of a thermo-electrochemical model for a lithium-ion battery". In: *Applied Mathematical Modelling* 80 (2020), pp. 724–754. DOI: 10.1016/j.apm.2019.11.018.

[151]   D. Zhang, B. N. Popov, and R. E. White. "Modeling Lithium Intercalation of a Single Spinel Particle under Potentiodynamic Control". In: *Journal of The Electrochemical Society* 147.3 (2000), p. 831. DOI: 10.1149/1.1393279.

[152]   S. Khaleghi Rahimian, S. Rayman, and R. E. White. "Extension of physics-based single particle model for higher charge–discharge rates". In: *Journal of Power Sources* 224 (2013), pp. 180–194. DOI: 10.1016/j.jpowsour.2012.09.084.

[153]   C. von Lüders, J. Keil, M. Webersberger, and A. Jossen. "Modeling of lithium plating and lithium stripping in lithium-ion batteries". In: *Journal of Power Sources* 414 (2019), pp. 41–47. DOI: 10.1016/j.jpowsour.2018.12.084.

[154]   A. Rheinfeld, J. Sturm, A. Noel, J. Wilhelm, A. Kriston, A. Pfrang, and A. Jossen. "Quasi-Isothermal External Short Circuit Tests Applied to Lithium-Ion Cells: Part II. Modeling and Simulation". In: *Journal of The Electrochemical Society* 166.2 (2019), A151–A177. DOI: 10.1149/2.0071902jes.

[155] W. Ai, L. Kraft, J. Sturm, A. Jossen, and B. Wu. "Electrochemical Thermal-Mechanical Modelling of Stress Inhomogeneity in Lithium-Ion Pouch Cells". In: *Journal of The Electrochemical Society* 167.1 (2020), p. 013512. DOI: 10.1149/2.0122001JES.

[156] P. W. C. Northrop, M. Pathak, D. Rife, S. De, S. Santhanagopalan, and V. R. Subramanian. "Efficient Simulation and Model Reformulation of Two-Dimensional Electrochemical Thermal Behavior of Lithium-Ion Batteries". In: *Journal of The Electrochemical Society* 162.6 (2015), A940–A951. DOI: 10.1149/2.0341506jes.

[157] C. Kupper and W. G. Bessler. "Multi-Scale Thermo-Electrochemical Modeling of Performance and Aging of a LiFePO 4 /Graphite Lithium-Ion Cell". In: *Journal of The Electrochemical Society* 164.2 (2017), A304–A320. DOI: 10.1149/2.0761702jes.

[158] D. Sauerteig, N. Hanselmann, A. Arzberger, H. Reinshagen, S. Ivanov, and A. Bund. "Electro chemical-mechanical coupled modeling and parameterization of swelling and ionic transport in lithium-ion batteries". In: *Journal of Power Sources* 378 (2018), pp. 235–247. DOI: 10.1016/j.jpowsour.2017.12.044.

[159] S. Carelli, M. Quarti, M. C. Yagci, and W. G. Bessler. "Modeling and Experimental Validation of a High-Power Lithium-Ion Pouch Cell with LCO/NCA Blend Cathode". In: *Journal of The Electrochemical Society* 166.13 (2019), A2990–A3003. DOI: 10.1149/2.0301913jes.

[160] M. Guo and R. E. White. "A distributed thermal model for a Li-ion electrode plate pair". In: *Journal of Power Sources* 221 (2013), pp. 334–344. DOI: 10.1016/j.jpowsour.2012.08.012.

[161] M. Guo and R. E. White. "Mathematical model for a spirally-wound lithium-ion cell". In: *Journal of Power Sources* 250 (2014), pp. 220–235. DOI: 10.1016/j.jpowsour.2013.11.023.

[162] A. Latz and J. Zausch. "Multiscale modeling of lithium ion batteries: thermal aspects". In: *Beilstein journal of nanotechnology* 6 (2015), pp. 987–1007. DOI: 10.3762/bjnano.6.102.

[163] S. Hein et al. "Influence of Conductive Additives and Binder on the Impedance of Lithium-Ion Battery Electrodes: Effect of Morphology". In: *Journal of The Electrochemical Society* 167.1 (2020), p. 013546. DOI: 10.1149/1945-7111/ab6b1d.

[164] B. S. Vishnugopi, A. Verma, and P. P. Mukherjee. "Fast Charging of Lithium-ion Batteries via Electrode Engineering". In: *Journal of The Electrochemical Society* 167.9 (2020), p. 090508. DOI: 10.1149/1945-7111/ab7fb9.

[165] F. Zhang, M. M. U. Rehman, H. Wang, Y. Levron, G. Plett, R. Zane, and D. Maksimovic. "State-of-charge estimation based on microcontroller-implemented sigma-point Kalman filter in a modular cell balancing system for Lithium-Ion battery packs". In: *2015 IEEE 16th Workshop on Control and Modeling for Power Electronics (COMPEL)* (2017), pp. 1–7. DOI: 10.1109/COMPEL.2015.7236525.

[166] Q. Yu, R. Xiong, and C. Lin. "Online Estimation of State-of-charge Based on the H infinity and Unscented Kalman Filters for Lithium Ion Batteries". In: *Energy Procedia* 105 (2017), pp. 2791–2796. DOI: 10.1016/j.egypro.2017.03.600.

[167] X. Shu, G. Li, J. Shen, W. Yan, Z. Chen, and Y. Liu. "An adaptive fusion estimation algorithm for state of charge of lithium-ion batteries considering wide operating temperature and degradation". In: *Journal of Power Sources* 462 (2020), p. 228132. DOI: 10.1016/j.jpowsour.2020.228132.

[168] F. M. Kindermann, J. Keil, A. Frank, and A. Jossen. "A SEI Modeling Approach Distinguishing between Capacity and Power Fade". In: *Journal of The Electrochemical Society* 164.12 (2017), E287–E294. DOI: `10.1149/2.0321712jes`.

[169] Jan Alexander Gerrit Rheinfeld. "Performance and Safety of Lithium-Ion Electrodes and Cells: Modeling, Simulation, and Validation at Elevated Temperatures and Currents". PhD thesis. Munich: Technical University of Munich, 20.09.2019. URL: `http://nbn-resolving.de/urn/resolver.pl?urn:nbn:de:bvb:91-diss-20190920-1506354-1-9` (visited on 09/18/2020).

[170] B. Rieger. "Methodology to model the mechanical behavior of Lithium-ion cells". PhD thesis. Munich: Technical University of Munich, 18.07.2017. URL: `http://nbn-resolving.de/urn/resolver.pl?urn:nbn:de:bvb:91-diss-20170718-1335562-1-3` (visited on 09/18/2020).

[171] N. Dawson-Elli, S. Kolluri, K. Mitra, and V. R. Subramanian. "On the Creation of a Chess-AI-Inspired Problem-Specific Optimizer for the Pseudo Two-Dimensional Battery Model Using Neural Networks". In: *Journal of The Electrochemical Society* 166.6 (2019), A886–A896. DOI: `10.1149/2.1261904jes`.

[172] B. Ng, P. T. Coman, W. E. Mustain, and R. E. White. "Non-destructive parameter extraction for a reduced order lumped electrochemical-thermal model for simulating Li-ion full-cells". In: *Journal of Power Sources* 445 (2020), p. 227296. DOI: `10.1016/j.jpowsour.2019.227296`.

[173] C.-H. Chen, F. Brosa Planella, K. O'Regan, D. E. Gastol, W. Widanage, and E. Kendrick. "Development of Experimental Techniques for Parameterization of Multi-scale Lithium-ion Battery Models". In: *Journal of The Electrochemical Society* 167.8 (2020), p. 080534. DOI: `10.1149/1945-7111/ab9050`.

[174] I. A. Hunt, Y. Zhao, Y. Patel, and J. Offer. "Surface Cooling Causes Accelerated Degradation Compared to Tab Cooling for Lithium-Ion Pouch Cells". In: *Journal of The Electrochemical Society* 163.9 (2016), A1846–A1852. DOI: `10.1149/2.0361609jes`.

[175] Y. Zhao, Y. Patel, T. Zhang, and G. J. Offer. "Modeling the Effects of Thermal Gradients Induced by Tab and Surface Cooling on Lithium Ion Cell Performance". In: *Journal of The Electrochemical Society* 165.13 (2018), A3169–A3178. DOI: `10.1149/2.0901813jes`.

[176] M. Doyle. "Design and Simulation of Lithium Rechargeable Batteries". PhD thesis. Berkeley: University of California, 8.1995. URL: `https://escholarship.org/uc/item/6j87z0sp` (visited on 09/18/2020).

[177] J. Newman and K. E. Thomas-Alyea. *Electrochemical Systems.* Hoboken, NJ, USA: Wiley-Interscience, 2004.

[178] K. E. Thomas and J. Newman. "Thermal Modeling of Porous Insertion Electrodes". In: *Journal of The Electrochemical Society* 150.2 (2003), A176–A196. DOI: `10.1149/1.1531194`.

[179] T. S. Chadha, B. Suthar, D. Rife, V. R. Subramanian, and P. Biswas. "Model Based Analysis of One-Dimensional Oriented Lithium-Ion Battery Electrodes". In: *Journal of The Electrochemical Society* 164.11 (2017), E3114–E3121. DOI: `10.1149/2.0141711jes`.

[180] L. O. Valøen and J. N. Reimers. "Transport Properties of LiPF6-Based Li-Ion Battery Electrolytes". In: *Journal of The Electrochemical Society* 152.5 (2005), A882–A891. DOI: `10.1149/1.1872737`.

[181] J. Schmalstieg. "Physico-electrochemical simulation of lithium-ion batteries : implementation, parametrization and application". PhD thesis. Aachen: RWTH Aachen University, 19.05.2017. URL: http://publications.rwth-aachen.de/record/689927/files/689927.pdf (visited on 09/18/2020).

[182] J. Landesfeind, J. Hattendorff, A. Ehrl, W. A. Wall, and H. A. Gasteiger. "Tortuosity Determination of Battery Electrodes and Separators by Impedance Spectroscopy". In: *Journal of The Electrochemical Society* 163.7 (2016), A1373–A1387. DOI: 10.1149/2.1141607jes.

[183] D. A. G. Bruggeman. "Calculation of different physical constants in heterogeneous substances. I. Di-electricity constants and conductivities in mixed solids using isotropical substances". In: *Annalen der Physik* 416.7 (1935), pp. 636–664. DOI: 10.1002/andp.19354160705.

[184] F. M. Kindermann. "Implications of Current Density Distribution in Lithium-Ion Battery Graphite Anodes on SEI Formation". PhD thesis. Munich: Technical University of Munich, 12.12.2017. URL: http://nbn-resolving.de/urn/resolver.pl?urn:nbn:de:bvb:91-diss-20171212-1380608-1-2 (visited on 09/18/2020).

[185] S. Arrhenius. "About the inversion rate of sucrose caused by acids," in: *Zeitschrift für Physikalische Chemie* 4U.1 (1889). DOI: 10.1515/zpch-1889-0416.

[186] J. Schmalstieg, C. Rahe, M. Ecker, and D. U. Sauer. "Full Cell Parameterization of a High-Power Lithium-Ion Battery for a Physico-Chemical Model: Part I. Physical and Electrochemical Parameters". In: *Journal of The Electrochemical Society* 165.16 (2018), A3799–A3810. DOI: 10.1149/2.0321816jes.

[187] C. Hong, Q. Leng, J. Zhu, S. Zheng, H. He, Y. Li, R. Liu, J. Wan, and Y. Yang. "Revealing the correlation between structural evolution and Li + diffusion kinetics of nickel-rich cathode materials in Li-ion batteries". In: *Journal of Materials Chemistry A* 8.17 (2020), pp. 8540–8547. DOI: 10.1039/D0TA00555J.

[188] Comsol Multiphysics. *Battery and Fuel Cells Module*. Ed. by Comsol Multiphysics. 2020. URL: https://www.comsol.de/batteries-and-fuel-cells-module (visited on 09/18/2020).

[189] T. Amietszajew, E. McTurk, J. Fleming, and R. Bhagat. "Understanding the limits of rapid charging using instrumented commercial 18650 high-energy Li-ion cells". In: *Electrochimica Acta* 263 (2018), pp. 346–352. DOI: 10.1016/j.electacta.2018.01.076.

[190] D. Bernardi. "A General Energy Balance for Battery Systems". In: *Journal of The Electrochemical Society* 132.1 (1985), p. 5. DOI: 10.1149/1.2113792.

[191] K. Kumaresan, G. Sikha, and R. E. White. "Thermal Model for a Li-Ion Cell". In: *Journal of Power Sources* 155.2 (2008), A164. DOI: 10.1149/1.2817888.

[192] B. Wu, V. Yufit, M. Marinescu, G. J. Offer, R. F. Martinez-Botas, and N. P. Brandon. "Coupled thermal–electrochemical modelling of uneven heat generation in lithium-ion battery packs". In: *Journal of Power Sources* 243 (2013), pp. 544–554. DOI: 10.1016/j.jpowsour.2013.05.164.

[193] W. Polifke and J. Kopitz. *Transfer of Heat - Fundamentals, Analytical and Numerical methods.* 2nd ed. Munich: Pearson, 2009. URL: https://www.pearson-studium.de/warmeubertragung.html.

[194] D. Werner, A. Loges, D. J. Becker, and T. Wetzel. "Thermal conductivity of Li-ion batteries and their electrode configurations – A novel combination of modelling and experimental approach". In: *Journal of Power Sources* 364 (2017), pp. 72–83. DOI: 10.1016/j.jpowsour.2017.07.105.

[195]   L. Sheng, L. Su, and H. Zhang. "Experimental determination on thermal parameters of prismatic lithium ion battery cells". In: *International Journal of Heat and Mass Transfer* 139 (2019), pp. 231–239. DOI: `10.1016/j.ijheatmasstransfer.2019.04.143`.

[196]   M. Steinhardt, E. I. Gillich, M. Stiegler, and A. Jossen. "Thermal conductivity inside prismatic lithium-ion cells with dependencies on temperature and external compression pressure". In: *Journal of Energy Storage* 32 (2020), p. 101680. DOI: `10.1016/j.est.2020.101680`.

[197]   J. Sturm, A. Rheinfeld, I. Zilberman, F. B. Spingler, S. Kosch, F. Frie, and A. Jossen. *Supplementary Material - Modeling and simulation of inhomogeneities in a 18650 nickel-rich, silicon-graphite lithium-ion cell during fast charging*. Ed. by Journal of Power Sources. 2019. URL: `https://www.sciencedirect.com/science/article/abs/pii/S0378775318312849` (visited on 09/18/2020).

[198]   J. Sturm, A. Rheinfeld, I. Zilberman, F. B. Spingler, S. Kosch, F. Frie, and A. Jossen. *Data set - Modeling and simulation of inhomogeneities in a 18650 nickel-rich, silicon-graphite lithium-ion cell during fast charging*. Ed. by 4TU.Centre for Research Data. 2018. URL: `https://doi.org/10.4121/uuid:e8735cd2-e478-4db5-80bc-b5051961a0ab` (visited on 09/18/2020).

[199]   J. Sturm, A. Frank, A. Rheinfeld, S. V. Erhard, and A. Jossen. *Supplementary Material - Impact of Electrode and Cell Design on Fast Charging Capabilities of Cylindrical Lithium-Ion Batteries*. Ed. by Journal of the Electrochemical Society. 2020. URL: `https://iopscience.iop.org/1945-7111/167/13/130505/media/JES_167_13_130505_suppdata.pdf` (visited on 09/18/2020).

[200]   The MathWorks. *MATLAB*. 2020. URL: `https://www.mathworks.com/products/matlab.html` (visited on 09/18/2020).

[201]   S. Wolfram. *Mathematica*. Ed. by The Wolfram Foundation. 2020. URL: `https://www.wolfram.com/mathematica/` (visited on 09/18/2020).

[202]   Maplesoft. *Maple*. Ed. by Cybernet Systems Group. 2020. URL: `https://www.maplesoft.com/products/maple/` (visited on 09/18/2020).

[203]   ANSYS Inc. *Ansys*. 2020. URL: `https://www.ansys.com/` (visited on 09/18/2020).

[204]   Comsol. *COMSOL Multiphysics*. 2020. URL: `https://www.comsol.de/` (visited on 09/18/2020).

[205]   J. Sturm, S. Ludwig, J. Zwirner, C. Ramirez-Garcia, B. Heinrich, M. F. Horsche, and A. Jossen. *Supplementary Material - Suitability of physicochemical models for embedded systems regarding a nickel-rich, silicon-graphite lithium-ion battery*. Ed. by Journal of Power Sources. 2019. URL: `https://www.sciencedirect.com/science/article/abs/pii/S0378775319308274` (visited on 09/18/2020).

[206]   J. Sturm, S. Ludwig, J. Zwirner, C. Ramirez-Garcia, B. Heinrich, M. F. Horsche, and A. Jossen. *Data set - Suitability of physicochemical models for embedded systems regarding a nickel-rich, silicon-graphite lithium-ion battery*. Ed. by 4TU.Centre for Research Data. 2019. URL: `https://doi.org/10.4121/uuid:6590260b-244c-4a17-b134-f7a7cda5b8b5` (visited on 09/18/2020).

[207]   J. Sturm, H. Ennifar, S. V. Erhard, A. Rheinfeld, S. Kosch, and A. Jossen. *Data set - State estimation of lithium-ion cells using a physicochemical model based extended Kalman filter*. Ed. by 4TU.Centre for Research Data. 2018. URL: `https://doi.org/10.4121/uuid:a588c059-0d82-42fb-931d-8e805da79388` (visited on 09/18/2020).

[208] A. Rheinfeld, A. Noel, J. Wilhelm, A. Kriston, A. Pfrang, and A. Jossen. "Quasi-Isothermal External Short Circuit Tests Applied to Lithium-Ion Cells: Part I. Measurements". In: *Journal of The Electrochemical Society* 165.14 (2018), A3427–A3448. DOI: `10.1149/2.0451814jes`.

[209] J. Sturm, A. Rheinfeld, D. Buzon, and A. Jossen. "On The Impact of the Locality on Short-Circuit Characteristics: Experimental Analysis and Multiphysics Simulation of External and Local Short-Circuits Applied to Lithium-Ion Batteries". In: *Journal of The Electrochemical Society* 167.9 (2020), p. 090521. DOI: `10.1149/1945-7111/ab8873`.

[210] J. Sturm, A. Rheinfeld, D. Buzon, and A. Jossen. *Supplementary Material - On The Impact of the Locality on Short-Circuit Characteristics: Experimental Analysis and Multiphysics Simulation of External and Local Short-Circuits Applied to Lithium-Ion Batteries*. Ed. by Journal of the Electrochemical Society. 2020. URL: `https://iopscience.iop.org/1945-7111/167/9/090521/media/JES_167_9_090521_suppdata.pdf` (visited on 09/18/2020).

[211] J. Sturm, F. B. Spingler, B. Rieger, A. Rheinfeld, and A. Jossen. "Non-Destructive Detection of Local Aging in Lithium-Ion Pouch Cells by Multi-Directional Laser Scanning". In: *Journal of The Electrochemical Society* 164.7 (2017), A1342–A1351. DOI: `10.1149/2.0161707jes`.

[212] F. B. Spingler, W. Wittmann, J. Sturm, B. Rieger, and A. Jossen. "Optimum fast charging of lithium-ion pouch cells based on local volume expansion criteria". In: *Journal of Power Sources* 393 (2018), pp. 152–160. DOI: `10.1016/j.jpowsour.2018.04.095`.

[213] J. Sturm, F. B. Spingler, B. Rieger, A. Rheinfeld, and A. Jossen. *Data set - Non-Destructive Detection of Local Aging in Lithium-Ion Pouch Cells by Multi-Directional Laser*. Ed. by 4TU.Centre for Research Data. 2018. URL: `https://doi.org/10.4121/uuid:c10a6b3f-efe9-41ce-99f6-4093df68c653` (visited on 09/18/2020).

List of Publications

Journal Papers

XIV **Sturm, J.**; Frank, A.; Rheinfeld, A.; Erhard, S.V.; Jossen, A.: *Impact of Electrode and Cell Design on Fast Charging Capabilities of Cylindrical Lithium-Ion Batteries*, in: *Journal of The Electrochemical Society 167 (13)*, p. 130505, 2020, DOI: 10.1149/1945-7111/abb40c.

XIII Li, A.; Ponchant, M.; **Sturm, J.**; Jossen, A.: *Reduced Order Electro-thermal Battery Model Ready for Software-in-the-loop and Hardware-in-the-loop BMS Evaluation for Electric Vehicle*, in: *33nd Electric Vehicle Symposium (EVS33)*, pp. 1-12, 2020, DOI: 10.5281/zenodo.4021345.

XII Schindler, M.; Durdel, A.; **Sturm, J.**; Jocher, P.; Jossen, A.: *On the Impact of Internal Cross-Linking and Connection Properties on the Current Distribution in Lithium-Ion Battery Modules*, in: *Journal of The Electrochemical Society 167 (12)*, p. 120542, 2020, DOI: 10.1149/1945-7111/abad6b.

XI **Sturm, J.**; Rheinfeld, A.; Buzon, D.; Jossen, A.: *On The Impact of the Locality on Short-Circuit Characteristics: Experimental Analysis and Multiphysics Simulation of External and Local Short-Circuits Applied to Lithium-Ion Batteries*, in: *Journal of The Electrochemical Society 167 (9)*, p. 090521, 2020, DOI: 10.1149/1945-7111/ab8873.

X Rheinfeld, A.; **Sturm, J.**; Frank, A.; Kosch, S.; Erhard, S.V.; Jossen, A.: *Impact of Cell Size and Format on External Short Circuit Behavior of Lithium-Ion Cells at Varying Cooling Conditions: Modeling and Simulation*, in: *Journal of The Electrochemical Society 167 (1)*, p. 013511, 2020, DOI: 10.1149/2.0112001JES.

IX Ai, W.; Kraft, L.; **Sturm, J.**; Jossen, A.; Wu, B.: *Electrochemical Thermal-Mechanical Modelling of Stress Inhomogeneity in Lithium-Ion Pouch Cells*, in: *Journal of The Electrochemical Society 167 (1)*, p. 013512, 2020, DOI: 10.1149/2.0122001JES.

VIII **Sturm, J.**; Ludwig, S.; Zwirner, J.; Ramirez-Garcia, C.; Heinrich, B.; Horsche, M.F.; Jossen, A.: *Suitability of Physicochemical Models for Embedded Systems Regarding a Nickel-rich, Silicon-Graphite Lithium-Ion Battery*, in *Journal of Power Sources 436*, p. 226834, 2019, DOI: 10.1016/j.jpowsour.2019.226834.

VII Zilberman, I.; **Sturm, J.**; Jossen, A.: *Reversible Self-Discharge and Calendar Aging of 18650 Nickel-rich, Silicon-Graphite Lithium-Ion Cells*, in *Journal of Power Sources 425*, pp. 217-226, 2019, DOI: 10.1016/j.jpowsour.2019.03.109.

VI **Sturm, J.**; Rheinfeld, A.; Zilberman, I.; Spingler, F.B.; Kosch, S.; Frie, F.; Jossen, A.: *Modeling and Simulation of Inhomogeneities in a 18650 Nickel-rich, Silicon-Graphite Lithium-Ion Cell during Fast Charging*, in *Journal of Power Sources 412*, pp. 204-223, 2019, DOI: 10.1016/j.jpowsour.2018.11.043.

V Rheinfeld, A.; **Sturm, J.**; Noel, A.; Kosch, S.; Wilhelm, J.; Kriston, A.; Pfrang, A.; Jossen, A.:

Quasi-Isothermal External Short Circuit Tests Applied to Lithium-Ion Cells: Part II. Modeling and Simulation, in: *Journal of The Electrochemical Society 166 (2)*, pp. A151-A177, 2019, DOI: 10.1149/2.0071902jes.

IV **Sturm, J.**; Ennifar, H.; Erhard, S.V.; Rheinfeld, A.; Kosch, S.; Jossen, A.: *State Estimation of Lithium-Ion Cells using a Physicochemical Model based Extended Kalman Filter*, in *Applied Energy 223*, pp. 103-123, 2018, DOI: 10.1016/j.apenergy. 2018.04.011.

III Spingler, F.B.; Wittmann, W.; **Sturm, J.**; Rieger, B.; Jossen, A.: *Optimum fast charging of lithium-ion pouch Cells based on local volume expansion criteria*, in *Journal of Power Sources 393*, pp. 152-160, 2018, DOI: 10.1016/j.jpowsour.2018.04.095.

II Kosch, S.; Zhao, Y.; **Sturm, J.**; Schuster, J.; Mulder, G.; Ayerbe, E.; Jossen, A.: *A Computationally Efficient Multi-Scale Model for Lithium-Ion Cells*, in: *Journal of The Electrochemical Society 165 (10)*, pp. A2374-A2388, 2018, DOI: 10.1149/2.1241810jes.

I **Sturm, J.**; Spingler, F.B.; Rieger, B.; Rheinfeld, A.; Jossen, A.: *Non-Destructive Detection of Local Aging in Lithium-Ion Pouch Cells by Multi-Directional Laser Scanning*, in: *Journal of The Electrochemical Society 164 (7)*, pp. A1342-A1351, 2017, DOI: 10.1149/2.0161707jes.

Oral Presentations

II **Sturm, J.**; Ludwig, S.; Zwirner, J.; Ramirez-Garcia, C.; Heinrich, B.; Zilberman, I.; Jossen, A.: *Suitability of Physicochemical Models in Microcontroller Systems for Monitoring Lithium-Ion Batteries*, at: *16th Symposium on Modeling and Validation of Electrochemical Energy Devices, Brunswick, Germany*, pp. 1-17, 2019, DOI: 10.13140/RG.2.2.21847.21920.

I **Sturm, J.**; Rheinfeld, A.; Jossen, A.: *Modelling the Electrochemical-Thermal Behaviour of Cylindrical Lithium-Ion Cells during Internal Short Circuit Scenarios*, at: *14th Symposium on Fuel Cell and Battery Modeling and Experimental Validation, Karlsruhe, Germany*, pp. 1-26, 2017, DOI: 10.13140/RG.2.2.33591.27042.

Poster Presentations

IV **Sturm, J.**; Rheinfeld, A.; Zilberman, I.; Spingler, F.B.; Kosch, S.; Erhard, S.V.; Frie, F.; Jossen, A.: *Multi-Dimensional Modelling and Simulation of a 18650 Nickel-rich, Silicon-Graphite Lithium-Ion Cell for Developing rapid Charging Methods*, at: *Oxford Battery Modelling Symposium, Oxford, UK*, p. 1, 2019, DOI: 10.13140/RG.2.2.35985.45926.

III **Sturm, J.**; Zilberman, I.; Rheinfeld, A.; Kosch, S.; Jossen, A.: *Comparison of Reduced Order Electrochemical Models and Multi-Physically coupled Models of a Lithium-Ion Cell during Fast Charging*, at: *19th International Meeting on Lithium Batteries, Kyoto, Japan*, p. 1, 2018, DOI: 10.13140/RG.2.2.36320.43528.

II **Sturm, J.**; Ennifar, H.; Erhard, S.V.; Kosch, S.; Rheinfeld, A.; Jossen, A.: *State Estimation of Lithium-Ion Cells using a Physicochemical Model based Extended Kalman Filter*, at: *15th Symposium on Modeling and Experimental Validation of Electrochemical Energy Devices, Arau, Switzerland*, p. 1, 2018, DOI: 10.13140/RG.2.2.11658.49606.

I **Sturm, J.**; Spingler, F.B.; Rieger, B.; Rheinfeld, A.; Jossen, A.: *Non-destructive Detection*

of Local Aging in Lithium-Ion Pouch Cells by Multi-Directional Laser-Scanning, at: *Kraftwerk Batterie, Aachen, Germany*, p. 1, 2017, DOI: 10.13140/RG.2.2.25080.26887.

Published Data Repositories

V **Sturm, J.**; Ludwig, S.; Zwirner, J.; Ramirez-Garcia, C.; Heinrich, B.; Horsche, M.F.; Jossen, A.: *Suitability of Physicochemical Models for Embedded Systems Regarding a Nickel-rich, Silicon-Graphite Lithium-Ion Battery - Data Set*, at *4TU.ResearchData, Netherlands*, 2019, DOI: 10.4121/ uuid:6590260b-244c-4a17-b134-f7a7cda5b8b5.

IV Zilberman, I.; **Sturm, J.**; Jossen, A.: *Reversible Self-Discharge and Calendar Aging of 18650 Nickel-rich, Silicon-Graphite Lithium-Ion Cells - Data Set*, at *4TU.ResearchData, Netherlands*, 2019, DOI: 10.4121/uuid:74e3e15c-1575-4d0d-bd38-f63148259158.

III **Sturm, J.**; Rheinfeld, A.; Zilberman, I.; Spingler, F.B.; Kosch, S.; Frie, F.; Jossen, A.: *Modeling and Simulation of Inhomogeneities in a 18650 Nickel-rich, Silicon-Graphite Lithium-Ion Cell during Fast Charging - Data Set*, at *4TU.ResearchData, Netherlands*, 2019, DOI: 10.4121/uuid:e8735 cd2-e478-4db5-80bc-b5051961a0ab.

II **Sturm, J.**; Ennifar, H.; Erhard, S.V.; Rheinfeld, A.; Kosch, S.; Jossen, A.: *State Estimation of Lithium-Ion Cells using a Physicochemical Model based Extended Kalman Filter - Data Set*, at *4TU.ResearchData, Netherlands*, 2018, DOI: 10.4121/uuid:a588c059-0d82-42fb-931d-8e805da793 88.

I **Sturm, J.**; Spingler, F.B.; Rieger, B.; Rheinfeld, A.; Jossen, A.: *Non-Destructive Detection of Local Aging in Lithium-Ion Pouch Cells by Multi-Directional Laser Scanning - Data Set*, at: *4TU.ResearchData, Netherlands*, 2017, DOI: 10.4121/uuid:c10a6b3f-efe9-41ce-99f6-4093df68c653.

Acknowledgment

Appendix

A Supplementary part of the article titled *Modeling and simulation of inhomogeneities in a 18650 nickel-rich, silicon-graphite lithium-ion cell during fast charging* (see section 2.2)

Supplementary material

Multi-dimensional model coupling

The multiphysical coupling of the multi-dimensional model (MuDiMod) is illustrated in Fig. 1.
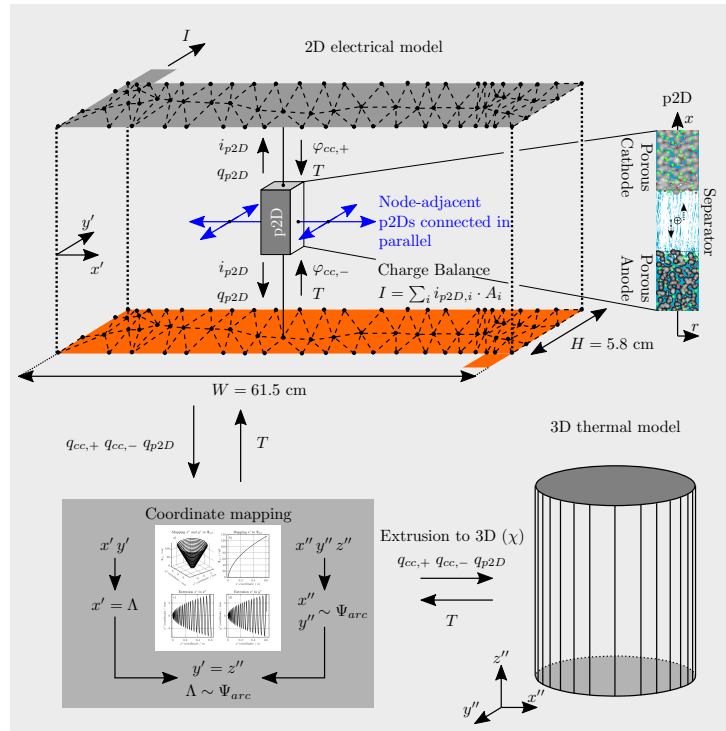

Figure 1: Coupling procedure for the MuDiMod incorporating several p2D models connected in parallel, the 2D electrical and 3D thermal model. The coordinate mapping between the 2D and 3D cartesian coordinates referring to Fig. 2 is used to exchange the locally calculated heat generation rate and temperature between 2D and 3D.

The basic multi-dimensional model description is presented in previous work [1, 2, 3] and the extension for the local coupling of heat generation and temperature between the 2D and 3D model is explained here.

Similar to other works [4, 5, 6], the coordinate mapping of 2D-plain to 3D-spirally-wound geometries uses the correlation of arc length (Λ) and azimuthal angle (Ψ_{arc}, see Eq. 1) of the spirally wound jelly roll.

$$\Lambda(\Psi_{arc}) = \frac{L_{stack}}{4\pi}\left[\left(\cosh\left(\operatorname{arcsin}(\Psi_{arc} + 4\pi)\right) \cdot (\Psi_{arc} + 4\pi)\right) + \operatorname{arcsin}(\Psi_{arc} + 4\pi)\right] \quad (1)$$

Looking into the 3D-spiral geometry of the jelly roll, every point in the x''-y''-plain is defined by an azimuthal angle and the radial distance from the starting point. Hence, every (x'', y'')-coordinate pair can be correlated to an (Ψ_{arc}, R_i)-coordinate pair according to Eq. 2.

$$\begin{bmatrix} x'' \\ y'' \end{bmatrix} = \begin{bmatrix} \cos(\Psi_{arc}) \cdot \left(\Psi_{arc} \cdot \frac{L_{stack}}{2\pi} + R_i\right) \\ \sin(\Psi_{arc}) \cdot \left(\Psi_{arc} \cdot \frac{L_{stack}}{2\pi} + R_i\right) \end{bmatrix} \quad \text{for} \quad \begin{array}{l} \Psi_{arc} \in \{0, 42.9\pi\} \\ R_i \in \{2 \cdot L_{stack} : \frac{L_{stack}}{10} : 3 \cdot L_{stack}\} \end{array} \quad (2)$$

To discretize the azimuthal direction, 2148 nodes are used ($\approx 0.3\,\mathrm{mm}$ element-length) to calculate the arc-length from inner start ($\Psi_{arc} = 0$) to the outer end ($\Psi_{arc} = 42.9\pi$) of the $61.5\,\mathrm{cm}$ length of electrode in the MJ1 cell. To discretize the radial direction (*i.e.* thickness of electrode stack), 10 spirals are defined by increasing the starting point ($R_i = 2 \cdot L_{stack}$) in $35.8\,\mathrm{\mu m}$-steps ($= L_{stack}/10$). In sum, a total number of $21\,480$ nodes were used to guarantee proper matching with the lumped finite element method (FEM) mesh in the 3D model.

Looking into the unwound, plain electrode geometry in the 2D model, the x'-coordinate along the electrode corresponds directly to the arc length (Λ)

and is correlated to the azimuthal angle according to Eq. 1. Both coordinate transformation to the azimuthal angle are illustrated in Fig. 2 a and b for the 3D- and 2D-model, respectively. The x'- and (x'', y'')-coordinates are correlated via the corresponding Ψ_{arc}-value as shown in Fig. 2 c and d.
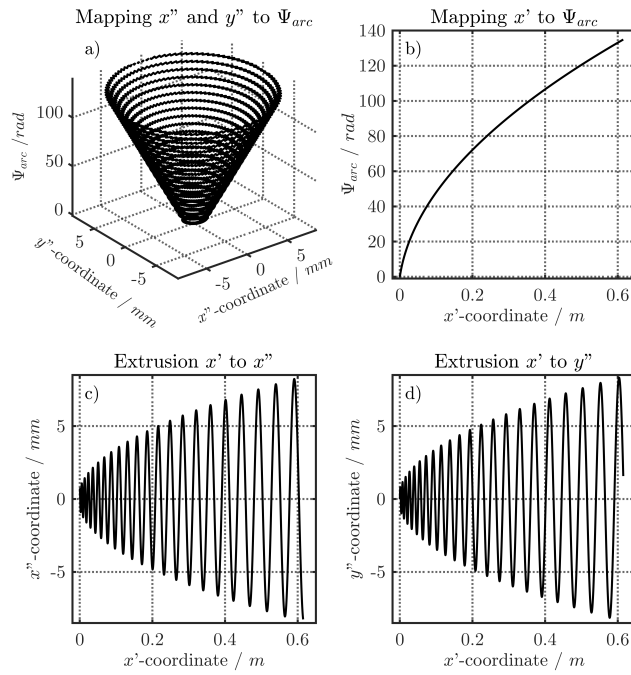

Figure 2: The coordinate mapping between the 2D- (x') and 3D-coordinates (x'', y'') is illustrated via the correlation of arclength (Λ) and azimuthal angle (Ψ_{arc}). Subplot a) and b) show the correlation of (x'', y'')- and x'-coordinates to the azimuthal angle Ψ_{arc} in the 2D- and 3D-model, respectively. Subplot c) and d) show the mapping of the x''- (c) and y''-coordinate (d) to the x'-coordinate, which corresponds to the arclength (Λ) of the spirally wound electrode stack.

3

The height of the electrode (H) corresponds to the y'- and z''-coordinate in the 2D and 3D model and can be correlated directly.

The local heat generation is extruded from the 2D model to the 3D model using the FEM. Therefore, the calculated heat generation terms from the p2D models and the 2D model are referenced to the thickness of the corresponding layers and multiplicated with the thickness ratio of corresponding layers and the total stack thickness.

Table 1: Thickness ratio for 2D heat generation rate

Thickness ratio	χ_{p2D}	$\chi_{cc,-}$	$\chi_{cc,+}$
	92.1 %	3.1 %	4.8 %
Heat generation terms	q_l; q_s; q_r; q_{rev}	$q_{cc,-}$	$q_{cc,+}$

Discretization and solving

In this work, FEM is used to discretize the fundamental equations of the single p2D model and the MuDiMod with the commercial solver COMSOL Multiphysics® 5.3a. Individual spatial discretization for the different length scales regarded in the submodels are shown in Table 2. A total of 1090 and

Table 2: FEM mesh configurations

Model	Mesh vertices	Mesh elements	Element size*	Method
p2D	45	44	Normal	FEM [I]
2D	87	125	Custom	FEM [II]
3D	1792	2448	Extremely fine/Custom	FEM [III]

* Settings of COMSOL in-built meshing-algorithm using the 'physics controlled' sequence

I = Ref. [7]   II = Ref. [8]   III = Ref. [9]

86400 degrees of freedom appears for solving the differential algebraic equation system of the single p2D and the MuDiMod, respectively. The solving process uses COMSOL Multiphysics® in-built multifrontal massively parallel sparse direct solver (MUMPS) [10] with a relative and absolute tolerance of 1×10^{-4} and 1×10^{-10}. The computation time for a 1C constant current discharge scenario at 25 °C takes around 17.5 min and 45.5 h for the single p2D and the MuDiMod, respectively. The models are computed on a Intel(R) Xeon(R) CPU E5-2687W 0 @ 3.1 GHz work station with 64 GB RAM under using a maximum time step of 1 s.

Regarding the tab design simulations with the MuDiMod, a total of 150, 134, 156 and 197 p2D models was used for the MJ1, 1x1, 1x2 and 2x3 configuration, which resulted in a total of 156351, 141599, 163010 and 200354 degrees of freedom.

Validation via infrared thermography

Table 3: Validation of the single p2D model using the thermography measurement under convective cooling I

Ambient Temperature	C-rate	Mode	$v_{air} = 1\,\mathrm{ms}^{-1}$ and $\alpha_{conv} = 22.1\,\mathrm{W\,m}^{-2}$			
			$\triangle V_{cell}$* in mV	$MSE(V_{cell})$** in $(mV)^2$	$\triangle T_{cell}$* in K	$MSE(T_{cell})$** in K^2
20 °C		CH	13	0.4	0.49	0.32
		DCH	25.3	1.3	0.39	0.21
25 °C		CH	9.9	0.2	0.43	0.31
		DCH	13.5	0.3	0.36	0.16
30 °C	1.0C	CH	14.5	0.4	0.34	0.17
		DCH	14.4	0.3	0.38	0.18
40 °C		CH	7.6	0.5	0.26	0.11
		DCH	13.1	0.2	0.33	0.17

* Mean absolute error   ** Mean squared error

Table 4: Validation of the MuDiMod using the thermography measurement under convective cooling I

| Ambient Temperature | C-rate | Mode | $\mathrm{v}_{air} = 1\,\mathrm{m\,s^{-1}}$ and $\alpha_{conv} = 22.1\,\mathrm{W\,m^{-2}}$ | | | |
			$\triangle\mathrm{V}_{\mathrm{cell}}^{*}$ in mV	$\mathrm{MSE(V_{cell})}^{**}$ in $(\mathrm{mV})^2$	$\triangle\mathrm{T}_{\mathrm{cell}}^{*}$ in K	$\mathrm{MSE(T_{cell})}^{**}$ in K^2
20 °C		CH	16.7	0.5	0.26	0.09
		DCH	19.9	0.9	0.41	0.21
25 °C		CH	23.5	0.7	0.32	0.13
	1.0C	DCH	15.2	0.5	0.33	0.14
30 °C		CH	13.7	0.4	0.28	0.11
		DCH	12.7	0.3	0.34	0.15
40 °C		CH	10.9	0.4	0.30	0.14
		DCH	13.8	0.3	0.31	0.13

* Mean absolute error   ** Mean squared error

Table 5: Validation of the single p2D model using the thermography measurement under convective cooling II

| Ambient Temperature | C-rate | Mode | $\mathrm{v}_{air} = 2\,\mathrm{m\,s^{-1}}$ and $\alpha_{conv} = 31.7\,\mathrm{W\,m^{-2}}$ | | | |
			$\triangle\mathrm{V}_{\mathrm{cell}}^{*}$ in mV	$\mathrm{MSE(V_{cell})}^{**}$ in $(\mathrm{mV})^2$	$\triangle\mathrm{T}_{\mathrm{cell}}^{*}$ in K	$\mathrm{MSE(T_{cell})}^{**}$ in K^2
20 °C		CH	18.5	0.6	0.44	0.24
		DCH	36.1	3.0	0.31	0.12
25 °C		CH	9.7	0.2	0.36	0.20
	1.0C	DCH	16.3	0.5	0.40	0.21
30 °C		CH	22.7	0.8	0.34	0.16
		DCH	25.1	1.3	0.34	0.15
40 °C		CH	21.3	0.6	0.23	0.09
		DCH	13.9	0.3	0.34	0.15

* Mean absolute error   ** Mean squared error
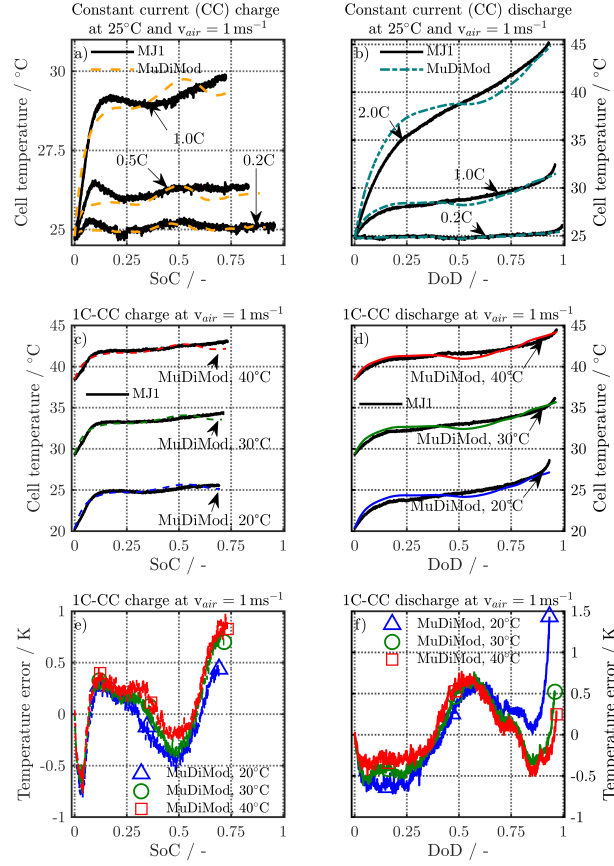
Figure 3: Thermography measurements of the MJ1 cell to validate the simulated cell temperature at different C-rates for charge (a) and discharge (b) at 25 °C in terms of the MuDiMod. 1C-CC charge (c) and discharge (d) validation at different ambient temperatures (20 °C, 30 °C and 40 °C) are shown for the MuDiMod simulation results together with the related error (e and f).

Influence of tab design on temperature distribution
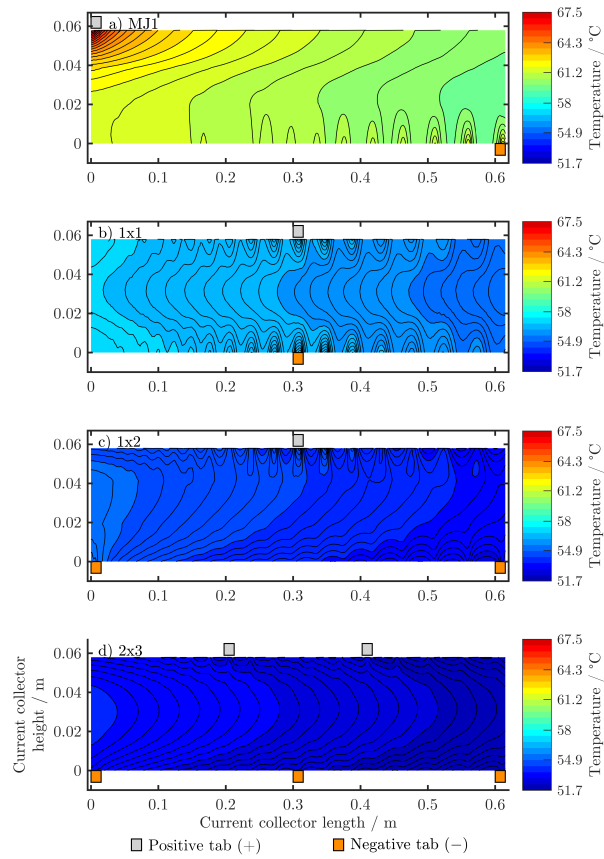
Figure 4: Simulated temperature distribution along the electrode. The calculated temperature distribution is shown for 3C constant current charging at EoC for the MJ1 (a), 1x1 (b), 1x2 (c) and 2x3 (d) tab design.

References

[1] S. V. Erhard, P. J. Osswald, J. Wilhelm, A. Rheinfeld, S. Kosch, A. Jossen, Simulation and measurement of local potentials of modified commercial cylindrical cells: Ii: Multi-dimensional modeling and validation, Journal of The Electrochemical Society 162 (14) (2015) A2707–A2719. doi:10.1149/2.0431514jes.

[2] B. Rieger, S. V. Erhard, S. Kosch, M. Venator, A. Rheinfeld, A. Jossen, Multi-dimensional modeling of the influence of cell design on temperature, displacement and stress inhomogeneity in large-format lithium-ion cells, Journal of The Electrochemical Society 163 (14) (2016) A3099–A3110. doi:10.1149/2.1051614jes.

[3] S. Kosch, Y. Zhao, J. Sturm, J. Schuster, G. Mulder, E. Ayerbe, A. Jossen, A computationally efficient multi-scale model for lithium-ion cells, Journal of The Electrochemical Society 165 (10) (2018) A2374–A2388. doi:10.1149/2.1241810jes.

[4] M. Guo, R. E. White, Mathematical model for a spirally-wound lithium-ion cell, Journal of Power Sources 250 (2014) 220–235. doi:10.1016/j.jpowsour.2013.11.023.

[5] J. N. Reimers, Accurate and efficient treatment of foil currents in a spiral wound li-ion cell, Journal of the Electrochemical Society 161 (1) (2013) A118–A127. doi:10.1149/2.046401jes.

[6] D. A. H. McCleary, J. P. Meyers, B. Kim, Three-dimensional modeling of electrochemical performance and heat generation of spirally and pris-

matically wound lithium-ion batteries, Journal of the Electrochemical Society 160 (11) (2013) A1931–A1943. doi:10.1149/2.023311jes.

[7] COMSOL Multiphysics, The heat transfer module user's guide (2017).
URL https://www.comsol.com/

[8] COMSOL Multiphysics, The batteries & fuel cells module user's guide (2017).
URL https://www.comsol.com/

[9] COMSOL Multiphysics, Comsol multiphysics reference manual (2017).
URL https://www.comsol.com/

[10] P. Amestoy, A. Buttari, A. Guermouche, J.-Y. L'Excellent, B. Ucar, Mumps: Multifrontal massively parallel sparse direct solver - version 5.1.2 (2017).
URL http://mumps.enseeiht.fr/

B Supplementary part of the article titled *Impact of Electrode and Cell Design on Fast Charging Capabilities of Cylindrical Lithium-Ion Batteries* (see section 2.3)

Impact of electrode and cell design on fast charging capabilities of cylindrical lithium-ion batteries

Sturm, J.,[*,†] Frank, A.,[†] Rheinfeld, A.,[†] Erhard, S.V.,[†] and Jossen, A.[†,‡]

†*Technical University of Munich (TUM), Institute for Electrical Energy Storage Technology (EES), Arcisstrasse 21, 80333 Munich, Germany*

‡*Munich School of Engineering (MSE), Technical University of Munich (TUM), Lichtenbergstr. 4a, 85748 Garching, Germany*

E-mail: johannes.sturm@tum.de

Phone: +49 (0) 89 289-26967

Supplementary material

Geometrical Design of the 21700#2 Cylindrical Lithium-Ion Cell

View A   21700 #2
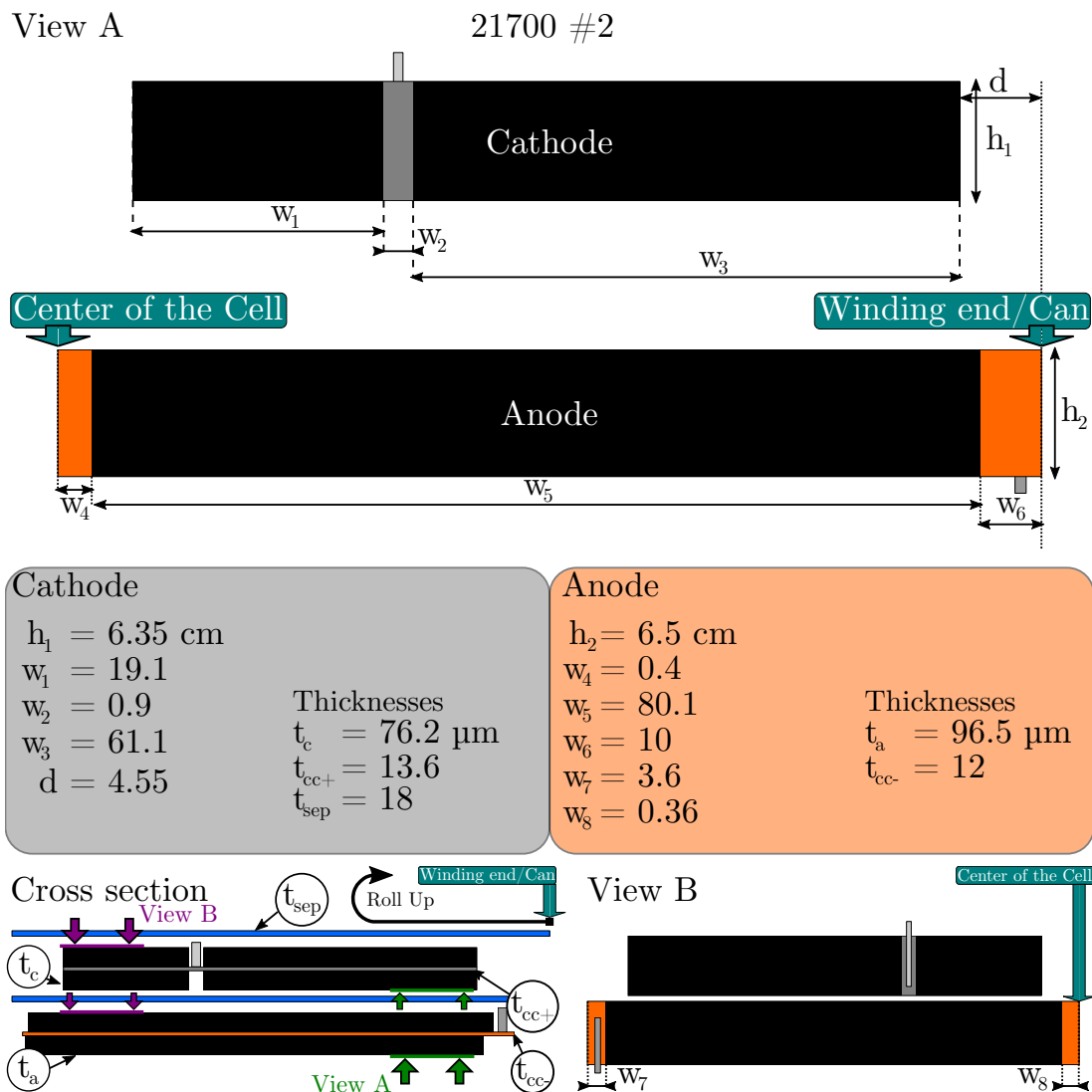
Figure 1: Design of the electrode stack derived from the measurement results of the dismantled and unrolled jelly roll of cell 21700#2 .

Cathode

$h_1 = 6.35$ cm
$w_1 = 19.1$
$w_2 = 0.9$
$w_3 = 61.1$
$d = 4.55$

Thicknesses
$t_c = 76.2$ µm
$t_{cc+} = 13.6$
$t_{sep} = 18$

Anode

$h_2 = 6.5$ cm
$w_4 = 0.4$
$w_5 = 80.1$
$w_6 = 10$
$w_7 = 3.6$
$w_8 = 0.36$

Thicknesses
$t_a = 96.5$ µm
$t_{cc-} = 12$
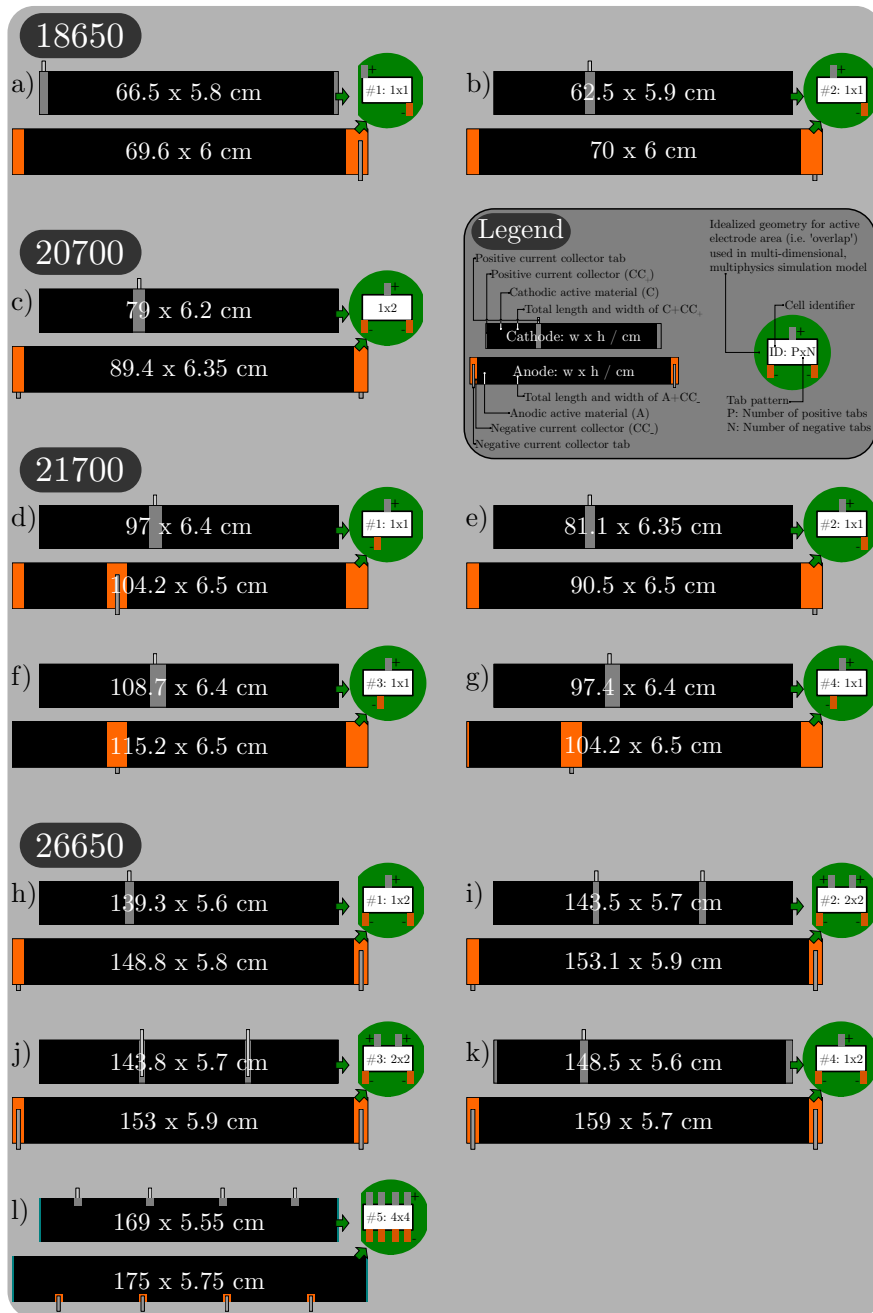
Figure 2: Dimensions of anode and cathode geometry incorporated in the jelly roll of the experimentally investigated 18650 (a,b), 20700 (c), 21700 (d-g), and 26650 (h-l) cylindrical lithium-ion batteries (LIBs). Additionally two high power type 26650 cells are depicted (see k and l) for comparison purposes, which are not discussed any further in this work.

3

Experimental Results of Rate Test Measurements

The surface temperature profiles of the rate test are shown in Fig. 3 and the corresponding analysis is shown in Table 1.

Table 1: Total temperature rise ($\triangle T$) and maximum surface temperatures ($T_{\max}$) at 1C constant current (CC) discharge and charge at 25 °C and free convection in a climate chamber

Format	Cell number	Discharge		Charge	
		$\triangle T$ / K	$T_{\max}$ / °C	$\triangle T$ / K	$T_{\max}$ / °C
18650	#1	12.4	37.4	11	36
	#2	7.1	32.1	5.1	30.1
20700		3.7	28.7	2.4	27.4
21700	#1	4.8	29.8	3.3	28.3
	#2	6.5	31.5	5.4	30.4
	#3	6.5	31.5	4.6	29.6
	#4	6.6	31.6	4.9	29.9
26650	#1	6.7	31.7	5.7	30.7
26650	#2	6.8	31.8	4.6	29.6
26650	#3	5.8	30.8	4	29
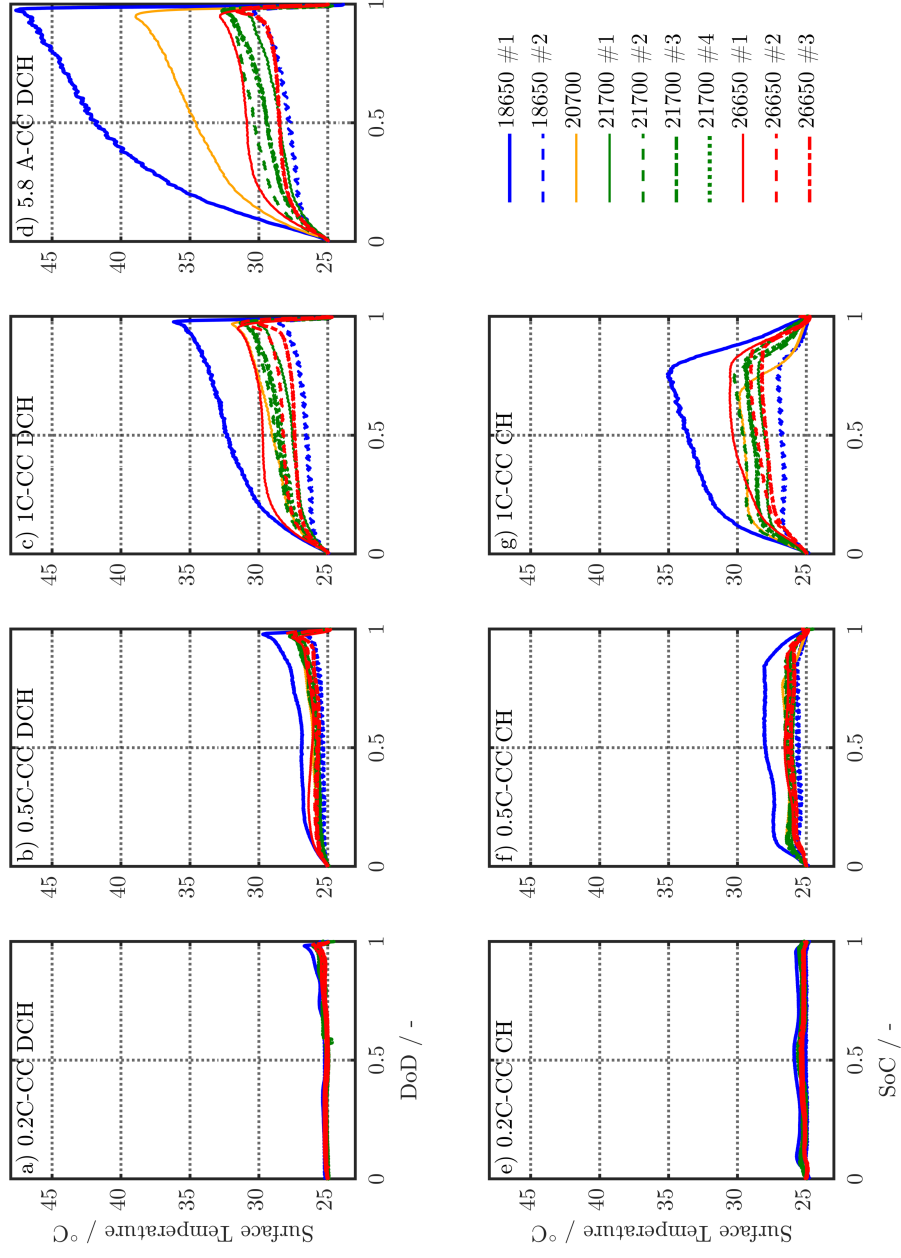
Figure 3: Experimental results of the surface temperatures gained from the rate test at 25 °C for all cylindrical formats from 0.2C-to 1C-CC charge (e,f,g) and discharge (a,b,c) with additional constant voltage (CV) phase terminated at 0.01C. Additionally, the maximum applicable current by the cycler ($\approx$ 5.8 A) is shown for the discharge scenario in subplot d.

Experimental Results of Open-Circuit Voltage Analysis

Fig. 4 shows the experimental results of the open-circuit potential (OCP) measurements for the anode (a and b) and the cathode (f) half cells vs. Li/Li$^+$ at 0.01C-CC and 25 °C. Differential voltage analysis (DVA) is applied to calculate the differential potential (c and g), differential capacity (d and h), and the temperature coefficient (e and i) derived from a linear interpolation between 10 °C, 25 °C, and 40 °C. The suplots c to e and g to i show magnifications at low anode and high cathode lithiation levels as indicated in the subplots a and f.

Regarding the anode results significant lower potentials as shown in subplot a appear for the pure graphite type 26650#1 cell compared to the silicon-containing types of the remaining high energy cells. The higher potentials as shown in magnification b appear due to the presence of silicon in the graphite host lattice. The higher differential potentials of the high energy cells as shown in subplot c are well in line with the aforementioned potential increase as well as the significantly increased differential capacity shown in subplot d between 200 mV and 300 mV. Similarly, a different temperature sensitivity appears showing a lower mean value between 5 % and 30 % SoC (see subplot e) for the silicon-containing graphite types compared to the pure graphite type.

Regarding the cathode results, the focus lies on the difference between the rather moderately-loaded NMC-type to high-energy nickel-rich NMC- or NCA-type cathodes. A deviation of the half-cell potential curves (f) appears between the moderate and the high-energy types, which is highlighted from 0 % to 48 % depth of discharge (DoD) of the cathode in the subplots g, h, and i. A more detailed discussion of the shown differential peaks (see g and h) can be found elsewhere.[1] A significantly increased temperature sensitivity appears for the high-energy types as shown in subplot i.

Figure 4: Summary of the OCP analysis for anode (a,b,c,d,e) and cathode (f,g,h,i) half cells vs. Li/Li$^+$. The results were gained at 0.01C-CC lithiation of the anode and delithiation of the cathode at 25°C for two 18650-, a single 20700-, four 21700-, and a single 26650-format. The enclosed sections in subplot a and f are magnified in terms of the potential (b), its 1st derivative (c and g), the differential capacity over the electrode's potential vs. Li/Li$^+$ (d and h), and the temperature coefficient (e and i) for the anode and cathode material derived from linearization at 10°C, 25°C, and 40°C.

Exemplarily the DVA results of cell 21700#2 are shown in Fig. 5 using the full- and half-cell data. The OCV of the full cell (see subplot a) is composed properly by the superposition of anode and cathode OCP, where the electrode balancing is determined via using the 1st derivative (see subplot b). Significant anode and cathode peaks appear in the differential potential, which can also be seen in the temperature coefficient (see subplot c) of the full cell. The temperature coefficient is shown to visualize the sensitivity of the OCV towards the temperature and is not meant to represent the actual entropic coefficient as shown in other works like Osswald et al.[2] The related slight deviances of the anode and cathode superposition to the full cell are most likely caused by manufacturing tolerances of the coin cells, change of the electrolyte, an expected influence of the constant current measurement procedure compared to more precise relaxation methods[2] and not completely extinguishable influences of the cell opening and handling process in the glovebox. Nevertheless, the significant, differential temperature marks can be attributed to either the anode or the cathode. The superposition of the differential capacity is well in line with the full cell characteristic as shown in subplot d.
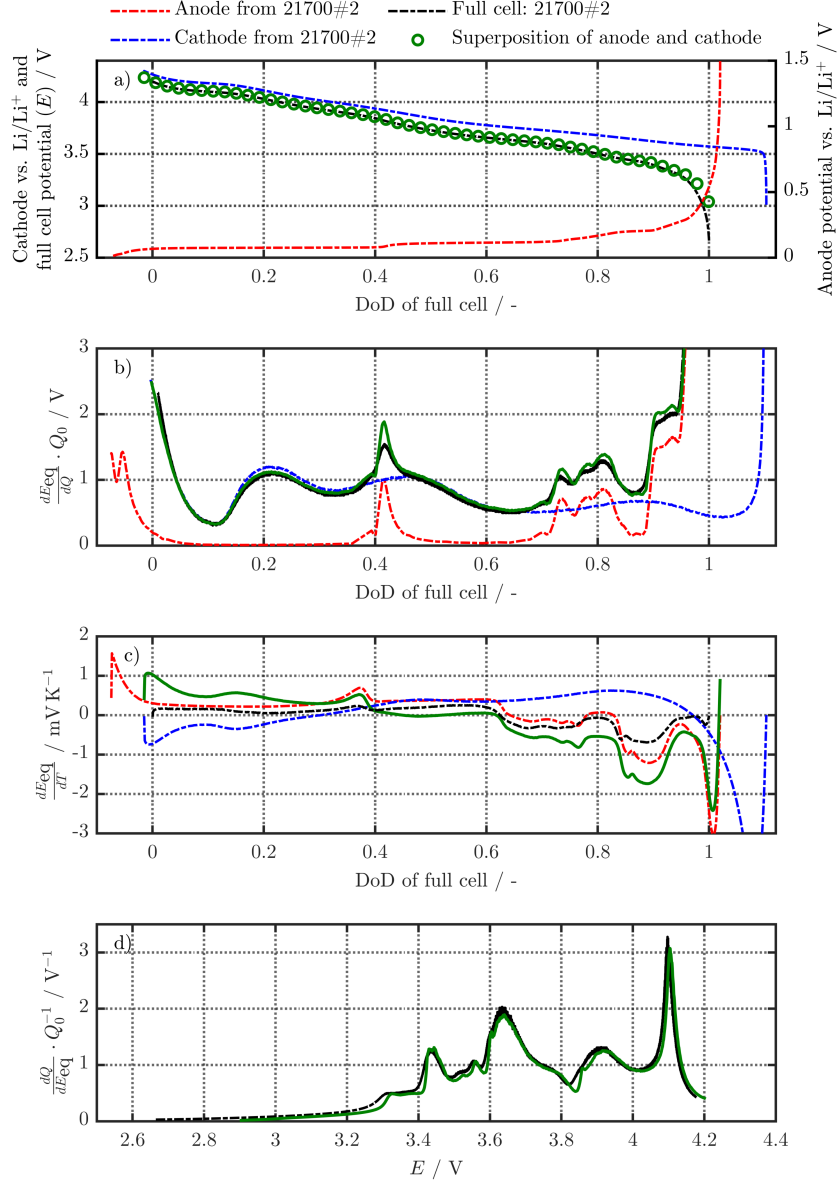
Figure 5: DVA results at 0.01C-CC discharge and 25 °C for the 21700#2 cell ('black'), its anode ('red') and cathode ('blue') half cells vs. lithium metal (Li/Li$^+$) and their superposition ('green'). The results comprise the OCP/OCV vs. the full cell DoD (a), its 1st derivative vs. the capacity, the linearized temperature coefficient at 10 °C, 25 °C, and 40 °C (c) and the differential capacity vs. the full cell voltage (d).

Experimental Results of Scanning Electron Microscopy and Energy-Dispersive X-Ray Spectroscopy

The results of the scanning electron microscopy (SEM, JCM-600 JEOL Ltd.) are shown in Fig. 6 for the anode and cathode samples extracted from the opened cells of the cylindrical state-of-the-art review. Rather flake-like and spherical particle shapes appear for all anode and cathode samples, respectively. The particle sizes appear in a comparable manner as seen in Fig. 6.

The results of the energy-dispersive X-ray (EDX, JCM-600 JEOL Ltd.) spectroscopy are shown in Fig. 7. Silicon (Si), oxygen (O) and carbon (C) were analyzed for the anode samples at a magnification level of 300. At a similar magnification level nickel (Ni), cobalt (Co), manganese (Mn), aluminum (Al), O and C were analyzed for the cathode samples. As seen in Fig. 7, a clear difference in indication of Si between the silicon-containing (e.g. 18650#1, 18650#2 and 20700) and the pure graphite-type host lattices of cell 26650#1 appears. For the high-energy nickel-rich cathode host lattices an amplified indication of Ni appears (e.g. 18650#1 and 18650#2 with indication in 'red' for Ni) compared to the rather moderately loaded NMC-532 cathode of cell 26650#1. Additionally a balanced NMC-111 type (CustomCells, Germany) is shown in Fig. 7 to visualize the difference to the remaining cathode types. Nickel-rich NMC and NCA types were distinguished via indication of either Mn or Al. In case of a Ni-rich NCA significant Al indication appeared on the surface of the cathode as seen in Fig. 7.

Table. 2 summarizes the EDX analysis with the measured thickness of the electrode stack layers gained from SEM and micro calliper measurements. Inductively Coupled Plasma-Optical Emission Spectroscopy (ICP-OES, Varian 7XX-ES ICP-OES Spectrometer, Agilent Technologies) and EDX spectroscopy showed a good accordance for the cathode experiments and in terms of the anode, slightly increased deviances were seen and the content of silicon was estimated using a correction factor derived from the ICP-OES reference measurement of cell 18650#1.

10
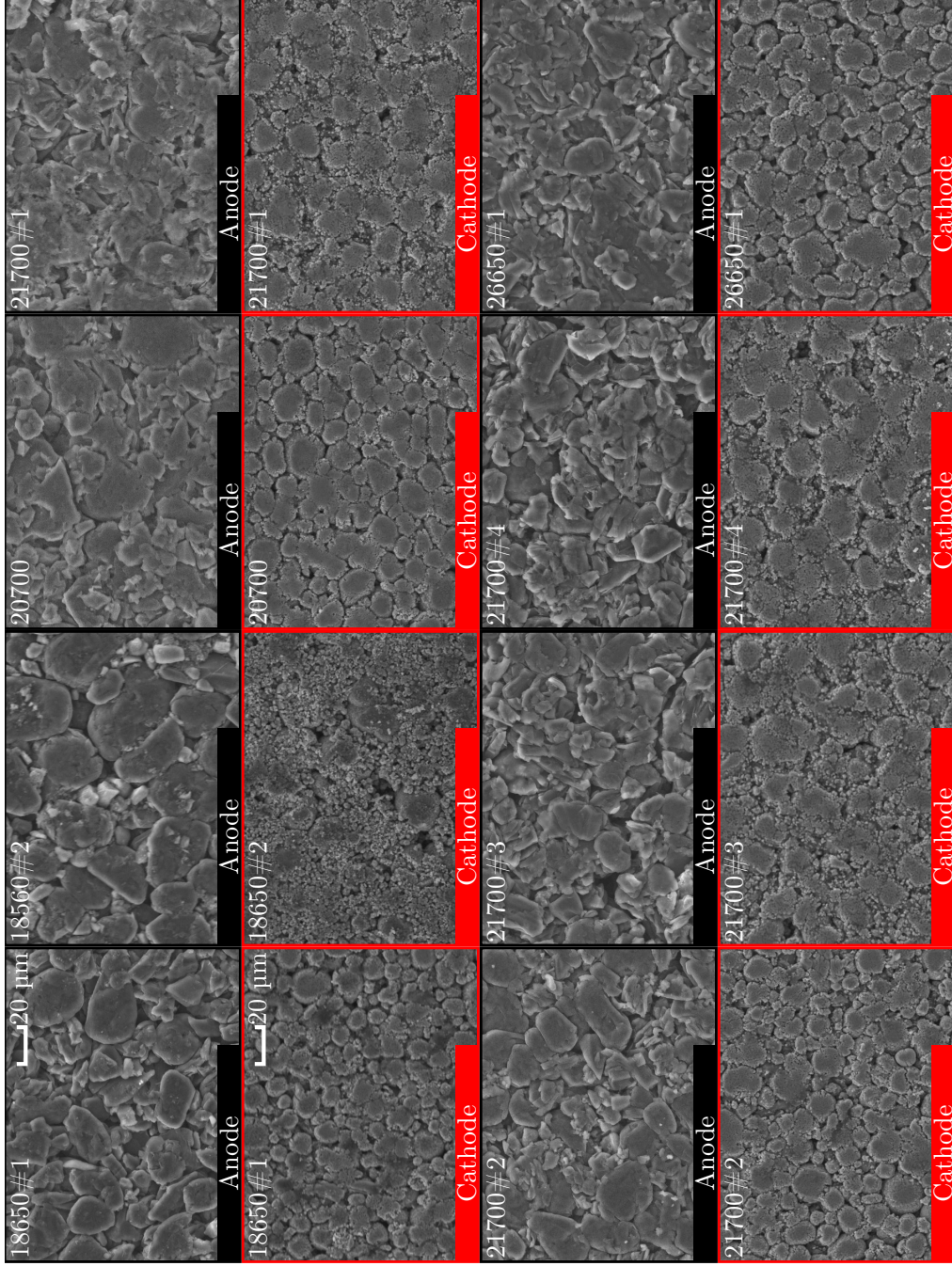
Figure 6: Experimental results of the SEM for the extracted anode and cathode samples from two 18650, a 20700, four 21700 and the 26650#1 cell. Every image was recorded at an acceleration voltage of 15 kV and a magnification level of 1000. The depicted scale bars refer to 20 μm and are applicable to all images.
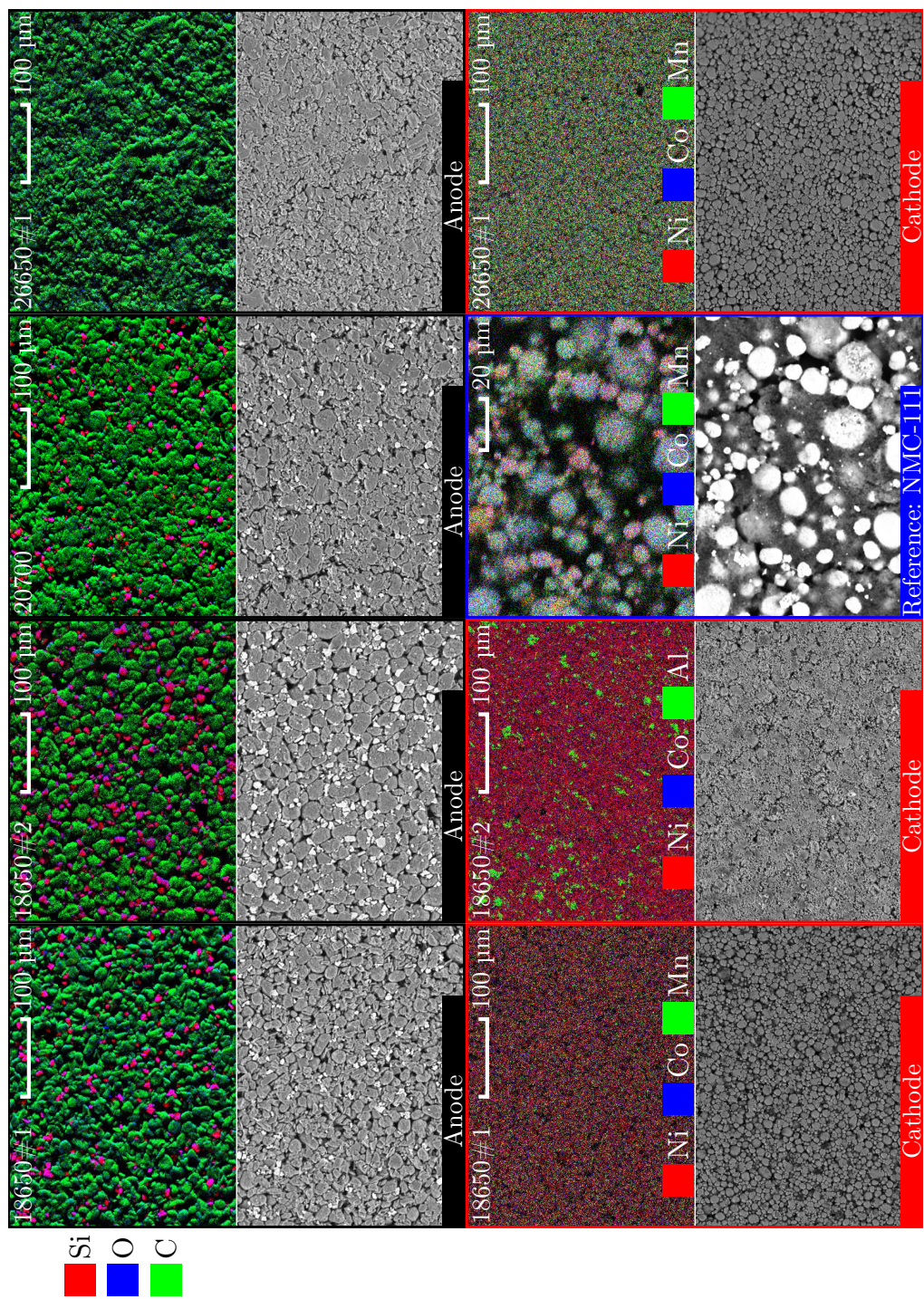
11

Figure 7: Experimental results of the EDX spectroscopy for the extracted anode and cathode samples from two 18650, a 20700 and the 26650#1 cell. Every image was recorded at an acceleration voltage of 15 kV and a magnification level of 300. The depicted scale bars refer to 100 μm and are applicable to all images except for the NMC-111 electrode (CustomCells, Germany), which is magnified at a level of 1000 with a respective scale bar at 20 μm.

Table 2: Results of the EDX spectroscopy measurements and the geometrical analysis of the electrode stack

Format	Number	Anode			Separator	Cathode						Electrode Stack
Symbol		Si	$t_{cc,-}$	t_a	t_{sep}	t_c	$t_{cc,+}$	Ni	Co	Mn	Al	t_{stack}[III]
Unit		wt.%	μm	μm	μm	μm	μm	wt.%	wt.%	wt.%	wt.%	μm
18650	#1	3.5[I]	11	86.7	12	66.2	17.3	82.4[II](82[I])	11.4[II](11.7[I])	6.2[II](6.3[I])	0[I,II]	358
	#2	≈7.2[IV]	12.5	78.8	15	77	16	85.6	8.9	0	5.5	370
20700		≈4.7[IV]	13	78	17	66.5	12	87.7	10.5	0	1.8	348
21700	#1	≈2.7[IV]	11	79.5	13	62.5	13	83.9	15.3	0	0.8	334
	#2	≈6.2[IV]	12	96.5	18	76.2	13.6	82	11.4	6	0	407
	#3	≈2.3[IV]	14	68	14	53	14	83.7	15.4	0	0.9	298
	#4	≈2.5[IV]	13	80	14	62	14	87	10.3	0	2.7	339
26650	#1	0	10	77.5	15	15	62	49.5	20.3	30.2	0	334
	#2	n.a.	11	70	19	59.5	17	n.a.	n.a.	n.a.	n.a.	325
	#3	n.a.	15	72.5	18	60	18	n.a.	n.a.	n.a.	n.a.	334

[I] Measured via ICP-OES
[II] Measured via EDX spectroscopy at 15 kV accelerating voltage at a surface magnification level of 300
[III] $t_{stack} = t_{cc,-} + 2 \cdot (t_a + t_{sep} + t_c) + t_{cc,+}$
[IV] Estimated from the EDX results of the anodes using the offset between the ICP-OES and EDX result from cell 18650#1 as a correction factor

The estimation only holds for an estimate of the actual Si content and more precise measurement techniques such as ICP-OES should be applied to validate the findings, which could not be carried out for each cell within this work.

Modeling Approach of the Multidimensional Multiphysics framework (MuDiMod)

A detailed description of the MuDiMod framework can be found in our previous work, where especially the coordinate mapping function and the physical meaningful coupling between the electrochemical p2D models, the 2D electrical and the 3D thermal model is presented.[3]

Discretization and Solving

Finite element method (FEM) is used within this work to discretize the fundamental equations of the the MuDiMod framework and the commercial solver COMSOL Multiphysics® 5.3a is used for the solving process. Individual spatial discretization configurations referring to the different length scales solved in each submodel (p2D, 2D and 3D) are shown in Table 3. Exemplary a total of 188222, 171219 and 193029 degrees of freedom result for the differential algebraic equation system of the MuDiMod framework to simulate the 18650, 21700 and 26650 configuration under 1C-CC charging with a 1x1 tab design. A total of 179, 158, and 168 p2D models are used in these models across the active electrode area, where their distribution follows a physical-meaningful concept based on a meshing algorithm incorporated in COMSOL Multiphysics® 5.3a. The solving process uses a COMSOL Multiphysics® in-built multifrontal massively parallel sparse direct solver (MUMPS)[7] with a relative and absolute tolerance of 1×10^{-4} and 1×10^{-10} at a maximum step-size of 1 s. The simulation studies were computed on Intel(R) Xeon(R) CPU E5-2687W 0 @ 3.1 GHz work stations with 64 GB RAM.

Table 3: FEM mesh configuration for the MuDiMod cases

Format	Model	Tab Design	Vertices	Elements [I]	Method	$\sum$DoF [II]
	p2D	n.a.	45	44	FEM [V]	
		1x1	191	308 [III]	FEM [VI]	188222
		1x1*	169	270 [III]	FEM [VI]	162154
18650	**2D**	1x2	175	277 [III]	FEM [VI]	164821
		2x2	183	284 [III]	FEM [VI]	169514
		2x3	237	359 [III]	FEM [VI]	214386
	3D	n.a.	2004	2766 [IV]	FEM [VII]	
	p2D	n.a.	45	44	FEM [V]	
		1x1	170	267 [III]	FEM [VI]	171219
		1x1*	179	290 [III]	FEM [VI]	179712
21700	**2D**	1x2	188	295 [III]	FEM [VI]	182432
		2x2	168	252 [III]	FEM [VI]	158097
		2x3	210	320 [III]	FEM [VI]	191701
	3D	n.a.	2256	3120 [IV]	FEM [VII]	
	p2D	n.a.	45	44	FEM [V]	
22800	**2D**	1x1*	118	178 [III]	FEM [VI]	120601
		1x2	131	195 [III]	FEM [VI]	127116
	3D	n.a.	2060	2850 [IV]	FEM [VII]	
	p2D	n.a.	45	44	FEM [V]	
23700	**2D**	1x2	130	189 [III]	FEM [VI]	133757
		2x2	166	246 [III]	FEM [VI]	161751
	3D	n.a.	2784	3900 [IV]	FEM [VII]	
	p2D	n.a.	45	44	FEM [V]	
		1x1	180	278 [III]	FEM [VI]	193029
		1x1*	192	300 [III]	FEM [VI]	204249
26650	**2D**	1x2	204	312 [III]	FEM [VI]	209791
		2x2	165	235 [III]	FEM [VI]	167702
		2x3	225	335 [III]	FEM [VI]	218124
	3D	n.a.	3448	4860 [IV]	FEM [VII]	

[I] User defined settings incorporating a COMSOL in-built meshing algorithm

[II] Total degrees of freedom for the specific MuDiMod case

[III] Triangular mesh elements   [IV] Prismatic mesh elements

[V] Ref.[4]   [VI] Ref.[5]   [VII] Ref.[6]

Simulation Studies

Fig. 8 illustrates the temperature sensitivity of the in- and through-plane polarization between different 18650 tab designs and Fig. 9 shows the temperature profile of the 18650, 21700 and 26650 format under rapid charging and active cooling.
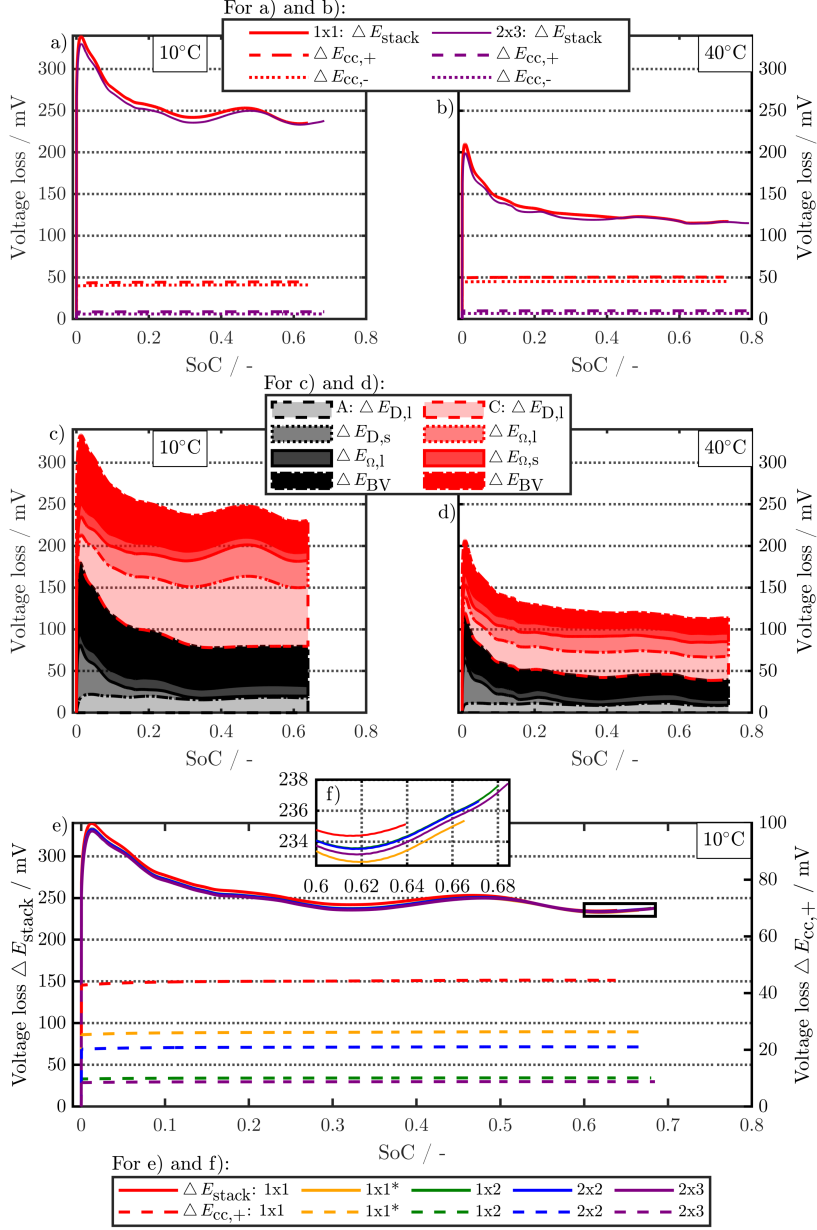
Figure 8: Simulation results of the 1C-CC charging from 3 V to 4.2 V at 10 °C, 25 °C and 40 °C for different 18650 tab design studies. Subplot a and b show the maximum through- and in-plane polarization parts for the 18650_1x1 and the 18650_2x3 study at 10 °C and 40 °C. Subplot c and d show the related composition of the major through-plane polarization parts and subplot e depicts the maximum through- and in-plane (here positive current collector) polarization of all 18650 tab design studies with the resulting variance of charged SoC magnified in subplot f.

16
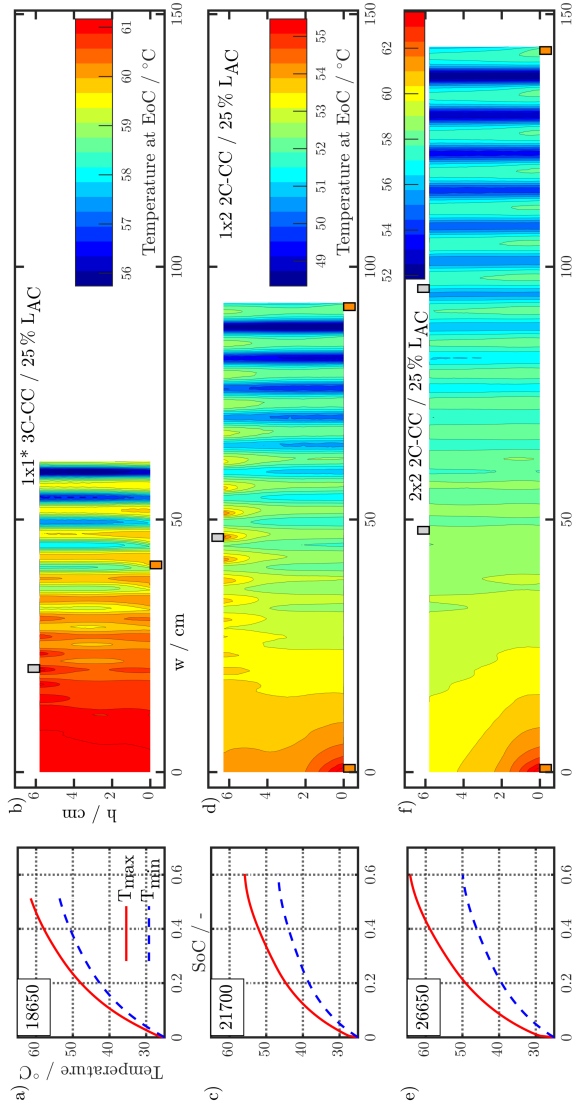
Figure 9: Simulation results of 3C- (18650_1x1*) and 2C-CC (21700_1x2 and 26650_2x2) charging from 3 V to 4.2 V at 25 °C. The subplots a, c and e show the maximum and minimum temperature for the 18650 (a), 21700 (c) and 26650 (e) study. The corresponding temperature distribution at the end of charge (EoC) is shown in the subplots b, d and f across the active electrode area.

References

(1) Jung, R.; Metzger, M.; Maglia, F.; Stinner, C.; Gasteiger, H. A. Oxygen Release and Its Effect on the Cycling Stability of LiNixMnyCozO2 (NMC) Cathode Materials for Li-Ion Batteries. *Journal of The Electrochemical Society* **2017**, *164*, A1361–A1377.

(2) Osswald, P. J.; Rosario, M. d.; Garche, J.; Jossen, A.; Hoster, H. E. Fast and Accurate Measurement of Entropy Profiles of Commercial Lithium-Ion Cells. *Electrochimica Acta* **2015**, *177*, 270–276.

(3) Sturm, J.; Rheinfeld, A.; Zilberman, I.; Spingler, F. B.; Kosch, S.; Frie, F.; Jossen, A. Modeling and simulation of inhomogeneities in a 18650 nickel-rich, silicon-graphite lithium-ion cell during fast charging. *Journal of Power Sources* **2019**, *412*, 204–223.

(4) COMSOL Multiphysics, The Batteries & Fuel Cells Module User's Guide. 2017; `https://www.comsol.com/`.

(5) COMSOL Multiphysics, The Heat Transfer Module User's Guide. 2017; `https://www.comsol.com/`.

(6) COMSOL Multiphysics, COMSOL Multiphysics Reference Manual. 2017; `https://www.comsol.com/`.

(7) Amestoy, P.; Buttari, A.; Guermouche, A.; L'Excellent, J.-Y.; Ucar, B. MUMPS: Multifrontal massively parallel sparse direct solver - version 5.1.2. 2017; `http://mumps.enseeiht.fr/`.

C Supplementary part of the article titled *Suitability of physicochemical models for embedded systems regarding a nickel-rich, silicon-graphite lithium-ion battery* (see section 3.2)

Supplementary

Parameterization and illustration of the equivalent circuit model (ECM)
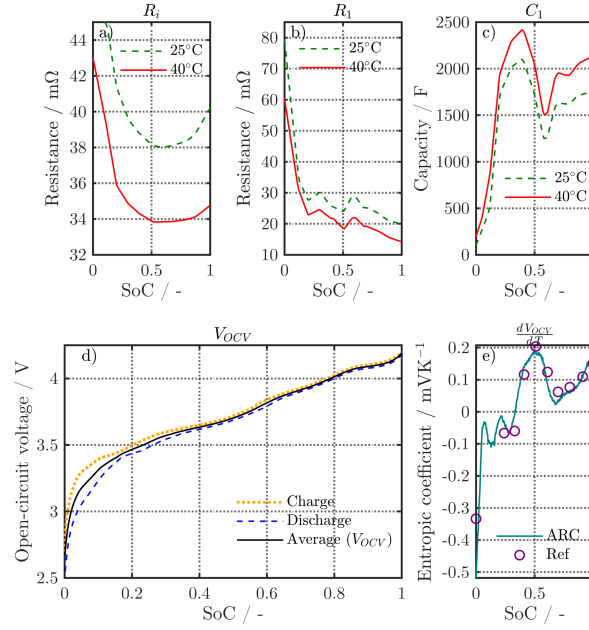
Figure 1: The parameterization of the ECM is illustrated for the ohmic resistance R_i (a) and the RC network consisting of the resistance R_1 (b) and the capacity C_1 (c) derived from pulse current tests for charge and discharge at 0.5C and 1.0C for two different cell temperatures (25 °C and 40 °C) using the electrochemical impedance spectroscopy (EIS) zero-crossing results as boundary condition for the R_i values. The voltage source V_{OCV} is derived from the averaged value of charge and discharge at 0.033C at 25 °C as shown in d. The entropic coefficient $\frac{dV_{OCV}}{dT}$ is used from accelerated rate calorimetry (ARC) and the comparison to the potentiometric method (Ref) according to Zilberman et al. [1] are shown in e.
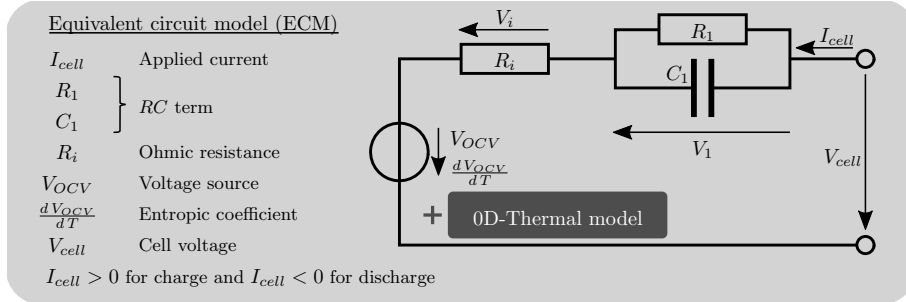
Figure 2: Schematic illustration of the equivalent circuit model for the NMC-811/SiC INR18650-MJ1 lithium-ion battery.

MATLAB$^\circledR$ solver ode15s transferred into stand-alone C-code

The solver MATLAB$^\circledR$ $ode15s$ [2] is referenced to the original fundamental works [3, 4] and outlined partly here, to comprehend better the transfer from MATLAB$^\circledR$ to C.

Using Chebyshev orthogonal collocation to reformulate the spatial discretization in the OC-PCM, only ordinary differential equations (ODEs) in time are left together with algebraic equations (AEs), which form a differential algebraic equation (DAE) system as

$$\boldsymbol{M}\boldsymbol{x}' = \boldsymbol{f}(t, \boldsymbol{x})$$

including the regular mass matrix $\boldsymbol{M}$ [3]. The solver is designed to handle stiffness issues caused by stiff equations in the DAE, where numerical integrations methods can become unstable unless the step-size is extremely reduced even if the solution curve is expected to be smooth [3]. Stiff problems are solved with a linear implicit, one-step method based on numerical differentiation formulas (NDFs) implemented in backward differences [3]. Multiplying

2

the general form of the DAE system with $\boldsymbol{M}^{-1}$, setting $\boldsymbol{F} = \boldsymbol{M}^{-1}\boldsymbol{f}(t, \boldsymbol{x})$ and applying backward differentiation formulas (BDFs) according to Shampine and Reichelt [3], the non-linear DAE system can be solved using a simplified Newton iteration scheme for a constant step-size h and a formula of order k (*i.e.* BDF of order k) for the integration step from n to $n+1$ as [3]

$$\sum_{m=1}^{k} \tfrac{1}{m}\nabla^m \boldsymbol{x}_{n+1} - h\boldsymbol{F}(t_{n+1}, \boldsymbol{x}_{n+1}) = 0$$

The equation can be solved for $\boldsymbol{x}_{n+1}$ using a simplified Newton iteration scheme and starts with a prediction step '(0)' as [3]

$$\boldsymbol{x}_{n+1}^{(0)} = \sum_{m=0}^{k} \nabla^m \boldsymbol{x}_n$$

According to Shampine and Reichelt [3] the aforementioned NDF [5] can be added in backward difference as

$$\sum_{m=1}^{k} \frac{1}{m}\nabla^m \boldsymbol{x}_{n+1} - h\boldsymbol{F}(t_{n+1}, \boldsymbol{x}_{n+1}) - \kappa\boldsymbol{\gamma}_k\left(\boldsymbol{x}_{n+1} - \boldsymbol{x}_{n+1}^{(0)}\right) = 0 \qquad (1)$$

$$\text{with } \boldsymbol{\gamma}_k = \sum_{j=1}^{k} \tfrac{1}{j}$$

where κ is a scalar parameter [3]. Using the identity [3]

$$\sum_{m=1}^{k} \tfrac{1}{m}\nabla^m \boldsymbol{x}_{n+1} = \boldsymbol{\gamma}_k\left(\boldsymbol{x}_{n+1} - \boldsymbol{x}_{n+1}^{(0)}\right) + \sum_{m=1}^{k} \boldsymbol{\gamma}_m \nabla^m \boldsymbol{x}_n$$

the formulation depicted in Eq. 1 is equivalent to the following formulation [3]

$$(1-\kappa)\boldsymbol{\gamma}_k\left(\boldsymbol{x}_{n+1} - \boldsymbol{x}_{n+1}^{(0)}\right) + \sum_{m=1}^{k} \boldsymbol{\gamma}_m \nabla^m \boldsymbol{x}_n - h\boldsymbol{F}(t_{n+1}, \boldsymbol{x}_{n+1}) = 0$$

The actual solving of the DAE system uses a Newton iteration scheme with the current iteration step i as [3]

$$\triangle^{(i)} = \boldsymbol{x}_{n+1}^{(i+1)} - \boldsymbol{x}_{n+1}^{(i)}$$

and the correction is gained by solving [3]

$$\left(\boldsymbol{I} - \frac{h}{(1-\kappa)\gamma_k}\boldsymbol{J_F} \right)\triangle^{(i)} \; = \; \frac{h}{(1-\kappa)\gamma_k}\boldsymbol{F}(t_{n+1}, \boldsymbol{x}_{n+1}^{(i)}) - \boldsymbol{\Gamma} - \left(\boldsymbol{x}_{n+1}^{(i)} - \boldsymbol{x}_{n+1}^{(0)} \right)$$

where $\boldsymbol{J_F}$ is an approximation of the jacobian matrix for $\boldsymbol{M}^{-1}\boldsymbol{f}$ and $\boldsymbol{\Gamma}$ is defined as

$$\boldsymbol{\Gamma} \; = \; \frac{1}{(1-\kappa)\gamma_k}\sum_{m=1}^{k}\boldsymbol{\gamma}_m\nabla^m\boldsymbol{x}_n$$

which remains constant during a single integration step. The jacobian $\boldsymbol{J}$ is multiplied via the inversed mass matrix $\boldsymbol{M}^{-1}$ and the iteration Matrix $\boldsymbol{M}_i$ is obtained via multiplying with $\boldsymbol{M}$ as [3]

$$\boldsymbol{M} - \frac{h}{(1-\kappa)\gamma_k}\boldsymbol{J}$$

Simulation error for CC charge and discharge of MATLAB®-code PCMs and benchmark models
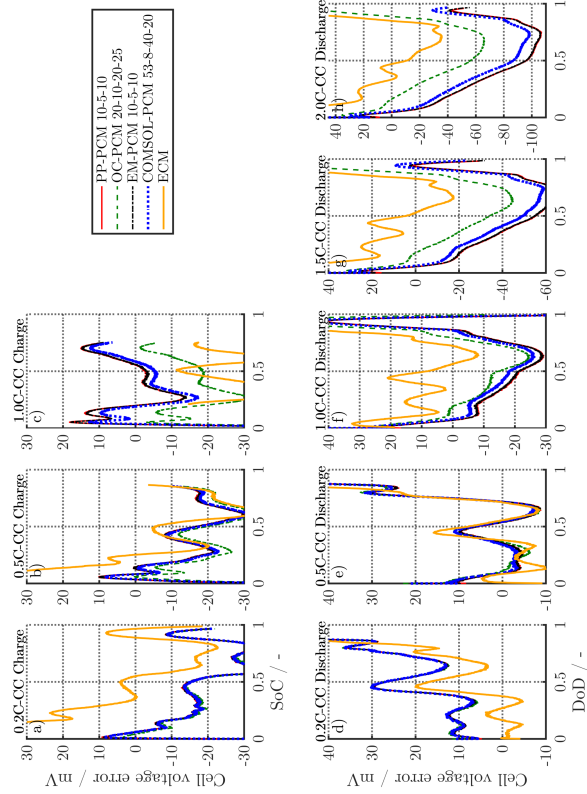
Figure 3: Cell voltage error for 0.2 (a), 0.5 (b) and 1.0C constant current charge and 0.2 (d), 0.5 (e), 1.0C (f), 1.5C (g) and 2.0C (h) constant current discharge to measurements of the INR18650-MJ1 LIB at 25 °C and convective cooling of $1\,\mathrm{m\,s^{-1}}$ [6]. The plot shows the simulation results of the MATLAB®-code PP- ('red'), EM- ('black') and OC-PCM ('green') with rigorous spatial configurations together with the ECM ('orange') and COMSOL-PCM ('blue') benchmark models.
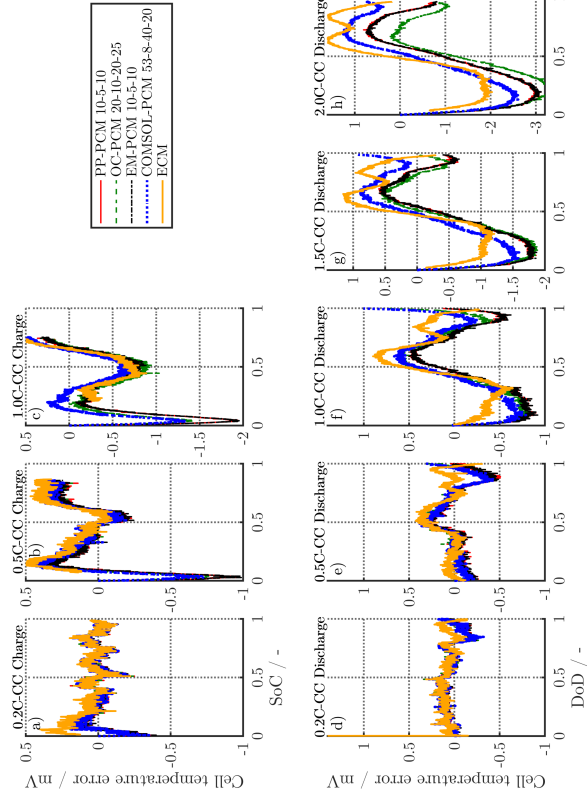
Figure 4: Cell temperature error at 0.2 (a), 0.5 (b) and 1.0C constant current charge and 0.2 (d), 0.5 (e), 1.0C (f), 1.5C (g) and 2.0C (h) constant current discharge to measurements of the INR18650-MJ1 LIB at 25 °C and convective cooling of 1 m s⁻¹ [6]. The plot shows the simulation results of the MATLAB®-code PP- ('red'), EM- ('black') and OC-PCM ('green') with rigorous spatial configurations together with the ECM ('orange') and COMSOL-PCM ('blue') benchmark models.

Simulation error for CC charge and discharge of C-Code PCMs on the STM32 microcontroller
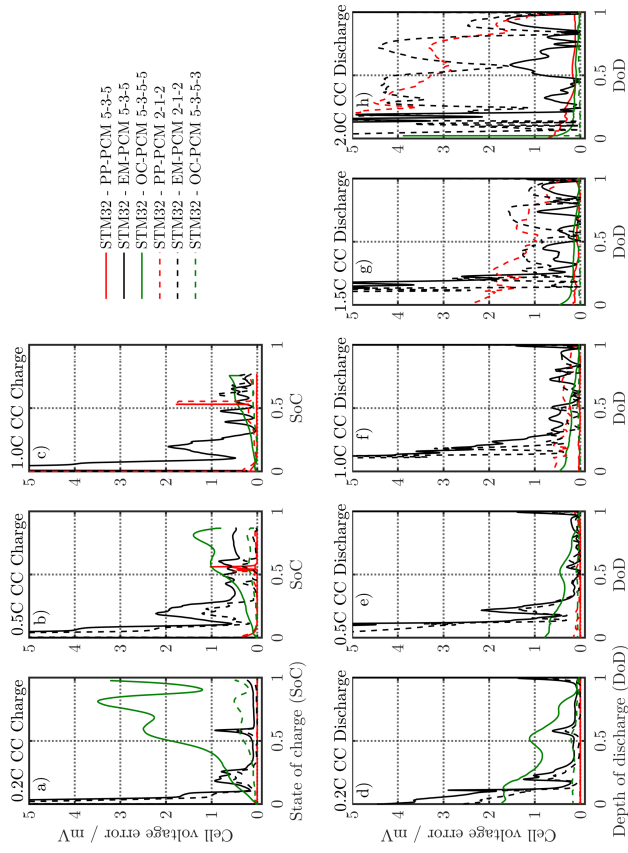
Figure 5: Implementation error on the STM32 microcontroller at 0.2 (a), 0.5 (b) and 1.0C constant current charge and 0.2 (d), 0.5 (e), 1.0C (f), 1.5C (g) and 2.0C (h) constant current discharge in reference to the corresponding MATLAB®-code PCM. The plot shows the errors of the C-code STM32 PP- ('red'), EM- ('black') and OC-PCM ('green') with coarse ('dotted line') and maximum ('solid line') spatial configuration.

Reducing measurement-related polarization effects for driving cycle scenario simulation
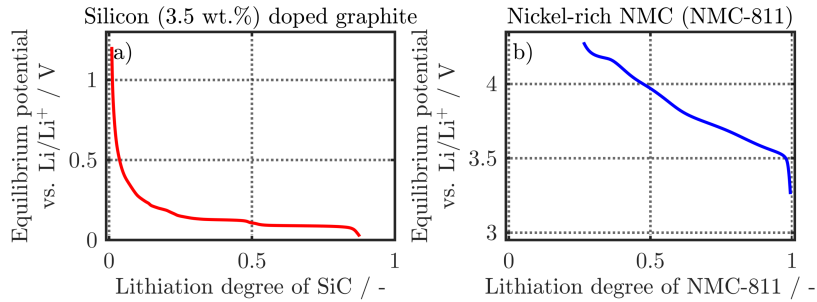
Figure 6: Equilibrium potential vs. Li/Li$^+$ of the graphite-silicon composite (3.5 wt.-% of Si, derived from ICP-OES [6]) anode (b) and the nickel-rich NMC (NMC-811, ICP-OES [6]) cathode (b) over the lithiation range. The averaged profiles are derived from measured charge and discharge open-circuit potentials ($0.01C \equiv 80\mu A$) of self-made, custom-built CR2032-type coin cells including $\oslash 14$ mm single-side coated electrode samples from the INR18650-MJ1 full cell versus lithium-metal [6].

Acknowledgement

References

[1] I. Zilberman, A. Rheinfeld, A. Jossen, Uncertainties in entropy due to temperature path dependent voltage hysteresis in li-ion cells, Journal of Power Sources 395 (2018) 179–184. doi:10.1016/j.jpowsour.2018.05.052.

8

[2] The MathWorks, Mathworks' documentation on 'solve stiff differential equations and daes — variable order method', url: https://www.mathworks.com/help/matlab/ref/ode15s.html 2018.

[3] L. F. Shampine, M. W. Reichelt, The matlab ode suite, SIAM Journal on Scientific Computing 18 (1) (1997) 1–22. doi:10.1137/S1064827594276424.

[4] L. F. Shampine, M. W. Reichelt, J. A. Kierzenka, Solving index-1 daes in matlab and simulink, SIAM Review 41 (3) (1999) 538–552. doi:10.1137/S003614459933425X.

[5] W. Klopfenstein, Numerical differentiation formulas for stiff systems of ordinary differential equations, RCA Review 32 (1971) 447–462.

[6] J. Sturm, A. Rheinfeld, I. Zilberman, F. B. Spingler, S. Kosch, F. Frie, A. Jossen, Modeling and simulation of inhomogeneities in a 18650 nickel-rich, silicon-graphite lithium-ion cell during fast charging, Journal of Power Sources 412 (2019) 204–223. doi:10.1016/j.jpowsour.2018.11.043.

D Supplementary part of the article titled *On The Impact of the Locality on Short-Circuit Characteristics: Experimental Analysis and Multiphysics Simulation of External and Local Short-Circuits Applied to Lithium-Ion Batteries* (see section 5.2)

On the Impact of the Locality on Short-Circuit Characteristics - Experimental Analysis and Multiphysics Simulation of External and Local Short-Circuits applied to Lithium-Ion Batteries

Sturm, J.,*,† Rheinfeld, A.,† Buzon, D.,‡,¶ and Jossen, A.†,§

†*Technical University of Munich (TUM), Institute for Electrical Energy Storage Technology (EES), Arcisstrasse 21, 80333 Munich, Germany*

‡*Univ. Grenoble Alpes, 38000 Grenoble, France*

¶*CEA, Liten, 38054 Grenoble, France*

§*Munich School of Engineering (MSE), Technical University of Munich (TUM), Lichtenbergstr. 4a, 85748 Garching, Germany*

E-mail: johannes.sturm@tum.de

Phone: +49 (0)89 289-26967

Supplementary material

Calibration of the calorimetric test bench

In accordance with our previous work,[1] the calibration and measurement procedure for the calorimetric test bench applied in this work was chosen adequately. The main steps to calculate the heat generation rate from the measured temperature signals are outlined

1

here. The calibration or test cells for applying short-circuits are both mechanically clamped between the copper bars as depicted in the manuscript (see Fig. 1). The applied heat rate ($\dot{Q}_{tot}^*$) from either the calibration procedure ($U_{app} \cdot I_{app}$) or the ESC/LSC tests translates into a rise in mean temperature ($\bar{T}$) of both the copper bars and the cell itself weighed with the individual heat capacities ($C_{p,i}$) and corrected with the heat exchange ($\alpha_{cu,i}$) of the copper bars with the environment (T_∞) as:

$$\dot{Q}_{tot}^* = C_{p,1} \frac{d\bar{T}_{cu,1}}{dt} + C_{p,2} \frac{d\bar{T}_{cu,2}}{dt} + C_{p,c} \frac{d\bar{T}_c}{dt} + \alpha_{cu,1} (\bar{T}_{cu,1} - T_\infty) + \alpha_{cu,2} (\bar{T}_{cu,2} - T_\infty) \tag{1}$$

The heat transfer coefficients ($\alpha_{cu,i}$) represent the heat losses from the test bench via wiring and insulation imperfections[1] which can be related to each of the two copper bars. For a first estimate of the overall heat capacities of the two copper bars and the cell itself ($C_{p,i}$), the weight and specific heat capacity of each component must be considered. As outlined in our previous work,[1] the temperature measured in the center of each copper bar can be used to estimate its average temperature ($\bar{T}_{cu,i}$), as the related error is below the measurement accuracy. The average cell temperature ($\bar{T}_{cell}$) is estimated from measuring the temperature at the positive terminal.[1]

By carrying out the calibration procedure, the heat exchange with the environment can be determined. After heating up the setup via using a calibration cell with two resistive heaters,[1] the cooling phase can be analyzed assuming a homogeneous temperature distribution within each copper bar:

$$C_{p,i} \frac{d\bar{T}_{cu,i}}{dt} = \alpha_{cu,i} (T_\infty - \bar{T}_{cu,i}) \quad \text{with} \quad i = 1, 2 \tag{2}$$

This resembles an ordinary differential equation (ODE) which can be solved via an exponential approach which essenially fits the predicted temperature to the measured temperature data[1]:

$$\Theta_i = exp\left(\frac{\alpha_{cu,i}}{C_{p,i}} \cdot t\right) \quad \text{with} \quad i = 1, 2 \quad \text{and} \quad \Theta_i = \frac{\bar{T}_{cu,i} - T_\infty}{\bar{T}_{cu,i,t=0} - T_\infty} \tag{3}$$

After quantifiying the heat losses, the adiabatic temperature ($\bar{T}_{ad,i}$) of each copper bar can be calculated as[1]:

$$\bar{T}_{ad,i} = \bar{T}_{cu,i} + \frac{\alpha_{cu,i}}{C_{p,i}} \int_t (\bar{T}_{cu,i} - T_\infty) \, dt \quad \text{with} \quad i = 1, 2 \tag{4}$$

The applied heat rate $(\dot{Q}_{tot}^*)$ can be finally calculated as[1] :

$$\dot{Q}_{tot}^* = C_{p,1}\frac{d\bar{T}_{ad,1}}{dt} + C_{p,2}\frac{d\bar{T}_{ad,2}}{dt} + C_{p,c}\frac{d\bar{T}_c}{dt} \tag{5}$$

which can be used to correct the calculated overall heat capacities of each individual component by applying a linear fit to the measured total heat Q_{tot}[1] :

$$Q_{tot} = C_{p,1}(\bar{T}_{ad,1} - \bar{T}_{cu,1,t=0}) + C_{p,2}(\bar{T}_{ad,2} - \bar{T}_{cu,2,t=0}) + C_{p,c}(\bar{T}_c - \bar{T}_{c,t=0}) \tag{6}$$

After determining the heat losses to the ambience in the calibration procedure, the actual heat rate and total amount of heat calculated from the temperature signals must be corrected due to thermal inertia of the calorimetric setup. In short, the measured temperature rise is delayed compared to the actual heat generation rate onset. To account for this time lag $(\triangle t_\infty)$ and to correct the estimated heat rate $(\dot{Q}_{tot}^*)$ and generated heat (Q_{tot}^*), dimensionless heat (Ψ) and time (τ) are introduced as[1] :

$$\Psi = \frac{Q}{\triangle Q_\infty} \quad \text{with} \quad \tau = \frac{\tau}{\triangle t_\infty} \tag{7}$$

The heat offset $(\triangle Q_\infty)$ resembles the amount of heat, which cannot be measured due to the time lag of the measurement equipement. Following the work of Rheinfeld et al.,[1] the corrected heat rate $(\dot{Q}_{tot})$ and heat dissipation (Q_{tot}) can be calculated as:

$$Q_{tot} = Q_{tot} + \triangle t_\infty \cdot \dot{Q}_{tot} \cdot \left(1 - exp\left(-\frac{t}{\triangle t_\infty}\right)\right) \tag{8}$$

$$\dot{Q}_{tot} = \dot{Q}_{tot}\left(1 + exp\left(-\frac{t}{\triangle t_\infty}\right)\right) \tag{9}$$

The calibration procedure for the applied heat rates of 0.1, 5, and 10 W is shown in Fig. 1 and results in a time lag of 5.902 s (see subplot c) and a linearized heat offset according to Fig. 1 b. The normalized heat of the two copper bars $(\Psi_{cu,i})$, the cell (Ψ_{tab}), their superposition (Ψ_{tot}) and linearization (Ψ_{lin}), as well as the actual applied heat (Ψ_{app}) by the calibration cell at 5 W is shown in Fig. 1 a. In terms of the ESC and LSC tests, the time lag and the linerarized heat rate are used
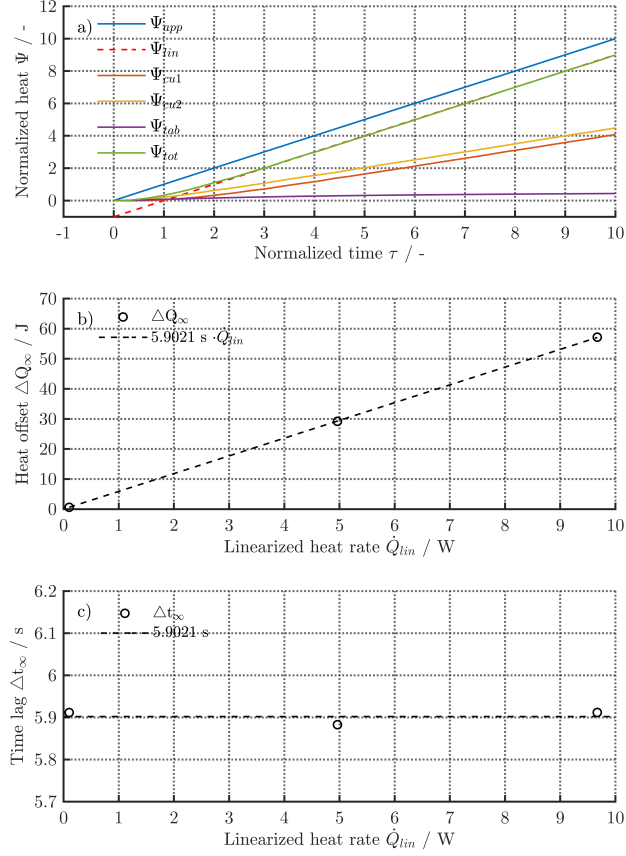
3

Figure 1: Calibration results for the calorimetric test bench showing the normalized heat (a) of the copper bars ($\Psi_{cu,i}$), the cell (Ψ_{tab}), their superposition (Ψ_{tot}) and linearization (Ψ_{lin}), as well as the applied heat via the calibration cell at $5\,\mathrm{W}$ (Ψ_{app}). Subplot b) shows the linearized heat offset ($\triangle Q_\infty$) and the time lag ($\triangle t_\infty$) for all three calibration procedures over the linearized heat rate in subplot c).

to correct the measured temperature rises in order to derive sufficiently accurate heat dissipation and heat generation rate during the shorting scenarios.

4

Effective polarization of ESC tests applied to single-layered pouch-type LIBs
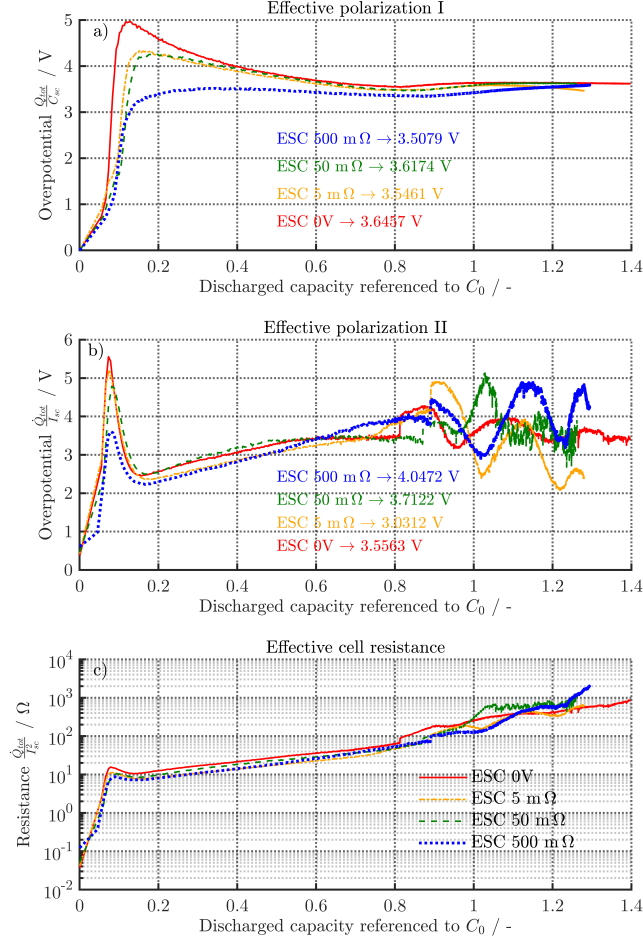
Figure 2: Effective polarization profiles (a and b) of the four ESC tests (i.e. 0 V as well as 5, 50, and 500 mΩ) calculated from the total heat and capacity ('Effective polarization I', $\frac{Q_{tot}}{C_{sc}}$) and the heat rate and the shorting current ('Effective polarization II', $\frac{\dot{Q}_{tot}}{I_{sc}}$) over the discharged capacity referenced to the capacity measured in the check-up cycles (C_0). The polarization values on average are depicted for all ESC tests in subplot a) and b). Subplot c) shows the calculated effective resistance from the heat rate and the shorting current ('Effective cell resistance', $\frac{\dot{Q}_{tot}}{I_{sc}^2}$).

5

Post-mortem analysis of ESC and LSC tests

The *post-mortem* analysis incorporates visual inspection, scanning electrode microscopy (SEM) at different magnification levels, and energy dispersive X-ray spectrometry (EDX) measurements for all ESCs applied to single-layerd pouch-type LIBs (i.e. $0\,\text{m}\Omega$ resp. $0\,\text{V}$ as well as 5, 50, and $500\,\text{m}\Omega$). In case of the LSC tests, a single cell of each configuration (i.e. P1, P2, P3, and P4) shorted with the $1\,\text{mm}$ stainless steel needle is analyzed.
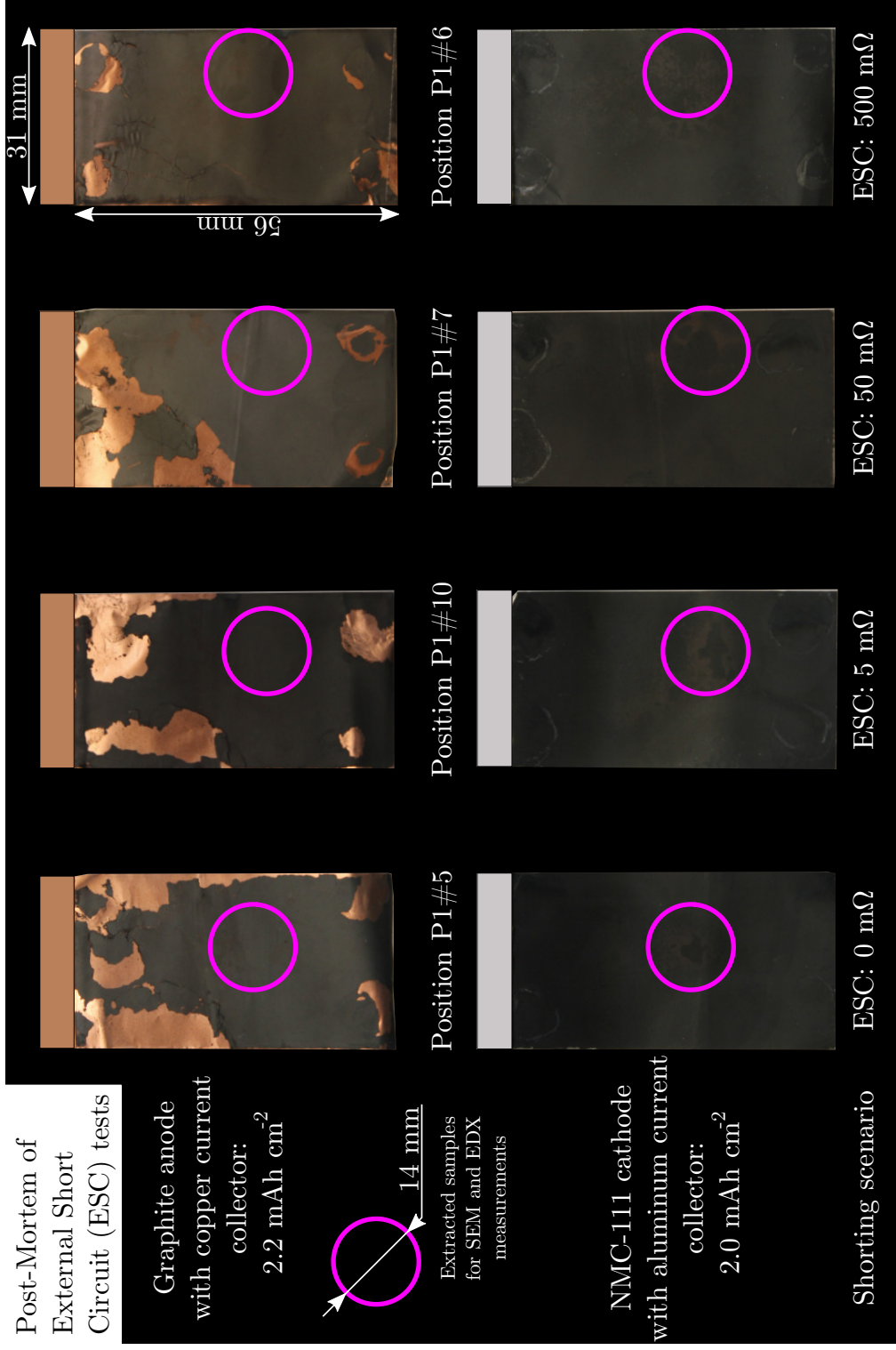
Figure 3: Visual inspection of the four ESC tests (i.e. $0\,\mathrm{m\Omega}$ resp. $0\,\mathrm{V}$ as well as 5, 50, and $500\,\mathrm{m\Omega}$) applied to single-layered (configuration P1) pouch-type graphite ($2.2\,\mathrm{mAh\,cm^{-2}}$)/NMC-111 ($2.0\,\mathrm{mAh\,cm^{-2}}$) LIBs. The position of the extracted samples for SEM and EDX analysis is depicted with the purple circle ($\oslash\,14\,\mathrm{mm}$) at every anode and cathode electrode sheet.
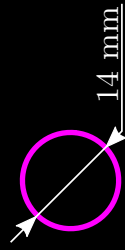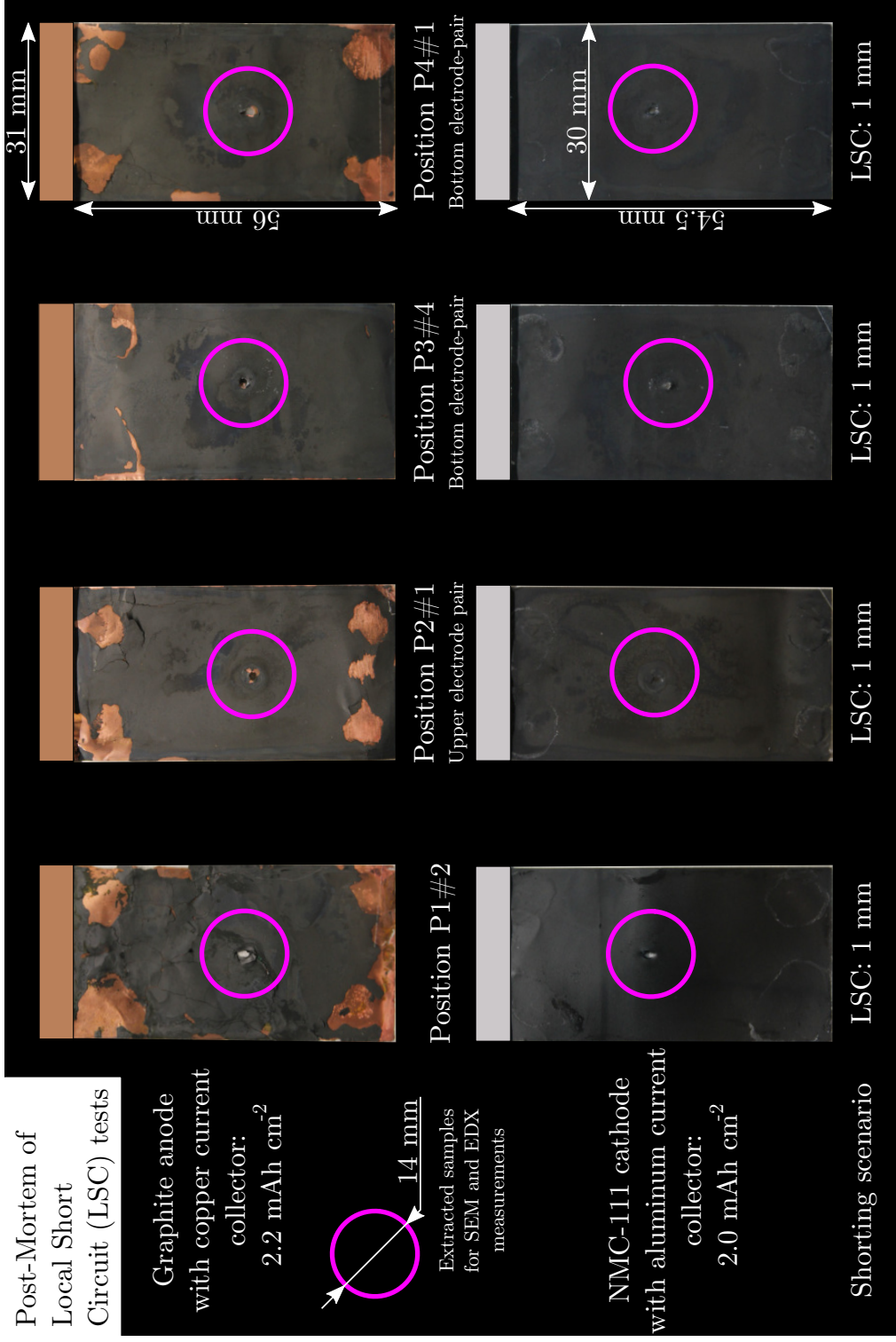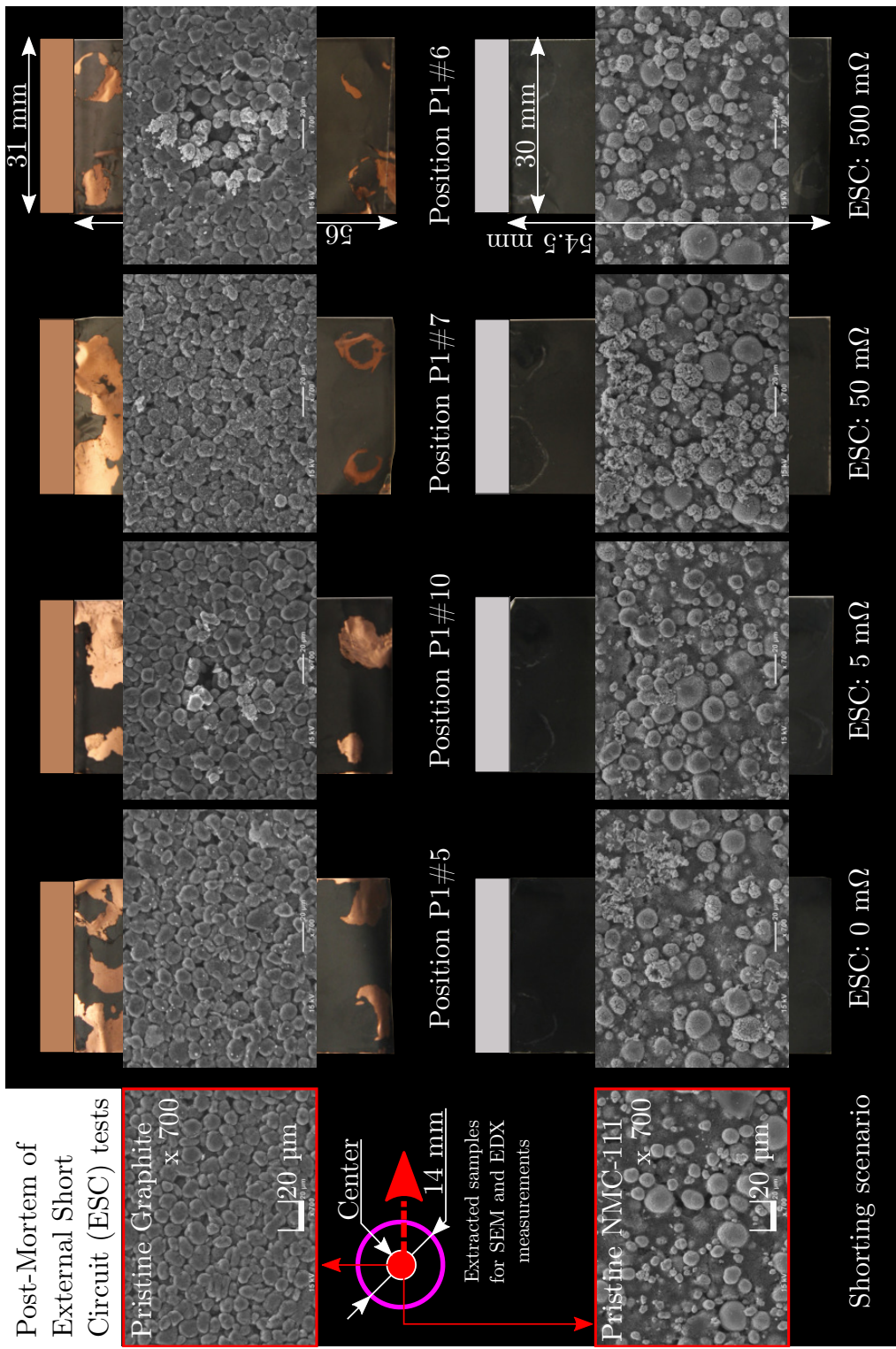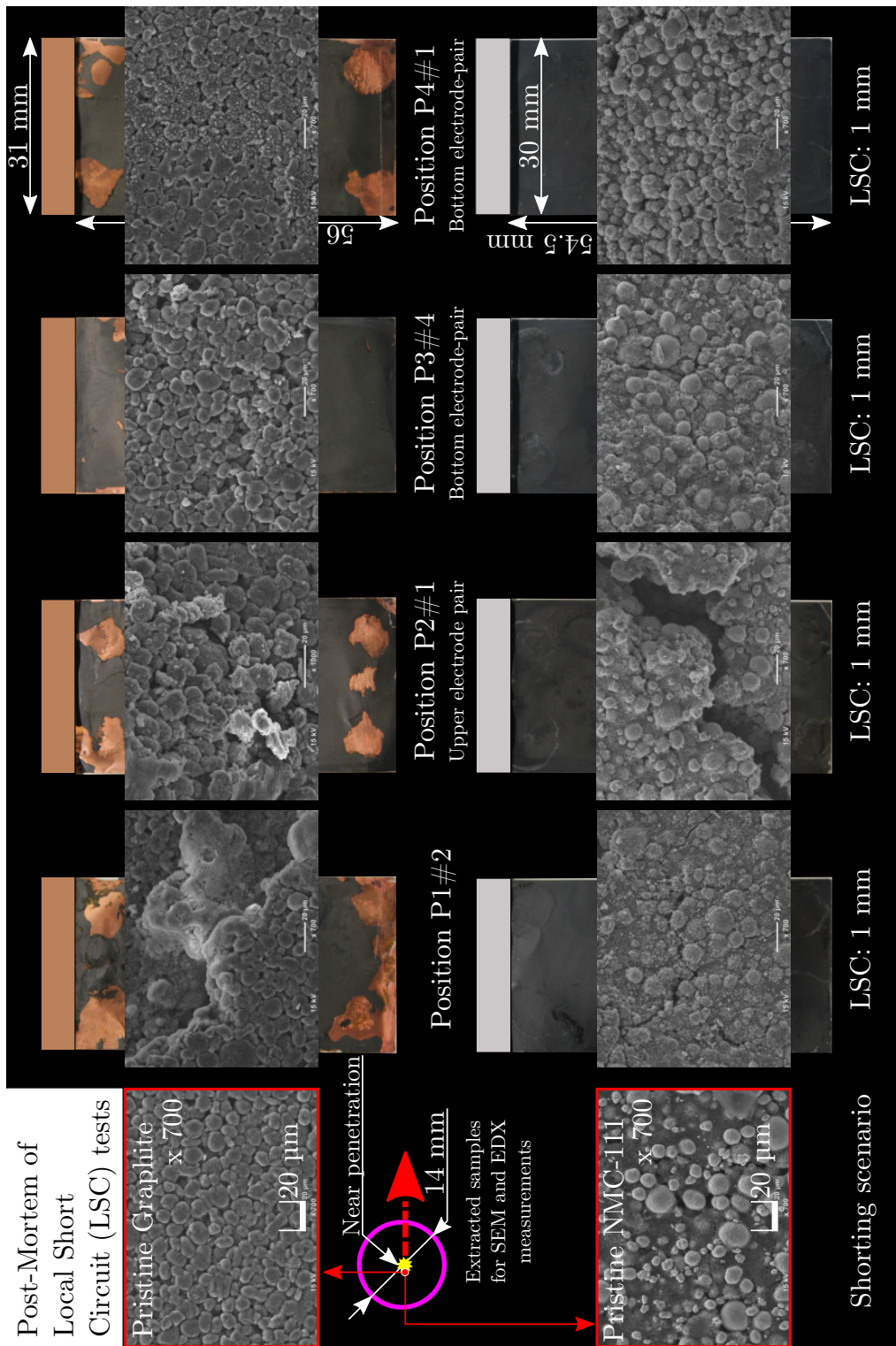
Figure 4: Visual inspection of the four analyzed LSC tests (i.e. a single cell of configuration P1, P2, P3, and P4) applied to the pouch-type graphite $(2.2\,\mathrm{mAh\,cm^{-2}})$/NMC-111 $(2.0\,\mathrm{mAh\,cm^{-2}})$ LIBs with the 1 mm stainless steel needle. In case of the double-layered LIBs (P2, P3, and P4), the chosen electrode pair (upper or bottom pair) for the analysis is denoted. The position of the extracted samples for SEM and EDX analysis is depicted with the purple circle ($\varnothing$ 14 mm) at every anode and cathode electrode sheet.

Figure 5: SEM images of the four ESC scenarios (i.e. $0\,\mathrm{m\Omega}$ resp. $0\,\mathrm{V}$ as well as 5, 50, and $500\,\mathrm{m\Omega}$) applied to single-layered (configuration P1) pouch-type graphite $(2.2\,\mathrm{mAh\,cm^{-2}})$/NMC-111 $(2.0\,\mathrm{mAh\,cm^{-2}})$ LIBs. The magnification level is chosen to 700 and the comparison to pristine graphite and NMC-111 (i.e. before the ESC) is given as a reference. The sample magnifications are taken from the center of the extracted samples described in Fig. 3.

9

Figure 6: SEM images of the four analyzed LSC scenarios (i.e. a single cell of configuration P1, P2, P3, and P4) applied to the pouch-type graphite (2.2 mAh cm^{-2})/NMC-111 (2.0 mAh cm^{-2}) LIBs with the 1 mm stainless steel needle. In case of the double-layered LIBs (P2, P3, and P4), the chosen electrode pair (upper or bottom pair) for the analysis is denoted. The magnification level is chosen to 700 and the comparison to pristine graphite and NMC-111 (i.e. before the LSC) is given as a reference. The sample magnifications are taken from the center of the extracted samples described in Fig. 4.

10
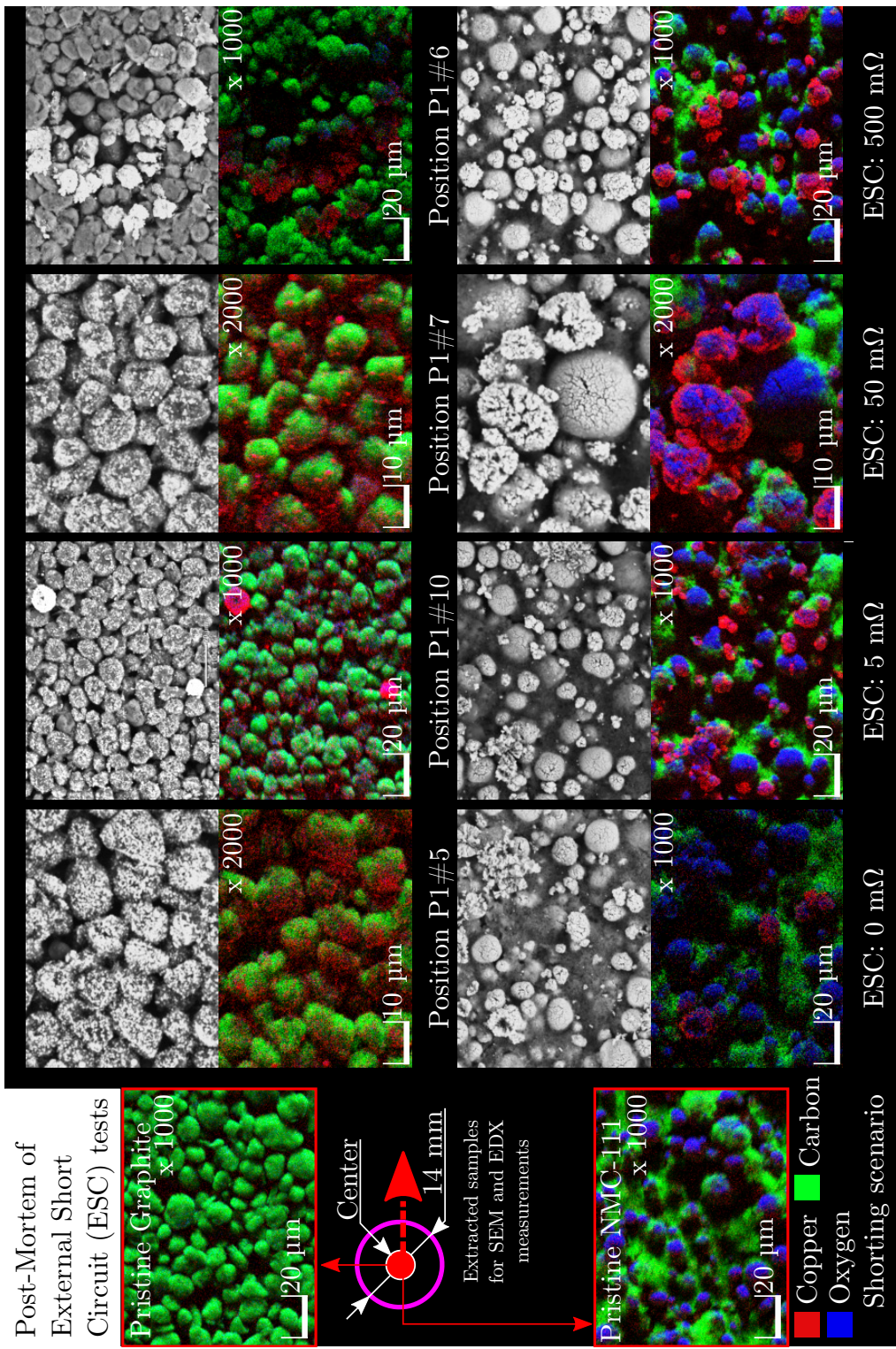
Figure 7: EDX analysis to detect copper (red), carbon (green), and oxygen (blue) of the four ESC scenarios (i.e. $0\,\mathrm{m\Omega}$ resp. $0\,\mathrm{V}$ as well as 5, 50, and $500\,\mathrm{m\Omega}$) applied to single-layered (configuration P1) pouch-type graphite ($2.2\,\mathrm{mAh\,cm^{-2}}$)/NMC-111 ($2.0\,\mathrm{mAh\,cm^{-2}}$) LIBs. The magnification level is chosen to 1000 or 2000 and the comparison to pristine graphite and NMC111 (i.e. before the ESC) is given as a reference. The sample magnifications are taken from the center of the extracted samples described in Fig. 3. Deposition of primarily dissolved copper from the negative current collector is clearly seen on both electrodes.
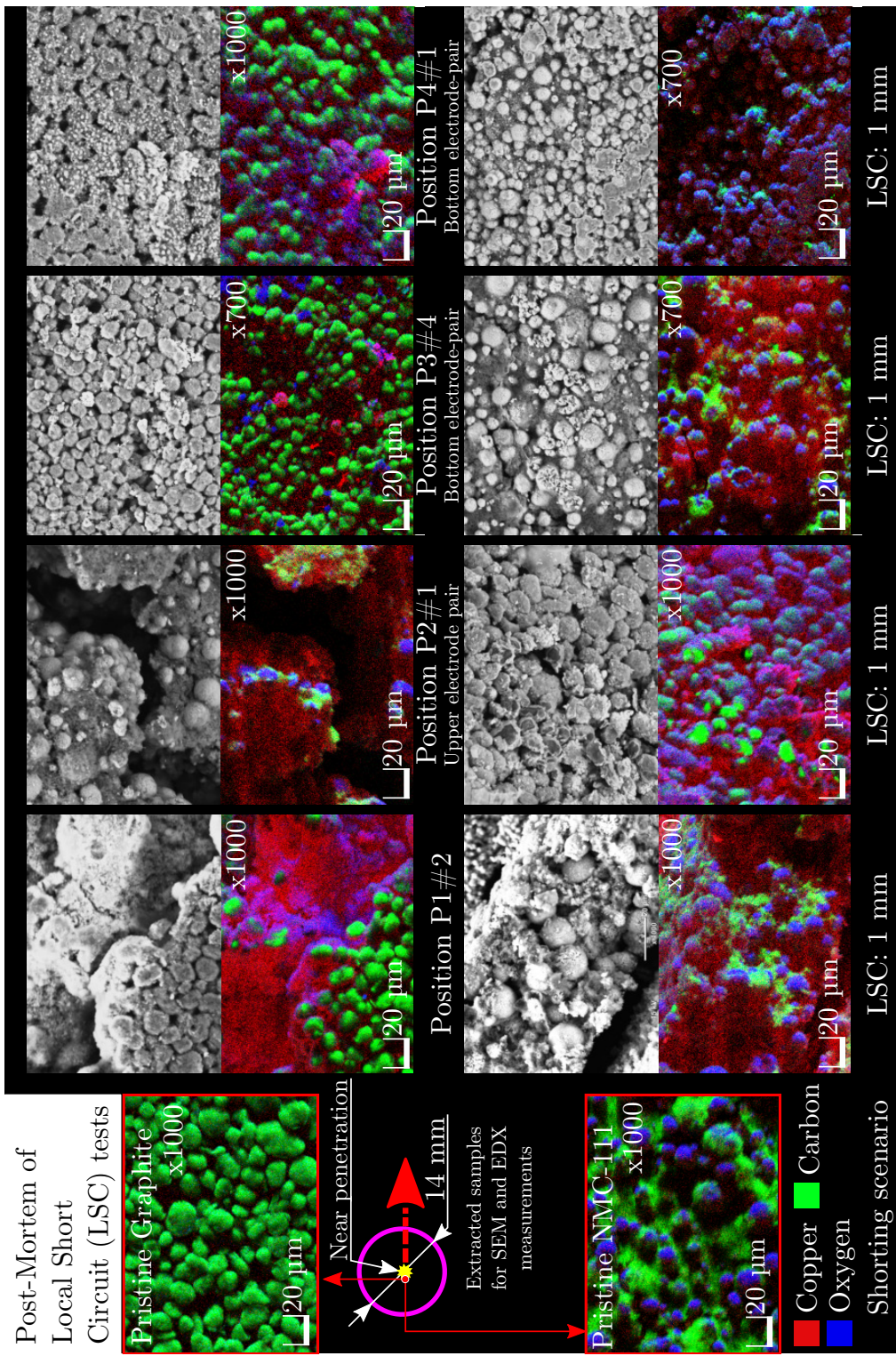
Figure 8: EDX analysis to detect copper (red), carbon (green), and oxygen (blue) of the four analyzed LSC tests (i.e. one single cell of pconfiguration P1, P2, P3, and P4) applied to the pouch-type graphite (2.2 mAh cm⁻²)/NMC-111 (2.0 mAh cm⁻²) LIBs with the 1 mm stainless steel needle. In case of the double-layered LIBs (P2, P3, and P4), the chosen electrode pair (upper or bottom pair) for the analysis is denoted. The magnification level is chosen to 700 or 1000 and the comparison to pristine graphite and NMC-111 (i.e. before the LSC) is given as a reference. The sample magnifications are taken from the center of the extracted samples described in Fig. 4. Deposition of primarily dissolved copper from the negative current collector is clearly seen on both electrodes.

Modelling and simulation of ESC and LSC applied to single-layered pouch-type LIBs

The basic modelling approach refers to our previous works[2–5] presenting our multi-dimensional modelling (MuDiMod) framework. Fig. 9 shows a schematic overview of the MuDiMod approach incorporating the electrochemical unit cell model[6] (so called pseudo two-dimensional model (p2D)) and the 2D electrical model. 25 p2D models are connected in parallel via the current collectors
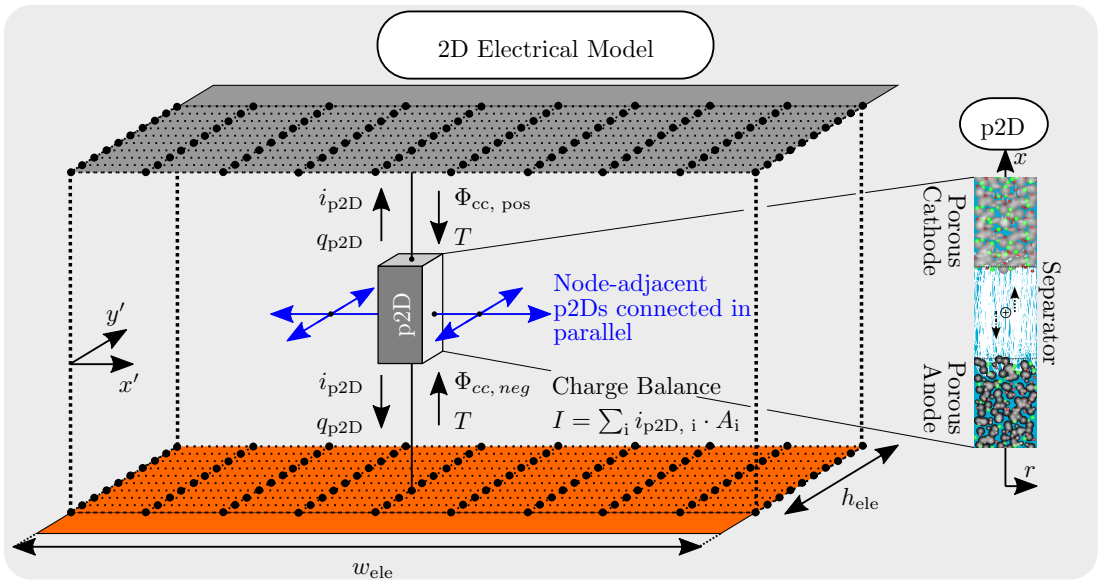

Figure 9: Schematic overview of the MuDiMod framework consisting of several, parallel-connected electrochemical unit cell models (i.e. p2D models) for the electrode stack and the 2D electrical model to simulate polarization effects on the current collectors.

in the 2D electrical model to simulate the concentrations, potentials , and intercalation reaction kinetics in and between the active material particles, the electrolyte, and the separator domain. The copper and aluminum current collector are represented in the 2D electrical model and depict the electrical potential distribution. In this work, we use the MuDiMod approach with several adaptions for the solid and liquid phase[7,8] in terms of the electrochemical unit cell model (i.e. p2D model) to simulate high current scenarios. Incorporating limiting mechanisms of the molar flux (j_n) referring to depletion or oversaturation of lithium-ions in the pore (i.e. electrolyte) or the particle (i.e. active material) is crucial[7,9] to correctly simulate the cell's behavior under high current

scenarios. These adaptions are depicted in Table. 1 accounting for modified Butler-Volmer equations together with the fundamental set of differential algebraic equations. To simulate ESC scenarios, the cell is shorted via an external resistance (R_{ESC}) as presented in our previous work.[7] Model validation was shown in our previous work[7] for a single, high current modified p2D model regarding P1-type, graphite/NMC-111 cells as investigated in this work. The related parameterization of the MuDiMod approach is depicted in Table 2 and Table 3. In case of the LSC simulation, a single p2D model is modified[10,11] enabling an electron current flux across the separator, which represents a shorted area of approximately 6 % of the entire active electrode area with an electrical conductivity of $2.857{\times}10^6\,\mathrm{S\,m^{-1}}$ approximating the short-circuit resistance of a stainless-steel needle penetrating the electrode stack.

The ESC and LSC simulation model can be then to simulate a shorting scenario which shows a similar current flux either across the terminals or through the shorted area of the separator. Due to computational limitations of the LSC simulation model, the maximum shorting current (I_{ESC} and I_{LSC}) at the beginning of the simulations ($t = 1\,\mathrm{ms}$) appears to be around 6.6 A as shown in Fig. 10 a, which corresponds to an ESC with an external resistance of $243.9\,\mathrm{m\Omega}$ similar to the cell's initial impedance seen in the experimental tests of this work. The highest deviance between the simulations appears in the transition zone I-II with maximum deviances around 580 mA. Nevertheless, in the very beginning (i.e. zone I) a good match appears and due to the different application of the shorting condition, different electrical potential distributions appear across the electrodes and the copper/aluminum current collector as shown in Fig. 11, which still deliver the same shorting current. The significant difference in the electrical potential distribution shown at 1 ms in Fig. 11 a/b for the ESC and e/f for the LSC simulation shows the different local polarization across the electrode (see also Fig. 11 d and h over time), which results in different terminal voltages (see Fig. 11 c and g) shown together in Fig.10 b with their related difference (10 e).
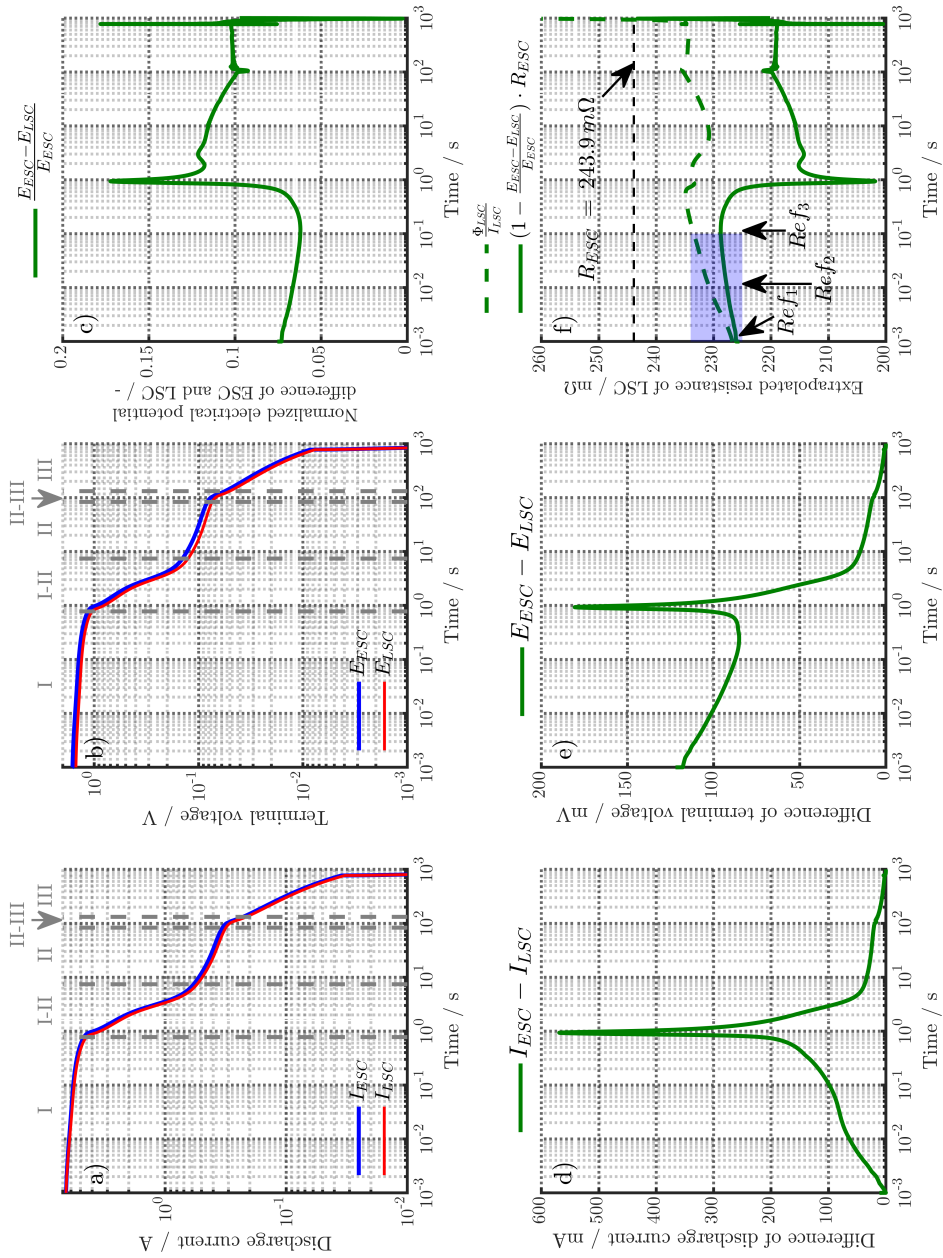
14

Figure 10: Simulation results of the ESC ($243.9\,\mathrm{m\Omega}$) and the LSC scenario resulting in the same shorting currents (see I_{ESC} and I_{LSC} in a) applied to the P1-type pouch-type cells of this work. The current deviance is shown in d) and the resulting terminal voltages (E_{ESC} and E_{LSC}) are shown in b) with the related error in e). The normalized error is shown in c), which is used for extrapolation of the shorting resistance from the ESC to the LSC scenario resulting in the resistance profile shown in f) together with the simulated resistance during the LSC $\frac{\Phi_{LSC}}{I_{LSC}}$ and the constant external resistance R_{ESC}.

15

As a result, simulating two shorting scenarios revealing the same shorting current show different local polarization across the electrode depending on the local application of the shorting condition, which result in a significant terminal voltage offset. Using the normalized terminal voltage offset ($\frac{E_{ESC}-E_{LSC}}{E_{ESC}}$) shown in Fig. 10 c, an extrapolation of the internal short-circuit resistance of the LSC simulation can be derived ($1 - \frac{E_{ESC}-E_{LSC}}{E_{ESC}} \cdot R_{ESC}$) as shown in Fig. 10 g. The comparison to the simulated resistance ($\frac{\Phi_{LSC}}{I_{LSC}}$) using the potential drop (Φ_{LSC}) between the current collectors as indicated in Fig. 11 (i.e. P2-P3), shows errors of 0.3, 1.3, and 2 % at 1, 10 and 100 ms (see Ref_1, Ref_2, and Ref_3 in Fig.10 f) for extrapolating the shorting resistance from the ESC to the LSC simulation.

The normalized terminal voltage error at 100 ms accounts to 0.062 and will be used in this work as correction factor for the measured terminal voltages of the LSC test applied to P1-type cells to correlate the shorting resistance and shorting current to the ESC tests appied to the P1-type cells, which showed higher and lower terminal voltages.

Future work will focuss on a more detailed validation of the simulation results and further improving both the quasi-isothermal test bench (i.e. damping of the mechanical oscillation effects in the very beginning of the short-circuit) and the multidimensional multiphysics model approach (i.e. incorporating degradation effects and investigating altering contact conditions at the penetration site).
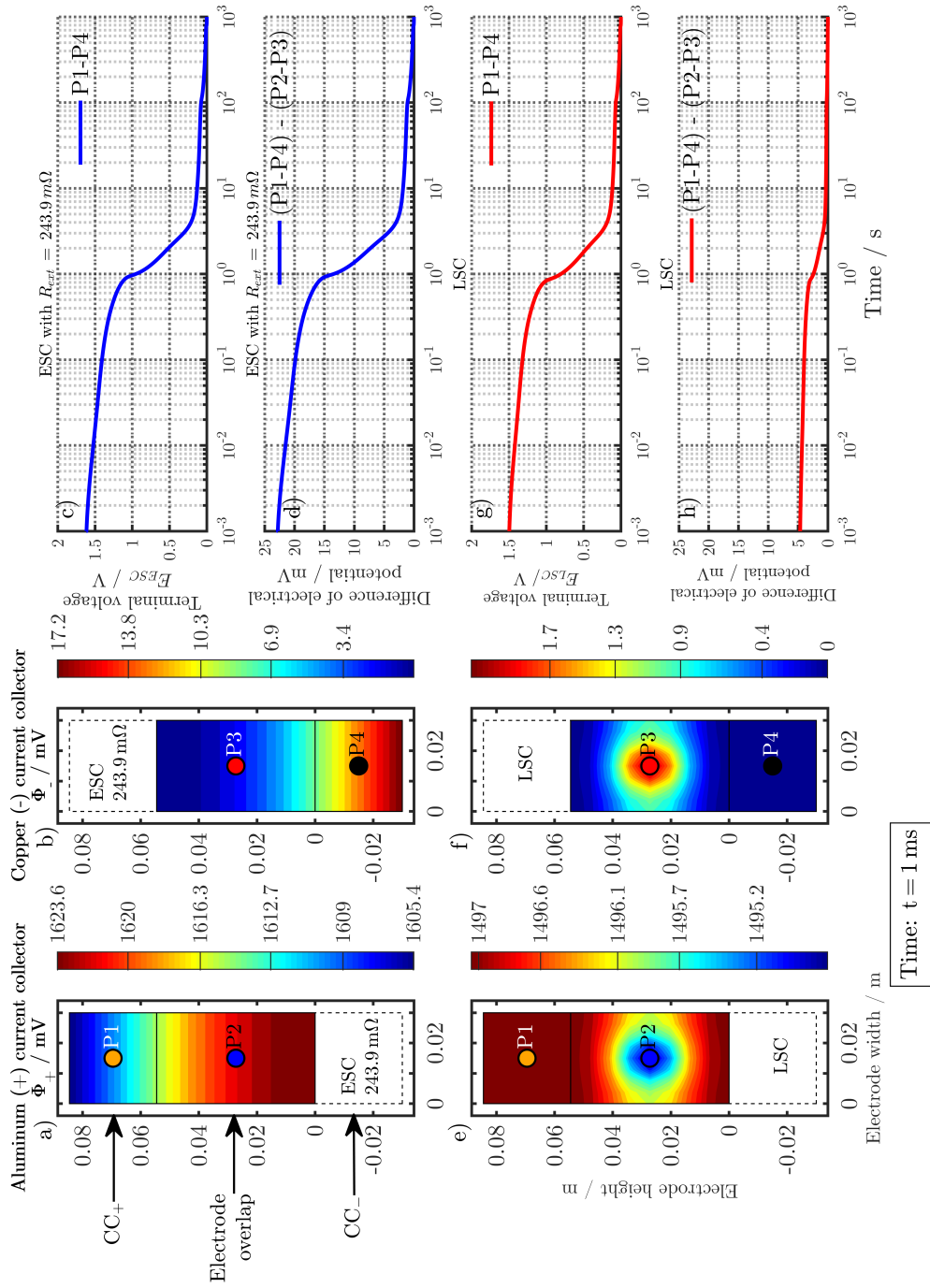
Figure 11: Simulation results of the ESC (243.9 mΩ) and the LSC scenario resulting in the same shorting currents (I_{ESC} and I_{LSC}) applied to the P1-type pouch-type cells of this work. The electrical potential ($\Phi_{\pm}$) across the positive (+, a and e) and negative (−, b and f) current collector (CC) is depicted for the ESC (a and b) and LSC (e and f) at 1 ms after the shorting. The terminal voltage corresponds to the electrical potential difference between the current collector tabs (see 'P1-P4', c and h) and the polarization difference from the terminals to the center of the cell is shown in subplot d) and h).

17

Table 1: Equations for the multidimensional multiphysics model (MuDiMod framework)

Electrochemical unit cell model (i.e. p2D model)	
Mass balance [I]	$\varepsilon_l \frac{\partial c_l(x,t)}{\partial t} = \frac{\partial}{\partial x}\left(D_l^{eff}\frac{\partial c_l(x,t)}{\partial x} + \frac{i_l(x,t)\,(1-t_+^0)}{F}\right)$
	$\varepsilon_s \frac{\partial c_s(x,t,r)}{\partial t} = \frac{1}{r^2}\frac{\partial}{\partial r}\left(D_s r^2 \frac{\partial c_s(x,t,r)}{\partial r}\right)$
Potentials [I]	$\frac{\partial \Phi_l(x,t)}{\partial x} = -\frac{i_l(x,t)}{\kappa_l^{eff}} + \frac{2\,R\,T}{F}\left(1-t_+^0\right)\left(1+\frac{d\,ln f_\pm}{d\,ln\,c_l(x,t)}\right)\frac{\partial\,ln\,c_l(x,t)}{\partial x}$
	$\frac{\partial \Phi_s(x,t)}{\partial x} = -\frac{i_{app}(t)-i_l(x,t)}{\sigma_s} \quad \text{with} \quad i_{app}(t) = i_s(x,t) + i_l(x,t) \quad \forall\, x, t$
Charge balance [I]	$\frac{\partial i_l(x,t)}{\partial x} + \frac{\partial i_s(x,t)}{\partial x} = 0 \quad \text{with} \quad \frac{\partial i_s(x,t)}{\partial x} = -\frac{3\varepsilon_s}{R_p}F j_n(x,t)$
Electrode kinetics [I,II]	$j_n(x,t) = \frac{i_0(x,t)}{F}\left[exp\left(\frac{\alpha_a\,F\,\eta(x,t)}{RT}\right) - exp\left(-\frac{\alpha_c\,F\,\eta(x,t)}{RT}\right)\right]\cdot d_i^*$
	$d_{anode}^* = 1 + \left(\frac{c_{s,lim}}{c_{ss}}\right)\cdot exp\left(\frac{\alpha_a\,F}{RT}\right)$
	$d_{cathode}^* = 1 + \left(\frac{c_{l,lim}}{c_l} + \frac{c_{s,lim}}{c_{s,max}-c_{ss}}\right)\cdot exp\left(\frac{\alpha_c\,F}{RT}\right)$
	$\eta(x,t) = \Phi_s(x,t) - \Phi_l(x,t) - E_{eq}(x,t) - j_n(x,t)FR_f$
	$i_0(x,t) = F\,k\,(c_{s,max}-c_{ss}(x,t))^{\alpha_c}\,(c_{ss}(x,t))^{\alpha_a}\,(c_l(x,t))^{\alpha_a}$

2D electrical model	
	$\nabla = (\frac{\partial}{\partial x'}, \frac{\partial}{\partial y'})^{\mathrm{T}} \qquad \boldsymbol{\sigma} = \begin{bmatrix} \sigma_{cc,x'} & 0 \\ 0 & \sigma_{cc,y'} \end{bmatrix}$
Charge Balance	$I = \sum_i i_{p2D,i}\cdot A_i$
Potentials	$\boldsymbol{\sigma}_{cc}\nabla^2\boldsymbol{\varphi}_{cc} = \pm^{**}\frac{i_{p2D}}{L_{cc}}$

[I] Ref.[6]   [II] Ref.[7]   [III] Ref.[12]

$x^* = L_{neg} + L_{sep} + L_{pos} \qquad x^{**} = x \in [0, L_{neg}] \wedge [L_{neg}+L_{sep}, L_{neg}+L_{sep}+L_{pos}]$

** < 0 for cc,- and > 0 cc,+

Table 2: Properties of the electrolyte

Electrolyte	1 M LiPF$_6$ in PC/EC/DMC
Salt diffusivity D_l [I] / m^{2}s^{-1}	$3.729E-9 \cdot exp\left(\frac{-1.557E3}{T}\right)$
Ionic conductivity κ_l [I] / S m^{-1}	$4.7557E2 \cdot exp\left(\frac{-5.725E2}{T}\right) \cdot \left(\frac{c_l}{1.173E4 \cdot exp\left(\frac{-5.725E2}{T}\right)}\right)^{0.73} \cdot exp\left(-\left(-5.0646E-4 \cdot c_l + \frac{1.25E2}{2.2879E2 + 5.0051E-3 \cdot c_l - T} + \frac{c_l}{1.173E4 \cdot exp\left(\frac{-5.725E2}{T}\right)}\right)\right)$
Activity $\frac{d\ln f_{\pm}}{d\ln c_l}$ [I] / -	$\left(6.01E-1 - 7.5895E-3 \cdot c_l^{0.5} + 2.4174E-3 \cdot exp\left(\frac{-3.3972E3}{1.0732E3-T}\right) c_l^{1.5}\right) \cdot (1-t_+^0)^{-1} - 1$
Transference t_+^0 [I] / -	0.38
Ref. concentration c_{ref} [I] / mol m^{-3}	1000

[I] modified from Ref.[13] according to Ref.[7]

Table 3: Parameterization of the single-layered, graphite/NMC-111 pouch-type LIB (i.e. P1-type)

Geometry	Graphite (C)	Separator	NMC-111
Thickness L	$67\,\mu m$ [m]	$25\,\mu m$ [m]	$79\,\mu m$ [m]
Particle radius R_p	$11\,\mu m$ [I,D50]		$7\,\mu m$ [II,D50]
Active material fraction ε_s	0.464 [II]		0.364 [II]
Inactive fraction $\varepsilon_{s,na}$	0.023 [II]		0.149 [II]
Porosity ε_l	0.513 [II]	0.5 [II]	0.487 [II]
Bruggeman coefficient β [IV,*]	1.8 [II]	1.8 [II]	1.1 [II]
Thermodynamics			
Equilibrium potential E_{eq}	Ref. [7]		Ref. [7]
Stoichiometry 100% SoC	0.766		0.425
0% SoC	0.0021		0.915
Max. concentration $c_{s,max}$	$29\,862\,mol\,m^{-3}$ [II]		$49\,242\,mol\,m^{-3}$ [II]
Lim. concentration $c_{s,lim}$	$1{\times}10^{-4}\,mol\,m^{-3}$ [II]		$1{\times}10^{-4}\,mol\,m^{-3}$ [II]
Lim. concentration $c_{l,lim}$	$1\,mol\,m^{-3}$ [II]		$1\,mol\,m^{-3}$ [II]
Transport			
Solid diffusivity D_s	Ref. [7]		Ref. [7]
Solid conductivity σ_s	$100\,S\,m^{-1}$ [I,II]		$10\,S\,m^{-1}$ [II]
Film resistance R_f	$0.0035\,\Omega\,m^2$ [III]		$0\,\Omega\,m^2$ [e]
Kinetics			
Reaction rate constant k	$2{\times}10^{-11}\,m\,s^{-1}$ [II]		$2{\times}10^{-11}\,m\,s^{-1}$ [II]
Transfer coefficient $\alpha_{a/c}$	0.5 [e]		0.5 [e]
Current collectors	**Copper**		**Aluminum**
Thickness L / νm	14		18
Height H / mm	54.5		56
Length W / mm	30		31
Conductivity σ_{cc} / $S\,m^{-1}$	$\dfrac{5.96{\cdot}10^7}{1+3.383{\cdot}10^{-3}(T-293.15\text{к})}$ [V]		$\dfrac{3.78{\cdot}10^7}{1+4.290{\cdot}10^{-3}(T-293.15\text{к})}$ [VI]

[I] Ref. [3]   [II] Ref. [7]   [III] Ref. [9]   [IV] Ref. [14]   [V] Ref. [15]   [VI] Ref. [16]

m = measured   e = estimated

* Effective transport correction according to Bruggeman (Ref. [14]): $\Psi_{eff} = \varepsilon^{\beta} \cdot \Psi_0$

Acknowledgement

Appendix

Table 4: Nomenclature

Latin symbols		
C_p	$\mathrm{J\,K^{-1}}$	Heat capacity
C_0	Ah	Initial capacity at 0.5C CC discharge
C_{sc}	Ah	Discharged capacity after the ESC test
d	m	Diameter of nail (i.e. stainless steel needle)
E_{eq}	V	Equilibrium potential vs. Li/Li$^+$
E_{sc}	V	Terminal voltage
$E_{sc,end}$	V	Terminal voltage after the short-circuit test
F	$96\,485\,\mathrm{As\,mol^{-1}}$	Faraday's constant
I_{sc}	A	Current flux during short-circuit scenario
$I_{LSC,est}$	A	Estimated current flux for LSC test
I_{max}	A	Maximum current flux for ESC test
m	kg	Mass of cell
R	$8.314\,\mathrm{J\,mol^{-1}\,K^{-1}}$	Gas constant
R_{ext}	Ω	External resistance for ESC test
$R_{i,0}$	Ω	Initial impedance from EIS measurement
$R_{i,sc}$	Ω	Final impedance from EIS measurement after the short-circuit test
$R_{LSC,est}$	Ω	Estimated shorting resistance of LSC test
$\dot{Q}_{tot}^*$	W	Uncorrected heat generation rate
$\dot{Q}_{tot}$	W	Calorimetric-corrected heat generation rate
Q_{tot}^*	W	Uncorrected total amount of heat
Q_{tot}	W	Calorimetric-corrected total amount of heat
t	s	Time
T	K	Temperature
Greek symbols		
Φ_{sc}	V	Electrical potential between the penetration site vs. the cell's negative tab

References

(1) Rheinfeld, A.; Noel, A.; Wilhelm, J.; Kriston, A.; Pfrang, A.; Jossen, A. *Journal of The Electrochemical Society* **2018**, *165*, A3427–A3448.

(2) Erhard, S. V.; Osswald, P. J.; Wilhelm, J.; Rheinfeld, A.; Kosch, S.; Jossen, A. *Journal of The Electrochemical Society* **2015**, *162*, A2707–A2719.

(3) Erhard, S. V. et al. *Journal of The Electrochemical Society* **2017**, *164*, A6324–A6333.

(4) Rieger, B.; Erhard, S. V.; Kosch, S.; Venator, M.; Rheinfeld, A.; Jossen, A. *Journal of The Electrochemical Society* **2016**, *163*, A3099–A3110.

(5) Sturm, J.; Rheinfeld, A.; Zilberman, I.; Spingler, F. B.; Kosch, S.; Frie, F.; Jossen, A. *Journal of Power Sources* **2019**, *412*, 204–223.

(6) Doyle, M.; Fuller, T. F.; Newman, J. *Journal of The Electrochemical Society* **1993**, *140*, 1526–1533.

(7) Rheinfeld, A.; Sturm, J.; Noel, A.; Wilhelm, J.; Kriston, A.; Pfrang, A.; Jossen, A. *Journal of The Electrochemical Society* **2019**, *166*, A151–A177.

(8) Rheinfeld, A. *PhD-Thesis, Technical University of Munich, Department of Electrical and Computer Engineering, Institute for Electrical Energy Storage Technology* **2019**, *2019*.

(9) Mao, J.; Tiedemann, W.; Newman, J. *ECS Transactions* **2014**, *58*, 71–81.

(10) Sturm, J.; Rheinfeld, A.; Jossen, A. *14th Symposium on Fuel Cell and Battery Modelling and Experimental Validation* **2017**,

(11) COMSOL Multiphysics, *COMSOL Multiphysics Application Galerie* **2018**,

(12) Bernardi, D. *Journal of The Electrochemical Society* **1985**, *132*, 5.

(13) Valoen, O. V.; Reimers, J. N. *Journal of The Electrochemical Society* **2005**, *152*, A882–A891.

(14) Bruggeman, D. A. G. *Ann. Phys.* **1935**, *24*, 636–664.

(15) Wolff, F. A.; Dellinger, J. H. *Proceeding of the American Institute of Electrial Engineers* **1910**, *29*, 1981–2008.

(16) Giancoli, D. G. *Physics: Principles with Application*, 4th ed.; Prentice Hall College Div, 1995.